Koordinationspolymere aus 3d-Übergangsmetallhalogeniden mit Cyanopyridinen: Synthese, Analytik und Kristallstrukturbestimmung aus Röntgenpulverdaten

Dissertation
zur Erlangung des Doktorgrades
der Naturwissenschaften

vorgelegt beim Fachbereich Biochemie, Chemie und Pharmazie der
Johann Wolfgang Goethe-Universität
in Frankfurt am Main

von
Miriam Heine
aus Korbach

Frankfurt 2021
(D30)

vom Fachbereich Biochemie, Chemie und Pharmazie der
Johann Wolfgang Goethe-Universität als Dissertation angenommen.

Dekan: Prof. Dr. Clemens Glaubitz

1. Gutachter: Prof. Dr. Martin U. Schmidt

2. Gutachter: Prof. Dr. Ullrich Englert

Datum der Disputation: 21. 07. 2021

Für Oma

meine Eltern, Julian und Opa (†).

Inhaltsverzeichnis

Danksagung

Herzlichen Dank an alle, die mich in meiner Promotionsphase unterstützt und gefördert haben! Mein besonderer Dank gilt namentlich unter anderem:

Prof. Dr. Martin U. Schmidt für die Möglichkeit, mich dem Arbeitskreis anzuschließen sowie für die Betreuung und hilfreichen Gespräche sowie

Prof. Dr. Ullrich Englert für die Übernahme des Zweitgutachtens.

Abkürzungsverzeichnis

B	Auslenkungsparameter
CCDC	**C**ambridge **C**rystallographic **D**ata **C**entre
Cif	**C**rystallographic **I**nformation **F**ile
CSD	**C**ambridge **S**tructural **D**atabase
DSC	**D**ifferential **S**canning **C**alorimetry
DTA	**D**ifferenz-**T**hermo**a**nalyse
ESI	**E**lectronic **S**upplementary **I**nformation / Zusatzmaterial einer Publikation
GOF	**G**oodness **o**f **F**it
HT	**H**och**t**emperatur-
ICCD	**I**nternational **C**entre for **D**iffraction **D**ata
IR	**I**nfra**r**ot-Spektroskopie
M	**M**etall(atom)
X	Halogen(atom)
PSD	**P**osition **s**ensitive **d**etector
R_{exp}	***R*****exp***ected* (erwarteter *R*-Wert)
R_{exp}'	***R*****exp***ected***'** (erwarteter *R*-Wert, untergrundkorrigiert)
R_p	***R*****p***rofile* (ungewichteter Profil-*R*-Wert)
R_p'	***R*****p***rofile***'** (ungewichteter Profil-*R*-Wert, untergrundkorrigiert)
R_{wp}	***R*****w***eighted* ***p****rofile* (gewichteter Profil-*R*-Wert)
R_{wp}'	***R*****w***eighted* ***p****rofile***'** (gewichteter Profil-*R*-Wert, untergrundkorrigiert)
RG	**R**aum**g**ruppe
RT	**R**aum**t**emperatur
TG	**T**hermo**g**ravimetrie
TT	**T**ief**t**emperatur-
SCXRD	**S**ingle **C**rystal **X**-**R**ay **D**iffraction
(T-)XRPD	(**T**emperature-Dependent-) **X**-**R**ay **P**owder **D**iffraction
Z	**Z**ahl der Formeleinheiten pro Elementarzelle

Vorbemerkungen

Auf die konsequente Darstellung von chemisch korrekten Lewis-Formeln wird in dieser Arbeit zwecks Übersichtlichkeit verzichtet. Dies gilt ebenso für die Darstellung von H-Atomen, welche in den hier abgebildeten Packungsmustern für gewöhnlich ausgeblendet werden. In den Abbildungen von Packungsmustern gilt folgender Farbencode:

Element	Farbe	Element	Farbe
H	weiß	Fe	rot-orange
C	hellgrau	Co	violett
N	blau	Ni	Grün
Cl	hellgrün	Cu	braun
Br	orange	Zn	dunkelgrau/ schwarz
Mn	rosa		

Für die vorliegende Dissertationsschrift wurde ein publikationsbasiertes Verfahren genehmigt. Die eigenen Veröffentlichungen werden durch das Kürzel MHx gekennzeichnet und sind gemeinsam mit ihrem Zusatzmaterial (ESI) im Anhang A abgedruckt. Eine kurze Darstellung des Eigenanteils dieser Publikationen findet sich in Anhang D. Folgende Zuordnung wurde getroffen:

MH1

4-Cyanopyridine, a versatile mono- and bidentate ligand. Crystal structures of related coordination polymers determined by X-ray powder diffraction.

Haishuang Zhao, Alexander Bodach, Miriam Heine, Yasar Krysiak, Jürgen Glinnemann, Edith Alig, Lothar Fink, and Martin U. Schmidt, In: CrystEngComm, 2017, 19, 2216-2228.

MH2

3-Cyanopyridine as a bridging and terminal ligand in coordination polymers.

Miriam Heine, Lothar Fink and Martin U. Schmidt, In: CrystEngComm, 2018**,** 20**,** 7556-7566.

MH3

Coordination compounds built up from $M^{II}Cl_2$ and 3-cyanopyridine: double chains, single chains and isolated complexes.

Miriam Heine, Lothar Fink and Martin U. Schmidt, In: CrystEngComm, 2019, 21, 4305-4318.

MH4

4-Cyanopyridine complexes $[MX_2(4\text{-CNpy})_x]_n$ (with X = Cl, Br and x = 1, 2): crystal structures, thermal properties and a comparison with $[MX_2(3\text{-CNpy})_x]_n$ complexes.

Miriam Heine, Lothar Fink and Martin U. Schmidt, In: CrystEngComm, 2020, 22, 2067-2082.

1. Einleitung

Die Synthese und Charakterisierung neuartiger metallorganischer Koordinationsverbindungen erlebt seit etlichen Jahren Hochkonjunktur. Oftmals wird in der Materialentwicklung der Ansatz eines „rationalen Designs“ verfolgt, d.h. der gezielten Darstellung von Verbindungen mit vordefinierten physikalischen oder chemischen Eigenschaften [26, 27]. Damit eng verbunden und inzwischen unumgänglich ist das Konzept des „*Crystal Engineerings*“, gemäß welchem ein umfassendes Verständnis von in kristallinen Festkörpern auftretenden Wechselwirkungen und Struktur-Eigenschafts-Beziehungen anzustreben ist [14, 15]. Dieses Konzept soll als Grundlage für die Entwicklung neuer Festkörperstrukturen mit entsprechend gewünschten physikalischen oder chemischen Eigenschaften dienen.

> „Crystal engineering is the understanding of intermolecular interactions in the context of crystal packing and in the utilisation of such understanding in the design of new solids with desired physical and chemical properties.” [14]

Seit geraumer Zeit setzen Forschung und Entwicklung dabei auf metallorganische Polymer- bzw. Gerüstverbindungen [26, 27]. Die Strukturvielfalt solcher Verbindungen ist beträchtlich, sodass die *International Union of Pure and Applied Chemistry* (IUPAC) seit 2013 folgende hierarchische Terminologie empfiehlt [4]:

a) **Koordinationspolymere**: Koordinationsverbindungen mit sich wiederholenden Einheiten, welche sich in ein, zwei oder drei Dimensionen erstrecken können.
b) **Koordinationsnetzwerke**: Koordinationsverbindungen mit sich wiederholenden Einheiten, die sich in einer Dimension erstrecken und Quervernetzungen zwischen den Ketten aufweisen. Koordinationsnetzwerke sind also eine Unterklasse von Koordinationspolymeren.
c) **Metal-Organic-Framework (MOF)**: Koordinationsnetzwerke mit potentiell nutzbaren Lücken, die zum Beispiel als Katalysatoren, Trennungsmedium oder (Gas-)Speichermaterial eingesetzt werden. MOFs sind also wiederum eine Untergruppe von Koordinationsnetzwerken.

Neben den unzähligen Arbeiten zu MOFs häufen sich in letzter Zeit Publikationen, die sich mit der Synthese von magnetischen Koordinationspolymeren beschäftigen. Dabei werden meist Übergangsmetallkationen wie Mangan, Eisen, Cobalt oder Nickel

eingesetzt, die bei Vorliegen bestimmter Elektronenkonfigurationen interessante magnetische Phänomene hervorzurufen vermögen [33]. An dieser Stelle sei ausdrücklich darauf hingewiesen, dass die magnetischen Eigenschaften von Koordinationspolymeren im Folgenden nicht weiter beachtet werden.

In der vorliegenden Arbeit werden ausschließlich Koordinationspolymere bzw. Koordinationsnetzwerke thematisiert, welche aus Halogeniden zweiwertiger 3d-Übergangsmetalle (bspw. $MnCl_2$ oder $FeBr_2$) und Pyridin bzw. Pyridinderivaten aufgebaut sind (vgl. Abb. 2.3 in Kapitel 2). Sie verfolgt das Ziel, Strukturtopologien in Abhängigkeit des Metalltyps, der Stöchiometrie und der Koordinationsmöglichkeiten des organischen Liganden zu ergründen. Da die Zielverbindungen in der Regel als mikrokristalline Pulver anfallen, ist die Strukturbestimmung aus Röntgenpulverbeugungsdaten substanzieller Bestandteil dieser Arbeit und nimmt einen dementsprechend großen Raum ein.

2. Stand der Forschung und Fragestellungen dieser Arbeit

Die ersten Untersuchungen des Arbeitskreises Schmidt konzentrierten sich auf die umfassende Darstellung und Strukturbestimmung von Koordinationspolymeren auf Basis von $CuCl_2$ oder $NiCl_2$ mit Pyridin (py) [1, 28]. Die stöchiometrische Zusammensetzung der Koordinationsverbindungen kann über die gezielte Entfernung von Pyridin, dem sog. thermischen Abbau, gesteuert und mittels Röntgenpulverbeugung (engl. *X-Ray Powder Diffraction*, XRPD) untersucht werden. Auf diese Weise wurden Koordinationspolymere mit unterschiedlichen Kettenmotiven erhalten (Refcodes[1] der CSD: PYNICL01 [1], QQQDDA02 [28], UWEBAB [28]), wie nachfolgend exemplarisch an der $[NiCl_2(py)_x]_n$-Serie illustriert sei (Abb. 2.1). Grundsätzlich ist zu konstatieren, dass: je niedriger der Pyridin-Gehalt des Koordinationspolymers, desto „bandartiger" die durch verbrückendende Cl-Atome entstehende Polymerkette. Die Bildung von Koordinationsnetzwerken, also miteinander vernetzen Ketten (vgl. Definition nach [4] in Kapitel 1), wurde bei dieser Serie nicht beobachtet, da Pyridin grundsätzlich als monodentater Ligand fungiert und somit keine Quervernetzungen zu generieren vermag.

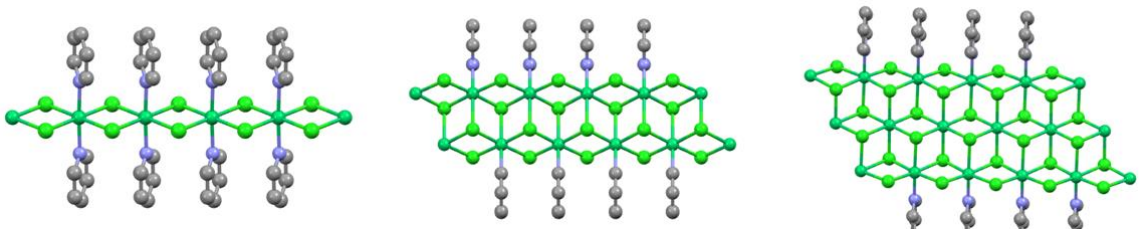

$[NiCl_2(py)_2]_n$ $[NiCl_2(py)_1]_n$ $[NiCl_2(py)_{2/3}]_n$

(a) (b) (c)

Abbildung 2.1: Kettenmotive in $[NiCl_2(py)_x]_n$-Polymeren. (a) Einzelketten bei x = 2, (b) Doppelketten bei x = 1, (c) Dreifachketten bei x = $^2/_3$.

[1] Die *Crystal Structure Database* (CSD) ist eine Datenbank für Kristallstrukturen (metall-)organischer Verbindungen. Jeder CSD-Eintrag wird über einen eindeutigen Refcode identifiziert, der für jede Verbindung aus 6 Buchstaben besteht. Bei polymorphen oder mehrfach bestimmten Phasen sind zusätzlich zwei Zahlen angehängt.

Um Koordinationspolymere in Koordinationsnetzwerke überführen zu können, muss der organische Ligand Pyridin folglich mit einer weiteren Donorfunktion ausgestattet werden. Deshalb wurde in weiterführenden Arbeiten des Arbeitskreises zunächst 4-Cyanopyridin (4-CNpy) als Ligand ausgewählt. Dieser kann neben dem Pyridinstickstoff (N_{py}) auch über den Cyanostickstoff (N_{CN}) eine koordinative Bindung eingehen und dadurch als bidentater Ligand Metallatome verbrücken. Dem HSAB-Prinzip (eng. *Principle of Hard and Soft Acids and Bases* [33]) folgend, bindet N_{py} bevorzugt an das Metallkation, sodass Quervernetzungen erst durch verbrückenden N_{CN} entstehen.

Erste Untersuchungen des Koordinationsverhaltens von 4-CNpy wurden mit $MnCl_2$ und $CuCl_2$ sowie erstmals $NiCl_2$ durchgeführt [MH1], da die Koordinationspolymere $[MnCl_2(4\text{-}CNpy)_2]_n$ bzw. $[CuCl_2(4\text{-}CNpy)_2]_n$ bereits literaturbekannt waren (NESYOZ, NESYUF [47]). In allen drei Kristallstrukturen $[MCl_2(4\text{-}CNpy)_2]_n$ mit M = Mn, Ni und Cu liegen Einfachketten vor (Abb. 2.2a), ähnlich dem in Abb. 2.1a dargestellten Kettenmotiv:

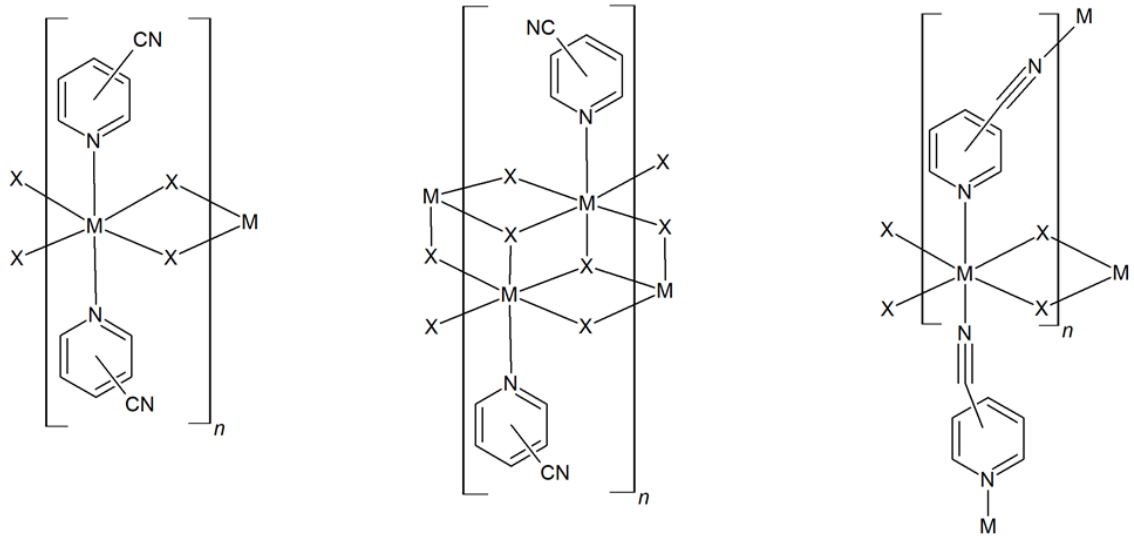

$[MX_2(CNpy)_2]_n$ $[MX_2(CNpy)_1]_n$ $[MX_2(CNpy)_1]_n$

(a) (b) (c)

Abbildung 2.2: Strukturmotive in Verbindungen des Typs $[MX_2(CNpy)_2]_n$ und $[MX_2(CNpy)_1]_n$. (a) Einzelkette, (b) Doppelkette, (c) Netzwerk mit verbrückendem CNpy. CNpy = 3-Cyanopyridin oder 4-Cyanopyridin.

Die Synthese von $[MCl_2(4\text{-}CNpy)_x]_n$ wurde über Abbaureaktionen der Ausgangsverbindungen $[MCl_2(4\text{-}CNpy)_2]_n$, auch als „Precursoren“ bezeichnet, gesteuert (siehe Kapitel 3.1). Ob 4-CNpy neben N_{py} auch mit N_{CN} an ein Metallatom koordiniert, kann über Beobachtung der asymmetrischen Valenzschwingung $\nu(N_{CN})$ im IR-Spektrum ermittelt werden (siehe Kapitel 3.3). Für $[CuCl_2(4\text{-}CNpy)_1]_n$ wurden zwei polymorphe Strukturen gefunden (UWEBEF, UWEBEF01 [28]). Beide Polymorphe zeigen das Doppelkettenmotiv, wie es bereits aus den Kristallstrukturen der Pyridin-Analoga $[CuCl_2(py)_1]_n$ und $[NiCl_2(py)_1]_n$ bekannt ist (vgl. Abb. 2.1b und Abb. 2.2b). Im Falle von $[MnCl_2(4\text{-}CNpy)_1]_n$ wurde erstmals die Bildung einer Netzstruktur beobachtet (CIRTIJ [MH1]), in der 4-CNpy tatsächlich als bidentater bzw. verbrückender Ligand in Erscheinung tritt. 4-CNpy koordiniert mit seinen beiden N-Atomen an zwei verschiedene Mn-Atome, wodurch die polymeren Ketten des Precursors zu einem Koordinationsnetzwerk verknüpft werden (Abb. 2.2c).

Dieser Befund wirft unter anderem folgende Fragen auf:

- Wie verhält es sich mit den übrigen Übergangsmetallen der vierten Periode, d.h. insbesondere Fe, Co, Ni und Zn? Welche Strukturtopolgie(n) ist (sind) für $[MCl_2(4\text{-}CNpy)_2]_n$ zu erwarten?
- Was geschieht, wenn MBr_2 als Edukt eingesetzt wird? Bestehen $[MBr_2(4\text{-}CNpy)_2]_n$-Verbindungen ebenfalls aus Polymerketten? Oder wird womöglich ein anderes Strukturmotiv, bspw. Dimere wie in $[Cu_2I_4(3\text{-}CNpy)_4]_n$ (IYUXIJ [25]) oder Trimere ausgebildet? Wie verhält es sich bei den Abbaustufen $[MBr_2(4\text{-}CNpy)_1]_n$?
- Was geschieht bei Verwendung eines trifunktionalen Liganden, z. Bsp. Dicyanopyridin? Sind mit diesem Pyridinderivat gar Gerüststrukturen, also MOFs, herstellbar?
- Wie weit können $[MCl_2(4\text{-}CNpy)_2]_n$ bzw. grundsätzlich $[MX_2(CNpy)_2]_n$ thermisch abgebaut werden? Sind (stabile) Abbaustufen mit $x \leq {}^2/_3$, also bspw. $[MCl_2(4\text{-}CNpy)_{1/2}]_n$ oder $[MCl_2(4\text{-}CNpy)_{1/4}]_n$, realisierbar? Bilden diese Verbindungen Ketten/ Bänder oder Netze? Oder entstehen sogar Gerüststrukturen (MOFs)?

Zu Klärung dieser Fragen stützt sich diese Arbeit auf folgenden „Fahrplan“:

1. Komplettierung der begonnenen Serie mit 4-CNpy: Umsetzung von $FeCl_2$, $CoCl_2$ sowie $NiCl_2$ mit 4-CNpy und anschließendem thermischen Abbau.
2. Umsetzung von MBr_2 (M = Mn, Fe, Co, Ni, Cu, Zn) mit 4-CNpy und anschließendem thermischen Abbau. Vergleich mit den Analoga der MCl_2-Serie.
3. Umsetzung von MCl_2 und MBr_2 mit 3-CNpy und anschließendem thermischen Abbau. Vergleich mit den Analoga der 4-CNpy-Serien.
4. Umsetzung von $NiCl_2$ mit einem trifunktionalen Liganden und anschließendem thermischen Abbau. Vergleich mit den Analoga der 3-CNpy und 4-CNpy-Serien. Wegen seiner Molekülsymmetrie und leichten Verfügbarkeit wird 3,5-CNpy als Ligand eingesetzt.

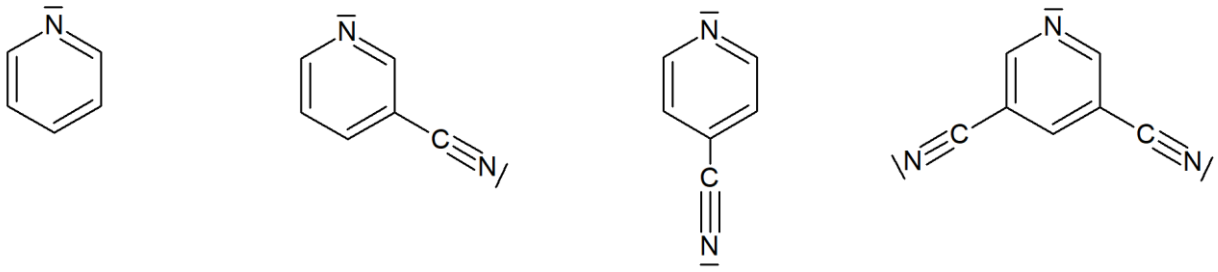

Pyridin	3-Cyanopyridin	4-Cyanopyridin	3,5-Dicyanopyridin
py	3-CNpy	4-CNpy	3,5-CNpy

Abbildung 2.3: Strukturformeln und Abkürzungsweise der eingesetzten Pyridin-Verbindungen. Mit CNpy ist 3- oder 4-Cyanopyridin gemeint.

Die Vorgehensweise zur Darstellung dieser Zielverbindungen wird in Kapitel 3.1 skizziert, wobei die Verbindungen grundsätzlich reihenweise dargestellt wurden. So wurden bspw. innerhalb der $[MnBr_2(3\text{-CNpy})_x]_{(n)}$-Abbaureihe die Verbindungen mit x = 4, 2 und 1 erhalten. Da die Zielverbindungen als mikrokristalline Pulver anfielen, erfolgte die Bestimmung ihrer Kristallstrukturen auf Basis von Röntgenpulverdaten (Kapitel 3.2). Für einige Abbaureihen waren Verbindungen herzustellen, deren Kristallstrukturen bereits aus Röntgeneinkristalldaten (engl. *Single-Crystal X-Ray Diffraction*, SCXRD) oder aus bei Nicht-Standardbedingungen aufgenommenen

Pulverdaten bekannt waren. In allen Fällen wurden die Kristallstrukturbestimmungen an einem (ggf. dann unter Standardbedingungen aufgenommenen) Pulverdatensatz wiederholt und die Ergebnisse an die *Crystal Structure Database* (CSD) zur Vervollständigung ihrer Datenlage übermittelt. Diese Strukturen sind an den entsprechenden Stellen im Text sowie in den Tabellen mit kristallographischen Daten (Kapitel 4 bzw. Publikationen MH1-4) gesondert ausgewiesen.

Die Ergebnisse dieser Promotionsarbeit werden in Form einer kumulativen Dissertation zusammengestellt und diskutiert (Kapitel 4), wobei die Kristallstrukturen in Reihen bzw. Serien gebündelt werden. So bilden bspw. $[MnBr_2(3\text{-}CNpy)_4]$, $[MnBr_2(3\text{-}CNpy)_2]_n$ und $[MnBr_2(3\text{-}CNpy)_1]_n$ eine (Abbau-)Reihe, bzw. $[MnBr_2(3\text{-}CNpy)_4]$, $[FeBr_2(3\text{-}CNpy)_4]$, $[CoBr_2(3\text{-}CNpy)_4]$ und $[NiBr_2(3\text{-}CNpy)_4]$ eine Serie.

3. Methoden

3.1 Kristallisationsexperimente und thermische Methoden (DTA-TG)

Die Darstellung der Koordinationsverbindungen mit Cyanopyridin erfolgte in erster Linie über gewöhnliche Kristallisationsexperimente in alkoholischer Lösung. Dabei wurden Metallsalz und organischer Ligand zunächst separat, aber in dasselbe Lösungsmedium eingebracht. Die Lösungen wurden anschließend vorsichtig und unter verschiedenen, dem Experiment angepassten Bedingungen, vereint. Auf diese Weise fielen in der Regel Reinphasen mit einem Metallsalz-zu-Ligand-Verhältnis von 1:2, also $[MX_2(CNpy)_2]_{(n)}$, an. Grundsätzlich ist diese Vorgehensweise zweifelsohne komfortabel, birgt jedoch für die Darstellung neuer Phasen unerwünschte Eventualitäten. Dazu zählen u. a. die Bildung von Solvaten oder die gleichzeitige Ausfällung von Phasen mit unterschiedlicher Stöchiometrie, also bspw. $[MX_2(CNpy)_2]_{(n)}$ und $[MX_2(CNpy)_1]_{(n)}$. Darüber hinaus besteht die Gefahr, thermodynamisch metastabile Phasen zu „verpassen“.

Eine Alternative und sinnvolle Ergänzung zur Synthese aus Lösung stellen thermische Abbaureaktionen dar [33]. Dabei werden die durch Lösungskristallisation erhaltenen Precursoren systematisch erhitzt („getempert“), was in der Regel zu einer stufenweisen und irreversiblen Abgabe eines Teils der Liganden führt, also bspw. von $[MX_2(CNpy)_2]_n$ zu $[MX_2(CNpy)_1]_n$. Auf diese Weise können die Abbauphasen in quantitativer Ausbeute und mit hoher Reinheit erhalten werden. Im Rahmen der vorliegenden Arbeit hat sich schlussendlich folgende Kombination der beiden Synthesevarianten bewährt: zunächst die Darstellung der ligandenreichsten Verbindung durch Lösungskristallisation und anschließend thermischer Abbau dieser Verbindung bis zur gewünschten Zielphase.

Thermische Abbaureaktionen wurden wahlweise in einem DTA-TG-Gerät (hier TGA 92 von SETARAM Instrumentation) oder *in-situ,* d.h. während des laufenden Röntgenbeugungsexperimentes auf dem Pulverdiffraktometer durchgeführt (siehe Kapitel 3.2.3). Die Differential-Thermoanalyse-Messung (DTA) untersucht das thermische Verhalten einer Probe als Funktion der Temperatur. Dazu werden die üblicherweise feste Probe (in einem Tiegel) und eine Referenzsubstanz (in einem anderen Tiegel) gleichzeitig erhitzt. Die Temperaturänderung der Referenzprobe ist konstant, während sich die der Probe aufgrund endothermer oder exothermer

Prozesse ändern kann. Die Temperaturdifferenz ΔT zwischen Probe und Referenzsubstanz wird als Funktion der Zeit aufgetragen (DTA-Kurve). Die Thermogravimetrische Analyse (TG) bestimmt die Gewichtsänderung einer Probe als Funktion der Temperatur oder auch Zeit, wobei jeder Gewichtsverlust der Probe als Stufe sichtbar ist (TG-Kurve). Die TG-Stufen ermöglichen eine quantitative Beschreibung der Änderung der Probenzusammensetzung. Im Falle der hier thematisierten Koordinationsverbindungen kann die Betrachtung aller TG-Stufen Aufschluss über Abbaureaktionen bzw. – mit Bedacht formuliert – theoretisch realisierbarer Abbaustufen des Precursors liefern. In Abb. 3.1 und Tab. 3.1 sind exemplarisch eine DTA-TG-Aufnahme mit Auswertungsschema der $[MnBr_2(3\text{-}CNpy)_4]$-Reihe abgebildet [MH2]. $[MnBr_2(3\text{-}CNpy)_4]$ wurde über eine Lösungskristallisation synthetisiert und die beiden Abbauphasen $[MnBr_2(3\text{-}CNpy)_2]_n$ bzw. $[MnBr_2(3\text{-}CNpy)_1]_n$ durch thermischen Abbau von $[MnBr_2(3\text{-}CNpy)_4]$ erhalten.

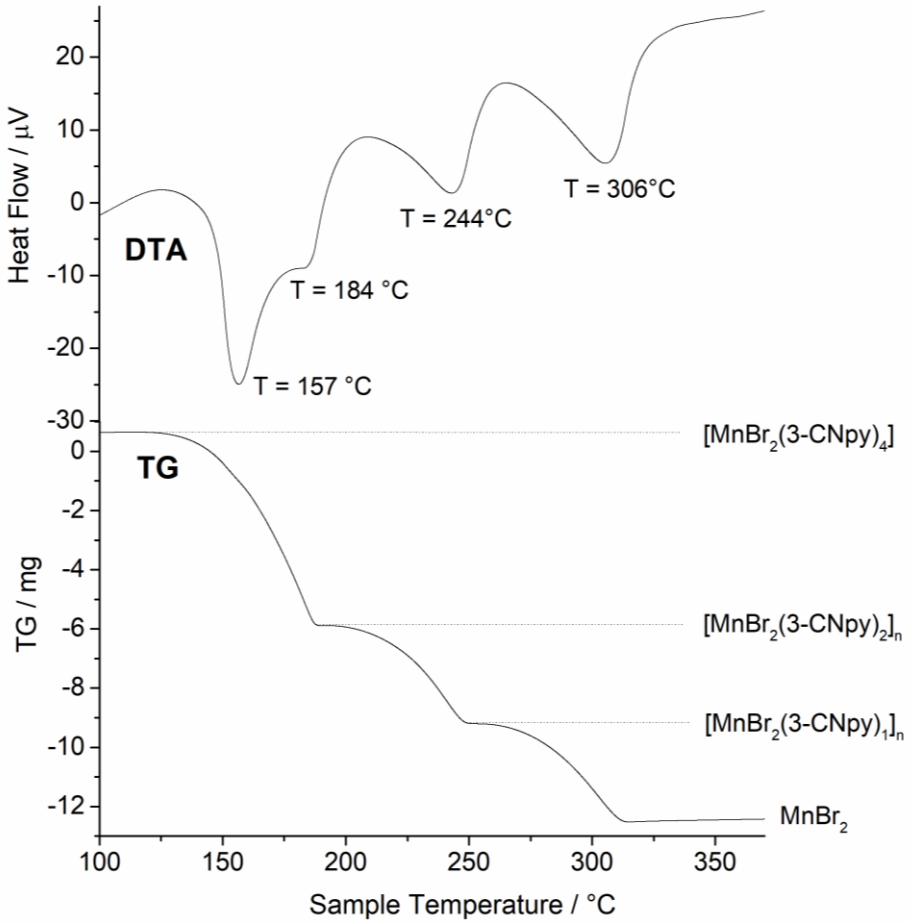

Abbildung 3.1: DTA-TG-Aufnahme von $[MnBr_2(3\text{-}CNpy)_4]$. Stufenweise Abgabe von 3-CNpy mit Angabe der jeweiligen DTA-Peaktemperaturen (T); Schutzgas: Ar, Heizrate: 5 °C/ min.

Tabelle 3.1: Auswertung der DTA-TG-Aufnahme von [$MnBr_2$(3-CNpy)$_4$] aus Abb. 3.1. *T*: DTA-Peaktemperatur(en), m_0: Einwaage der Startverbindung, Δm_{exp}: Masseverlust (absolut), $\Delta m_{exp}/m_0$: experimenteller Masseverlust (relativ), $\Delta m_{cal}/m_0$: theoretischer Masseverlust (relativ).

Verbindung	***T*** **[°C]**	m_0 **[mg]**	Δm_{exp} **[mg]**	$\Delta m_{exp}/m_0$ **[%]**	$\Delta m_{cal}/m_0$ **[%]**
[$MnBr_2$(3-CNpy)$_4$]		20,72	0	0	0
[$MnBr_2$(3-CNpy)$_2$]$_n$	157/ 184		6,54	31,54	32,99
[$MnBr_2$(3-CNpy)$_1$]$_n$	244		3,32	26,97	24,61
$MnBr_2$	306		3,30	30,43	32,66

In dem o.g. DTA-TG-Gerät erfolgten beiden Messungen gleichzeitig, sodass die Kombination ihrer jeweiligen Ergebnisse zu folgenden Erkenntnissen führte:

- endothermes oder exothermes Ereignis, aber kein Gewichtsverlust:
  → Phasenumwandlung der Probe; also Experiment auf dem Diffraktometer wiederholen!
- endothermes oder exothermes Ereignis, und Gewichtsverlust:
  → Zersetzung oder Entfernung von anhaftendem Rest-Lösungsmittel; also Massenverlust berechnen und die Stöchiometrie der Probe vorher bzw. nachher ermitteln!

Die Messkurve der Thermogravimetrie von einer Reihe von experimentellen Parametern bestimmt. Dazu zählen Heizrate, Art und Durchflussrate des Schutzgases sowie natürlich auch die Probeneigenschaften selbst. Daher empfiehlt es sich gelegentlich, mehrere Messungen mit variierten Parametern durchzuführen, damit etwaige Messartefakte identifiziert werden können. So waren beispielsweise einige Precursor-Proben aufgrund der oben skizzierten Kristallisationsmethode noch mit etwas Restlösungsmittel (Methanol oder Ethanol) behaftet, welches in der TG-Kurve zu sichtbaren Masseverlusten im Bereich bis 100 °C geführt hat. Allerdings überlagerten sich diese indes nicht mit den eigentlich “interessanten“ Masseabnahmen der Probe ab ca. 140 °C, sodass die Auswertung dieser TG-Kurven dahingehend nicht beeinträchtigt wurde.

Für die DTA-TG-Messungen dieser Arbeit wurden ca. 20 mg der Probesubstanz in einen Tiegel aus α-Al_2O_3 eingewogen und in einem konstanten Schutzgasstrom aus Ar oder N_2 von RT bis 440 °C erhitzt. Stellvertretend ist in diesem Unterkapitel eine DTA-TG-Aufnahme inklusive Auswertung von $[MnBr_2(3\text{-}CNpy)_4]$ abgebildet (Abb. 3.1 und Tab 3.1 [MH2]). In Kapitel 3.2.3 sei dann am Beispiel von $[CoCl_2(4\text{-}CNpy)_2]_n$ skizziert, wie sich die in der DTA-TG-Aufnahme beobachteten Abbaureaktionen praktisch auf dem Röntgenpulverdiffraktometer reproduzieren lassen.

3.2 Röntgenographische Methoden

Laue, Friedrich und Knipping gelang 1912 der Nachweis der Beugung von Röntgenstrahlung am Kristallgitter [29]. Das Kristallgitter wirkt als Beugungsgitter, am dem die auftreffende Röntgenstrahlung aus ihrer Strahlungsrichtung abgelenkt wird. William Laurence Bragg und William Henry Bragg erkannten schon früh, dass (kristalline) Stoffe charakteristische Beugungsmuster der von ihnen abgelenkten Röntgenstrahlung zeigen [7]. Dieses Beugungsmuster ist für jeden (kristallinen) Stoff einzigartig und kann, bildlich gesprochen, als sein Fingerabdruck verstanden werden. Da die Röntgenbeugung (nahezu) zerstörungsfrei abläuft, hat sie sich als Verfahren zur Strukturaufklärung in Forschung und Industrie etabliert.

Die Bragg-Gleichung

Bragg/ Bragg führten die Röntgenbeugung auf Reflexion an den kernnahen Bereichen der Atome einer Netzebene im Kristallgitter zurück, wobei parallele und in demselben Abstand zueinander liegende Netzebenen zu sog. Netzebenenscharen zusammengefasst werden. Die räumliche Lage einer Netzebene wird über die Miller-Indizes *h*, *k* und *l* beschrieben, welche den reziproken (und ganzzahlig gemachten) Achsabschnitten der betrachteten Netzebene entsprechen (Abb. 3.2).

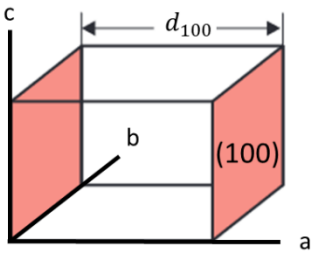

Abbildung 3.2: Indizierung der Netzebene (100) und interplanarer Abstand d_{100} in der entsprechenden Schar [nach 19].

Setzt man einen Kristall monochromatischer Röntgenstrahlung aus, dann wird diese sowohl an der Kristalloberfläche (Strahl I) als auch an Netzebenen im Kristallinneren gebeugt (Strahl II) (Abb. 3.3) Die ausfallenden Strahlen überlagern sich und sind aufgrund der verschieden zurückgelegten Strecken phasenverschoben. Ist die längere Wegstrecke (Strahl II) ein ganzzahliges Vielfaches der kürzeren (Strahl I), entsteht eine Verstärkung („konstruktive Interferenz“). Ist die Wegstrecke kein ganzzahliges Vielfaches, wird die ausfallende Röntgenstrahlung abgeschwächt oder gar ausgelöscht („destruktive Interferenz“).

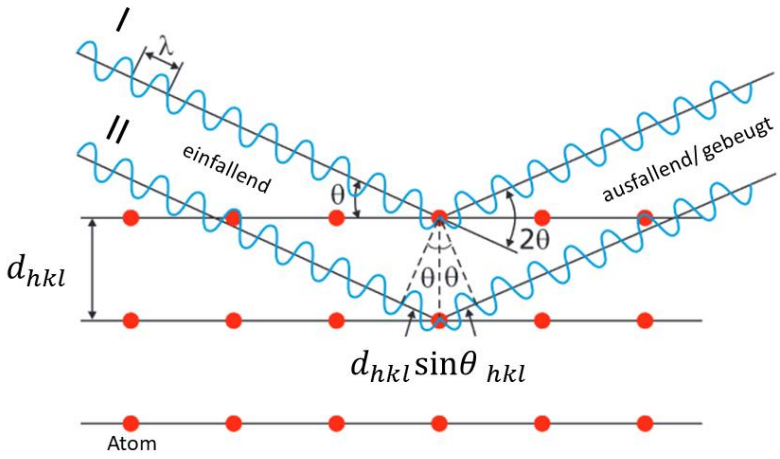

Abbildung 3.3: Beugung von Röntgenstrahlen an parallelen Netzebenen eines Kristallgitters und Ableitung der Bragg-Gleichung [nach 19].

Reflexion findet nur dann statt, wenn der Winkel (θ) zwischen einfallender Röntgenstrahlung (Primärstrahlung) und der Netzebene ganz bestimmte Werte hat. Dieser Winkel wird üblicherweise auch als Glanz- oder Bragg-Winkel bezeichnet. Seine Werte hängen vom interplanaren Ebenenabstand der betrachteten Schar (d_{hkl}) sowie der Wellenlänge der Primärstrahlung (λ) ab. Der Faktor n (n = 1, 2, …) gibt die

„Ordnung“ der Interferenz an, da $n \cdot \lambda$ die Wegdifferenz zwischen jenen Strahlen darstellt, welche an benachbarten Netzebenen gebeugt werden. Er wird typischerweise *n* = 1 gesetzt.

$$n \cdot \lambda = 2 \cdot d_{hkl} \cdot \sin\theta_{hkl} \qquad \text{(Bragg-Gleichung)}$$

Ist die Bragg-Gleichung also für eine Schar paralleler Netzebenen erfüllt, entsteht konstruktive Interferenz der ausfallenden Röntgenstrahlen. Jede Netzebenenschar einer Kristallphase erzeugt einen spezifischen Reflex, dessen Lage durch die Gitterkonstanten dieser Phase bestimmt wird und dessen Intensität vom Streuvermögen und der Position der auf dieser Netzebenenschar liegenden Atomsorte(n) abhängt. Dadurch kann in einem mehrstufigen und vielschichtigen Prozess (siehe Kapitel 3.2.1) schlussendlich die Struktur eines kristallinen Stoffes aus seinem Beugungsbild ermittelt werden.

Was ist ein Kristall?

Kristalle sind Körper, die eine dreidimensional periodische Anordnung ihrer Bausteine (Atome, Moleküle, Ionen, …) aufweisen (vgl. z. Bsp. [3]). Unter „Kristallstruktur“ versteht man die regelmäßige Verteilung der Atomkerne und Elektronen in einem Kristall. Zur Beschreibung der Struktur wird der Kristall in Basis und (Punkt-)Gitter zerlegt. Die Basis ist der sich periodisch wiederholende, physikalische Baustein des Kristalls. Dieser wird mathematisch als Punkt erfasst, und die einzelnen Punkte wiederum über verschiedene Symmetrieoperationen zu einem (Punkt-)Gitter zusammengefasst. Erst die Überlagerung von (physikalischer) Basis und (mathematischem Punkt-)Gitter führt zu einer realen Kristallstruktur. Das (Punkt-)Gitter wird durch ein Vektortripel (z. Bsp. $\vec{a}$, $\vec{b}$ und $\vec{c}$) beschrieben, welches die sog. Elementarzelle aufspannt. Die Längen der drei Basisvektoren, also $|\vec{a}|$, $|\vec{b}|$ und $|\vec{c}|$, heißen Gitterkonstanten (wobei im Sprachgebrauch gerne auch die entsprechenden Basiswinkel *α*, *β* und *γ* als Gitterkonstanten bezeichnet werden). Durch periodische Wiederholung der Elementarzelle wird der gesamte Körper aufgebaut. Nach Bravais lassen sich alle Kristallgitter durch eines von 14 Gittern, die sog. Bravais-Gitter darstellen, die sich ihrerseits wiederum sieben Kristallsysteme zuordnen lassen (Abb. 3.4). Es gibt sieben primitive (P) Gitter, bei denen nur die Ecken des Kristallgitters

besetzt sind. Drei Gitter sind innenzentriert (I) und je zwei Gitter basisflächenzentriert (C) bzw. allseits flächenzentriert (F).

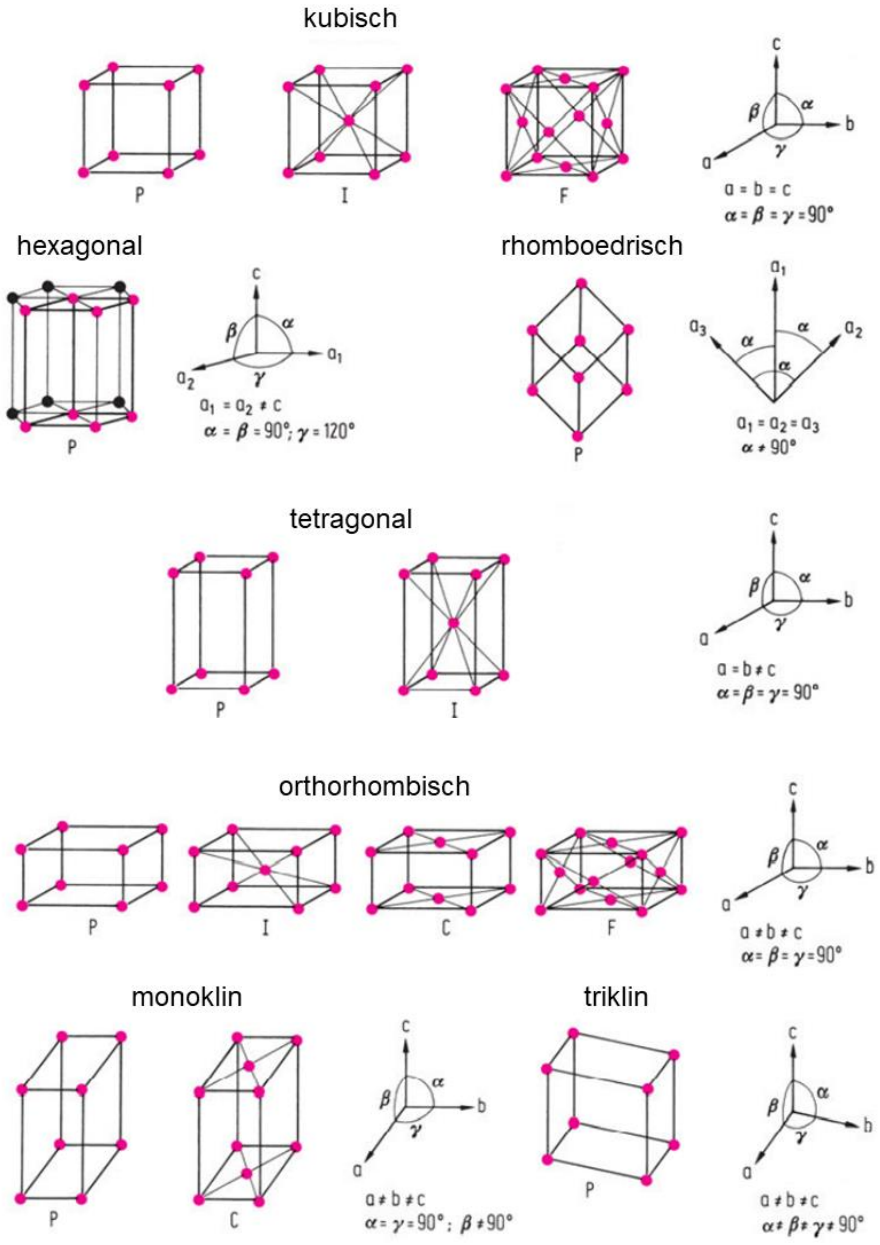

Abbildung 3.4: Graphische Darstellung der 14 Bravais-Gitter und 7 Kristallsysteme mit ihren jeweiligen Beschreibungsgrößen [nach 39].

Einkristall- und Pulverdiffraktion

Ziel der Kristallstrukturanalyse ist nun die Bestimmung der Atomlagen (*x*, *y*, *z*) und ihrer Besetzungsverteilung in einer vorgegebenen bzw. zuvor bestimmten Elementarzelle. Zu diesem Zweck müssen Strukturfaktoren (*F*) bestimmt werden, die

sich aus den im Beugungsexperiment beobachteten Intensitäten (*I*) ableiten lassen. Die Intensität eines Röntgenreflexes I_{hkl} ist proportional zu dem Quadrat des Strukturfaktors $|F_{hkl}|^2$:

$$I_{hkl} \sim |F_{hkl}|^2 \qquad \text{mit} \qquad F_{hkl} = |f_{hkl}|e^{i*\varphi_{hkl}}$$

Dadurch können die Atomlagen allerdings nicht direkt aus F_{hkl} ermittelt werden, weil die Phaseninformation φ_{hkl} der Streuwelle eben nicht direkt zugänglich ist. Dieses sog. „Phasenproblem der Kristallstrukturanalyse“ führt zu einem erheblichen Mehraufwand bei der Kristallstrukturlösung, für den in Einkristall- und Pulverdiffraktion verschiedene Lösungsansätze vorliegen. Der Atomformfaktor *f* gibt das Streuvermögen des Atoms an und ist die Fouriertransformierte der atomaren Elektronendichteverteilung. Die Atomformfaktoren sind in den „International Tables for Crystallography, Vol C“ [3] tabelliert.

Nach wie vor erfolgt die Mehrzahl der Kristallstrukurbestimmungen durch Röntgeneinkristalldiffraktion, für die Einkristalle mit hinreichender Größe (u. a. abhängig von verwendeter Röntgenquelle und Absorptionsverhalten der Probe, als Faustregel gilt mind. 1000µm^3) und Qualität notwendig sind. Allerdings stehen nicht immer geeignete Einkristalle zur Verfügung, sodass – wie in dieser Arbeit – auf die Röntgenpulverdiffraktion zurückgegriffen werden „muss“. Im Falle der Einkristallbeugung erhält man Beugungsreflexe auf Punkten im dreidimensionalen reziproken Raum, wobei jede Orientierung des Einkristalls zu einem spezifischen Beugungsbild mit spezifischen Reflexintensitäten führt. Pulverproben bestehen aus unzähligen kleinen, statistisch orientierten Kristalliten (max. 10 µm^3), die jeweils ein eigenes Beugungsbild erzeugen. Diese überlagern und bilden sich auf Kreisbögen ab, sodass bei einem „idealen“ Pulver gleichmäßige Ringe (Debye-Scherrer-Ringe) entstehen (Abb. 3.5).

Da der Informationsgehalt „idealerweise“ an jedem Punkt des Rings derselbe ist, wird schlussendlich der dreidimensionale reziproke Raum auf eine Dimension, nämlich die 2θ-Achse des Pulverdiffraktogramms, projiziert. Pulverdiffraktogramme enthalten also deutlich weniger separierte Reflexe als Einkristallaufnahmen, sodass eine Kristallstrukturanalyse aus XRPD-Daten zunächst quasi unmöglich erschien.

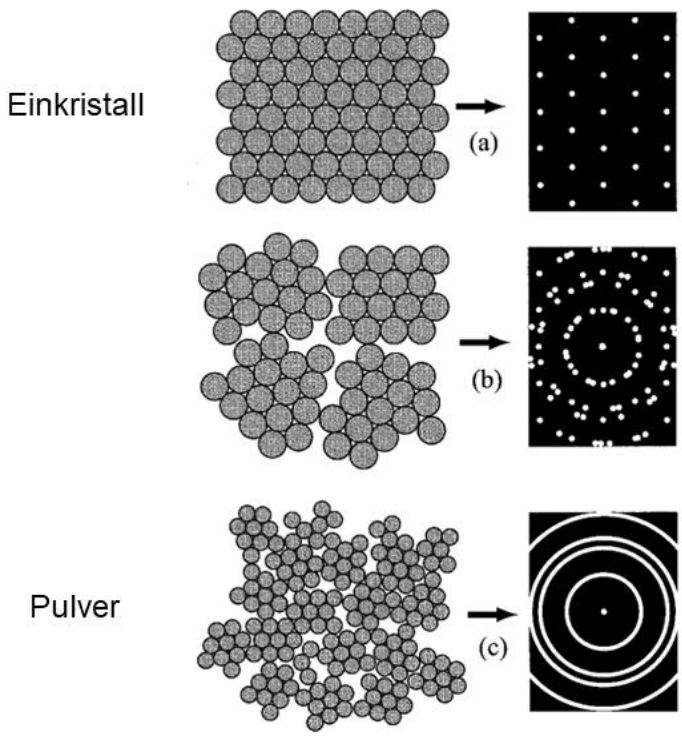

Abbildung 3.5: Zusammenhang Zahl und Orientierung der Kristallite / resultierendes Beugungsbild [nach 21].

Die Rietveld-Methode

Loopstra und Rietveld stellten 1967 und 1969 eine Methode vor, bei der ein theoretisch errechnetes bzw. simuliertes Pulverdiffraktogramm der Zielstruktur mit dem gemessenen Diffraktogramm zur Deckung gebracht werden soll [40, 41]. Ausgehend von einem dem tatsächlichen Ergebnis schon sehr nahekommenden Anfangsmodell der Kristallstruktur werden die Atomlagen des Modells so lange variiert, bis eine möglichst hohe Übereinstimmung zwischen dem simulierten und dem gemessenen Diffraktogramm vorliegt. Somit ist die Rietveld-Methode also ein Anpassungsverfahren für das gesamte Beugungsdiagramm, dessen einzelne Messpunkte *i* (mit gemessener Intensität y_{io}) durch analytische Funktionen beschrieben werden (was zur berechneten Intensität y_{ic} führt). Mit diesen Funktionen können sowohl Struktur- als auch gerätespezifische Parameter beschrieben werden. Im Anpassungsprozess („Verfeinerung“) werden diese Parameter mit der Methode der kleinsten Fehlerquadrate (engl. *least squares*) simultan angepasst („gefittet“), wobei es die gewichtete (w_i) Fehlerquadratsumme S_y zu minimieren gilt:

$$S_y = \sum w_i |y_{io} - y_{ic}|^2 \qquad \text{mit } w_i = \frac{1}{\sigma(y_{io})^2}$$

Die Güte der Verfeinerung, also die Minimierung von S_y, kann mit diversen *R*-Werten (Residuen) abgeschätzt werden, wobei R_p, R_{wp} und R_{exp} (theoretischer Minimalwert von R_p) die wichtigsten Profilübereinstimmungsindikatoren sind. Üblicherweise werden diese auch untergrundkorrigiert (y_{ib}) berechnet, weil sie im Falle eines dürftigen Reflexintensität-zu-Untergrundintensität-Verhältnisses aussagekräftiger sind:

Profil-R-Wert: **Gewichteter Profil-R-Wert:** **Erwarteter Profil-R-Wert:**

$$R_p = \frac{\sum_i |y_{io} - y_{ic}|}{\sum_i y_{io}} \qquad R_{wp} = \sqrt{\frac{\sum_i w_i (y_{io} - y_{ic})^2}{\sum_i w_i (y_{io})^2}} \qquad R_{exp} = \sqrt{\frac{(N-P)}{\sum_i w_i (y_{io})^2}}$$

N = Anzahl der Messpunkte
P = Zahl der verfeinerten Parameter

Mit Untergrundkorrektur:

$$R_{p'} = \frac{\sum_i |y_{io} - y_{ic}|}{\sum_i |y_{io} - y_{ib}|} \qquad R_{wp'} = \sqrt{\frac{\sum_i w_i (y_{io} - y_{ic})^2}{\sum_i w_i (y_{io} - y_{ib})^2}} \qquad R_{exp'} = \sqrt{\frac{(N-P)}{\sum_i w_i (y_{io} - y_{ib})^2}}$$

Ein weiteres wichtiges Kriterium ist der Quotient aus R_{wp} und R_{exp}, der für gewöhnlich als *Goodness of Fit* (GOF) bezeichnet wird. Eine Verfeinerung mit einem abschließenden GOF zwischen 1,0 und 1,5 wird als gut bewertet [17]:

$$GOF = \frac{R_{wp}}{R_{exp}} = \sqrt{\frac{\sum_k w_i (y_{io} - y_{ic})^2}{(N-P)}}$$

Zwecks Vergleich mit Einkristalldaten wird außerdem der Bragg-*R*-Wert R_{Bragg} verwendet, welcher auf integralen Intensitäten (I_k) statt Intensitäten an einem einzelnen Messpunkt basiert:

$$R_{Bragg} = \frac{\sum_k |I_{ko} - I_{kc}|}{\sum_k I_{ko}}$$

In der vorliegenden Arbeit sind die hier aufgeführten *R*-Werte stets in Tabellen mit kristallographischen Daten zu finden.

3.2.1 Kristallstrukturbestimmung aus Röntgenpulverdaten

Da die Zielverbindungen ausschließlich in Pulverform anfielen, wurden alle Kristallstrukturbestimmungen aus XRPD-Daten durchgeführt. Der Bestimmung einer Kristallstruktur liegt prinzipiell folgender Ablauf zu Grunde [vgl. 31]:

a) Probenpräparation
b) Messung des XRPD-Diagramms
c) Indizierung der Reflexe des Diagramms zur Bestimmung der Gitterkonstanten und möglicher Raumgruppen, Bestimmung der Anzahl der Formeleinheiten in der Elementarzelle
d) Strukturlösung
e) Strukturverfeinerung
f) kritische Prüfung der in e) erhaltenen Kristallstruktur

a) Probenpräparation

Einen wichtigen Anteil an der Qualität von Röntgenpulverdaten hat zweifelsohne die Probenpräparation, der wiederum die Herstellung eines gut kristallinen Pulvers vorausgeht. Letzteres gestaltet sich oft als schwieriges Unterfangen, sodass eine gute Probenpräparation trotz der inzwischen hoch entwickelten Hard- und Softwaremöglichkeiten entscheidend ist. Um einen Datensatz mit akkuraten Peakpositionen und Reflexintensitäten zu erhalten, an dem im Nachgang möglichst wenige Korrekturen vorzunehmen sind, sind insbesondere folgende Kriterien zu beachten:

- phasenreine Probenpräparation
- homogene Verteilung aller Kristallorientierungen (Vorzugsorientierung ist jedoch manchmal unvermeidbar)
- homogene Kristallitgrößenverteilung sowie ein geringer amorpher Anteil

b) Messung eines XRPD-Diagramms

Alle Proben dieser Arbeit wurden mit Diffraktometern der Firma STOE & Cie GmbH in Transmissionsgeometrie vermessen (Abb. 3.6). Für die Analysen wurden ca. 5-20 mg gemörserte Probensubstanz wahlweise in eine Glaskapillare (0,5 mm < d < 1,0 mm) gefüllt oder zwischen zwei Polymerfolien gespannt. In beiden Fällen rotierte die Probe während der Messung permanent um die Kapillarachse bzw. in der Folienebene. Die Diffraktometer wurden mit Cu- oder Mo-Strahlung betrieben, welche mithilfe eines gebogenen Ge(111)-Einkristalls monochromatisiert wurde. Die gebeugte Röntgenstrahlung wurde mit ortsempfindlichen Detektoren (*position sensitive detector,* PSD) registriert.

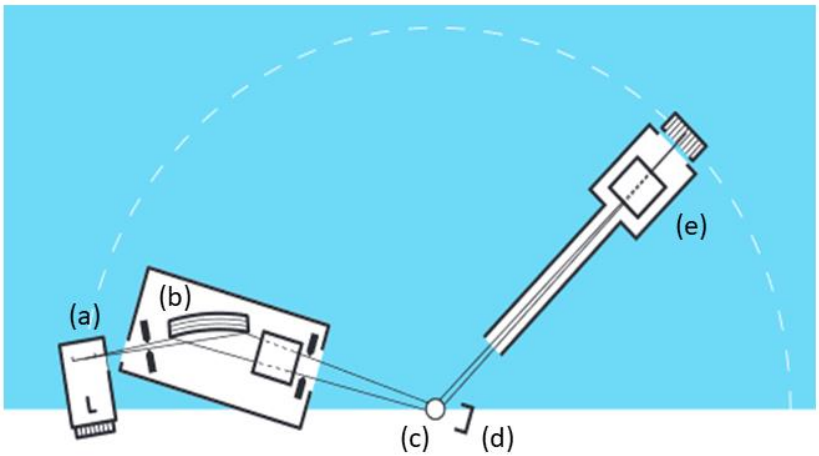

Abbildung 3.6: Skizze eines Transmissionsdiffraktometers mit fokussierendem Strahl. (a) Röntgenröhre, (b) Monochromator, (c) Kapillare mit Probe, (d) Primärstrahlfänger, (e) Punktdetektor [nach 19].

c) Indizierung und Raumgruppenbestimmung

Bei der Indizierung erfolgt die Zuordnung der gemessenen Reflexe zu den Netzebenscharen. Zur (Lage-)Beschreibung der Netzebenenschar benutzt man die Miller-Indizes (*hkl*). Anschließend werden die Gitterparameter *a, b, c, α, β* und *γ* (Metrik der Elementarzelle) bestimmt. Die Indizierung erfolgte mit den Programmen DASH (Dicvol-Algorithmus) [10, 11, 12] und/ oder Conograph [20, 34, 35]. Zur Überprüfung der Verlässlichkeit eines Indiziervorschlages wurden die Volumeninkremente nach Hofmann [24] herangezogen. Hierbei wird das Volumen einer Formeleinheit (basierend auf den Atomvolumina bei 25 °C) abgeschätzt und *Z*, also die Anzahl der Formeleinheiten in der vorgeschlagenen Elementarzelle, ermittelt. Diese Methode

kann indes nur angewendet werden, wenn die Summenformel der Verbindung, so wie in der vorliegenden Arbeit durch gravimetrische Analysen, bekannt ist.

Ist eine Indizierung sinnvoll und reproduzierbar, muss nach systematischen Auslöschungen, also nach der Abwesenheit von Reflexen bestimmter Netzebenenscharen, geschaut werden. Daraus lassen sich mögliche Raumgruppen ableiten, in denen dann Strukturlösungsversuche (siehe Punkt d) durchgeführt werden. Unter Umständen lässt sich die Zahl der möglichen Raumgruppen reduzieren, weil sie zum Beispiel aus chemischer Sicht „unsinnig“ sind (Beispiel: Vorschlag $P2_1/c$ für eine chirale Verbindung). Des Weiteren wird eine Pawley-Anpassung („Pawley-Fit“) durchgeführt [36], bei der Gitterparameter, Untergrundparameter, der Nullpunktsfehler, Parameter zur Beschreibung der Reflexform sowie alle Reflexintensitäten nach der Methode der kleinsten Fehlerquadrate gefittet werden. Die hierbei extrahierten Intensitäten werden bei der nachfolgenden Strukturlösung herangezogen.

d) Strukturlösung

Zur Strukturlösung bzw. Lösung des Phasenproblems wird im Fall von Röntgenpulverdaten gerne auf sog. Realraummethoden zurückgegriffen (während die aus der SCXRD bekannten konventionellen Methoden im reziproken Raum arbeiten), bei denen sozusagen reale Modelle entwickelt und deren berechnete Pulverdiffraktogramme mit dem tatsächlich gemessenen Diffraktogramm abgeglichen werden (vgl. [31]). Dazu wird zunächst ein Startmodell benötigt, das im Falle einer organischen Verbindung dann ein Molekülfragment ist (das Startmodell kann auch aus mehreren Fragmenten bestehen). Bindungslängen, Bindungswinkel und Torsionswinkel können aus verwandten Verbindungen, oder kristallographischen Datenbanken wie der CSD abgeleitet werden. Optional kann die Zahl der Freiheitsgrade bei der Strukturlösung eingeschränkt werden, indem beispielsweise einzelne Atome auf bestimmten Lagen in der Elementarzelle fixiert werden. Die Startmodelle werden nun systematisch und in Abhängigkeit der zuvor festgelegten Parameter, in Position, Orientierung und Konformation variiert (*move*), sodass die Differenz zwischen theoretischem und experimentellem Diffraktogramm möglichst gering wird. Dafür wird nach jeder Parametermodifikation ein programmabhängiger *R*-Wert berechnet. Die in dieser Arbeit vorgestellten Kristallstrukturen wurden mit Hilfe

des *Simulated Annealing*-Ansatzes und dem Programm DASH [10, 11, 12] gelöst. Bei diesem Verfahren wird die Molekülstruktur am Ende jedes *set of moves* langsam eingefroren um verifizieren, ob die Struktur stabil bleibt und damit der Algorithmus in einem Minimum der *R*-Werte geendet ist. Dieser Prozess (*run*) wird mehrfach wiederholt. Abschließend sind die Strukturlösungsvorschläge aller *runs* sorgfältig zu begutachten. Zu berücksichtigen sind u. a. Molekülgeometrie, Anordnung der Fragmente in der Elementarzelle, intermolekulare Verknüpfungsmuster, Häufigkeit identischer oder ähnlicher Ergebnisse. Die besten bzw. sinnvollsten Strukturvorschläge werden sodann einer Strukturverfeinerung unterzogen.

e) Strukturverfeinerung

Alle Strukturverfeinerungen in dieser Arbeit wurden mit dem Programms TOPAS 4.2 [9] durchgeführt. An dieser Stelle folgt eine grobe Skizze der Vorgehensweise einer Rietveld-Verfeinerung, da alle relevanten Details der Strukturverfeinerungen in den jeweiligen Publikationen bzw. im Anhang dieser Arbeit nachzulesen sind. Für weitere Ratschläge in der praktischen Umsetzung sei die Lektüre von Dinnebier et al. [17], McCusker et al. [32] und Young [46] empfohlen. Zu Beginn des Verfeinerungsprozesses wird ein Pawley-Fit vorgenommen, um die aus dem Strukturlösungsdurchlauf (siehe Punkt d) erhaltenen Parameter für Gitterkonstanten, Profil, Untergrund und Nullpunkt anzupassen. Außerdem wird ein Gesamtskalierungsfaktor eingeführt, mit dem die simulierten Intensitäten (aus der folgenden Strukturverfeinerung) an die berechneten Intensitäten (aus der Strukturlösung in Punkt d)) angepasst werden. Anschließend wird schrittweise die Kristallstruktur verfeinert, indem erst die Lageparameter der Atome (*x, y, z*) und anschließend die atomaren Auslenkungsparameter (*B*) angepasst werden. In der Regel wird ein Auslenkungsparameter für alle H-Atome (Parameter in TOPAS: bh) und ein zweiter Auslenkungsparameter für alle Nicht-H-Atome eingeführt (TOPAS: bnonh), beide werden dann isotrop verfeinert. Falls nötig, können außerdem Vorzugsorientierung (TOPAS*:* PO) und Besetzungsdichten (TOPAS*:* occ) verfeinert werden. Da die Zahl der zu verfeinernden Parameter sehr schnell sehr groß werden kann, bedient man sich für gewöhnlich sog. *restraints* und/ oder *constraints,* mit Hilfe derer externe bzw. messunabhängige Informationen (wie bspw. die Planarität eines Benzolrings) in die Verfeinerung eingepflegt werden können. Diese Einschränkungen

stabilisieren den Verfeinerungsprozess in erheblichem Maße und tragen zu einer plausiblen Fehlerverteilung bei.

Obwohl inzwischen mehrere sehr gute und hoch entwickelte (und zum Teil bedienerfreundliche) Programme existieren, erfordert die Kristallstrukturanalyse aus Röntgenpulverdaten nach wie vor einen erfahrenen und stets prüfenden Programmnutzer. Nach Allmann [2] sollte dieser bei der Beurteilung über die Güte einer Rietveld-Verfeinerung mindestens folgende Kriterien berücksichtigen:

- konsistente *R*-Werte (s.o.)
- eine möglichst glatte Differenzkurve
- sinnvolle und niedrige Standardabweichungen der verfeinerten Parameter
- physikalisch und chemisch sinnvolle Ergebnisse

3.2.2 Qualitative und quantitative Phasenanalyse

Bei einer quantitativen Phasenanalyse werden die Massenanteile der einzelnen Phasen einer Phasenmischung bestimmt. Dazu werden entweder Reflexintensitäten bzw. die Intensitätsverhältnisse der Reflexe der jeweiligen Phasen ausgewertet, oder aber die Informationen des gesamten Beugungsdiagramms nach dem Rietveld-Ansatz ausgeschöpft. Im Rahmen dieser Arbeit wurde in zwei Fällen eine quantitative Phasenanalyse durchgeführt (siehe MH2), da die Zielverbindungen nicht reinphasig erhalten wurden. Für Ratschläge in der praktischen Anwendung bzw. Umsetzung sei auch hier die Lektüre von Dinnebier et al. [17] empfohlen.

<u>Methode mit äußerem Standard</u>

Bei diesem Ansatz wird eine Reinphase der Mischung (bspw. CaO) unter denselben experimentellen Bedingungen (!) gemessen wie die Mischung (bswp. SiO_2/ CaO), und die integralen Intensitäten der Reinphase mit denen des Kristallgemisches in Beziehung gesetzt. Vorteil dieser Variante ist die Möglichkeit, den amorphen Anteil in einer Mischung zu bestimmen, ohne der Probe einen inneren Standard beigeben zu müssen. Daher eignet sich dieser Ansatz bspw. für die industrielle Großproduktion, wo Proben (aus mitunter verschiedenen Produktionsstufen) rasch geprüft werden müssen und sich deshalb die Messbedingungen bzw. die Gerätekonfiguration vorläufig nicht ändern.

Methode mit innerem/ internem Standard

Besteht eine Mischung aus mehr als zwei Phasen (amorpher Anteil ausgenommen), sollte ihre quantitative Analyse besser an einer sog. „gespikten“ Probe durchgeführt werden. Hier wird der zu quantifizierenden Phasenmischung ein Standardmaterial mit definierter Masse bzw. Volumen, innerer Standard bzw. „Spike“ genannt, beigemischt. Vorteil dieses Ansatzes ist die Möglichkeit, auch einzelne Phasen des Phasengemisches quantifizieren zu können, ohne dabei die restlichen Phasen analysieren zu müssen.

Quantitative Phasenanalyse mit der Rietveld-Methode

Im Gegensatz zu den zuvor skizzierten Möglichkeiten zur quantitativen Phasenanalyse wird bei dem Rietveld-Ansatz nicht zwangsläufig ein zusätzlicher Standard benötigt. Dies ermöglicht auch eine Phasenanalyse an Proben, denen per se kein Standard zugesetzt werden kann, weil die Probe zum Beispiel – wie in dieser Arbeit bei β-$[CoBr_2(3\text{-}CNpy)]_n$ der Fall (siehe MH2) – unter Inertbedingungen gehalten werden muss, oder *in-situ* auf dem Pulverdiffraktometer erzeugt wird. Voraussetzung dafür ist allerdings die Kenntnis aller Kristallstrukturen der in der Mischung vorhandenen Phasen. Bei Anwesenheit einer amorphen Phase muss die Probe also trotzdem gespikt werden.

PONKCS-Methode

Hat man eine Phasenmischung mit einer Phase, deren Kristallstruktur noch nicht gelöst ist, zumindest aber deren Gitterkonstanten bekannt sind (und damit auch die zu erwartenden Reflex-Positionen), kann ihr Anteil über den PONKCS-Ansatz (***p****artial* ***o****r* ***n****o* ***k****nown* ***c****rystal* ***s****tructure*) im Programm TOPAS bestimmt werden. In der Verfeinerung einer solchen Mischung wird die PONCKS-Phase über einen Pawley-Fit beschrieben und alle Reflexintensitäten fixiert bzw. über einen Parameter, den Skalierungsfaktor, verfeinert. Die übrigen Phasen mit bekannten Kristallstrukturen können Rietveld verfeinert werden. Diese Methode wurde bei der Kristallstrukturbestimmung bzw. Verfeinerung von $[MnCl_2(3\text{-}CNpy)_1]_n$ und $[CuCl_2(3\text{-}CNpy)_1]_n$ eingesetzt (siehe MH3). Ihre Proben enthielten in geringem Maße die Nachfolgeabbaustufen $[MnCl_2(3\text{-}CNpy)_{1/3}]_n$ resp. $[CuCl_2(3\text{-}CNpy)_{1/2}]_n$, deren

Kristallstrukturen bislang noch nicht gelöst werden konnten, aber für die eine reproduzierbare Indizierung vorlag.

3.2.3 Temperaturabhängige Röntgenpulverdiffraktometrie (T-XRPD)

Wie zuvor in Kapitel 3.1 erwähnt, wurde der thermische Abbau des Precursors teilweise in temperaturabhängigen Röntgenpulvermessungen (T-XRPD) auf dem Diffraktometer nachgestellt. Dazu wurde der Precursor in eine Quarzkapillare gefüllt und während der Messung (rotierende Kapillare in Transmissionsgeometrie) mit einem von oben auf die Kapillare gerichteten Heizsystem temperiert. Dabei wurde die Probe fortlaufend einem Schutzgasstrom (Ar oder N_2) ausgesetzt, sodass die mitunter luft- und feuchtigkeitsempfindlichen Abbauverbindungen der Hochtemperaturserien (HT-XRPD) geschützt wurden. An dieser Stelle ist grundsätzlich zu beachten, dass infolge des nicht vorhandenen kontinuierlichen Gasdurchflusses (welcher den sich verflüchtigenden Liganden im DTA-TG-Gerät ja förmlich mitreißt und dadurch das Reaktionsgleichgewicht zugunsten der Abbaustufe verschiebt), ein gewisser zeitlicher Versatz zu korrespondierenden DTA-TG-Aufnahme vorliegt. Für Tieftemperaturmessungen (TT-XRPD) wurde ein analoges, aber mit N_2(-Gas) betriebenes Heizsystem eingesetzt, das einen Temperaturbereich von - 180 °C bis + 230 °C abdeckte. In Kombination mit ortsempfindlichen Detektoren (linearer PSD) konnten mit beiden Messvorrichtungen Röntgenpulverdaten gesammelt werden, deren Qualität die Kristallstrukturbestimmung von TT- bzw. HT-Phasen zuließ/ermöglichte. Darüber hinaus diente die T-XRPD zur Detektion von Polymorphen und Untersuchung von Polymorphieänderungen – vor allem solcher, die mit Abbaureaktionen zusammenfallen und deshalb in der DTA-TG-Analyse quasi „untergehen“. Dank dieser apparativen Möglichkeiten konnten ganze Temperaturserien in *in-situ*-Pulvermessungen realisiert wurden, was nachfolgend exemplarisch an der Abbaureihe von $[CoCl_2(4\text{-}CNpy)_2]_n$ illustriert sei (vgl. auch MH4). Zunächst wurde eine DTA-TG-Messung vorgenommen, die zwei dezidierte Abbaustufen zeigte (Abb. 3.7). Dabei handelte es sich um die Phasen $[CoCl_2(4\text{-}CNpy)_1]_n$ und $[CoCl_2(4\text{-}CNpy)_{1/3}]_n$. Allerdings konnten diese in dem DTA-TG-Gerät nicht phasenrein präpariert werden, da die Proben beim Überführen aus dem Korundtiegel in die Quarzkapillare aufgrund ihrer Luft- und Feuchtigkeitsempfindlichkeit oxidierten. Daher wurde die Präparation auf dem

Pulverdiffraktometer reproduziert (Abb. 3.8), sodass die Kristallstruktur von $[CoCl_2(4\text{-}CNpy)_1]_n$ aus einem Datensatz (aufgenommen bei 250 °C) dieser *in-situ*-Messung bestimmt werden konnte.

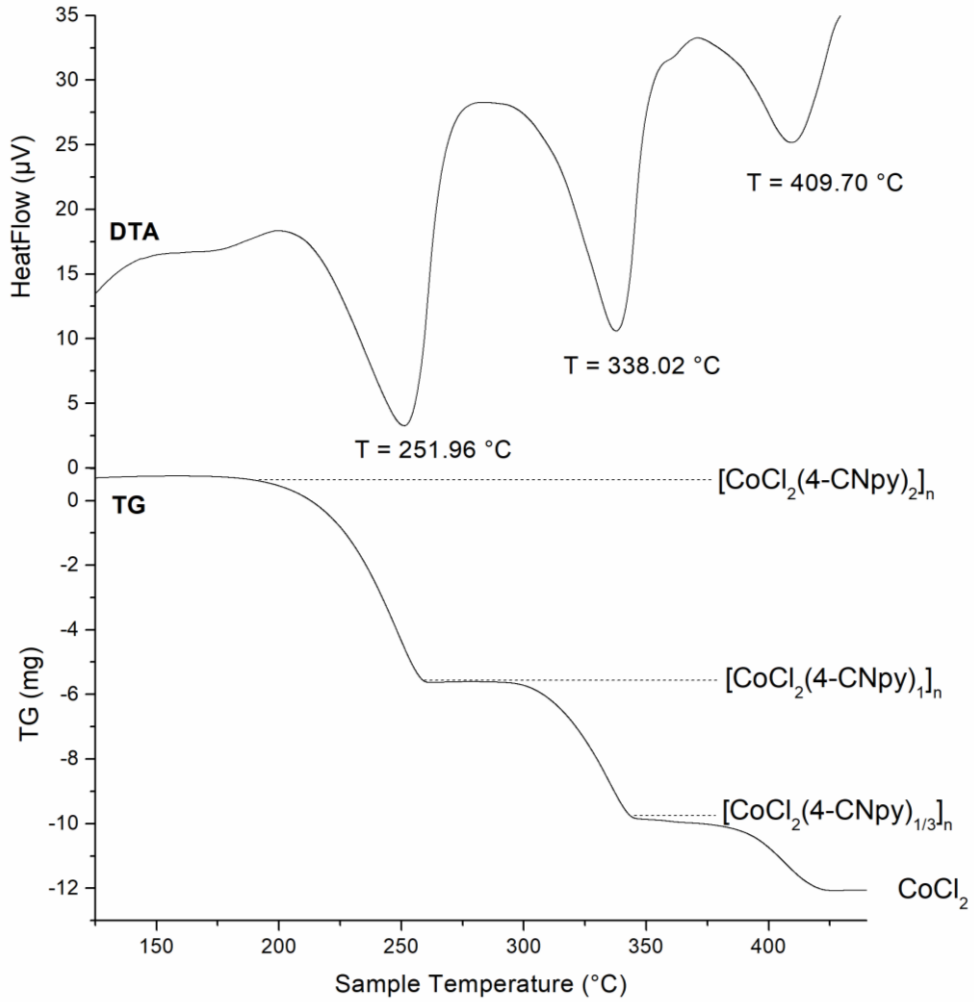

Abbildung 3.7: DTA-TG-Aufnahme von $[CoCl_2(4\text{-}CNpy)_2]_n$: thermischer Abbau von $[CoCl_2(4\text{-}CNpy)_2]_n$ über $[CoCl_2(4\text{-}CNpy)_1]_n$ zu $CoCl_2$ [MH4].

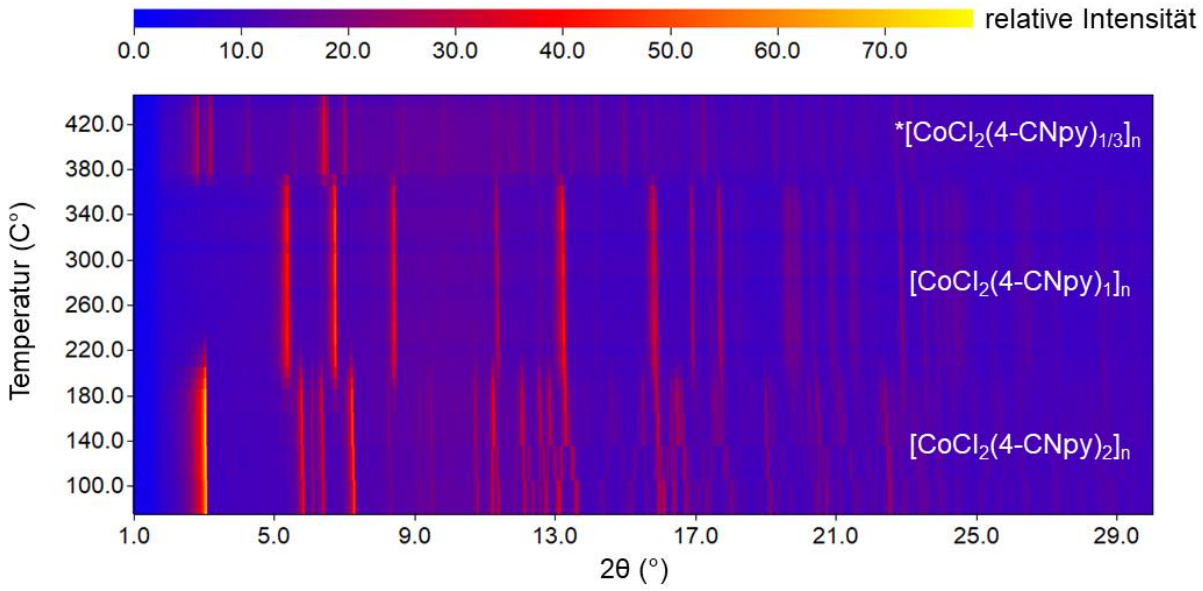

(a)

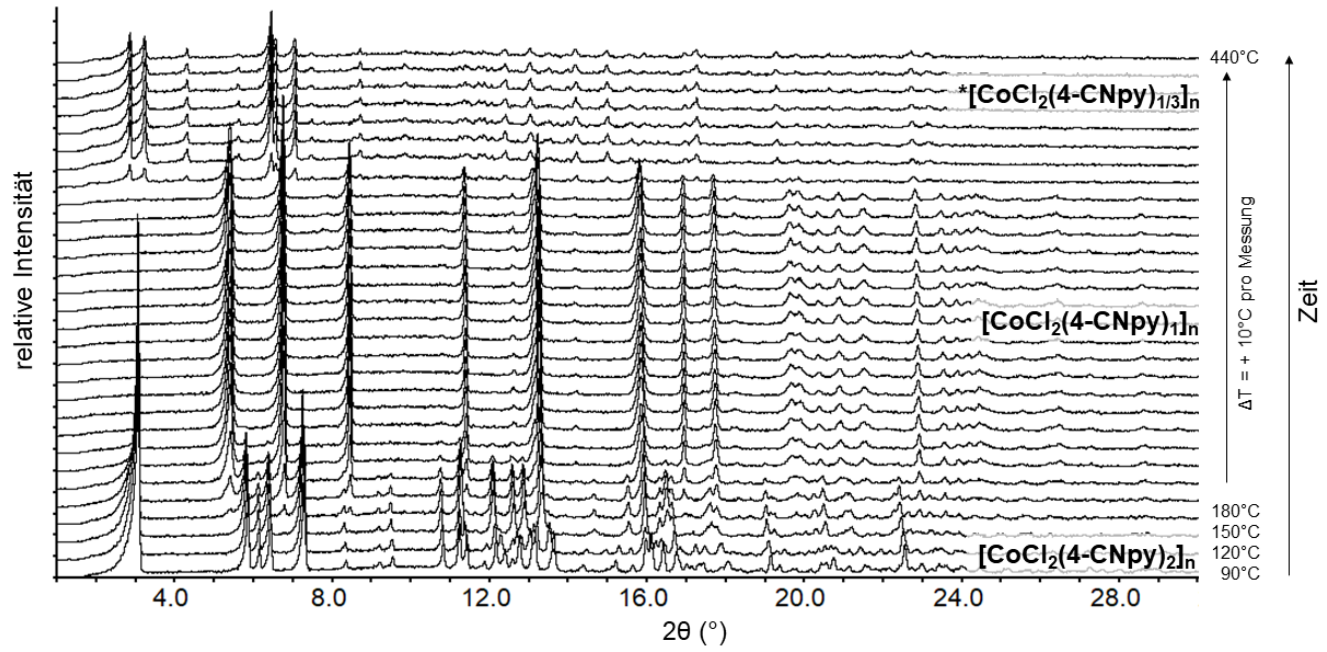

(b)

Abbildung 3.8: XRPD-Aufnahme der HT-Serie von $[CoCl_2(4\text{-}CNpy)_2]_n$: (a) Draufsicht und (b) gestaffelte Darstellung. * Die Kristallstruktur von $[CoCl_2(4\text{-}CNpy)_{1/3}]_n$ konnte trotz reproduzierbarer Indizierung bislang nicht gelöst werden (vgl. MH4).

3.3 Infrarot-Spektroskopie (IR)

Die Infrarot-Spektroskopie (IR) beruht auf der Tatsache, dass Moleküle elektromagnetische Strahlung des infraroten Spektrums (750 nm -1 mm) absorbieren und sich dadurch Schwingungszustände der kovalenten Bindungen eines Moleküls ändern. Die für einen Zustandswechsel benötigte Energieportion ist spezifisch für jede Bindung des Moleküls, weshalb das IR-Spektrum für gewöhnlich auch als „molekularer Fingerabdruck“ bezeichnet wird. Es ermöglicht u. a. die Identifikation bzw. „Beschaffenheit“ funktioneller Gruppen, was für die vorliegende Arbeit von Relevanz ist. Standardmäßig werden heutzutage Fourier-Transform-IR-Spektrometer (FTIR) eingesetzt, welche die Absorption der IR-Strahlung in Abhängigkeit der Wellenlänge λ, bzw. der Wellenzahl ν (cm^{-1}) messen. Alle Messungen dieser Arbeit wurden mit einem SHIMADZU IRAffinity-1S FTIR-Spektrophotometer aufgenommen. Grundsätzlich lassen sich die Molekülschwingungen in zwei Schwingungsformen einteilen: Valenzschwingungen (es ändern sich hauptsächlich die Bindungslängen) und Deformationsschwingungen (es ändern sich die Bindungswinkel). Des Weiteren wird nach dem Symmetrieverhalten unterschieden: symmetrische Schwingungen (die Symmetrie des Moleküls bleibt erhalten) und antisymmetrische Schwingungen (die Symmetrie des Moleküls ändert sich).

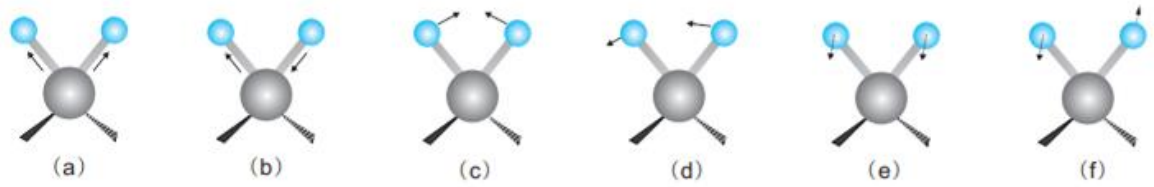

Abbildung 3.9: Valenzschwingungen und Deformationsschwingungen des Methan-Moleküls [nach 23]. (a): C-H symmetrische Valenzschwingung (ν_s), (b): C-H antisymmetrische Valenzschwingung (ν_{as}), (c) und (d): C-H Deformationsschwingungen (ν_δ) innerhalb der Ebene, (e) und (f): C-H Deformationsschwingungen (ν_γ) aus der Ebene heraus.

Für diese Arbeit wurde das Verhalten der antisymmetrischen Valenzschwingung der Cyanogruppe ν_{as}(C≡N) ausgewertet, da hieraus das Koordinationsverhalten der CN-Gruppe, d. h. ob der Cyanostickstoff N_{CN} terminal oder verbrückend vorliegt, abgeleitet werden kann. ν_{as}(C≡N)-Banden treten typischerweise im Bereich von 2260 - 2200 cm^{-1} [42] auf, die der sog. „freien“ Cyanopyridine im Bereich von 2243 - 2230 cm^{-1} (siehe Abb. 3.10 bzw. ebenfalls [42] sowie Tab. 3.2).

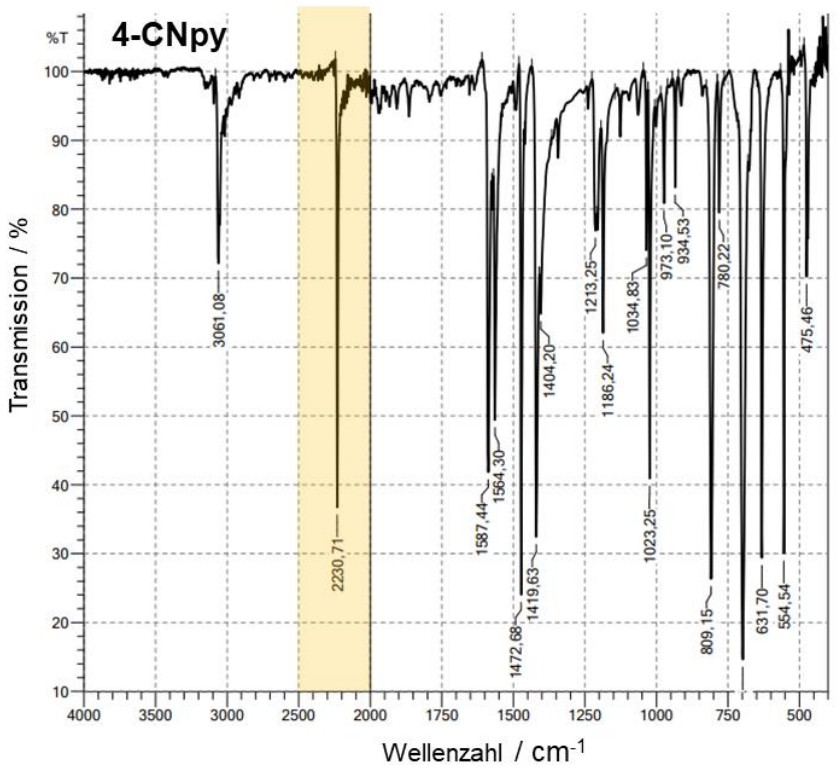

(a)

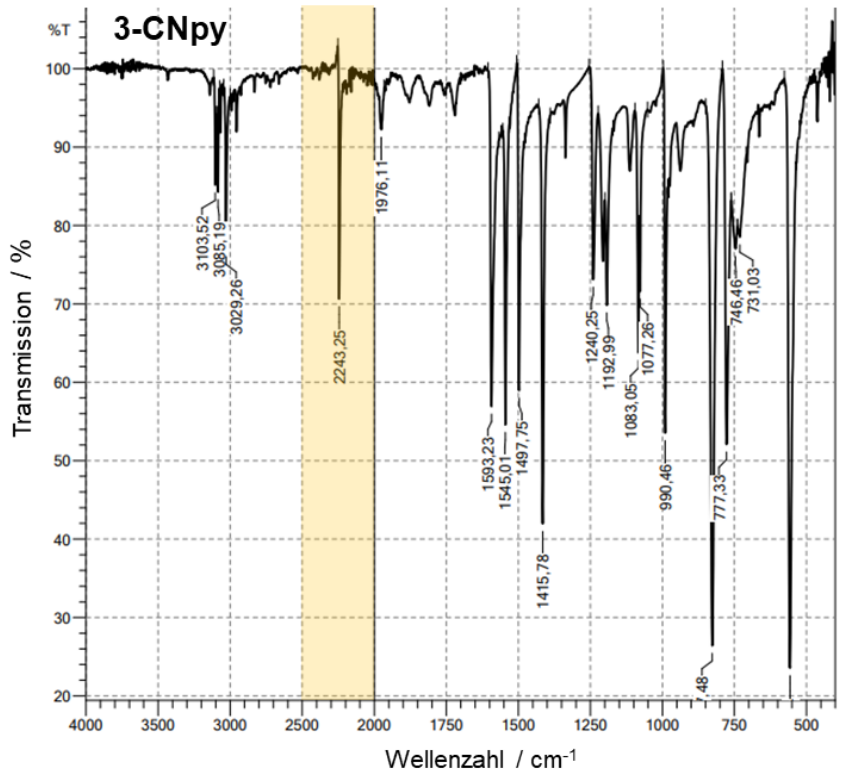

(b)

Abbildung 3.10: IR-Aufnahmen von 4-CNpy (a) und 3-CNpy (b). Die relevante antisymmetrische Valenzschwingung der Cyanogruppe ν_{as}(C≡N) ist gelb unterlegt.

Ist die Bandenlage von ν_{as}(C≡N) des in $[MX_2(CNpy)_x]_n$ gebundenen Cyanopyridins ähnlich der des „freien“ Cyanopyridins, liegt CNpy als monodentater Ligand mit einem terminalen N_{CN}-Atom vor. Es koordiniert ausschließlich der Pyridinstickstoff N_{py} an ein Metallatom (vgl. bspw. 4-CNpy in der $[MCl_2(4\text{-}CNpy)_2]_n$-Serie). Ist die Bande von ν_{as}(C≡N) allerdings zu nennenswert größeren Wellenzahlen verschoben, dann agiert CNpy als bidentater, sprich verbrückender Ligand. N_{CN} koordiniert ebenfalls an ein Metallatom, woraus die Bildung eines zweidimensionalen Netzwerks resultiert. In Abb. 3.11 sind die IR-Aufnahmen von $[MnBr_2(3\text{-}CNpy)_2]_n$ und $[MnBr_2(3\text{-}CNpy)_1]_n$ abgedruckt [MH2], in denen das 3-CNpy-Fragment frei (ν_{as}(C≡N): 2239 cm^{-1}) bzw. verbrückend (ν_{as}(C≡N): 2275 cm^{-1}) vorliegt.

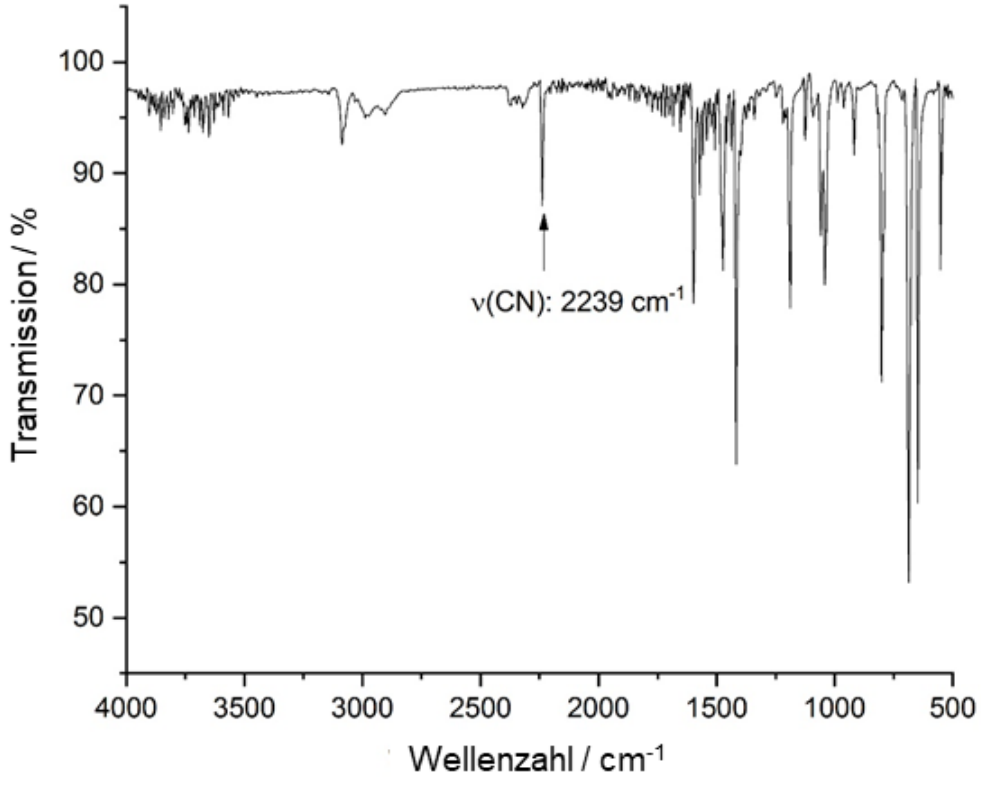

(a)

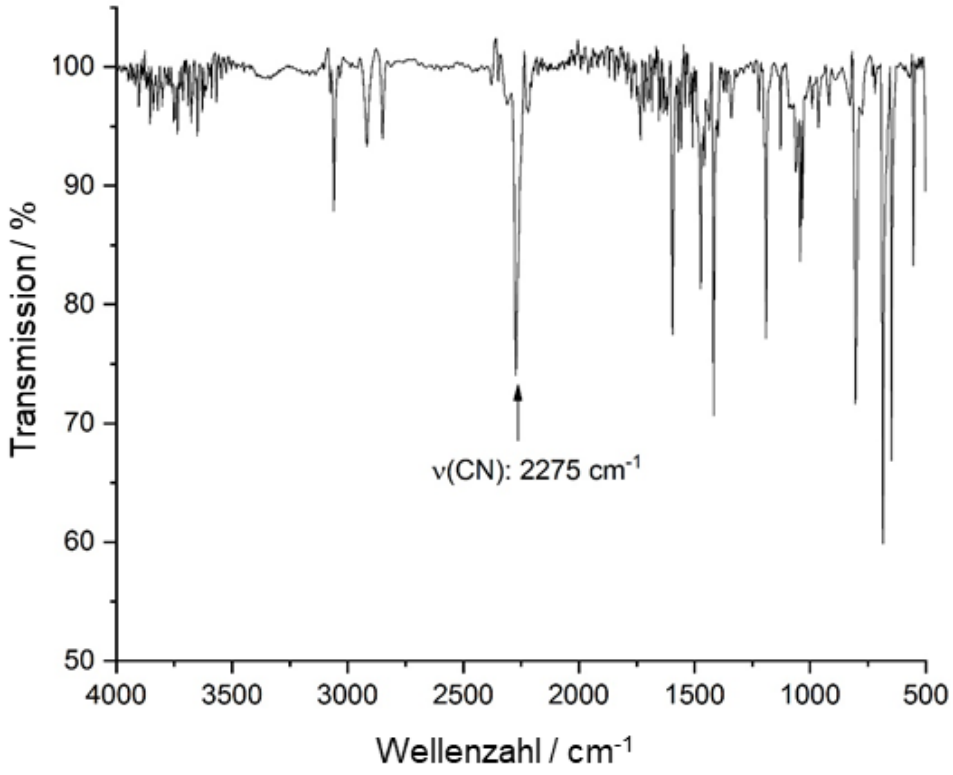

(b)

Abbildung 3.11: IR-Aufnahmen von $[MnBr_2(3\text{-}CNpy)_2]_n$ (a) und $[MnBr_2(3\text{-}CNpy)_1]_n$ (b) [MH2]. In $[MnBr_2(3\text{-}CNpy)_1]_n$ koordinieren auch die N_{CN}-Atome an Mn-Atome, sodass die ν_{as}(C≡N)-Bande bei einer höheren Wellenzahl erscheint.

Dank der IR-Spektroskopie wurden also im Vorfeld strukturrelevante Informationen erhalten, die bei Strukturlösung und anschließender Kristallstrukturbestimmung berücksichtigt werden konnten. So signalisiert das IR-Spektrum von $[CuCl_2(4\text{-}CNpy)_1]_n$ bereits, dass diese Verbindung, als einzige der $[MCl_2(4\text{-}CNpy)_1]_n$-Serie, keine Netzwerkstruktur besitzt (vgl. ESI von MH1).

Tabelle 3.2: Charakteristische ν_{as}(C≡N) von 3-CNpy, 4-CNpy und ihren Koordinationspolymeren. Die IR-Aufnahmen finden sich im Begleitmaterial von MH1, MH2, MH3 und MH4 sowie im Anhang B. IR-Aufnahmen von 3-CNpy und 4-CNpy wurden mit den Einträgen in der SDBS [28] abgeglichen.

		ν_{as}(C≡N) [cm^{-1}]	
M^{II}	**Verbindung**	**4-Cyanopyridin**	**Zustand des N_{CN}**
	4-CNpy	2230	terminal
		$[MX_2(4\text{-CNpy})_2]_n$	
Mn, Fe, Co, Ni, Cu, Zn	$[MCl_2(4\text{-CNpy})_2]_n$	2241-2242	terminal
Mn, Fe, Co, Ni, Cu, Zn	$[MBr_2(4\text{-CNpy})_2]_n$	2234-2235	terminal
		$[MX_2(4\text{-CNpy})_1]_n$	
Mn, Fe, Ni, Co *	$[MCl_2(4\text{-CNpy})_1]_n$	2275-2288	verbrückend
Cu	$[CuCl_2(4\text{-CNpy})_1]_n$	2243	terminal
Mn, Fe, Ni, Co *	$[MBr_2(4\text{-CNpy})_1]_n$	2281-2298	verbrückend
		3-Cyanopyridin	**Zustand des N_{CN}**
	3-CNpy	2243	terminal
		$[MX_2(3\text{-CNpy})_2]_n$	
Mn, Fe, Co, Ni, Cu, Zn	$[MCl_2(3\text{-CNpy})_2]_n$	2236-2243	terminal
Mn, Fe, Co, Ni, Cu, Zn	$[MBr_2(3\text{-CNpy})_2]_n$	2236-2239	terminal
		$[MX_2(3\text{-CNpy})_1]_n$	
Mn, Co, Ni, Cu	$[MCl_2(3\text{-CNpy})_1]_n$	2236-2239	terminal
Mn, Fe, Co, Ni	$[MBr_2(3\text{-CNpy})_1]_n$	2275-2288	verbrückend
		3,5-Dicyanopyridin	**Zustand beider N_{CN}**
	3,5-CNpy	2245	terminal
Ni	$[NiCl_2(3,5\text{-CNpy})_2]_n$	2253	terminal

* Diese Kristallstruktur wurde aus Daten einer *in-situ*-Messung bestimmt. Daher fehlt eine IR-Aufnahme.

4. Ergebnisse

In der nachfolgenden Zusammenstellung werden zunächst Koordinationsverbindungen auf Basis von MCl_2 und 3-CNpy ($[MCl_2(3\text{-}CNpy)_x]_{(n)}$-Reihe), 4-CNpy ($[MCl_2(4\text{-}CNpy)_x]_{(n)}$-Reihe) sowie 3,5-CNpy präsentiert und diskutiert. Es folgen die Verbindungen auf Basis von MBr_2 und 3-CNpy ($[MBr_2(3\text{-}CNpy)_x]_{(n)}$-Reihe) bzw. 4-CNpy ($[MBr_2(4\text{-}CNpy)_x]_{(n)}$-Reihe). Innerhalb einer Reihe werden die jeweiligen Kristallstrukturen zudem in Serien (beginnend in Kapitel 4.1 mit der Serie $[MCl_2(3\text{-}CNpy)_2]_n$ mit M = Mn, Fe, …) zusammengefasst und dann innerhalb ihrer Serie diskutiert. Außerdem werden die Serien, bzw. einzelne Kristallstrukturen verschiedener Serien, über Querverweise an entsprechenden Stellen verglichen.

4.1 $[MCl_2(3\text{-}CNpy)_2]_{(n)}$

Die Synthesen dieser Verbindungen erfolgten über Reaktionen des entsprechenden Chlorids MCl_2 (mit M = Mn, Fe, Co, Ni, Cu und Zn) mit 3-Cyanopyridin in alkoholischen Lösungen. Sämtliche Versuchsansätze führten stets zu der Bildung von pulverförmigen Verbindungen mit einem Metall(chlorid)-zu-Ligand-Verhältnis von 1:2, also der Stöchiometrie $[MCl_2(3\text{-}CNpy)_2]_{(n)}$. Trotz Variation der Reaktionsbedingungen oder der eingesetzten Eduktstoffmengen konnten keine Verbindungen mit einem höheren Anteil an 3-Cyanopyridin erhalten werden. Im Fall von $[ZnCl_2(3\text{-}CNpy)_2]$ führte die Änderung der Reaktionstemperatur jedoch zur Bildung eines weiteren Polymorphs.

Aus der $[MCl_2(3\text{-}CNpy)_2]_n$-Serie war bisher einzig die Kristallstruktur von $[CuCl_2(3\ CNpy)_2]_n$ literaturbekannt. Diese wurde 2011 von Chen et al. aus TT-Einkristalldaten bestimmt (UTIHAH [8]). Zwecks Vergleichbarkeit mit den anderen Kristallstrukturen dieser Serie wurde eine Kristallstrukturbestimmung von $[CuCl_2(3\text{-}CNpy)_2]_n$ aus RT-Pulverdaten ergänzt.

Wichtige kristallographische Daten und Ergebnisse der Strukturverfeinerungen der $[MCl_2(3\text{-}CNpy)_2]_{(n)}$-Serie sind in den Tabellen 4.1.1 (Kap. 4.1.1) und 4.1.2 (Kap. 4.1.2) aufgeführt. Weitere Ergebnisse sind im Detail in den Publikationen MH3 und MH4 nachzulesen.

4.1.1 $[MCl_2(3\text{-}CNpy)_2]_n$ mit M = Mn, Fe, Co, Ni und Cu

In allen Kristallstrukturen werden die Metallatome von jeweils vier Cl Atomen und zwei N_{py}-Atomen koordiniert, sodass Oktaeder aus MCl_4N_{py2}-Einheiten aufgespannt werden. Die Cl-Atome fungieren als μ_2-Brückenliganden, die die MCl_4N_{py2}-Oktaeder eckenverknüpfen. Dadurch entstehen (eindimensionale) Ketten aus $[MCl_2(3\text{-}CNpy)_2]_n$ entlang [100] (Abb. 4.1.1), und die kurze Gitterkonstante *a* entspricht dem Metall-Metall-Abstand innerhalb einer Kette. Dieser nimmt innerhalb der $[MCl_2(3\text{-}CNpy)_2]_n$-Serie erwartungsgemäß ab (und zwar von 3,7030(4) Å für Mn auf 3,5837(3) Å für Ni, Tab. 4.1.1). Dieser Trend setzt sich in $[CuCl_2(3\text{-}CNpy)_2]_n$ mit *a* = 3,7560(1) Å nicht fort, da die $CuCl_4N_{py2}$-Koordinationsoktaeder aufgrund der d^9-Elektronenkonfiguration des Cu stark Jahn-Teller verzerrt sind und in Kettenrichtung gestreckt werden (Abb. 4.1.1).

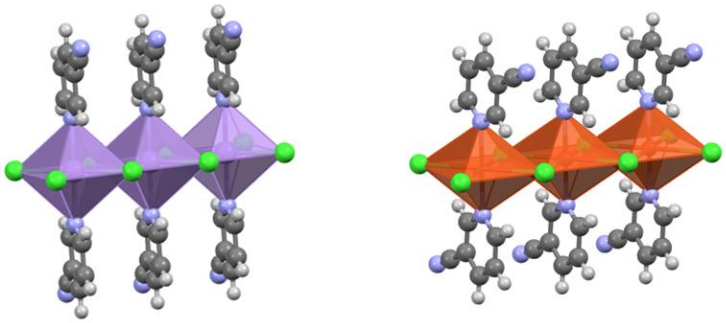

$[MnCl_2(3\text{-}CNpy)_2]_n$ $[CuCl_2(3\text{-}CNpy)_2]_n$

Abbildung 4.1.1: Polyederdarstellung eines Kettenausschnitts von $[MnCl_2(3\text{-}CNpy)_2]_n$ (links) und $[CuCl_2(3\text{-}CNpy)_2]_n$ (rechts).

Benachbarte Cyanopyridin-Liganden einer Kette sind stets planparallel. Die Interplanar-Abstände der Ebenen der C_5N_{py}-Ringfragmente variieren zwischen 3,535 Å in $[MnCl_2(3\text{-}CNpy)_2]_n$ und 3,599 Å in $[CoCl_2(3\text{-}CNpy)_2]_n$, sodass π-π-Wechselwirkungen auftreten.

Tabelle 4.1.1: Ausgewählte kristallographische Daten von $[MCl_2(3\text{-}CNpy)_2]_n$ mit M = Mn, Fe, Co, Ni und Cu.

Verbindung	**$[MnCl_2(3\text{-}CNpy)_2]_n$**	**$[FeCl_2(3\text{-}CNpy)_2]_n$**	**$[CoCl_2(3\text{-}CNpy)_2]_n$**
Literaturstelle	MH3	MH3	MH3
CSD Refcode	JOWYOM	JOXFAG	JOXDIM
Strukturbestimmung erfolgte aus	Pulverdaten	Pulverdaten	Pulverdaten
Summenformel	$C_{12}H_8Cl_2MnN_4$	$C_{12}H_8Cl_2FeN_4$	$C_{12}H_8Cl_2CoN_4$
Kristallsystem	monoklin	monoklin	monoklin
Raumgruppe (Nr.)	*P* 2₁/*c* (14)	*P* 2₁/*c* (14)	*C c* (9)
***a* /Å**	3,7030(4)	3,6440(2)	3,6186(2)
***b* /Å**	15,4310(4)	13,8135(8)	27,504(2)
***c* /Å**	11,5780(3)	13,1192(11)	13,2081(12)
***α* /°**	90	90	90
***ß* /°**	91,438(2)	98,532(7)	97,49(2)
***γ* /°**	90	90	90
***V* /Å³**	661,3(6)	653,0(8)	1302,6(9)
Z, Z'	2, ½	2, ½	4, 1
Lagesymmetrie von M	$\bar{1}$	$\bar{1}$	1
T /K	298	298	298
Strahlungsart	Cu $K\alpha_1$	Mo $K\alpha_1$	Mo $K\alpha_1$
Wellenlänge /Å	1,5406	0,70930	0,70930

Verbindung	**$[NiCl_2(3\text{-}CNpy)_2]_n$**	**$[CuCl_2(3\text{-}CNpy)_2]_n$**	**$[CuCl_2(3\text{-}CNpy)_2]_n$**
Literaturstelle	MH3	MH3	[8]
CSD Refcode	BUHVOS	UTIHAH01	UTIHAH
Strukturbestimmung erfolgte aus	Pulverdaten	Pulverdaten	Einkristalldaten
Summenformel	$C_{12}H_8Cl_2N_4Ni$	$C_{12}H_8Cl_2CuN_4$	$C_{12}H_8Cl_2CuN_4$
Kristallsystem	monoklin	monoklin	monoklin
Raumgruppe (Nr.)	*C c* (9)	*P* 2₁/*c* (14)	*P* 2₁/*c* (14)
***a* /Å**	3,5837(3)	3,7560(1)	3,710(2)
***b* /Å**	27,2889(3)	13,4653(3)	13,420(4)
***c* /Å**	13,1815(3)	13,0443(5)	12,987(2)
***α* /°**	90	90	90
***ß* /°**	97,715(4)	97,347(3)	97,48 *
***γ* /°**	90	90	90
***V* /Å³**	1277,4(2)	654,3(4)	641,0(9)
Z, Z'	4, 1	2, ½	2, ½
Lagesymmetrie von M	1	$\bar{1}$	$\bar{1}$
T /K	298	298	123
Strahlungsart	Cu $K\alpha_1$	Cu $K\alpha_1$	Mo $K\alpha$
Wellenlänge /Å	1,5406	1,5406	0,71073
***** Für *β* liegt keine Fehlerangabe vor.			

In allen Kristallstrukturen der $[MCl_2(3\text{-}CNpy)_2]_n$-Serie sind die Ketten fischgrätenartig angeordnet (Abb. 4.1.2 und 4.1.3). $[CoCl_2(3\text{-}CNpy)_2]_n$ und $[NiCl_2(3\text{-}CNpy)_2]_n$ sind isostrukturell und kristallisieren in der monoklinen Raumgruppe *C c* mit vier Formeleinheiten pro Elementarzelle (*Z* = 4). Folglich befinden sich alle Atome auf allgemeiner Lage, d.h. ihre Lagesymmetrie ist 1.

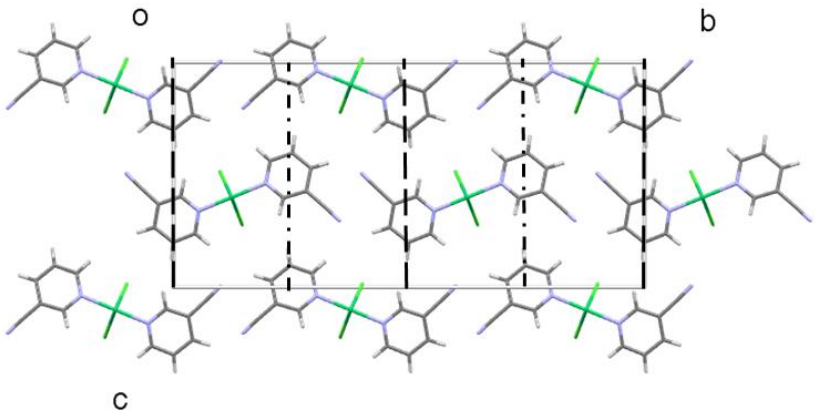

$[NiCl_2(3\text{-}CNpy)_2]_n$

Abbildung 4.1.2: Fischgrätenmotiv und Symmetrieelemente in $[NiCl_2(3\text{-}CNpy)_2]_n$, RG *C c*. Projektionsrichtung [010].

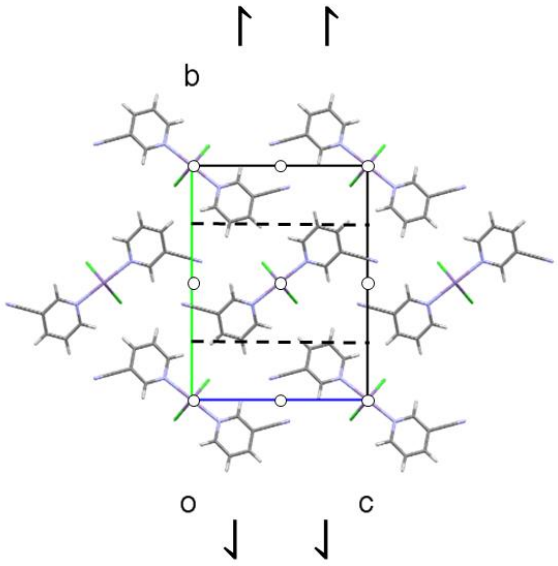

$[MnCl_2(3\text{-}CNpy)_2]_n$

Abbildung 4.1.3: Fischgrätenmotiv und Symmetrieelemente in $[MnCl_2(3\text{-}CNpy)_2]_n$, RG $P\,2_1/c$. Projektionsrichtung [100].

In diesen beiden Kristallstrukturen ist jede zweite Kette um *a*/2 entlang [010] verschoben, was in einer AABBAA… Stapelabfolge resultiert (Abb. 4.1.4 links). Hingegen liegt in $[FeCl_2(3\text{-}CNpy)_2]_n$, $[MnCl_2(3\text{-}CNpy)_2]_n$ sowie $[CuCl_2(3\text{-}CNpy)_2]_n$ keine derartige Verschiebung vor, sodass die Ketten uniform (also in AAA… Motiv) entlang [010] stapeln (Abb. 4.1.4 rechts).

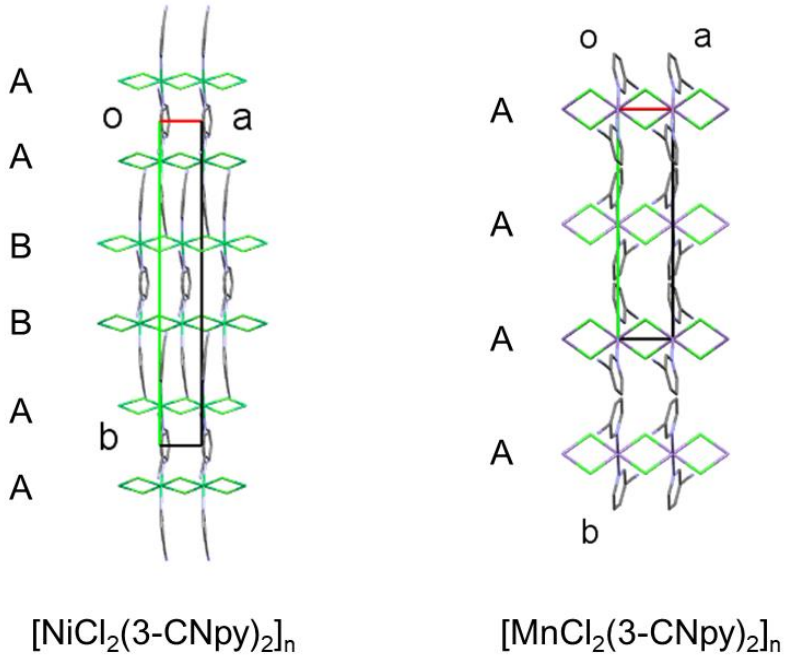

$[NiCl_2(3\text{-}CNpy)_2]_n$ $[MnCl_2(3\text{-}CNpy)_2]_n$

Abbildung 4.1.4: Packungsmuster mit Stapelabfolge entlang [010] in $[NiCl_2(3\text{-}CNpy)_2]_n$ (links) und $[MnCl_2(3\text{-}CNpy)_2]_n$ (rechts). Projektionsrichtung [001].

Die drei genannten Verbindungen kristallisieren in der monoklinen Raumgruppe *P* $2_1/c$ mit *Z* = 2. $[FeCl_2(3\text{-}CNpy)_2]_n$ ist zudem isotyp zu $[CuCl_2(3\text{-}CNpy)_2]_n$. Die Packung von $[MnCl_2(3\text{-}CNpy)_2]_n$ unterscheidet sich hingegen deutlich von den übrigen Strukturen (vgl. Abb. 4.1.4 bzw. 4.1.5). Wegen *Z* = 2 sind spezielle Lagen zu besetzen und in den drei genannten Strukturen befinden sich alle Metallatome auf Lagen mit $\bar{1}$ Symmetrie. Alle übrigen Atome befinden sich auf allgemeinen Lagen (Lagesymmetrie 1).

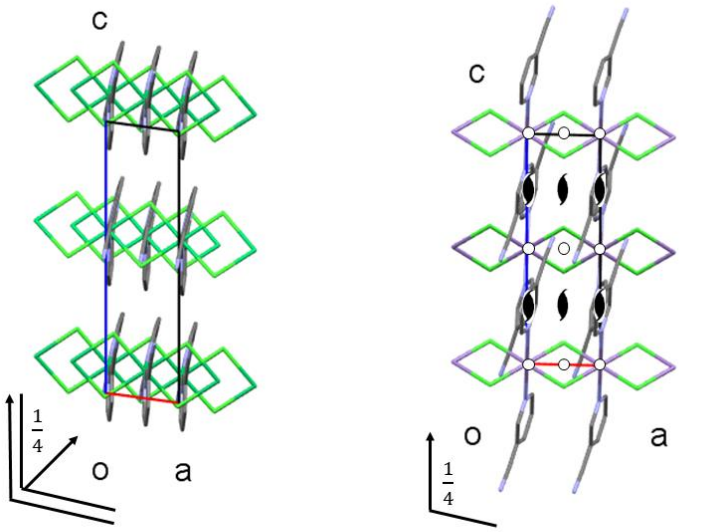

$[NiCl_2(3\text{-}CNpy)_2]_n$ $[MnCl_2(3\text{-}CNpy)_2]_n$

Cc $P2_1/c$

Abbildung 4.1.5: Packungsmuster und Symmetrieelemente in $[NiCl_2(3\text{-}CNpy)_2]_n$ (links) und $[MnCl_2(3\text{-}CNpy)_2]_n$ (rechts). Projektionsrichtung [010].

In allen Strukturen der $[MCl_2(3\text{-}CNpy)_2]_n$-Serie packen die 3-CNpy-Liganden stets leicht schief bezüglich der Ketten, sodass die Pyridin-Ringebene (also die durch das C_5N_{py}-Ringfragment aufgespannte Ebene) einen Winkel zwischen 84,3° (für Co) und 88,3° (für Mn) mit ihrer Ankerkette (also die durch das $[MCl_4]$-Kettenfragment aufgespannte Ebene) bildet. Folglich weisen alle Strukturen ein monoklines Gitter auf.

4.1.2 $[ZnCl_2(3\text{-}CNpy)_2]$

Im Gegensatz zu den zuvor diskutierten Verbindungen bildet $[ZnCl_2(3\text{-}CNpy)_2]$ keine Kettenstruktur. Stattdessen liegen diskrete Komplexmoleküle vor, in denen die Zn-Atome jeweils von zwei Cl-Atomen und zwei N_{py}-Atomen nahezu tetraedrisch koordiniert werden (Abb. 4.1.6). Diese Koordinationsgeometrie ist typisch für Metallatome mit einer vollständigen d^{10}-Valenzschale und findet sich ebenfalls in der verwandten Br-Verbindung $[ZnBr_2(3\text{-}CNpy)_2]$ (siehe Kapitel 4.7) sowie in $[ZnCl_2(4\text{-}CNpy)_2]$ und $[ZnCl_2(py)_2]$ (CYPYZN, ZNPYRC01).

Die Kristallstrukturen der beiden Polymorphe von $[ZnCl_2(3\text{-}CNpy)_2]$ zeigen jede für sich ein eigentümliches Packungsmuster. In α-$[ZnCl_2(3\text{-}CNpy)_2]$ formen die Moleküle, von außen betrachtet, aufgrund der abständigen CNpy-Fragmente eine Art Chips, die entlang [100] gestapelt werden (Abb. 4.1.6c). Die Moleküle stapeln jedoch leicht versetzt, sodass etwaige die Packung stabilisierende π-π-Wechselwirkungen nahezu ausbleiben.

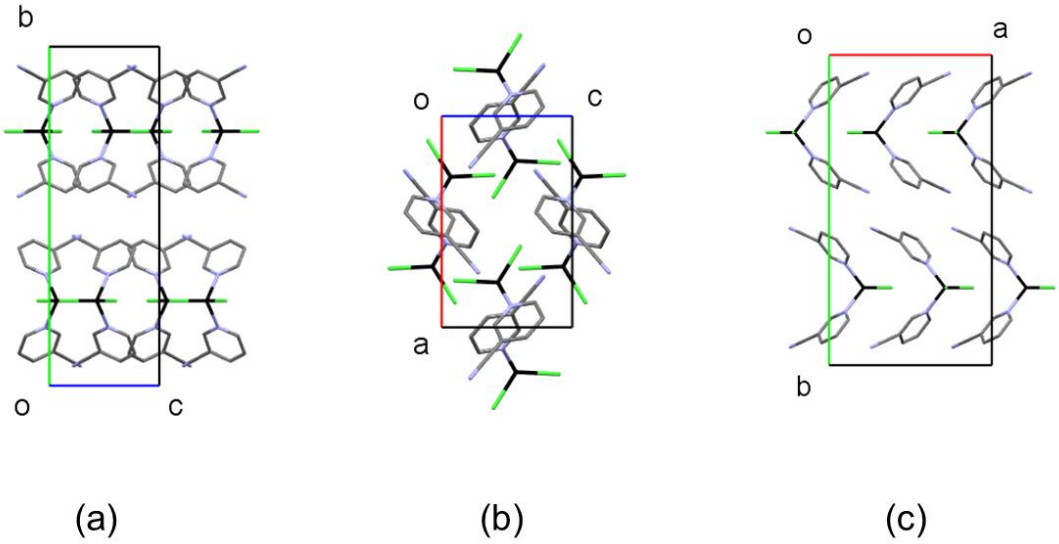

Abbildung 4.1.6: Packungsmuster in α-$[ZnCl_2(3\text{-}CNpy)_2]$. Projektionsrichtung [100] in (a), [010] in (b) und [001] in (c).

Anders verhält sich es in der Kristallstruktur von β-$[ZnCl_2(3\text{-}CNpy)_2]$, in der π-π-Interaktionen zwischen benachbarten CNpy-Liganden gleich durch zwei unabhängige Symmetrieoperationen erzeugt werden. Die eine Hälfte wird durch die *c*-Gleitung entlang [001] gestapelt (gelb eingefärbt in Abb. 4.1.7), ihr Ring-zu-Ring-Abstand (gemessen über die C_5N_{py}-Mitten) beträgt ca. 4,0 Å. Die andere Hälfte ist über Inversionszentren zu Paaren verknüpft (lila eingefärbt in Abb. 4.1.7). Hier beträgt der Ring-zu-Ring-Abstand (gemessen über die C_5N_{py}-Ebenen) ca. 3,53 Å und ist vergleichbar mit den Abständen benachbarter Pyridin-Liganden in den übrigen Strukturen der $[MCl_2(3\text{-}CNpy)_2]_n$-Serie. Aus energetischer Perspektive ist die Packung in β-$[ZnCl_2(3\text{-}CNpy)_2]$ also günstiger als die der α-Phase (und auch geringfügig dichter mit 1,616 g/cm^3 für β gegenüber 1,59 g/cm^3 für α), sodass α-$[ZnCl_2(3\text{-}CNpy)_2]$ bereits binnen weniger Stunden in die thermodynamisch stabilere β-Phase zu übergehen vermag.

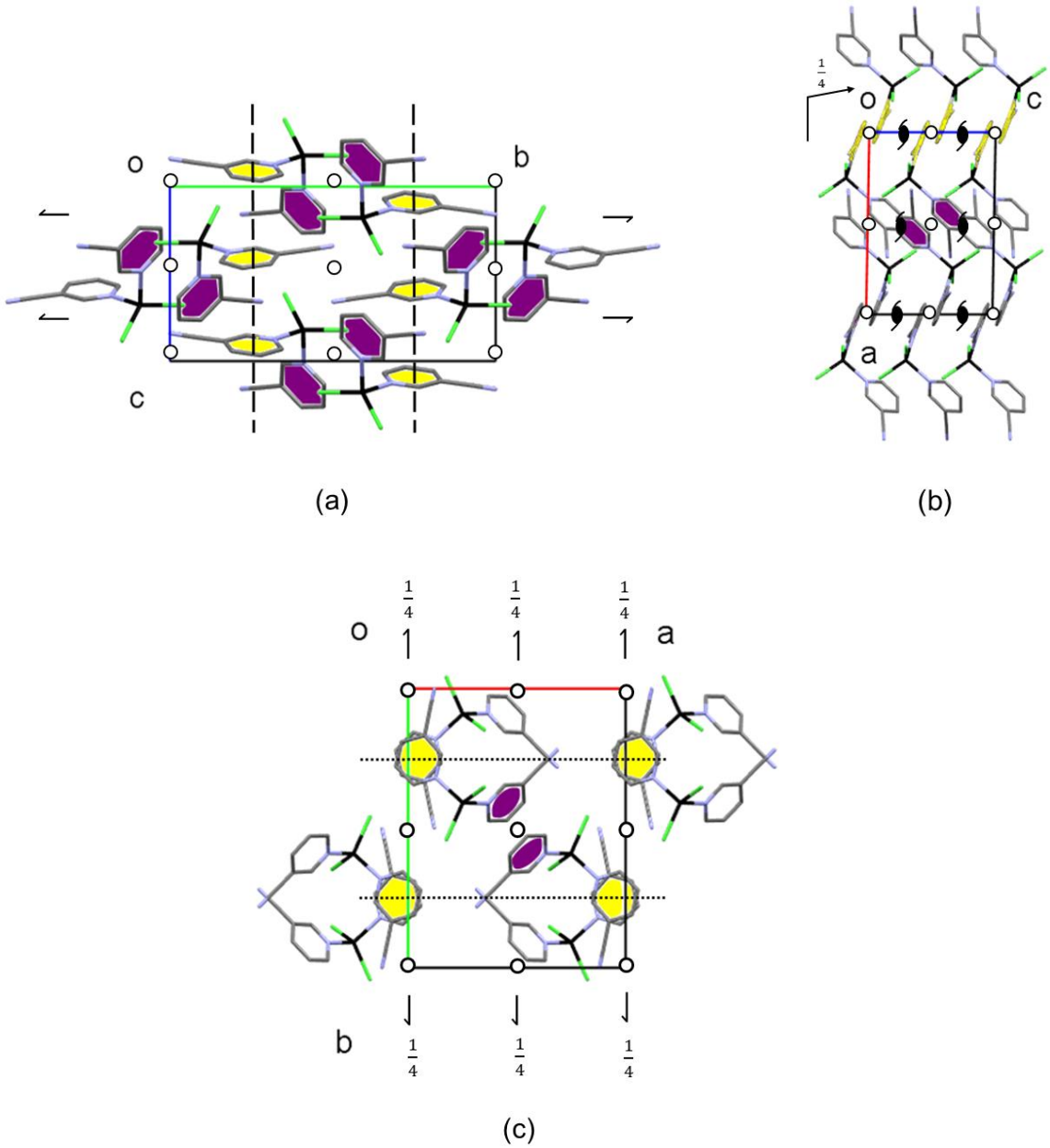

Abbildung 4.1.7: Packungsmuster und Symmetrieelemente in β-[$ZnCl_2$(3-CNpy)$_2$]. Projektionsrichtung [100] in (a), [010] in (b) und [001] in (c). Die Struktur enthält zwei kristallographisch unabhängige 3-CNpy-Liganden (gelb bzw. lila eingefärbt).

Tabelle 4.1.2: Ausgewählte kristallographische Daten von $[ZnCl_2(3\text{-}CNpy)_2]$.

Verbindung	**α-$[ZnCl_2(3\text{-}CNpy)_2]$**	**β-$[ZnCl_2(3\text{-}CNpy)_2]$**
Literaturstelle	MH3	MH3
CSD Refcode	BUHVUY	BUHVUY01
Strukturbestimmung erfolgte aus	Pulverdaten	Pulverdaten
Summenformel	$C_{12}H_8Cl_2N_4Zn$	$C_{12}H_8Cl_2N_4Zn$
Kristallsystem	orthorhombisch	monoklin
Raumgruppe (Nr.)	*Pnma* (62)	$P\,2_1/c$ (14)
***a* /Å**	10,6653(3)	11,6619(15)
***b* /Å**	20,3998(5)	15,0731(18)
***c* /Å**	6,6114(17)	8,0572(10)
***α* /°**	90	90
***ß* /°**	90	91,0112(9)
***γ* /°**	90	90
***V* /Å³**	1438,4(6)	1416,0(7)
Z, Z'	4, ½	4, 1
Lagesymmetrie von M	*.m.*	1
T /K	298	298
Strahlungsart	Cu $K\alpha_1$	Cu $K\alpha_1$
Wellenlänge /Å	1,5406	1,5406

4.2 $[MCl_2(3\text{-}CNpy)_1]_n$

Der synthetische Zugang zu Verbindungen der Stöchiometrie $[MCl_2(3\text{-}CNpy)_1]_n$ erfolgte durch Tempern der Ausgangsverbindungen $[MCl_2(3\text{-}CNpy)_2]_n$. Durch gezielten thermischen Abbau konnten für M = Mn, Fe, Co, Ni und Cu die entsprechenden $[MCl_2(3\text{-}CNpy)_1]_n$-Verbindungen erhalten werden. Erhitzen von $[ZnCl_2(3\text{-}CNpy)_2]$ führte unmittelbar zur vollständigen Verflüchtigung des gebundenen Cyanopyridins ohne Bildung eines Intermediates. Von $[FeCl_2(3\text{-}CNpy)_1]_n$ konnte noch keine Kristallstruktur bestimmt werden, da die Qualität der Pulverprobe bzw. der Röntgenpulverdaten bislang mangelhaft war.

Wichtige kristallographische Daten und Ergebnisse der Strukturverfeinerungen von $[MCl_2(3\text{-}CNpy)_1]_n$-Verbindungen sind in Tabelle 4.2 aufgeführt. Weitere Ergebnisse sind im Detail in Publikation MH3 nachzulesen.

In allen Kristallstrukturen werden die Metallatome von jeweils fünf Cl-Atomen und einem N_{py}-Atom koordiniert, sodass Oktaeder aus MCl_5N_{py}-Einheiten aufgespannt werden. Die MCl_5N_{py}-Oktaeder sind über zwei μ_2-Cl-Atome und drei μ_3-Cl-Atome zu Doppelketten verknüpft (Abb. 4.2.1). Das Doppelkettenmotiv ist das charakteristische Strukturmerkmal der $[MCl_2(3\text{-CNpy})_1]_n$-Serie, welches zuvor einzig in beiden Polymorphen von $[CuCl_2(4\text{-CNpy})_1]_n$ beobachtet wurde (vgl. MH1). Bei den hier aufgeführten vier Kristallstrukturen handelt es sich somit um die ersten Verbindungen mit 3-CNpy als Ligand, die dieses Doppelkettenmuster zeigen.

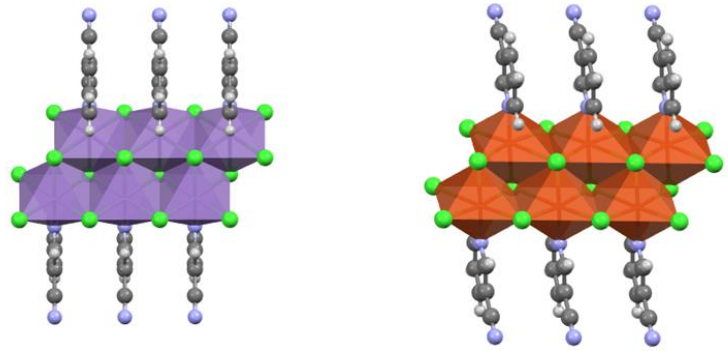

$[MnCl_2(3\text{-CNpy})_1]_n$ $[CuCl_2(3\text{-CNpy})_1]_n$

Abbildung 4.2.1: Polyederdarstellung eines Doppelkettenausschnitts von $[MnCl_2(3\text{-CNpy})_1]_n$ (links) und $[CuCl_2(3\text{-CNpy})_2]_n$ (rechts).

Plastisch lässt sich die Bildung solcher Doppelketten als Fusion zweier Einzelketten der Vorläuferverbindung $[MCl_2(3\text{-CNpy})_2]_n$ nachvollziehen. Beim Tempern von $[MCl_2(3\text{-CNpy})_2]_n$ wird pro Formeleinheit einer Kette, bzw. pro Metallatom, eines der beiden gebundenen 3-Cyanopyridinmoleküle ausgetrieben. Die freiwerdende Koordinationsstelle des Metallatoms einer Kette wird dann von einem Cl-Atom einer anderen Kette belegt, wodurch die Koordinationsoktaeder der Metallatome zusätzlich über Kanten verknüpft werden. Die Metallatome der Doppelketten sind also nunmehr von fünf Cl-Atomen, d.h. zwei μ_2- und drei μ_3-Atomen umgeben. Die sechste Koordinationsstelle wird von dem verbliebenen 3-CNpy-Liganden belegt, der weiterhin terminal mit seinem N_{py}-Atom an das Metall koordiniert.

Auch in allen Kristallstrukturen der $[MCl_2(3\text{-CNpy})_1]_n$-Serie sind die Doppelketten fischgrätenartig angeordnet (Abb. 4.2.2). Die Strukturen von $[MnCl_2(3\text{-CNpy})_1]_n$, $[CoCl_2(3\text{-CNpy})_1]_n$ und $[NiCl_2(3\text{-CNpy})_1]_n$ sind isotyp und kristallisieren in der

orthorhombischen Raumgruppe *P nma* mit *Z* = 4. Die Doppelketten laufen entlang [010], sodass hier die Gitterkonstante *b* den Metall-Metall-Abstand angibt. Da in den orthorhombischen Strukturen $\beta = 90°$ ist, stehen die Pyridinliganden (exakt) senkrecht auf den Ketten. Benachbarte Pyridinliganden einer Kette sind planparallel, sodass ihr Abstand ebenfalls *b* entspricht. Alle Atome liegen auf Spiegelebenen *m* und auch die Metallatome besetzen Lagen mit *.m.* Symmetrie. Zusammen mit *n*- und *a*-Gleitspiegelebenen senkrecht zu *m*, wird die Raumgruppe *P* $2_1/n$ $2_1/m$ $2_1/a$ (also *P nma*) aufgebaut (Abb. 4.2.2 unten und 4.2.3 rechts).

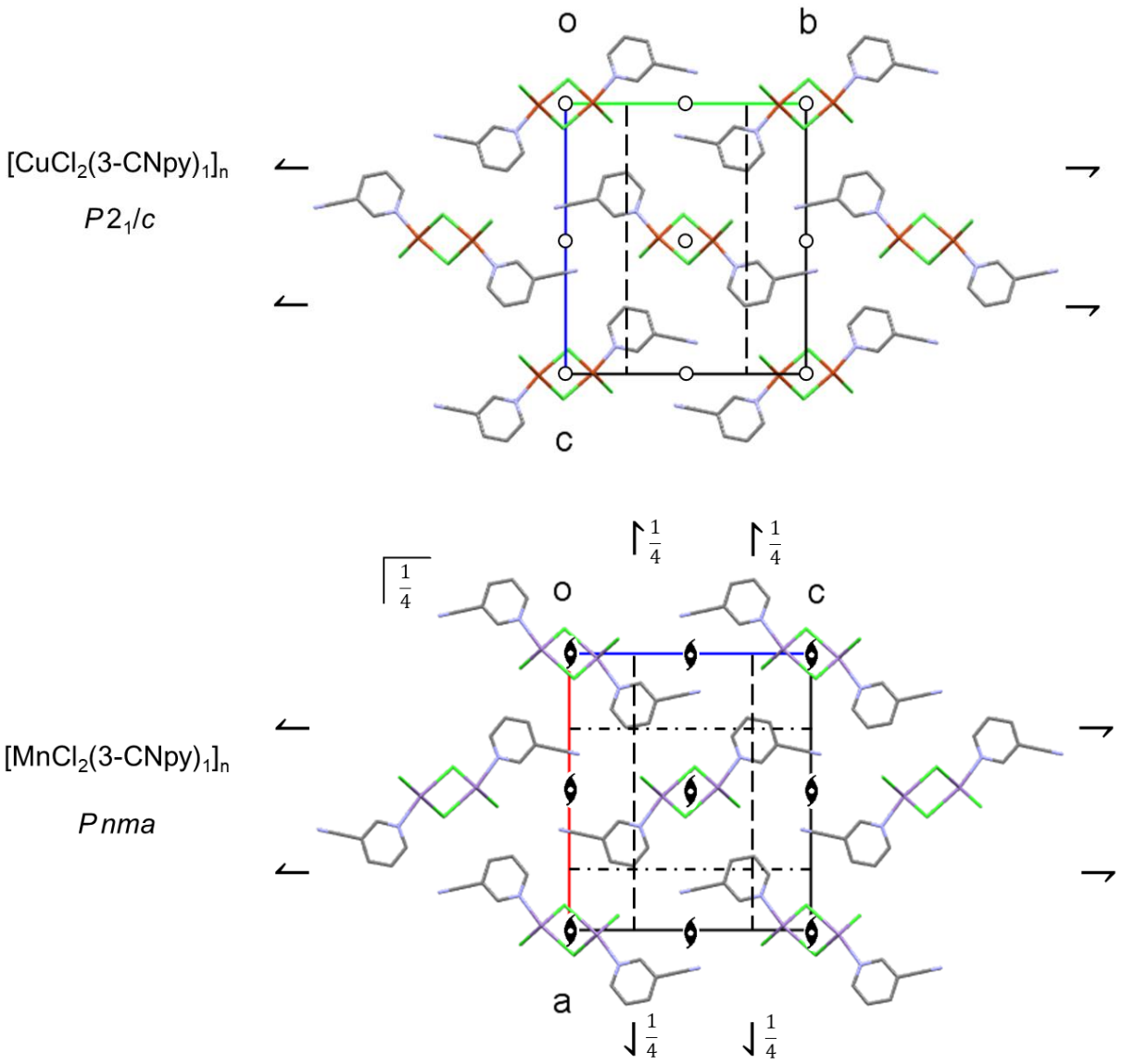

Abbildung 4.2.2: Fischgrätenmotiv und Symmetrieelemente in $[CuCl_2(3\text{-}CNpy)_1]_n$ (oben) mit Projektionsrichtung [100] und $[MnCl_2(3\text{-}CNpy)_1]_n$ (unten) mit Projektionsrichtung [010]. Hinweis: $[CuCl_2(3\text{-}CNpy)_1]_n$ ist in der Standardaufstellung *P* $2_1/c$ abgebildet.

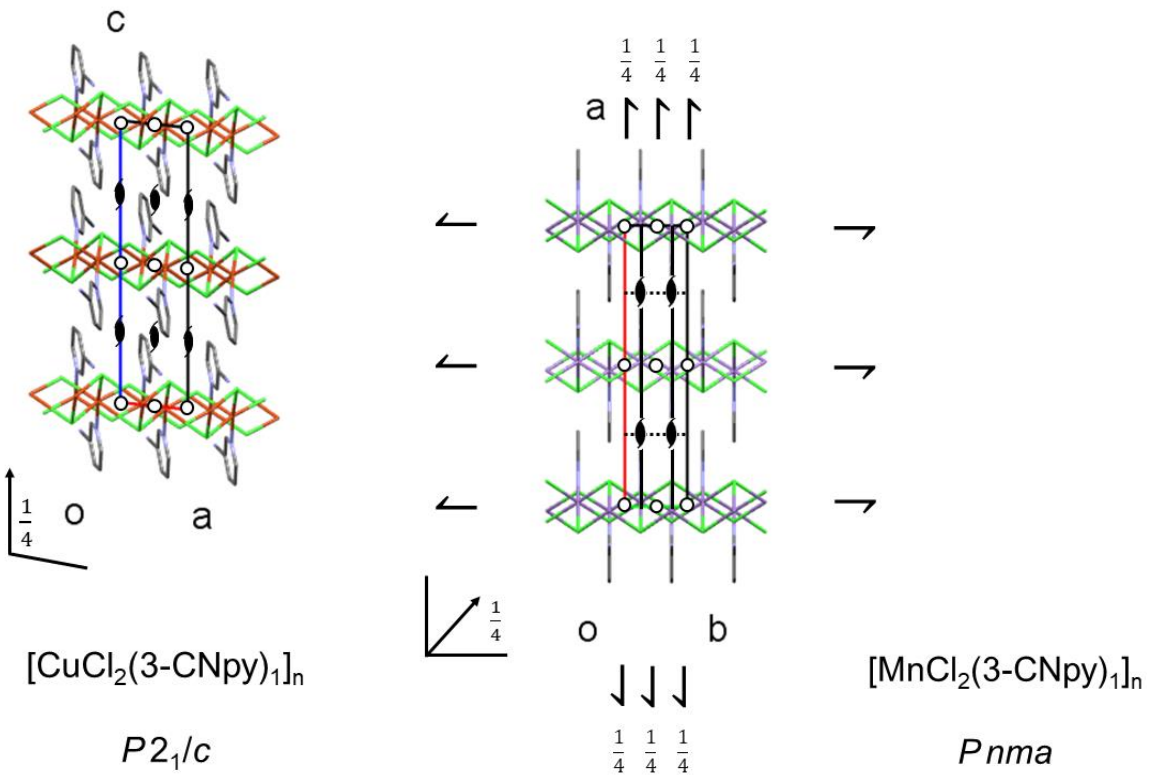

Abbildung 4.2.3: Packungsmuster und Symmetrieelemente in $[CuCl_2(3\text{-}CNpy)_2]_n$ (links) mit Projektionsrichtung [010], und $[MnCl_2(3\text{-}CNpy)_2]_n$ (rechts) mit Projektionsrichtung [001].

Die Kristallstruktur von $[CuCl_2(3\text{-}CNpy)_1]_n$ ist ähnlich zu den genannten drei Strukturen. Benachbarte Pyridinliganden einer Kette sind ebenfalls planparallel ausgerichtet, allerdings stehen diese nicht senkrecht auf den Ketten, sodass $\beta \neq 90°$, also das Gitter monoklin wird (vgl. Abb. 4.2.4). Dadurch fallen die Spiegelebenen weg und alle Atome befinden sich in $[CuCl_2(3\text{-}CNpy)_1]_n$ auf allgemeiner Lage (siehe Abb. 4.2.2 oben und Abb. 4.2.3 links). Die Symmetrie wird ausgehend von *P* $2_1/n$ $2_1/m$ $2_1/a$ um den Faktor 2 auf die maximale Untergruppe *P* 1 1 $2_1/a$ reduziert (Nicht-Standardaufstellung von *P* 1 $2_1/c$ 1).

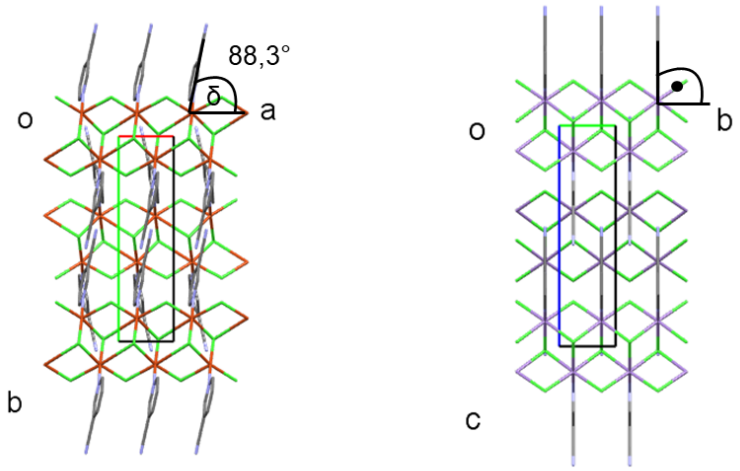

$[CuCl_2(3\text{-}CNpy)_1]_n$ $[MnCl_2(3\text{-}CNpy)_1]_n$

$P2_1/c$ $Pnma$

Abbildung 4.2.4: Packungsmuster in $[MnCl_2(3\text{-}CNpy)_2]_n$ (links) mit Projektionsrichtung [100] und $[CuCl_2(3\text{-}CNpy)_2]_n$ (rechts) mit Projektionsrichtung [001]. In $[MnCl_2(3\text{-}CNpy)_2]_n$ stehen alle 3-CNpy-Liganden senkrecht von ihrer Doppelkette ab.

Tabelle 4.2: Ausgewählte kristallographische Daten von $[MCl_2(3\text{-}CNpy)_1]_n$ mit M = Mn, Co, Ni und Cu.

Verbindung	**$[MnCl_2(3\text{-}CNpy)_1]_n$**	**$[CoCl_2(3\text{-}CNpy)_1]_n$**	**$[NiCl_2(3\text{-}CNpy)_1]_n$**	**$[CuCl_2(3\text{-}CNpy)_1]_n$**
Literaturstelle	MH3	MH3	MH3	MH3
CSD Refcode	JOXFAG	JOWYUS	JOXFEK	JOWZAZ
Struktur bestimmt aus	Pulverdaten	Pulverdaten	Pulverdaten	Pulverdaten
Summenformel	$C_6H_4Cl_2MnN_2$	$C_6H_4Cl_2CoN_2$	$C_6H_4Cl_2N_2Ni$	$C_6H_4Cl_2CuN_2$
Kristallsystem	monoklin	orthorhombisch	orthorhombisch	monoklin
Raumgruppe (Nr.)	*Pnma* (62)	*Pnma* (62)	*Pnma* (62)	*P*2₁/*c* (14)
***a* /Å**	16,5338(9)	16,0863(5)	15,9027(4)	3,77530(8)
***b* /Å**	3,6933(12)	3,5874(10)	3,5328(6)	13,9311(4)
***c* /Å**	14,4596(9)	14,1910(5)	14,0807(4)	15,6849(3)
***α* /°**	90	90	90	90
***ß* /°**	90	90	90	96,114(3)
***γ* /°**	90	90	90	90
***V* /Å³**	882,96(3)	818,9(1)	791,0(5)	820,2(4)
Z, Z'	4, ½	4, ½	4, ½	4, 1
Lagesymmetrie von M	*.m.*	*.m.*	*.m.*	1
T /K	298	298	298	298
Strahlungsart	Mo $K\alpha_1$	Mo $K\alpha_1$	Cu $K\alpha_1$	Cu $K\alpha_1$
Wellenlänge /Å	0,70930	0,70930	1,5406	1,5406

4.3 $[MCl_2(4\text{-}CNpy)_2]_n$

Alle Verbindungen der $[MCl_2(4\text{-}CNpy)_2]_n$-Serie konnten über Reaktionen des jeweiligen Chlorids MCl_2 mit 4-Cyanopyridin in alkoholischer Lösung synthetisiert werden. Wie eingangs bei der $[MCl_2(3\text{-}CNpy)_2]_n$-Serie (Kap. 4.1) berichtet, endeten auch hier sämtliche Versuchsansätze in der Bildung von Phasen mit einem Metall-zu-Ligand-Verhältnis von 1:2. Verbindungen der allgemeinen Zusammensetzung $[MCl_2(CNpy)_{x>2}]_{(n)}$ scheinen also ohne weiteres nicht zugänglich zu sein.

Die Kristallstrukturen von $[MnCl_2(4\text{-}CNpy)_2]_n$ (NESYUF), $[CoCl_2(4\text{-}CNpy)_2]_n$, (UTIHIP), $[CuCl_2(4\text{-}CNpy)_2]_n$, (NESYOZ) und $[ZnCl_2(4\text{-}CNpy)_2]$ (CYPYZN) waren bereits aus Einkristalldaten bekannt. In vorherigen Arbeiten des Arbeitskreises konnten außerdem die Abbaustufen $[MnCl_2(4\text{-}CNpy)_1]_n$ und $[CuCl_2(4\text{-}CNpy)_1]_n$ strukturell charakterisiert werden (siehe MH1). Für die vorliegende Arbeit standen daher noch die Strukturbestimmungen aus Pulverdaten von $[CoCl_2(4\text{-}CNpy)_2]_n$ und $[FeCl_2(4\text{-}CNpy)_2]_n$, sowie deren Abbaustufen $[CoCl_2(4\text{-}CNpy)_1]_n$ und $[FeCl_2(4\text{-}CNpy)_1]_n$ (siehe Kap. 4.4) aus.

Wichtige kristallographische Daten und Ergebnisse der Strukturverfeinerungen von $[MCl_2(4\text{-}CNpy)_2]_n$-Verbindungen sind in Tabelle 4.3 aufgeführt. Weitere Ergebnisse sind im Detail in den Publikationen MH1 und MH4 nachzulesen.

In allen Kristallstrukturen werden die Metallatome von jeweils vier Cl-Atomen und zwei N_{py}-Atomen koordiniert, sodass Oktaeder aus MCl_4N_{py2}-Einheiten aufgespannt werden. Die Cl-Atome fungieren als μ_2-Brückenliganden, die die MCl_4N_{py2}-Oktaeder eckenverknüpfen. Dadurch entstehen Ketten, welche in den Kristallstrukturen der $[MCl_2(4\text{-}CNpy)_2]_n$-Serie bei der in Tab. 4.3 gewählten Zellaufstellung entlang [001] laufen (Abb. 4.3.1b). Der Metall-Metall-Abstand innerhalb einer Kette findet sich somit in der Gitterkonstanten *c* wieder.

Die Abstände bzw. *c* verringern sich von 3,700(2) Å für Mn auf 3,5890(1) Å für Ni, analog zur korrespondieren $[MCl_2(3\text{-}CNpy)_2]_n$-Serie (vgl. Tab. 4.3 mit Tab. 4.1.1). In $[CuCl_2(4\text{-}CNpy)_2]_n$ sind die $CuCl_4N_{py2}$-Koordinationsoktaeder aufgrund der d^9-Konfiguration des Cu-Atoms in Kettenrichtung gestreckt, sodass der längere Cu-Cu-Abstand bzw. *c* mit 3,779(2) Å auffällt.

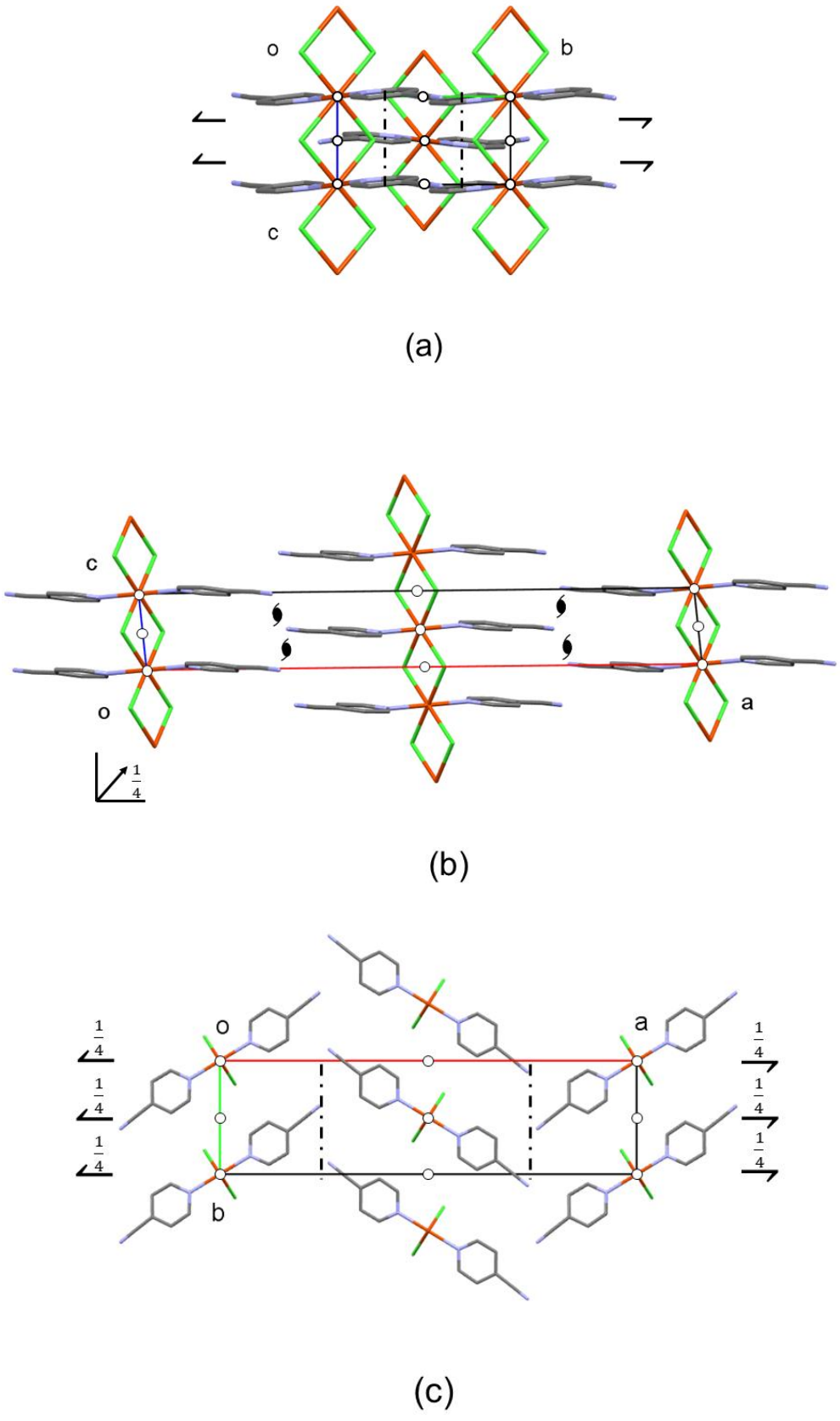

Abbildung 4.3.1: Packungsmuster und Symmetrieelemente in $[FeCl_2(4\text{-}CNpy)_2]_n$, RG $P2_1/n$. Projektionsrichtung in (a): [100], in (b): [010], in (c): [001].

Erwartungsgemäß sind benachbarte Cyanopyridin-Fragmente einer Kette planparallel angeordnet (Abb. 4.3.1a/b). Die Interplanar-Abstände der Ebenen der C_5N_{py}-Ringfragmente variieren zwischen 3,373 Å in $[NiCl_2(4\text{-}CNpy)_2]_n$ und 3,579 Å in $[FeCl_2(4\text{-}CNpy)_2]_n$, sodass π-π-Wechselwirkungen auftreten können.

Auch in allen Kristallstrukturen der $[MCl_2(4\text{-}CNpy)_2]_n$-Serie sind die Ketten fischgrätenartig angeordnet, wobei die Gitterkonstante *b* stets den Abstand benachbarter, paralleler Ketten angibt (Abb. 4.3.1c). Alle Verbindungen sind isotyp und kristallisieren in der Raumgruppe *P* $2_1/n$ (bzw. *P* $2_1/c$, aber von der Standardaufstellung nach *P* $2_1/n$ transformiert) mit *Z* = 2. Die Kristallstrukturen von $[MnCl_2(4\text{-}CNpy)_2]_n$, $[FeCl_2(4\text{-}CNpy)_2]_n$ und $[CuCl_2(4\text{-}CNpy)_2]_n$ sind außerdem isotyp zu ihren 3-CNpy-Analoga (also zu $[MnCl_2(3\text{-}CNpy)_2]_n$, $[FeCl_2(3\text{-}CNpy)_2]_n$ und $[CuCl_2(3\text{-}CNpy)_2]_n$). Folglich belegen die Metallatome spezielle Lagen mit $\bar{1}$ Symmetrie. Die übrigen Atome befinden sich auf allgemeinen Lagen (Lagesymmetrie 1). Wie auch in allen Strukturen der $[MCl_2(3\text{-}CNpy)_2]_n$-Reihe (siehe Kapitel 4.1), packen die 4-CNpy-Liganden stets leicht schief bezüglich der Ketten, und die C_5N_{py}-Ebenen bilden einen Winkel zwischen 83,2° (in $[MnCl_2(4\text{-}CNpy)_2]_n$) und 88,6° (in $[CuCl_2(4\text{-}CNpy)_2]_n$) mit ihrer Ankerkette (also die durch das $[MCl_4]$-Kettenfragment aufgespannte Ebene). Somit werden grundsätzlich in allen polymeren Verbindungen der Stöchiometrie $[MCl_2(CNpy)_2]_n$ monokline Gitter ausgebildet.

Tabelle 4.3: Ausgewählte kristallographische Daten von $[MCl_2(4\text{-}CNpy)_2]_n$ mit M = Mn, Fe, Co, Ni und Cu.

Verbindung	**$[MnCl_2(4\text{-}CNpy)_2]_n$ ***	**$[FeCl_2(4\text{-}CNpy)_2]_n$**	**$[CoCl_2(4\text{-}CNpy)_2]_n$ ***
Literaturstelle	[47]	MH4	[8]
CSD Refcode	NESYUF	ZUDZUF	UTIHIP
Strukturbestimmung erfolgte aus	Einkristalldaten	Pulverdaten	Einkristalldaten
Summenformel	$C_{12}H_8Cl_2MnN_4$	$C_{12}H_8Fe_2FeN_4$	$C_{12}H_8Cl_2CoN_4$
Kristallsystem	monoklin	monoklin	monoklin
Raumgruppe (Nr.)	*P* $2_1/n$ (14)	*P* $2_1/n$ (14)	*P* $2_1/n$ (14)
***a* /Å**	26,640(5)	26,5605(10)	26,4959(3)
***b* /Å**	7,198(2)	7,1868(2)	7,15642(12)
***c* /Å**	3,700(2)	3,66280(7)	3,6288(4)
***α* /°**	90	90	90
***ß* /°**	95,85(4)	95,365(3)	94,465(5)
***γ* /°**	90	90	90
***V* /Å³**	705,8(4)	696,11(4)	686,02(18)

Z, Z'	2, ½	2, ½	2, ½
Lagesymmetrie von M	$\bar{1}$	$\bar{1}$	$\bar{1}$
T /K	294	298	293
Strahlungsart	Mo *Kα*	Cu $K\alpha_1$	Mo *Kα*
Wellenlänge /Å	0,71073	1,5406	0,71073
* Elementarzelle transformiert von *P* 2_1/*c* nach *P* 2_1/*n*, Transformationsmatrix (*P, p*):	*a*' = *a* + *c*, *b*' = *b*, *c*' = -*a*, 0, 0, 0		*a'* = -*a* - *c*, *b'* = *b*, *c'* = *a* 0, 0, 0

Verbindung	**$[CoCl_2(4\text{-}CNpy)_2]_n$ ***	**$[NiCl_2(4\text{-}CNpy)_2]_n$**	**$[CuCl_2(4\text{-}CNpy)_2]_n$**
Literaturstelle	MH4	MH1	[47]
CSD Refcode	UTIHIP02	LATKOJ	NESYOZ
Strukturbestimmung erfolgte aus	Pulverdaten	Pulverdaten	Einkristalldaten
Summenformel	$C_{12}H_8Cl_2CoN_4$	$C_{12}H_8Cl_2N_4Ni$	$C_{12}H_8Cl_2CuN_4$
Kristallsystem	monoklin	monoklin	monoklin
Raumgruppe (Nr.)	*P* 2_1/*n* (14)	*P* 2_1/*n* (14)	*P* 2_1/*n* (14)
***a* /Å**	26,4959(3)	26,4504(7)	3,779(2)
***b* /Å**	7,15642(12)	7,1667(2)	25,711(12)
***c* /Å**	3,6288(4)	3,5890(1)	7,104(4)
***α* /°**	90	90	90
***ß* /°**	94,465(5)	92,474(3)	95,98(4)
***γ* /°**	90	90	90
***V* /Å³**	686,02(18)	679,71(1)	686,48(4)
Z, Z'	2, ½	2, ½	2, ½
Lagesymmetrie von M	$\bar{1}$	$\bar{1}$	$\bar{1}$
T /K	298	298	294
Strahlungsart	Mo $K\alpha_1$	Cu $K\alpha_1$	Cu *Kα*
Wellenlänge /Å	0,70930	1,5406	1,54178
* Elementarzelle transformiert von *P* 2_1/*c* nach *P* 2_1/*n*, Transformationsmatrix (*P, p*):	*a'* = -*a* - *c*, *b'* = *b*, *c'* = *a* 0, 0, 0		

4.4 $[MCl_2(4\text{-}CNpy)_1]_n$

Thermischer Abbau von $[MCl_2(4\text{-}CNpy)_2]_n$ (bei M = Mn, Fe, Co, Ni und Cu) führt zur Bildung der Abbaustufen mit einem Metall-zu-Ligand-Verhältnis von 1:1. Aus der $[MCl_2(4\text{-}CNpy)_1]_n$-Reihe wurden im Rahmen von Bachelor- und Masterprojekten bereits die Verbindungen $[MnCl_2(4\text{-}CNpy)_1]_n$, $[CuCl_2(4\text{-}CNpy)_1]_n$ und $[NiCl_2(4\text{-}CNpy)_1]_n$ strukturell charakterisiert und gemeinsam mit weiteren Strukturen dieser Arbeit in MH1 publiziert. Für die vorliegende Arbeit fielen also noch die Strukturbestimmungen von $[CoCl_2(4\text{-}CNpy)_1]_n$ und $[FeCl_2(4\text{-}CNpy)_1]_n$ an.

Wichtige kristallographische Daten und Ergebnisse der Strukturverfeinerungen von $[MCl_2(4\text{-}CNpy)_2]_n$-Verbindungen sind in Tabelle 4.4 aufgeführt. Weitere Ergebnisse sind im Detail in den Publikationen MH1 und MH4 nachzulesen.

In allen Kristallstrukturen, ausgenommen $[CuCl_2(4\text{-}CNpy)_1]_n$, werden die Metallatome von jeweils vier Cl-Atomen, einem N_{py}- und einem N_{CN}-Atom eines zweiten 4-CNpy Liganden koordiniert. Die $MCl_4N_{py}N_{CN}$-Oktaeder sind durch verbrückende μ_2-Cl-Atome eckenverknüpft, wodurch in erster Dimension Ketten entstehen. Diese Ketten laufen entlang [010], sodass die Gitterkonstante *b* dem Metall-Metall-Abstand innerhalb dieser Verkettung entspricht (Abb. 4.4.2). Mit 3,6593(2) Å für Mn bzw. 3,5132(1) Å für Ni bewegt sich *b* im Rahmen der entsprechenden Gitterkonstanten aus der $[MCl_2(3\text{-}CNpy)_1]_n$-Reihe (vgl. Tab. 4.2 in Kapitel 4.2 mit Tab. 4.4).

Doch im Gegensatz zur $[MCl_2(3\text{-}CNpy)_1]_n$-Serie mit ihrem charakteristischen Doppelkettenmotiv weisen die Verbindungen $[MCl_2(4\text{-}CNpy)_1]_n$ (ausgenommen $[CuCl_2(4\text{-}CNpy)_1]_n$) netzartige Strukturen auf (siehe Abb. 4.4.1 auf der übernächsten Seite). Tatsächlich tritt 4-CNpy als bidentater Ligand in Erscheinung, der die Ketten über seine beiden N-Atome verknüpft. Somit handelt es sich um die ersten Kristallstrukturen der $[MCl_2(4\text{-}CNpy)_1]_n$-Serie, in denen 4-CNpy 3d-Übergangsmetallatome der 4. Periode verbrückt. Wie kommt es dazu?

Tabelle 4.4: Ausgewählte kristallographische Daten von $[MCl_2(4\text{-}CNpy)_1]_n$ mit M = Mn, Fe, Co, Ni und Cu.

Verbindung	**$[MnCl_2(4\text{-}CNpy)_1]_n$**	**$[FeCl_2(4\text{-}CNpy)_1]_n$**	**$[CoCl_2(4\text{-}CNpy)_1]_n$**
Literaturstelle	MH1	MH4	MH4
CSD Refcode	CIRTIJ	ZUDZOQ	ZUFCAH
Strukturbestimmung erfolgte aus	Pulverdaten	Pulverdaten	Pulverdaten
Summenformel	$C_6H_4Cl_2MnN_2$	$C_6H_4Cl_2FeN_2$	$C_6H_4Cl_2CoN_2$
Kristallsystem	monoklin	monoklin	monoklin
Raumgruppe (Nr.)	*P* 2/*m* (10)	*P m* (6)	*P m* (6)
***a* /Å**	12,0318(9)	7,6656(8)	7,7426(4)
***b* /Å**	3,6493(2)	3,57945(15)	3,57685(7)
***c* /Å**	9,8938(6)	7,7986(10)	7,6901(4)
***α* /°**	90	90	90
***ß* /°**	90,808(15)	102,157(3)	102,664(2)
***γ* /°**	90	90	90
***V* /Å³**	434,25(4)	209,18(4)	207,790(16)
Z, Z'	2, 1	1, ½	1, ½
Lagesymmetrie von M	*m*	*m*	*m*
T /K	298	298	523
Strahlungsart	Mo $K\alpha_1$	Cu $K\alpha_1$	Mo $K\alpha_1$
Wellenlänge /Å	0,70930	1,54056	0,70930

Verbindung	**$[NiCl_2(4\text{-}CNpy)_1]_n$**	**α-$[CuCl_2(4\text{-}CNpy)_1]_n$**	**β-$[CuCl_2(4\text{-}CNpy)_1]_n$**
Literaturstelle	MH1	MH1	MH1
CSD Refcode	LATKID	LATKAV	LATKAV01
Strukturbestimmung erfolgte aus	Pulverdaten	Pulverdaten	Pulverdaten
Summenformel	$C_6H_4Cl_2N_2Ni$	$C_6H_4Cl_2CuN_2$	$C_6H_4Cl_2CuN_2$
Kristallsystem	monoklin	triklin	monoklin
Raumgruppe (Nr.)	*P m* (6)	*P* $\bar{1}$ (2)	*P* $2_1/n$ (14)
***a* /Å**	7,5810(5)	13,8312(3)	7,9609(4)
***b* /Å**	3,5132(1)	7,9385(2)	27,3362(2)
***c* /Å**	9,5049(3)	3,7907(5)	3,7947(2)
***α* /°**	90	96,171(2)	90
***ß* /°**	128,019(4)	94,914(2)	97,482(2)
***γ* /°**	90	96,825(2)	90
***V* /Å³**	199,43(2)	408,83(2)	818,76(7)
Z, Z'	1, 1	2, 1	4, 1
Lagesymmetrie von M	*m*	1	1
T /K	298	298	298
Strahlungsart	Cu $K\alpha_1$	Cu $K\alpha_1$	Cu $K\alpha_1$
Wellenlänge /Å	1,54056	1,54056	1,54056

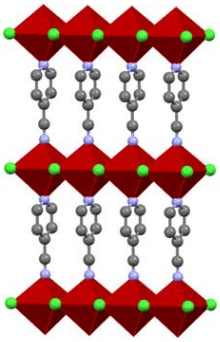

Abbildung 4.4.1: Polyederdarstellung eines Netzausschnittes von $[FeCl_2(4\text{-}CNpy)_1]_n$.

Beim thermischen Abbau von $[MCl_2(4\text{-}CNpy)_2]_n$ zu $[MCl_2(4\text{-}CNpy)_1]_n$ (ausgenommen $[CuCl_2(4\text{-}CNpy)_1]_n$) wird pro Metallatom ein 4-CNpy ausgetrieben. Die vakanten Koordinationsstellen werden durch die verbliebenen 4-CNpy-Liganden belegt, die dazu mit ihrem N_{CN}-Atom koordinieren müssen. Dadurch werden die entlang [010] verketteten Oktaeder bei M = Fe, Ni und Co zusätzlich in zweiter Dimension senkrecht zu [010] und bei M = Mn entlang [001] vernetzt. In allen Strukturen schichten die Netze planparallel, und in allen Strukturen erzeugt die Verkettung entlang [010] Spiegelebenen, sodass alle Metallatome und 4-CNpy-Liganden die Lagesymmetrie *m* besitzen (Abb. 4.4.2).

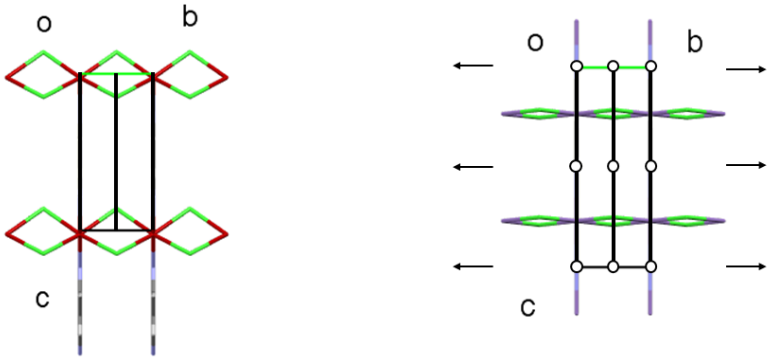

$[FeCl_2(4\text{-}CNpy)_1]_n$ $[MnCl_2(4\text{-}CNpy)_1]_n$

Pm *P2/m*

Abbildung 4.4.2: Packungsmuster und Symmetrieelemente in $[FeCl_2(4\text{-}CNpy)_1]_n$ (links) und $[MnCl_2(4\text{-}CNpy)_1]_n$ (rechts). Projektionsrichtung [100].

In $[FeCl_2(4\text{-}CNpy)_1]_n$, $[NiCl_2(4\text{-}CNpy)_1]_n$ und $[CoCl_2(4\text{-}CNpy)_1]_n$ sind die verbrückenden 4-CNpy aller Schichten uniform orientiert (Abb. 4.4.3 links) Diese Strukturen sind isotyp und kristallisieren in der Raumgruppe *P* 1 *m* 1 mit *Z* = 1. In $[MnCl_2(4\text{-}CNpy)_1]_n$ sind die 4-CNpy-Liganden innerhalb einer Schicht uniform orientiert, aber jede zweite Schicht ist invertiert (Abb. 4.4.3 rechts). Dadurch werden zweizählige Drehachsen senkrecht zu den Spiegelebenen, also in [010]-Richtung, erzeugt. Folglich kristallisiert $[MnCl_2(4\text{-}CNpy)_1]_n$ in der höhersymmetrischen Raumgruppe *P* 1 2/*m* 1 mit *Z* = 2.

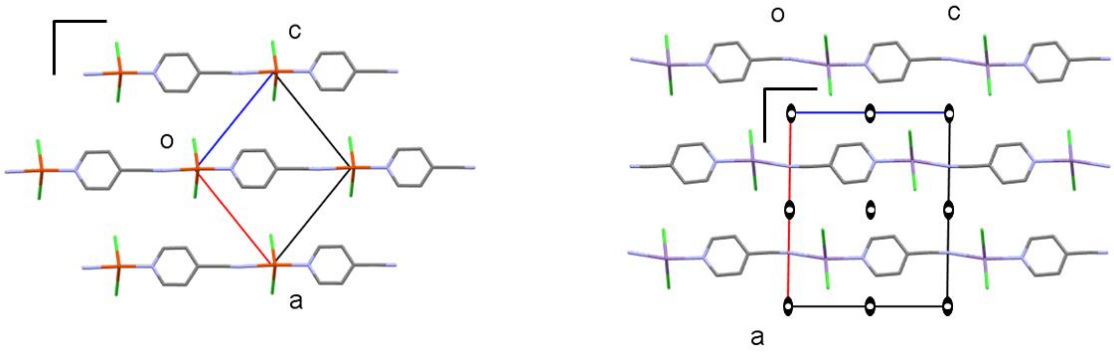

$[FeCl_2(4\text{-}CNpy)_1]_n$ $[MnCl_2(4\text{-}CNpy)_1]_n$

Pm *P*2/*m*

Abbildung 4.4.3: Packungsmuster und Symmetrieelemente in $[FeCl_2(4\text{-}CNpy)_1]_n$ (links) und $[MnCl_2(4\text{-}CNpy)_1]_n$ (rechts), Projektionsrichtung [010]. In $[FeCl_2(4\text{-}CNpy)_1]_n$ besitzen alle 4-CNpy-Fragmente dieselbe Orientierung. In $[MnCl_2(4\text{-}CNpy)_1]_n$ ist die Orientierung jeder zweiten Schicht invertiert.

In Kapitel 4.2 wurde zuvor bereits skizziert, dass alle bekannten Kristallstrukturen der $[MCl_2(3\text{-}CNpy)_1]_n$-Serie ein charakteristisches Doppelkettenmotiv (vgl. Kapitel 4.2) zeigen. In diesen Verbindungen sind alle, oktaedrisch koordinierten Metallatome von fünf Cl-Atomen umgeben. Die letzte Koordinationsstelle wird von einem N_{py}-Atom des gebundenen 3-CNpy eingenommen. Das gleiche Arrangement beobachtet man auch bei $[CuCl_2(4\text{-}CNpy)_1]_n$, wobei hier an dem N_{py}-Atom dessen 4-CNpy-Rest hängt, der auf die sterischen Verhältnisse keinen nennenswerten Einfluss hat. Daher scheint es auf den ersten Blick umso verwunderlicher, dass die übrigen vier Verbindungen der $[MCl_2(4\text{-}CNpy)_1]_n$-Serie Netzwerkstrukturen zeigen.

Das M-pyCN-M-System ist resonanzstabilisiert, wie am Beispiel von $[NiCl_2(4\text{-}CNpy)_1]_n$ in Abb. 4.4.4 skizziert. Die Stabilisierung resultiert aus einer π-Rückbindung des Metallatoms an sein gebundenes N_{py} sowie durch eine dative π-Bindung des CN-Fragments an das jeweils nächst gebundene Metallatom. Diese Wechselwirkungen erzeugen einen Domino-Effekt, der wiederum zu einer infiniten Mesomeriestabilisierung innerhalb eines Netzes führt. Im Falle von $[MCl_2(3\text{-}CNpy)_1]_n$-Verbindungen mit gedachter Netzwerkstruktur bleibt dieser aus (Abb. 4.4.5), sodass die Resonanzstabilisierung des Pyridin-Fragmentes insgesamt weniger ausgeprägt ist. Folglich bilden alle bislang bekannten Verbindungen der $[MCl_2(3\text{-}CNpy)_1]_n$-Serie nicht Netze, sondern Doppelketten aus. Letztlich bleibt dennoch die Frage offen, wieso $[CuCl_2(4\text{-}CNpy)_1]_n$ Doppelketten statt Netze bildet.

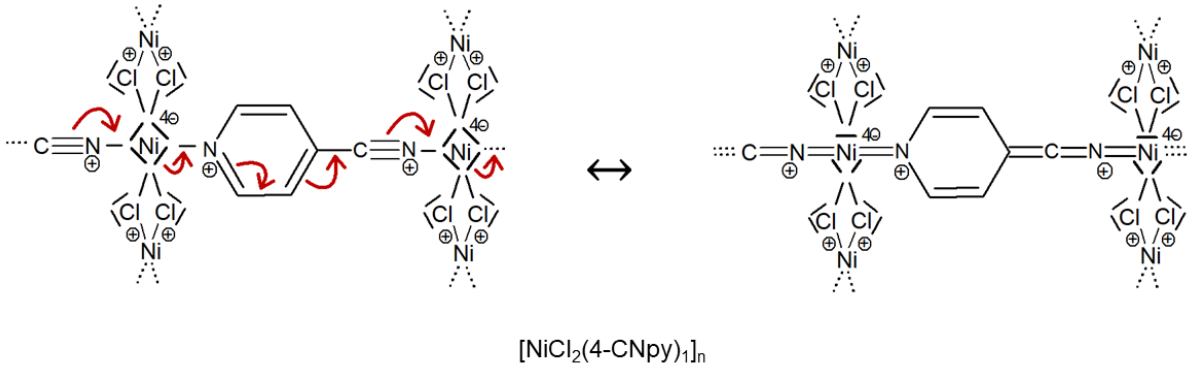

$[NiCl_2(4\text{-}CNpy)_1]_n$

Abbildung 4.4.4: Mesomerie in $[NiCl_2(4\text{-}CNpy)_1]_n$.

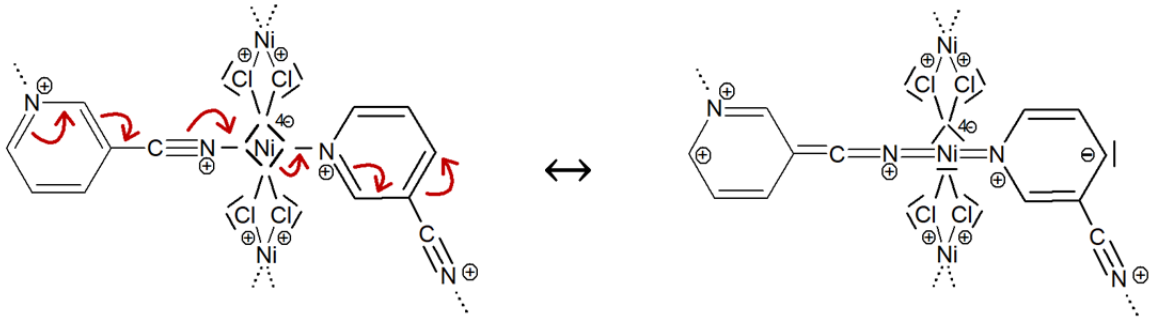

$[NiCl_2(3\text{-}CNpy)_1]_n$

mit Netzwerkstruktur

Abbildung 4.4.5: Mesomerie in $[NiCl_2(3\text{-}CNpy)_1]_n$ mit gedachter Netzwerkstruktur.

4.5 $[NiCl_2(3,5\text{-}CNpy)_2]_n$

Die Verbindung $[NiCl_2(3,5\text{-}CNpy)_2]_n$ wurde durch Reaktion von $NiCl_2$ (Hexahydrat) mit 3,5-Dicyanopyridin aus methanolischer Lösung erhalten. Details dieses Syntheseansatzes sind im Anhang B zusammengestellt. Gemäß DTA-TG-Analysen zersetzt sich $[NiCl_2(3,5\text{-}CNpy)_2]_n$ ohne Bildung einer intermediären Abbaustufe zu $NiCl_2$ und 3,5-CNpy (siehe DTA-TG-Aufnahme in Anhang B2).

Wichtige kristallographische Daten und Ergebnisse der Strukturverfeinerung von $[NiCl_2(3,5\text{-}CNpy)_2]_n$ sind in Tabelle 4.5 aufgeführt. Weitere relevante Informationen zu Indizierung und Strukturlösung sind ebenfalls Anhang B2 zu entnehmen.

In der Kristallstruktur von $[NiCl_2(3,5\text{-}CNpy)_2]_n$ werden die Ni-Atome von je vier Cl- und zwei N_{py}-Atomen nahezu oktaedrisch koordiniert. IR-Aufnahmen bestätigen, dass 3,5-CNpy nicht über den Stickstoff der Cyanogruppe (N_{CN}) an Nickel bindet, d.h. trotz dreier möglicher Koordinationsstellen monodentat agiert (siehe IR-Aufnahme in Anhang B2). Die Koordinationsoktaeder aus MCl_4N_{py2}-Einheiten werden über μ_2-Cl-Atome eckenverknüpft, wodurch eine Verkettung entlang [001] resultiert (Abb. 4.5.1). Die Gitterkonstante *c* = 3,6101(2) Å entspricht dem Ni-Ni-Abstand innerhalb einer Kette. Die bezüglich der Kette *trans*-gebundenen 3,5-CNpy-Liganden stapeln planparallel. Der Interplanar-Abstand der Ebenen der C_5N_{py}-Ringfragmente beträgt ca. 3,48 Å, sodass π-π-Interaktionen greifen können.

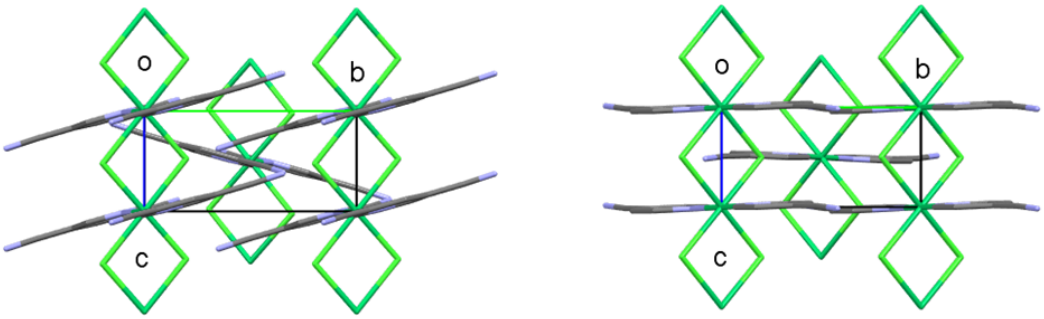

$[NiCl_2(3,5\text{-}CNpy)_2]_n$ $[NiCl_2(4\text{-}CNpy)_2]_n$

Abbildung 4.5.1: Packungsmuster in $[NiCl_2(3,5\text{-}CNpy)_2]_n$ (links) und $[NiCl_2(4\text{-}CNpy)_2]_n$ (rechts). Projektionsrichtung [100].

Die Kristallstruktur von $[NiCl_2(3,5\text{-}CNpy)_2]_n$ ist homöotyp zu der Struktur von $[NiCl_2(4\text{-}CNpy)_2]_n$. Beide Verbindungen kristallisieren in der monoklinen Raumgruppe *P* $2_1/n$ mit *Z* = 2 (vgl. Tab. 4.5). Die Ni-Atome befinden sich auf spezieller Lage, d.h. ihre Lagesymmetrie ist $\bar{1}$. Die Ketten sind ähnlich fischgrätenartig angeordnet und der Abstand benachbarter paralleler Ketten findet sich in der Gitterkonstanten *b* wieder (Abb. 4.5.2). Die 3,5-CNpy Fragmente stehen leicht verkippt von ihren jeweiligen $[NiCl_2]_n$-Bändern ab (ca. 87,8° in $[NiCl_2(4\text{-}CNpy)_2]_n$ und 83,7° in $[NiCl_2(3,5\text{-}CNpy)_2]_n$, bestimmt über die Ebene des C_5N_{py}-Ringfragmentes und seiner $[NiCl_4]$-Ebene), sodass der monokline Winkel *β* geringfügig ≠ 90° ist und beide Strukturen als pseudo-orthorhombisch bezeichnet werden können (Abb. 4.5.3).

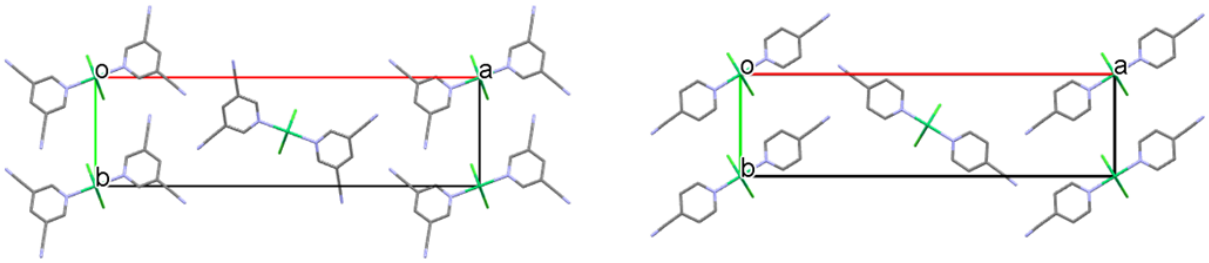

$[NiCl_2(3,5\text{-}CNpy)_2]_n$ $[NiCl_2(4\text{-}CNpy)_2]_n$

Abbildung 4.5.2: Fischgrätenmuster in den Packungen von $[NiCl_2(3,5\text{-}CNpy)_2]_n$ (links) und $[NiCl_2(4\text{-}CNpy)_2]_n$ (rechts). Projektionsrichtung [001].

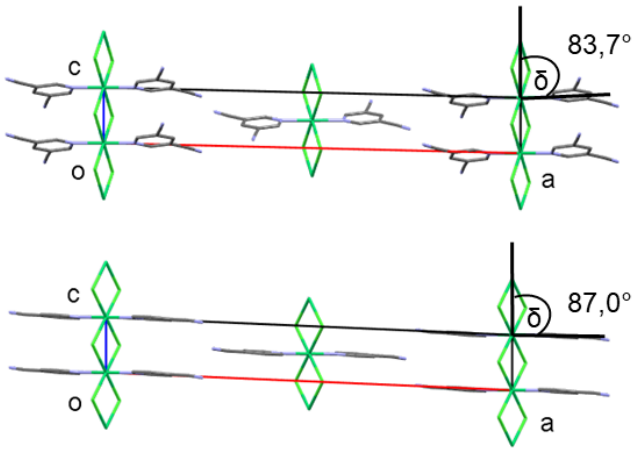

$[NiCl_2(3,5\text{-}CNpy)_2]_n$

$[NiCl_2(4\text{-}CNpy)_2]_n$

Abbildung 4.5.3: Packungsmuster in $[NiCl_2(3,5\text{-}CNpy)_2]_n$ (oben) und $[NiCl_2(4\text{-}CNpy)_2]_n$ (unten). Wegen δ ≠ 90° liegt kein orthorhombisches Gitter vor. Projektionsrichtung [010].

Tabelle 4.5: Ausgewählte kristallographische Daten von $[NiCl_2(3,5\text{-}CNpy)_2]_n$ und $[NiCl_2(4\text{-}CNpy)_2]_n$ im Vergleich.

Verbindung	**$[NiCl_2(3,5\text{-}CNpy)_2]_n$**	**$[NiCl_2(4\text{-}CNpy)_2]_n$**
Literaturstelle	unveröffentlicht	MH1
CSD Refcode	DUQTIV	LATKOJ
Strukturbestimmung erfolgte aus	Pulverdaten	Pulverdaten
Summenformel	$C_{14}H_6Cl_2N_6Ni$	$C_{12}H_8Cl_2N_4Ni$
Kristallsystem	monoklin	monoklin
Raumgruppe (Nr.)	*P* $2_1/n$ (14)	*P* $2_1/n$ (14)
***a* /Å**	27,1288(4)	26,4504(7)
***b* /Å**	7,62666(15)	7,16668(19)
***c* /Å**	3,6101(2)	3,58904(7)
***α* /°**	90	90
***ß* /°**	91,389(7)	92,474(4)
***γ* /°**	90	90
***V* /Å³**	746,72(5)	679,71(1)
Z, Z'	2, ½	2, ½
Lagesymmetrie von M	$\bar{1}$	$\bar{1}$
T /K	298	298
Strahlungsart	Cu $K\alpha_1$	Cu $K\alpha_1$
Wellenlänge /Å	1,5406	1,5406

4.6 $[MBr_2(3\text{-}CNpy)_4]$

Alle Verbindungen der $[MBr_2(3\text{-}CNpy)_4]$-Serie (mit M = Mn, Fe, Co und Ni) wurden über Reaktionen des jeweiligen Bromids MBr_2 mit 3-CNpy aus alkoholischer Lösung synthetisiert. Alle Versuchsansätze führten zu der Bildung von Phasen mit einem Metall(salz)-zu-Ligand von Verhältnis von 1:4. Auch Ansätze mit einem Stoffmengenverhältnis von 1:2 auf Eduktseite endeten in der Bildung von $[MBr_2(3\text{-}CNpy)_4]$ und nicht $[MBr_2(3\text{-}CNpy)_2]_n$. Dieses Verhalten ist bemerkenswert, da in allen anderen Serien stets Phasen mit einem Metall(salz)-zu-Ligand-Verhältnis von 1:2 anfielen und selbst ein enormer Überschuss an Cyanopyridin dort nicht zur Bildung von $[MX_2(CNpy)_4]$ führte. Indes wurden bei M = Cu und Zn stets Phasen der Zusammensetzung $[MBr_2(3\text{-}CNpy)_2]_{(n)}$ erhalten.

Wichtige kristallographische Daten und Ergebnisse der Strukturverfeinerungen von $[MBr_2(3CNpy)_4]$ -Verbindungen sind in Tabelle 4.6 aufgeführt. Weitere Ergebnisse sind im Detail in Publikation MH2 nachzulesen.

Alle Kristallstrukturen der $[MBr_2(3\text{-}CNpy)_4]$ -Serie sind isotyp und kristallisieren in der Raumgruppe *P* 4*nc* mit *Z* = 2. Die Verbindungen bestehen aus diskreten Komplexmolekülen, in denen die Metallatome oktaedrisch koordiniert sind (Abb. 4.6.1a). Jedes Metallatom ist an zwei Br-Atome und vier N_{py}-Atome gebunden. Dominierendes Symmetrieelement dieser Kristallstruktur ist die vierzählige Drehachse, die wegen *Z* = 2 von M- und Br-Atomen belegt ist (Abb. 4.4.1b). Die Lagesymmetrie dieser Atome ist folglich 4.. . Bezüglich dieser Drehachse sind die vier Pyridinliganden propellerartig angeordnet (Abb. 4.4.1b/c). Die Pyridinringe (d.h. die C_5N_{py}-Ebenen) bilden mit der $[MN_{py2}Br_2]$-Ebene einen Winkel von ca. 46°. Symmetriebedingt sind alle M-N_{py}-Bindungen einer Kristallstruktur gleich lang und die beiden M-Br-Bindungen verschieden lang. In $[NiBr_2(3\text{-}CNpy)_4]$ und $[CoBr_2(3\text{-}CNpy)_4]$ sind die beiden M-Br-Bindungslängen gar signifikant unterschiedlich, was auf eine Jahn-Teller-Verzerrung der Oktaeder hindeutet. Insgesamt verringern sich die M-N_{py}- sowie die M-Br-Abstände von $[MnBr_2(3\text{-}CNpy)_4]$ zu $[NiBr_2(3\text{-}CNpy)_4]$ um jeweils ca. 0,05 Å wegen des schrumpfenden Atomvolumens (von Mn zu Ni).

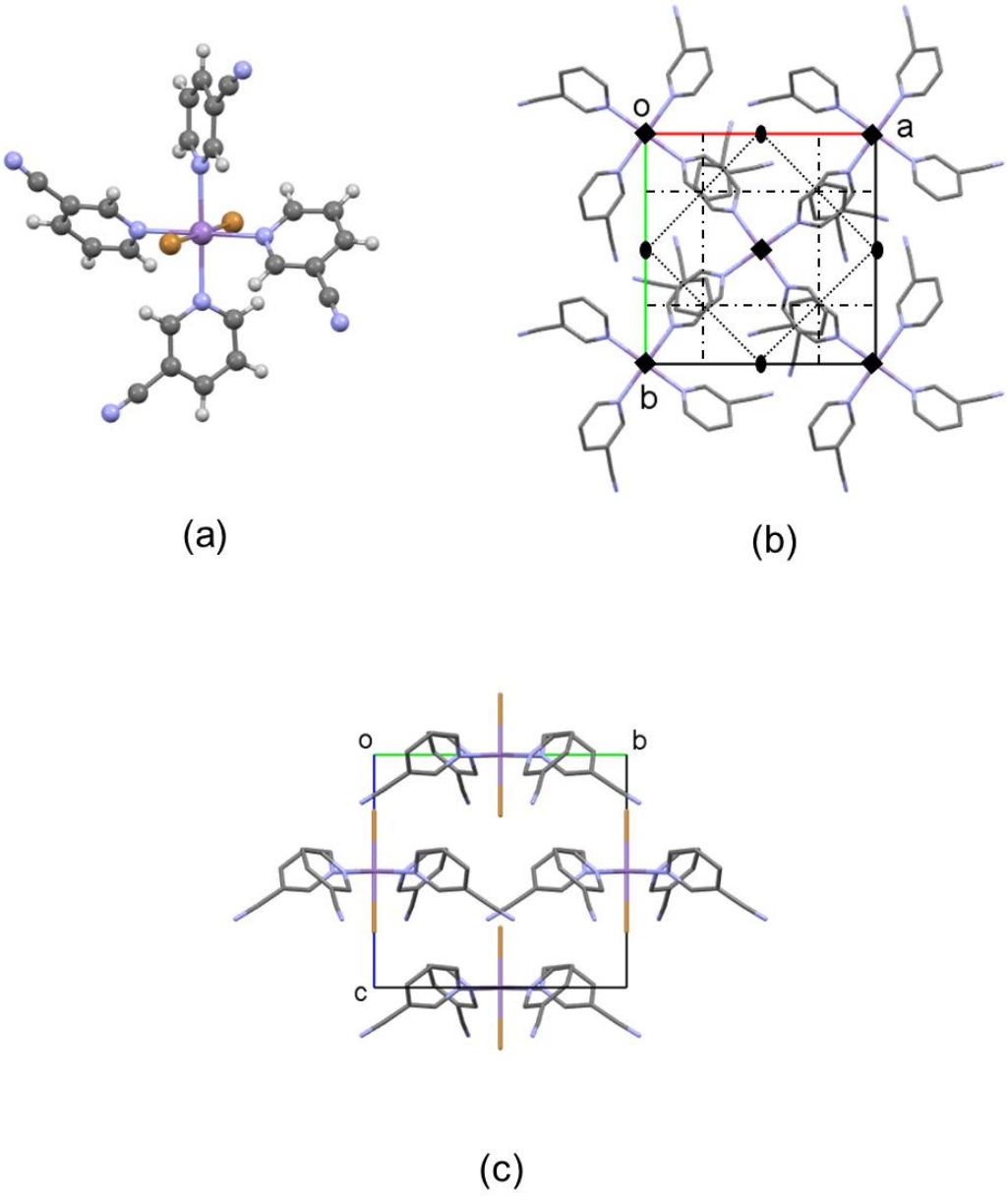

Abbildung 4.6.1: $[MnBr_2(3\text{-}CNpy)_4]$: (a) diskretes Molekül, (b) Packungsmuster und Darstellung ausgewählter Symmetrieelemente bei Projektionsrichtung [001], (c) Packungsmuster bei Projektionsrichtung [100].

Tabelle 4.6: Ausgewählte kristallographische Daten von $[MnBr_2(3\text{-}CNpy)_4]$ mit M = Mn, Fe, Co und Ni.

Verbindung	**$[MnBr_2(3\text{-}CNpy)_4]$**	**$[FeBr_2(3\text{-}CNpy)_4]$**	**$[CoBr_2(3\text{-}CNpy)_4]$**	**$[NiBr_2(3\text{-}CNpy)_4]$**
Literaturstelle	MH2	MH2	MH2	MH2
CSD Refcode	XOSLID	XOSMIE	XOSNAX	XOSNUR
Strukturbestimmung erfolgte aus	Pulverdaten	Pulverdaten	Pulverdaten	Pulverdaten
Summenformel	$C_{24}H_{16}Br_2MnN_8$	$C_{24}H_{16}Br_2FeN_8$	$C_{24}H_{16}Br_2CoN_8$	$C_{24}H_{16}Br_2N_8Ni$
Kristallsystem	tetragonal	tetragonal	tetragonal	tetragonal
Raumgruppe (Nr.)	*P*4*nc* (104)	*P*4*nc* (104)	*P*4*nc* (104)	*P*4*nc* (104)
***a* /Å**	11,2178(5)	11,1484(2)	11,0587(4)	10,9722(9)
***c* /Å**	10,3309(6)	10,3205(2)	10,4149(5)	10,4600(3)
***V* /Å³**	1300,0(3)	1282,7(1)	1273,7(1)	1259,3(2)
Z, Z'	2, ¼	2, ¼	2, ¼	2, ¼
Lagesymmetrie von M	4..	4..	4..	4..
T /K	298	298	298	298
Strahlungsart	Cu *K*α$_1$	Cu *K*α$_1$	Cu *K*α$_1$	Cu *K*α$_1$
Wellenlänge /Å	1,5406	1,5406	1,5406	1,5406

4.7 $[MBr_2(3\text{-}CNpy)_2]_n$

Die Verbindungen $[MBr_2(3\text{-}CNpy)_2]_n$ (mit M = Mn, Fe, Co und Ni) wurden durch thermischen Abbau der Precursoren $[MBr_2(3\text{-}CNpy)_4]$ dargestellt (Details in MH2). Im Gegensatz zur $[MCl_2(3\text{-}CNpy)_2]_n$-Serie führten hier analoge Versuchsansätze zur Reaktion von MBr_2 mit 3-Cyanopyridin in (alkoholischer) Lösung nicht zur Bildung von phasenreinem bzw. lösungsmittelfreiem $[MBr_2(3\text{-}CNpy)_2]_n$. Hingegen konnten $[CuBr_2(3\text{-}CNpy)_2]_n$ sowie $[ZnBr_2(3\text{-}CNpy)_2]$ durch Lösungskristallisation synthetisiert werden (Details siehe Anhang B1 und B3). Im Fall von $[CuBr_2(3\text{-}CNpy)_2]_n$ bildete sich ein bislang unbekanntes Polymorph, β-$[CuBr_2(3\text{-}CNpy)_2]_n$. Des Weiteren existieren jeweils zwei Polymorphe von $[CoBr_2(3\text{-}CNpy)_2]_n$ und $[NiBr_2(3\text{-}CNpy)_2]_n$, deren Phasenumwandlungen in temperaturabhängigen Beugungsexperimenten beobachtet werden konnten (Details in MH2).

Die Kristallstrukturen von α-$[CuBr_2(3\text{-}CNpy)_2]_n$ (MAHVOH) und $[ZnBr_2(3\text{-}CNpy)_2]$ (QAHZAC) waren bereits aus SCXRD-Daten literaturbekannt. Da der Datensatz von $[ZnBr_2(3\text{-}CNpy)_2]$ aus Messungen bei 120K stammte, wurde eine Strukturbestimmung

aus RT-Pulverdaten ergänzt (siehe Anhang B1). Auf eine Diskussion der Kristallstruktur von $[ZnBr_2(3\text{-}CNpy)_2]$ wird allerdings an dieser Stelle verzichtet, da diese nicht grundsätzlich neu und zudem der in Kapitel 4.1 diskutierten Struktur von $[ZnCl_2(3\text{-}CNpy)_2]$ ähnelt.

Wichtige kristallographische Daten und Ergebnisse der Strukturverfeinerungen der $[MBr_2(3\text{-}CNpy)_2]_n$-Verbindungen sind in den Tabellen 4.7.1 und 4.7.2 aufgeführt. Weitere Ergebnisse sind im Detail in Publikation MH2 sowie in Anhang B1 und B3 nachzulesen.

Analog zu den Verbindungen der $[MCl_2(3\text{-}CNpy)_2]_n$-Serie werden die Metallatome von jeweils vier Br- und zwei N_{py}-Atomen koordiniert, sodass Oktaeder aus MBr_4N_{py2}-Einheiten aufgespannt werden. Die Br-Atome fungieren als μ_2-Brückenliganden, welche die MBr_4N_{py2}-Oktaeder eckenverknüpfen und folglich zu Ketten aus $[MBr_2(3\text{-}CNpy)_2]_n$-Einheiten führen. In $[MnBr_2(3\text{-}CNpy)_2]_n$, $[FeBr_2(3\text{-}CNpy)_2]_n$, α-$[CoBr_2(3\text{-}CNpy)_2]_n$ sowie β-$[CuBr_2(3\text{-}CNpy)_2]_n$ laufen die Ketten entlang [001] und in den restlichen Strukturen entlang [100] (Abb. 4.7.1). Die kurzen Gitterkonstanten *a* bzw. *c* entsprechen den M-M-Abständen innerhalb einer Kette. Sie rangieren im Bereich von 3,829(7) Å für Mn und 3,7097(7) Å für Ni (α-Phase) und fallen wegen des voluminöseren Halogenatoms naturgemäß größer aus als in der $[MCl_2(3\text{-}CNpy)_2]_n$-Serie (vgl. Tab. 4.7.1 und 4.7.2 mit Tab. 4.1.1) . Auch in β-$[CuBr_2(3\text{-}CNpy)_2]_n$ sind die $CuBr_4N_{py2}$-Koordinationsoktaeder aufgrund der d^9-Konfiguration des Cu-Atoms in Kettenrichtung gestreckt, sodass die Gitterkonstante *c* mit 3,937(9) Å die längste der $[MBr_2(3\text{-}CNpy)_2]_n$-Serie ist (Tab. 4.7.2)

Tabelle 4.7.1: Ausgewählte kristallographische Daten von $[MBr_2(3\text{-}CNpy)_2]_n$ mit M = Mn, Fe und Co.

Verbindung	**$[MnBr_2(3\text{-}CNpy)_2]_n$**	**$[FeBr_2(3\text{-}CNpy)_2]_n$**	**α-$[CoBr_2(3\text{-}CNpy)_2]_n$**	**β-$[CoBr_2(3\text{-}CNpy)_2]_n$**
Literaturstelle	MH2	MH2	MH2	MH2
CSD Refcode	XOSLOJ	XOSMOK	LATJOI02	LATJOI03
Summenformel	$C_{12}H_8Br_2MnN_4$	$C_{12}H_8Br_2FeN_4$	$C_{12}H_8Br_2CoN_4$	$C_{12}H_8Br_2CoN_4$
Strukturbestimmung erfolgte aus	Pulverdaten	Pulverdaten	Pulverdaten	Pulverdaten
Kristallsystem	orthorhombisch	orthorhombisch	orthorhombisch	triklin
Raumgruppe (Nr.)	*P n n m* (58)	*P n n m* (58)	*P n n m* (58)	*P* $\bar{1}$ (2)
***a* /Å**	27,304(6)	27,128(5)	27,019(1)	3,727(5)
***b* /Å**	7,221(9)	7,172(2)	7,124(2)	13,629(6)

***c* /Å**	3,829(7)	3,788(1)	3,759(7)	13,868(6)
***α* /°**	90	90	90	87,37(7)
***ß* /°**	90	90	90	82,34(4)
***γ* /°**	90	90	90	82,40(5)
***V* /Å³**	755,1(8)	737,0(2)	723,7(1)	697,2(2)
Z, Z'	2, ¼	2, ¼	2, ¼	2, 1
Lagesymmetrie von M	2/*m*	2/*m*	2/*m*	$\bar{1}$, $\bar{1}$ *
T /K	298	298	298	298
Strahlungsart	Cu $K\alpha_1$	Cu $K\alpha_1$	Cu $K\alpha_1$	Cu $K\alpha_1$
Wellenlänge /Å	1,54056	1,54056	1,54056	1,54056
* Enthält zwei symmetrieunabhängige Co-Atome.				

Tabelle 4.7.2: Ausgewählte kristallographische Daten von $[MBr_2(3\text{-}CNpy)_2]_n$ mit M = Ni und Cu.

Verbindung	**α-$[NiBr_2(3\text{-}CNpy)_2]_n$**	**β-$[NiBr_2(3\text{-}CNpy)_2]_n$**	**α-$[CuBr_2(3\text{-}CNpy)_2]_n$**	**β-$[CuBr_2(3\text{-}CNpy)_2]_n$**
Literaturstelle	MH2	MH2	[30]	unveröffentlicht
CSD Refcode	XOSPAZ	XOSPAZ02	MAHVOH	DUNVIU
Summenformel	$C_{12}H_8Br_2N_4Ni$	$C_{12}H_8Br_2N_4Ni$	$C_{12}H_8Br_2CuN_4$	$C_{12}H_8Br_2CuN_4$
Strukturbestimmung erfolgte aus	Pulverdaten	Pulverdaten	Einkristalldaten	Pulverdaten
Kristallsystem	monoklin	triklin	triklin	monoklin
Raumgruppe (Nr.)	*C c* (9)	*P* $\bar{1}$ (2)	*P* $\bar{1}$ (2)	*P* $2_1/n$ (14)
***a* /Å**	3,709(1)	3,727(4)	7,0410(10)	26,3672(7)
***b* /Å**	26,801(4)	13,574(9)	7,2791(10)	7,21068(16)
***c* /Å**	13,706(8)	13,761(6)	8,0673(11)	3,93786(8)
***α* /°**	90	86,86(2)	116,563(2)	90
***ß* /°**	97,67(8)	82,40(1)	107,909(2)	96,333(4)
***γ* /°**	90	82,12(1)	98,437(3)	90
***V* /Å³**	1350,5(8)	683,1(5)	331,70(8)	744,12(3)
Z, Z'	4, 1	2, 1	1, ½	2, ½
Lagesymmetrie von M	1	$\bar{1}$, $\bar{1}$ *	$\bar{1}$	$\bar{1}$
T /K	125	298	298	298
Strahlungsart	Cu $K\alpha_1$	Cu $K\alpha_1$	Mo $K\alpha$	Cu $K\alpha_1$
Wellenlänge /Å	1,54056	1,54056	0,71073	1,54056
* Enthält zwei symmetrieunabhängige Ni-Atome.				

In allen Strukturen sind benachbarte Cyanopyridin-Liganden einer Kette planparallel (Abb. 4.7.1). Die Interplanar-Abstände der Ebenen der C_5N_{py}-Ringfragmente variieren zwischen 3,703 Å in α-$[NiBr_2(3\text{-}CNpy)_2]_n$ und 3,829 Å in $[MnBr_2(3\text{-}CNpy)_2]_n$, sodass π-π-Wechselwirkungen im Vergleich zu der analogen $[MCl_2(3\text{-}CNpy)_2]_n$-Serie etwas schwächer sind.

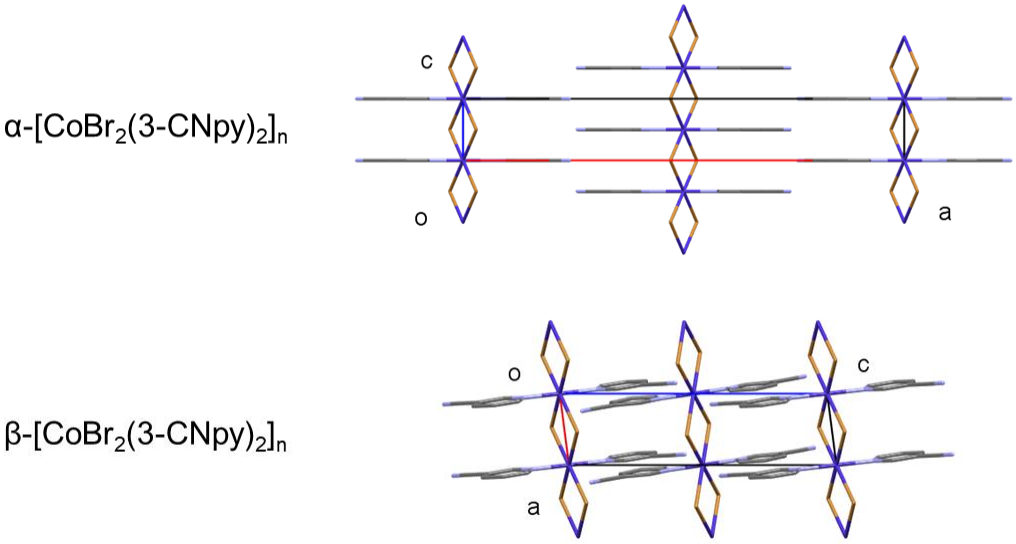

Abbildung 4.7.1: Kettenanordnung und Packungsmuster in α-$[CoBr_2(3\text{-}CNpy)_2]_n$ und β-$[CoBr_2(3\text{-}CNpy)_2]_n$, Projektionsrichtung [010].

In allen Kristallstrukturen sind die Ketten in dem bekannten Fischgrätenmuster angeordnet (Abb. 4.7.2), wobei in $[MnBr_2(3\text{-}CNpy)_2]_n$, $[FeBr_2(3\text{-}CNpy)_2]_n$ und α-$[CoBr_2(3\text{-}CNpy)_2]_n$ der Abstand unmittelbar benachbarter, paralleler Ketten durch die Gitterkonstante *b* wiedergegeben wird (Abb. 4.7.2).

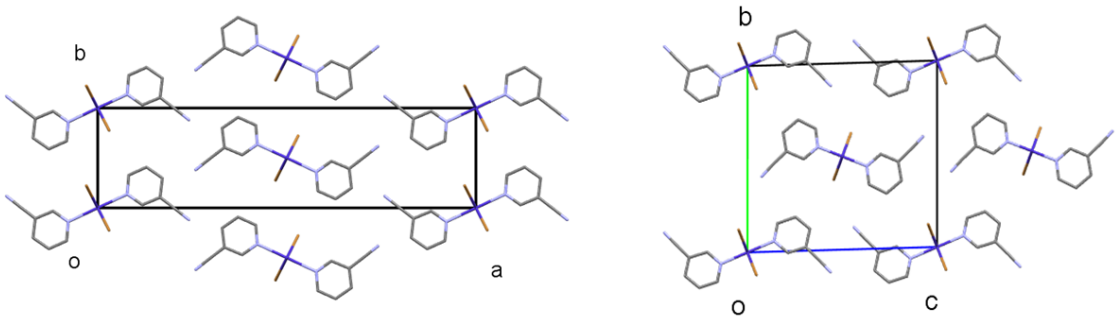

α-$[CoBr_2(3\text{-}CNpy)_2]_n$ β-$[CoBr_2(3\text{-}CNpy)_2]_n$

Abbildung 4.7.2: Fischgrätenmotiv und Packungsmuster in α-$[CoBr_2(3\text{-}CNpy)_2]_n$ (Projektionsrichtung $[00\bar{1}]$), und β-$[CoBr_2(3\text{-}CNpy)_2]_n$ (Projektionsrichtung [100]).

Diese Verbindungen sind isostrukturell und kristallisieren in der orthorhombischen Raumgruppe *P nnm* mit *Z* = 2. Die Pyridinliganden zeigen (exakt) senkrecht von den Ketten weg, sodass der Bezugswinkel β = 90° und die Kristallstruktur orthorhombisch ist. Da benachbarte Pyridinliganden einer Kette planparallel sind, findet sich deren Abstand zueinander ebenfalls in der korrespondieren Gitterkonstante *a* wieder (Abb. 4.7.1 oben). Aufgrund dieser orthogonalen Anordnung existieren Spiegelebenen parallel zu (001). Folglich besetzen die Pyridinliganden Lagen mit *m* Symmetrie und die Metallatome Lagen mit 2/*m* Symmetrie. Des Weiteren liegen *n*-Gleitspiegelebenen senkrecht zu *m* vor, wodurch für $[MnBr_2(3\text{-}CNpy)_2]_n$, $[FeBr_2(3\text{-}CNpy)_2]_n$ und α-$[CoBr_2(3\text{-}CNpy)_2]_n$ die Raumgruppe *P* $2_1/n$ $2_1/n$ 2/*m* (kurz: *P nnm*) resultiert.

Die Kristallstruktur von β-$[CuBr_2(3\text{-}CNpy)_2]_n$ ist ähnlich zu diesen drei Strukturen. Benachbarte Pyridinliganden einer Kette sind ebenfalls planparallel, allerdings stehen diese nicht senkrecht auf (001), sodass $\beta \neq 90°$ wird und Spiegelebenen wegfallen (Abb. 4.7.3). Dadurch besetzen die Pyridinliganden allgemeine Lagen, und die Lagesymmetrie der Cu-Atome wird auf $\bar{1}$ reduziert. Folglich kristallisiert β-$[CuBr_2(3\text{-}CNpy)_2]_n$ in der monoklinen Untergruppe *P* 1 $2_1/n$ 1 (kurz *P* $2_1/n$), die eine maximale translationengleiche Untergruppe von *P* $2_1/n$ $2_1/n$ 2/*m* ist. Eine solcher „Symmetriebruch“ liegt ebenfalls in den entsprechenden Kristallstrukturen der $[MCl_2(4\text{-}CNpy)_2]_n$-Serie vor, deren Gitter allesamt monoklin sind (vgl. Kapitel 4.3 und Abb. 4.3.1).

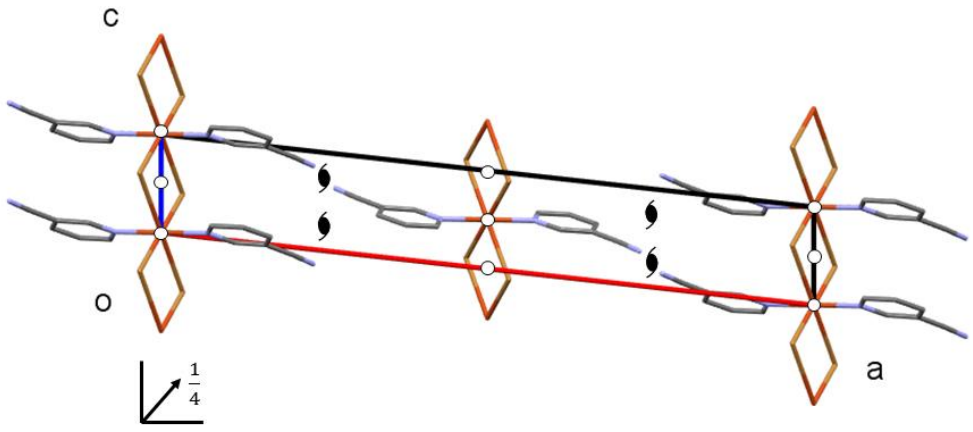

Abbildung 4.7.3: Packungsmuster in Symmetrieelemente β-$[CuBr_2(3\text{-}CNpy)_2]_n$, RG *P* $2_1/n$. Projektionsrichtung [010].

Auch in β-[$CoBr_2(3\text{-}CNpy)_2]_n$, α-[$NiBr_2(3\text{-}CNpy)_2]_n$ und β-[$NiBr_2(3\text{-}CNpy)_2]_n$ stehen die Pyridinliganden nicht orthogonal zu der (001)-Ebene, sondern zeigen quasi flügelartig von ihren Ketten weg (Abb. 4.7.1 unten und 4.7.4 rechts). In diesen Strukturen befinden sich alle Atome auf allgemeiner Lage. β-[$CoBr_2(3\text{-}CNpy)_2]_n$ und β-[$NiBr_2(3\text{-}CNpy)_2]_n$ sind ihrerseits isostrukturell und kristallisieren in der triklinen Raumgruppe $P\ \bar{1}$ mit Z = 2, also zwei unabhängigen Ketten(fragmenten) in der Elementarzelle. Die beiden Strukturen sind ähnlich zu α-[$NiBr_2(3\text{-}CNpy)_2]_n$, das hingegen ein monoklines Gitter ausbildet und in *Cc* mit Z = 4 kristallisiert (Abb. 4.7.4).

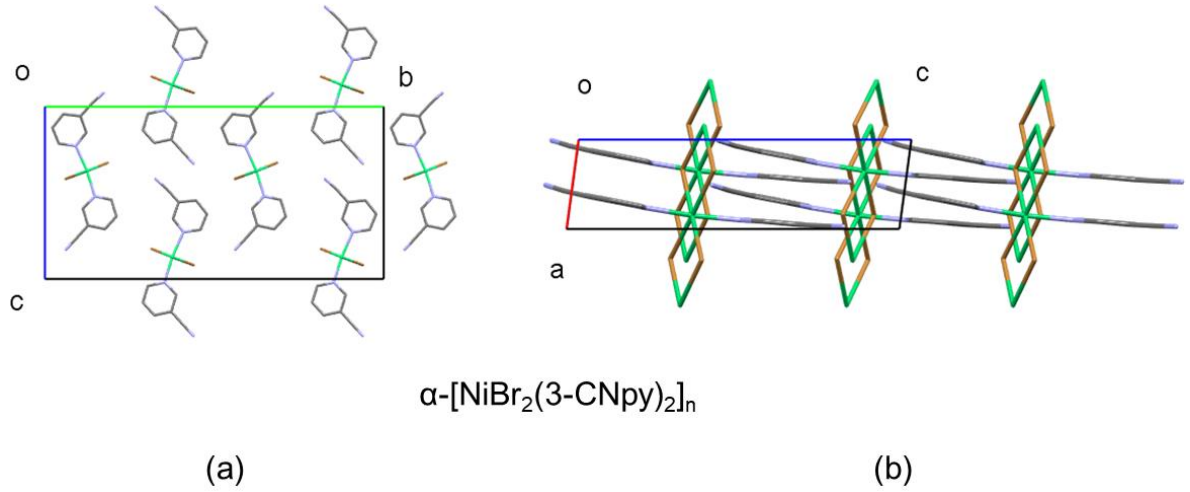

Abbildung 4.7.4: Fischgrätenmotiv und Packungsmuster in α-[$NiBr_2(3\text{-}CNpy)_2]_n$. Hier ist Z = 4. Projektionsrichtung in (a): [100], in (b): [010].

In α-[$NiBr_2(3\text{-}CNpy)_2]_n$ sind benachbarte Ketten abwechselnd um *a*/2 und 0 verschoben, sodass die Ketten entlang [010] in einem (ABBA)A… Muster gestapelt werden, wie es gleichermaßen in [$NiCl_2(3\text{-}CNpy)_2]_n$ zu finden ist (Abb. 4.7.5 links). In β-[$CoBr_2(3\text{-}CNpy)_2]_n$ und β-[$NiBr_2(3\text{-}CNpy)_2]_n$ sind benachbarte Ketten stets um ca. *a*/4 verschoben, sodass die Ketten entlang [010] einem (ABCD)A… Muster gehorchen (Abb. 4.7.5 rechts und 4.7.6 rechts).

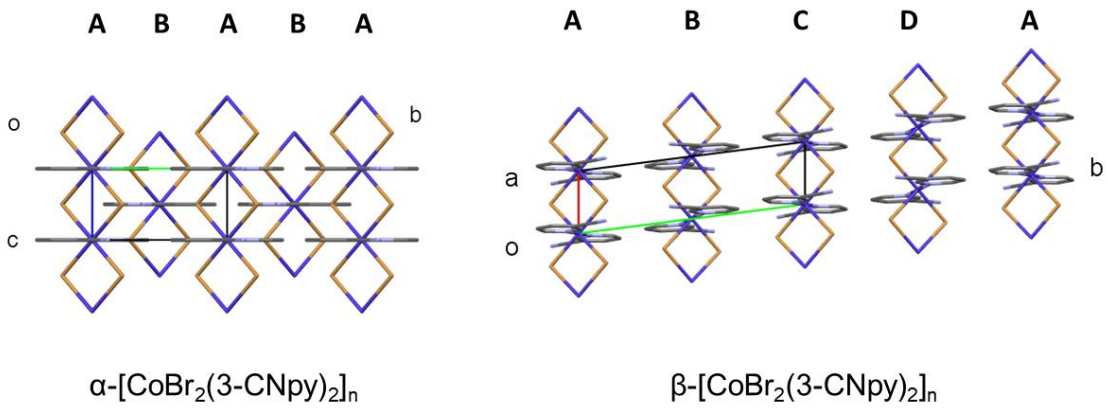

α-[$CoBr_2(3\text{-}CNpy)_2]_n$ β-[$CoBr_2(3\text{-}CNpy)_2]_n$

Abbildung 4.7.5: Packungsmuster und Stapelabfolgen in α-[$CoBr_2(3\text{-}CNpy)_2]_n$ (Projektionsrichtung [100]) und β-[$CoBr_2(3\text{-}CNpy)_2]_n$ (Projektionsrichtung [001]).

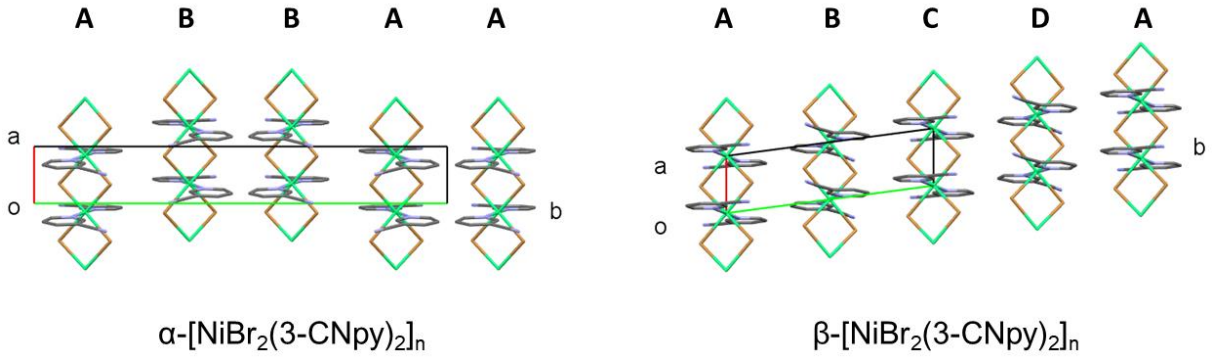

α-[$NiBr_2(3\text{-}CNpy)_2]_n$ β-[$NiBr_2(3\text{-}CNpy)_2]_n$

Abbildung 4.7.6: Packungsmuster und Stapelabfolgen in α-[$NiBr_2(3\text{-}CNpy)_2]_n$ und β-[$NiBr_2(3\text{-}CNpy)_2]_n$, Projektionsrichtung [001].

4.8 [$MBr_2(3\text{-}CNpy)_1]_n$

Der synthetische Zugang zu [$MBr_2(3\text{-}CNpy)_1]_n$ (mit M = Mn, Fe, Co und Ni) erfolgte durch thermischen Abbau der Vorläuferverbindungen [$MBr_2(3\text{-}CNpy)_2]_n$ (die wiederum als Abbauprodukte der Precursoren [$MBr_2(3\text{-}CNpy)_4$] anfielen). Tempern von [$CuBr_2(3\text{-}CNpy)_2]_n$ führte unmittelbar zur vollständigen Verflüchtigung des gebundenen Cyanopyridins sowie Reduktion des Cu^{II}, sodass CuBr zurückblieb. [$ZnBr_2(3\text{-}CNpy)_2$] zersetzte sich ebenfalls ohne Bildung von Intermediaten in seine Ausgangsstoffe.

Wichtige kristallographische Daten und Ergebnisse der Strukturverfeinerungen der [$MBr_2(3\text{-}CNpy)_1]_n$-Verbindungen sind in Tabelle 4.8 aufgeführt. Weitere Ergebnisse sind im Detail in Publikation MH2 nachzulesen.

In allen Kristallstrukturen werden die Metallatome von jeweils vier Cl-Atomen, einem N_{py}- sowie einem N_{CN}-Atom koordiniert, wodurch Koordinationsoktaeder aus MCl_4N_2-Einheiten aufgespannt werden. Im Gegensatz zu $[MCl_2(3\text{-}CNpy)_1]_n$ bilden alle Verbindungen der $[MBr_2(3\text{-}CNpy)_1]_n$-Serie Netzwerkstrukturen aus (Abb. 4.8.1). Somit handelt es sich hierbei um die ersten Kristallstrukturen mit 3-Cyanopyridin als verbrückendes Element zwischen zweiwertigen 3d-Übergangsmetallatomen der 4. Periode. Die Metallatome sind von je vier μ_2-Br-Atomen umgeben, wodurch Bänder aus $[MBr_2]_n$-Einheiten erzeugt werden. Zusätzlich wird jedes Metallatom von je einem N_{py} und einem N_{CN} eines zweiten 3-CNpy-Liganden koordiniert. Benachbarte $[MBr_2]_n$-Bänder werden durch bidentates 3-CNpy zu Netzen verknüpft, die infolge der in meta-Position eingeführten Cyanogruppe gewellt sind.

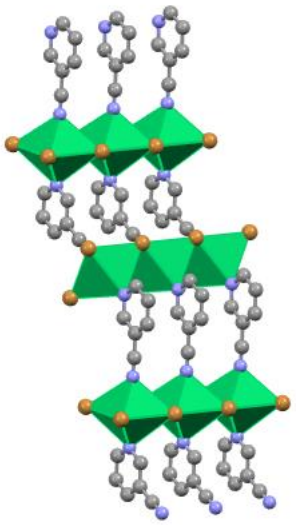

Abbildung 4.8.1: Polyederdarstellung eines Netzausschnittes von $[NiBr_2(3\text{-}CNpy)_1]_n$.

Die Netze werden entlang [010] geschichtet, sodass der Schichtabstand der Gitterkonstanten *b* entspricht. In $[FeBr_2(3\text{-}CNpy)_1]_n$, $[CoBr_2(3\text{-}CNpy)_1]_n$ und $[NiBr_2(3\text{-}CNpy)_1]_n$ befinden sich alle Atome auf Spiegelebenen *m*, parallel zu (100). Aufgrund ihrer Wellenstruktur erzeugen die Netze weitere Symmetrieelemente: eine 2_1-Schraubenachse entlang [001] sowie eine Gleitspiegelebene *c* senkrecht zu *m* bzw. parallel zu (010). Somit kristallisieren die Phasen $[MBr_2(3\text{-}CNpy)_1]_n$ mit M = Fe, Co und Ni in der Raumgruppe $Pmc2_1$ (Abb. 4.8.2).

$[NiBr_2(3\text{-}CNpy)_1]_n$

$Pmc2_1$

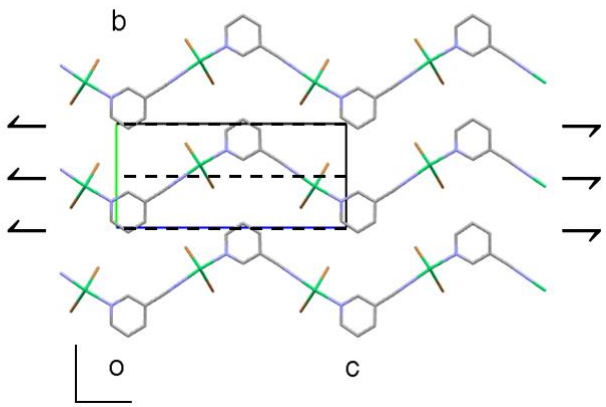

Abbildung 4.8.2: Packungsmuster und Symmetrieelemente in $[NiBr_2(3\text{-}CNpy)_1]_n$, Projektionsrichtung [100].

Die Verbindung $[MnBr_2(3\text{-}CNpy)_1]_n$ zeigt zwar dieselbe Strukturtopologie, ihre Kristallstruktur lässt sich, mit Bezug auf die anderen drei Strukturen, als „pseudo-orthorhombisch“ bezeichnen. Bereits ein Vergleich aller vier Pulverdiffraktogramme (Abb. 4.8.3) signalisiert, dass $[MnBr_2(3\text{-}CNpy)_1]_n$ zwar ähnlich, aber nicht isostrukturell zu $[MBr_2(3\text{-}CNpy)_1]_n$ mit M = Fe, Co und Ni ist.

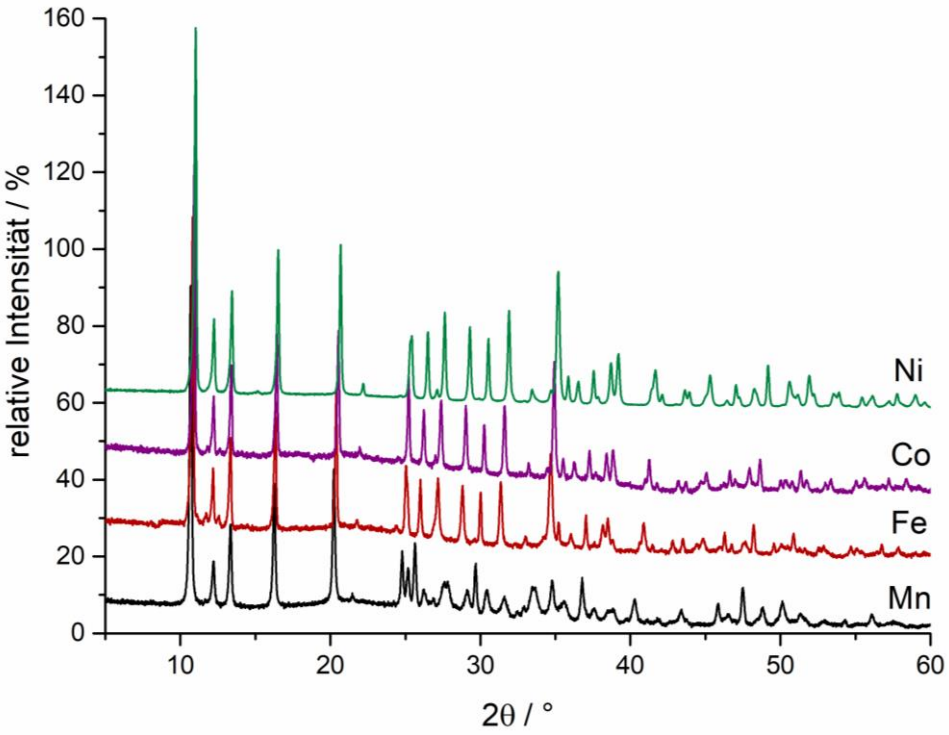

Abbildung 4.8.3: XRPD-Aufnahmen von $[MBr_2(3\text{-}CNpy)_1]_n$ mit M = Mn (schwarz), Fe (rot), Co (violett) und Ni (türkis). Zwecks Vergleichbarkeit wurde auf relative Intensitäten skaliert und ein y-Offset von 20 gewählt.

Tatsächlich sind die Koordinationsoktaeder der Mn-Atome derart verzerrt, dass Spiegelebenen und *c*-Gleitung wegfallen (Abb. 4.8.4 und 4.8.5). Daher kristallisiert $[MnBr_2(3\text{-}CNpy)_1]_n$ in der Untergruppe *P* 1 1 2_1 (einer Nicht-Standardaufstellung von *P* 2_1).

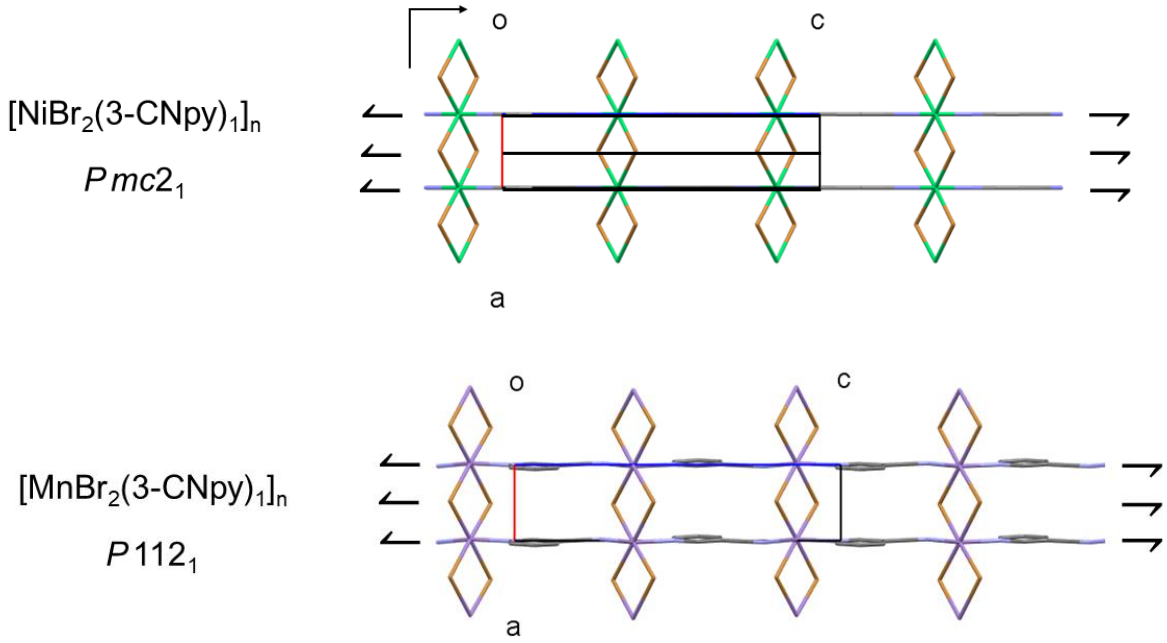

$[NiBr_2(3\text{-}CNpy)_1]_n$ *P*m*c*2_1

$[MnBr_2(3\text{-}CNpy)_1]_n$ *P*112$_1$

Abbildung 4.8.4: Packungsmuster und Symmetrieelemente in $[NiBr_2(3\text{-}CNpy)_1]_n$ und $[MnBr_2(3\text{-}CNpy)_1]_n$, Projektionsrichtung [010]. Wegen der verzerrten Koordinationsoktaeder der Mn-Atome liegen weder Spiegelebenen noch Gleitspiegelebenen vor.

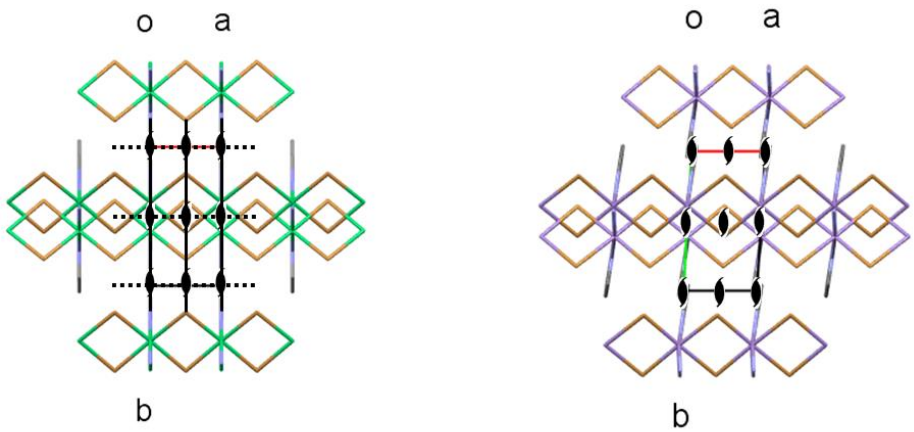

$[NiBr_2(3\text{-}CNpy)_1]_n$ *P*m*c*2_1

$[MnBr_2(3\text{-}CNpy)_1]_n$ *P*112$_1$

Abbildung 4.8.5: Packungsmuster und Symmetrieelemente in $[NiBr_2(3\text{-}CNpy)_1]_n$ und $[MnBr_2(3\text{-}CNpy)_1]_n$, Projektionsrichtung [001]. In $[MnBr_2(3\text{-}CNpy)_1]_n$ liegen nur 2_1-Schraubenachsen vor.

Alle bekannten Kristallstrukturen der analogen $[MCl_2(3\text{-}CNpy)_1]_n$-Serie zeichnen sich durch ihr Doppelkettenmotiv (vgl. Kapitel 4.2) aus, das bislang auch ausschließlich bei Cl-Verbindungen in Erscheinung trat. In diesen Verbindungen sind die Metallatome von fünf Halogenatomen umgeben. Aufgrund des größeren Atomvolumens eines Br-Atoms ist ein vergleichbares Koordinationsarrangement in den $[MBr_2(3\text{-}CNpy)_1]_n$-Verbindungen schlechter möglich, sodass diese Kristallstrukturen ein Netzwerkmotiv aufweisen.

Tabelle 4.8: Ausgewählte kristallographische Daten von $[MBr_2(3\text{-}CNpy)_1]_n$ mit M = Mn, Fe, Co und Ni.

Verbindung	**$[MnBr_2(3\text{-}CNpy)_1]_n$ ***	**$[FeBr_2(3\text{-}CNpy)_1]_n$**	**$[CoBr_2(3\text{-}CNpy)_1]_n$**	**$[NiBr_2(3\text{-}CNpy)_1]_n$**
Literaturstelle	MH2	MH2	MH2	MH2
CSD Refcode	XOSMEA	XOSMUQ	XOSNOL	XOSPIH
Strukturbestimmung erfolgte aus	Pulverdaten	Pulverdaten	Pulverdaten	Pulverdaten
Summenformel	$C_6H_4Br_2MnN_2$	$C_6H_4Br_2FeN_2$	$C_6H_4Br_2CoN_2$	$C_6H_4Br_2N_2Ni$
Kristallsystem	orthorhombisch	orthorhombisch	orthorhombisch	orthorhombisch
Raumgruppe (Nr.)	*P* 1 1 2_1 (4)	*P m c* 2_1 (26)	*P m c* 2_1 (26)	*P m c* 2_1 (26)
***a* /Å**	3,834(7)	3,772(2)	3,740(1)	3,701(5)
***b* /Å**	7,258(1)	7,251(2)	7,231(2)	7,204(8)
***c* /Å**	16,547(7)	16,31(1)	16,167(6)	16,000(4)
***α* /°**	90	90	90	90
***ß* /°**	90	90	90	90
***γ* /°**	93,41(1)	90	90	90
***V* /Å³**	459,7(5)	446,1(8)	437,2(1)	426,7(1)
Z, Z'	2, 1	2, ½	2, ½	2, ½
Lagesymmetrie von M	1	*m*	*m*	*m*
T /K	298	298	298	298
Strahlungsart	Cu *K*α_1	Cu *K*α_1	Cu *K*α_1	Cu *K*α_1
Wellenlänge /Å	1,54056	1,54056	1,54056	1,54056
* Zwecks Vergleichbarkeit wurde für $[MnBr_2(3\text{-}CNpy)_1]_n$ an dieser Stelle eine Nicht-Standardaufstellung gewählt.				

4.9 $[MBr_2(4\text{-}CNpy)_2]_{(n)}$

Alle Verbindungen der $[MBr_2(4\text{-}CNpy)_2]_n$-Serie (mit M^{II} = Mn, Fe, Co, Ni, Cu und Zn) wurden durch Reaktion des jeweiligen Bromids MBr_2 mit 4-Cyanopyridin in alkoholischer Lösung synthetisiert. Im Gegensatz zu Kristallisationsexperimenten der 3-CNpy-Serie (siehe Kapitel 4.6) bildeten sich in allen Versuchsansätzen stets Verbindungen mit einem Metall-zu-Ligand-Verhältnis von 1:2. Verbindungen der allgemeinen Zusammensetzung $[MX_2(4\text{-}CNpy)_{x>2}]_{(n)}$ scheinen also grundsätzlich ohne weiteren Aufwand nicht zugänglich zu sein. Im Fall von $[ZnBr_2(4\text{-}CNpy)_2]$ fielen indes zwei polymorphe Phasen an.

Wichtige kristallographische Daten und Ergebnisse der Strukturverfeinerungen der $[MBr_2(4\text{-}CNpy)_2]_n$-Verbindungen sind in den Tabellen 4.9.1 und 4.9.2 aufgeführt. Weitere Ergebnisse sind im Detail in den Publikation MH1 und MH4 nachzulesen.

4.9.1 $[MBr_2(4\text{-}CNpy)_2]_n$ mit M = Mn, Fe, Co, Ni und Cu

Analog zu den Verbindungen der $[MBr_2(3\text{-}CNpy)_2]_n$-Serie werden die Metallatome von jeweils vier Br- und zwei N_{py}-Atomen oktaedrisch koordiniert. Die Br-Atome fungieren als μ_2-Brückenliganden und verknüpfen die MBr_4N_{py2}-Oktaeder über deren Ecken. Dadurch entstehen Ketten, die in den Kristallstrukturen von $[MBr_2(4\text{-}CNpy)_2]_n$ entlang [001] laufen, sodass in diesen Strukturen die Gitterkonstante *c* den Metall-Metall-Abstand innerhalb einer Kette angibt. Dieser nimmt von 3,86070(12) Å bei γ-Mn auf 3,6898(5) Å bei Ni ab, korreliert also mit den Abständen der $[MBr_2(3\text{-}CNpy)_2]_n$-Serie. In $[CuBr_2(4\text{-}CNpy)_2]_n$ sind die Koordinationsoktaeder in Kettenrichtung gestreckt, sodass hier die kurze Gitterkonstante *c* mit 3,98420(7) Å beträchtlich größer ausfällt.

Erwartungsgemäß stapeln benachbarte 4-CNpy-Liganden einer Kette planparallel. Die Interplanar-Abstände der Ebenen der C_5N_{py}-Ringfragmente variieren zwischen 3,662 Å in $[CuBr_2(4\text{-}CNpy)_2]_n$ und 3,86070(12) Å in γ-$[MnBr_2(4\text{-}CNpy)_2]_n$ (entspricht ebenfalls *c*), wodurch die π-π-Wechselwirkungen im Vergleich zu den $[MCl_2(4\text{-}CNpy)_2]_n$ schwächer sind.

Tabelle 4.9.1: Ausgewählte kristallographische Daten von $[MBr_2(4\text{-}CNpy)_2]_n$ mit M = Mn, Fe, Co, Ni und Cu.

Verbindung	**β-$[MnBr_2(4\text{-}CNpy)_2]_n$**	**γ-$[MnBr_2(4\text{-}CNpy)_2]_n$**	**$[FeBr_2(4\text{-}CNpy)_2]_n$**
Literaturstelle	MH4	MH4	MH4
CSD Refcode	ZUFBEK	ZUFBEK03	ZUDZIK
Strukturbestimmung erfolgte aus	Pulverdaten	Pulverdaten	Pulverdaten
Summenformel	$C_{12}H_8Br_2MnN_4$	$C_{12}H_8Br_2MnN_4$	$C_{12}H_8Br_2FeN_4$
Kristallsystem	monoklin	orthorhombisch	orthorhombisch
Raumgruppe (Nr.)	*P*2$_1$/*n* (14)	*Pnnm* (58)	*Pnnm* (58)
***a* /Å**	27,0744(7)	27,1046(6)	26,9168(11)
***b* /Å**	7,38192(18)	7,4288(3)	7,3429(2)
***c* /Å**	3,83783(11)	3,86070(12)	3,79547(10)
***α* /°**	90	90	90
***ß* /°**	91,182(3)	90	90
***γ* /°**	90	90	90
***V* /Å^3**	766,87(4)	777,37(4)	750,17(4)
Z, Z'	2, ½	2, ¼	2, ¼
Lagesymmetrie von M	$\bar{1}$	2/*m*	2/*m*
T /K	298	478	298
Strahlungsart	Cu *Kα*$_1$	Cu *Kα*$_1$	Cu *Kα*$_1$
Wellenlänge /Å	1,5406	1,5406	1,5406

Verbindung	**$[CoBr_2(4\text{-}CNpy)_2]_n$**	**$[NiBr_2(4\text{-}CNpy)_2]_n$**	**$[CuBr_2(4\text{-}CNpy)_2]_n$**
Literaturstelle	MH4	MH1	MH4
CSD Refcode	LATJOI	LATJUO	ZUDZAC
Strukturbestimmung erfolgte aus	Pulverdaten	Pulverdaten	Pulverdaten
Summenformel	$C_{12}H_8Br_2CoN_4$	$C_{12}H_8Br_2N_4Ni$	$C_{12}H_8Br_2CuN_4$
Kristallsystem	orthorhombisch	orthorhombisch	monoklin
Raumgruppe (Nr.)	*Pnnm* (58)	*Pnnm* (58)	*P*2$_1$/*n* (14)
***a* /Å**	26,8461(15)	26,6981(4)	7,30106(14)
***b* /Å**	7,3191(3)	7,2936(1)	25,8712(6)
***c* /Å**	3,7708(11)	3,7359(4)	3,98420(7)
***α* /°**	90	90	90
***ß* /°**	90	90	97,3176(13)
***γ* /°**	90	90	90
***V* /Å^3**	740,92(6)	727,48(2)	746,44(3)
Z, Z'	2, ¼	2, ¼	2, ½
Lagesymmetrie von M	2/*m*	2/*m*	$\bar{1}$
T /K	298	298	298
Strahlungsart	Mo *Kα*$_1$	Cu *Kα*$_1$	Cu *Kα*$_1$
Wellenlänge /Å	0,70930	1,5406	1,5406

In allen Kristallstrukturen sind die Ketten in dem bekannten Fischgrätenmuster angeordnet. In γ-$[MnBr_2(4\text{-}CNpy)_2]_n$, $[FeBr_2(4\text{-}CNpy)_2]_n$, $[CoBr_2(4\text{-}CNpy)_2]_n$ und $[NiBr_2(4\text{-}CNpy)_2]_n$ wird der Abstand unmittelbar benachbarter, paralleler Ketten durch die Gitterkonstante *b* wiedergegeben wird. Wie zuvor bei der $[MBr_2(3\text{-}CNpy)_2]_n$-Reihe aufgezeigt (vgl. Kapitel 4.7), stehen die Pyridinliganden senkrecht auf den Ketten, sodass $\beta = 90°$ und das Kristallgitter folglich orthorhombisch ist (Abb. 4.9.1). Diese Verbindungen kristallisieren wie ihre verwandten $[MBr_2(3\text{-}CNpy)_2]_n$-Verbindungen ebenfalls in der Raumgruppe *Pnnm* mit $Z = 2$ (vgl. Kapitel 4.7).

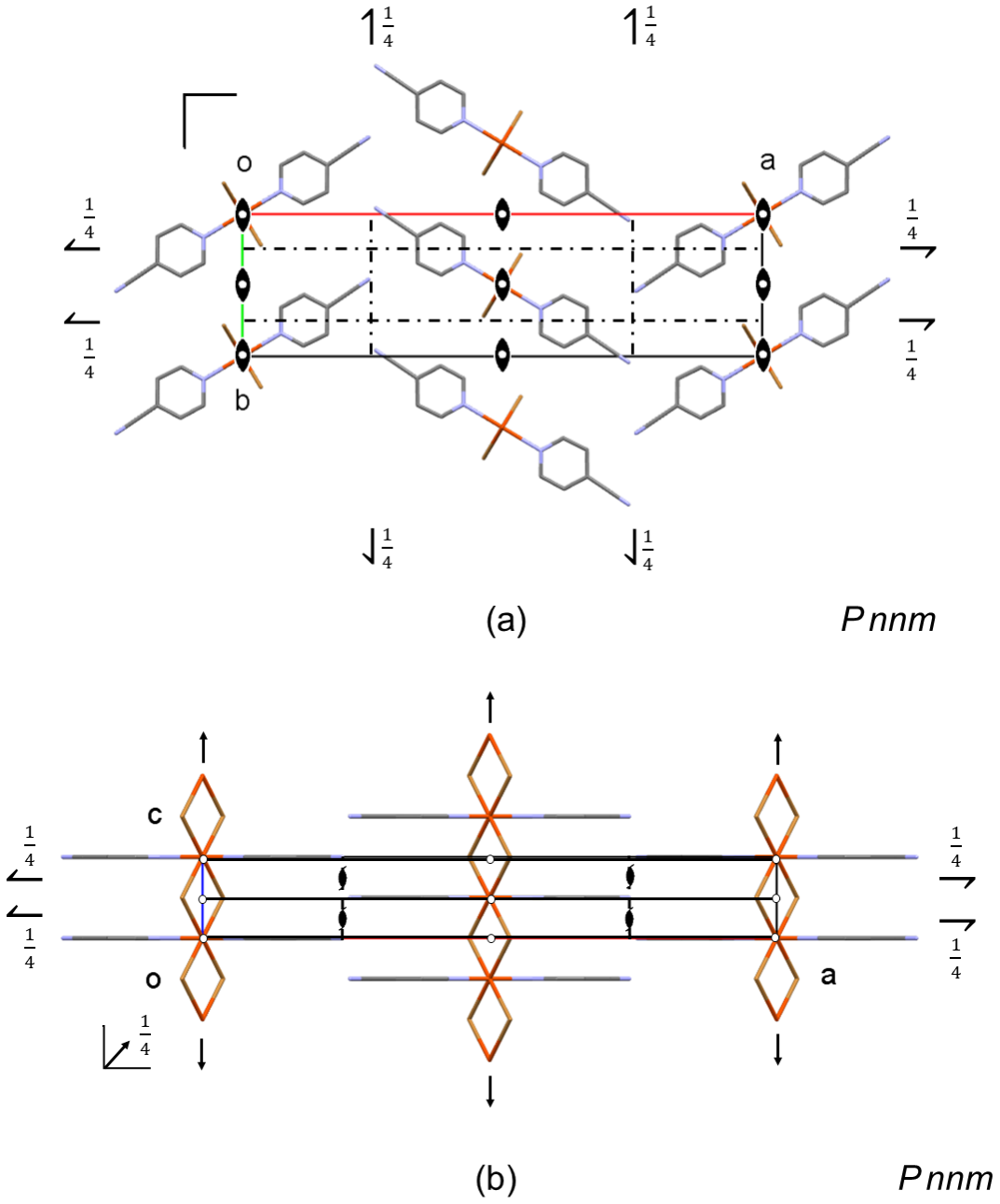

Abbildung 4.9.1: Packungsmuster und Symmetrieelemente in $[FeBr_2(4\text{-}CNpy)_2]_n$. Projektionsrichtung in (a): [001], in (b): [010].

Die Kristallstrukturen von β-$[MnBr_2(4\text{-}CNpy)_2]_n$ und $[CuBr_2(4\text{-}CNpy)_2]_n$ sind ähnlich zu den zuvor diskutierten vier Strukturen. Da die 4-CNpy-Liganden leicht schief auf ihren $[MBr_4]$-Ketten(ebenen) stehen, wird die Spiegelsymmetrie gebrochen. Somit reduziert sich die Lagesymmetrie für 4-CNpy auf 1 bzw. für die Metallatome auf $\bar{1}$. Infolgedessen kristallisieren β-$[MnBr_2(4\text{-}CNpy)_2]_n$ und $[CuBr_2(4\text{-}CNpy)_2]_n$ wie auch die komplette $[MCl_2(4\text{-}CNpy)_2]_n$-Serie in der monoklinen Untergruppe *P* 1 2_1/*n* 1 (Abb. 4.9.2). Grundsätzlich lässt sich jedoch konstatieren, dass Br-haltige Strukturen gegenüber ihren Cl-Analogen in der Regel höhere Symmetrie zeigen. Dadurch eignen sich einen Vergleich zweier Kristallstrukturen lassen sich, wie an dieser Stelle, wunderbar Symmetriebeziehungen bzw. Obergruppe-Untergruppe-Beziehung veranschaulichen.

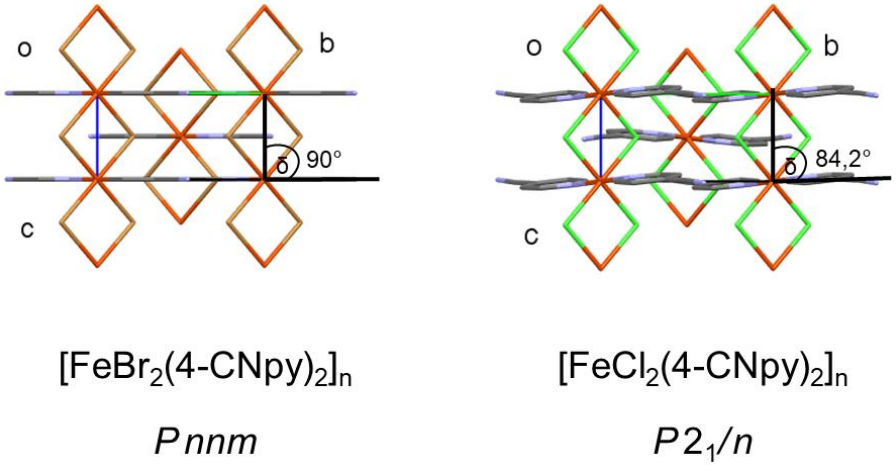

Abbildung 4.9.2: Packungsmuster in $[FeBr_2(4\text{-}CNpy)_2]_n$ und $[FeCl_2(4\text{-}CNpy)_2]_n$, Projektionsrichtung [100]. In $[FeCl_2(4\text{-}CNpy)_2]_n$ ist wegen δ ≠ 90° das Gitter monoklin.

Im Falle von β-$[MnBr_2(4\text{-}CNpy)_2]_n$ und γ-$[MnBr_2(4\text{-}CNpy)_2]_n$ ist der Symmetrieverlust bzw. Symmetriegewinn bei Phasenumwandlung sogar in temperaturabhängigen Röntgenbeugungsaufnahmen sichtbar (siehe Abb. 4.9.3). Wie eingangs beschrieben, liegen in γ-$[MnBr_2(4\text{-}CNpy)_2]_n$ alle Atome auf kristallographischen Spiegelebenen, wohingegen in β-$[MnBr_2(4\text{-}CNpy)_2]_n$ keine Spiegelebenen existieren.

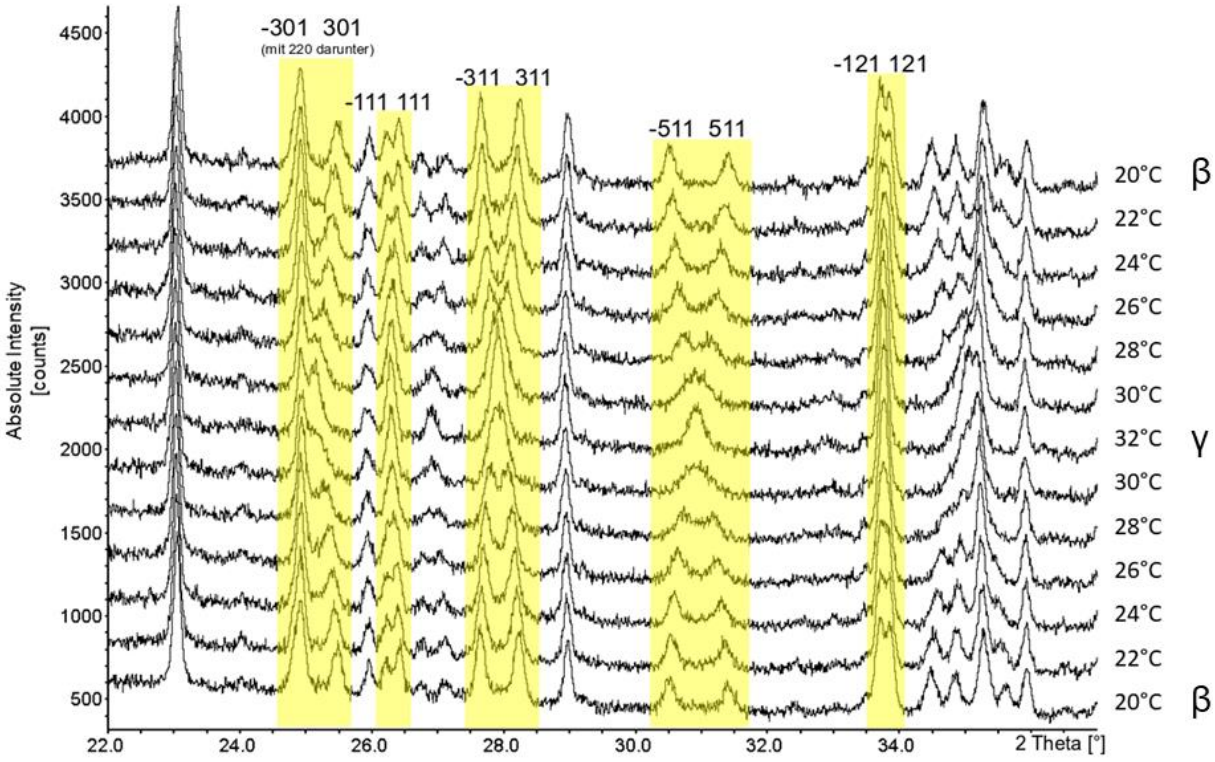

Abbildung 4.9.3: T-abhängige XRPD-Aufnahme von $[MnBr_2(4\text{-}CNpy)_2]_n$: reversibler Phasenübergang von β zu γ mit „wandernden“ Bragg-Reflexen.

In der XRPD- Aufnahme von γ-$[MnBr_2(4\text{-}CNpy)_2]_n$ fallen also Reflexe wie -301 und 301 zusammen, d.h. sie erscheinen unter einem gemeinsamen Beugungswinkel in 2θ. Verfolgt man nun den Übergang der orthorhombischen γ- zur monoklinen β-Phase, so erkennt man ein egales „Auseinanderlaufen“ dieser Reflexe zu zwei dezidierten Beugungswinkeln und mit jeweils etwa der halben Intensität. Leider treten in der Pulveraufnahme von β-$[MnBr_2(4\text{-}CNpy)_2]_n$ keine der zusätzlichen (und in *P nnm* ausgelöschten) 0*kl* Reflexe ($k + l \neq 2n$) wie zum Beispiel 021 oder 041 isoliert auf, sondern fallen mit anderen Reflexen des monoklinen Systems zusammen.

4.9.1 [$ZnBr_2(4\text{-}CNpy)_2$]

In beiden Polymorphen von [$ZnBr_2(4\text{-}CNpy)_2$] liegen wie in [$ZnCl_2(3\text{-}CNpy)_2$] und [$ZnBr_2(3\text{-}CNpy)_2$] (vgl. Kapitel 4.1 und 4.7) diskrete Komplexmoleküle vor, in denen die Zn-Atome jeweils von zwei Br- und zwei N_{py}-Atomen nahezu tetraedrisch koordiniert werden. Die Packungsmuster der beiden Polymorphe unterscheiden sich deutlich.

Die Packung von α-[$ZnBr_2(4\text{-}CNpy)_2$] ähnelt der von [$ZnCl_2(4\text{-}CNpy)_2$], das ebenfalls in der Raumgruppe *C* 2/*c* kristallisiert. Die Komplexmoleküle werden durch (schwache) π-π-Wechselwirkungen der 4-CNpy-Fragmente zusammengehalten. Ein 4-CNpy-Ligand formt mit dem 4-CNpy-Liganden des Nachbarmoleküls über ein Inversionszentrum ($\bar{1}$) ein Paar (gelb markiert in Abb. 4.9.4b und 4.9.4c). Der zweite 4-CNpy-Ligand ist ebenfalls „gepaart“, jedoch mit dem 4-CNpy eines anderen Nachbarmoleküls. Diese Paarung wird über die zweizählige Drehachse (2) in [010]-Richtung fortgepflanzt (blau markiert in Abb. 4.9.4b und 4.9.4c). Die Interplanar-Abstände der Ebenen der C_5N_{py}-Ringfragmente betragen ca. 4,6 Å bzw. 3,9 Å. Außerdem packen die 4-CNpy-Liganden in α-[$ZnBr_2(4\text{-}CNpy)_2$] nicht flächendeckend, sondern sind wegen der „sperrigen“ Br-Atome leicht versetzt zueinander angeordnet.

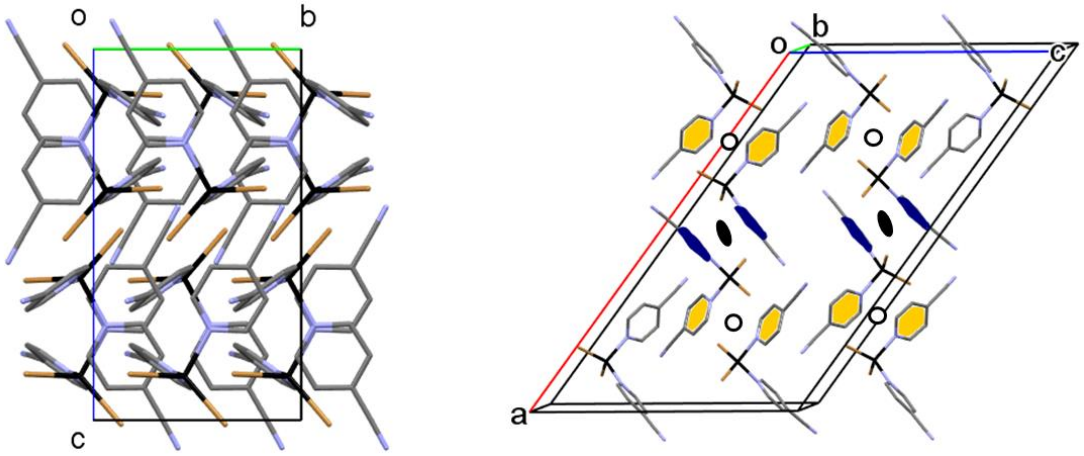

(a) (b)

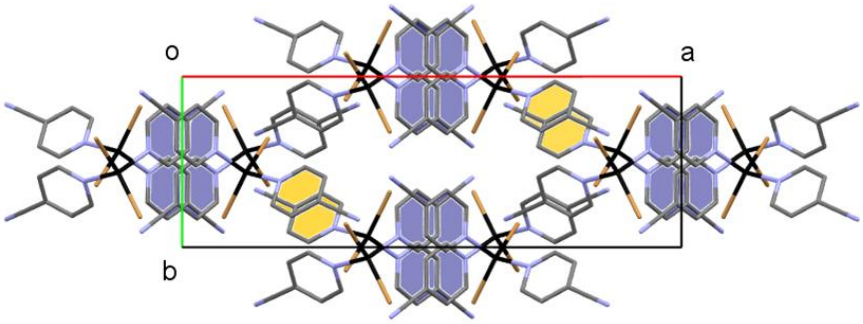

(c)

Abbildung 4.9.4: Packungsmuster in α-[$ZnBr_2(4\text{-}CNpy)_2$]. Projektionsrichtung [100] in (a), schräg entlang [010] in (b), [010] in (c). Über $\bar{1}$ gepaarte 4-CNpy-Liganden in gelb bzw. über 2-Drehachsen aufgereihte 4-CNpy in blau eingefärbt.

Die Kristallstruktur von β-[$ZnBr_2(4\text{-}CNpy)_2$] ähnelt den Strukturen von β-[$ZnCl_2(3\text{-}CNpy)_2$] und [$ZnCl_2(py)_2$]; alle drei Verbindungen kristallisieren in der Raumgruppe *P* $2_1/c$. Im Gegensatz zu α-[$ZnBr_2(4\text{-}CNpy)_2$] liegt nur ein π-π-Paarungsmotiv vor, das entlang [001] greift (Obacht: je nach Projektionsrichtung werden über $\bar{1}$ gepaarte 4-CNpy-Fragmente vorgetäuscht). Über die *c*-Gleitspiegelebenen wird die Hälfte der Liganden kettenförmig aufgereiht (in Abb. 4.9.5 grün eingefärbt). Der Ligand-zu-Ligand-Abstand beträgt hier ca. 4,0 Å (bestimmt über die Mittelpunkte der C_5N_{py}-Ebenen). Bezüglich dieser Ketten ist die andere Hälfte Ligand sozusagen paddelförmig angeordnet (Abb. 4.9.5b).

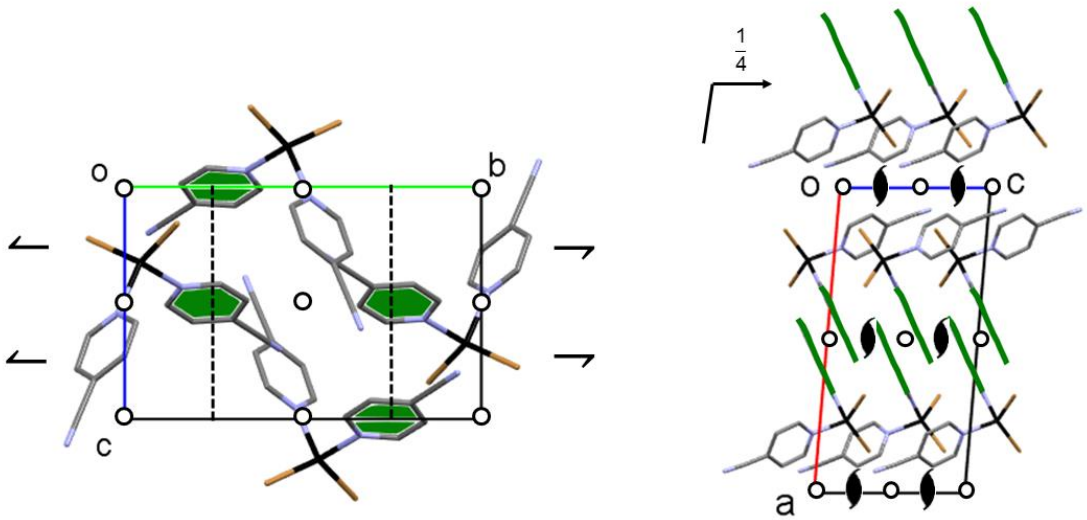

(a) (b)

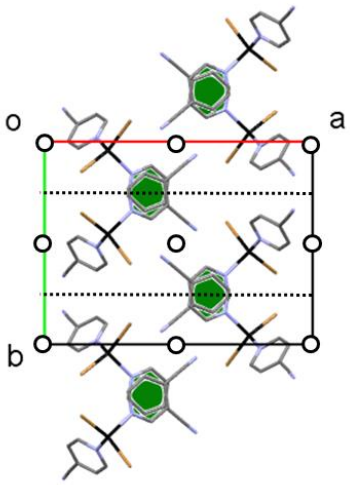

(c)

Abbildung 4.9.5: Packungsmuster und Symmetrieelemente in β-[$ZnBr_2(4\text{-}CNpy)_2$]. Projektionsrichtung in (a): [100], in (b): [010], in (c): [001], 2_1-Schraubenachsen aus Gründen der Übersichtlichkeit nicht abgebildet. Über *c* aufgereihte 4-CNpy-Liganden in grün eingefärbt.

Tabelle 4.9.2: Ausgewählte kristallographische Daten von $[ZnBr_2(4\text{-}CNpy)_2]_n$.

Verbindung	**α-[$ZnBr_2(4\text{-}CNpy)_2$]**	**β-[$ZnBr_2(4\text{-}CNpy)_2$]**
Literaturstelle	MH4	MH4
CSD Refcode	ZUFBEK	ZUFBEK03
Strukturbestimmung erfolgte aus	Pulverdaten	Pulverdaten
Summenformel	$C_{12}H_8Br_2N_4Zn$	$C_{12}H_8Br_2N_4Zn$
Kristallsystem	monoklin	monoklin
Raumgruppe (Nr.)	*C* 2/*c* (15)	*P* 2_1/*c* (14)
***a* /Å**	28,4031(3)	16,0185(4)
***b* /Å**	7,73326(8)	12,09069(19)
***c* /Å**	17,2427(2)	7,89902(13)
***α* /°**	90	90
***ß* /°**	126,9230(6)	94,8775(12)
***γ* /°**	90	90
***V* /Å³**	3027,76(6)	1524,30(5)
Z, Z'	8, 1	4, 1
Lagesymmetrie von M	1	1
T /K	298	298
Strahlungsart	Cu $K\alpha_1$	Cu $K\alpha_1$
Wellenlänge /Å	1,54056	1,54056

4.9 $[MBr_2(4\text{-}CNpy)_1]_n$

Der thermische Abbau von $[MBr_2(4\text{-}CNpy)_2]_n$ (mit M = Mn, Fe, Co oder Ni) führte zur Bildung von Verbindungen der Stöchiometrie $[MBr_2(4\text{-}CNpy)_1]_n$. Von $[ZnBr_2(4\text{-}CNpy)_2]$ und $[CuBr_2(4\text{-}CNpy)_2]$ waren keine Abbaustufen zugänglich, da diese Verbindungen wie $[ZnBr_2(3\text{-}CNpy)_2]$ bzw. $[CuBr_2(4\text{-}CNpy)_2]$ bei Erhitzen unmittelbar in ihre Ausgangsstoffe zerfallen (vgl. Kapitel 4.7).

Wichtige kristallographische Daten und Ergebnisse der Strukturverfeinerungen der $[MBr_2(4\text{-}CNpy)_1]_n$-Serie sind in Tabelle 4.10 aufgeführt. Weitere Ergebnisse sind im Detail in den Publikationen MH1 und MH4 nachzulesen.

In allen Kristallstrukturen werden die Metallatome von jeweils vier Br-, einem N_{py}- und einem N_{CN}-Atom eines zweiten 4-CNpy-Liganden koordiniert. Die $MBr_4N_{py}N_{CN}$-Oktaeder sind durch verbrückende μ_2-Br-Atome eckenverknüpft, wodurch in erster Dimension Ketten entstehen. Diese Ketten laufen entlang [010], sodass die Gitterkonstante *b* dem M-M-Abstand innerhalb dieser Verkettung entspricht (Abb. 4.10.1b).

Alle Kristallstrukturen der $[MBr_2(4\text{-}CNpy)_1]_n$-Serie sind isotyp. Wie auch die $[MBr_2(3\text{-}CNpy)_1]_n$- und $[MCl_2(4\text{-}CNpy)_1]_n$-Serien zeigen sie Netzwerkstrukturen, in denen 4-CNpy als bidentater Ligand fungiert und über seine beiden N-Atome an zwei M-Atome koordiniert. Analog zur $[MCl_2(4\text{-}CNpy)_1]_n$-Serie werden die in [010]-Richtung laufenden Ketten durch verbrückende 4-CNpy Liganden entlang [001] vernetzt (Abb. 4.10.1.a). Alle Netze schichten parallel zu (100) (Abb. 4.10.1b). Ihr Abstand entspricht $\frac{a}{2}\sin\beta$, der wegen $\beta \approx 90°$ also knapp $\frac{a}{2}$ ist. Senkrecht zu (100) verlaufen Spiegelebenen, welche von 4-CNpy-Liganden und Metallatomen belegt werden (Abb. 4.10.1c). Diese besitzen folglich die Lagesymmetrie *m*. Außerdem existieren zweizählige Drehachsen senkrecht zu den Spiegelebenen, sodass die Strukturen in der Raumgruppe *P* 2/*m* mit *Z* = 2 kristallisieren.

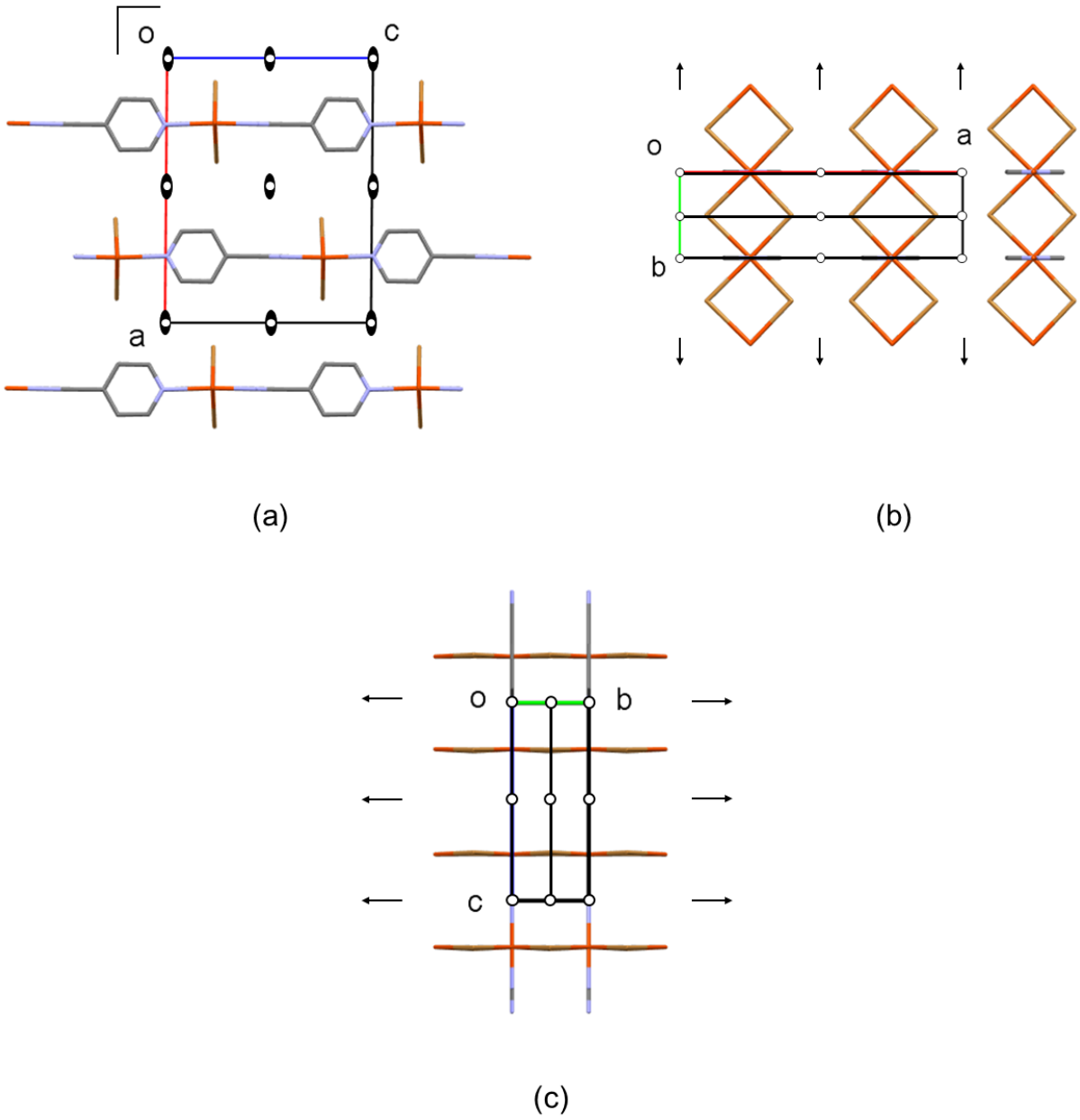

Abbildung 4.10.1: Packungsmuster und Symmetrieelemente in $[FeBr_2(4\text{-}CNpy)_1]_n$, RG *P*2/*m*. Projektionsrichtung in (a): [010], in (b): [001], in (c): [100]. Nur eine Orientierung des verbrückenden 4-CNpy in $[FeBr_2(4\text{-}CNpy)_1]_n$ abgebildet.

Alle Kristallstrukturen der $[MBr_2(4\text{-}CNpy)_1]_n$-Serie können als „pseudo-orthorhombisch“ bezeichnet werden, da der monokline Winkel *β* nur geringfügig von 90° abweicht. Tatsächlich sind die $[MBr_4]$-Ebenen nicht parallel zu (001), sodass die Symmetriebedingungen für ein orthorhombisches Gitter knapp nicht erfüllt werden. Die korrespondierende Obergruppe wäre *P* $2_1/m$ 2/*m* 2/*a* (kurz *P mma*) und bei *Z* = 2 würden die Metallatome Lagen mit *mm*2 Symmetrie (statt *m* bei *P* 2/*m*) belegen. Da die verwandten $[MBr_2(3\text{-}CNpy)_1]_n$-Verbindungen mit M = Fe, Co und Ni (vgl. Kapitel

4.3) in einer höhersymmetrischen bzw. orthorhombischen Struktur kristallisieren (und Brom-Strukturen grundsätzlich ja tendenziell höhere Symmetrie zeigen), wurden bei der $[MBr_2(4\text{-}CNpy)_1]_n$-Serie zusätzlich Strukturverfeinerungen in *P mma* durchgeführt. Allerdings lieferten die Rietveld-Verfeinerungen mehrheitlich schlechtere Gütewerte, sodass für die $[MBr_2(4\text{-}CNpy)_1]_n$-Serie eine monokline Beschreibung in *P* 2/*m* vorzuziehen ist (vgl. ESI von MH4).

In allen Kristallstrukturen von $[MBr_2(4\text{-}CNpy)_1]_n$ liegt eine sogenannte „Kopf-Schwanz-Fehlordnung“ der verbrückenden 4-CNpy-Fragmente vor (Abb. 4.10.2). Grundsätzlich sind die Metallatome in Verbindungen mit Netzwerkstrukturen (also auch in $[MCl_2(4\text{-}CNpy)_1]_n$ und $[MBr_2(3\text{-}CNpy)_1]_n$) stets an das N_{py}-Atom eines 4-CNpy-Liganden sowie an das N_{CN}-Atom eines zweiten Liganden gebunden. Hingegen werden die Metallatome in den fehlgeordneten Kristallstrukturen teilweise von je zwei N_{py}- bzw. von je zwei N_{CN}-Atomen koordiniert. Diese zusätzlichen Koordinationsvarianten sind möglich, da die Pyridinmoleküle in den $[MBr_2(4\text{-}CNpy)_1]_n$-Strukturen zwei verschiedenen Orientierungen im Kristallgitter einnehmen können. Diese kann man sich plastisch als „Kopf-Schwanz“-Alternation vorstellen.

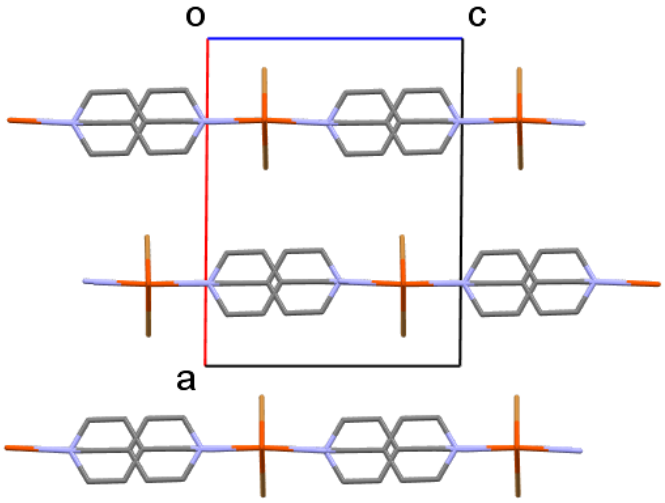

Abbildung 4.10.2: Fehlgeordnete 4-CNpy-Fragmente in $[FeBr_2(4\text{-}CNpy)_1]_n$, RG *P* 2/*m*. Projektionsrichtung [010].

Angenommen, die Netze sind in sich geordnet, dann erzeugt diese Fehlordnung in Röntgenbeugungsexperimenten diffuse Streuung parallel zu a^*, die sich in den Pulverdiffraktogrammen aller betroffenen Strukturen wiederum in charakteristischen „Warren-Reflexen“ äußert [45]. Diese Reflexe weisen einen asymmetrischen

Peakabfall auf, welcher vornehmlich bei Warren-Reflexen im niedrigen 2θ-Bereich der Diffraktogramme zur Geltung kommt (siehe Abb. 4.10.3).

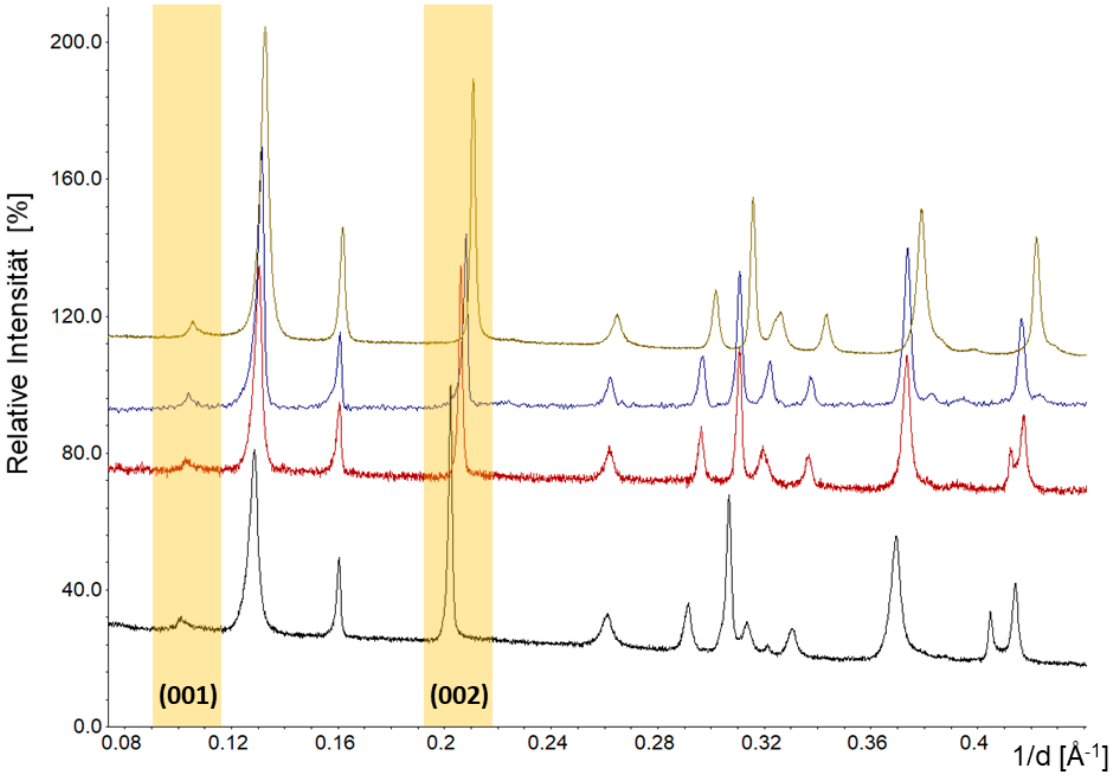

Abbildung 4.10.3: XRDP-Aufnahmen von $[MBr_2(4\text{-}CNpy)_1]_n$ mit M = Mn (schwarz), Fe (rot), Co (blau) und Ni (gelb). Die charakteristische Reflexform der Warren-Reflexe ist nur an den ersten beiden 00*l* Reflexen erkennbar, da diese isoliert auftreten. Hinweis: Die XRPD-Aufnahmen sind in 1/d aufgetragen, da mit unterschiedlicher Strahlung gemessen wurde (vgl. Tabelle 4.10).

Bei den Rietveld-Verfeinerungen der vier Kristallstrukturen wurde u. a. ein zusätzlicher Parameter zur Beschreibung der Besetzungsdichten in beiden Orientierungsvarianten eingeführt (FO), der bei allen Verfeinerungen auf eine Besetzung von ca. 0,5 : 0,5 hinauslief. Das heißt, in allen Kristallstrukturen der $[MBr_2(4\text{-}CNpy)_1]_n$-Serie weist die Hälfte der 4-CNpy-Fragmente die „richtige“ bzw. „normale“ Anordnung zwischen zwei Metallatomen auf, und die andere Hälfte der Moleküle ist „falsch“ bzw. „verkehrt herum“ orientiert.

Bislang wurde dieses Fehlordnungsmuster ausschließlich in der $[MBr_2(4\text{-}CNpy)_1]_n$-Serie beobachtet. Analoge Rietveld-Verfeinerungen der verwandten $[MCl_2(4\text{-}CNpy)_1]_n$ Kristallstrukturen führten in allen Fällen zu schlechteren Gütewerten, verglichen mit

jenen aus den Verfeinerungen nicht-fehlgeordneter Modelle (siehe ESI aus MH4). Grundsätzlich ist der Schicht-zu-Schicht-Abstand (also *a*/2) in allen $[MBr_2(4\text{-}CNpy)_1]_n$-Strukturen wegen der voluminöseren Br-Atome größer (als in den$[MCl_2(4\text{-}CNpy)_1]_n$-Strukturen) und bietet dadurch den 4-CNpy-Liganden „Spielraum“, beide Orientierungsmöglichkeiten wahrzunehmen.

Tabelle 4.10: Ausgewählte kristallographische Daten von $[MBr_2(4\text{-}CNpy)_1]_n$ mit M = Mn, Fe, Co und Ni. Diese Strukturen sind fehlgeordnet.

Verbindung	**$[MnBr_2(4\text{-}CNpy)_1]_n$**	**$[FeBr_2(4\text{-}CNpy)_1]_n$**	**$[CoBr_2(4\text{-}CNpy)_1]_n$**	**$[NiBr_2(4\text{-}CNpy)_1]_n$**
Literaturstelle	MH4	MH4	MH4	MH1
CSD Refcode	ZUFBAG	ZUDZEG	ZUDYOP	LATJIC
Strukturbestimmung erfolgte aus	Pulverdaten	Pulverdaten	Pulverdaten	Pulverdaten
Summenformel	$C_6H_4Br_2MnN_2$	$C_6H_4Br_2FeN_2$	$C_6H_4Br_2CoN_2$	$C_6H_4Br_2N_2Ni$
Kristallsystem	monoklin	monoklin	monoklin	monoklin
Raumgruppe (Nr.)	*P* 2/*m* (10)	*P* 2/*m* (10)	*P* 2/*m* (10)	*P* 2/*m* (10)
***a* /Å**	12,4448(6)	12,4397(9)	12,4692(10)	12,3468(3)
***b* /Å**	3,82332(12)	3,75800(17)	3,76053(17)	3,6898(5)
***c* /Å**	9,8744(5)	9,6919(7)	9,6232(7)	9,4827(2)
***α* /°**	90	90	90	90
***ß* /°**	90,569(8)	90,459(8)	89,870(15)	90,423(7)
***γ* /°**	90	90	90	90
***V* /Å³**	469,81(4)	453,07(5)	451,24(5)	431,99(2)
Z, Z'	2, ½	2, ½	2, ½	2, ½
Lagesymmetrie von M	*m*	*m*	*m*	*m*
T /K	298	298	523	298
Strahlungsart	Cu *K*α₁	Cu *K*α₁	Mo *K*α₁	Cu *K*α₁
Wellenlänge /Å	1,54056	1,54056	0,70930	1,54056

5. Zusammenfassung

Ausgangspunkt dieser Arbeit bildeten frühere Untersuchungen an MX_2-Koordinationspolymeren mit zweiwertigen Mn-, Cu- oder Ni-Atomen, sowie Pyridin oder 4-Cyanopyridin als neutralen Co-Liganden. In der hier vorliegenden Arbeit wurden diese Untersuchungen systematisch fortgesetzt und darüber hinaus auf FeX_2 und 3-Cyanopyridin als Edukte ausgeweitet. Ein besonderes Interesse galt Koordinationsverbindungen der Stöchiometrie $[MX_2(CNpy)_1]_n$, denen bis dato wenig Aufmerksamkeit geschenkt wurde. Hierfür wurden zunächst ligandenreichere Precursoren der Stöchiometrie $[MX_2(CNpy)_2]_n$ oder $[MX_2(CNpy)_4]$ (d.h. $[MBr_2(3\text{-}CNpy)]_4$) dargestellt, die anschließend systematisch thermisch abgebaut wurden. Diese Abbaureaktionen wurden wahlweise in einem DTA-TG-Gerät oder einem speziell ausgerüsteten Pulverdiffraktometer durchgeführt und resultierten in Phasen mit Einzelketten, Doppelketten oder Netzwerktopologie (Tab. 5a/b).

Tabelle 5a: Übersicht der Raumgruppen und Strukturtopologien von $[MX_2(CNpy)_2]_n$. K = Kette, M = diskretes Molekül. * Diese Kristallstrukturen waren bereits aus SCXRD-Aufnahmen bekannt.

	$[MX_2(3\text{-}CNpy)_2]_n$				**$[MX_2(4\text{-}CNpy)_2]_n$**			
M^{II}	**X = Cl**		**X = Br**		**X = Cl**		**X = Br**	
Mn	*P* $2_1/n$	K	*P nnm*	K	* *P* $2_1/n$	K	*P* $2_1/c$ *P nnm*	K
Fe	*P* $2_1/n$	K	*P nnm*	K	*P* $2_1/n$	K	*P nnm*	K
Co	*C c*	K	*P nnm* *P* $\bar{1}$	K	* *P* $2_1/c$	K	*P nnm*	K
Ni	*C c*	K	*C c* *P* $\bar{1}$	K K	*P* $2_1/n$	K	*P nnm*	K
Cu	* *P* $2_1/c$	K	*P* $2_1/c$ * *P* $\bar{1}$	K M	*P* $2_1/n$	K	*P* $2_1/n$	K
Zn	*P nma* *P* $2_1/c$	M M	* *P bca*	M	* *I* 2/*a*	M	*C* 2/*c* *P* $2_1/c$	M M

Tabelle 5b: Übersicht der Raumgruppen und Strukturtopologien von $[MX_2(CNpy)_1]_n$. DK = Doppelkette, N = Netzwerk.

	$[MX_2(3\text{-}CNpy)_1]_n$				$[MX_2(4\text{-}CNpy)_1]_n$			
M^{II}	**X = Cl**		**X = Br**		**X = Cl**		**X = Br**	
Mn	*P* $2_1/n$	DK	*P* 2_1	N	*P* 2/*m*	N	*P* 2/*m*	N
Fe	- [a]		*P mc*2_1	N	*P m*	N	*P* 2/*m*	N
Co	*P nma*	DK	*P mc*2_1	N	*P m*	N	*P* 2/*m*	N
Ni	*P nma*	DK	*P mc*2_1	N	*P m*	N	*P* 2/*m*	N
Cu	*P* $2_1/c$	DK	- [b]		*P* $2_1/n$ *P* $\bar{1}$	DK DK	*P* 2/*m*	N
Zn	- [b]		- [b]		- [b]		- [b]	

a) Verbindung existiert, Strukturbestimmung bislang erfolglos.
b) Verbindung existiert nicht laut DTA-TG-Daten.

Insgesamt wurden im Rahmen dieser Arbeit 42 Kristallstrukturen aus Röntgenpulverdaten neu bestimmt, wobei davon 38 Phasen zudem erstmalig synthetisiert wurden. Für die übrigen vier Verbindungen lagen bereits aus Einkristalldaten bestimmte Strukturen vor, sodass ergänzend Röntgenpulverdaten gesammelt und Rietveld-Verfeinerungen durchgeführt wurden. In sechs Fällen wurde polymorphes Verhalten beobachtet, dabei handelte es sich ausschließlich um Phasen der Zusammensetzung $[MX_2(CNpy)_2]_{(n)}$. Alle neuen Kristallstrukturen wurden in die CSD eingepflegt sowie (mit Ausnahme der in Anhang B aufgeführten drei Strukturen) im Rahmen von vier Publikationen ausführlich diskutiert (siehe MH1-4, Anhang A). Zusammenfassend ergibt sich folgendes Bild:

3-Cyanopyridin

Im Falle der MBr_2-Serie wurden für M = Mn, Fe, Co und Ni Koordinationsverbindungen der Stöchiometrie $[MBr_2(3\text{-}CNpy)_4]$ erhalten, deren Kristallstrukturen aus diskreten Komplexmolekülen bestehen. Derart ligandenreiche Verbindungen konnten bei keiner der übrigen Serien erhalten werden. Alle Kristallstrukturen der Zusammensetzung $[MX_2(3\text{-}CNpy)_2]_n$ zeigen bei M = Mn, Fe, Co, Ni und Cu eine Kettenstruktur, in der die Halogenatome als μ_2-Brückenliganden fungieren. Die Ketten weisen eine Fischgrät-Anordnung auf. Im Falle von $[ZnX_2(3\text{-}CNpy)_2]$ werden ausschließlich diskrete Komplexmoleküle beobachtet. In allen Kristallstrukturen der $[MCl_2(3\text{-}CNpy)_1]_n$-Serie

liegen Doppelketten mit μ_2- und μ_3-verbrückenden Cl-Atomen vor. Hingegen weisen die Verbindungen der $[MBr_2(3\text{-}CNpy)_1]_n$-Serie Netzwerkstrukturen auf, in denen, zusätzlich zu μ_2-Cl-Atomen, über N_{CN}-Atome gebrückt wird. (Veröffentlichungen: MH2, MH3)

3,5-Dicyanopyridin

Aufgrund der umfassenden Erkenntnislage bei $[NiCl_2(CNpy)_x]_n$ und $[NiCl(py)_x]_n$-Verbindungen wurde $NiCl_2$ für erste Experimente mit 3,5-Dicyanopyridin als neuem, bifunktionalem Liganden ausgewählt. Erwartungsgemäß führte deren Umsetzung zur Bildung von $[NiCl_2(3,5\text{-}CNpy)_2]_n$, dessen Kristallstruktur das hinlänglich bekannte charakteristische Kettenmotiv aufweist. Thermischer Abbau von $[NiCl_2(3,5\text{-}CNpy)_2]_n$ führt indes nicht zur Bildung von $[NiCl_2(3,5\text{-}CNpy)_1]_n$ (bzw. grundsätzlich zu $[NiCl_2(3,5\text{-}CNpy)_{x<2}]_n$ (mit bi- oder gar tridentaten Liganden), sondern unmittelbar zur vollständigen Zersetzung in $NiCl_2$ und 3,5-CNpy. Daher sollten weitere Experimente mit $NiBr_2$ als Edukt durchgeführt werden, da in $[NiBr_2(CNpy)_1]_n$ neben N_{py} auch N_{CN} an Ni-Atome zu koordinieren vermag, wodurch ja deren Netzwerkstrukturen resultieren (Kapitel 4.5 u. 4.8). (Noch nicht veröffentlicht.)

4-Cyanopyridin

Alle Kristallstrukturen der Zusammensetzung $[MX_2(4\text{-}CNpy)_2]_n$ zeigen bei M = Mn, Fe, Co, Ni und Cu ebenfalls eine Kettenstruktur, in der die Halogenatome als μ_2-Brückenliganden fungieren. Auch in diesen Kristallstrukturen liegt eine Fischgrät-Anordnung der Ketten vor. Im Falle von $[ZnX_2(4\text{-}CNpy)_2]$ werden ausschließlich diskrete Komplexmoleküle beobachtet. In allen Kristallstrukturen der $[MX_2(4\text{-}CNpy)_1]_n$-Serie liegen Netzwerkstrukturen vor, in denen die Metallatome über μ_2-Halogenatome und N_{CN}-Atome verbrückt werden. Alle Kristallstrukturen der $[MBr_2(4\text{-}CNpy)_1]_n$-Serie sind charakteristisch fehlgeordnet, da die Orientierung der 4-CNpy-Liganden invertiert wird (Kopf-Schwanz-Fehlordnung). (Veröffentlichungen: MH1, MH4)

6. Literaturverzeichnis

[1] Alig. E., Bernert, T., Fink, L., Kulcu, N., Yesilkaynak, T.: Catena-*Poly[[dipyridine-nickel(II)]-trans-di-μ-chlorido] from powder data.* Acta Cryst. E66: m239, 2010.

[2] Allmann, R.: *Röntgen-Pulverdiffraktometrie.* Springer-Verlag Heidelberg, 2013.

[3] Aroyo, M. I. (Ed.): *International Tables for Crystallography:* Volume A - *Space-group symmetry.* Wiley, 2016.

[4] Batten, S. R., Champness, N. R., Chen, X.-M., Garcia-Martinez, J., Kitagawa, S., Öhrström, L., O'Keeffe, M., Suh, M. P., Reedijk, J.: *Terminology of metal-organic frameworks and coordination polymers (IUPAC Recommendations 2013)*. Pure Appl. 85: 1715-1724, 2013.

[5] Borchardt-Ott, W., Sowa, H.: *Kristallographie*. Springer Heidelberg, 2018.

[6] Boultif, A., Louër, D.: *Indexing of powder diffraction patterns for low-symmetry lattices by the successive dichotomy method.* J. Appl. Cryst. 24: 987-993, 1991.

[7] Bragg, W. L.: *The diffraction of short electromagnetic waves by a crystal*. Proc. Camb. Phys. Soc. 17: 43-57, 1912.

[8] Chen, W.-T., Luo, Z.-G., Xu, Y.-P., Luo, Q.-Y., Liu, J.-H.: *Syntheses, structures and photoluminescence of a series of transition metal-cyanopyridine polymers.* Journal of Chemical Research 35: 253-256, 2011.

[9] Coelho, A.: *TOPAS and TOPAS-Academic: an optimization program integrating computer algebra and crystallographic objects written in C++.* J. Appl. Cryst. 51: 210-218, 2018.

[10] David, W. I. F., Shankland, K., van de Streek, J., Pidcock, E., Motherwell, W. D. S., Cole, J. C.: *DASH: a programm for crystal structure determination from powder diffraction data.* J. Appl. Cryst. 39: 910-915, 2006.

[11] David, W. I. F., Shankland, K., McCusker L. B., Baerlocher, C.: *Structure determination from powder diffraction data.* Oxford University Press, 2006.

[12] David, W. I. F., Shankland, K.: *Structure determination from powder diffraction data.* Acta Cryst. A 64: 52-64, 2008.

[13] Debye, P., Scherrer, P.: *Interferenzen an regellos orientierten Teilchen im Röntgenlicht.* Nachrichten Kgl. Gesell. Wiss. Göttingen I. 1-15; II. 16-26, 1916.

[14] Desiraju, G. R.: *Crystal Engineering: The Design of Organic Solids*. Elsevier, Amsterdam, 1989.

[15] Desiraju, G. R.: *Crystal Engineering: A Holistic View.* Angew. Chem. Int. Ed. 46: 8342-8356, 2007.

[16] De Wolff, P. M.: *A simplified criterion for the reliability of a powder pattern indexing.* J. Appl. Cryst. 1: 108-113, 1968.

[17] Dinnebier, R. E., Leineweber, A., Evans, J. S. O.: *Rietveld Refinement*. De Gruyter, 2019.

[18] Dinnebier, R. E., Billinge, S. J. L.: *Powder diffraction - theory and practice.* RCS Cambridge UK, 2008.

[19] Ermrich, M., Opper, D.: *XRD for the analyst*. PANalytical B.V., 2013.

[20] Esmaeili, A., Kamiyama, T., Oishi-Tomiyasu, R.: *New functions and graphical user interface attached to powder indexing software*. J. Appl. Cryst. 50: 651-659, 2017.

[21] Gesellschaft Deutscher Chemiker https://www.gdch.de/fileadmin/downloads/Netzwerk_und_Strukturen/Fachgruppen/ Analytische_Chemie/chemkrist/pulverdiffraktometrie.pdf (zuletzt aufgerufen am 23.01.2021)

[22] Ghiasi, R.: *Dibromidobis(pyridine-3-carbo-nitrile-κN^{1})zinc(II).* Acta Cryst. E 67: m101. 2011.

[23] Hesse, M., Meier, H., Zeeh, B.: *Spektroskopische Methoden in der Organischen Chemie.* Thieme Stuttgart, 2005.

[24] Hofmann, D. W. M.: *Fast estimation of crystal densities.* Acta Cryst. B 58 : 489-493, 2002.

[25] Huang, X.-C., Ng, S. W.: *$[Cu_2I_2(C_6H_4N_2)_4]$*. Acta Cryst. E 60: m1055-m1056, 2004.

[26] Janiak, C.: *Engineering coordination polymers towards applications*. Dalton Trans.: 2781-2804, 2003.

[27] Janiak, C.; Vieth, J. K.: *MOFs, MILs and more: concepts, properties and applications for porous coordination networks (PCNs)*. New J. Chem. 34: 2366-2388, 2010.

[28] Krysiak, Y., Fink, L., Bernert, T., Glinnemann, J., Kapuscinski, M., Zhao, H., Alig, E., Schmidt, M. U.: *Crystal Structures and Polymorphism of Nickel and Copper Coordination Polymers with Pyridine Ligands.* Z. Anorg. Allg. Chem. 640: 3190, 2014.

[29] Laue, M. von, Friedrich, W., Knipping, P.: *Interferenz-Erscheinungen bei Röntgenstrahlen. Vorgelegt am 8. Juni 1912. / Eine quantitative Prüfung der Theorie für die Interferenz-Erscheinungen bei Röntgenstrahlen. Vorgelegt am 6. Juli 1912.* Verl. d. Königl. Bayer. Akad. d. Wiss. München, 1912.

[30] Li, X.-H., Wu, H.-Y., Hu, J.-G.: *Poly[[*trans-*dibromocopper(II)]-di*-μ-*3-pyridine-carbonitrile*-κ^4N^1:N^3*].* Acta Cryst E 60: m1533, 2004.

[31] Massa, W.: *Kristallstrukturbestimmung*. Springer Spektrum, 2015.

[32] McCusker, L. B., Von Dreele, R. B., Cox, D. E., Louer, D., Scardi, P.: *Rietveld refinement guidelines.* J. Appl. Cryst. 32: 36-50, 1999.

[33] Näther, C., Wöhlert, S., Boeckmann, J., Wriedt, M., Jeß, I.: *A Rational Route to Coordination Polymers with Condensed Networks and Cooperative Magnetic Properties.* Z. Anorg. Allg. Chem. 639: 2696-2714, 2013.

[34] Oishi-Tomiyasu, R.: *Robust powder auto-indexing using many peaks*. J. Appl. Cryst. 47: 593-598, 2014.

[35] Oishi-Tomiyasu, R.: *Method to generate all the geometrical ambiguities of powder indexing solutions*. J. Appl. Cryst. 47: 2055-2059, 2014.

[36] Pawley, G. S.: *Unit-cell refinement from powder diffraction scans.* J. Appl. Cryst. 14: 357-361, 1981.

[37] Pearson, R. G.: *Hard and Soft Acids and Bases.* J. Am. Chem. Soc. 85: 3533-3539, 1963.

[38] Prince, E. (Ed.): *International Tables for Crystallography:* Volume C – *Mathematical, physical and chemical tables.* Wiley, 2006.

[39] Riedel, E., Janiak, C.: *Anorganische Chemie.* De Gruyter Berlin, 2007.

[40] Rietveld, H. M.: *A profile refinement method for nuclear and magnetic structures*. J. Appl. Cryst. 2: 65-71, 1967.

[41] Rietveld, H. M.: *Line profiles of neutron powder-diffraction peaks for structure refinement.* Acta. Cryst. 22: 151-152, 1967.

[42] Warren, B. E.: *X-Ray diffraction in random layer lattices*. Phys. Rev. 59: 693-698, 1941.

[43] SDBS: Spectral Database for Organic Compounds (zuletzt aufgerufen am 23.01.2020)

[44] Smith, G. S., Snyder, R. L.: F_N: *A criterion for rating powder diffraction patterns and evaluating the reliability of powder-pattern indexing.* J. Appl. Cryst. 12: 60-65, 1979.

[45] Sturala, J., Bohacova, S., Chudoba, J., Metelkova, R., Cibulka, R.: *Electron-Deficient Heteroarenium Salts: An Organocatalytic Tool for Activation of Hydrogen Peroxide in Oxidations.* J. Org. Chem. 80: 2676-2699, 2015.

[46] Young, R. A: *The Rietveld method*. Oxford University Press, 1993.

[47] Zhang, W., Jeitler, J. R., Turnbull, M. M., Landee, C. P., Wie, M., Willett, R. D.: *Synthesis, X-ray structures and magnetic properties of linear chain 4-cyanopyridine compounds*: *[Cu(4-CNpy)$_4$H$_2$O)](ClO$_4$)$_2$ and M(4-CNpy)$_2$Cl$_2$ (M= Mn, Fe, Co, Ni, Cu)*. Inorg. Chim. Acta 256: 183-198, 1997.

A Eigene Veröffentlichungen

[MH1]

4-Cyanopyridine, a versatile mono- and bidentate ligand. Crystal structures of related coordination polymers determined by X-ray powder diffraction.
Haishuang Zhao, Alexander Bodach, Miriam Heine, Yasar Krysiak, Jürgen Glinnemann, Edith Alig, Lothar Fink, and Martin U. Schmidt, In: CrystEngComm, 2017, 19, 2216-2228.

CrystEngComm

PAPER

View Article Online
View Journal | View Issue

Cite this: *CrystEngComm*, 2017, **19**, 2216

4-Cyanopyridine, a versatile mono- and bidentate ligand. Crystal structures of related coordination polymers determined by X-ray powder diffraction†

Haishuang Zhao, ‡ Alexander Bodach, Miriam Heine, Yasar Krysiak,‡ Jürgen Glinnemann, Edith Alig, Lothar Fink* and Martin U. Schmidt

4-Cyanopyridine (4-CNpy, also known as isonicotinonitrile) can act as a monodentate ligand in transition metal complexes *via* the pyridine nitrogen atom (N_{py}), or as a bidentate ligand *via* both nitrogen atoms (N_{py} and N_{CN}), resulting in a linear bridge between two metal atoms. Seven new polymeric transition metal compounds, $[CuCl_2(4\text{-CNpy})]_n$ (**1b**), $[MnCl_2(4\text{-CNpy})]_n$ (**2b**), $[NiCl_2(4\text{-CNpy})_2]_n$ (**3a**), $[NiCl_2(4\text{-CNpy})]_n$ (**3b**), $[CoBr_2(4\text{-CNpy})_2]_n$ (**4a**), $[NiBr_2(4\text{-CNpy})_2]_n$ (**5a**) and $[NiBr_2(4\text{-CNpy})]_n$ (**5b**), are reported. Compounds **1b**, **2b**, **3b** and **5b** were obtained from the corresponding $[M(II)X_2(4\text{-CNpy})_2]_n$ compounds by careful thermal decomposition under controlled conditions. Compounds **3a**, **4a** and **5a** were synthesized from 4-cyanopyridine and transition metal halides. For all compounds, IR-spectroscopy was used to distinguish between mono- or bi-coordination of the 4-cyanopyridine ligand: in bi-coordinated compounds the asymmetric stretching vibrations of the cyano group ν_{as}(C≡N) are shifted to higher frequencies. All crystal structures were determined from X-ray powder diffraction data. Compounds **1b**, **3a**, **4a** and **5a** consist of polymeric chains of octahedra (double chains for **1b**; single chains for **3a**, **4a** and **5a**), in which 4-cyanopyridine acts as a monodentate ligand *via* the N_{py} atom. Compound **1b** exists in two polymorphs, a triclinic (**α-1b**) and a monoclinic phase (**β-1b**); both exhibit a strong Jahn–Teller distortion of the $CuCl_5N$-octahedra. On the other hand, **2b**, **3b** and **5b** exhibit layered structures, in which the 4-cyanopyridine acts as a bidentate ligand. Both nitrogen atoms coordinate to metal atoms, resulting in a linear M(II)-py-C≡N–M(II) bridge. These are the first examples of Mn and Ni compounds in which two 3d metal atoms are connected by a 4-cyanopyridine bridge. Due to the linearity of this bridge, 4-cyanopyridine lends itself to the construction of new metal–organic frameworks.

Received 28th February 2017,
Accepted 21st March 2017

DOI: 10.1039/c7ce00425g

rsc.li/crystengcomm

Introduction

Coordination polymers with 4-cyanopyridine as ligand belong to a class of materials which have attracted much attention due to their potential properties with applications in many fields,[1–10] *e.g.*, adsorption, catalysis, optical and magnetic materials, and separation.

The neutral ligand 4-cyanopyridine (4-CNpy, also known as isonicotinonitrile) contains two atoms with donor functions, the N_{py} atom and the N_{CN} atom, and has therefore the potential to form linear M(II)-py-C≡N–M(II) bridges, which may be used to construct coordination polymers or even metal–organic frameworks. In spite of these promising abilities 4-cyanopyridine has relatively rarely been used for the design of transition metal polymers and networks. The Cambridge Structure Database (CSD)[11,12] contains only about 140 crystal structures of transition metal complexes with 4-cyanopyridine. Structures with bridging 4-cyanopyridine groups are very rare. In the CSD there are only eleven structures with bridging 4-cyanopyridines between two metal atoms, each one with Cu,[13–16] Ru,[17] Rh,[18] Ag (ref. 19 and 20) and Cd.[21,22] Astonishingly, bridging 4-cyanopyridine ligands have not been observed in Mn and Ni complexes hitherto. When 4-cyanopyridine acts as a monodentate ligand, the N_{py} atom coordinates due to its stronger Lewis-base character. This leads to the question of whether the monodentate or the bidentate behaviour can be controlled *via* the

Institute of Inorganic and Analytical Chemistry, Goethe University, Max-von-Laue-Str. 7, 60438 Frankfurt am Main, Germany. E-mail: fink@chemie.uni-frankfurt.de; Fax: +49 69798 29235; Tel: +49 69798 29123

† Electronic supplementary information (ESI) available: DTA/TG curves of **3a**, **4a** and **5a**; results of DTA/TG measurements of **1a**–**5a**; combined Rietveld plot of **1b** (sample 2); fragment of crystal structure **3b**, schematic representation for the preparation of compound **1b**; IR spectra of all 4-cyanopyridine compounds. Results of quantitative Rietveld analysis for **1b**. CCDC 1535269–1535275. For ESI and crystallographic data in CIF or other electronic format see DOI: 10.1039/c7ce00425g

‡ Present address: Institute of Inorganic Chemistry and Analytical Chemistry, Johannes Gutenberg University, Jakob-Welder-Weg 11, 55128 Mainz, Germany.

'concentration' of the ligand during the preparation of a compound. Whether one-dimensional coordination polymers or higher dimensional networks will occur should depend on the chemical composition as well as on the donating ability of the donors.

In previous work, using pyridine instead of 4-cyanopyridine, we investigated the compounds $[M(II)Cl_2(pyridine)_x]_n$ (M(II) = Cu, Ni) with three different metal–ligand ratios: x = 2, 1, and 2/3.[23] In all these compounds, pyridine acts as a terminal ligand. The metal atoms are connected by the Cl atoms into single chains for x = 2, double chains for x = 1 and triple chains for x = 2/3. In the present work, we investigated the ability of 4-cyanopyridine to act as a mono- or bidentate ligand, *i.e.* to coordinate the metal atom as a terminal or as a bridging ligand, depending on the metal–ligand ratio and on the type of metal and halide atom. Therefore, we synthesized compound $[M(II)X_2(4\text{-}CNpy)_x]_n$ with M(II) = Cu, Mn, Ni, Co; X = Cl, Br and x = 1, 2 (Scheme 1). Compounds with a metal–ligand ratio of 1 : 2 were synthesized from 4-cyanopyridine and the corresponding metal dihalides. Compounds with a metal–ligand ratio of 1 : 1 were obtained from the corresponding 1 : 2 compounds by thermal decomposition under controlled conditions. In order to determine whether the 4-cyanopyridine motif is coordinated as a mono- or bidentate ligand, IR-spectra of all the compounds were recorded and the frequencies of the asymmetric stretching vibrations of the cyano groups ν_{as}(C≡N) were analyzed.

Only the crystal structures of **1a** and **2a** have previously been determined.[24] In both structures, the 4-cyanopyridine molecule acts as a monodentate ligand. All other compounds are new. We were unable to obtain single crystals of the new compounds. In particular, the 1 : 1 compounds (**1b**, **2b**, **3b**, **5b**) prepared by thermal decomposition were always microcrystalline or nanocrystalline powders. Hence, all crystal structures were determined by X-ray powder diffraction.

Results and discussion

Synthesis and thermal investigation

The compounds with a metal–ligand ratio of 1 : 2, $[M(II)X_2(4\text{-}CNpy)_2]_n$ (**1a–5a**) were synthesized using 4-cyanopyridine and the corresponding anhydrous metal dihalides in alcoholic solution. The thermal behaviour of these compounds was investigated by differential thermal and thermogravimetric analyses (DTA/TG) under nitrogen atmosphere. Compounds $[M(II)X_2(4\text{-}CNpy)]_n$ (**1b–5b**), were prepared by thermal decomposition of the corresponding $[M(II)X_2(4\text{-}CNpy)_2]_n$ at an appropriate temperature. $[CuCl_2(4\text{-}CNpy)_2]_n$ (**1a**) slowly releases one equivalent of 4-cynopyridine between 200 °C and 270 °C and forms compound $[CuCl_2(4\text{-}CNpy)]_n$ (**1b**), which decomposes to 4-cyanopyridine and $CuCl_2$ at 314 °C (Fig. 1a and Table S1†). Similarly, $[NiCl_2(4\text{-}CNpy)_2]_n$ (**3a**) transforms to $[NiCl_2(4\text{-}CNpy)]_n$ (**3b**) between 200 °C and 260 °C, which finally decomposes to $NiCl_2$ and 4-cynopyridine at 374 °C (Fig. S1 and Table S1†).

The TG curve of $[MnCl_2(4\text{-}CNpy)_2]_n$ (**2a**) shows three steps of weight loss (Fig. 1b and Table S1†), which correspond to the endothermic signals in the DTA curve. The first endothermic signal is assigned to the liberation of the first 4-cyanopyridine molecule at 253 °C to form $[MnCl_2(4\text{-}CNpy)]_n$ (**2b**), according to eqn (1). The second endothermic signal at

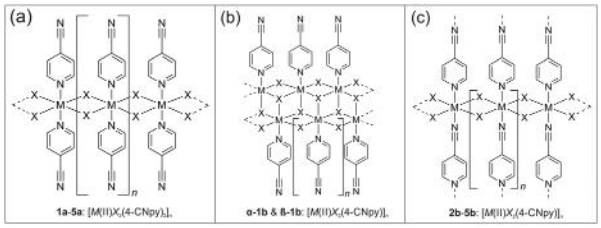

Scheme 1 Connectivity pattern of investigated coordination polymers $[M(II)X_2(4\text{-}CNpy)_2]_n$ (a) and $[M(II)X_2(4\text{-}CNpy)]_n$ (b and c).

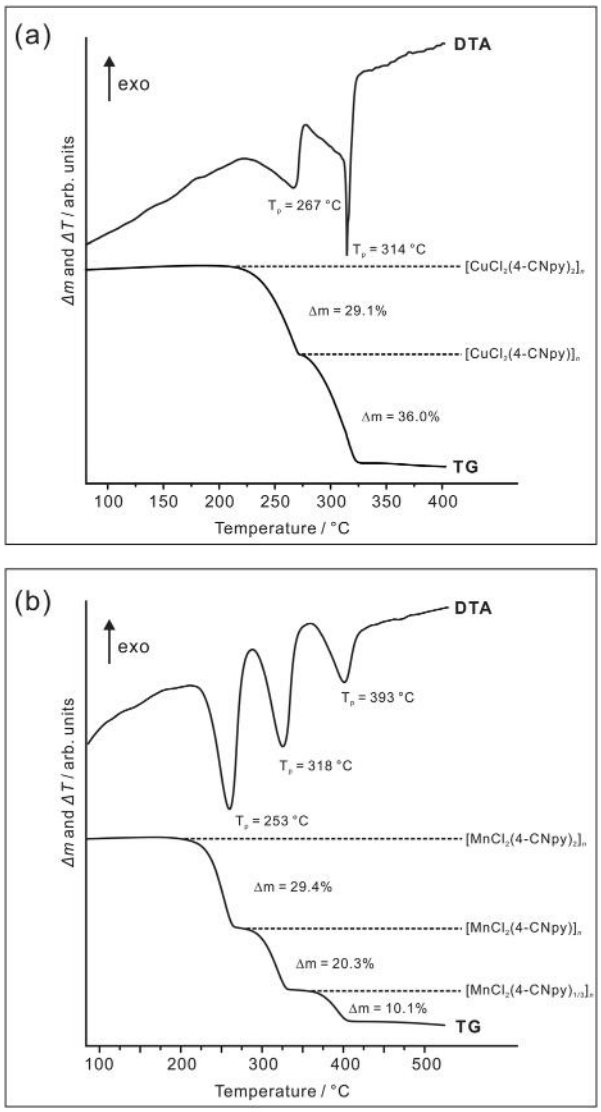

Fig. 1 DTA/TG curves of (a) $[CuCl_2(4\text{-}CNpy)_2]_n$ (**1a**) and (b) $[MnCl_2(4\text{-}CNpy)_2]_n$ (**2a**).

318 °C is attributed to the decomposition of this intermediate compound to form $[MnCl_2(4\text{-}CNpy)_{1/3}]_n$ (**2c**), according to eqn (2). The remaining 4-cyanopyridine is released in the third decomposition step at 393 °C to leave $MnCl_2$, according to eqn (3).

$$MnCl_2(4\text{-}CNpy)_2 \rightarrow MnCl_2(4\text{-}CNpy) + 4\text{-}CNpy \quad (1)$$

$$MnCl_2(4\text{-}CNpy) \rightarrow MnCl_2(4\text{-}CNpy)_{1/3} + 2/3(4\text{-}CNpy) \quad (2)$$

$$MnCl_2(4\text{-}CNpy)_{1/3} \rightarrow MnCl_2 + 1/3(4\text{-}CNpy) \quad (3)$$

Similarly, $[CoBr_2(4\text{-}CNpy)_2]_n$ (**4a**) reacts with $[CoBr_2(4\text{-}CNpy)]_n$ (**4b**) at 241 °C, which releases two thirds of the remaining ligand to form $[CoBr_2(4\text{-}CNpy)_{1/3}]_n$ (**4c**) at 339 °C. Finally, at 374 °C, $CoBr_2$ remains (Fig. S2 and Table S1†). $[NiBr_2(4\text{-}CNpy)_2]_n$ (**5a**) reacts to $[NiBr_2(4\text{-}CNpy)]_n$ (**5b**) at 237 °C, which decomposes to $NiBr_2$ and 4-cyanopyridine at 374 °C (Fig. S3 and Table S1†). Various attempts to synthesize pure phases of $[MnCl_2(4\text{-}CNpy)_{1/3}]_n$ (**2c**) and $[CoBr_2(4\text{-}CNpy)_{1/3}]_n$ (**4c**) failed.

Investigation of the coordination of the cyano group by FT-IR

FT-IR-spectroscopy was used to investigate whether the cyano group coordinates to a metal atom or not. A shifted value of the asymmetric stretching vibration ν_{as}(C≡N) indicates that the cyano group coordinates to a metal atom, while a value similar to that of 4-cyanopyridine itself indicates that the cyano group remained unchanged, *i.e.* the 4-cyanopyridine coordinates only *via* the N atom of the pyridine ring.[25–27] In **1a–5a** and **1b**, the frequency is similar to the frequency of the noncoordinated 4-cyanopyridine (Table 1). In contrast, the asymmetric stretching vibration ν_{as}(C≡N) in **2b–5b** is shifted to higher values (Table 1). This reveals that 4-cyanopyridine forms a bridge between the metal atoms in these compounds while in all the other compounds a monodentate behaviour of the ligand is observed.

Table 1 Characteristic asymmetric stretching vibrations ν_{as}(C≡N) for 4-cyanopyridine and its coordination polymers

Compound	ν_{as}(C≡N)/cm^{-1}
Cyanopyridine	2236–2243
Compounds with a metal : ligand ratio of 1 : 2	
$[CuCl_2(4\text{-}CNpy)_2]_n$ (**1a**)	2242
$[MnCl_2(4\text{-}CNpy)_2]_n$ (**2a**)	2241
$[NiCl_2(4\text{-}CNpy)_2]_n$ (**3a**)	2242
$[CoBr_2(4\text{-}CNpy)_2]_n$ (**4a**)	2234
$[NiBr_2(4\text{-}CNpy)_2]_n$ (**5a**)	2235
Compounds with a metal : ligand ratio of 1 : 1	
$[CuCl_2(4\text{-}CNpy)]_n$ (**1b**)	2243
$[MnCl_2(4\text{-}CNpy)]_n$ (**2b**)	2275
$[NiCl_2(4\text{-}CNpy)]_n$ (**3b**)	2288
$[CoBr_2(4\text{-}CNpy)]_n$ (**4b**)	2281
$[NiBr_2(4\text{-}CNpy)]_n$ (**5b**)	2298

Structure determination from powder data

The crystal structures of **3a–5a**, **1b–3b** and **5b** were determined from X-ray powder data. (For details see the Experimental section). For ease of comparison of the individual crystal structures, the unit cell for all structures was set up in such a way that the metal–halogen polymeric chains are parallel to the *c* axis. For some of the crystal structures, this leads to non-standard space-group settings ($P11m$ instead of $P1m1$ for **2b** and $P112/m$ instead of $P12/m1$ for **3b** and **5b**). Selected crystallographic data are summarized in Tables 2 and 3. Rietveld plots are shown in Fig. 4 (combined Rietveld refinement of **1b** sample 2, see Fig. S4 in the ESI†). For $[CoBr_2(4\text{-}CNpy)]_n$ (**4b**) no reliable indexing of the powder diffraction data succeeded.

Polymorphism of 1b

For $[CuCl_2(4\text{-}CNpy)]_n$ (**1b**), the X-ray powder data were inconsistent. The compound was prepared three times, under slightly different conditions, at 207 °C and 220 °C (see the Experimental section for details); the X-ray powder diagrams (measured at room temperature) show identical peak positions, but significantly different reflection intensities (Fig. 2). It turned out that compound **1b** exists in two polymorphic forms, **α-1b** and **β-1b**. All three samples contained a phase mixture with different amounts of the two polymorphs.

Powder data of the individual polymorphs were obtained by subtracting the data of the phase mixtures from each other. Subsequently the structure could be solved in a routine manner. Finally, the combined Rietveld refinements of both phases were performed, using the original powder diffraction data of polymorph mixtures. The monoclinic phase prefers to appear at a higher synthesis temperature. (For details see the Experimental section, Fig. 2 and Table S2.†)

Monitoring the formation of α- and β-1b by temperature-dependent X-ray diffraction

The reaction from **1a** to **1b** was investigated by temperature-dependent X-ray diffraction, recording powder patterns from 170 °C to 250 °C in steps of 5 °C every 15 minutes. The 3D plot of the X-ray powder patterns (Fig. 3) confirms the first structural changes at about 190 °C, corresponding to a decomposition of **1a** and the formation of **α-1b**. At about 220 °C this transformation is completed. In the DTA/TG measurement, where the heating rate is much faster (5 K min^{-1}), this reaction from **1a** to **1b** occurs between about 210 °C and 270 °C. Under further heating, additional changes are observed, starting at about 230 °C. These changes do not correspond to a further decomposition, but to the polymorphic phase transition from **α-1b** to **β-1b**. In the DTA curve this transformation is indicated as a shoulder at about 290 °C (Fig. 1a).

Crystal structures

General. In all the crystal structures the M(II) atoms are octahedrally coordinated by 4 halogen and 2 nitrogen atoms

Table 2 Selected crystallographic data and Rietveld refinement parameters for compounds **1a–5a**. In all structures the $[M(II)_2X_4]_n$ chains run along the *c* axis

	1a[a]	**2a**[b]	**3a**	**4a**	**5a**
Compound	$[CuCl_2(4\text{-CNpy})_2]_n$	$[MnCl_2(4\text{-CNpy})_2]_n$	$[NiCl_2(4\text{-CNpy})_2]_n$	$[CoBr_2(4\text{-CNpy})_2]_n$	$[NiBr_2(4\text{-CNpy})_2]_n$
CCDC number/CSD code	NESYOZ	NESYUF	1535275	1535270	1535271
Ref.	24	24	This work	This work	This work
Structure determined from	Single-crystal	Single-crystal	Powder	Powder	Powder
Formula	$C_{12}H_8Cl_2CuN_4$	$C_{12}H_8Cl_2MnN_4$	$C_{12}H_8Cl_2NiN_4$	$C_{12}H_8Br_2CoN_4$	$C_{12}H_8Br_2NiN_4$
MW/g mol^{-1}	342.67	334.06	337.82	426.95	426.49
Crystal system	Monoclinic	Monoclinic	Monoclinic	Orthorhombic	Orthorhombic
Space group (no.)	$P2_1/n11$ (14)	$P12_1/n1$ (14)	$P12_1/n1$ (14)	*Pnnm* (58)	*Pnnm* (58)
a/Å	25.711(12)	26.640(5)	26.4504(7)	26.8461(15)	26.6981(4)
b/Å	7.104(4)	7.198(2)	7.1667(2)	7.3191(3)	7.2936(1)
c/Å	3.779(2)	3.700(2)	3.5890(1)	3.7708(11)	3.7359(4)
α/°	95.98(4)	90	90	90	90
β/°	90	95.85(4)	92.474(3)	90	90
γ/°	90	90	90	90	90
V/Å^3	686.48(4)	705.8(4)	679.71(1)	740.92(6)	727.48(2)
Z, *Z*′	2, 1/2	2, 1/2	2, 1/2	2, 1/2	2, 1/2
D_{calc}/Mg m^{-3}	1.658	1.572	1.651	1.914	1.948
T/K	294	294	298	298	298
Radiation type	Cu Kα	Mo Kα	Cu Kα$_1$	Mo Kα$_1$	Cu Kα$_1$
Wavelength/Å	1.54178	0.71073	1.54056	0.70930	1.54056
θ_{max}/°	30	30	55	30	50
R_p/%			2.59	1.39	3.50
R_{wp}/%	6.39	6.37	3.56	1.89	4.60
R_{exp}/%			2.61	1.78	3.11
GOF			1.37	1.06	1.48
R_p'[c]/%			7.43	17.81	8.98
R_{wp}'[c]/%			9.04	13.06	10.24
R_{exp}'[c]/%			6.62	12.32	6.92
Pyridine stacking angle[d]/°	88.6	83.2	87.8	90	90

[a] Unit cell transformed from the literature data with $a' = b$, $b' = c$, $c' = a$ to correspond to the other structures. [b] Unit cell transformed from the literature data with $a' = a + c$, $b' = b$, $c' = -a$ to correspond to the other structures. [c] R', R_{wp}' and R_p' values are background corrected according to ref. 28. [d] Angle between the pyridine ring mean plane and the stacking direction [001].

(N_{py} and N_{CN}) or 5 halogen atoms and 1 nitrogen atom (N_{py}). Neighbouring octahedra are connected, in the first instance, by two μ_2-bridging halogen atoms each, resulting in a linear $[M(II)_2X_4]_n$ chain of edge-sharing octahedra. Within these chains, the metal–metal distances range from 3.51 Å (for **3b**) to 3.79 Å (for **1b**). Since the $[M(II)_2X_4]_n$ chains are running parallel in each structure, the metal-to-metal distance is the shortest translational periodicity in the structures and accounts for a short lattice parameter *c* in all structures.

In the $[M(II)_2X_4]_n$ chains, the metal atoms are coordinated by four halogen atoms. The fifth coordination position of the octahedra is always occupied by a cyanopyridine ligand coordinating with its pyridine-nitrogen atom. Thereby the cyanopyridine ligands form lateral "wings" on one side of the $[M(II)_2X_4]_n$ chains.

For the sixth position at the metal coordination octahedra (*i.e.* in *trans*-position to the N atom), there are three possibilities:

(1) The position is filled by a second cyanopyridine ligand, also coordinating with its pyridine-nitrogen atom, resulting in single chains with a second wing at the other side of the $[M(II)_2X_4]_n$ chain (Scheme 1a, Fig. 5). This is the case for all compounds with a metal : ligand ratio of 1 : 2 (**1a–5a**).

(2) The cyanopyridine ligand of a neighbouring chain coordinates with the N atom of the cyano group (Scheme 1c). Thereby the cyanopyridine acts as a linker between the two chains in compounds **2b**, **3b**, **4b** and **5b**.

(3) The sixth coordination position is filled by a Cl atom of a neighbouring $[M(II)_2X_4]_n$ chain, *i.e.* two $[M(II)_2X_4]_n$ chains aggregate *via* μ^3-Cl atoms into a double chain (Scheme 1b). This situation is found for both polymorphs of **1b**.

In the corresponding series of polymeric copper and nickel chloride complexes with unsubstituted pyridine as ligand, $[M(II)Cl_2(py)_x]_n$, case (1) is found for all compounds with $x = 2$, and case (3) for all compounds with $x = 1$.[23,24] For $x = 2/3$, triple chains are formed.[23] Phases with $x = 1/3$ were not observed. The phases of 4-cyanopyridine compounds with $x = 1/3$, $[MnCl_2(4\text{-CNpy})_{1/3}]_n$ (**2c**) and $[CoBr_2(4\text{-CNpy})_{1/3}]_n$ (**4c**), can be observed in the DTA/TG curves (Fig. 1b and S2†), but could not be isolated. The stoichiometry would agree with a structure formed from triple chains connected by 4-cyanopyridine bridges.

The distances between the metal atoms and the coordinating atoms are compiled in Table 4. From the pronounced variation of the metal–halogen distances, it is evident that the copper compounds **1a**, **α-1b** and **β-1b**, and the nickel

Table 3 Selected crystallographic data and Rietveld refinement parameters for compounds **1b–3b** and **5b**. In all structures the $[M(II)_2X_4]_n$ chains run along the *c* axis

	α-**1b** (sample **1**)	β-**1b** (sample **3**)	**2b**	**3b**	**5b**
Compound	$[CuCl_2(4\text{-CNpy})]_n$	$[CuCl_2(4\text{-CNpy})]_n$	$[MnCl_2(4\text{-CNpy})]_n$	$[NiCl_2(4\text{-CNpy})]_n$	$[NiBr_2(4\text{-CNpy})]_n$
CCDC number	1535272	1535273	1535276	1535274	1535269
Ref.	This work	This work	This work	This work	This work
Structure determined from	Powder	Powder	Powder	Powder	Powder
Formula	$C_6H_4Cl_2CuN_2$	$C_6H_4Cl_2CuN_2$	$C_6H_4Cl_2MnN_2$	$C_6H_4Cl_2NiN_2$	$C_6H_4Br_2NiN_2$
MW/g mol^{-1}	238.56	238.56	229.95	233.71	322.49
Crystal system	Triclinic	Monoclinic	Monoclinic	Monoclinic	Monoclinic
Space group (no.)	$P\bar{1}$ (2)	$P12_1/n1$ (14)	$P112/m$ (10)	$P11m$ (6)	$P112/m$ (10)
a/Å	13.8312(3)	7.9609(4)	9.8938(6)	9.5049(3)	9.4827(2)
b/Å	7.9385(2)	27.3362(2)	12.0318(9)	7.5810(5)	12.3468(3)
c/Å	3.7907(5)	3.7947(2)	3.6493(2)	3.5132(1)	3.6898(5)
α/°	96.171(2)	90	90	90	90
β/°	94.914(2)	97.482(2)	90	90	90
γ/°	96.825(2)	90	90.808(15)	128.019(4)	90.423(7)
V/Å^3	408.83(2)	818.76(7)	434.25(4)	199.43(2)	431.99(2)
Z, *Z*′	2, 1	4, 1	2, 1	1, 1	2, 1
D_{calc}/Mg m^{-3}	1.938	1.935	1.758	1.947	2.480
T/K	298	298	298	298	298
Radiation type	Cu Kα_1	Cu Kα_1	Mo Kα_1	Cu Kα_1	Cu Kα_1
Wavelength/Å	1.54056	1.54056	0.70930	1.54056	1.54056
θ_{max}/°	55	55	40	55	50
R_p/%	3.35	4.28	3.01	3.35	3.55
R_{wp}/%	4.41	5.89	3.94	4.43	4.65
R_{exp}/%	2.53	2.82	2.10	2.99	2.86
GOF	1.74	2.09	1.88	1.49	1.63
R_p'[a]/%	9.49	13.24	11.23	10.76	9.65
R_{wp}'[a]/%	10.66	10.04	11.93	10.81	10.21
R_{exp}'[a]/%	6.12	7.19	6.35	7.28	6.27
Pyridine stacking angle[b]/°	86.4	84.5	90	90	90

[a] *R*′, R_{wp}' and R_p' values are background corrected according to ref. 28. [b] Angle between pyridine ring mean plane and the stacking direction [001].

compounds **3a**, **5a** and **5b** exhibit a Jahn–Teller distortion of the octahedra.

In all structures, the pyridine rings of the cyanopyridine ligands have centre-to-centre distances, which are equivalent to the metal–metal-distances, *i.e.* 3.51 to 3.79 Å. This allows a good π···π stacking of the 4-cyanopyridine rings. In fact, neighbouring pyridine rings are always parallel to each other.

In **2b**, **3b**, **4a**, **5a** and **5b**, the pyridine rings are situated on mirror planes parallel to (001), hence the rings are exactly perpendicular to the stacking direction [001]. In contrast, the rings are not exactly perpendicular to the stacking direction in the other structures (**1a**, **2a**, **3a**, **1b**), with angles of 83.2° to 88.6° between the pyridine ring plane and the stacking direction. This inclination leads to a more efficient space filling and better van der Waals contacts. We cannot exclude that

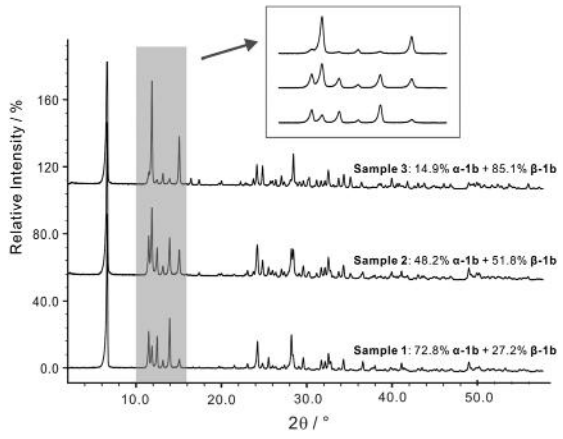

Fig. 2 X-ray powder patterns of three samples of compound **1b** (Cu Kα_1 radiation).

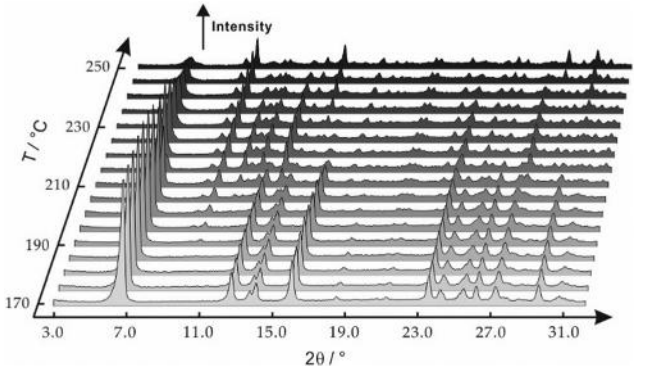

Fig. 3 Temperature dependent X-ray powder diffraction diagrams of the thermal decomposition of compound **1a** (Cu Kα_1 radiation), yielding the triclinic phase (α-**1b**) first, which starts to transform to the monoclinic phase (**β-1b**) upon further heating.

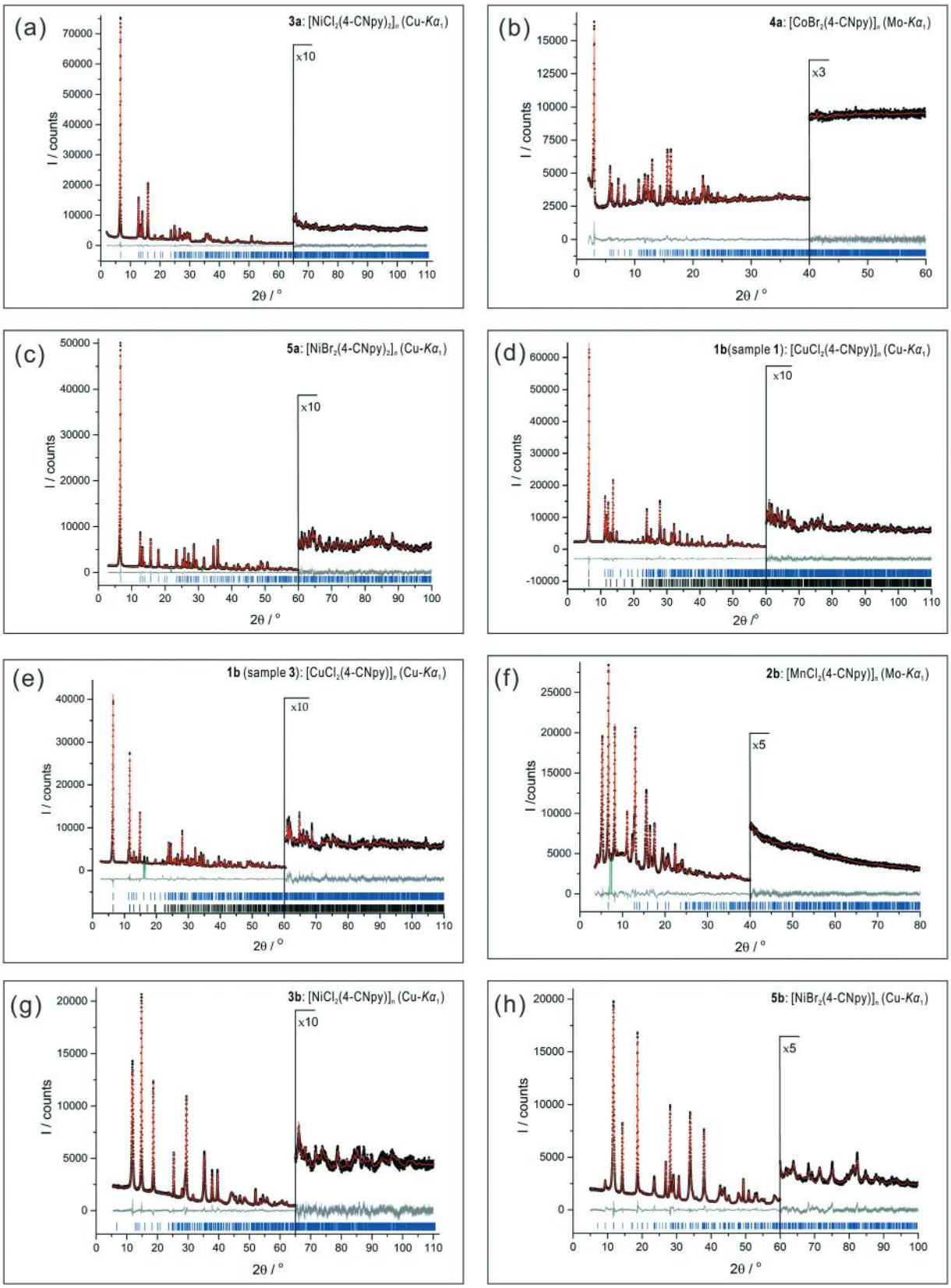

Fig. 4 Rietveld plots of **3a–5a** (a–c) **1b–3b** (d–g), **5b** (h). Observed powder diagram (black points), simulated powder diagram (red solid line), difference profile (grey solid line), and reflection positions (blue tick marks, black for **β-1b**). Change of the scales with corresponding factors is indicated in the diagrams. Combined Rietveld refinements of **α-1b** and **β-1b** for sample **1** (d) and sample **3** (e). Excluded 2θ ranges are indicated by green lines (c, e and f).

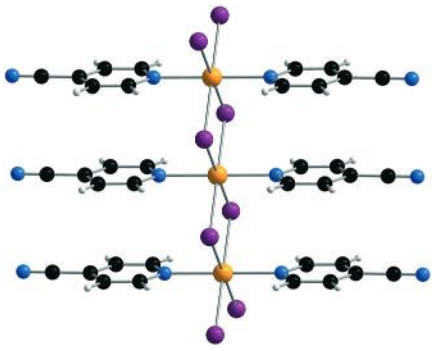

Fig. 5 Single chain of $[M(II)_2X_4]_n$ with lateral cyanopyridine 'wings' in the crystal structure of $[CoBr_2(4\text{-CNpy})_2]_n$ (**4a**).

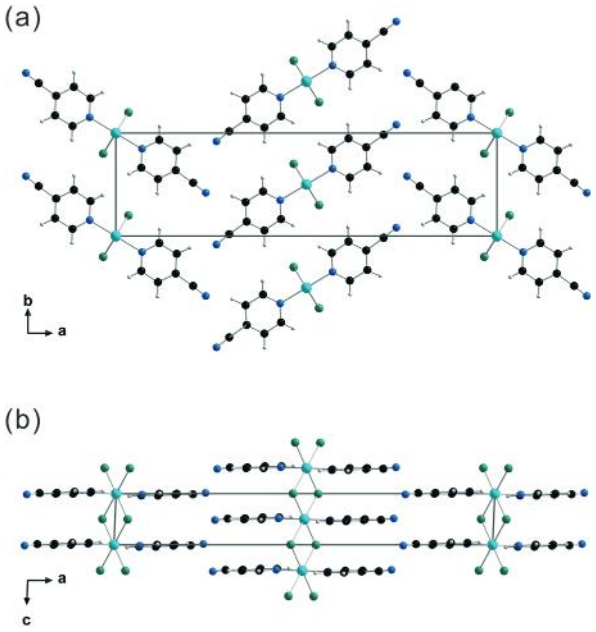

Fig. 6 Crystal structure of $[NiCl_2(4\text{-CNpy})_2]_n$ (**3a**). View along [00$\bar{1}$] (a) and [0$\bar{1}$0] (b).

also in **2b**, **3b** and **4a** the pyridine rings are actually slightly inclined as well, and exhibit an orientational disorder across the mirror plane; such a disorder can hardly be detected from the powder diffraction data. But the small atomic displacement parameters indicate the absence of such a disorder. In all structures of $[M(II)X_2(4\text{-CNpy})_x]_n$ compounds all chains are parallel.

Structures built from single chains (1a–5a). All compounds $[M(II)X_2(4\text{-CNpy})_2]_n$ (**1a–5a**), having a metal : ligand ratio of 1 : 2, are built of linear $[M(II)_2X_4]_n$ single chains, which are equipped with two lateral cyanopyridine wings at each metal atom. The cyanopyridine ligands occupy the *trans*-positions of the octahedra. In all structures, the chains are arranged in a herringbone packing motif (see Fig. 6a and 7a). Neighbouring 'sheets' are shifted by 0.5 in the chain direction to ensure a better van der Waals packing (Fig. 6b and 7b).

Although this herringbone arrangement is identical for the compounds **1a–5a**, there are small differences between the structures, caused by differences in the electronic structure of the metal atoms and the sites of the different halogen atoms. These differences become visible by viewing perpendicular to the chain direction. In the bromo compounds **4a** and **5a**, the pyridine rings are exactly perpendicular to the chain direction, leading to a crystallographic mirror plane (Fig. 7b). The angle β is 90°, the lattice is orthorhombic and the space group is $P2_1/n2_1/n2/m$, with the Co atom occupying a $2/m$ site. The structure of **3a** is only pseudo-orthorhombic: all ligands are still co-planar, but the stacking direction is off the normal vector of the pyridine ring plane by 87.8° (Fig. 6b). The angle β changes from 90° to 92.47°, the lattice becomes monoclinic, and the space group is reduced to $P12_1/n1$, which is a maximal *translationengleiche* subgroup of $P2_1/n2_1/n2/m$. The Ni atom has a site symmetry of $\bar{1}$ only. Compounds **2a** and $[CoCl_2(4\text{-CNpy}]$[29] are isotopic to **3a**, but the inclination of the pyridine rings is even stronger (Fig. 8).

In **1a**, the chains form a slight herringbone arrangement also when viewed from the side (Fig. 9). This leads to the space group $P2_1/n11$, which is another maximal *translationengleiche* subgroup of $P2_1/n2_1/n2/m$. Note that $P2_1/n11$ (for **1a**) is different from $P12_1/n1$ (for **2a** and **3a**): in **1a**, the monoclinic axis is the long axis (25.7 Å), but in **2a** and **3a**, it is the medium axis (7 Å).

Structures with double chains (α-1b and β-1b). For structures with a metal : ligand ratio of 1 : 1 there are two possibilities to fill the position of the missing ligand. Either a cyanopyridine of a neighbouring $[M(II)_2X_4]_n$ chain additionally coordinates with its cyano-nitrogen, thereby acting as a linker between the $[M(II)_2X_4]_n$ chains. Alternatively, two chains fuse into a double chain. Both possibilities were found in the compounds $[M(II)X_2(4\text{-CNpy})]_n$.

The copper compound $[CuCl_2(4\text{-CNpy})_2]_n$ (**1b**) is the only compound with a metal : ligand ratio of 1 : 1, which does not

Table 4 Selected bond distances between metal atoms and donor atoms (X = Cl or Br)

	1a	2a	3a	4a	5a	α-1b	β-1b	2b	3b	5b
M(II)–N_{py}/Å	2 × 2.015(6)	2 × 2.286(8)	2 × 2.123(3)	2 × 2.202(9)	2 × 2.162(2)	2.001(7)	1.993(4)	2.311(8)	2.034(8)	2.185 (mean)
M(II)–X(1)/Å	2 × 2.957(3)	2 × 2.526(3)	2 × 2.437(2)	4 × 2.617(4)	4 × 2.588(1)	2.295(3)	2.284(4)	2 × 2.565(6)	2 × 2.415(5)	2 × 2.561(3)
M(II)–X(2)/Å						2.302(4)	2.301(4)			
M(II)–X(3)/Å	2 × 2.276(3)	2 × 2.555(3)	2 × 2.123(3)			2.360(5)	2.311(4)	2 × 2.581(6)	2 × 2.436(4)	2 × 2.570(3)
M(II)–X(4)/Å						2.742(4)	2.569(4)			
M(II)–X(5)/Å						3.126(4)	3.225(4)			
M(II)–N_{CN}/Å								2.349(10)	2.079(6)	1.990 (mean)

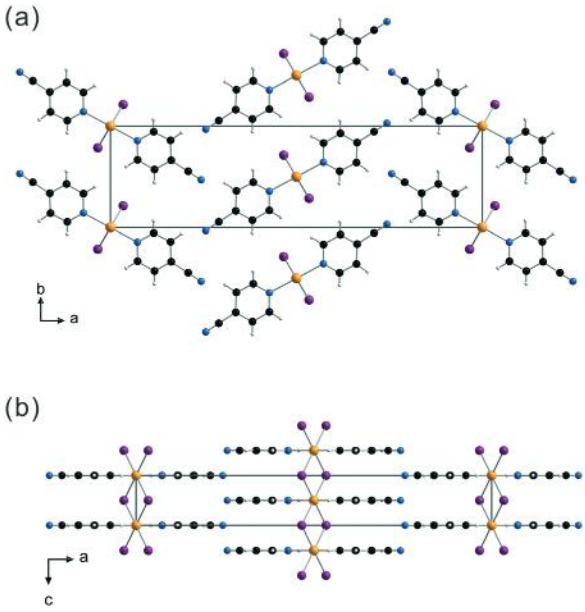

Fig. 7 Crystal structure of $[CoBr_2(4\text{-}CNpy)_2]_n$ (**4a**). View along [00$\bar{1}$] (a) and [0$\bar{1}$0] (b).

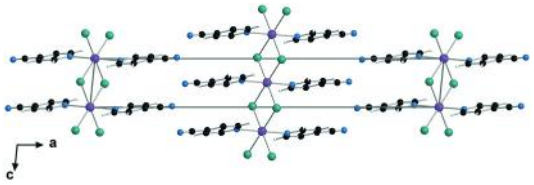

Fig. 8 Crystal structure of $[MnCl_2(4\text{-}CNpy)_2]_n$ (**2a**). View along [0$\bar{1}$0].

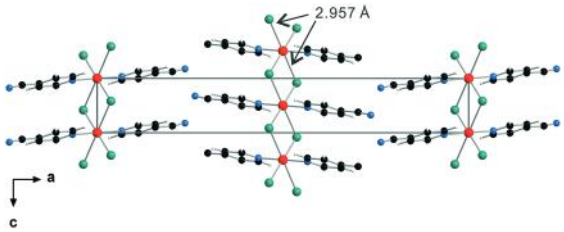

Fig. 9 Crystal structure of $[CuCl_2(4\text{-}CNpy)_2]_n$ (**1a**). View along [0$\bar{1}$0]. Note: there are two strongly different Cu–Cl distances caused by Jahn–Teller distortion.

contain bridging 4-cyanopyridine units, but form double chains with lateral cyanopyridine "wings" at both sides. Obviously, the Cu(II) as a d^9-ion is responsible for the resulting Jahn–Teller distortion and, therefore, for the occurrence of μ_3-Cl atoms, resulting in double chains instead of layers. As mentioned above, **1b** is polymorphic. The topology of the double chains is identical for both phases. The double chains, having the stoichiometry $[M(II)_2X_4]_n$, are formed by fusion of two single $[M(II)_2X_4]_n$ chains. Thereby two of the four chlorine atoms change from μ_2- to μ_3-bridging, *i.e.* they are connected to three different Cu atoms (Fig. 10). This leads to a double chain of edge-sharing octahedra (Fig. 10).

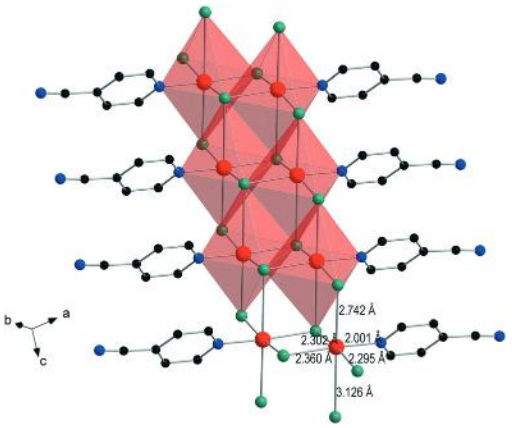

Fig. 10 Double chain $[M(II)_2X_4]_n$ of edge-sharing octahedra with adjacent ligands in the crystal structure of α-**1b** (H atoms omitted for clarity).

In both polymorphs, the coordination octahedra of Cu^{2+} show a remarkable Jahn–Teller distortion leading towards octahedra with two longer bonds in *trans*-positions. The three "equatorial" Cu–Cl bonds are quite short, with bond lengths between 2.295(3) and 2.360(5) Å for α-**1b** (and similar values for **β-1b**). The two 'axial' Cu–Cl distances are significantly longer, with values of 2.742(4) and 3.126(4) Å for α-**1b**, and 2.569(4) and 3.225(4) Å for **β-1b**. The Jahn–Teller effect is much stronger than the bond length difference between μ_2- and μ_3-coordinated chlorine ions: from the two Cu–Cl bonds of the μ_2-bridging chlorine atom, one is short, the other is long; from the three Cu–Cl bonds of the μ_3-connecting chlorine atoms, two are short, one is long (see Table 4). The two polymorphs of **1b** differ from each other in their arrangement of the $[M(II)_2X_4]_n$ chains. In the triclinic α-phase all double chains are parallel (Fig. 11); in contrast, a herringbone arrangement appears in the monoclinic phase (Fig. 12).

In both polymorphs, the cyanopyridine groups of neighbouring double chains show a vertical offset of *c*/2 to ensure a good van der Waals packing (see Fig. 13).

Structures with bridging cyanopyridine ligands (2b, 3b, 5b). The crystal structures of $[MnCl_2(4\text{-}CNpy)]_n$ (**2b**), $[NiCl_2(4\text{-}$

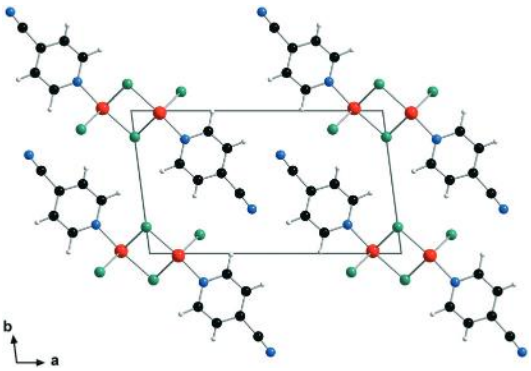

Fig. 11 Parallel arrangement of double chains in the crystal structure of α-**1b**. View along [00$\bar{1}$].

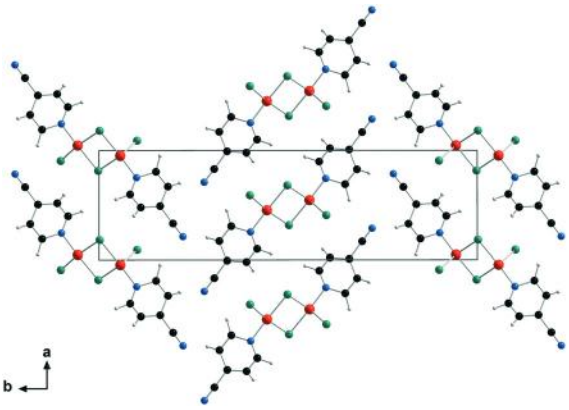

Fig. 12 Herringbone arrangement of double chains in the crystal structure of β-**1b**. View along [00$\bar{1}$].

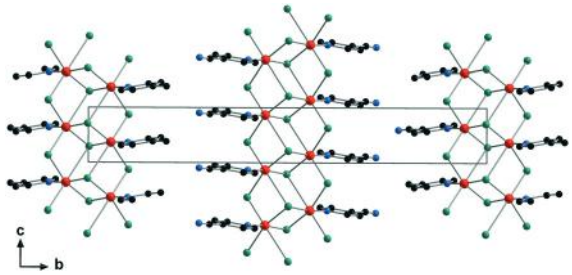

Fig. 13 Vertical arrangement of neighbouring chains in the crystal structure of β-**1b**. View along [$\bar{1}$00]. H atoms omitted for clarity.

CNpy)]$_n$ (**3b**) and [NiBr$_2$(4-CNpy)]$_n$ (**5b**), determined here, are the first crystal structures where the 4-cyanopyridine acts as a linker between two 3d transitional metal atoms. The 4-cyanopyridine coordinates not only with the nitrogen atom of the pyridine ring but also with its cyano nitrogen atom, as was also revealed by the IR data.

The bridges between the [M(II)$_2$X$_4$]$_n$ chains lead to a layer parallel to (010) (see Fig. 14). Each metal atom is coordinated by one 4-cyanopyridine ligand with its pyridine-nitrogen atom, and a second one with its cyano group. The theoretically possible case of a metal atom surrounded either by two cyano groups or by two pyridine rings, is not observed. Within a layer, all cyanopyridine bridges have the same orientation. In the neighbouring layers, either the orientation may be inverted, or the orientation of the cyanopyridine can be the same in all layers.

The former case leads to the non-polar crystal structure of **2b** in space group $P112/m$, with all atoms on mirror planes parallel to (001) (Fig. 14a). The structure is pseudo-orthorhombic, with a monoclinic angle of 90.81(2)° only. The orthorhombic space group would be $P2/b2_1/m2/m$, which is a non-standard setting of *Pmma*. In this space group, Ni and N atoms would be situated on sites with *2mm* symmetry. The main deviation from the orthorhombic symmetry is that the [M(II)$_2$X$_4$]$_n$ chain is not exactly parallel to the (100) plane but forms an angle of 6.0° with it.

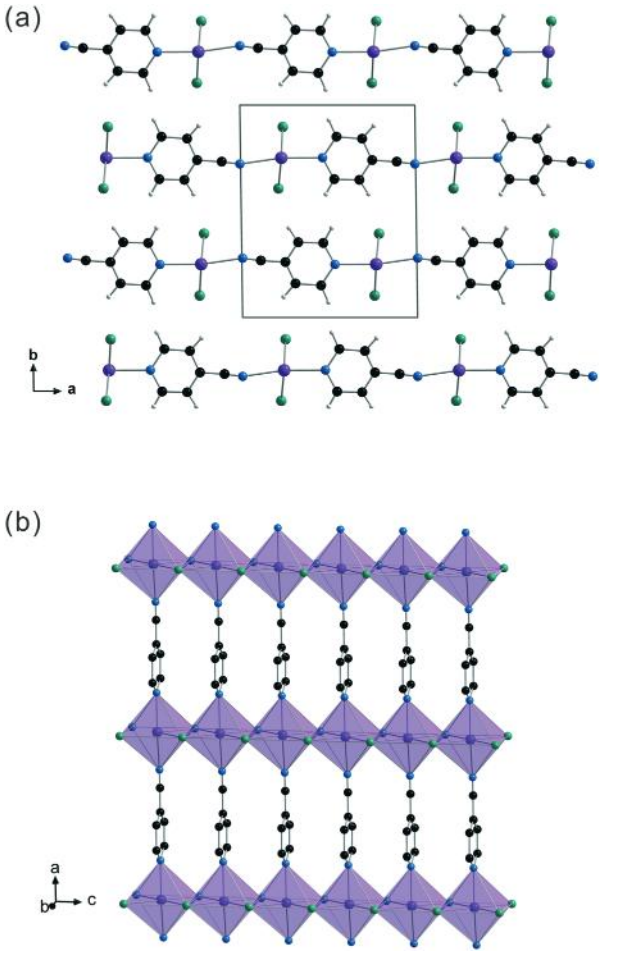

Fig. 14 Crystal structure of [MnCl$_2$(4-CNpy)]$_n$ (**2b**). (a) View along [00$\bar{1}$]. (b) One single layer (H atoms omitted for clarity). All atoms are on vertical mirror planes parallel to (001).

In the crystal structure of **3b** (Fig. 15 and S5†), all cyanopyridine fragments have an identical orientation. This leads to the polar structure of **3b** in the space group $P11m$, $Z = 1$, with all cyanopyridine rings being exactly parallel. Here, all atoms are situated on crystallographic mirror planes.

The M(II)–(4-CNpy)–M(II) fragments are not exactly linear, but show a slight zigzag shape. The cyano group exhibits a C≡N–M(II) angle of 171.5° for **2b**, 176.7° for **3b** and 172.0° for **5b**. These values are in good agreement with the C≡N–

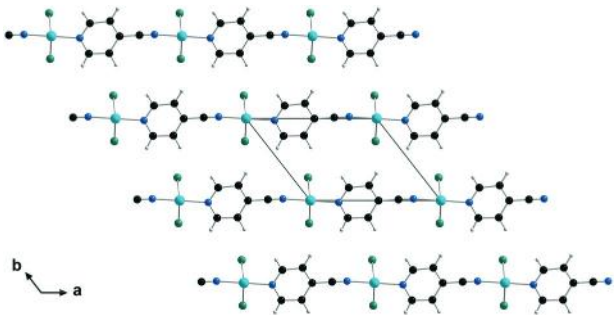

Fig. 15 Crystal structure of [NiCl$_2$(4-CNpy)]$_n$ (**3b**). View along [00$\bar{1}$].

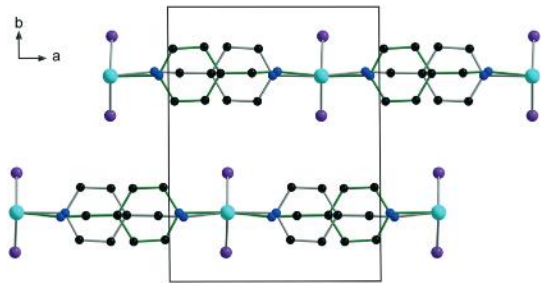

Fig. 16 Head-to-tail disorder of the 4-cyanopyridine ligands in the crystal structure of **5b**. View along [00$\bar{1}$]. H atoms omitted for clarity.

M(II) angle of 178.1° in the known single-crystal structure of $[Ag(4\text{-CNpy})]_n(nBF_3)$.[19] However, the C≡N–M angle is even more strongly bent in other structures, with a C≡N–Cd angle of 148.7°, in the single-crystal structure of $[Cd(SCN)_2(4\text{-CNpy})]_n$.[21]

In **3b**, the Ni(II) coordination octahedra are slightly contracted in comparison to the Mn(II) octahedra of **2b**. Furthermore, a significant Jahn–Teller distortion is visible for the nickel compound (**3b**): the mean M(II)–N distances decrease from 2.33 Å for the manganese compound to 2.08 Å for the nickel compound, whereas the M(II)–Cl distances decrease only by 0.15 Å.

In the crystal structure of $[NiBr_2(4\text{-CNpy})_2]_n$ (**5b**), the arrangement of the layers is the same as in **2b**. However, the cyanopyridine bridges of **5b** show a head-to-tail-disorder with two molecular orientations (Fig. 16). In both orientations, both nitrogen atoms bind to the nickel atoms, but the carbon (and hydrogen) atoms swap their positions. The occupancies for the two orientations are 0.468 (green marked 4-cyanopyridine in Fig. 16) and 0.532. From the powder data themselves, it is not evident if the cyanopyridine groups within one layer are disordered, or if the disorder concerns an orientational disorder of ordered layers. In all cases, the disorder causes diffuse scattering. In the powder diagram of **5b**, this diffuse scattering is visible as Warren peaks, *i.e.* peaks with tails towards higher diffraction angles, especially pronounced for the marked reflections (see Fig. 17).

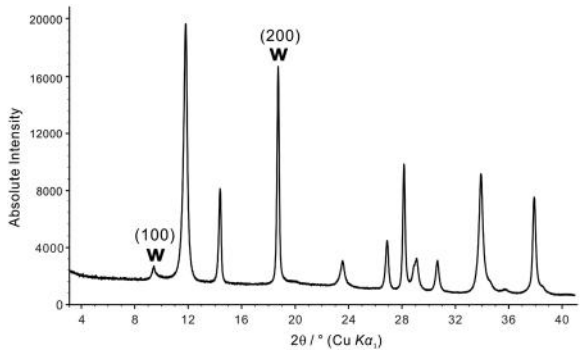

Fig. 17 Low-range part of powder pattern of **5b**. The Warren peaks (100) and (200) are marked by "W".

For **2b** and **3b**, a head-to-tail disorder cannot be completely excluded, but the Rietveld refinements with a disorder model reveal that the occupancy of the second molecular orientation must be lower than 10%. Also, two of the four literature structures of 4d metals with bridging 4-cyanopyridine rings show this head-to-tail disorder of the cyanopyridine fragment: the complexes with Ru (ref. 17) and Rh (ref. 18) are disordered, whereas the structures with Ag (ref. 19 and 20) and Cd (ref. 21) are ordered.

Conclusions

This work has shown that 4-cyanopyridine can be used as a versatile ligand. The new compounds $[MnCl_2(4\text{-CNpy})]_n$ (**2b**), $[NiCl_2(4\text{-CNpy})]_n$ (**3b**) and $[NiBr_2(4\text{-CNpy})]_n$ (**5b**) are the first known compounds in which 4-cyanopyridine acts as a linker between two 3d transitional metal atoms (Mn, Ni).

The choice of whether 4-cyanopyridine acts as a bidentate or as a monodentate ligand depends on the metal(II) atom, the halogen atom and the stoichiometric metal : ligand ratio. All 1 : 2 compounds of the type $[M(II)X_2(4\text{-CNpy})_2]_n$ with Mn, Co, Ni or Cu, and X = Cl or Br (**1a–5a**) exhibit a monodentate behaviour of the ligand which results in linear polymeric $[M(II)_2X_4]_n$ single chains built by edge-sharing octahedra. The ligands are attached as lateral 'wings' on both sides of the chains. The chains are arranged in a herringbone packing motif. The structural differences between the five compounds **1a–5a** are small but lead to four different structures in three different space groups.

For the 1 : 1 compounds $[M(II)X_2(4\text{-CNpy})]_n$, two different structure types are observed: a) two-dimensional networks, in which the $[M(II)_2X_4]_n$ chains are connected through bridging 4-cyanopyridine linkers, which coordinate the M(II) atoms additionally by their N_{CN} atoms; b) polymeric double chains, which emerge by fusing two $[M(II)_2X_4]_n$ chains through μ_3-Cl atoms. For the copper compound $[CuCl_2(4\text{-CNpy})]_n$ (**1b**), we found the double chains, whereas for all other compounds ($[MnCl_2(4\text{-CNpy})]_n$ (**2b**), $[NiCl_2(4\text{-CNpy})]_n$ (**3b**) and $[NiBr_2(4\text{-CNpy})]_n$ (**5b**)), we observed the intended formation of two-dimensional networks with 4-cyanopyridine bridges between the metal atoms.

The topology of the networks of **2b** and **3b** is identical, however the arrangement is different: in **2b**, the layers are stacked in an anti-parallel orientation to each other. For **3b**, we found an arrangement of parallel layers leading to a polar structure with space group *P*11*m*. Therefore, **3b** may possess optical activity, pyroelectricity, piezoelectricity and second-harmonic generation. The crystal structure of **5b** shows an interesting head-to-tail disorder of the 4-cyanopyridine groups with a distribution of about 4 : 6 for the two orientations of the ligand.

The copper compound $[CuCl_2(4\text{-CNpy})]_n$ is the only 1 : 1 compound in which the 4-cyanopyridine acts as a monodentate ligand. The compound is polymorphic. In both phases, the Cu(II) atoms, having a d^9 configuration, show a strong Jahn–Teller distortion of the octahedra with Cu–Cl

bond lengths varying from 2.28 to 3.26 Å. We found the monodentate behaviour of the organic ligand due to the d^9-configuration of the copper, causing Jahn–Teller distortion of the coordination octahedra in **1b**. The two polymorphic phases of **1b** differ by the arrangement of the double chains, which can be either parallel (α-**1b**) or in a herringbone pattern (β-**1b**). The formation of the different polymorphs depends on the synthetic conditions, especially on the temperature profiles. Temperature-dependent XRPD should in the future be made also on the other coordination polymers in order to investigate a possible polymorphism as well.

With 4-cyanopyridine as a ligand, a spectrum of various coordination chemistry is available. One-dimensional single chains or double chains and two-dimensional networks are realized. The degree of polymerization can be tuned by thermal decomposition from chains to double chains and 2D networks. By further increase of the metal : ligand ratio or a variation of the counterions, even new three-dimensional frameworks (*e.g.* MOFs) should be conceivable.

Experimental section

Materials

Methanol, ethanol and 4-cyanopyridine were purchased from Sigma-Aldrich. $MnCl_2{\cdot}4H_2O$, $NiCl_2{\cdot}6H_2O$ and $CuCl_2{\cdot}2H_2O$ were obtained from Fluka. $CoBr_2$ and $NiBr_2$ were purchased from Alfa Aesar.

Synthesis of $[CuCl_2(4\text{-CNpy})_2]_n$ (1a). $CuCl_2{\cdot}2H_2O$ was dried at 100 °C for 120 minutes. Anhydrous $CuCl_2$ (1.983 g, 14.75 mmol) was dissolved in 60 mL of methanol. The solution was added dropwise to 60 mL solution of 4-cyanopridine (3.07 g, 29.5 mmol) in methanol. After constant stirring for 90 minutes the mixture was filtered and washed with methanol. The final residue was dried in a vacuum desiccator (drying agent: silica gel) for one night to obtain **1a** as a light blue powder. The compound was identified by X-ray powder diffraction data by comparing with a calculated powder pattern. Yield: 4.683 g (92.26%). IR (cm^{-1}): *ν* 2242(w), 1611(s), 1551(m), 1494(m), 1415(s), 1219(s), 1065(m), 1027(m), 829(s), 785(m) (Fig. S6†).

Preparation of $[CuCl_2(4\text{-CNpy})]_n$ (1b). Compound **1b** was prepared by thermal decomposition reaction of **1a**. Sample **1** of **1b** was prepared in a glass capillary on a STOE Stadi-P diffractometer equipped with a heating device which gives a hot nitrogen flow (about 220 °C). The other samples were obtained from thermal decomposition in a snap cap vial in a tube furnace under nitrogen atmosphere at 207 °C for 150 minutes (sample **2**) and at 220 °C for 120 minutes (sample **3**). A schematic representation of the preparation of samples **2** and **3** can be found in the ESI† (Fig. S7). Yield: 99.96% for sample **2** and 94.94% for sample **3**. IR of sample **2** (cm^{-1}): 3102(w), 3058(w), 3012(w), 2243(w), 1698(w), 1612(m), 1497(w), 1417(s), 1219(m), 1067(w), 1029(w), 834(s), 785(w), 671 (w) (Fig. S8†).

Synthesis of $[MnCl_2(4\text{-CNpy})_2]_n$ (2a). $MnCl_2{\cdot}4H_2O$ was dried at 100 °C for 120 minutes. Anhydrous $MnCl_2$ (1.346 g, 10.7 mmol) was dissolved in 50 mL ethanol. A 50 mL ethanol solution of 4-cyanopridine (2.227 g, 21.38 mmol) was mixed with the prepared $MnCl_2$/methanol solution. The mixture was stirred for 90 minutes at room temperature. The precipitate was isolated by filtration and washed with ethanol. The final residue was dried in a vacuum desiccator (drying agent: silica gel) for one night to give a white powder. It was identified by X-ray powder diffraction data by comparing with a calculated powder pattern. Yield: 2.821 g (78.95%). IR (cm^{-1}): 3096(w), 3051(w), 2241(w), 1606(s), 1550(m), 1494(m), 1413(s), 1226(s), 1216(m), 1194(w), 1065(s), 1011(s), 826(s), 789(s) (Fig. S9†).

Preparation of $[MnCl_2(4\text{-CNpy})]_n$ (2b). Compound **2b** was prepared by thermal decomposition reaction of $[MnCl_2(4\text{-CNpy})_2]_n$. $[MnCl_2(4\text{-CNpy})_2]_n$ (0.1432 g, 0.429 mmol) was placed in a snap cap vial and heated in a muffle furnace at 220 °C for 120 minutes. After cooling, a white crystalline powder (0.0976 g, 0.424 mmol) was obtained. Yield: 99.02%. IR (cm^{-1}): 3093(w), 3070(w), 2275(w), 1603(m), 1550(w), 1490(w), 1411(s), 1215(m), 1067(w), 1012(w), 959(w), 821(s), 799(s) (Fig. S10†).

Synthesis of $[NiCl_2(4\text{-CNpy})_2]_n$ (3a). Compound **3a** was synthesized similarly to the synthesis of $[MnCl_2(4\text{-CNpy})_2]_n$. A light green crystalline product was obtained by a reaction of nickel chloride hexahydrate (2.347 g, 9.87 mmol) and cyanopyridine (2.056 g, 19.75 mmol) in ethanol for 90 minutes. Yield: 2.958 g (88.68%). IR (cm^{-1}): 3105(w), 2242(w), 1610(s), 1551(m), 1492(m), 1414(s), 1220(s), 1066(m), 1020(m), 821(s), 782(m) (Fig. S11†).

Preparation of $[NiCl_2(4\text{-CNpy})]_n$ (3b). Compound **3b** was prepared by thermal decomposition reaction of **3a**. Compound **3a** (0.2261 g, 0.669 mmol) was placed in a snap cap vial and heated in a muffle furnace at 220 °C for 180 minutes. After cooling, a light blue residue (0.1564 g, 0.669 mmol) was obtained. Yield: 99.98%. IR (cm^{-1}): 3176(w), 2288(w), 1605(m), 1551(w), 1490(w), 1411(s), 1215(s), 1067(w), 1019(w), 821(s), 792(m) (Fig. S12†).

Synthesis of $[CoBr_2(4\text{-CNpy})_2]_n$ (4a). Anhydrous cobalt bromide (0.53 g, 2.4 mmol) was dissolved in 8 mL ethanol, and 4-cyanopyridine (0.55 g, 5.3 mmol) was dissolved in 5 mL ethanol. Both solutions were stirred, heated to 70 °C and mixed to form a violet precipitate. After stirring for an additional hour, the slurry was cooled to room temperature, filtered and washed three times with 5 mL ethanol. The final residue was dried in air for 1 h and overnight in a desiccator (drying agent: silica gel). The product (yield: 0.99 g, 2.3 mmol, 96%) was characterized by thermal analysis IR and X-ray powder diffraction. IR (cm^{-1}): 3102(w), 3056(w), 2234(w), 1606(s), 1547(m), 1487(m), 1408(s), 1209(s), 1187(m), 1058(s), 1016(s), 819(s), 776(s), 674(m) (Fig. S13†).

Synthesis of $[CoBr_2(4\text{-CNpy})]_n$ (4b). An evacuated and sealed glass ampoule, filled with a well distributed 1 : 1 molar mixture of $CoBr_2$ (0.12 g, 0.55 mmol) and **4a** (0.23 g, 0.54 mmol), was placed in a tube furnace with a temperature gradient (maximum temperature 360 °C) for 22 h. After cooling down within 4 h different phases of $[CoBr_2(4\text{-CNpy})_x]_n$ (x = 0–2) ranging from **4a** to pure $CoBr_2$ were obtained (Fig. S14†).

Fraction 2, $[CoBr_2(4\text{-}CNpy)]_n$ (**4b**), was isolated as a grey powder of poor crystallinity. IR (cm^{-1}): 3096(w), 3072(w), 3046(w), 2281(w), 1605(m), 1549(m), 1496(w), 1409(s), 1216(s), 1096(m), 1063(s), 1015(s), 819(s), 787(m), 671(w), 560(s), 458(w) (Fig. S15†).

Synthesis of $[NiBr_2(4\text{-}CNpy)_2]_n$ (5a). Anhydrous nickel bromide (0.25 g, 2.29 mmol) was dissolved in 35 mL 4-hydroxy-4-methylpentan-2-one (DAA), and 4-cyanopyridine (0.477 g, 9.16 mmol) was dissolved in 10 mL DAA. Both solutions were mixed and put in a fridge at 8 °C. A light yellow powder was formed after 3 days. The powder was washed four times with 2 mL methanol and dried overnight in a desiccator (drying agent: silica gel). The product was characterized by thermal analysis, X-ray powder diffraction and IR spectroscopy (cm^{-1}): 3105(w), 2235(w), 1607(s), 1549(m), 1489(m), 1412(s), 1219(s), 1196(m), 1063(s), 1018(s), 816(s), 783(s), 675(m) (Fig. S16†).

Preparation of $[NiBr_2(4\text{-}CNpy)]_n$ (5b). Compound **5b** was prepared by thermal decomposition reaction of **5a**. Compound **5a** (0.02216 g, 0.0520 mmol) was heated in a thermogravimetric device (for details see below) at 280 °C for 10 minutes under argon atmosphere. After cooling, an ochre powder (0.01712 g) was obtained and immediately transferred into a glass capillary. The capillary was sealed and put on the diffractometer. The product was characterized by X-ray powder diffraction and IR spectroscopy (cm^{-1}): 3310(w), 3229(w) 2298(w), 1630(m), 1551(w), 1418(s), 1217(s), 1067(w), 1024(w), 831(s), 820(s), 783(m) (Fig. S17†).

Spectroscopy

FT-IR spectra were recorded using a NICOLET 6700 Fourier transform infrared reflection–absorption spectrometer.

Differential thermal analysis and thermogravimetry (DTA/TG)

Differential thermal and thermogravimetric analyses (DTA/TG) were performed on a SETARAM (TGA 92) device. The samples were filled into Al_2O_3 crucibles and measured under nitrogen atmosphere with a heating rate of 5 K min^{-1} and a constant flow rate of about 75 mL min^{-1}. The heating ranges for the compounds were from 293 K to 873 K for $[MnCl_2(4\text{-}CNpy)_2]_n$, from 293 K to 713 K for $[NiCl_2(4\text{-}CNpy)_2]_n$ and from 293 K to 723 K for $[CuCl_2(4\text{-}CNpy)_2]_n$.

X-ray powder diffraction

For the crystal structure determination from X-ray powder diffraction data, the XRPD experiments were performed on a STOE Stadi-P diffractometer equipped with a Ge(111) monochromator and a linear position-sensitive detector (PSD) using Cu $K\alpha_1$ radiation (λ = 1.54056 Å) for **1b**, **3a**, **3b**, **5a**, and **5b** and Mo $K\alpha_1$ radiation (λ = 0.70930 Å) for **2b** and **4a**. The specimens were measured in borosilicate glass capillaries with a diameter of 1.0 mm for **1b**, **3a**, **3b**, **5a**, and **5b** and 0.5 mm for **2b** and **4a**. The data were collected using WinXPOW software.[30]

The temperature dependent XRPD measurements for compound **1a** were performed on a STOE Stadi-P diffractometer equipped with a ceramic oven and an imaging plate position-sensitive detector using Cu $K\alpha_1$ radiation. The measurements were carried out in a 1.0 mm glass capillary under static air.

Structure determinations from X-ray powder data

General. All the powder patterns were indexed with DICVOL91.[31] The space group determination was carried out in DASH.[32] All structures were solved with a starting molecular structure model in direct space using simulated annealing in DASH. Rietveld refinements were performed with TOPAS.[28] First, a Pawley refinement was carried out to refine the background, zero point error, unit cell parameters, peak width and peak asymmetry parameters. In the Rietveld refinements, the cyanopyridine ring including H atoms was restrained to be flat; the bond lengths and bond angles in the pyridine ring and the cyano group were restrained to a statistical mean value from the Cambridge Structural Database (CSD) (Fig. S18 and Table S3†). The values of isotropic thermal parameters of H atoms were constrained to be 1.2 times those of the non-hydrogen atoms.

$[CuCl_2(4\text{-}CNpy)]_n$ (α-1b and β-1b). The samples of **1b**, measured carefully at room temperature, always contained a mixture of the α- and the β-phase. The powder pattern of **α-1b** could be obtained by subtracting the pattern of sample 2 from that of sample **1**, and the pattern of **β-1b** by subtracting the patterns of sample 3 and sample 2. For the β-phase of **1b**, the indexing of the extracted X-ray powder pattern with 21 peaks led to a monoclinic unit cell with $M(21)$ = 24.9; $F(21)$ = 49.6. A comparison of the unit cell volume (814.2 $Å^3$) with Hofmann's volume increments[33] indicated Z = 4. The same molecular structure model as **1a** was applied in the structure solution.

For **α-1b**, a total of 21 peaks in the low angle range were selected for indexing of the extracted X-ray powder of the pure phase. The indexing led to a triclinic unit cell with a figure of merit[34,35] of $M(21)$ = 14.0; $F(21)$ = 24.9. A comparison of the unit cell volume from indexing (406.4 $Å^3$) with Hofmann's volume increments led to Z = 2. The starting molecular geometry for structure solution of **α-1b** was constructed from the known crystal structure of $[CuCl_2(4\text{-}CNpy)_2]_n$.

Rietveld refinements were performed on the original data of sample **1**, refining the structures of both phases simultaneously (Fig. 4d and e). The same procedure was also applied to sample 2 (Fig. S4†). The resulting crystal structures were virtually identical. *R*-values and relative amounts of both phases are given in Table S2.† The highest content of **α-1b** was found in sample **1** (72%), and the highest amount of **β-1b** in sample 3 (86%). Correspondingly, the final crystallographic data of **α-1b** were taken from the Rietveld refinement of sample **1**, and that of **β-1b** from the refinement of sample **3**.

$[MnCl_2(4\text{-}CNpy)]_n$ (2b). Indexing with the first 20 peaks led to a monoclinic unit cell. A starting molecular geometry was generated from the known crystal structure of $[MnCl_2(4\text{-}$

CNpy)$_2$]$_n$.[24] Due to the slight residue of compound **2a** the 2θ range from 7.1° to 7.4° was excluded from the Rietveld refinement.

[NiCl$_2$ (4-CNpy)$_2$]$_n$ (3b). The first 28 peaks were selected for indexing, which resulted in a monoclinic unit cell. The starting molecular geometry was derived from the known crystal structure of [MnCl$_2$(4-CNpy)$_2$]$_n$, in which the Mn atom was replaced by Ni.

[NiCl$_2$(4-CNpy)]$_n$ (3a). Indexing with 19 low-angle peaks led to a monoclinic unit cell. The molecular structure model was derived from the previously determined crystal structure of **3b**.

[CoBr$_2$(4-CNpy)$_2$]$_n$ (4a). Indexing of the X-ray powder pattern led to an orthorhombic unit cell. A starting molecular geometry was generated from the known crystal structure of compound **3b** and force field methods in AVOGADRO.[36]

[NiBr$_2$(4-CNpy)$_2$]$_n$ (5a). Indexing with 19 low-angle peaks led to an orthorhombic unit cell. The molecular structure model was derived from the previously determined crystal structure of **4a**. Due to the slight residue of a decomposition intermediate of **5b**, the 2θ ranges from 21.7° to 22.0° and 31.0° to 31.3° were excluded from the Rietveld refinement.

[NiBr$_2$(4-CNpy)]$_n$ (5b). Indexing with 21 low-angle peaks led to a monoclinic unit cell. The molecular structure model was derived from the previously determined crystal structure of **5a**.

Acknowledgements

Haishuang Zhao gratefully acknowledges financial support by the Carl-Zeiss-Stiftung.

References

1 T. Watabe and K. Yogo, *Bull. Chem. Soc. Jpn.*, 2014, **87**, 740–745.
2 J. Hasegawa, M. Higuchi, Y. Hijikata and S. Kitagawa, *Chem. Mater.*, 2009, **21**, 1829–1833.
3 Z. Wang, G. Chen and K. Ding, *Chem. Rev.*, 2008, **109**, 322–359.
4 S.-H. Cho, B. Ma, S. T. Nguyen, J. T. Hupp and T. E. Albrecht-Schmitt, *Chem. Commun.*, 2006, 2563–2565.
5 O. R. Evans and W. Lin, *Acc. Chem. Res.*, 2002, **35**, 511–522.
6 S. Wöhlert, L. Fink, M. Schmidt and C. Näther, *CrystEngComm*, 2013, **15**, 945–957.
7 Y.-S. Bae, O. K. Farha, A. M. Spokoyny, C. A. Mirkin, J. T. Hupp and R. Q. Snurr, *Chem. Commun.*, 2008, 4135–4137.
8 M. Wriedt, S. Sellmer and C. Näther, *Dalton Trans.*, 2009, 7975–7984.
9 J. Lee, O. K. Farha, J. Roberts, K. A. Scheidt, S. T. Nguyen and J. T. Hupp, *Chem. Soc. Rev.*, 2009, **38**, 1450–1459.
10 S. L. James, *Chem. Soc. Rev.*, 2003, **32**, 276–288.
11 F. H. Allen, *Acta Crystallogr., Sect. B: Struct. Sci.*, 2002, **58**, 380–388.
12 I. J. Bruno, J. C. Cole, P. R. Edgington, M. Kessler, C. F. Macrae, P. McCabe, J. Pearson and R. Taylor, *Acta Crystallogr., Sect. B: Struct. Sci.*, 2002, **58**, 389–397.
13 D. T. Cromer and A. C. Larson, *Acta Crystallogr., Sect. B: Struct. Crystallogr. Cryst. Chem.*, 1972, **28**, 1052–1058.
14 A. J. Graham, P. C. Healy, J. D. Kildea and A. H. White, *Aust. J. Chem.*, 1989, **42**, 177–184.
15 M. K. Broderick, C. Yang, R. D. Pike, A. Nicholas, D. May and H. H. Patterson, *Polyhedron*, 2016, **114**, 333–343.
16 H. Hanika-Heidl, S. E. H. Etaiw, M. S. Ibrahim, A. S. B. El-din and R. D. Fischer, *J. Organomet. Chem.*, 2003, **684**(1), 329–337.
17 A. Bacchi, G. Cantoni, P. Pelagatti and S. Rizzato, *J. Organomet. Chem.*, 2012, **714**, 81–87.
18 W. H. Leung, W. Lai and I. D. Williams, *J. Organomet. Chem.*, 2000, **604**, 197–201.
19 L. Carlucci, G. Ciani, D. M. Proserpio and A. Sironi, *J. Chem. Soc., Chem. Commun.*, 1994, 2755–2756.
20 X. L. Zhao and T. C. W. Mak, *Dalton Trans.*, 2004, 3212–3217.
21 W. Chen, F. Liu and X. You, *Bull. Chem. Soc. Jpn.*, 2002, **75**, 1559–1560.
22 R. D. Bailey and W. T. Pennington, *Chem. Commun.*, 1998, 1181–1182.
23 Y. Krysiak, L. Fink, T. Bernert, J. Glinnemann, M. Kapuscinski, H. Zhao, E. Alig and M. U. Schmidt, *Z. Anorg. Allg. Chem.*, 2014, **640**, 3190–3196.
24 W. Zhang, J. R. Jeitler, M. M. Turnbull, C. P. Landee, M. Wei and R. D. Willett, *Inorg. Chim. Acta*, 1997, **256**, 183–198.
25 M. L. Hernández, M. G. Barandika, M. K. Urtiaga, R. Cortés, L. Lezama, M. I. Arriortua and T. Rojo, *J. Chem. Soc., Dalton Trans.*, 1999, 1401–1406.
26 S. Wöhlert, I. Jess, U. Englert and C. Näther, *CrystEngComm*, 2013, **15**, 5326–5336.
27 S. Wöhlert, L. Fink, M. U. Schmidt and C. Näther, *Z. Anorg. Allg. Chem.*, 2013, **639**, 2186–2194.
28 A. Coelho, *TOPAS Acad. User Man. & Tech. Ref.*, Brisbane, Australia, 2009.
29 W. T. Chen, Z. G. Luo, Y. P. Xu, Q. Y. Luo and J. H. Liu, *J. Chem. Res.*, 2011, **35**, 253–256.
30 STOE & Cie GmbH, *STOE WinXPOW 210*, Darmstadt, Germany, 2004.
31 A. Boultif and D. Louër, *J. Appl. Crystallogr.*, 1991, **24**, 987–993.
32 W. I. F. David, K. Shankland, J. van de Streek, E. Pidcock, W. D. S. Motherwell and J. C. Cole, *J. Appl. Crystallogr.*, 2006, **39**, 910–915.
33 D. W. M. Hofmann, *Acta Crystallogr., Sect. B: Struct. Sci.*, 2002, **58**, 489–493.
34 P. M. de Wolff, *J. Appl. Crystallogr.*, 1968, **1**, 108–113.
35 G. S. Smith and R. L. Snyder, *J. Appl. Crystallogr.*, 1979, **12**, 60–65.
36 M. D. Hanwell, D. E. Curtis, D. C. Lonie, T. Vandermeersch, E. Zurek and G. R. Hutchison, *J. Cheminf.*, 2012, **4**, 17.

Supporting information

4-Cyanopyridine, a versatile mono- and bidentate ligand. Crystal structures of related coordination polymers determined by X-ray powder diffraction.

Haishuang Zhao,[a, b] Alexander Bodach,[a] Miriam Heine,[a] Yasar Krysiak,[a, b] Jürgen Glinnemann[a], Edith Alig[a] Lothar Fink,*[a] and Martin U. Schmidt[a]

[a] Institute of Inorganic and Analytical Chemistry, Goethe-University, Max-von-Laue-Str. 7, 60438 Frankfurt am Main, Germany. E-Mail: fink@chemie.uni-frankfurt.de; Fax: +49 69798 29235; Tel: +49 69798 29123

[b] Institute of Inorganic Chemistry and Analytical Chemistry, Johannes Gutenberg-University, Jakob-Welder-Weg 11, 55128 Mainz, Germany.

Figures

Tables

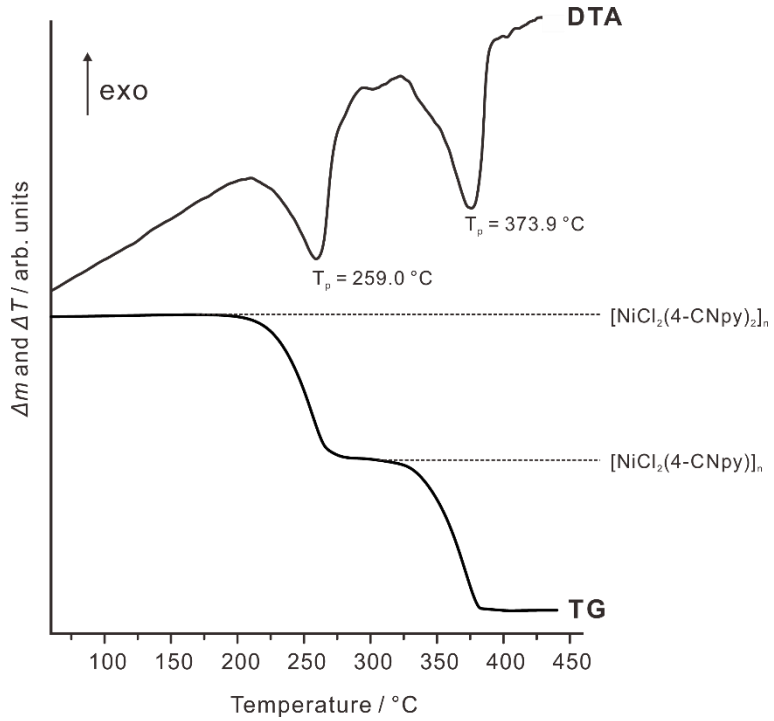

Fig. S1 DTA/TG curves of $[NiCl_2(4\text{-}CNpy)_2]_n$ (**3a**). Weight of starting compounds: 31.92 mg, Heating rate: 5 K/min, N_2 atmosphere, Al_2O_3 crucible, Tp: peak temperature.

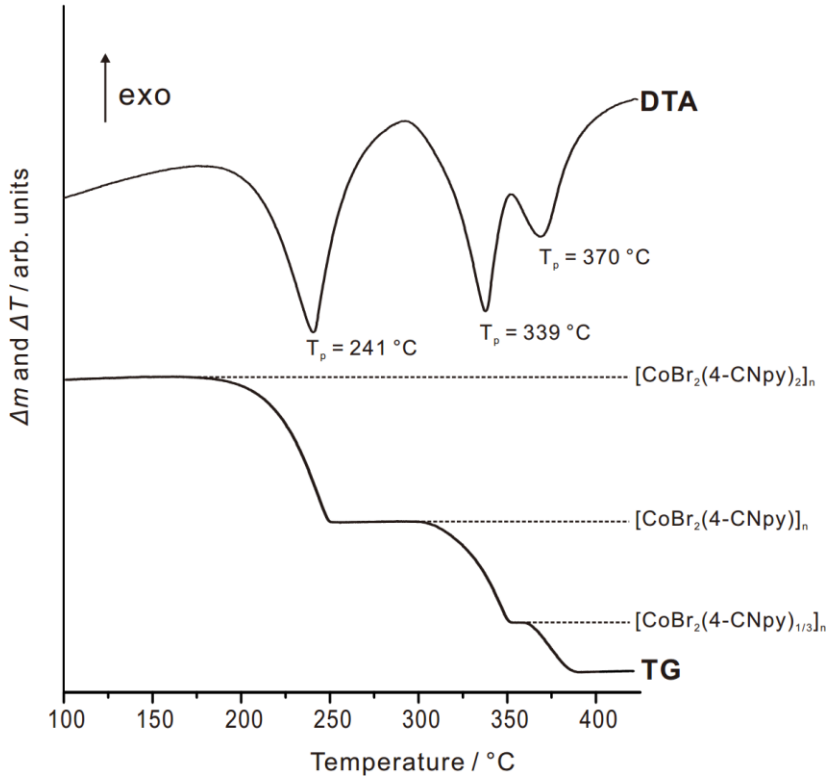

Fig. S2 DTA/TG curves of $[CoBr_2(4\text{-}CNpy)_2]_n$ (**4a**). Weight of starting compounds: 19.72 mg, Heating rate: 5 K/min, N_2 atmosphere, Al_2O_3 crucible, T_p: peak temperature.

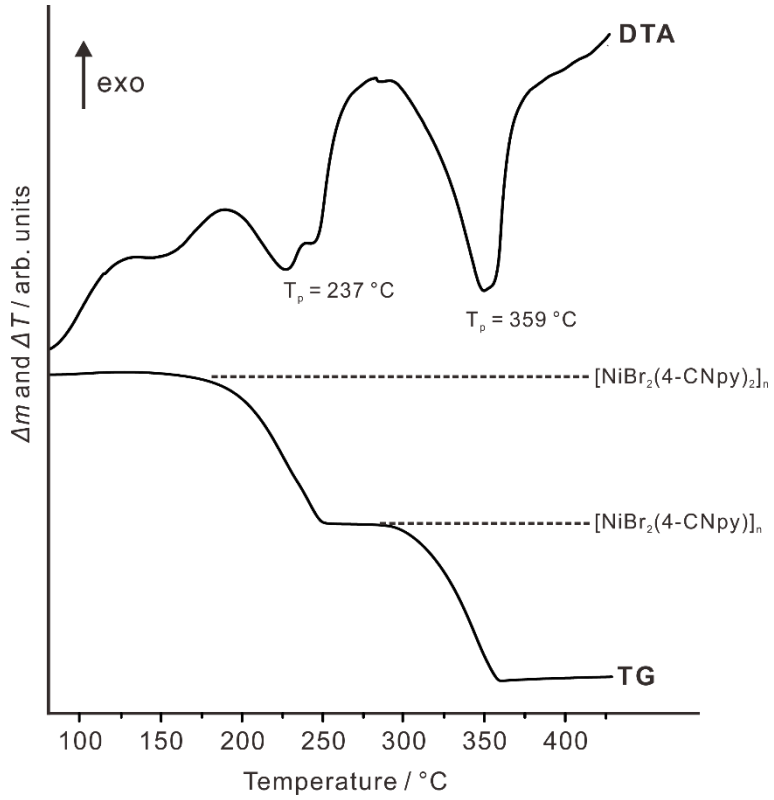

Fig. S3 DTA/TG curves of $[NiBr_2(4\text{-}CNpy)_2]_n$ (**5a**). Weight of starting compounds: 16.89 mg, Heating rate: 5 K/min, N_2 atmosphere, Al_2O_3 crucible, Tp: peak temperature.

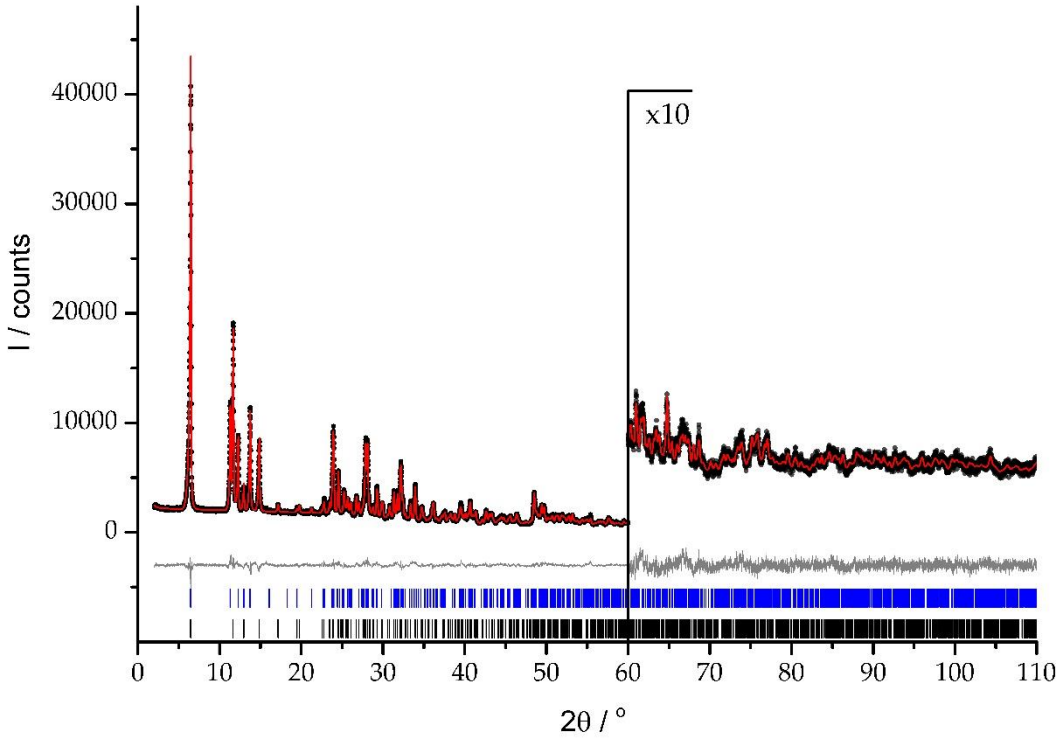

Fig. S4 Plot of combined Rietveld refinement of $[CuCl_2(4\text{-}CNpy)]_n$ **1b** (sample **2**). Observed powder diagram (black points), simulated powder diagram (red solid line), difference profiles (grey solid line), and reflection positions (blue (**α-1b** and black (**β-1b**) vertical lines). Change of the scale at 60º is with a factor of 10. Radiation type: Cu $K\alpha_1$ (λ= 1.54056 Å).

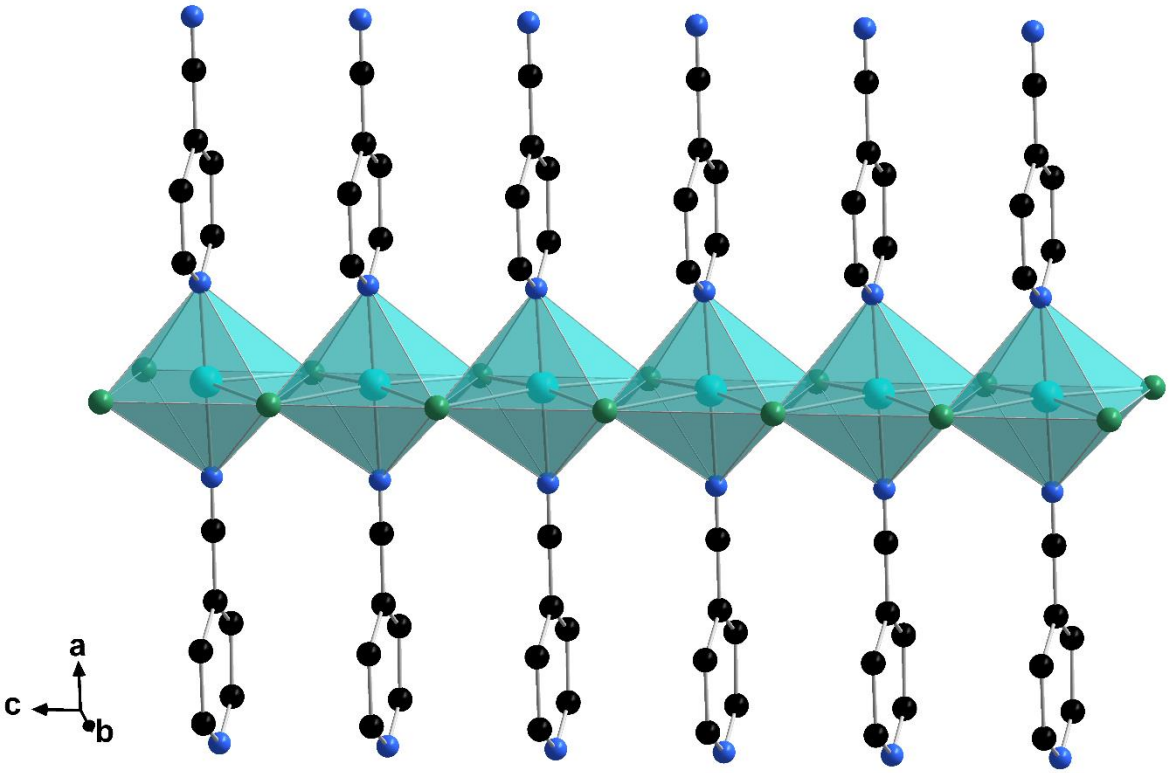

Fig. S5 Fragment of one layer in $[NiCl_2(4\text{-}CNpy)]_n$ (**3b**). H atoms have been removed for clarity.

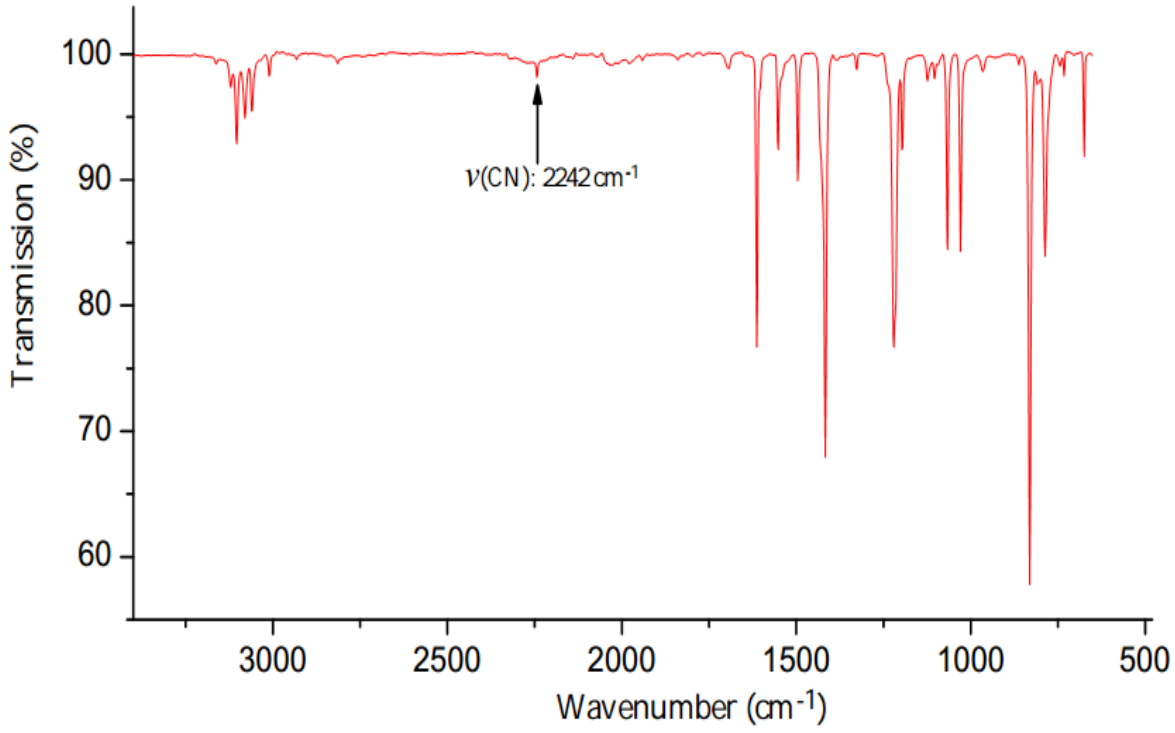

Fig. S6 IR spectrum of $[CuCl_2(4\text{-}CNpy)_2]_n$ (**1a**).

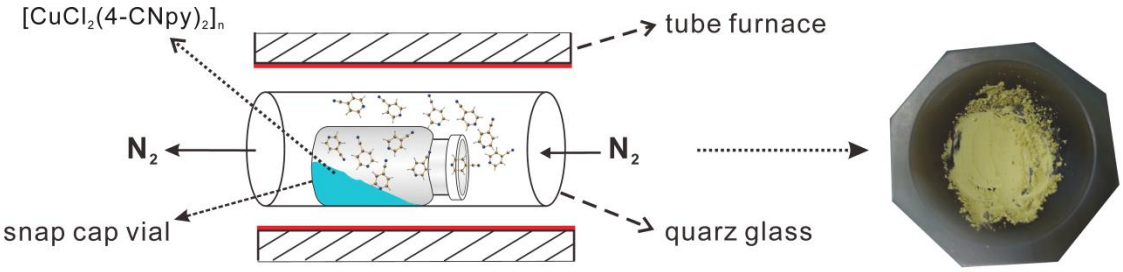

Fig. S7 Schematic representation for preparation of $[CuCl_2(4\text{-}CNpy)]_n$ (1b). According to the DTA/TG-curves of $[CuCl_2(4\text{-}CNpy)_2]_n$ (**1a**), the preparation of pure $[CuCl_2(4\text{-}CNpy)]_n$ (**1b**) was carried out using a snap cap vial as sample carrier under a controlled nitrogen flow.

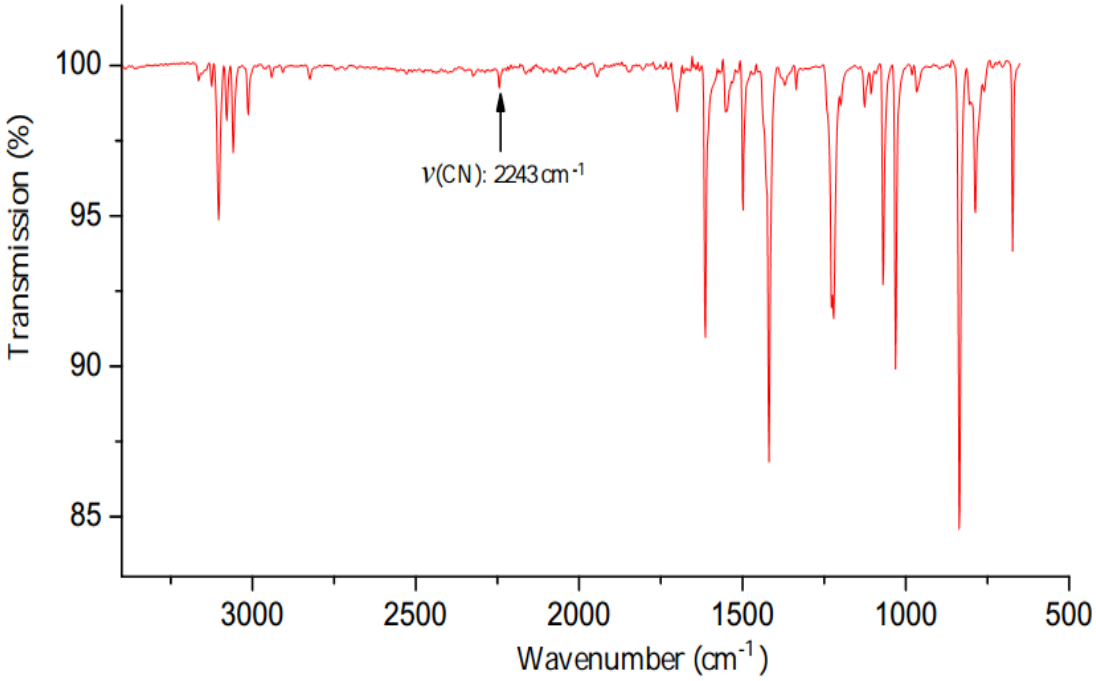

Fig. S8 IR spectrums of $[CuCl_2(4\text{-}CNpy)]_n$ **(1b)**.

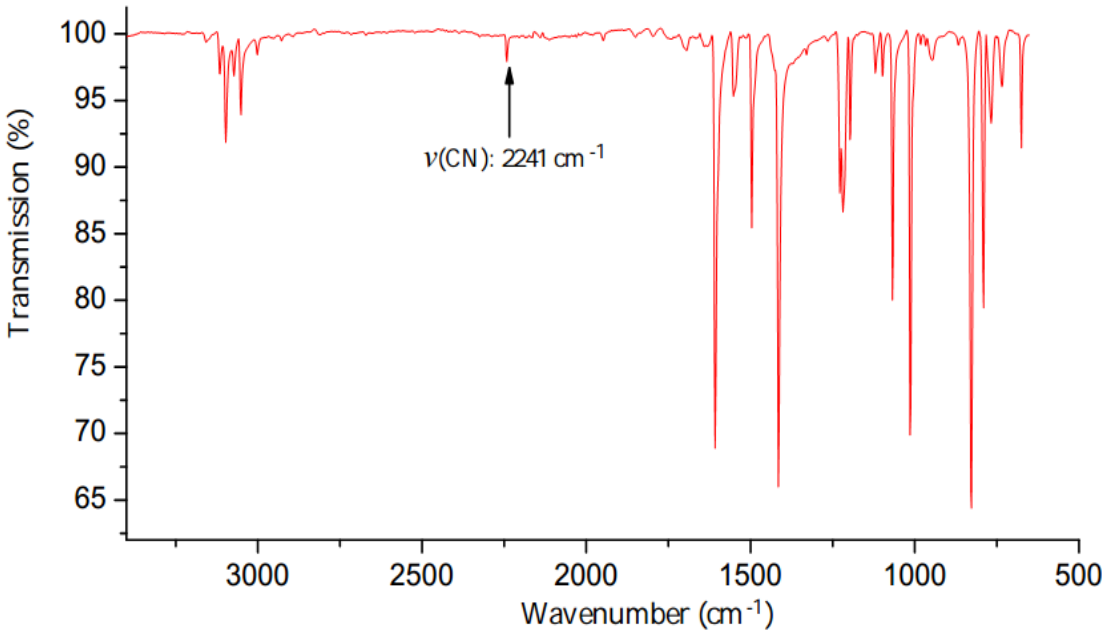

Fig. S9 IR spectrum of $[MnCl_2(4\text{-}CNpy)_2]_n$ **(2a)**.

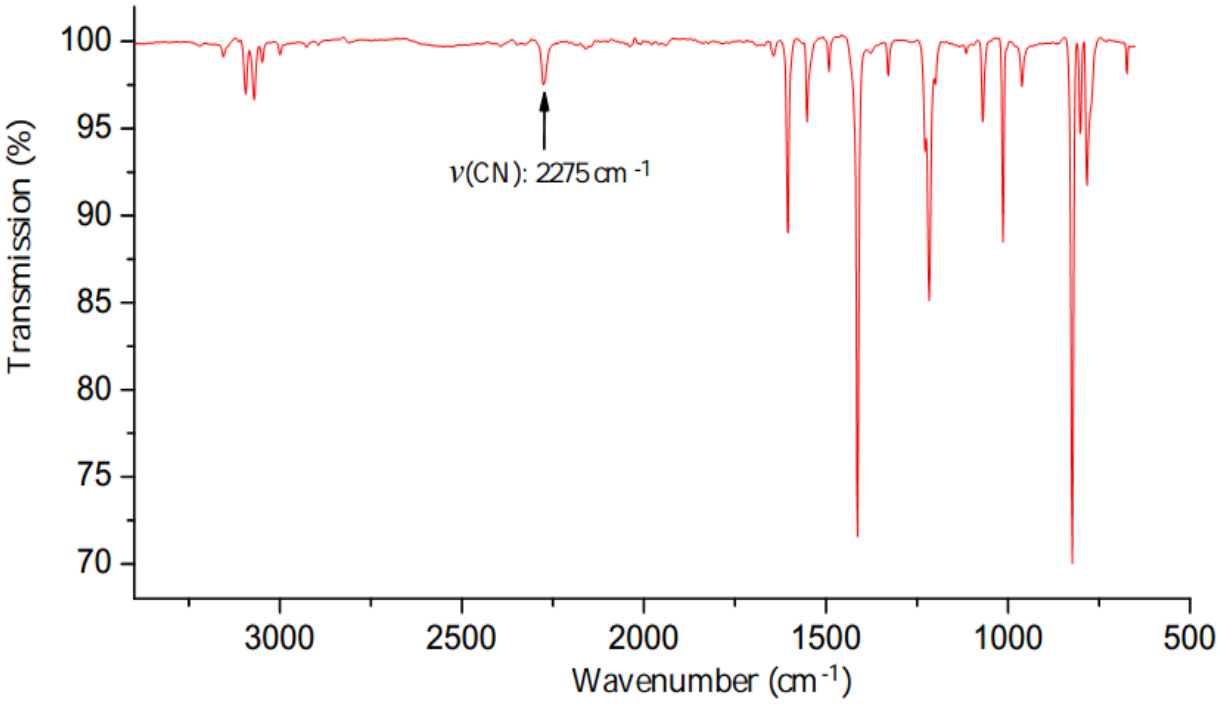

Fig. S10 IR spectrum of $[MnCl_2(4\text{-}CNpy)]_n$ **(2b)**.

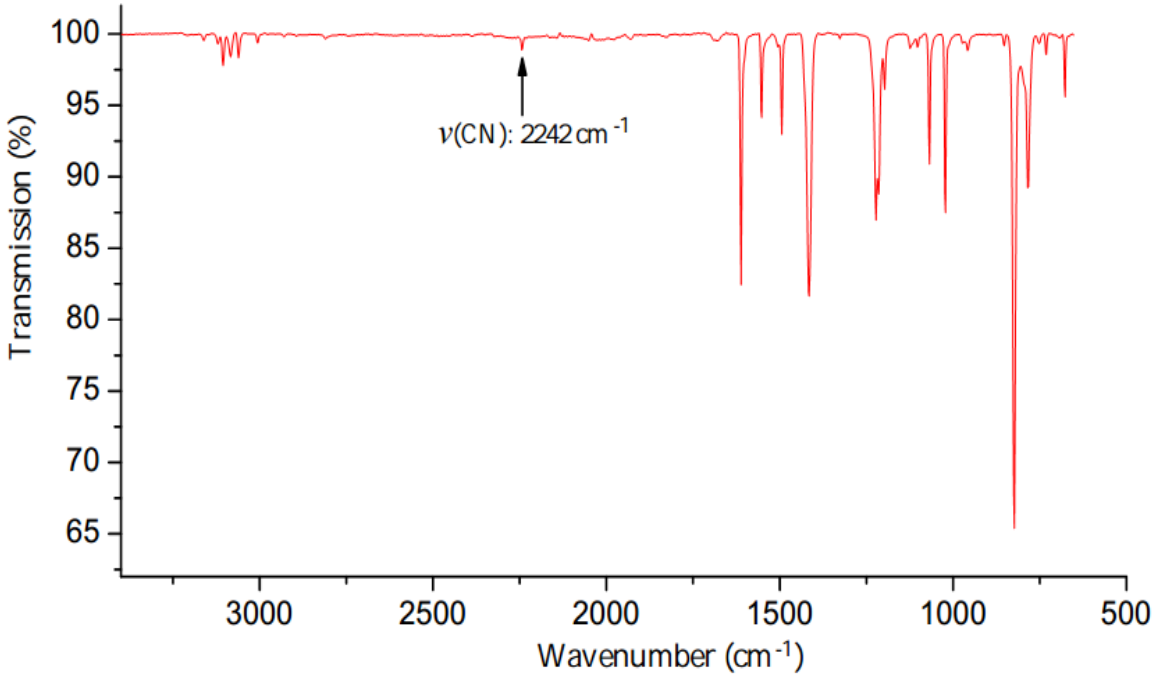

Fig. S11 IR spectrum of $[NiCl_2(4\text{-}CNpy)_2]_n$ **(3a)**.

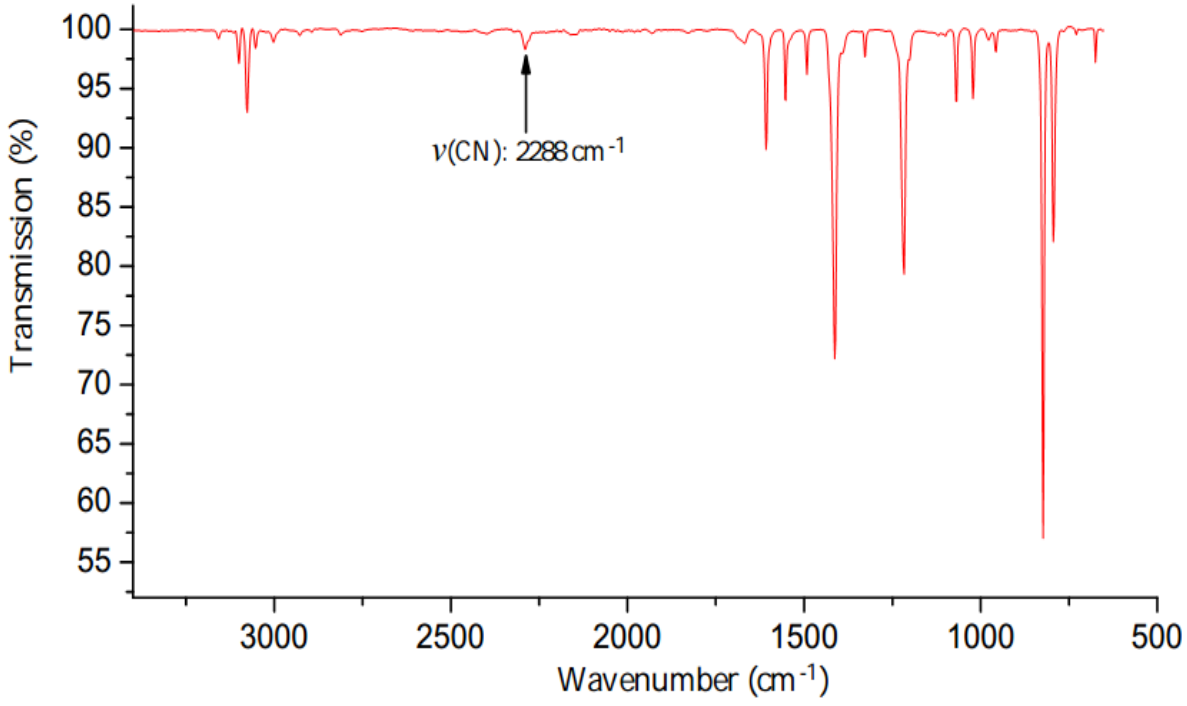

Fig. S12 IR spectrum of $[NiCl_2(4\text{-}CNpy)]_n$ **(3b)**.

.

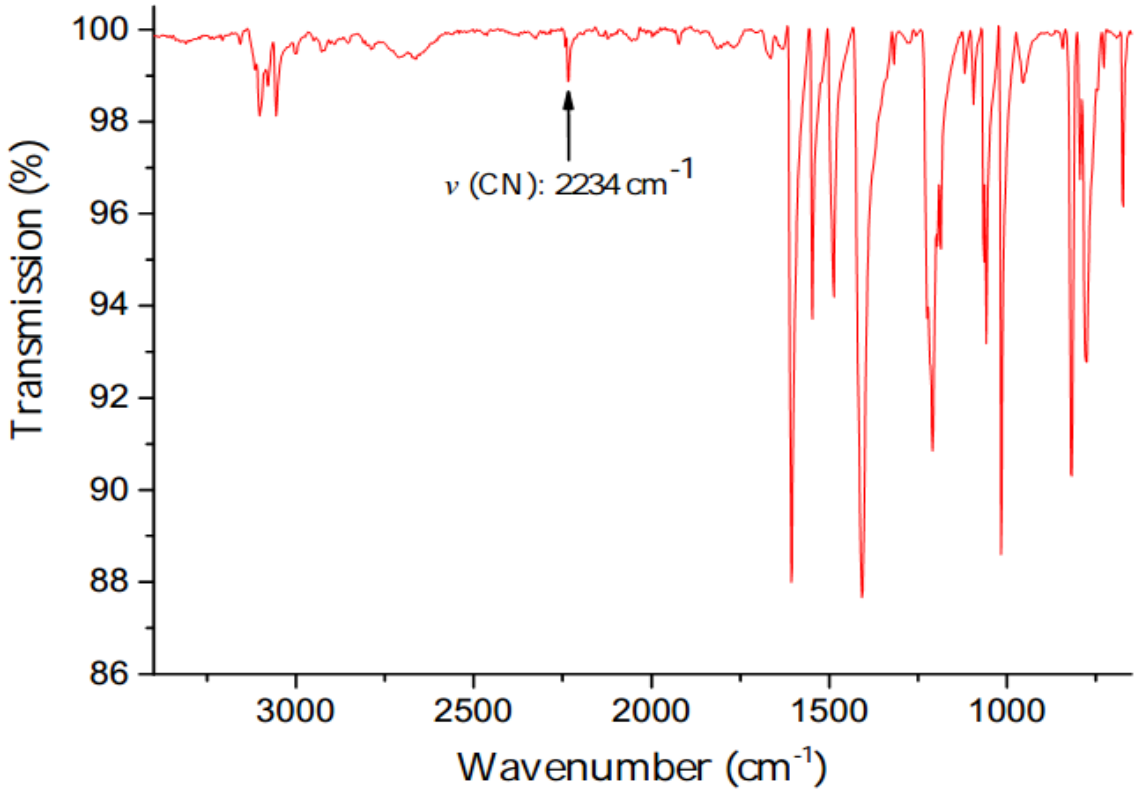

Fig. S13 IR spectrum of $[CoCl_2(4\text{-}CNpy)_2]_n$ **(4a)**.

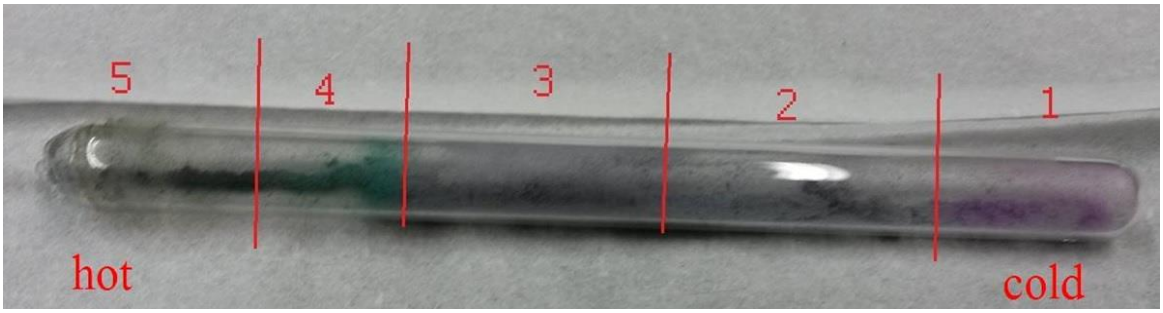

Fig. S 14 Schematic representation for preparation of $[CoBr_2(4\text{-}CNpy)]_n$ (**4b**).

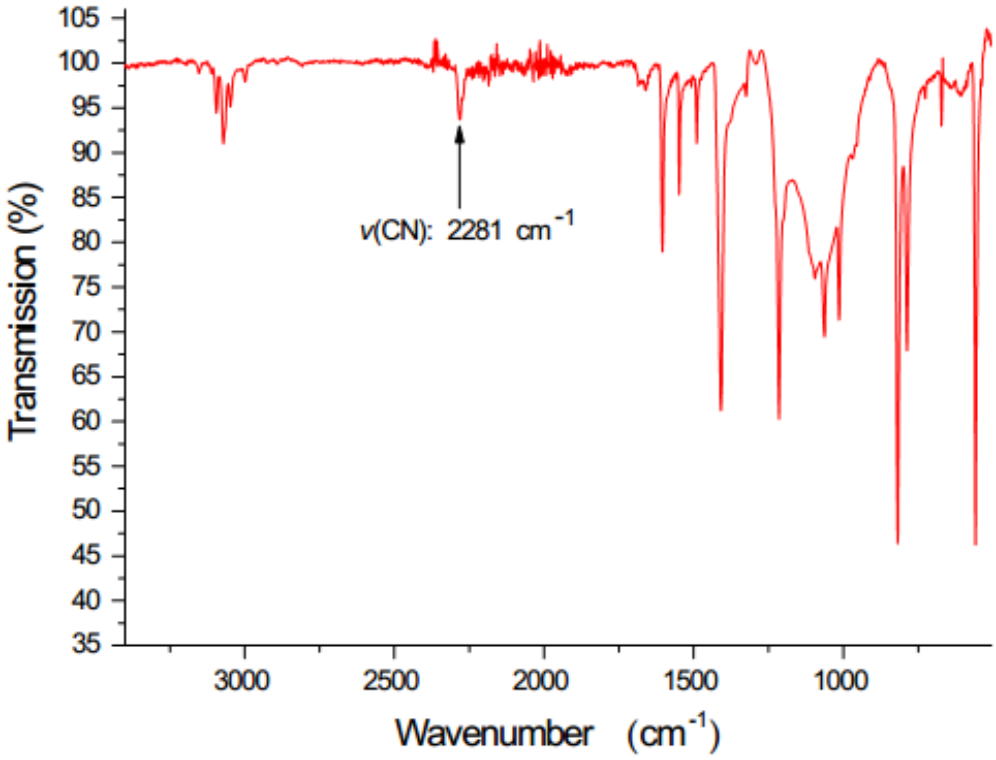

Fig. S 15 IR spectrum of $[CoCl_2(4\text{-}CNpy)]_n$ (**4b**).

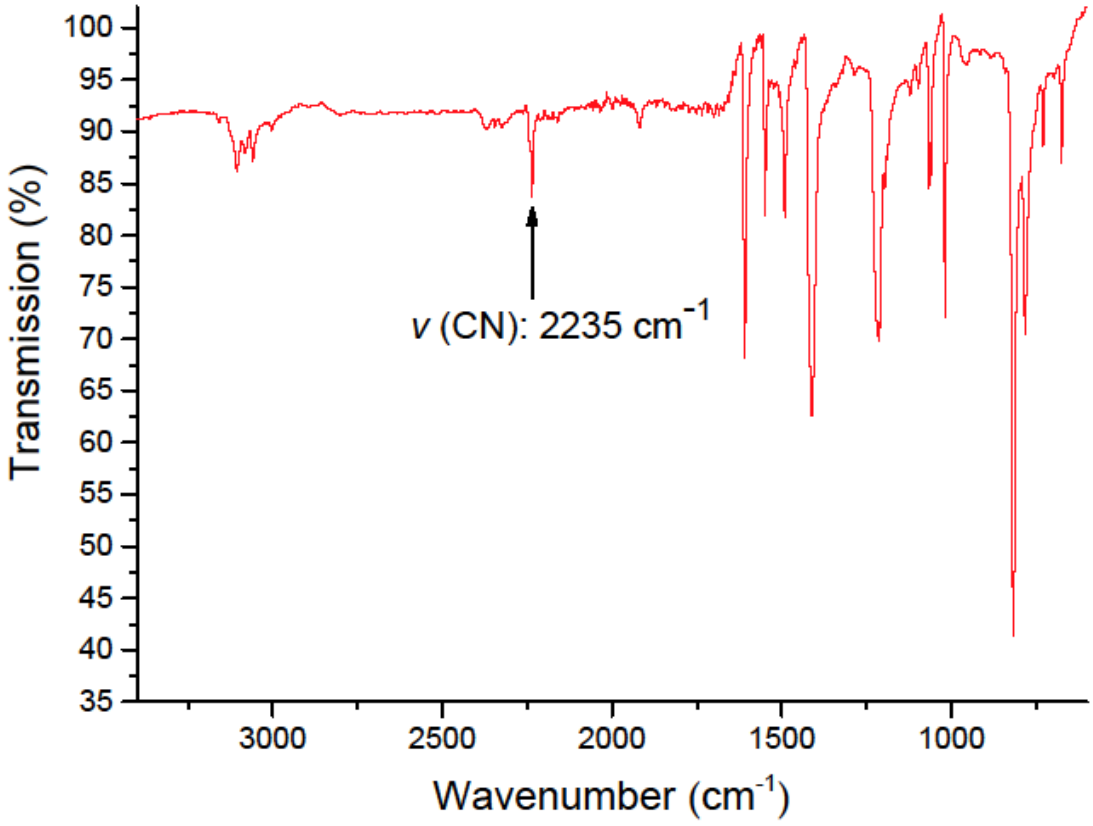

Fig. S16 IR spectrum of $[NiBr_2(4\text{-}CNpy)_2]_n$ **(5a)**.

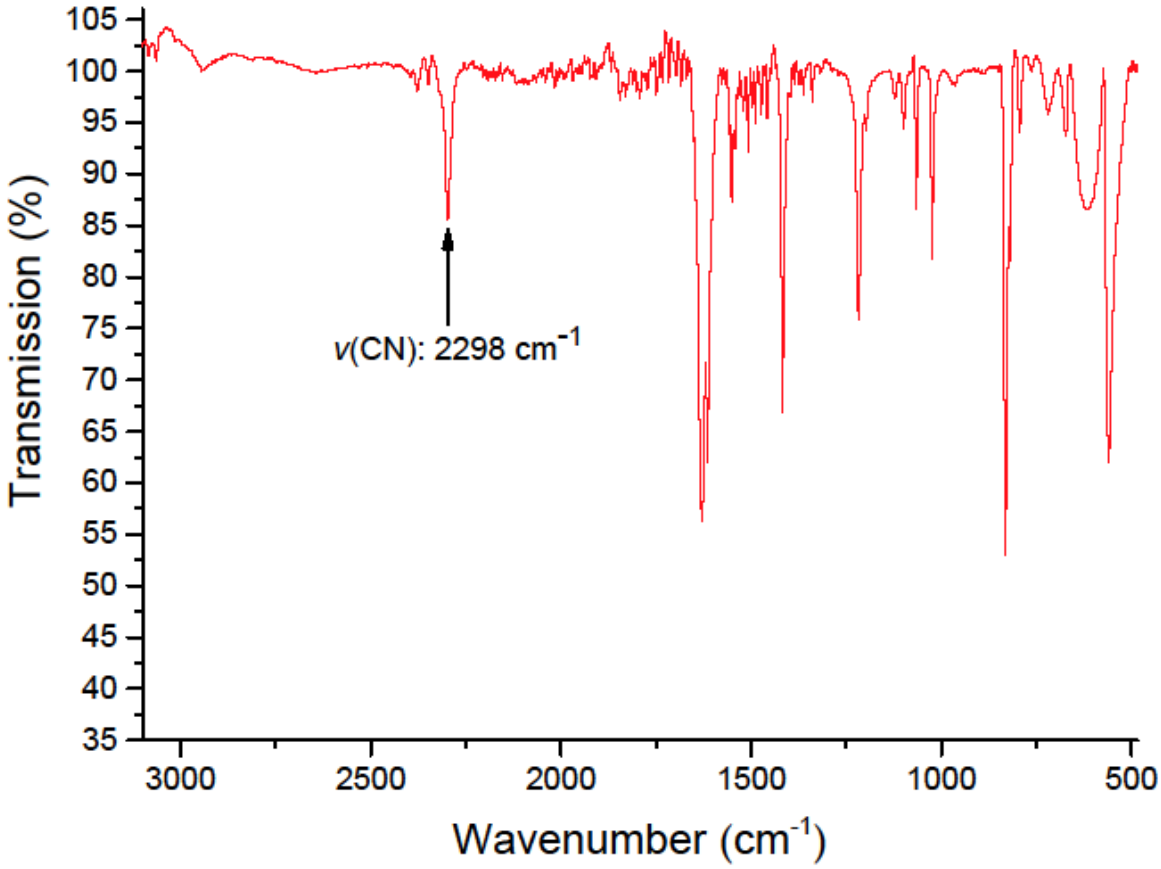

Fig. S17 IR spectrum of $[NiBr_2(4\text{-CNpy})]_n$. **(5b)**.

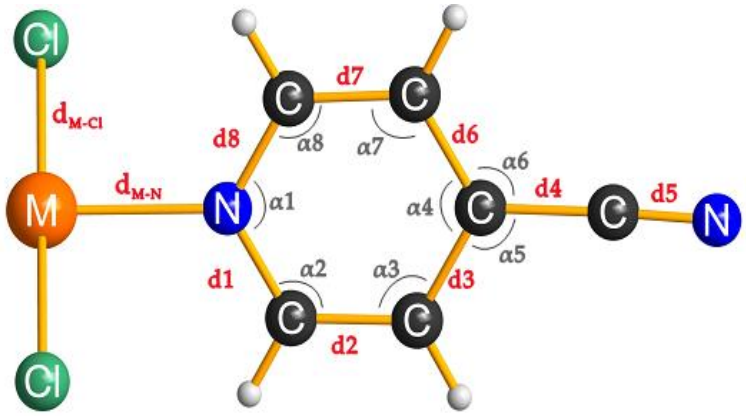

Fig. S18 Molecular structure model for structure solution. Note: model for compound **1b** - **4b**: MX_2(4-CNpy); for **3a** – **5a**: *MX*(4-CNpy) (*M* = Cu(II), Mn(II), Ni(II), Co(II), *X* = Cl, Br).

Table S1 Results of DTA/TG measurements of $[M(II)X_2(4\text{-}CNpy)_2]_n$ (M(II)= Cu, Mn, Ni, Co; X = Cl, Br). T: DTA peak temperatures, m_0: weight of starting compound, Δm_{exp}: relative experimental weight loss, experimental $\Delta m_{exp}/m_0$, calculated $\Delta m_{cal}/m_0$.

Compound	T /°C	m_0 /mg	Δm_{exp} /mg	$\Delta m_{exp}/m_0$ /%	$\Delta m_{cal}/m_0$ /%
$CuCl_2(4\text{-}CNpy)_2$	195	12.49	0	0	0
$CuCl_2(4\text{-}CNpy)$	267		3.63	29.1	30.38
$CuCl_2$	314		8.13	65.1	60.76
$MnCl_2(4\text{-}CNpy)_2$	190	17.18	0	0	0
$MnCl_2(4\text{-}CNpy)$	253		5.05	29.4	31.16
$MnCl_2(4\text{-}CNpy)_{1/3}$	318		8.54	49.7	51.94
$MnCl_2$	393		10.26	59.8	62.32
$NiCl_2(4\text{-}CNpy)_2$	200	31.92	0	0	0
$NiCl_2(4\text{-}CNpy)$	259		9.13	28.6	30.82
$NiCl_2$	374		18.79	58.9	61.63
$CoBr_2(4\text{-}CNpy)_2$	175	19.72	0	0	0
$CoBr_2(4\text{-}CNpy)$	241		4.51	22.9	24.38
$CoBr_2(4\text{-}CNpy)_{1/3}$	339		7.66	38.8	40.64
$CoBr_2$	370		9.20	46.7	48.77
$NiBr_2(4\text{-}CNpy)_2$	203	16.89	0	0	0
$NiBr_2(4\text{-}CNpy)$	325		3.81	22.58	24.37
$NiBr_2$	360		7.72	29.93	32.22

Table S2 Results of quantitative Rietveld analysis for the three samples of compound **1b**.

	α-1b /w%	**β-1b** /w%	R_{wp} /%	R_{exp} /%	*gof*
Sample **1**	72.76(18)	27.24(18)	4.41	2.53	1.74
Sample **2**	48.21(11)	51.79(11)	5.17	2.65	1.95
Sample **3**	14.87(20)	85.13(20)	5.89	2.82	2.09

Table S3 The mean bond lengths and bond angles in the given models after a statistic in CSD. $d1 = d8$, $d2 = d7$, $d3 = d6$; $a2 = a8$, $a3 = a7$, $a5 = a6$.

	1	**2**	**3**	**4**	**5**
bond angle ***a*** (º)	118.64	122.45	118.65	119.35	120.30
bond length ***d*** (Å)	1.338	1.377	1.381	1.447	1.138

[MH2]

3-Cyanopyridine as a bridging and terminal ligand in coordination polymers.
Miriam Heine, Lothar Fink and Martin U. Schmidt, In: CrystEngComm, 2018, 20**,** 7556-7566.

CrystEngComm

PAPER

View Article Online
View Journal | View Issue

Cite this: *CrystEngComm*, 2018, **20**, 7556

3-Cyanopyridine as a bridging and terminal ligand in coordination polymers†

Miriam Heine, Lothar Fink and Martin U. Schmidt*

3-Cyanopyridine (3-CNpy) can act as a bridging or terminal ligand in transition metal coordination polymers. The compounds $[M^{II}Br_2(3\text{-CNpy})_4]$ with M = Mn, Fe, Co, Ni (**1a–4a**) consist of individual complexes, in which the metal atom is octahedrally coordinated by two bromine atoms and four 3-cyanopyridine ligands, which coordinate through their pyridine N atoms only. Thermal decomposition at around 160 °C leads to the release of two 3-cyanopyridine molecules and the formation of $[M^{II}Br_2(3\text{-CNpy})_2]_n$ with M = Mn, Fe, Co, Ni (**1b–4b**). For **3b** and **4b** two polymorphs were observed each (**α-3b**, **β-3b**, **α-4b**, **β-4b**). In all six phases the metal atoms are linked by bromine bridges into $[M^{II}Br_2]_n$ chains. The 3-cyanopyridine ligands again act as terminal ligands coordinating with their pyridine N atoms. Upon further heating to around 250 °C, the compounds $[M^{II}Br_2(3\text{-CNpy})_1]_n$ with M = Mn, Fe, Co, Ni (**1c–4c**) are obtained. **1c–4c** are again built up from $[M^{II}Br_2]_n$ chains with lateral 3-CNpy ligands, but additionally the cyano groups coordinate to the metal atoms. **1c–4c** are the first compounds with 3-cyanopyridine as a bridging ligand between two 3d M^{2+} ions. The bridges connect neighbouring $[M^{II}Br_2]_n$ chains and this results in the formation of a wavy, two-dimensional network. All crystal structures were determined from X-ray powder diffraction data.

Received 13th September 2018,
Accepted 3rd November 2018

DOI: 10.1039/c8ce01568f

rsc.li/crystengcomm

1. Introduction

In recent years new coordination polymers based on transition metals have attracted much attention, due to their useful physical properties and their various potential applications in many areas such as catalysis, gas adsorption or magnetic materials.[1–9] A number of coordination polymers built up by transition metal halides or pseudohalides and additional heteroaromatic ligands have already been reported (see *e.g.* ref. 10 and 11). In the last few years we focused on the systematic investigation of polymeric compounds with the neutral N-donor ligands pyridine (py), 4-cyanopyridine (4-CNpy) and 3-cyanopyridine (3-CNpy). Especially 4-CNpy and 3-CNpy are less frequently used to prepare coordination polymers with novel structural topologies. As cyanopyridine contains two nitrogen donors, the N_{py} and the N_{CN} atoms, it can generally act as a bridge to connect two metal ions. On account of its weaker Lewis-base character, the donating ability of the N_{CN} is lower than of the N_{py} atom. Correspondingly, in most compounds cyanopyridine acts as a monodentate ligand coordinating with the N_{py} atom only. Structures with bridging cyanopyridine groups are rare.[12–21] Previously, we reported on polymeric compounds of the composition $[M^{II}Cl_2(py)_x]_n$ (M^{II} = Ni, Cu) with x = 2, 1, 2/3[22] and $[M^{II}X_2(4\text{-CNpy})_x]_n$ (M^{II} = Mn, Co, Ni; X = Cl, Br) with x = 2, 1.[23] In all of these compounds the metal atoms are connected by μ-bridging Cl or Br atoms to two neighbouring metal atoms, thus forming $[M^{II}X_2]_n$ chains. For x = 2, single chains are built up, in which pyridine or 4-cyanopyridine act as a terminal, monodentate ligand (see Scheme 1b). For x = 1 with X = Cl, two different structure types were observed: (1) two-dimensional networks; (2) polymeric double chains. In case (1) 4-cyanopyridine acts as bidentate ligand connecting two neighbouring $[M^{II}Cl_2]_n$-chains (Scheme 1d). In case (2) two $[M^{II}Cl_2]_n$ chains are fused together by μ_3-chlorine atoms while pyridine or 4-cyanopyridine acts as a terminal ligand only (Scheme 1c).

In the present work we investigated the ability of 3-cyanopyridine to act as mono- or bidentate ligand. The Cambridge Structural Database (CSD)[45,47] contains only about 40 structures of transition metal compounds with 3-cyanopyridine as ligand (in contrast to about 140 structures with 4-cyanopyridine, and about 43 800 structures with pyridine).[24–28] In only three structures 3-cyanopyridine behaves as a bidentate ligand:[29,30] in these structures 3-cyanopyridine links two Ag^I or two Cu^I ions respectively. We now prepared compounds that contain M^{2+} metal ions: $[M^{II}Br_2(3\text{-CNpy})_x]_n$ with M^{II} = Mn, Fe, Co, Ni and x = 1, 2 and 4. The compounds $[M^{II}Br_2(3\text{-CNpy})_4]$ (**1a–4a**) were synthesised by the reaction of 3-cyanopyridine and the corresponding metal bromide in solution. Thermal decomposition[31]

Institute of Inorganic and Analytical Chemistry, Goethe University, Max-von-Laue-Str. 7, 60438 Frankfurt am Main, Germany.
E-mail: m.schmidt@chemie.uni-frankfurt.de; Fax: +49 69 798 29235; Tel: +49 69 798 29123

† Electronic supplementary information (ESI) available. See DOI: 10.1039/c8ce01568f

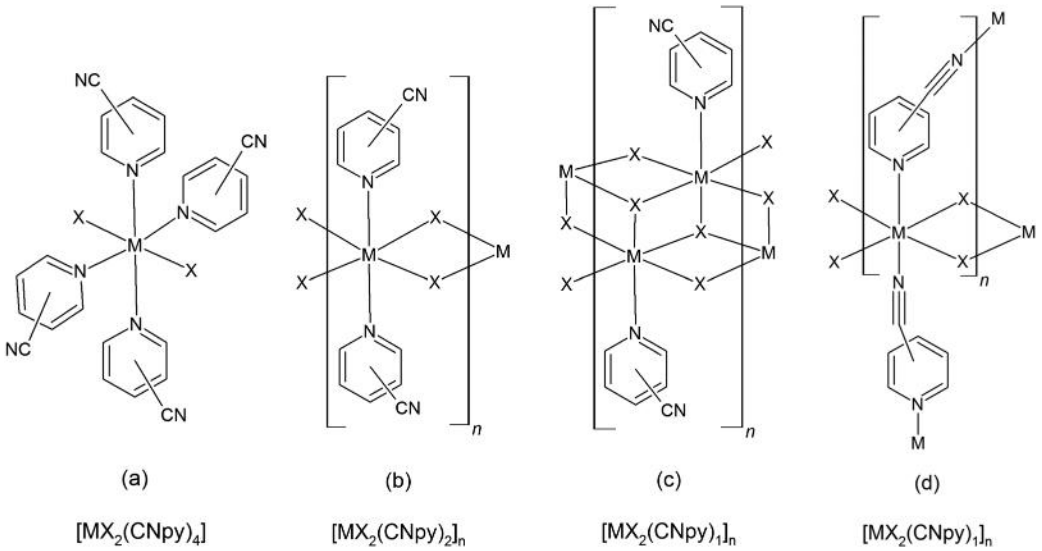

Scheme 1 Connectivity patterns of cyanopyridine compounds $[MX_2(CNpy)_x]_n$ with M = Mn, Fe, Co, Ni, Cu; X = Cl, Br. (a) $x = 4$; (b) $x = 2$; (c) $x = 1$, double chains; (d) $x = 1$, bridging ligand.

of $[M^{II}Br_2(3\text{-}CNpy)_4]$ led to compounds with the metal–ligand ratios of 1:2 ($[M^{II}Br_2(3\text{-}CNpy)_2]_n$, **1b–4b**) and further of 1:1 ($[M^{II}Br_2(3\text{-}CNpy)_1]_n$, **1c–4c**). Generally, compounds obtained by thermal decomposition tend to be micro- or nanocrystalline powders. Indeed, this was the case for the 1:2 as well as the 1:1 compounds. The compounds $[M^{II}Br_2(3\text{-}CNpy)_2]_n$ (**1b–4b**) and $[M^{II}Br_2(3\text{-}CNpy)_1]_n$ (**1c–4c**) are sensitive to moisture and air and easily react with water and polar solvents. In non-polar solvents they are insoluble. Correspondingly, recrystallization was not possible. Sublimation did not work, either. Hence the crystal structures of **1b–4b** and **1c–4c** were determined by X-ray powder diffraction (XRPD). Likewise, the structures of **1a–4a** were determined from powder data. IR spectroscopy[32–34] was used to determine the bridging character of the cyano group.

2. Results and discussion

2.1 Synthesis from solution and by thermal decomposition

Well crystalline material of the composition $[M^{II}Br_2(3\text{-}CNpy)_4]$ (M = Mn, Fe, Co, Ni) (**1a–4a**) was yielded by mixing $M^{II}Br_2$ with 3-cyanopyridine in a solvent (*e.g.* methanol, ethanol or diacetone alcohol). Changing the ratio between $M^{II}Br_2$ and 3-cyanopyridine did not lead to further crystalline compounds, *e.g.* a ratio of 1:2 did not lead to the formation of $[M^{II}Br_2(3\text{-}CNpy)_2]_n$. To check if the discrete complexes can be transformed into compounds of the composition $[M^{II}Br_2(3\text{-}CNpy)_{x<4}]_n$, thermogravimetric analysis (TG) combined with differential thermoanalysis (DTA) was performed.

The TG curve of $[MnBr_2(3\text{-}CNpy)_4]$ (**1a**) shows three steps of mass loss (Fig. 1 and Table S1 in the ESI†). These steps correspond to the endothermic signals in the DTA curve. The first endothermic signal at 157 °C is assigned to the liberation of two of the four 3-cyanopyridine ligands to form $[MnBr_2(3\text{-}CNpy)_2]_n$ (**1b**), according to eqn (1). The second endothermic signal at 244 °C is attributed to the decomposition of this intermediate compound to form $[MnBr_2(3\text{-}CNpy)_1]_n$ (**1c**), according to eqn (2). The remaining 3-cyanopyridine moiety is released in the third decomposition step at 306 °C, leaving $MnBr_2$, according to eqn (3).

$$n[MnBr_2(3\text{-}CNpy)_4] \rightarrow [MnBr_2(3\text{-}CNpy)_2]_n + 2n\ 3\text{-}CNpy \quad (1)$$

$$[MnBr_2(3\text{-}CNpy)_2]_n \rightarrow [MnBr_2(3\text{-}CNpy)_1]_n + n\ 3\text{-}CNpy \quad (2)$$

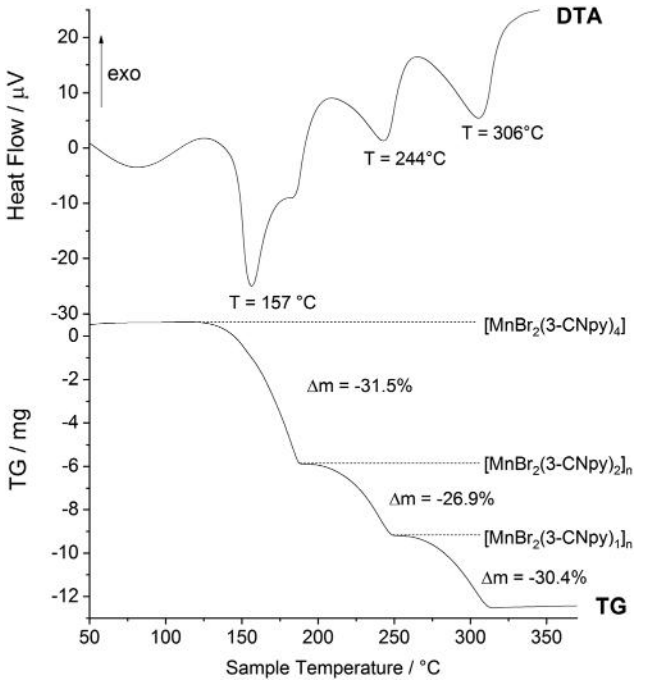

Fig. 1 DTA/TG curves of $[MnBr_2(3\text{-}CNpy)_4]$ (**1a**), showing the decomposition of **1a** *via* **1b** and **1c** to $MnBr_2$.

Table 1 Characteristic asymmetric stretching vibrations ν_{as}(C≡N) for 3-cyanopyridine, 4-cyanopyridine and their coordination polymers

Compound	ν_{as}(C≡N) [cm^{-1}]	Interaction
3-Cyanopyridine and its compounds		
3-Cyanopyridine	2230–2232	Free ligand
Compounds with a metal–ligand ratio of 1 : 4		
$[MnBr_2(3\text{-}CNpy)_4]$ (**1a**)	2241	Terminal ligand
$[FeBr_2(3\text{-}CNpy)_4]$ (**2a**)	2241	
$[CoBr_2(3\text{-}CNpy)_4]$ (**3a**)	2241	
$[NiBr_2(3\text{-}CNpy)_4]$ (**4a**)	2243	
Compounds with a metal–ligand ratio of 1 : 2		
$[MnBr_2(3\text{-}CNpy)_2]_n$ (**1b**)	2239	Terminal ligand
$[FeBr_2(3\text{-}CNpy)_2]_n$ (**2b**)	2239	
$[CoBr_2(3\text{-}CNpy)_2]_n$ (**3b**)	2236	
$[NiBr_2(3\text{-}CNpy)_2]_n$ (**4b**)	2236	
Compounds with a metal–ligand ratio of 1 : 1		
$[MnBr_2(3\text{-}CNpy)_1]_n$ (**1c**)	2275	Bridging ligand
$[FeBr_2(3\text{-}CNpy)_1]_n$ (**2c**)	2278	
$[CoBr_2(3\text{-}CNpy)_1]_n$ (**3c**)	2288	
$[NiBr_2(3\text{-}CNpy)_1]_n$ (**4c**)	2288	
4-Cyanopyridine and its compounds [23]		
4-Cyanopyridine	2238–2240	Free ligand
$[M^{II}X_2(4\text{-}CNpy)_x]_n$	2235–2242	Terminal ligand
$[M^{II}X_2(4\text{-}CNpy)_x]_n$	2275–2298	Bridging ligand

$$[MnBr_2(3\text{-}CNpy)_1]_n \rightarrow MnBr_2 + n\ 3\text{-}CNpy \quad (3)$$

For the corresponding iron compounds (**2a–2c**) the decomposition temperatures are 241 °C, 339 °C and 374 °C; for the cobalt compounds (**3a–3c**) 166 °C, 230 °C and 314 °C; and for the nickel compounds (**4a–4c**) 218 °C, 254 °C and 317 °C (see Fig. S1–S3 and Table S1 in the ESI†).

Compounds $[M^{II}Br_2(3\text{-}CNpy)_2]_n$ (**1b–4b**) and $[M^{II}Br_2(3\text{-}CNpy)_1]_n$ (**1c–4c**) were then prepared by thermal decomposition of the corresponding precursors $[M^{II}Br_2(3\text{-}CNpy)_4]$ at appropriate temperatures, either on the X-ray diffractometer or in the TG device. Details are given in the Experimental section and the ESI.†

2.2 Investigation of the coordination of the cyano group by FT-IR

In aromatic cyano compounds, IR spectroscopy can be used to determine whether the cyano group of an aromatic compound coordinates to a metal atom. If the frequency of the asymmetric stretching vibration ν_{as}(C≡N) is considerably higher than in the free ligand, the cyano group is likely to be coordinated to a metal atom, while a value similar to that of the free ligand indicates that the cyano group of the aromatic compound remained unchanged, *i.e.* it does not coordinate to a metal.[32–34]

In **1a–4a** and **1b–4b**, the ν_{as}(C≡N) frequency is similar to that of the non coordinated 3-cyanopyridine (Table 1). In contrast, in **1c–4c** the asymmetric stretching vibration ν_{as}(C≡N) is shifted to higher values. This indicates that 3-cyanopyridine forms a bridge between the metal atoms in **1c–4c**, while in all of the other compounds 3-cyanopyridine coordinates with its pyridine nitrogen atom (N_{py}) only.

2.3 Crystal structures of $[M^{II}Br_2(3\text{-}CNpy)_4]$ (1a–4a)

The crystal structures were determined from XRPD data. Details on the measurements are given in Table S2 (ESI†), Rietveld plots of structures **1a–4a** are shown in Fig. S17–S20 (ESI†).

In all the crystal structures of the type $[M^{II}Br_2(3\text{-}CNpy)_x]$ the metal ions are octahedrally coordinated by bromine atoms and by nitrogen atoms of the 3-cyanopyridine ligands. The compounds $[M^{II}Br_2(3\text{-}CNpy)_4]$ (**1a–4a**) consist of discrete complexes, in which the metal atoms are surrounded by two bromine atoms and four 3-cyanopyridine molecules, which coordinate with their N_{py} atoms (Fig. 2).

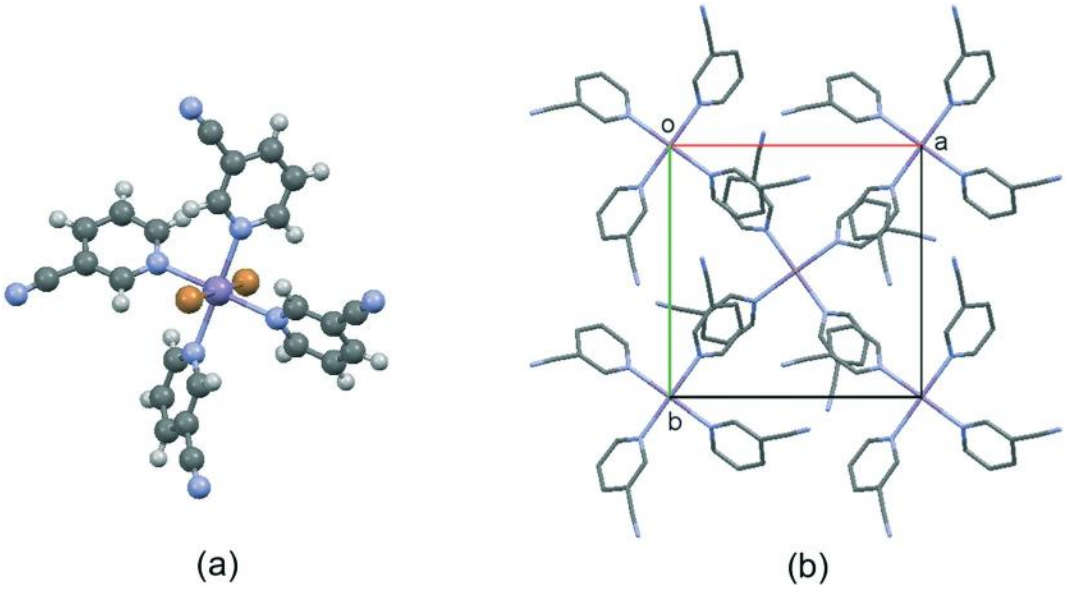

Fig. 2 (a) Molecular structure of $[MnBr_2(3\text{-}CNpy)_4]$ (**1a**). (b) Molecular packing in $[MnBr_2(3\text{-}CNpy)_4]$ (**1a**), H-atoms omitted for clarity. The compounds **2a–4a** are isostructural to **1a**. Color code: Mn violet, Br orange, N blue, C grey, H white.

Table 2 Crystallographic data of $[M^{II}Br_2(3\text{-CNpy})_4]$. All measurements were performed at room temperature

	1a	2a	3a	4a
Compound	$[MnBr_2(3\text{-CNpy})_4]$	$[FeBr_2(3\text{-CNpy})_4]$	$[CoBr_2(3\text{-CNpy})_4]$	$[NiBr_2(3\text{-CNpy})_4]$
CSD number	1845140	1845149	1845152	1845162
Formula	$C_{24}H_{16}Br_2MnN_8$	$C_{24}H_{16}Br_2FeN_8$	$C_{24}H_{16}Br_2CoN_8$	$C_{24}H_{16}Br_2NiN_8$
Crystal system	Tetragonal	Tetragonal	Tetragonal	Tetragonal
Space group (no.)	*P4nc* (104)	*P4nc* (104)	*P4nc* (104)	*P4nc* (104)
a/Å	11.2178(5)	11.1484(2)	11.0587(4)	10.9722(9)
c/Å	10.3309(6)	10.3205(2)	10.4149(5)	10.4600(3)
V/Å^3	1300.0(3)	1282.7(1)	1273.7(1)	1259.3(2)
Z, *Z*′	2, 1/4	2, 1/4	2, 1/4	2, 1/4
Site symmetry of M^{II}	4	4	4	4

The compounds **1a–4a** are isostructural and crystallise in the space group *P4nc*. Crystallographic data are given in Table 2. The complexes possess a fourfold crystallographic symmetry axis with the metal atom and the two bromine atoms positioned on the fourfold axis. Thus all M^{II}–N_{py} bond distances within the molecule are equal. In the series Mn–Fe–Co–Ni the M^{II}–N_{py} distances decrease by about 0.05 Å from one metal to the next metal, due to the shrinking atomic volume of the metal atoms (Table 3). In the Fe compound (**2a**) the Fe^{II}–Br(1) and Fe^{II}–Br(2) distances are equal. Also in the Mn compound (**1a**), the distances are not significantly different. In contrast, in the Co and Ni compounds (**3a** and **4a**) the M^{II}–Br(1) bond is appreciably longer than the M^{II}–Br(2) bond which points to a Jahn–Teller distortion.

The 3-cyanopyridine ligands are arranged in a propeller-like fashion around the metal atoms (see Fig. 2a). In **1a–4a** the plane of the pyridine ring is twisted by about 46° to the $[MN_4]$ plane. This propeller-like geometry is caused by the steric repulsion between the four pyridine groups. The packing of the molecules is shown in Fig. 2b.

Table 3 Selected bond distances between metal atoms and bromine atoms for $[M^{II}Br_2(3\text{-CNpy})_4]$. The given standard deviations are those resulting from the Rietveld refinements. The actual accuracy is much lower

	1a	2a	3a	4a
M^{II}	Mn	Fe	Co	Ni
M^{II}–Br(1)/Å	2.674(16)	2.615(9)	2.663(7)	2.653(5)
M^{II}–Br(2)/Å	2.656(16)	2.612(9)	2.579(7)	2.579(5)
M^{II}–N_{py}/Å	4 × 2.275(2)	4 × 2.212(3)	4 × 2.158(3)	4 × 2.131(2)

2.4 Crystal structures of $[M^{II}Br_2(3\text{-CNpy})_2]_n$ (1b–4b)

The crystal structures were determined from XRPD data. Details on the measurements are given in Table S3 (ESI†), Rietveld plots of structures **1b–4b** are shown in Fig. S21–S25 (ESI†).

In compounds **1b–4b** the metal atoms are coordinated by four bromine atoms and two N_{py} atoms forming a $M^{II}Br_4(N_{py})_2$ octahedron. These $M^{II}Br_4(N_{py})_2$ octahedra are connected by edges with two neighbouring octahedra, resulting in an infinite chain (Fig. 3a). In atomic view, the metal atoms are interconnected *via* two bridging μ_2-Br atoms each, resulting in a $[M^{II}Br_2]_n$ chain. The $[M^{II}Br_2(3\text{-CNpy})_2]_n$ chains are stacked parallel. In structures **1b**, **2b** and **α-3b**, the chains are running along the *c*-axis, and in **β-3b**, **α-4b** and **β-4b** along the *a*-axis (Fig. 6). In all structures of **1b–4b**, these chains are arranged in a herringbone packing motif and linked by weak intermolecular C–H···N contacts into a three-dimensional network (Fig. 3b). The metal–metal distances range from 3.70 Å (**α-4b**) to 3.82 Å (**1b**) which correspond to the short lattice parameter (Table 4).

In contrast, the iso-stoichiometric compounds $[M^{II}Br_2(3\text{-CNpy})_2]$ with d^9 and d^{10} metal atoms (Cu, Zn, Hg) do not

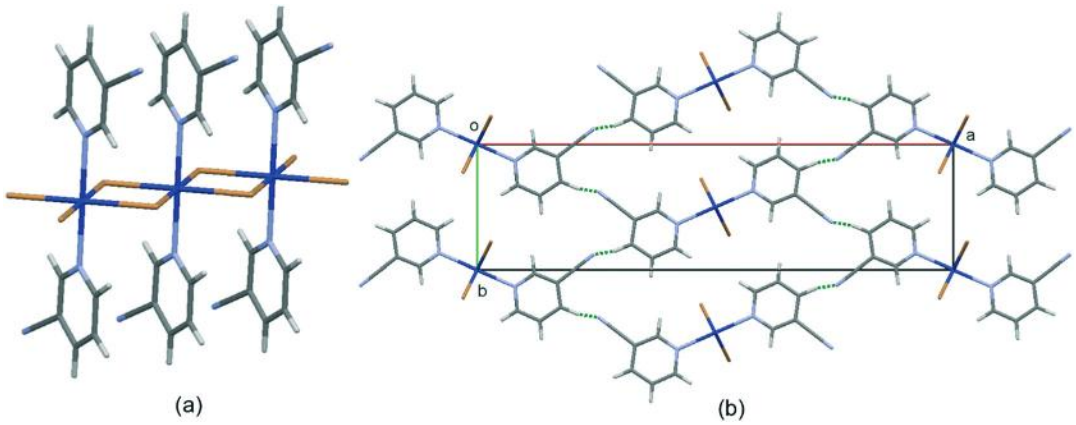

Fig. 3 Crystal structure of $[CoBr_2(3\text{-CNpy})_2]_n$ (**α-3b**). (a) One $[CoBr_2]_n$ chain with lateral 3-cyanopyridine ligands. (b) View along the *c*-axis. Intermolecular C–H···N contacts are shown as dotted green lines. Color code: Co violet, Br orange, N blue, C grey, H white.

Table 4 Crystallographic data of $[M^{II}Br_2(3\text{-CNpy})_2]_n$. Measurements of **1b**, **2b**, **α-3b**, **β-3b** and **β-4b** were performed at room temperature; the measurement **α-4b** was performed at −150 °C

	1b	**2b**	**α-3b**	**β-3b**	**α-4b**	**β-4b**
Compound	$[MnBr_2(3\text{-CNpy})_2]_n$	$[FeBr_2(3\text{-CNpy})_2]_n$	$[CoBr_2(3\text{-CNpy})_2]_n$	$[CoBr_2(3\text{-CNpy})_2]_n$	$[NiBr_2(3\text{-CNpy})_2]_n$	$[NiBr_2(3\text{-CNpy})_2]_n$
CSD number	1845141	1845150	1845157	1845160	1845163	1845164
Formula	$C_{12}H_8Br_2MnN_4$	$C_{12}H_8Br_2FeN_4$	$C_{12}H_8Br_2CoN_4$	$C_{12}H_8Br_2CoN_4$	$C_{12}H_8Br_2NiN_4$	$C_{12}H_8Br_2NiN_4$
Crystal system	Orthorhombic	Orthorhombic	Orthorhombic	Triclinic	Monoclinic	Triclinic
Space group (no.)	*Pnnm* (58)	*Pnnm* (58)	*Pnnm* (58)	$P\bar{1}$ (2)	*Cc* (9)	$P\bar{1}$ (2)
a/Å	27.304(6)	27.128(5)	27.019(1)	3.727(5)	3.709(1)	3.727(4)
b/Å	7.221(9)	7.172(2)	7.124(2)	13.629(6)	26.801(4)	13.574(9)
c/Å	3.829(7)	3.788(1)	3.759(7)	13.868(6)	13.706(8)	13.761(6)
α/°	90	90	90	87.37(7)	90	86.86(2)
β/°	90	90	90	82.34(4)	97.67(8)	82.40(1)
γ/°	90	90	90	82.40(5)	90	82.12(1)
V/Å^3	755.1(8)	737.0(2)	723.7(1)	697.2(2)	1350.5(8)	683.1(5)
Z, *Z*′	2, 1/4	2, 1/4	2, 1/4	2, **1**	4, 1	2, 1
Site symmetry of M^{II}	2/*m*	2/*m*	2/*m*	$\bar{1}$, $\bar{1}$	1	$\bar{1}$, $\bar{1}$

contain polymeric $[M^{II}Br_2]_n$ chains, but are built up by discrete complexes.[24,26,27] In the Zn and Hg compounds, the metal atom is tetrahedrally coordinated by two Br atoms and two 3-cyanopyridine ligands (Fig. 4). In $[CuBr_2(3\text{-CNpy})_2]$ the coordination geometry of the Cu is square-planar and the Cu atom in one molecule is stabilized by a weak intermolecular (py)-C–N⋯ contact of one 3-cyanopyridine ligand of the neighbouring molecule.

Compounds **1b**, **2b** and **α-3b** are isostructural and crystallise in the orthorhombic space group *Pnnm* with 2 formula units in the unit cell. The asymmetric unit consists of one metal atom on a 2/*m* site, one cyanopyridine ligand on a site with *m* symmetry (on the same mirror plane as the metal atom) and a bromine atom on a *m* site (neighbouring mirror plane), see Fig. 5a. Structure **α-4b** is not isotypic to these polymers and crystallises in the monoclinic space group *Cc* with *Z* = 4. The asymmetric unit consists of one metal-atom, two bromines atoms and two 3-cyanopyridine rings, all on general position (Fig. 5b). Structures **β-3b**, **α-4b** and **β-4b** are similar to the orthorhombic structures, differences are especially visible in the stacking orientations between of the 3-cyanopyridine ligands. In the orthorhombic structures (**1b**, **2b**, **α-3b**) the pyridine rings are located on mirror planes, so that the pyridine ligand of one metal atom completely eclipses with the ligand of its neighbouring metal atom, resulting in a "perfect" π–π-stacking (Fig. 5a). For **α-4b** the angle *β* inclines from 90° to 97.67°, the lattice type changes to monoclinic centred and the pyridine rings are no longer stacked face-to-face, but are arranged as slightly curved "wings" around the Ni atoms (Fig. 5b).

Structures **β-3b** and **β-4b** are very similar to **α-4b**, the main difference is visible in the mutual arrangement of neighbouring $[M^{II}Br_2(3\text{-CNpy})_2]_n$-chains along the *b*-axis (Fig. 6). In **β-4b** neighbouring $[NiBr_2(3\text{-CNpy})_2]$-chains are shifted by about a/5 each (Fig. 6b). In contrast, in **α-4b**, neighbouring $[NiBr_2(3\text{-CNpy})_2]$-chains are alternatingly shifted by 0 or a/2,

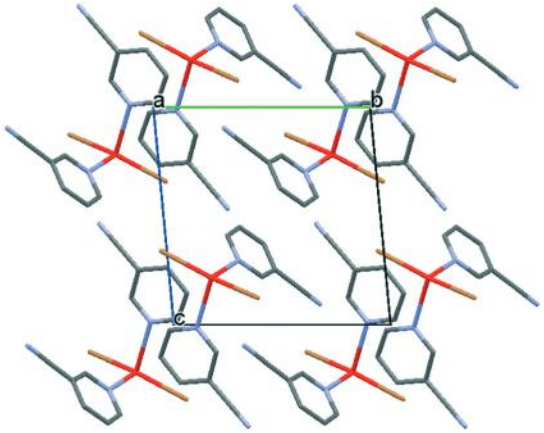

Fig. 4 Crystal structure of $[HgBr_2(3\text{-CNpy})_2]$ with discrete molecules.[27] Color code: Hg red, Br orange, N blue, C grey, H-atoms omitted for clarity.

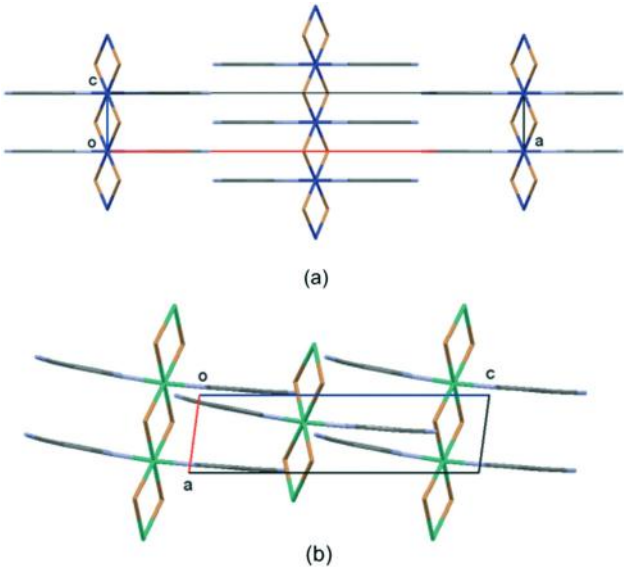

Fig. 5 Crystal structures of **α-3b** (a). Fragment of the crystal structure of (region $0 < y < \frac{1}{4}$). Views along the *b*-axis. Color code: Co violet, Ni green, Br orange, N blue, C grey, H-atoms omitted for clarity.

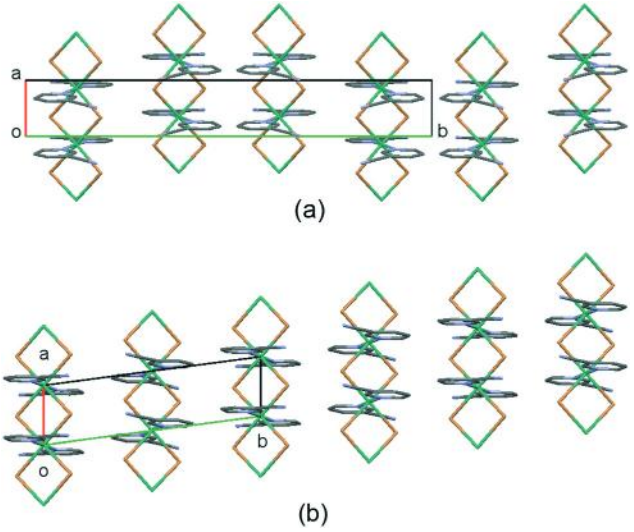

Fig. 6 Crystal structures of α-**4b** (a) and **β-4b** (b). View along the *c*-axis. Color code: Ni green, Br orange, N blue, C grey. H-Atoms omitted for clarity.

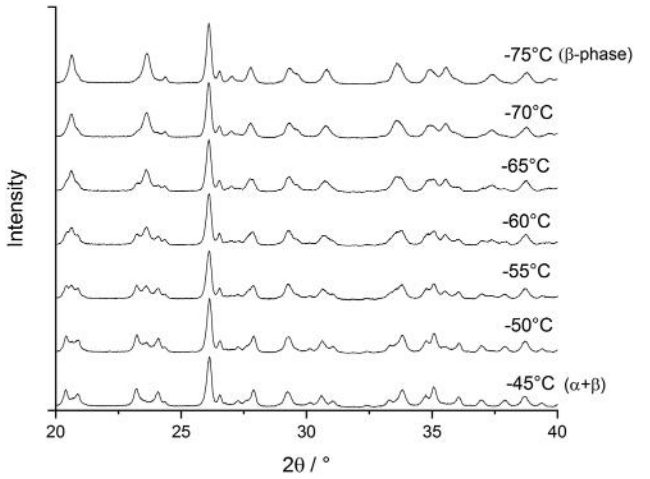

Fig. 7 Low-temperature XRPD series of $[NiBr_2(3\text{-}CNpy)_2]_n$ (**4b**): enlargement of the 2θ range 20–40°. One entire cooling–heating cycle showing the reversibility of the phase transition is shown in Fig. S30 in the ESI.†

resulting in an ABBAABBA… pattern (Fig. 6a). Within the experimental uncertainties the metal-Br distances point to a declination from the Mn- to the Ni-compound (Table 5).

Polymorphism of $[NiBr_2(3\text{-}CNpy)_2]_n$ (4b) and $[CoBr_2(3\text{-}CNpy)_2]_n$ (3b). Initially, none of the powder diagrams of the samples of $[NiBr_2(3\text{-}CNpy)_2]_n$ (**4b**) could be indexed, although the powders were well crystalline and the patterns contained a high number of sharp reflections. This observation pointed to the possibility that the samples might contain a mixture of phases. In the corresponding series of 4-cyanopyridine compounds, $[M^{II}X_2(4\text{-}CNpy)_2]_n$, a temperature-dependent polymorphism was observed in several cases.[23] Therefore, temperature-dependent X-ray powder diffraction (T-XRPD) of **4b** was performed. Between the temperature of the synthesis (190 °C) and room temperature, no phase changes took place (Fig. S32 in the ESI†). On further cooling, at −50 °C the reflection intensities started to change, indicating a phase transition (Fig. 7). At −75 °C this phase transition was completed, and no further changes occurred down to −150 °C. The low temperature phase was denominated as α-phase, the high temperature phase as β-phase. The phase transition is reversible: heating the low-temperature phase back to room temperature again lead to a mixture of α- and β-phases (Fig. S30 in the ESI†). In differential scanning calorimetry (DSC) cycles between room temperature and −150 °C, no signals for a phase transition were detectable (Fig. S4 in the ESI†). Obviously, both polymorphs have similar energies. The temperature-dependent behavior of $[NiBr_2(3\text{-}CNpy)_2]_n$ is stunning and further investigations should be made to clarify the reason for this behavior.

The structure of the α-phase (**α-4b**) could be solved from XRPD data collected at −150 °C. A pure β-phase could not be obtained, neither by synthesis, nor by heating the sample up to its decomposition point. Hence the crystal structure of **β-4b** had to be determined from a phase mixture containing around 18.5% of the α- and 81.5% of the β-phase, measured at room temperature (Fig. S24 in the ESI†).

The corresponding Co compound (**3b**) shows polymorphism, too: synthesis by thermal decomposition of $[CoBr_2(3\text{-}CNpy)_4]$ (**3a**) in a capillary, placed in the heating device of the X-ray diffractometer, generally led to a mixture of two polymorphs, **α-3b** and **β-3b**. A pure β-phase of **3b** was obtained only once. Upon cooling a phase mixture or the pure β-phase

Table 5 Selected bond distances between metal atoms and donor atoms in compounds $[M^{II}Br_2(3\text{-}CNpy)_2]_n$. **β-3b** and **β-4b** contain two symmetrically independent M^{II} atoms. The given standard deviations are those resulting from the Rietveld refinements. The actual accuracy is much lower

	1b	**2b**	**α-3b**	**β-3b**	**α-4b**	**β-4b**
M^{II}–M^{II}/Å	3.829(7)	3.788(14)	3.759(7)	3.757(4)	3.709(7)	3.727(29)
M^{II}–Br(1)/Å	2.689(7)	2.648(21)	2.593(22)	2.597(22)	2.668(5)	2.632(7)
				2.572(21)		2.628(3)
M^{II}–Br(2)/Å	2.689(7)	2.648(21)	2.593(22)	2.597(22)	2.569(09)	2.632(7)
				2.572(21)		2.628(3)
M^{II}–Br(3)/Å	2.689(7)	2.648(21)	2.593(22)	2.611(24)	2.525(8)	2.540(9)
				2.602(21)		2.570(6)
M^{II}–Br(4)/Å	2.689(7)	2.648(21)	2.593(22)	2.611(24)	2.536(4)	2.540(9)
				2.602(21)		2.570(6)
M^{II}–N_{py}/Å	2.280(3)	2.199(8)	2.337(13)	1.908(17)	2.090(15)	2.195(8)
				2.103(17)	2.177(14)	2.197(25)

to −100 °C, or upon heating to its decomposition point, no phase changes were observed (Fig. S33 in the ESI†). The only sample of the pure β-phase had a limited crystallinity, and the powder pattern was considerably worse than the patterns of the phase mixture. Therefore, we used the pattern of the phase mixture to determine the crystal structure of the β-phase, as well as of the α-phase which was never obtained as pure phase.

2.5 Crystal structures of $[M^{II}Br_2(3\text{-CNpy})_1]_n$ (1c–4c)

The crystal structures were determined from XRPD data. Details on the measurements are given in Table S4 (ESI†), Rietveld plots of structures **1b–4b** are shown in Fig. S26–S29 (ESI†).

The four crystal structures of $[M^{II}Br_2(3\text{-CNpy})_1]_n$ determined here are the first crystal structures, in which the 3-cyanopyridine acts as a linker between two 3d M^{II} transition metal atoms. The 3-cyanopyridine moiety coordinates not only with the nitrogen atom of the pyridine ring (N_{py}), but also with its cyano nitrogen atom (N_{CN}), as it was confirmed by IR data. Each metal atom is thus coordinated by four bromine atoms, one N_{py} atom and one N_{CN} atom. The M–Br and M–N_{CN} distances decrease from Mn to Ni, whereas the M–N_{py} distances remain similar (Table 7).

Structures **2c–4c** are isostructural, and the structure of **1c** is similar as well. The metal atoms are connected through two μ_2-Br atoms into $[M^{II}Br_2]_n$ chains, which are stacked run parallel to [100]. These chains are further connected by the 3-CNpy ligands, resulting in zigzag-shaped layers, which are orientated parallel to (010) (Fig. 8a and b). The distance between the layers corresponds to the lattice parameter *b* (Table 6).

A similar network has already been found for the corresponding 4-cyanopyridine compounds $[M^{II}X_2(4\text{-CNpy})_1]_n$ with M = Mn, Co, Ni and X = Cl, Br.[2,3] There, all atoms are on mirror planes, which are perpendicular to the $[M^{II}Br_2]_n$ chains (Fig. 8c). This observation is also valid for the phases **2c**, **3c** and **4c**: all atoms are situated on crystallographic mirror planes parallel to the stacking direction, *i.e.* parallel to (100). The zig-zag shape of the layers permits additional symmetry elements within the layer, namely a 2_1 screw axis along [001] and a *c*-glide plane parallel to (010), perpendicular to the mirror plane (Fig. 8a–c). Correspondingly the individual layers have $Pmc2_1$ symmetry (which is a non-standard setting of $Pm2_1b$, no. 28[46]). Upon stacking of the layers in the crystal, the full layer symmetry is maintained, resulting in space group $Pmc2_1$.

The manganese compound **1c** shows an identical topology, but the structure is only pseudo-orthorhombic, with a monoclinic angle of $\gamma = 93.41(1)°$. The atoms are no longer located on mirror planes and the coordination octahedra of

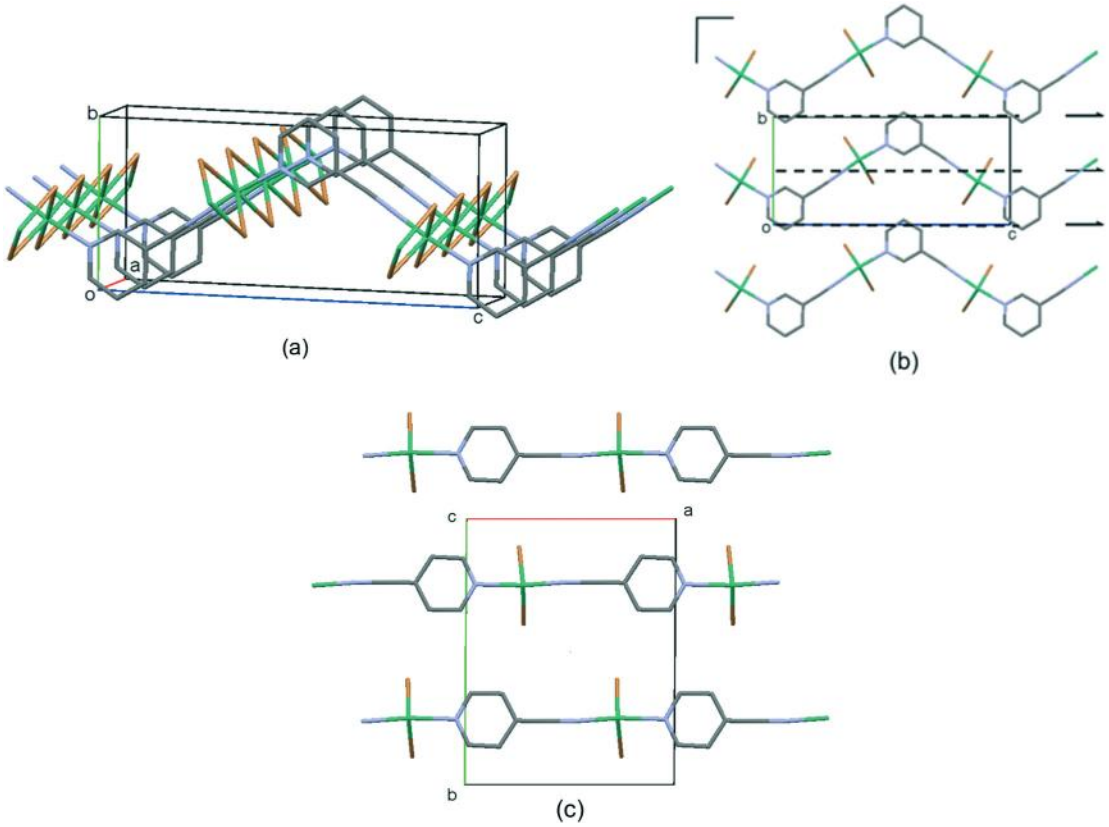

Fig. 8 (a) Fragment of the crystal structure of **4c**: perspective view of a single layer. The $[M^{II}Br_2]_n$ chains are connected by the 3-cyanopyridine ligands. (b) Crystal structure of **4c**: view along the $[M^{II}Br_2]_n$ chains, view direction $[\bar{1}00]$. The symmetry elements are shown as well (space group $Pmc2_1$). (c) Crystal structure of the corresponding 4-cyanopyridine compound $[NiBr_2(4\text{-CNpy})_1]_n$ (space group $P112/m$[23]), view direction $[00\bar{1}]$. Color code: Ni green, Br orange, N blue, C grey, H-atoms omitted for clarity.

Table 6 Crystallographic data of $[M^{II}Br_2(3\text{-CNpy})_1]_n$. All measurements were performed at room temperature

	1c	2c	3c	4c
Compound	$[MnBr_2(3\text{-CNpy})_1]_n$	$[FeBr_2(3\text{-CNpy})_1]_n$	$[CoBr_2(3\text{-CNpy})_1]_n$	$[NiBr_2(3\text{-CNpy})_1]_n$
CSD number	1845142	1845151	1845161	1845165
Formula	$C_6H_4Br_2MnN_2$	$C_6H_4Br_2FeN_2$	$C_6H_4Br_2CoN_2$	$C_6H_4Br_2NiN_2$
Crystal system	Monoclinic	Orthorhombic	Orthorhombic	Orthorhombic
Space group (no.)	$P112_1$[a] (4)	$Pmc2_1$ (26)	$Pmc2_1$ (26)	$Pmc2_1$ (26)
a/Å	3.834(7)	3.772(2)	3.740(1)	3.701(5)
b/Å	7.258(1)	7.251(2)	7.231(2)	7.204(8)
c/Å	16.547(7)	16.31(1)	16.167(6)	16.000(4)
α/°	90	90	90	90
β/°	90	90	90	90
γ/°	93.41(1)	90	90	90
V/Å^3	459.7(5)	446.1(8)	437.2(1)	426.7(1)
Z, Z'	2, 1	2, 1/2	2, 1/2	2, 1/2
Site symmetry of M	1	m	m	m

[a] For ease of comparison of **1c** to **4c** a non-standard space-group setting was used for **1c**. $P112_1$ is a non-standard setting of $P2_1$.

Mn are distorted (Fig. 9). The crystallographic mirror planes as well as the c glide planes vanish, and only the 2_1 screw axis remain, resulting in space group $P112_1$ (non-standard setting of $P2_1$).

In all of the compounds **1c–4c** the cyano groups exhibit a C≡N–M angle deviating from 180°: 174.6° for **4c**, 173.1° for **3c**, 172.9° for **2c** and, the largest deviation, 168.2° for **1c**. This tendency is in good agreement with the C≡N–M angles found in the analogous 4-cyanopyridine compounds,[23] which indicates that the deviation from linearity is not caused by the zigzag shape of the layers. Furthermore, in each of the compounds **2c–4c** all M–Br distances are nearly equal, whereas in **1c** the four Mn–Br distances differ (Table 7), resulting in a considerable distortion of the Mn coordination octahedron. It should be noted, that in the last steps of the Rietveld refinement of all structures all restraints on M–Br and M–N_{py} distances were omitted on purpose.

In the 4-cyanopyridine compound $[NiBr_2(4\text{-CNpy})_1]_n$ we observed a head-to-tail disorder of the 4-cyanopyridine ligands:[23] NC_5H_4–C≡N *vs.* N≡C–C_5H_4N, *i.e.* two different molecular orientations. In principal, a similar disorder for the analogous $[NiBr_2(3\text{-CNpy})_1]_n$ compound with a swapped orientation of one bridging 3-cyanopyridine is spatially possible: the distance between to 3-cyanopyridine rings (equal to the distance between two neighbouring nickel atoms within one chain, *i.e.* the shortest lattice parameter) is almost identical (3.69 Å for $[NiBr_2(4\text{-CNpy})_1]_n$[23] and 3.70 Å for $[NiBr_2(3\text{-CNpy})_1]_n$, Table 6) and the distance between two Ni atoms of neighbouring chains within one layer is comparable as well (8.07 Å for $[NiBr_2(4\text{-CNpy})_1]_n$ and 8.14 Å for $[NiBr_2(4\text{-CNpy})_1]_n$). This type of disorder would cause diffuse scattering and the corresponding reflections should show a Warren type peak shape, *i.e.* peaks with tails towards higher diffraction angle. The XRPD pattern of **4c** does not show such peak shapes (at least it is not pronounced) and there is no indication for disorder.

Table 7 Selected bond distances between metal atoms and bridging atoms in $[M^{II}Br_2(3\text{-CNpy})_1]_n$

	1c	2c	3c	4c
M^{II}	Mn	Fe	Co	Ni
M^{II}–Br(1)/Å	2.671(16)	2.649(6)	2.609(15)	2.579(8)
M^{II}–Br(2)/Å	2.735(5)	2.649(6)	2.609(15)	2.579(8)
M^{II}–Br(3)/Å	2.605(16)	2.631(6)	2.604(7)	2.564(11)
M^{II}–Br(4)/Å	2.701(3)	2.631(6)	2.604(7)	2.564(11)
M^{II}–N_{CN}/Å	2.330(5)	2.209(10)	2.168(09)	2.110(3)
M^{II}–N_{py}/Å	2.104(11)	2.115(12)	2.084(11)	2.034(7)

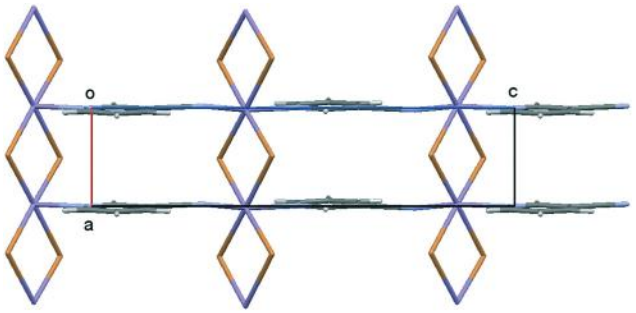

Fig. 9 Crystal structure of **1c**, view direction [0$\bar{1}$0]. Color code: Mn violet, Br orange, N blue, C grey, H white.

In case of the analogues 4-cyanopyridine compounds $[CoBr_2(4\text{-CNpy})_1]_n$ and $[MnCl_2(4\text{-CNpy})_1]_n$ thermal decomposition further leads to compounds with a metal–ligand ratio of 1 : 1/3, $[CoBr_2(4\text{-CNpy})_{1/3}]$ and $[MnCl_2(4\text{-CNpy})_{1/3}]_n$.[23] However, the powders were of limited quality, and the crystal structures could not be determined yet. Thermal investigations of the decomposition steps of $[MnBr_2(3\text{-CNpy})_4]$ (**1a**), as well as $[NiBr_2(3\text{-CNpy})_4]$ (**4a**), didn't reveal phases with a metal–ligand ratio of 1 : 1/3 or 1 : 1/2. The corresponding 1 : 1 compounds, $[MnBr_2(3\text{-CNpy})_1]_n$ (**1c**) and $[NiBr_2(3\text{-CNpy})_1]_n$ (**4c**), decompose directly into $M^{II}Br_2$.

For the 3-cyanopyridine compounds, the DTA and TG curves of $[FeBr_2(3\text{-CNpy})_4]$ (**2a**) and $[CoBr_2(3\text{-CNpy})_4]$ (**3a**) showed shoulders at about 340–350 °C, which indicate the formation of a decomposition product of $[M^{II}Br_2(3\text{-CNpy})_x]_n$ with $x < 1$ (Fig. S1 and S2 in the ESI†). A second hint for the existence of such products is the presence of a few weak

Table 8 Preparation type (Diffractometer or DTA) and heating temperatures for decomposition compounds **1b–4b** and **1c–4c**

Compound	**1b**	**1c**	**2b**	**2c**	**α-3b/β-3b**	**3c**	**α-4b/β-4b**	**4c**
Procedure	Diff.	Diff.	DTA	Diff.	Diff.	Diff.	Diff.	DTA
Heating temperature/°C	160	190	180	220	160	190	190	240
Heating time	1 h	11 h	10 min	1 h	2 h	2 h	12 h	10 min

peaks of an unidentified compound in the powder patterns of $[FeBr_2(3\text{-}CNpy)_1]_n$ (**2c**) and $[CoBr_2(3\text{-}CNpy)_1]_n$ (**3c**) (Fig. S27 and S28 in the ESI†). However, we were not able to isolate these products, or (at least) to obtain samples with a higher amount of these decomposition products.

3. Experimental section

3.1 Materials

$FeBr_2$, $CoBr_2$, $NiBr_2$, methanol and 3-cyanopyridine were purchased from Alfa Aesar. $MnBr_2$ and ethanol were purchased from Sigma Aldrich. Diacetonealcohole (DAA = 4-hydroxy-4-methylpentan-2-one) was obtained from B. Kraft. All chemicals were used without further purification.

3.2 Synthesis

Synthesis of $[M^{II}Br_2(3\text{-}CNpy)_4]$. The compounds $[MX_2(3\text{-}CNpy)_4]$ (**1a–4a**) were prepared by stirring the metal salts and 3-cyanopyridine in the respective solvents at room temperature overnight. The obtained powders were isolated by filtration, washed 3 times with 5 mL ethanol and dried in air.

Preparation of $[M^{II}Br_2(3\text{-}CNpy)_2]_n$ and $[M^{II}Br_2(3\text{-}CNpy)_1]_n$. Compounds **1b–4b** and **1c–4c** were prepared by thermal decomposition at the corresponding temperatures. Two different procedures were used:

(A) For compounds **1b**, **1c**, **2c**, **α-3b**, **β-3b**, **3c**, **α-4b** and **β-4b** the thermal decomposition was performed on the diffractometer (Diff.). The starting material (**1a–4a**, resp.) was filled in a glass capillary (diameter: 0.7 mm or 0.5 mm). The capillary was mounted on a STOE Stadi-P diffractometer equipped with an Oxford Cryosystems device, which uses nitrogen as heating or cooling agent. The open capillary was heated to 160–220 °C (Table 8). Subsequently the capillary was cooled to room temperature under a constant nitrogen flow.

(B) Compounds **2b** and **4c** were prepared by thermal decomposition of the starting material (**2a** and **4a** resp.) in a thermogravimetric device (DTA). Around 30 mg of **2a** or **4a**, respectively were placed in an Al_2O_3 crucible and heated for 10 minutes at the appropriate temperature under argon atmosphere. After cooling the powders were immediately transferred into a glass capillary that was sealed afterwards.

All products were characterized by DTA/TG, IR and X-ray powder diffraction. Details on all syntheses are given in the ESI.†

3.3 Spectroscopy

FT-IR spectra were recorded with a SHIMADZUIRaffinity 1S Fourier transform infrared reflection–absorption spectrometer.

3.4 Differential thermal analysis and thermogravimetry (DTA/TG)

Differential thermal and thermogravimetric analysis (DTA/TG) were performed on a SETARAM (TGA 92) device. The samples were placed in Al_2O_3 crucibles and measured under argon atmosphere with a heating rate of 5 K min^{-1} and a constant flow rate of about 75 mL min^{-1}. The compounds **1a–4a** were heated from 293 K to 713 K (for details see Fig. S1–S3 in the ESI†).

3.5 X-ray powder diffraction (XRPD)

All specimens were measured in borosilicate glass capillaries of Hilgenberg (diameter 0.5 or 0.7 mm). For the crystal structure determination from X-ray powder diffraction data, the XRPD experiments were performed on a STOE Stadi-P diffractometer equipped with a Ge (111) monochromator and a linear position-sensitive detector (PSD, Kr/CH_4) using Cu-Kα_1 radiation (λ = 1.54056 Å). Temperature-dependent XRPD measurements were performed on an identical Stoe STADI-P diffractometer which was equipped with an Oxford Cryostream 800. The data were collected with WinXPOW software 3.4.[35]

3.6 Structure determinations from XRPD data

The powder patterns of **1a–1c**, **2a**, **2c**, **3a–3c**, and **4a** were indexed with DICVOL91[36] within the DASH package[39] using the first 20 reliable peaks. The powder patterns of the other compounds were indexed by CONOGRAPH[37,38] using the first 25 peaks. Indexing results were checked with regard to expected cell volumes using Hofmann's volume increments.[42] Space group determination was carried out in DASH or CONOGRAPH. The structures (except **2c**, **3c** and **β-3b**) were solved with the simulated annealing algorithm in DASH, using a starting structure model in direct space. The starting model was built up of one metal atom, one (or two) bromine atoms and one (or two) 3-cyanopyridine ligands using AVOGADRO.[43] Structure solution was then performed with respect to the space group and site symmetry. All structures could be solved without further trouble. In case of **2c**, **3c** and **β-3b**, cif-files of the known crystal structures of **4c** and **α-3b** were used as starting point for the Rietveld refinement.[44]

Rietveld refinements were performed with TOPAS.[40,41] At first, a Pawley refinement was carried out to refine background, zero point error, lattice parameters and peak shape parameters, including peak asymmetry. In the subsequent Rietveld refinement the pyridine ring was restrained to be flat; all bond lengths and bond angles were restrained to a statistical mean value from the CSD; all C–C and C–H angles of the pyridine ring were restrained to 120°. At the end of the

refinement, the restraints for the M–Br and M–N_{py} distances and all restraints on angles involving M atoms (Br–M–N, M–N–C *etc.*) were omitted, in order to search for possible Jahn–Teller-distortions of the octahedra. Further details on structure determination from XRPD data are given in the ESI.† Cif-files can be found in the ESI,† too.

4. Conclusion

In the present contribution new coordination compounds, based on $M^{II}Br_2$ and 3-cyanopyridine, were synthesised and structurally characterized. Compounds $[M^{II}Br_2(3\text{-CNpy})]_4$ (**1a–4a**) consist of discrete complexes. The metal atoms are octahedrally coordinated by two bromine atoms and four 3-cyanopyridine ligands. Upon heating, the molecules lose half of the organic ligands and transform into chain compounds of the composition $[M^{II}Br_2(3\text{-CNpy})_2]_n$ (**1b–4b**). In these structures the metal atoms are linked *via* bridging bromine atoms into $[M^{II}Br_2]_n$ single chains, in which the metal atoms coordinate to four bromine atoms and two 3-cyanopyridine ligands. The chains are arranged in a herringbone packing motif. This coordination motif is in contrast to the Cu analogue, $[CuBr_2(3\text{-CNpy})_2]$,[24] that contains discrete complexes. Temperature-dependent XRPD revealed two polymorphic phases for the cobalt and nickel compounds (**α-3b/β-3b**, **α-4b/β-4b**). The structural differences between the polymorphs are small, but lead to different symmetries and different space groups.

Thermal decomposition of $[M^{II}Br_2(3\text{-CNpy})_2]_n$ leads again to the removal of half of the 3-cyanopyridine ligands, resulting in network compounds of the composition $[M^{II}Br_2(3\text{-CNpy})_1]_n$ (**1c–4c**). The metal atoms are linked into $[M^{II}Br_2]_n$ chains. The chains are linked *via* the 3-cyanopyridine ligands into wavy networks. These four compounds are the first known structures with M^{II} atoms, in which 3-cyanopyridine acts as bidentate ligand, coordinating *via* its N_{py} and its N_{CN} atoms. This coordination chemistry confirms the results of 4-cyanopyridine in some of the analogues $[M^{II}X_2(4\text{-CNpy})_1]_n$ compounds. There are hints for the formation of further decomposition products $[M^{II}Br_2(3\text{-CNpy})_x]_n$ with $0 < x < 1$ at high temperatures, at least for Fe and Co. However, the products could not be isolated. Therefore, additional synthetic investigations should be made to synthesise further ligand-deficient compounds and to determine their compositions and structures.

Conflicts of interest

There are no conflicts of interest to declare.

Acknowledgements

The authors thank Edith Alig for the TG/DTA and DSC measurements. Miriam Heine thanks Justine Ruhl and Carlo Kulig for their passionate but futile efforts to prepare single crystals.

References

1 T. Watabe and K. Yogo, *Bull. Chem. Soc. Jpn.*, 2014, **87**, 740–745.
2 S. Noro, K. Fukuhara, K. Kubo and T. Nakamura, *Cryst. Growth Des.*, 2011, **11**, 2379–2385.
3 J. Hasegawa, M. Higuchi, Y. Hijikata and S. Kitagawa, *Chem. Mater.*, 2009, **21**, 1829–1833.
4 Z. Wang, G. Chen and K. Ding, *Chem. Rev.*, 2008, **109**, 322–359.
5 S.-H. Cho, B. Ma, S. T. Nguyen, J. T. Hupp and T. E. Albrecht-Schmitt, *Chem. Commun.*, 2006, 2563–2565.
6 O. R. Evans and W. Lin, *Acc. Chem. Res.*, 2002, **35**, 511–522.
7 S. Wöhlert, L. Fink, M. U. Schmidt and C. Näther, *CrystEngComm*, 2013, **15**, 945–957.
8 J. Hu, H. Yao, Y. Bai, D. Zhao, S. Chen and J. Zhao, *Polyhedron*, 2014, **78**, 1–9.
9 Y.-S. Bae, O. K. Farha, A. M. Spokoyny, C. A. Mirkin, J. T. Hupp and R. Q. Snurr, *Chem. Commun.*, 2008, 4135–4137.
10 M. Wriedt, S. Sellmer and C. Näther, *Dalton Trans.*, 2009, 7975–7984.
11 S. Wöhlert, T. Runčevski, R. E. Dinnebier, S. G. Ebbinghaus and C. Näther, *Cryst. Growth Des.*, 2014, **14**, 1902–1913.
12 D. T. Cromer and A. C. Larson, *Acta Crystallogr., Sect. B: Struct. Crystallogr. Cryst. Chem.*, 1972, **28**, 1052–1058.
13 A. J. Graham, P. C. Healy, J. D. Kildea and A. H. White, *Aust. J. Chem.*, 1989, **42**, 177–184.
14 M. K. Broderick, C. Yang, R. D. Pike, A. Nicholas, D. May and H. H. Patterson, *Polyhedron*, 2016, **114**, 333–343.
15 H. Hanika-Heidl, S. E. H. Etaiw, M. S. Ibrahim, A. S. B. Eldin and R. D. Fischer, *J. Organomet. Chem.*, 2003, **684**(1), 329–337.
16 A. Bacchi, G. Cantoni, P. Pelagatti and S. Rizzato, *J. Organomet. Chem.*, 2012, **714**, 81–87.
17 W. H. Leung, W. Lai and I. D. Williams, *J. Organomet. Chem.*, 2000, **604**, 197–201.
18 L. Carlucci, G. Ciani, D. M. Proserpio and A. Sironi, *J. Chem. Soc., Chem. Commun.*, 1994, 2755–2756.
19 X. L. Zhao and T. C. W. Mak, *Dalton Trans.*, 2004, 3212–3217.
20 W. Chen, F. Liu and X. You, *Bull. Chem. Soc. Jpn.*, 2002, **75**, 1559–1560.
21 R. D. Bailey and W. T. Pennington, *Chem. Commun.*, 1998, 1181–1182.
22 Y. Krysiak, L. Fink, T. Bernert, J. Glinnemann, M. Kapuscinski, H. Zhao, E. Alig and M. U. Schmidt, *Z. Anorg. Allg. Chem.*, 2014, **640**, 3190–3196.
23 H. Zhao, A. Bodach, M. Heine, Y. Krysiak, J. Glinnemann, E. Alig, L. Fink and M. U. Schmidt, *CrystEngComm*, 2017, **19**, 2216–2228.
24 X.-H. Li, H.-Y. Wu and J.-G. Hu, *Acta Crystallogr., Sect. E: Struct. Rep. Online*, 2004, **60**, m1533.
25 M. Du, X.-J. Zhao, S. R. Batten and J. Ribas, *Cryst. Growth Des.*, 2005, **5**, 901–909.
26 R. Ghiasi, *Acta Crystallogr., Sect. E: Struct. Rep. Online*, 2011, **67**, m101.

27 R. Ghiasi, *Acta Crystallogr., Sect. E: Struct. Rep. Online*, 2011, **67**, m595.
28 W.-T. Chen, Z.-G. Luo, Y.-P. Xu, Q.-Y. Luo and J.-H. Liu, *J. Chem. Res.*, 2011, **35**, 253–256.
29 X.-L. Zhao and T. Mak, *Dalton Trans.*, 2004, 3212–3217.
30 M. K. Broderick, C. Yang, R. D. Pike, A. Nicholas, D. May and H. H. Patterson, *Polyhedron*, 2016, **114**, 333–343.
31 C. Näther, S. Wöhlert, J. Boeckmann, M. Wriedt and I. Jeß, *Z. Anorg. Allg. Chem.*, 2013, **639**, 2696–2714.
32 M. L. Hernández, M. G. Barandika, M. K. Urtiaga, R. Cortés, L. Lezama, M. I. Arriortua and T. Rojo, *J. Chem. Soc., Dalton Trans.*, 1999, 1401–1406.
33 S. Wöhlert, I. Jess, U. Englert and C. Näther, *CrystEngComm*, 2013, **15**, 5326–5336.
34 S. Wöhlert, L. Fink, M. U. Schmidt and C. Näther, *Z. Anorg. Allg. Chem.*, 2013, **639**, 2186–2194.
35 *STOE WinXPOW 310*, STOE & Cie GmbH, Darmstadt, Germany, 2016.
36 A. Boultif and D. Louër, *J. Appl. Crystallogr.*, 2004, **37**, 724–731.
37 R. Oishi-Tomiyasu, *J. Appl. Crystallogr.*, 2014, **47**, 593–598.
38 R. Oishi-Tomiyasu, *J. Appl. Crystallogr.*, 2014, **47**, 2055–2059.
39 W. I. F. David, K. Shankland, J. van de Streek, E. Pidcock, W. D. S. Motherwell and J. C. Cole, *J. Appl. Crystallogr.*, 2006, **39**, 910–915.
40 A. Coelho, *TOPAS Acad. User Man. & Tech. Ref*, Brisbane, Australia, 2009.
41 A. Coelho, *J. Appl. Crystallogr.*, 2018, **51**, 210–218.
42 D. W. M. Hofmann, *Acta Crystallogr., Sect. B: Struct. Sci.*, 2002, **58**, 489–493.
43 *Avogadro Chemistry*, 2018.
44 S. Habermehl, P. Mörschel, P. Eisenbrandt and S. M. Hammer, *Acta Crystallogr., Sect. B: Struct. Sci., Cryst. Eng. Mater.*, 2014, **70**, 347–359.
45 I. J. Bruno, J. C. Cole, P. R. Edgington, M. Kessler, C. F. Macrae, P. McCabe, J. Pearson and R. Taylor, *Acta Crystallogr., Sect. B: Struct. Sci.*, 2002, **58**, 389–397.
46 V. Kopský and D. B. Litvin, *International Tables for Crystallography, Volume E: Subperiodic Groups*, 2010, 280–281.
47 F. H. Allen, *Acta Crystallogr., Sect. B: Struct. Sci.*, 2002, **58**, 380–388.

3-Cyanopyridine as bridging and terminal ligand in coordination polymers

Miriam Heine, Lothar Fink, Martin U. Schmidt*

Institute of Inorganic and Analytical Chemistry, Goethe University, Max-von-Laue-Str. 7, 60438 Frankfurt am Main, Germany. E-Mail: m.schmidt@chemie.uni-frankfurt.de; Fax: +49 69798 29235; Tel: +49 69798 29123

Figures

Tables

Experimental Details

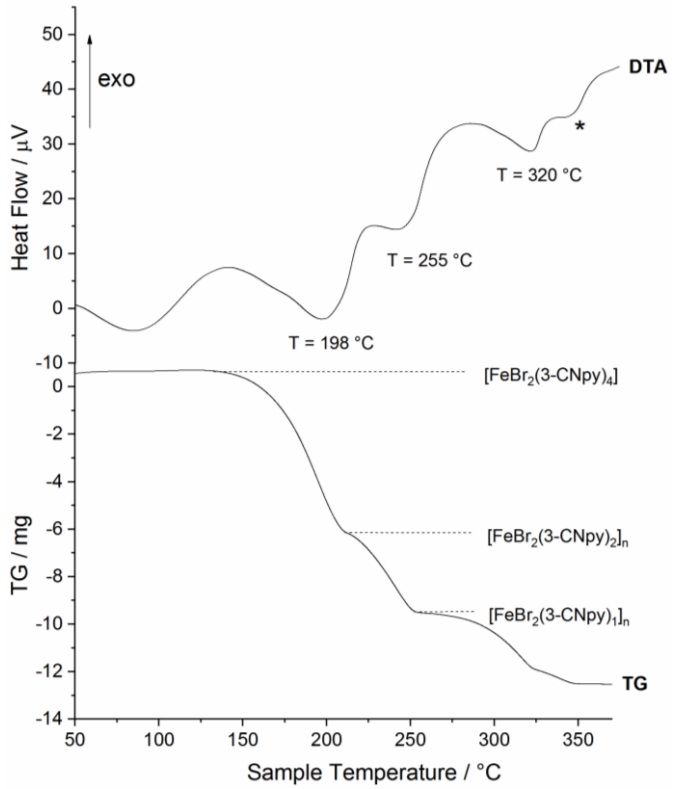

Figure S1. DTA/TG curves of $[FeBr_2(3\text{-}CNpy)_4]$ (**2a**). Heating rate: 5 K/min, Ar atmosphere, Al_2O_3 crucible. The shoulder marked by a * points to a fourth decomposition product $[FeBr_2(3\text{-}CNpy)_{1-x}]_n$, which could not be isolated in the Fe series, but would explain foreign reflections in the XRPD pattern of $[FeBr_2(3\text{-}CNpy)_1]_n$.

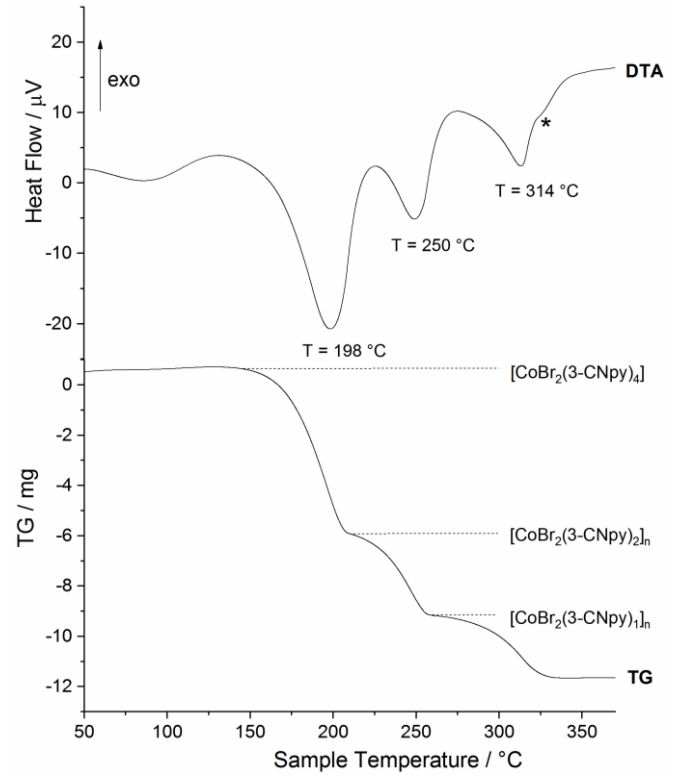

Figure S2. DTA/TG curves of $[CoBr_2(3\text{-}CNpy)_4]$ (**3a**). Heating rate: 5 K/min, Ar atmosphere, Al_2O_3 crucible. The shoulder marked by a * points to a fourth decomposition product $[CoBr_2(3\text{-}CNpy)_{1-x}]_n$, which could not be isolated in the Co series, but would explain foreign reflections in the XRPD pattern of $[CoBr_2(3\text{-}CNpy)_1]_n$.

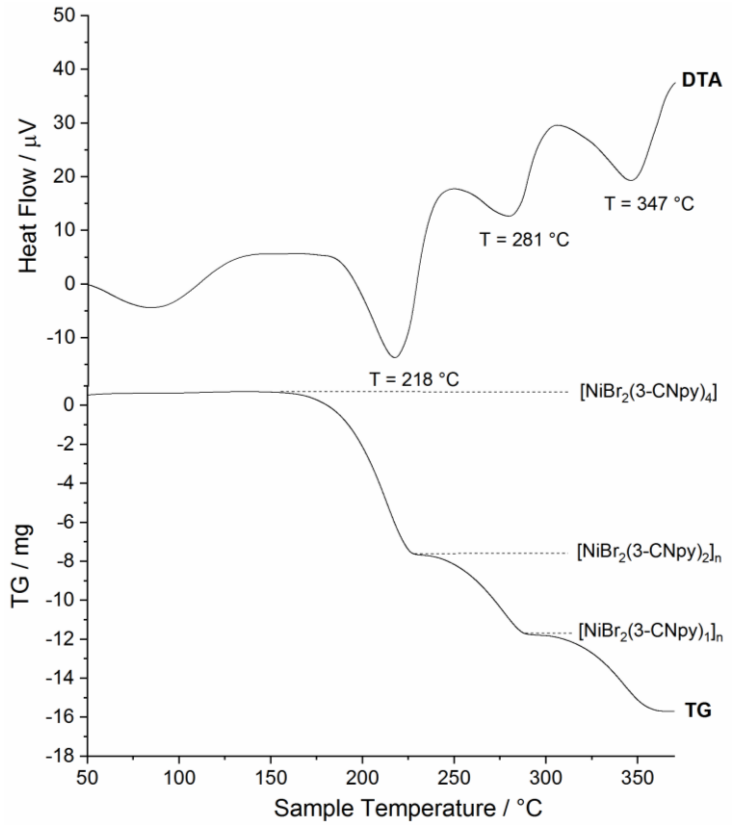

Figure S3. DTA/TG curves of $[NiBr_2(3\text{-}CNpy)_4]$ (**4a**). Heating rate: 5 K/min, Ar atmosphere, Al_2O_3 crucible.

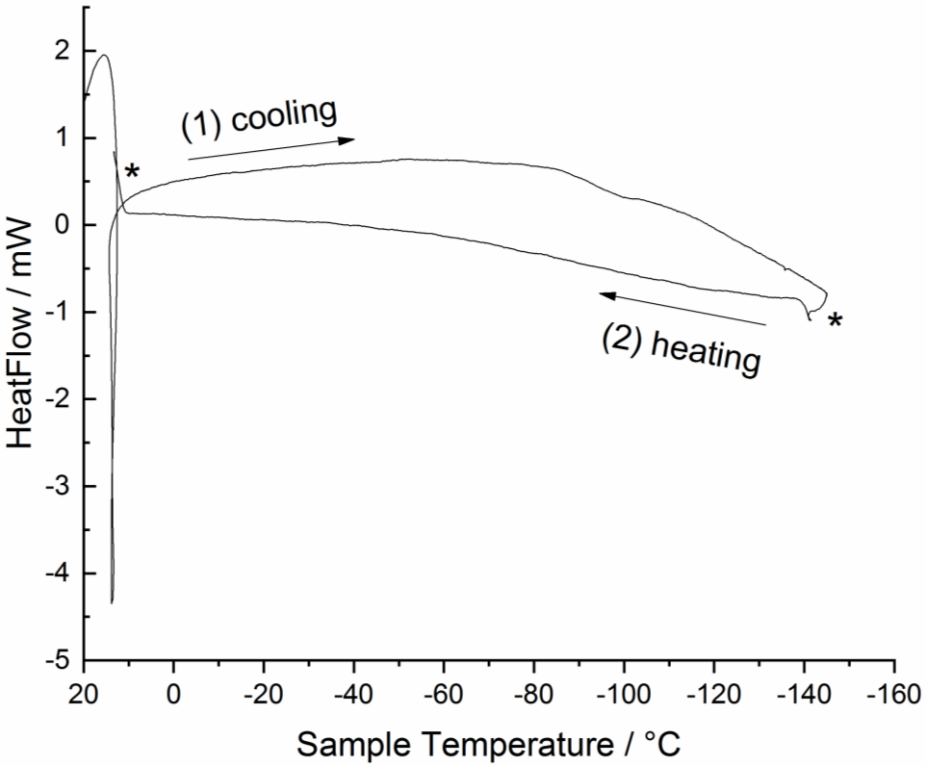

Figure S4. DSC-curve of $[NiBr_2(3\text{-}CNpy)_2]_n$ (**β-4b**). (1) cooling from room temperature to -150°C, then (2) heating to room temperature. Instrumental artefacts are marked by stars.

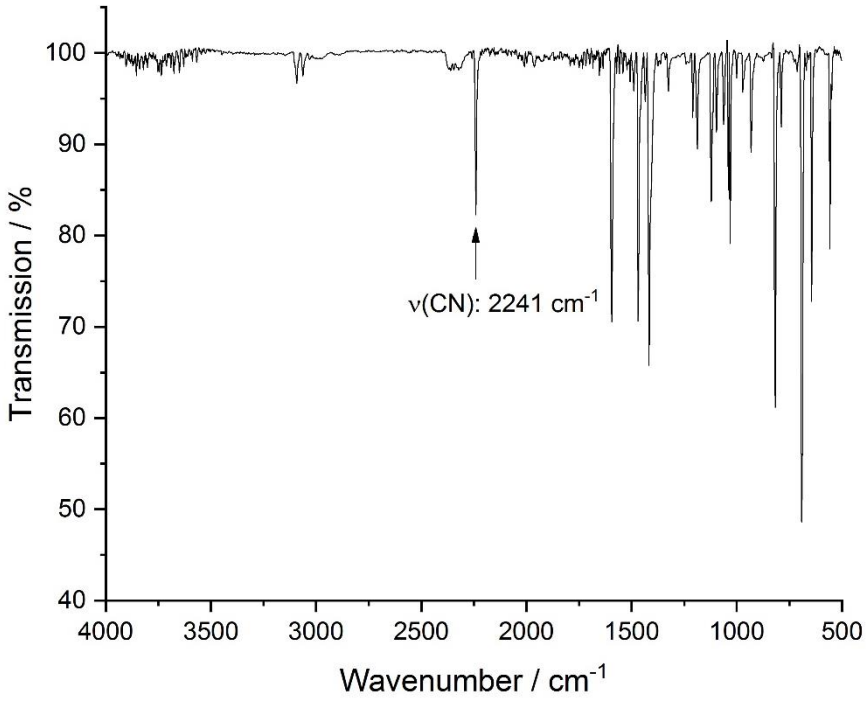

Figure S5. IR spectrum of $[MnBr_2(3\text{-}CNpy)_4]$ (**1a**)

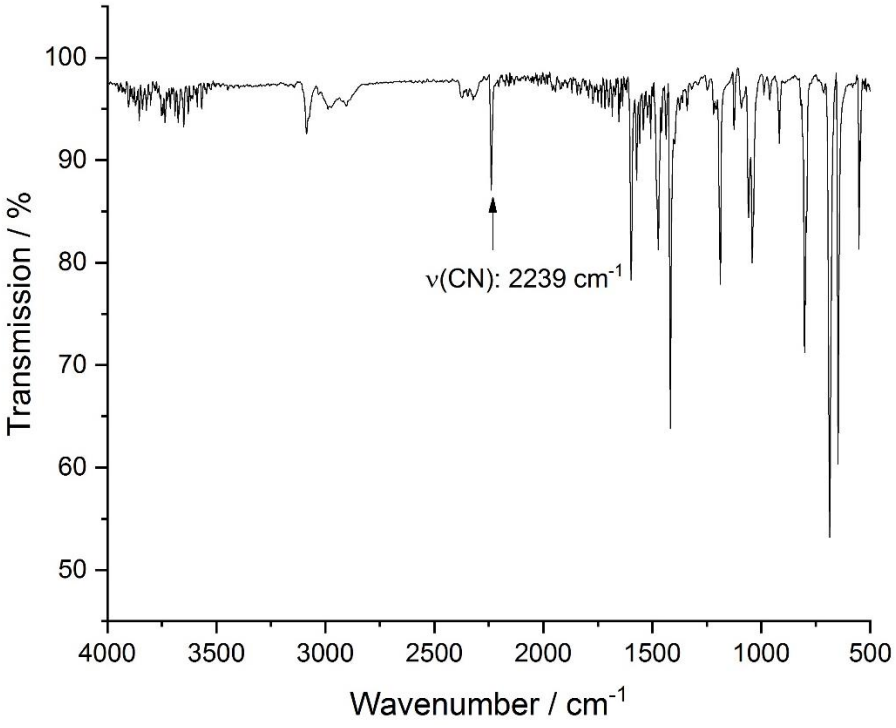

Figure S6. IR spectrum of $[MnBr_2(3\text{-}CNpy)_2]_n$ (**1b**)

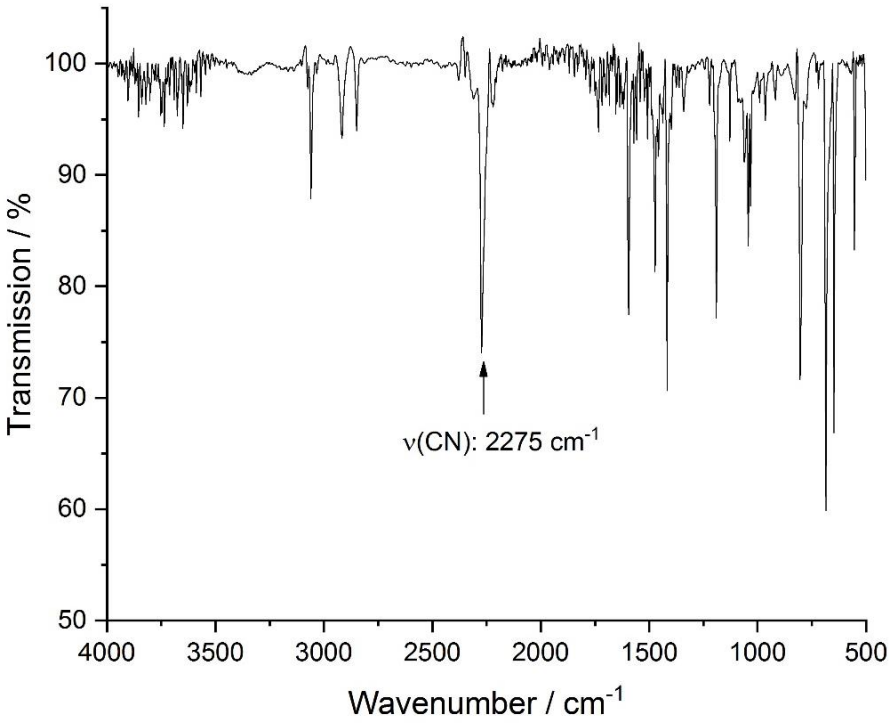

Figure S7. IR spectrum of $[MnBr_2(3\text{-}CNpy)_1]_n$ (**1c**)

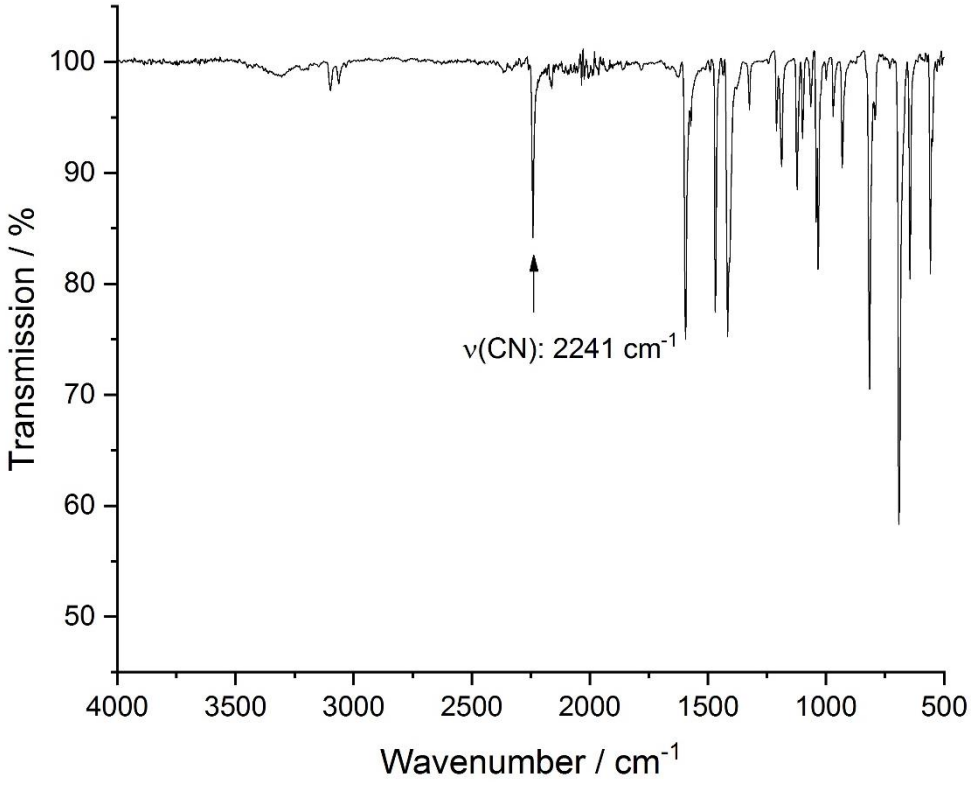

Figure S8. IR spectrum of $[FeBr_2(3\text{-}CNpy)_4]$ (**2a**)

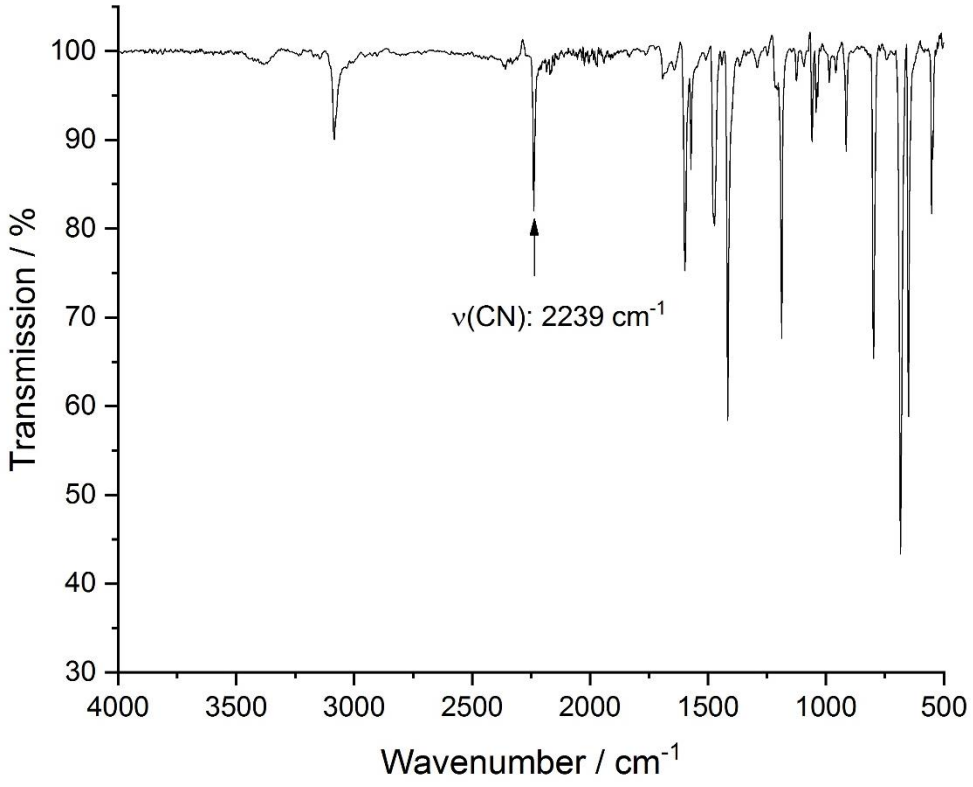

Figure S9. IR spectrum of $[FeBr_2(3\text{-}CNpy)_2]_n$ (**2b**)

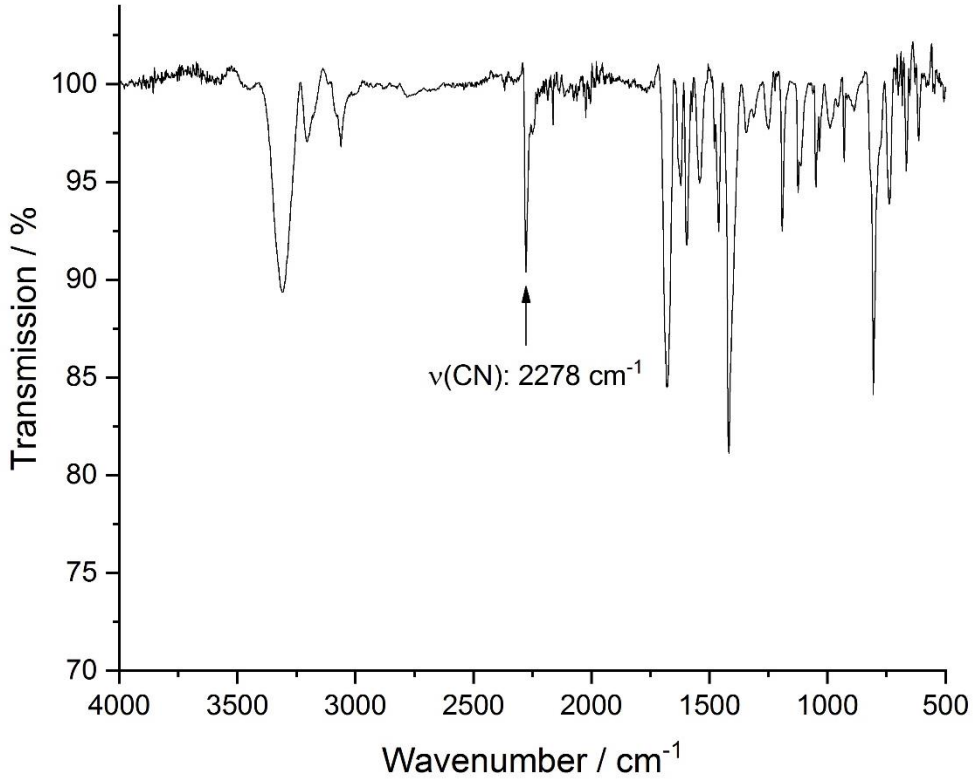

Figure S10. IR spectrum of $[FeBr_2(3\text{-}CNpy)_1]_n$ (**2c**)

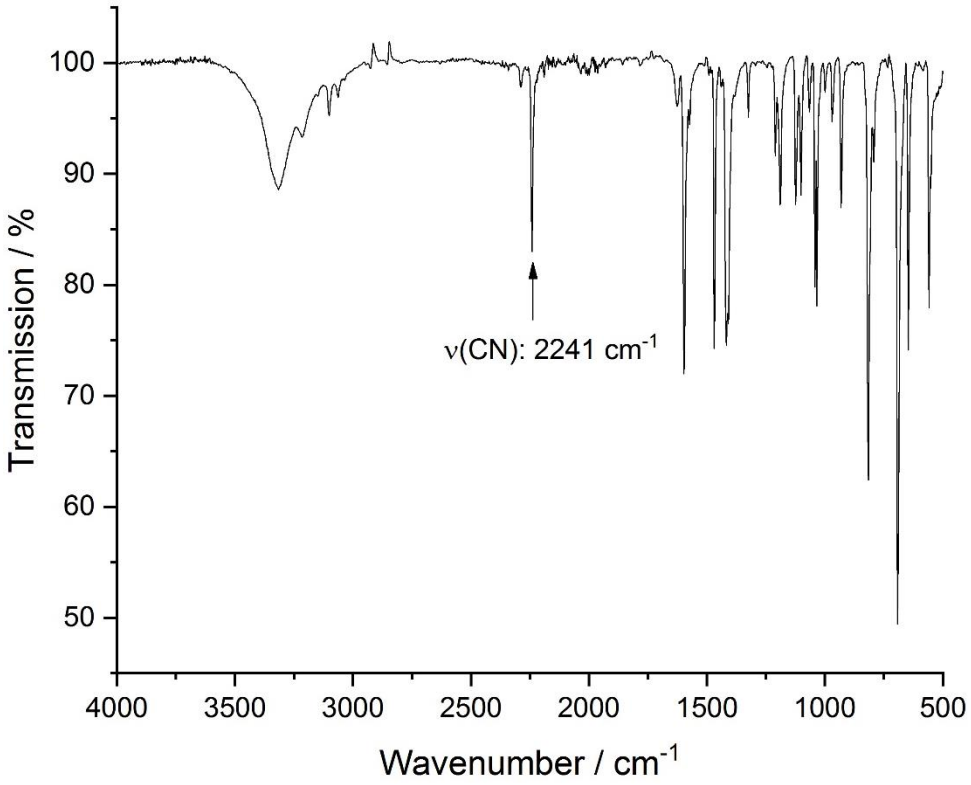

Figure S11. IR spectrum of $[CoBr_2(3\text{-}CNpy)_4]$ (**3a**)

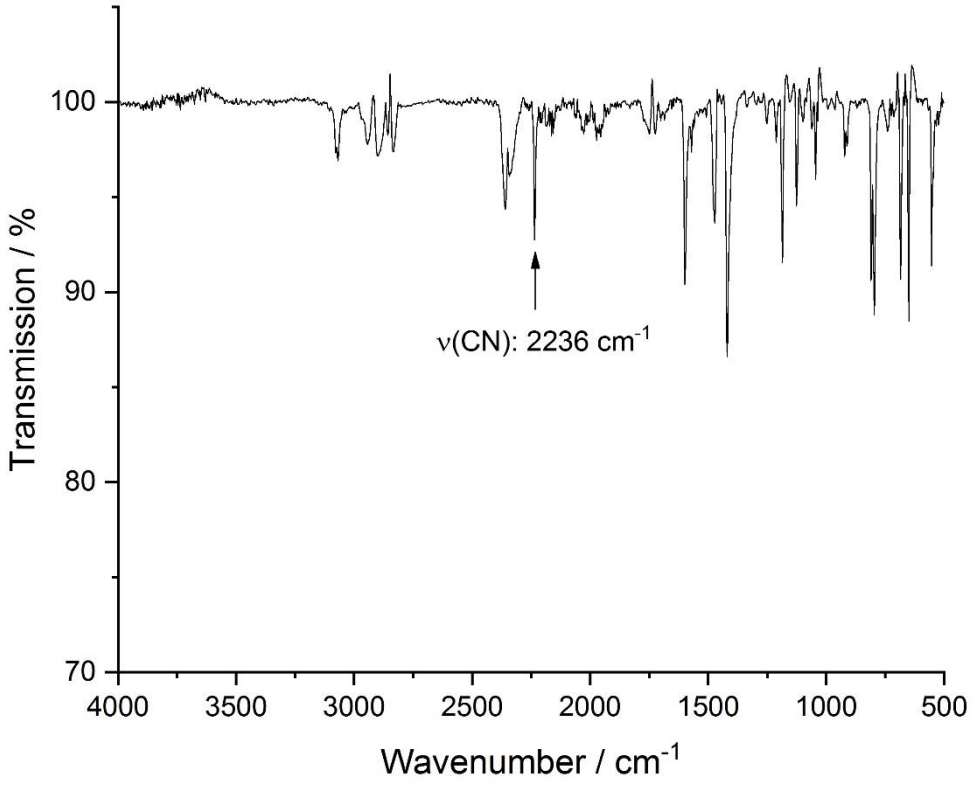

Figure S12. IR spectrum of $[CoBr_2(3\text{-}CNpy)_2]_n$: mixture of **α-3b** and **β-3b**

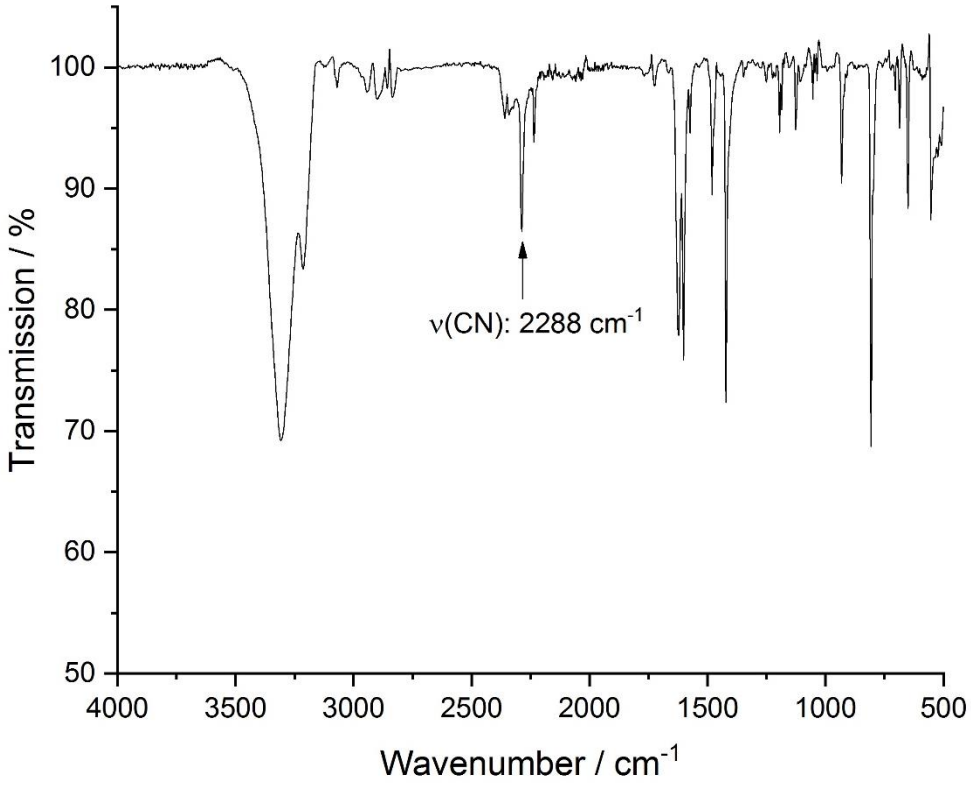

Figure S13. IR spectrum of $[CoBr_2(3\text{-}CNpy)_1]_n$ (**3c**)

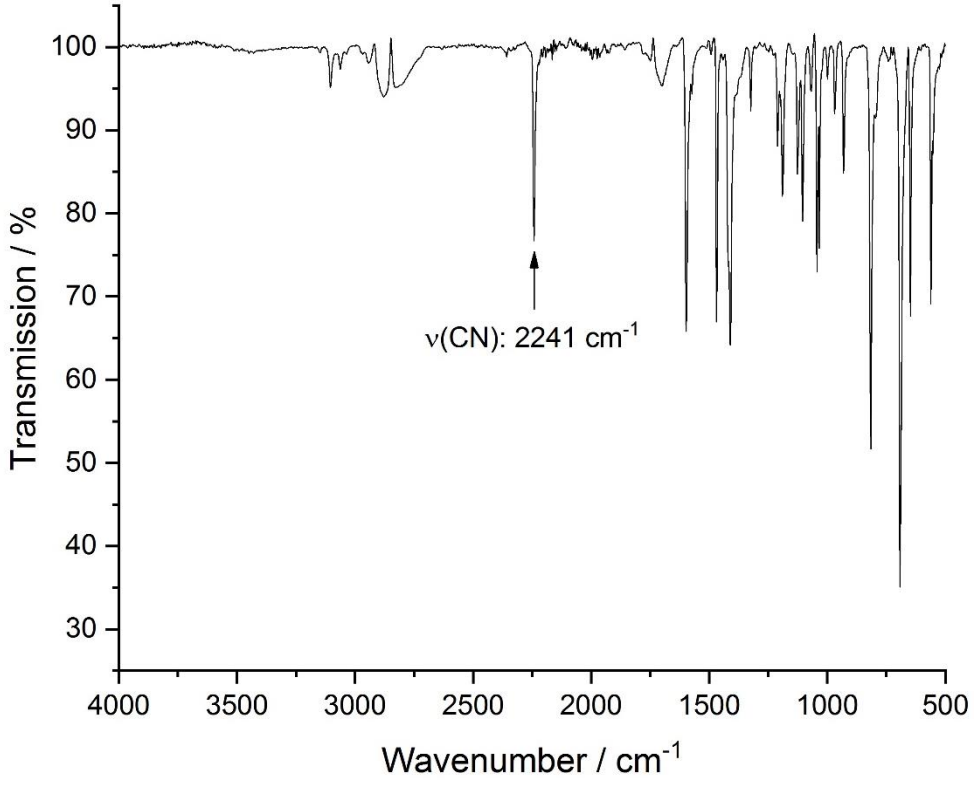

Figure S14. IR spectrum of $[NiBr_2(3\text{-}CNpy)_4]$ (**4a**)

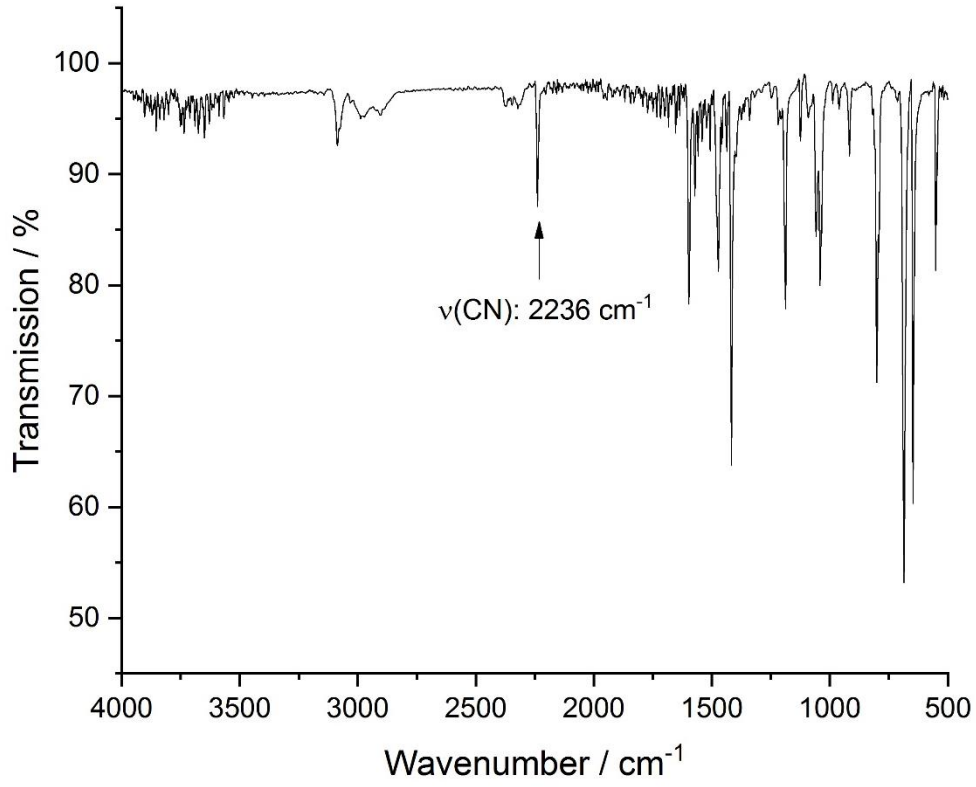

Figure S15. IR spectrum of $[NiBr_2(3\text{-}CNpy)_2]_n$: mixture of **α-4b** and **β-4b**

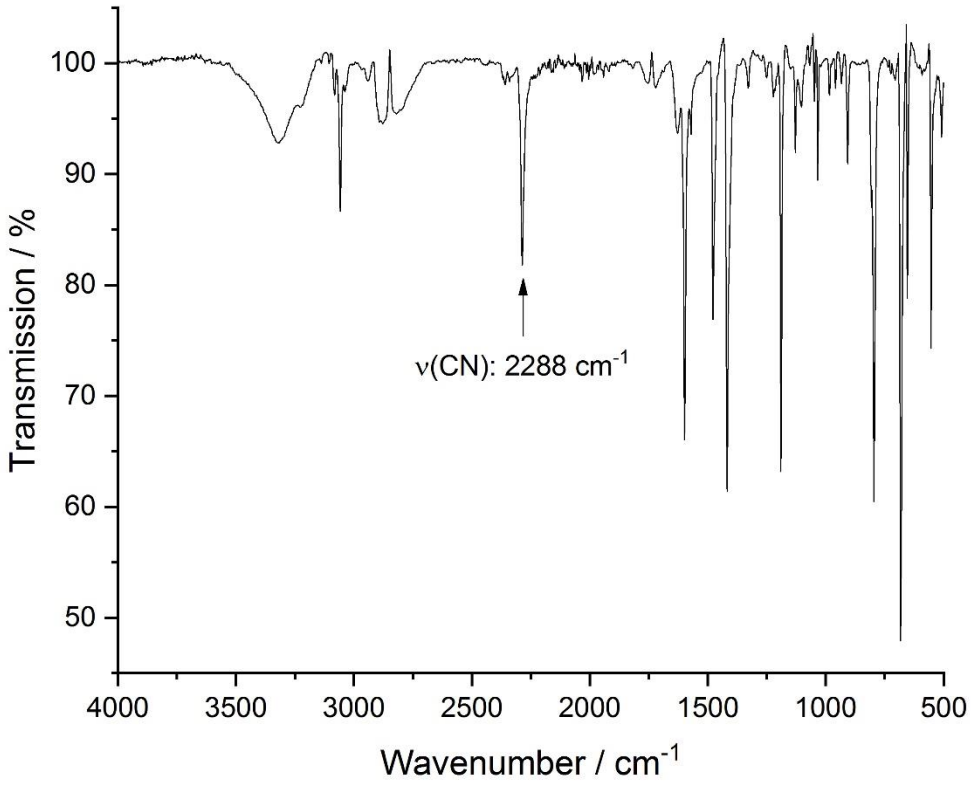

Figure S16. IR spectrum of $[NiBr_2(3\text{-}CNpy)_1]_n$ (**4c**)

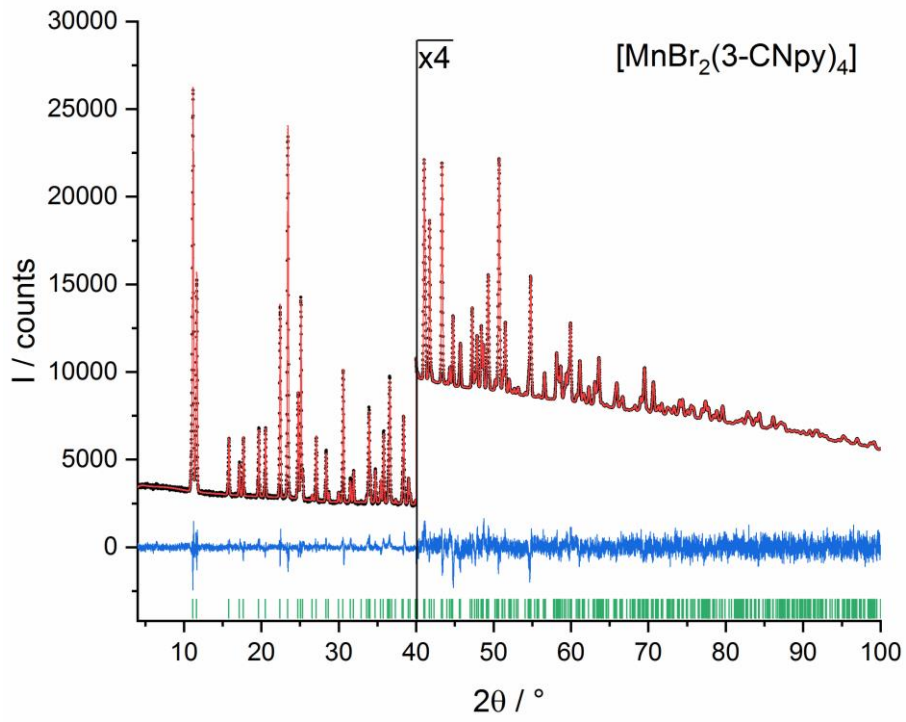

Figure S17. Rietveld plot of **1a**. Observed powder diagram (black points), simulated powder diagram (red solid line), difference profile (blue solid line) and reflection positions (green tick marks). Change of the scale with corresponding factor is indicated in the diagram.

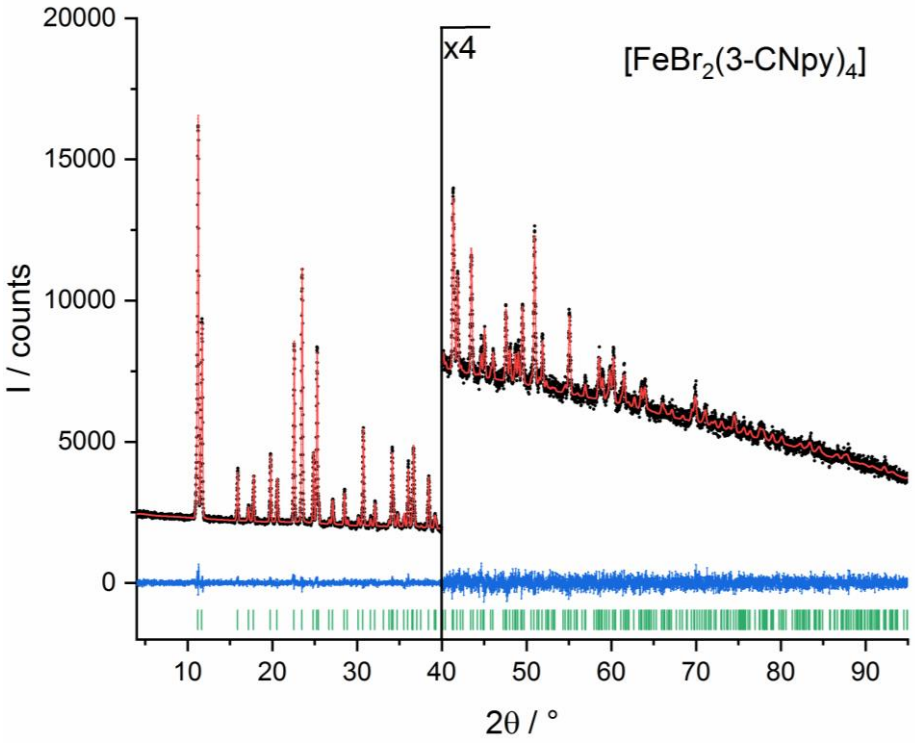

Figure S18. Rietveld plot of **2a**. Observed powder diagram (black points), simulated powder diagram (red solid line), difference profile (blue solid line) and reflection positions (green tick marks). Change of the scale with corresponding factor is indicated in the diagram.

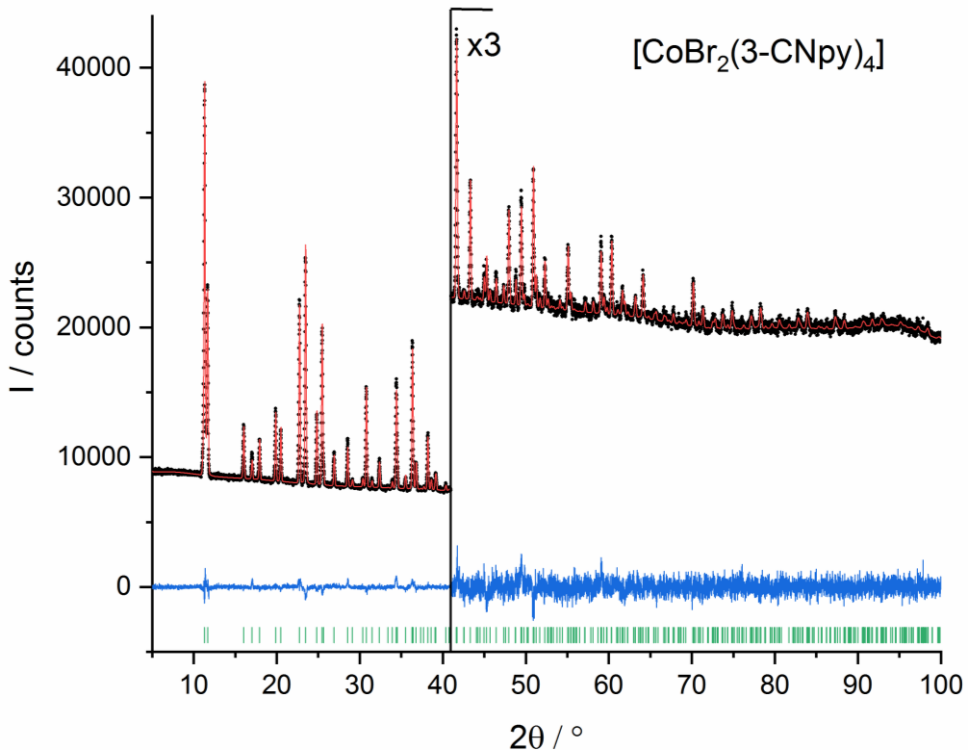

Figure S19. Rietveld plot of **3a**. Observed powder diagram (black points), simulated powder diagram (red solid line), difference profile (blue solid line) and reflection positions (green tick marks). Change of the scale with corresponding factor is indicated in the diagram.

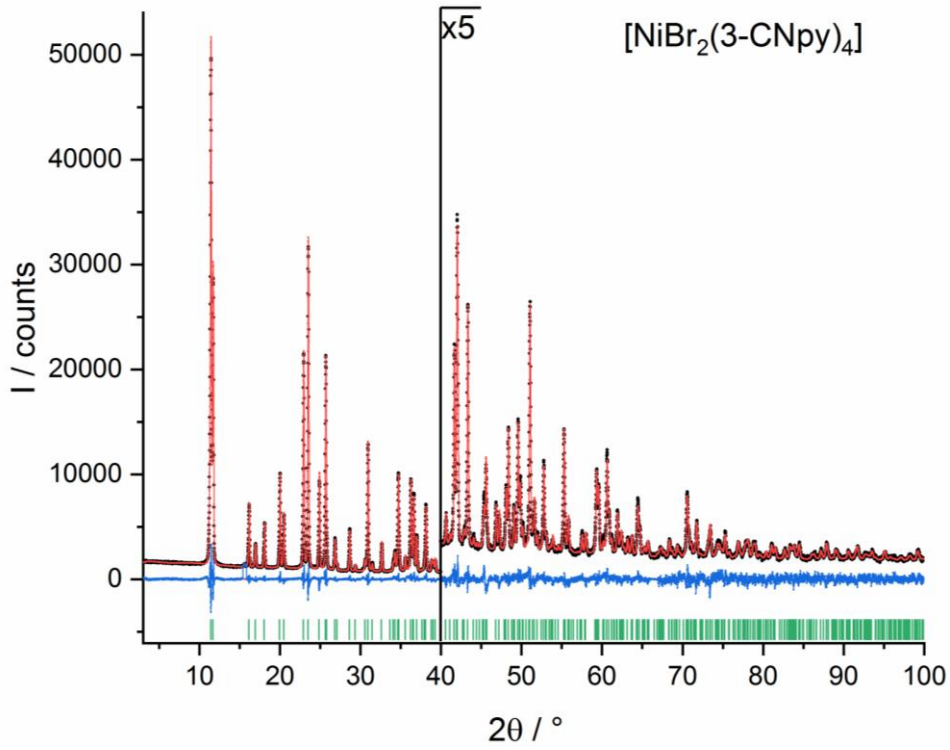

Figure S20. Rietveld plot of **4a**. Observed powder diagram (black points), simulated powder diagram (red solid line), difference profile (blue solid line) and reflection positions (green tick marks). Change of the scale with corresponding factor is indicated in the diagram.

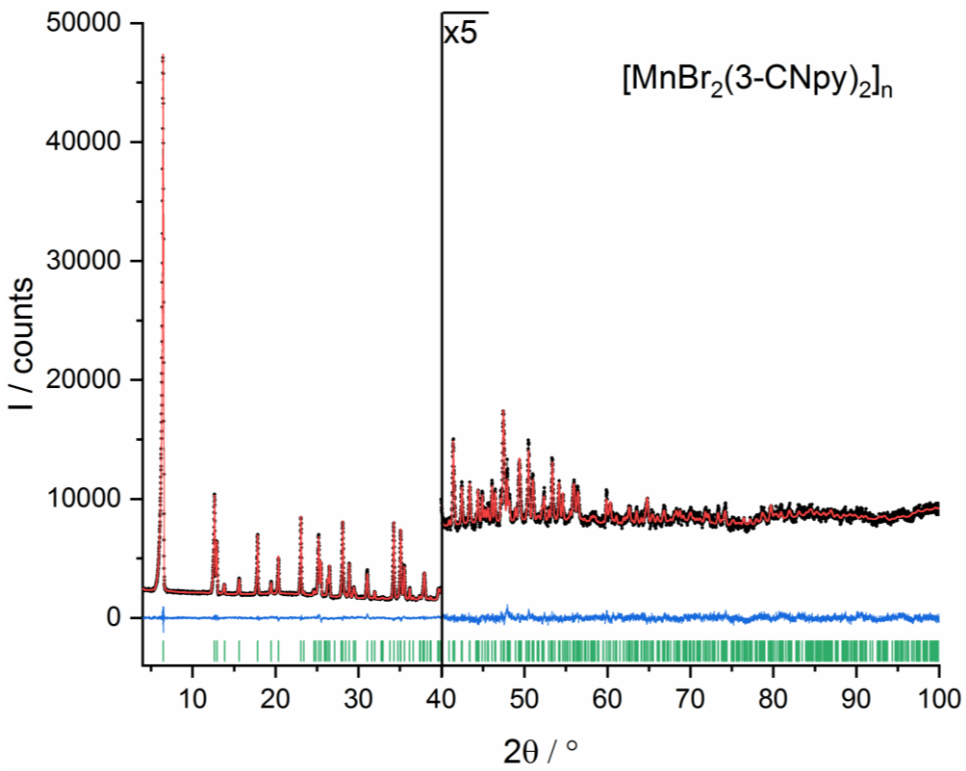

Figure S21. Rietveld plot of **1b**. Observed powder diagram (black points), simulated powder diagram (red solid line), difference profile (blue solid line) and reflection positions (green tick marks). Change of the scale with corresponding factor is indicated in the diagram.

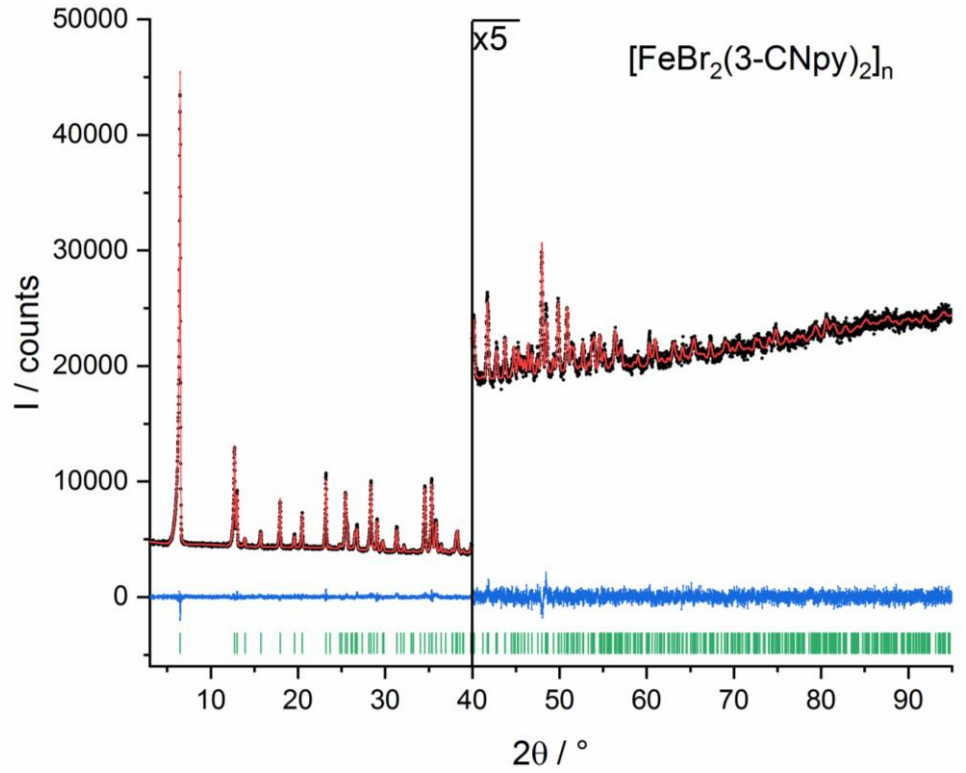

Figure S22. Rietveld plot of **2b**. Observed powder diagram (black points), simulated powder diagram (red solid line), difference profile (blue solid line) and reflection positions (green tick marks). Change of the scale with corresponding factor is indicated in the diagram.

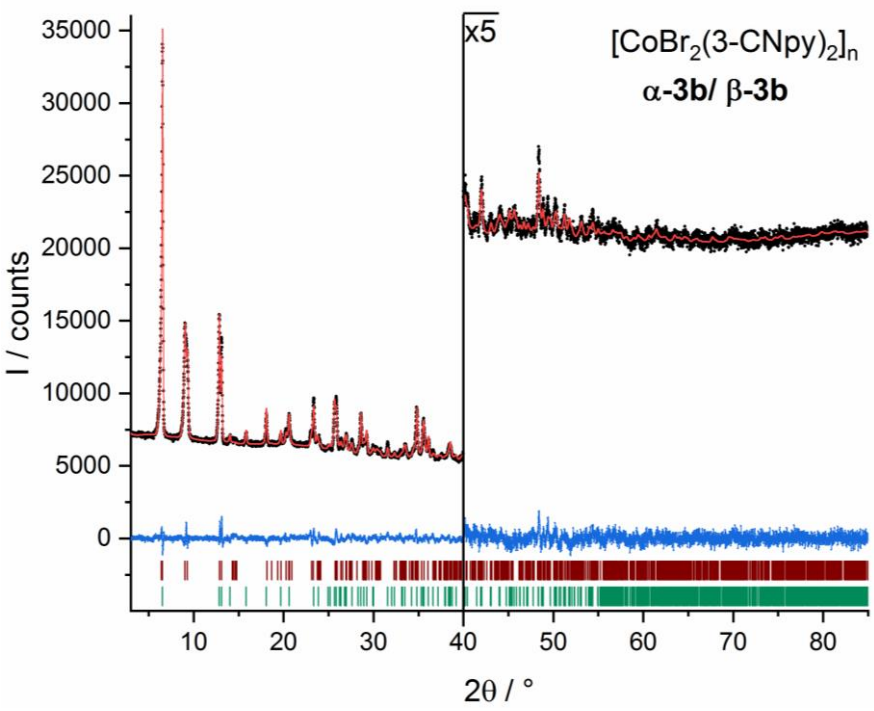

Figure S23. Rietveld plot of **3b**. The crystal structures of **α-3b** and **β-3b** were refined from a phase mixture. Observed powder diagram (black points), simulated powder diagram (red solid line), difference profile (blue solid line) and reflection positions (green tick marks for **α-3b**, brown tick marks for **β-3b**). Change of the scale with corresponding factor is indicated in the diagram.

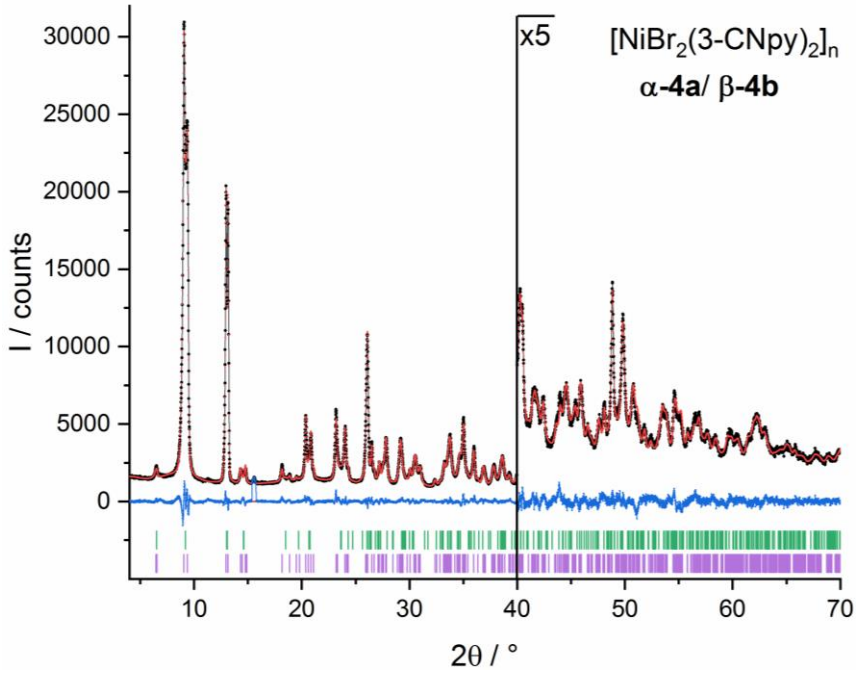

Figure S24. Rietveld plot of **4b**. The crystal structures of **β-4b** was refined from a phase mixture of **α-4b** and **β-4b**. Observed powder diagram (black points), simulated powder diagram (red solid line), difference profile (blue solid line) and reflection positions (green tick marks for **α-4b**, violet tick marks for **β-4b**). Change of the scale with corresponding factor is indicated in the diagram. Excluded region is indicated.

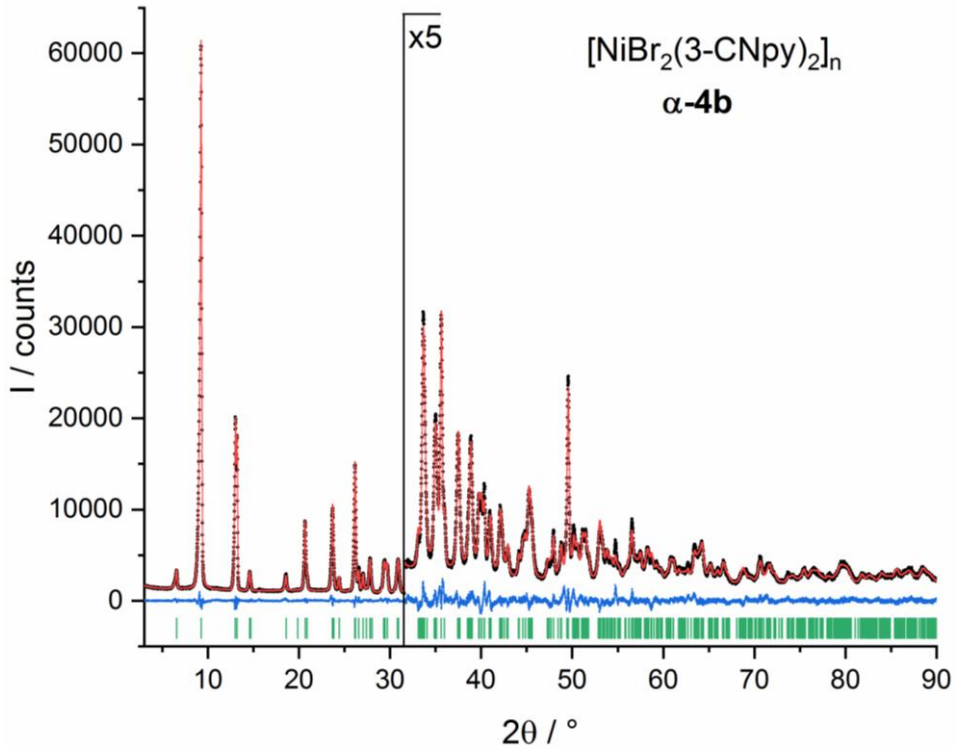

Figure S25. Rietveld plot of **α-4b**. Observed powder diagram (black points), simulated powder diagram (red solid line), difference profile (blue solid line) and reflection positions (green tick marks). Change of the scale with corresponding factor is indicated in the diagram.

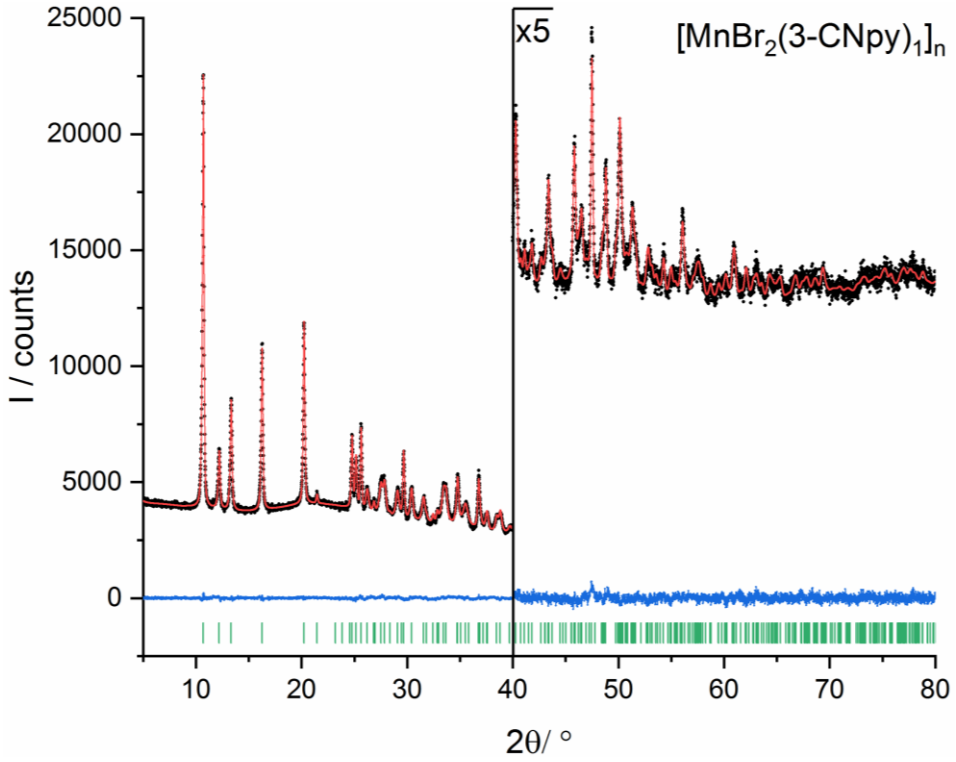

Figure S26. Rietveld plot of **1c**. Observed powder diagram (black points), simulated powder diagram (red solid line), difference profile (blue solid line) and reflection positions (green tick marks). Change of the scale with corresponding factor is indicated in the diagram.

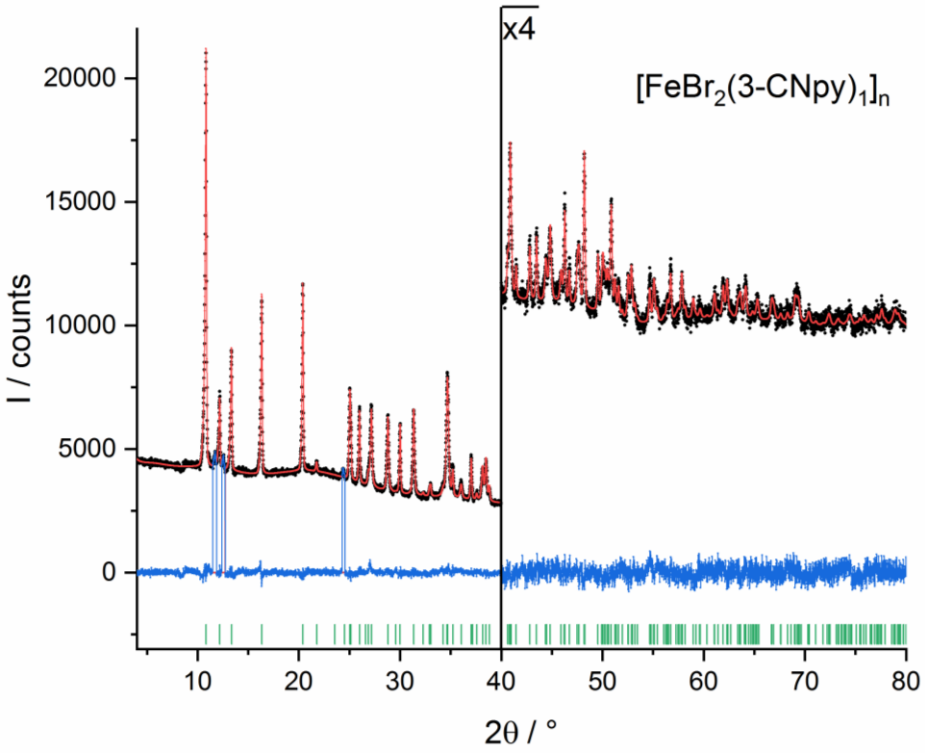

Figure S27. Rietveld plot of **2c**. Observed powder diagram (black points), simulated powder diagram (red solid line), difference profile (blue solid line) and reflection positions (green tick marks). Change of the scale with corresponding factor is indicated in the diagram. Reflections of a foreign phase are excluded.

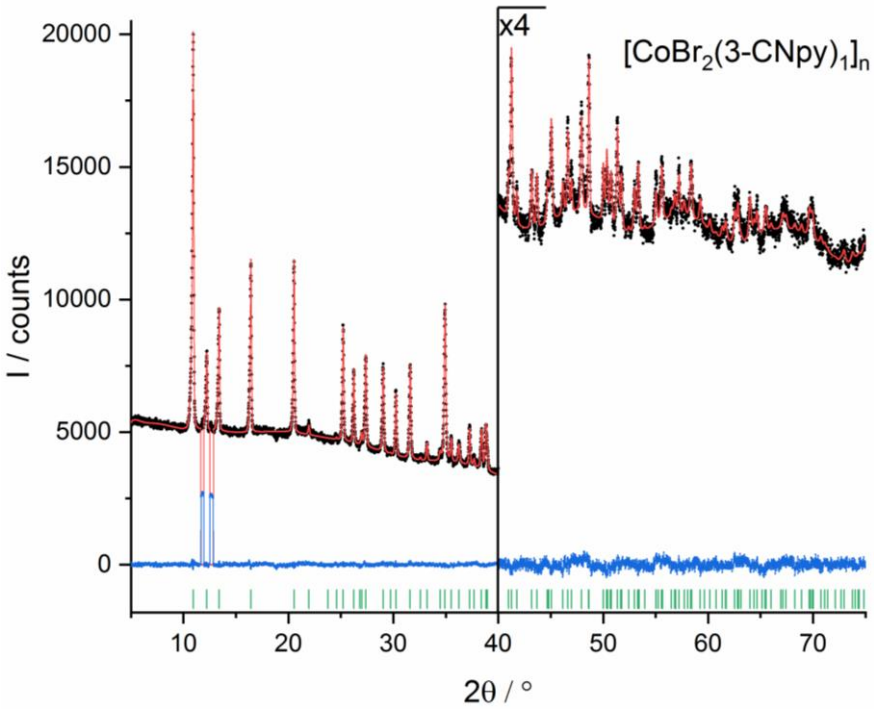

Figure S28. Rietveld plot of **3c**. Observed powder diagram (black points), simulated powder diagram (red solid line), difference profile (blue solid line) and reflection positions (green tick marks). Change of the scale with corresponding factor is indicated in the diagram. Reflections of a foreign phase are excluded.

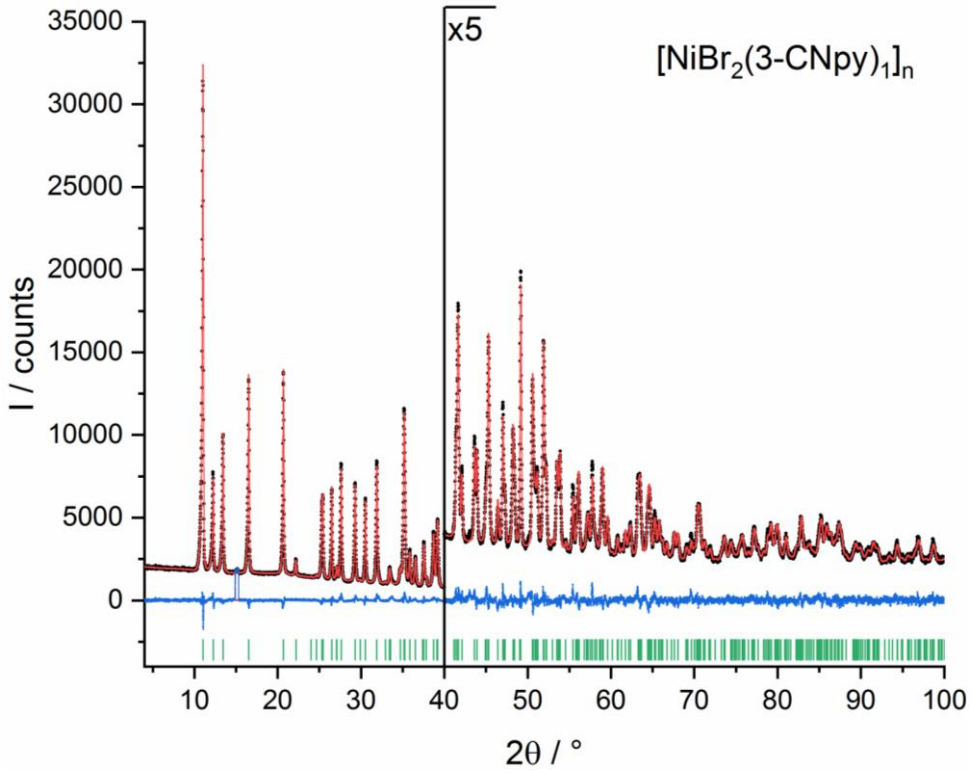

Figure S29. Rietveld plot of **4c**. Observed powder diagram (black points), simulated powder diagram (red solid line), difference profile (blue solid line) and reflection positions (green tick marks). Change of the scale with corresponding factor is indicated in the diagram. An appearing reflection of $NiCl_2$ was excluded.

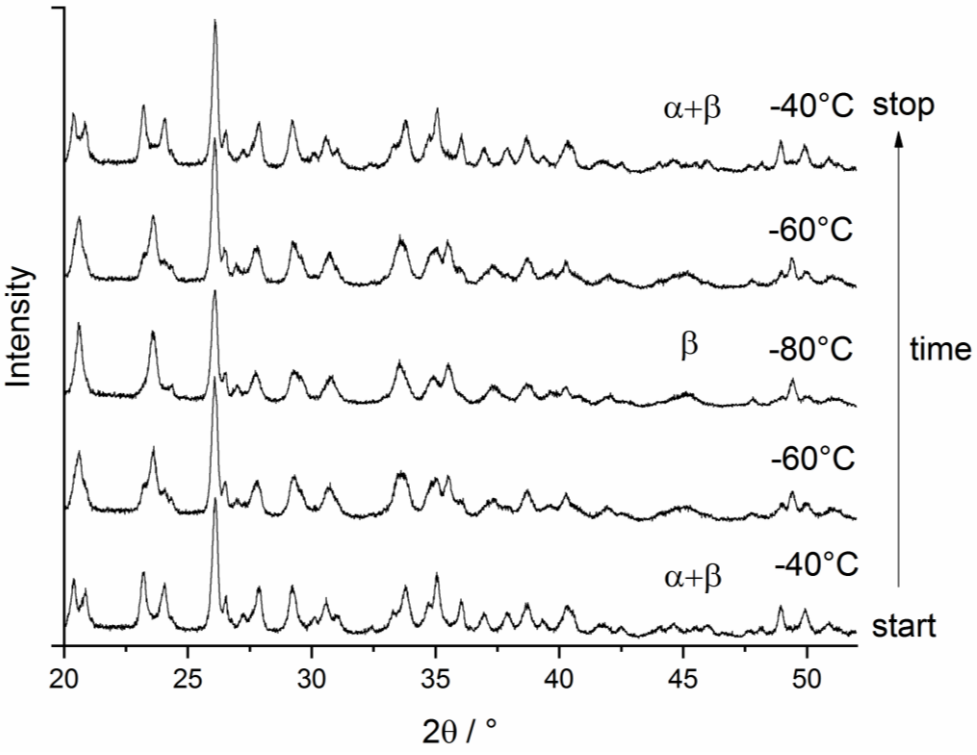

Figure S30. Low-temperature-XRPD series of $[NiBr_2(3\text{-}CNpy)_2]_n$ (**4b**): the phase transition of **β-4b** into **α-4b** is reversible.

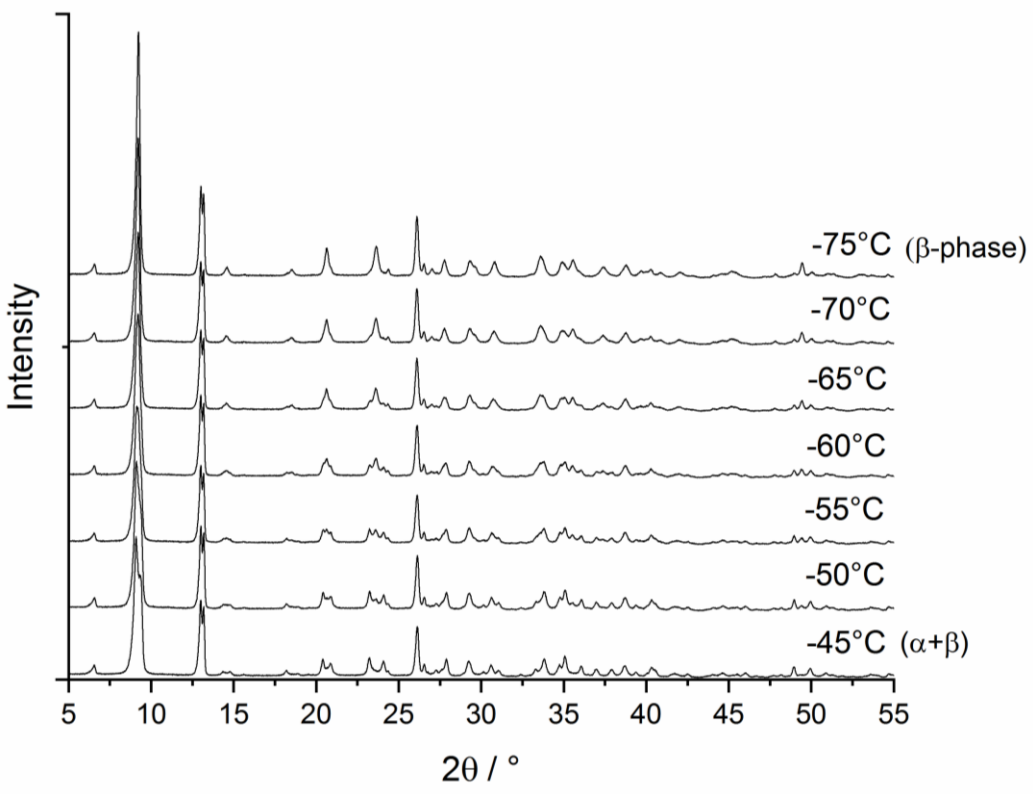

Figure S31. Low-temperature-XRPD series of $[NiBr_2(3\text{-}CNpy)_2]_n$ (**4b**) showing the phase transition in detail. At -75°C the phase transition is completed.

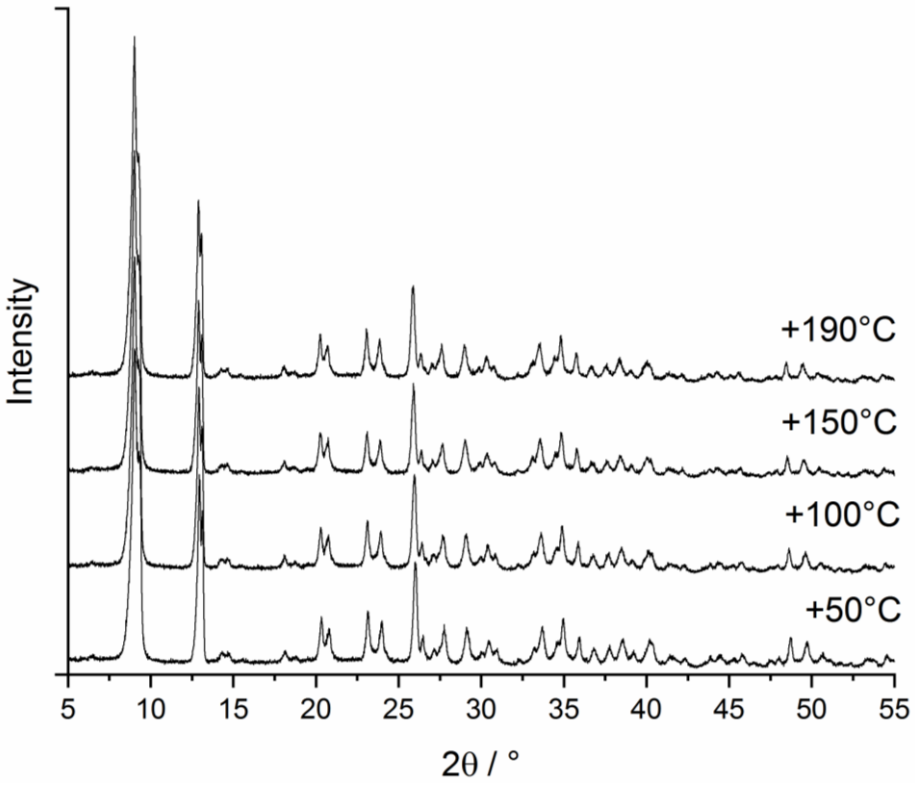

Figure S32. High-temperature-XRPD series of $[NiBr_2(3\text{-}CNpy)_2]_n$ (**4b**): no further phase transition up to 190°C.

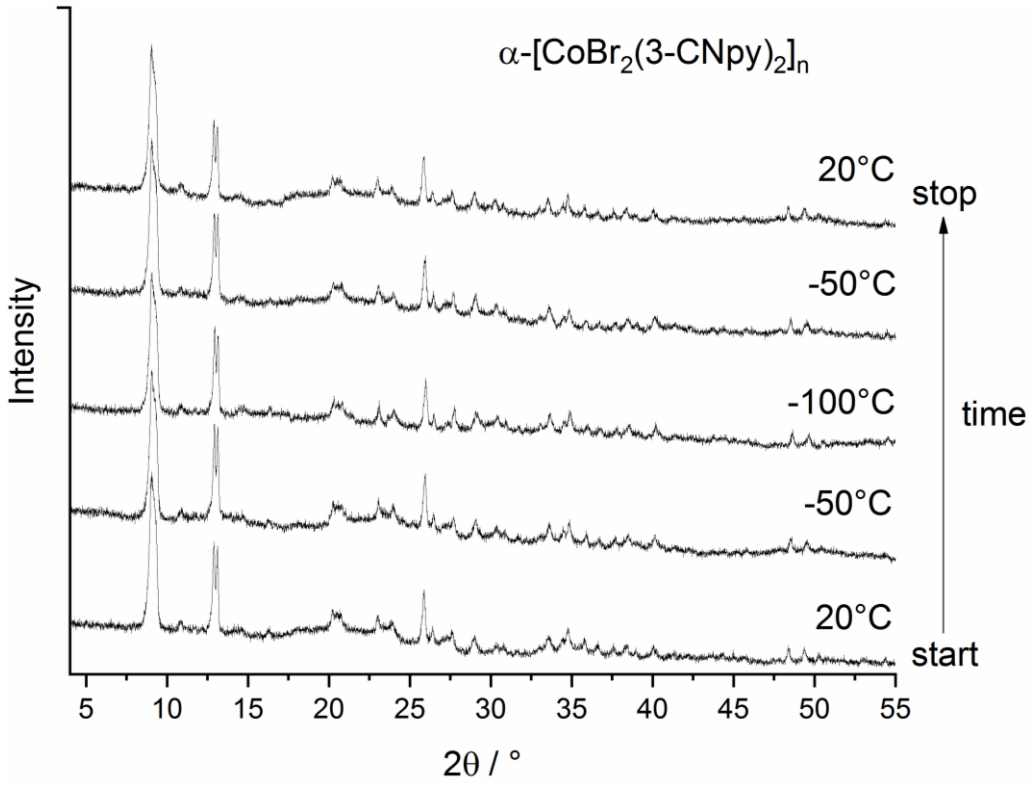

Figure S33. Low-temperature-XRPD series of α-$[CoBr_2(3\text{-}CNpy)_2]_n$ (**α-4b**): no further phase transition down to -100°C.

Table S1. Results of DTA/TG measurements of $[M^{II}Br_2(3\text{-}CNpy)_4]$ (M^{II} = Mn, Fe, Co, Ni). *T*: DTA peak temperatures, m_0: weight of starting compound, Δm_{exp}: relative experimental weight loss, experimental $\Delta m_{exp}/m_0$, calculated $\Delta m_{cal}/m_0$.

Compound	*T* / °C	m_0 / mg	Δm_{exp} / mg	$\Delta m_{exp}/m_0$ / %	$\Delta m_{cal}/m_0$ / %
$[MnBr_2(3\text{-}CNpy)_4]$		20.72	0	0	0
$[MnBr_2(3\text{-}CNpy)_2]_n$	156.9		6.54	31.54	32.99
$[MnBr_2(3\text{-}CNpy)_1]_n$	244.1		3.32	26.97	24.61
$MnBr_2$	306.4		3.30	30.43	32.66
$[FeBr_2(3\text{-}CNpy)_4]$		21.50	0	0	0
$[FeBr_2(3\text{-}CNpy)_2]_n$	197.4		6.83	31.76	32.94
$[FeBr_2(3\text{-}CNpy)_1]_n$	245.8		3.35	22.82	24.56
$FeBr_2$	318		2.79	24.56	32.55
$[CoBr_2(3\text{-}CNpy)_4]$		20.72	0	0	0
$[CoBr_2(3\text{-}CNpy)_2]_n$	198.8		6.61	31.90	32.78
$[CoBr_2(3\text{-}CNpy)_1]_n$	250.3		3.25	23.05	24.37
$CoBr_2$	313.63		2.37	21.90	32.24
$[NiBr_2(3\text{-}CNpy)_4]$		26.43	0	0	0
$[NiBr_2(3\text{-}CNpy)_2]_n$	217.8		8.32	31.52	32.77
$[NiBr_2(3\text{-}CNpy)_1]_n$	281.2		4.04	22.33	24.37
$NiBr_2$	346.8		3.92	27.88	32.22

Table S2. Crystallographic data of $[M^{II}Br_2(3\text{-}CNpy)_4]$.

	1a	**2a**	**3a**	**4a**
Compound	$[MnBr_2(3\text{-}CNpy)_4]$	$[FeBr_2(3\text{-}CNpy)_4]$	$[CoBr_2(3\text{-}CNpy)_4]$	$[NiBr_2(3\text{-}CNpy)_4]$
CSD number	1845140	1845149	1845152	1845162
Formula	$C_{24}H_{16}Br_2MnN_8$	$C_{24}H_{16}Br_2FeN_8$	$C_{24}H_{16}Br_2CoN_8$	$C_{24}H_{16}Br_2NiN_8$
Crystal system	Tetragonal	Tetragonal	Tetragonal	Tetragonal
Space group (No.)	*P*4*nc* (104)	*P* 4*nc* (104)	*P*4*nc* (104)	*P* 4*nc* (104)
MW /g·mol^{-1}	631.19	632.10	635.20	634.94
***a* /Å**	11.2178(5)	11.1484(2)	11.0587(4)	10.9722(9)
***c* /Å**	10.3309(6)	10.3205(2)	10.4149(5)	10.4600(3)
***V* /Å^3**	1300.0(3)	1282.7(1)	1273.7(1)	1259.3(2)
Z, Z'	2, 1/4	2, 1/4	2, 1/4	2, 1/4
Site symmetry of M^{II}	4	4	4	4
D_{calc} /Mg·m^{-3}	1.612	1.637	1.656	1.674
T /K	298	298	298	298
Radiation type	Cu $K\alpha_1$	Cu $K\alpha_1$	Cu $K\alpha_1$	Cu $K\alpha_1$
Wavelength /Å	1.54056	1.54056	1.54056	1.54056
$2\Theta_{max}$ /°	100	95	100	100
R_p /%	1.587	1.821	1.039	4.179
R_{wp} /%	2.038	2.315	1.335	5.366
R_{exp} /%	1.959	2.279	1.150	2.891
GOF	1.042	1.015	1.162	1.856
R_p' /% [a]	11.095	16.854	18.098	8.492
R_{wp}' /% [a]	8.292	10.980	12.177	9.616
R_{exp}' /% [a]	7.971	10.812	10.484	5.181
(a) R_{exp}', R_{wp}' and R_p' values are background corrected according to the reference [41].				

Table S3. Crystallographic data of $[M^{II}Br_2(3\text{-}CNpy)_2]_n$.

	1b	**2b**	**α-3b**	**β-3b**	**α-4b**	**β-4b**
Compound	$[MnBr_2(3\text{-}CNpy)_2]_n$	$[FeBr_2(3\text{-}CNpy)_2]_n$	$[CoBr_2(3\text{-}CNpy)_2]_n$	$[CoBr_2(3\text{-}CNpy)_2]_n$	$[NiBr_2(3\text{-}CNpy)_2]_n$	$[NiBr_2(3\text{-}CNpy)_2]_n$
CSD number	1845141	1845150	1845157	1845160	1845163	1845164
Formula	$C_{12}H_8Br_2MnN_4$	$C_{12}H_8Br_2FeN_4$	$C_{12}H_8Br_2CoN_4$	$C_{12}H_8Br_2CoN_4$	$C_{12}H_8Br_2NiN_4$	$C_{12}H_8Br_2NiN_4$
MW /g·mol^{-1}	422,96	423,87	426,95	426,95	426,71	426,71
Crystal system	Orthorhombic	Orthorhombic	Orthorhombic	Triclinic	Monoclinic	Triclinic
Space group (No.)	*P n n m* (58)	*P n n m* (58)	*P n n m* (58)	*P* $\bar{1}$ (2)	*C c* (9)	*P* $\bar{1}$ (2)
***a* /Å**	27.304(6)	27.128(5)	27.019(1)	3.727(5)	3.709(1)	3.727(4)
***b* /Å**	7.221(9)	7.172(2)	7.124(2)	13.629(6)	26.801(4)	13.574(9)
***c* /Å**	3.829(7)	3.788(1)	3.759(7)	13.868(6)	13.706(8)	13.761(6)
***α* /°**	90	90	90	87.37(7)	90	86.86(2)
***ß* /°**	90	90	90	82.34(4)	97.67(8)	82.40(1)
***γ* /°**	90	90	90	82.40(5)	90	82.12(1)
***V* /Å^3**	755.1(8)	737.0(2)	723.7(1)	697.2(2)	1350.5(8)	683.1(5)
Z, Z'	2, 1/4	2, 1/4	2, 1/4	2, 1	4, 1	2, 1
Site symmetry of M^{II}	2/*m*	2/*m*	2/*m*	$\bar{1}$, $\bar{1}$	1	$\bar{1}$, $\bar{1}$
***D*$_{calc}$ /Mg·m^{-3}**	1.860	1.910	1.959	2.034	2.099	2.075
T /K	298	298	298	298	125	298
Radiation type	Cu *Kα*$_1$	Cu *Kα*$_1$	Cu *Kα*$_1$	Cu *Kα*$_1$	Cu *Kα*$_1$	Cu *Kα*$_1$
Wavelength /Å	1.54056	1.54056	1.54056	1.54056	1.54056	1.54056
2Θ$_{max}$ /°	100	95	85 [a]	85 [a]	90	70
***R$_p$* /%**	2.095	1.315	1.388 [a]	1.388 [a]	3.547	3.277 [b]
***R$_{wp}$* /%**	2.694	1.674	1.823 [a]	1.823 [a]	5.026	4.294 [b]
***R$_{exp}$* /%**	2.231	1.484	1.286 [a]	1.286 [a]	2.753	2.473 [b]
GOF	1.208	1.127	1.417 [a]	1.417 [a]	1.825	1.737 [b]
***R$_p$'* /% [c]**	12.388	16.206	20.614 [a]	20.614 [a]	6.262	5.999 [b]
***R$_{wp}$'* /% [c]**	10.234	11.332	15.842 [a]	15.842 [a]	5.026	7.376 [b]
***R$_{exp}$'* /% [c]**	8.474	10.052	11.182 [a]	11.182 [a]	4.568	4.294 [b]
Pyridine stacking angle /° [d]	90	90	90	88.9(8)	86.7(3)	88.8(2)

(a) Rietveld refinement of a sample containing a mixture of α-phase (59.4%) and β-phase (41.6%).
(b) Rietveld refinement of a sample containing a mixture of α-phase (18.7%) and β-phase (81.3%).
(c) R_{exp}', R_{wp}' and R_p' values are background corrected according to the reference [41].
(d) Angle between the pyridine ring mean plane and the stacking direction
(for **1b** - **α-3b**: [001] and for **β-3b** - **β-4b** [100].)

Table S4. Crystallographic data of $[M^{II}Br_2(3\text{-}CNpy)_1]_n$.

	1c	2c	3c	4c
Compound	$[MnBr_2(3\text{-}CNpy)_1]_n$	$[FeBr_2(3\text{-}CNpy)_1]_n$	$[CoBr_2(3\text{-}CNpy)_1]_n$	$[NiBr_2(3\text{-}CNpy)_1]_n$
CSD number	1845142	1845151	1845161	1845165
Formula	$C_6H_4Br_2MnN_2$	$C_6H_4Br_2FeN_2$	$C_6H_4Br_2CoN_2$	$C_6H_4Br_2NiN_2$
MW /g·mol^{-1}	318.86	319.76	322.85	322.61
Crystal system	Monoclinic	Orthorhombic	Orthorhombic	Orthorhombic
Space group (No.)	*P* 1 1 2_1 [a] (4)	*P m c* 2_1 (26)	*P m c* 2_1 (26)	*P m c* 2_1 (26)
***a* /Å**	3.834(7)	3.772(2)	3.740(1)	3.701(5)
***b* /Å**	7.258(1)	7.251(2)	7.231(2)	7.204(8)
***c* /Å**	16.547(7)	16.31(1)	16.167(6)	16.000(4)
***α* /°**	90	90	90	90
***ß* /°**	90	90	90	90
***γ* /°**	93.41(1)	90	90	90
***V* /Å^3**	459.7(5)	446.1(8)	437.2(1)	426.7(1)
Z, Z'	2, 1	2, 1/2	2, 1/2	2, 1/2
Site symmetry of M	1	*m*	*m*	*m*
***D*$_{calc}$ /Mg·m^{-3}**	2.303	2.381	2.452	2.511
T /K	298	298	298	125
Radiation type	Cu *Kα*$_1$	Cu *Kα*$_1$	Cu *Kα*$_1$	Cu *Kα*$_1$
Wavelength /Å	1.54056	1.54056	1.54056	1.54056
2Θ$_{max}$ /°	80	100	100	100
***R*$_p$ /%**	1.696	1.633	1.506	2.715
***R*$_{wp}$ /%**	2.147	2.077	1.912	3.520
***R*$_{exp}$ /%**	1.695	1.714	1.555	2.757
GOF	1.266	1.212	1.230	1.277
***R*$_p$*'* /%** [b]	14.577	18.079	21.223	7.416
***R*$_{wp}$*'* /%** [b]	12.191	12.838	14.320	7.626
***R*$_{exp}$*'* /%** [b]	9.630	10.594	11.642	5.973

(a) For ease of comparison of 1c to 4c a non-standard space-group setting was used for 1c. *P* 112_1 is a non-standard setting of *P* 2_1.
(b) R_{exp}', R_{wp}' and R_p' values are background corrected according to the reference [41].

Text S1

Details on syntheses of [$M^{II}Br_2$(3-CNpy)$_4$]

Synthesis of [$MnBr_2$(3-CNpy)$_4$] (1a). $MnBr_2$ (0.5 g, 2.33mmol) was dissolved in 15mL ethanol, 3-cyanopyridine (0.96 g, 9.22 mmol) was dissolved in 35 mL ethanol. By mixing both solutions, a colorless powder was obtained. IR (cm^{-1}): 3091(w), 2241(m) 1595(s); 1470(s), 1418(s), 1039(s), 1032(s), 818(s), 691(s), 644(s).

Synthesis of [$FeBr_2$(3-CNpy)$_4$] (2a). $FeBr_2$ (0.2 g, 0.93 mmol) was dissolved in 15 mL ethanol, 3-cyanopyridine (0.96 g, 9.22 mmol) was dissolved in 35 mL ethanol. By mixing both solutions, a yellow powder was obtained. IR (cm^{-1}): 3092(w), 2241(m), 1595(s), 1468(s), 1418(s), 1042(m), 1034(m), 816(s), 691(s), 644(s).

Synthesis of [$CoBr_2$(3-CNpy)$_4$] (3a). $CoBr_2$ (0.5 g, 2.286 mmol) was dissolved in 30 mL methanol, 3-cyanopyridine (1g, 9.605mmol) was dissolved in 35 mL methanol. By mixing both solutions, a violett powder was obtained. IR(cm^{-1}): 3102(w), 2241(m), 1597(s), 1470(m), 1418(m), 1042(m), 1034(m), 816(s), 692(s), 646(s).

Synthesis of [$NiBr_2$(3-CNpy)$_4$] (4a). $NiBr_2$ (0.202 g, 0.924 mmol) was dissolved in 30 mL DAA, 3-cyanopyridine (0.4 g, 3.839 mmol) was dissolved in 35 mL DAA. By mixing both solutions, a light green powder was obtained. IR (cm^{-1}): 3103 (w), 2243(s) 1597(s); 1470(s), 1410(s), 1044(m), 1034(m), 816(s), 692(s), 648(m).

Text S2

Details on preparation of $[M^{II}Br_2(3\text{-}CNpy)_2]_n$

Preparation of $[MnBr_2(3\text{-}CNpy)_2]_n$ (1b). 1b was prepared by thermal decomposition of $[MnBr_2(3cypy)_4]$ (**1a**). A flesh-colored powder was obtained. IR (cm^{-1}): 3086(w), 2239(m), 1597(m), 1474(m), 1418(s), 1059(m), 1042(m), 800(s), 687(s), 648(s).

Preparation of $[FeBr_2(3\text{-}CNpy)_2]_n$ (2b). 2b was prepared by thermal decomposition of $[FeBr_2(3cypy)_4]$ (**2a**). A red powder was obtained and immediately transferred into a glass capillary (diameter: 0.5mm) that was sealed afterwards. IR (cm^{-1}): 3084(w), 2240(m), 1597(m), 1474(m), 1418(s), 1042(m), 799(s), 685(s), 650(s).

Preparation of $[CoBr_2(3\text{-}CNpy)_2]_n$ (3b). 3b was prepared by thermal decomposition of $[CoBr_2(3cypy)_4]$ (**3a**). A lilac powder was obtained. XRPD data revealed that this procedure generally leads to a mixture of **α-3b** and **β-3b**. A phase-pure sample of **α-3b** could not be obtained. Only once **β-3b** as pure phase could be obtained. IR(cm^{-1}) of the mixture: 3102(w), 2236(m), 1599(s), 1472(m), 1419(s), 1045(m), 810(s), 797(s) 685(s), 650(s).

Preparation of $[NiBr_2(3\text{-}CNpy)_2]_n$ (4b). α-4b and **β-4b** were prepared by thermal decomposition of $[NiBr_2(3cypy)_4]$ (**4a**). XRPD data revealed that this procedure generally leads to a mixture of **β-4b** with a slight amount of **α-4b**. **α-4b** as pure phase can be obtained by cooling the mixture to -100°C. Pure **β-4b** could not be obtained. IR(cm^{-1}) of the mixture: 3071(w), 2236(s), 1601(s), 1474(m), 1423(m), 1047(w), 1036(m) 808(s), 687(s).

Text S3

Details on preparation of $[M^{II}Br_2(3\text{-}CNpy)_1]_n$

Preparation of $[MnBr_2(3\text{-}CNpy)_1]_n$ (1c). 1c was prepared by thermal decomposition of $[MnBr_2(3cypy)_2]_n$ (**1b**). A light grey powder was obtained. IR (cm^{-1}): 3059(w), 2272(s), 1597(m), 1474(m), 1418(s), 1059(m), 1043(m), 800(s), 687(s), 648(s).

Preparation of $[FeBr_2(3\text{-}CNpy)_1]_n$ (2c). 2c was prepared by thermal decomposition of $[FeBr_2(3cypy)_2]_n$ (**2b**). An ochre powder was obtained. IR (cm^{-1}): 3061(w), 2278(s), 1680(s), 1595(m), 1541(m), 1460(m), 1417(s), 1049(m), 1034(m), 806(s), 682(w), 667(m).

Preparation of $[CoBr_2(3\text{-}CNpy)_1]_n$ (3c). 3c was prepared by thermal decomposition of $[CoBr_2(3cypy)_2]_n$ (**3b**). A light lilac powder was obtained. IR (cm^{-1}): 3102(w), 2287(m), 1622(s), 1603(s), 1573(w), 1481(m), 1422(s), 808(s), 687(m), 652(s).

Preparation of $[NiBr_2(3\text{-}CNpy)_1]_n$ (4c) was prepared by thermal decomposition of $[FeBr_2(3cypy)_4]$ (**4a**). A greyish ochre powder was obtained. IR (cm^{-1}): 3057(m), 2288(s), 1599(s), 1477(m), 1418(s), 1034(m) 797(s), 683(s), 654(m).

Text S4

Details on structure solutions

$[FeBr_2(3\text{-}CNpy)_1]_n$ (2c). The structure of **4c** was used as starting point for the Rietveld refinement. Reflections of an unknown foreign phase were excluded during Pawley and Rietveld refinement (2θ range from 11.51° to 11.85°, 12.40° to 12.71°, 24.30° to 24.54°).

$[CoBr_2(3\text{-}CNpy)_2]_n$ (α-3b/ β-3b). XRPD data were collected at room temperature**.** For **α-3b** 20 reflections in the low angle range were carefully selected for indexing, which led in an orthorhombic unit cell with $Z = 2$ and lattice parameters similar to those of compounds **1b** and **2b**. In the first Rietveld refinement reflections of **β-3b** were excluded. For the subsequent simultaneous refinement of both phases, the structure of **β-4b** was used as starting point for **β-3b**. The investigated sample contained 59.4 % of **α-3b** and 41.6 % of **β-3b**. The final crystallographic data of both phases were taken from the simultaneous refinement.

$[CoBr_2(3\text{-}CNpy)_1]_n$ (3c). The structure of **4c** was used as starting point for the Rietveld refinement. Reflections of an unknown foreign phase were excluded during Pawley and Rietveld refinement (2θ range from 11.675° to 11.93°, 12.52° to 12.83°).

$[NiBr_2(3\text{-}CNpy)_2]_n$ (α-4b). XRPD data of a phase-pure sample were collected at -150 °C.

$[NiBr_2(3\text{-}CNpy)_2]_n$ (β-4b). The structure of **α-4b** was used as a starting point for the structure solution of **β-4b**. The structure was solved by a fit to the room-temperature powder diagram (measured at room temperature) of the β-phase using the program FIDEL “Fit with deviating lattice parameters” [43], which uses a similarity index based on cross-correlation functions. Details will be published elsewhere [44]. The final Rietveld refinement revealed that the investigated sample contained 18.7 % of the α-phase and 81.3 % of the β-phase.

[MH3]

Coordination compounds built up from $M^{II}Cl_2$ and 3-cyanopyridine: double chains, single chains and isolated complexes.

Miriam Heine, Lothar Fink and Martin U. Schmidt, In: CrystEngComm, 2019, 21, 4305-4318.

CrystEngComm

PAPER

View Article Online
View Journal | View Issue

Cite this: *CrystEngComm*, 2019, **21**, 4305

Coordination compounds built up from $M^{II}Cl_2$ and 3-cyanopyridine: double chains, single chains and isolated complexes†

Miriam Heine, Lothar Fink and Martin U. Schmidt*

The coordination polymers $[M^{II}Cl_2(3\text{-CNpy})_2]_n$, with 3-CNpy = 3-cyanopyridine and M^{II} = Mn, Fe, Co, Ni, Cu, Zn (**1a–6a**), were synthesised and the related structures determined by X-ray powder diffraction (XRPD). In **1a–5a** the metal atoms are octahedrally coordinated by four chlorine atoms and two 3-CNpy ligands. The Cl atoms are bridging two M atoms, leading to infinite $[M^{II}Cl_2]_n$ chains. The 3-CNpy molecules coordinate through their pyridine N atoms (N_{py}) and form lateral "wings" on the chains. Upon heating to 230–290 °C, compounds **1a–5a** release half of the organic ligands and transform into $[M^{II}Cl_2(3\text{-CNpy})_1]_n$ (**1b–5b**). The crystal structures of **1b** and **3b–5b** were also determined from X-ray powder data. Compounds **1b** and **3b–5b** are built up by double chains of $[M_2^{II}Cl_4]_n$ units. Each metal atom is coordinated by two μ_2- and three μ_3-bridging chlorine atoms and one 3-CNpy ligand. In none of the investigated compounds does the 3-CNpy molecule act as a bridging ligand, which is in contrast to $[M^{II}Br_2(3\text{-CNpy})_1]_n$. The compound $[Zn^{II}Cl_2(3\text{-CNpy})_2]$ shows two polymorphic forms (**α-6a** and **β-6a**). In both polymorphs, the Zn atoms are tetrahedrally coordinated by two chlorine atoms and two 3-CNpy ligands to form discrete complexes. Upon heating to 290 °C, **α-6a** and **β-6a** decompose into $ZnCl_2$ and 3-CNpy without forming intermediate phases. In all compounds, the coordination mode of the 3-CNpy ligand was investigated by IR spectroscopy.

Received 20th March 2019,
Accepted 15th May 2019

DOI: 10.1039/c9ce00412b

rsc.li/crystengcomm

1. Introduction

In recent years the investigation of coordination polymers based on transition metals and organic linkers has taken an upward trend. Such inorganic–organic hybrid compounds offer various useful physical properties suitable for catalysis, molecular recognition, gas adsorption and separation.[1] In order to prepare new compounds with the desired properties, structure–property relationships have to be examined in detail. In the last few years a number of coordination polymers built up from transition metal halides (or pseudohalides) and heteroaromatic ligands have been investigated.[2] We focused on the systematic preparation and structural characterisation of coordination compounds with the neutral N-donor ligands pyridine (py), 4-cyanopyridine (4-CNpy) and 3-cyanopyridine (3-CNpy).[3–6] Cyanopyridines contain two nitrogen donors, the N_{py} and the N_{CN} atom. They can therefore generally act as a bridge to connect two metal atoms, making novel structural topologies accessible. However, in most compounds cyanopyridine molecules act as monodentate ligands coordinating with the N_{py} atom only, because the Lewis-base character and donating ability of the N_{py} atom is considerably higher than that of the N_{CN} atom. Therefore, structures with bridging cyanopyridine groups are rarely found.[7–21] The Cambridge Structural Database (CSD)[14,15] contains about 60 crystal structures with terminal 3-CNpy and about 190 structures with terminal 4-CNpy, in which the N_{py} atom coordinates to a transition metal atom. In only 15 structures, 3- or 4-CNpy acts as a bidentate ligand bridging two metal atoms *via* its N atoms. Among these few structures are only 7 polymeric compounds. We reported recently the syntheses and crystal structures of $[M^{II}Cl_2(4\text{-CNpy})_1]_n$ (M = Mn, Ni), $[NiBr_2(4\text{-CNpy})_1]_n$[6] and $[M^{II}Br_2(3\text{-CNpy})_1]_n$ (M = Mn, Fe, Co, Ni).[3] The compounds $[M^{II}Br_2(3\text{-CNpy})_1]_n$ are even considered to be the first ones with 3-cyanopyridine as a linker between two 3d M^{2+} ions. They can be prepared by thermal decomposition of $[M^{II}Br_2(3\text{-CNpy})_4]$ *via* $[M^{II}Br_2(3\text{-CNpy})_2]_n$. In all compounds $[M^{II}X_2(CNpy)_x]_n$ (M^{II} = Mn, Fe, Co, Ni; X = Cl, Br) with x = 1 or 2, the metal atoms are connected to the neighbouring metal atoms by two μ-bridging Cl or Br atoms, leading to $[M^{II}X_2]_n$ chains (Scheme 1). For x = 2 with X = Br, single chains are built up, in which cyanopyridine acts as a terminal, *i.e.* monodentate, ligand (Scheme 1a). For x = 1 with X = Br, cyanopyridine acts as a bidentate ligand connecting two

Institute of Inorganic and Analytical Chemistry, Goethe University, Max-von-Laue-Str. 7, 60438 Frankfurt am Main, Germany.
E-mail: m.schmidt@chemie.uni-frankfurt.de; Fax: +49 69 798 29235; Tel: +49 69 798 29171

† Electronic supplementary information (ESI) available. See DOI: 10.1039/c9ce00412b

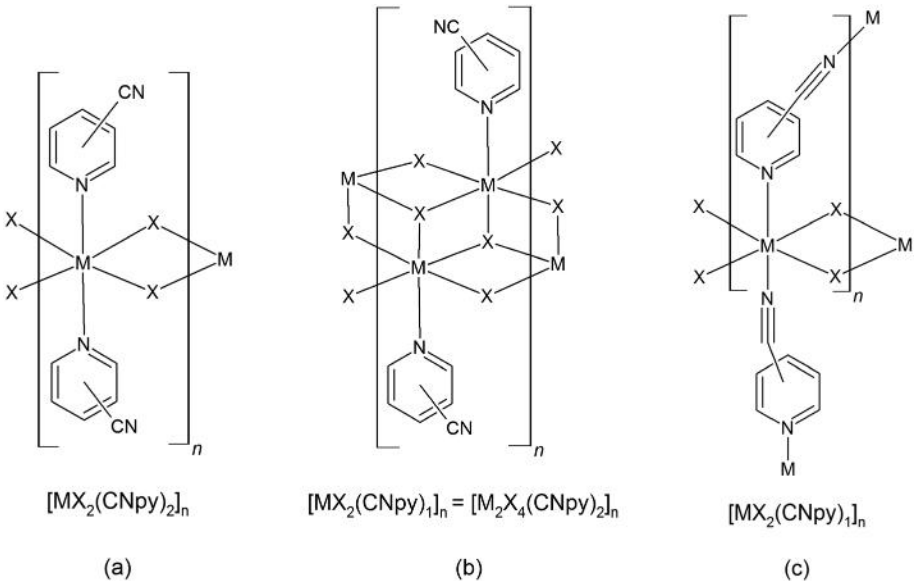

Scheme 1 Connectivity patterns of cyanopyridine compounds $[MX_2(CNpy)_2]_n$ and $[MX_2(CNpy)_1]_n$ with M = Mn, Fe, Co, Ni, Cu and X = Cl, Br. (a) Single chains, (b) double chains and (c) bridging organic ligands.

neighbouring $[M^{II}Br_2]_n$ chains, thus forming two-dimensional networks (Scheme 1c). Astonishingly, in the corresponding chloro compounds with x = 1, two different structure types can be observed: (1) a two-dimensional network (*e.g.* in $[MnCl_2(4\text{-}CNpy)_1]_n$, Scheme 1c) or (2) polymeric double chains (*e.g.* in $[CuCl_2(4\text{-}CNpy)_1]_n$): here two $[CuCl_2]_n$ chains are fused by μ_3-chlorine atoms leading to $[Cu_2Cl_4]_n$ chains, and 4-CNpy is a terminal ligand only (Scheme 1b and Table 1).

Thus the question rose: which structures will be observed for the corresponding 3-CNpy compounds with X = Cl and x = 1? Will they show two-dimensional networks, similar to $[M^{II}Br_2(3\text{-}CNpy)_1]_n$? Or will they exhibit polymeric double chains similar to $[CuCl_2(4\text{-}CNpy)_1]_n$?

The compounds $[M^{II}Cl_2(3\text{-}CNpy)_1]_n$, with M = Mn, Fe, Co, Ni, Cu (**1b–5b**), have not been described before. We prepared these materials by thermal decomposition of $[M^{II}Cl_2(3\text{-}CNpy)_2]_n$ (**1a–5a**).[22] The crystal structures of **1a–5a** are hitherto unpublished too, except for M = Cu (**5a**). Additionally, the corresponding zinc compound (**6a**) was synthesized and investigated. All obtained phases **1a–6a** and **1b–5b** are micro- or nanocrystalline powders. They are sensitive to moisture and react easily with water and polar solvents. In non-polar solvents they are insoluble. Hence, recrystallisation was not possible and all structures (except **2b**) were determined from X-ray powder diffraction (XRPD) data. IR spectroscopy was used to determine whether the cyano group coordinates to a metal atom.[22,23]

2. Results and discussion

2.1 Synthesis from solution and by thermal decomposition

Synthesis of $[M^{II}Cl_2(3\text{-}CNpy)_2]_n$ (1a–6a). The compounds $[M^{II}Cl_2(3\text{-}CNpy)_2]_{(n)}$ (M = Mn, Fe, Co, Ni, Cu, Zn; **1a–6a**) were synthesised using 3-cyanopyridine and the corresponding $M^{II}Cl_2$ (hydrate) in an alcoholic solution. Various stoichiometric ratios of the reactants were used. In the case of the corresponding bromine series this synthetic route leads to the formation of compounds $[M^{II}Br_2(3\text{-}CNpy)_4]$ with a metal-to-ligand ratio of 1 : 4. However, in the chlorine series all experiments led to compounds of the composition $[M^{II}Cl_2(3\text{-}CNpy)_2]_{(n)}$ with a metal-to-ligand ratio of 1 : 2. More ligand-rich phases, *e.g.* $[M^{II}Cl_2(3\text{-}CNpy)_4]$, were never observed. The formation of a coordination octahedron $[M^{II}Cl_2(CNpy)_4]$ seems to be hindered as the N-donating ligand forces a relatively short M^{II}–N bond. An elongation of the metal–chlorine bond would be necessary; this seems to be energetically unfavoured.

Thermal behaviour of 1a–6a. The thermal behaviour of **1a–5a**, **α-6a** and **β-6a** was investigated by a combined differential thermal and thermogravimetric analysis (DTA–TG). Upon heating $[M^{II}Cl_2(3\text{-}CNpy)_2]_{(n)}$ in a thermobalance to 400 °C, several well-separated mass loss steps are observed, which reveal the existence of compounds with a lower metal-to-ligand ratio.[24] The thermogravimetry (TG) curve of $[MnCl_2(3\text{-}CNpy)_2]_n$ (**1a**) exhibits three steps of weight loss (Fig. 1 and

Table 1 Topology of crystal structures of the type $[M^{II}X_2(CNpy)_1]_n$

$[M^{II}X_2(CNpy)_1]_n$	3-CNpy	4-CNpy
X = Cl	Double chains (Scheme 1b)	Double chains (Scheme 1b) for M = Cu Network (Scheme 1c) for M = Mn, Fe, Ni
X = Br	Network (Scheme 1c) for M = Mn, Fe, Co, Ni	Network (Scheme 1c) for M = Mn, Fe, Co, Ni

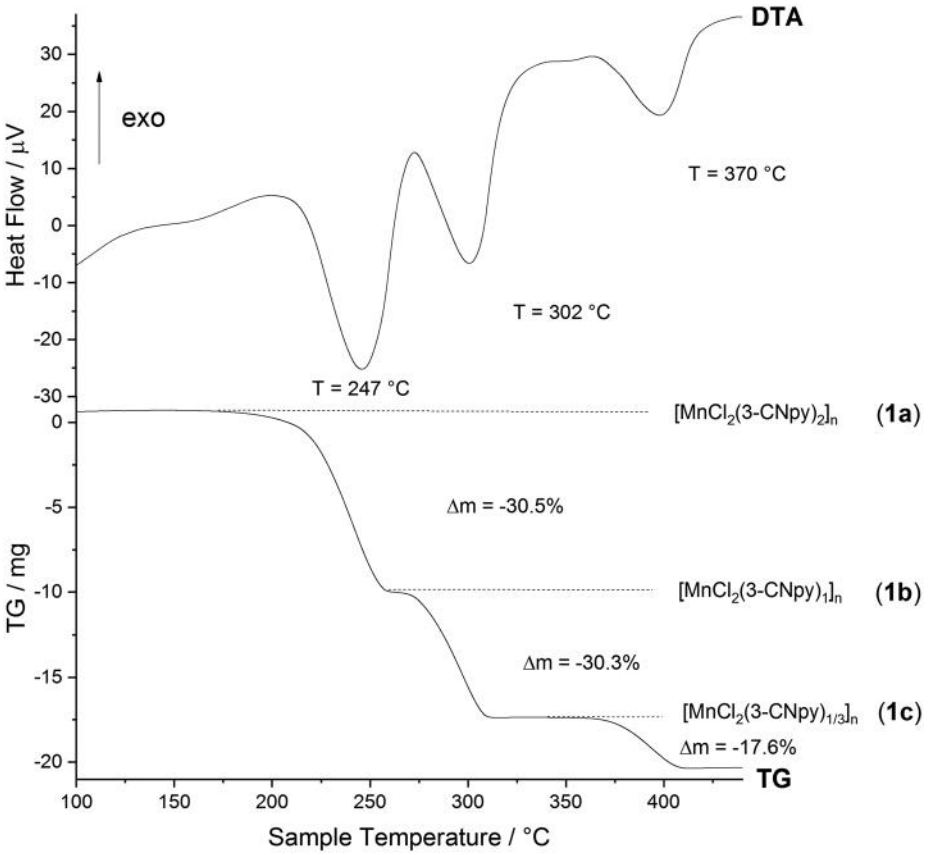

Fig. 1 DTA/TG curve of $[MnCl_2(3\text{-CNpy})_2]_n$ (**1a**) showing the decomposition of **1a** *via* **1b** and *via* **1c** to $MnCl_2$.

Table S1 in the ESI†), which correspond to the endothermic signals in the differential thermoanalysis (DTA) curve. The first endothermic signal at 247 °C is assigned to the liberation of half of the 3-CNpy ligands to form $[MnCl_2(3\text{-CNpy})_1]_n$ (**1b**), according to eqn (1). The second endothermic signal at 302 °C is attributed to the decomposition of this intermediate compound to form $[MnCl_2(3\text{-CNpy})_{1/3}]_n$ (**1c**), according to eqn (2). The remaining 3-CNpy is released in the third decomposition step at 370 °C, leaving $MnCl_2$, according to eqn (3).

$$[MnCl_2(3\text{-CNpy})_2]_n \rightarrow [MnCl_2(3\text{-CNpy})_1]_n + n\ 3\text{-CNpy} \quad (1)$$

$$[MnCl_2(3\text{-CNpy})_1]_n \rightarrow [MnCl_2(3\text{-CNpy})_{1/3}]_n + 2/3n\ 3\text{-CNpy} \quad (2)$$

$$[MnCl_2(3\text{-CNpy})_{1/3}]_n \rightarrow MnCl_2 + 1/3n\ 3\text{-CNpy} \quad (3)$$

For the 1 : 2 compounds **1a–5a**, the corresponding 1 : 1 compounds are available (**1b–5b**). As in the manganese series (Fig. 1), the DTA–TG results of the cobalt series point to the formation of $[CoCl_2(3\text{-CNpy})_{1/3}]_n$ (**3c**). In contrast, the DTA–TG results of the iron and copper series point to the formation of $[FeCl_2(3\text{-CNpy})_{1/2}]_n$ (**2c**) and $[CuCl_2(3\text{-CNpy})_{1/2}]_n$ (**5c**), respectively (Table S1 in the ESI†). However, the determination of the chemical composition of a coordination polymer from TG data at 250–400 °C bears some uncertainties and the given stoichiometry of **2c** and **3c** should be regarded with caution.

For the iron compounds, the decomposition temperatures are 243 °C (formation of **1b**), 320 °C (**1c**) and 373 °C ($FeCl_2$); for the cobalt compounds, 238 °C (**3b**), 293 °C (**3c**) and 362 °C ($CoCl_2$); for the nickel compounds, 296 °C (**4b**) and 369 °C ($NiCl_2$); and for the copper compounds, 275 °C (**5b**), 303 °C (**5c**) and 323 °C ($CuCl/CuCl_2$). The two polymorphs of the Zn compound, **α-6a** and **β-6a**, decompose at around 187 °C directly into $ZnCl_2$ without any hint of intermediate compounds with $x < 2$ (Table S1 in the ESI†).

Synthesis of $[M^{II}Cl_2(3\text{-CNpy})_1]_n$ (1b–5b). Samples of $[M^{II}Cl_2(3\text{-CNpy})_1]_n$ (**1b–5b**) were prepared by thermal decomposition of the corresponding precursors $[M^{II}Cl_2(3\text{-CNpy})_2]_n$ (**1a–5a**) at appropriate temperatures in the thermogravimetric device and subsequently cooled to room temperature. The resulting powders were used for IR and XRPD measurements without any further treatment. Details on the syntheses and the IR and XRPD measurements are given in the Experimental section. Despite various preparation trials, **1b** and **5b** could not be obtained as pure phases. The powders were always obtained as mixtures (**1b**: with **1a** or **1c**, **5b**: with **5a** or **5c**). Hence, their crystal structures had to be determined from phase mixtures. Unfortunately, the powder of **2b** was always of limited crystallinity and not phase pure (Fig. S29 in the ESI†). Neither was it possible to decide whether **2b** is isotypic to **1b** and **3b–5b**; hence the structure solution of **2b** failed.

Table 2 Characteristic asymmetric stretching vibrations ν_{as}(C≡N) for 3-cyanopyridine, 4-cyanopyridine and their coordination polymers

	Compound	ν_{as}(C≡N) [cm^{-1}]	Bonding mode
	3-Cyanopyridine and its compounds		
	3-Cyanopyridine	2230–2232	Free ligand
	Compounds with a metal–ligand ratio of 1 : 2		
X = Cl	$[MnCl_2(3\text{-CNpy})_2]_n$ (**1a**)	2236	Terminal ligand
	$[FeCl_2(3\text{-CNpy})_2]_n$ (**2a**)	2237	Terminal ligand
	$[CoCl_2(3\text{-CNpy})_2]_n$ (**3a**)	2238	Terminal ligand
	$[NiCl_2(3\text{-CNpy})_2]_n$ (**4a**)	2237	Terminal ligand
	$[CuCl_2(3\text{-CNpy})_2]_n$ (**5a**)	2237	Terminal ligand
	$[ZnCl_2(3\text{-CNpy})_2]_n$ (α-/β-**6**)	2242	Terminal ligand
X = Br	$[M^{II}Br_2(3\text{-CNpy})_2]_n$	2236–2239	Terminal ligand
	Compounds with a metal–ligand ratio of 1 : 1		
X = Cl	$[MnCl_2(3\text{-CNpy})_1]_n$ (**1b**)[a]	2236	Terminal ligand
	$[CoCl_2(3\text{-CNpy})_1]_n$ (**3b**)	2237	Terminal ligand
	$[NiCl_2(3\text{-CNpy})_1]_n$ (**4b**)	2238	Terminal ligand
	$[CuCl_2(3\text{-CNpy})_1]_n$ (**5b**)[b]	2237	Terminal ligand
X = Br	$[M^{II}Br_2(3\text{-CNpy})_1]_n$	2275–2288	Bridging ligand
	4-Cyanopyridine and its compounds		
	4-Cyanopyridine	2238–2240	Free ligand
	Compounds with a metal–ligand ratio of 1 : 2		
X = Cl	$[M^{II}Cl_2(4\text{-CNpy})_2]_n$	2241–2242	Terminal ligand
X = Br	$[M^{II}Br_2(4\text{-CNpy})_2]_n$	2234–2235	Terminal ligand
	Compounds with a metal–ligand ratio of 1 : 1		
X = Cl	$[CuCl_2(4\text{-CNpy})_1]_n$	2243	Terminal ligand
	$[M^{II}Cl_2(4\text{-CNpy})_1]_n$	2275–2288	Bridging ligand
X = Br	$[M^{II}Br_2(4\text{-CNpy})_1]_n$	2281–2298	Bridging ligand

[a] Phase mixture with **1b** as dominant phase. [b] Phase mixture with **5b** as dominant phase.

2.2 Investigation of the coordination of the cyano group by FT-IR

Infrared (IR) spectroscopy is a useful tool to check whether the cyano group of an aromatic compound coordinates to a metal atom (see Table 2). If the 3-CNpy ligand coordinates through its N_{py} atom, but not through its cyano group, then the asymmetric stretching vibration ν_{as}(C≡N) is expected to have a value similar to that of the free 3-cyanopyridine

Table 3 Crystallographic data of $[M^{II}Cl_2(3\text{-CNpy})_2]_n$ (**1a**–**5a**)

	1a	2a	3a	4a	5a	5a-SXRD[25]
Compound	$[MnCl_2(3\text{-CNpy})_2]_n$	$[FeCl_2(3\text{-CNpy})_2]_n$	$[CoCl_2(3\text{-CNpy})_2]_n$	$[NiCl_2(3\text{-CNpy})_2]_n$	$[CuCl_2(3\text{-CNpy})_2]_n$	$[CuCl_2(3\text{-CNpy})_2]_n$
CCDC number/CSD code	1904113	1904107	1904105	1904110	1904106	UTIHAH
Structure determined from	Powder	Powder	Powder	Powder	Powder	Single crystal
Formula	$C_{12}H_8Cl_2MnN_4$	$C_{12}H_8Cl_2FeN_4$	$C_{12}H_8Cl_2CoN_4$	$C_{12}H_8Cl_2NiN_4$	$C_{12}H_8Cl_2CuN_4$	$C_{12}H_8Cl_2CuN_4$
Crystal system	Monoclinic	Monoclinic	Monoclinic	Monoclinic	Monoclinic	Monoclinic
Space group (no.)	$P2_1/c$ (14)	$P2_1/c$ (14)	Cc (9)	Cc (9)	$P2_1/c$ (14)	$P2_1/c$ (14)
a/Å	3.7030(4)	3.6440(2)	3.6186(2)	3.5837(3)	3.7560(1)	3.710(2)
b/Å	15.4310(4)	13.8135(8)	27.504(2)	27.2889(3)	13.4653(3)	13.420(4)
c/Å	11.5780(3)	13.1192(11)	13.2081(12)	13.1815(3)	13.0443(5)	12.987(2)
α/°	90	90	90	90	90	90
β/°	91.438(2)	98.532(7)	97.49(2)	97.715(4)	97.347(3)	97.48[a]
γ/°	90	90	90	90	90	90
V/Å^3	661.3(6)	653.0(8)	1302.6(9)	1277.4(2)	654.3(4)	641.0(9)
Z, Z'	2, 1/2	2, 1/2	4, 1	4, 1	2, 1/2	2, 1/2
Site symmetry of M^{II}	$\bar{1}$	$\bar{1}$	1	1	$\bar{1}$	$\bar{1}$
T/K	298	298	298	298	298	123
Radiation type	Cu Kα_1	Mo Kα_1	Mo Kα_1	Cu Kα_1	Cu Kα_1	Mo Kα

[a] For the monoclinic angle, no standard deviation is given in ref. 25.

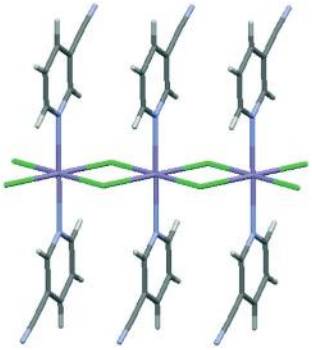

Fig. 2 Part of a $[MnCl_2(3\text{-CNpy})_2]_n$ chain (**1a**). Color code: Mn rose, Cl green, N blue, C grey, H white.

molecule (2230–2232 cm^{-1}). For a bidentate 3-CNpy ligand coordinating through its N_{py} and N_{CN} atoms, the asymmetric stretching vibration ν_{as}(C≡N) would be shifted to higher values of about 2275–2298 cm^{-1}, as is observed for $[M^{II}Br_2(3\text{-CNpy})_1]_n$[3] and also for bridging 4-CNpy ligands.[6] In all compounds of the type $[M^{II}Cl_2(3\text{-CNpy})_2]_n$ (**1a–5a**, α-**6a** and β-**6a**), the ν_{as}(C≡N) frequency is similar to that of the analogous bromine compounds, $[M^{II}Br_2(3\text{-CNpy})_2]_n$, with 3-CNpy as terminal ligand. For compounds of the type $[M^{II}Cl_2(3\text{-CNpy})_1]_n$ (**1b** and **3b–5b**) the values of ν_{as}(C≡N) remain almost unchanged, too, clearly indicating that 3-CNpy coordinates exclusively through the N_{py} atom. This reveals that 3-CNpy does not form a bridge between two metal atoms, which is in contrast to the bromine compounds $[M^{II}Br_2(3\text{-CNpy})_1]_n$, which form two-dimensional networks. For **2b** no measurement was run because we could not obtain a reliable sample.

2.3 Crystal structures of $[M^{II}Cl_2(3\text{-CNpy})_2]_n$ with M = Mn, Fe, Co, Ni, Cu (1a–5a)

The crystal structures of **1a–5a** were determined from XRPD data. Rietveld plots for **1a–5a** are shown in Fig. S16–S20 (ESI†). Table 3 shows the main crystallographic data of **1a–5a**. Further details are given in Table S2 – Part 1 (ESI†). In 2011, the crystal structure of **5a** was determined by Chen *et al.* from single crystal X-ray diffraction data (SXRD) at 123 K.[25] Room temperature data have not been published. In order to compare the crystal structure of **5a** with the structures of **1a–4a**, which were determined at room temperature, we redetermined the structure of **5a** at room temperature from powder data, too. The single crystal data of **5a** are included in Table 3. All samples of **1a–5a** were investigated for phase purity and polymorphism using XRPD. Only one phase was observed for each.

Compounds **1a–5a** crystallise in monoclinic space groups. The cobalt (**3a**) and nickel (**4a**) compounds are isotypic and crystallise in the centered space group *Cc* with $Z = 4$. All other compounds (**1a**, **2a**, **5a**) crystallise in $P2_1/c$ with $Z = 2$. Astonishingly the iron compound (**2a**) is isostructural with the copper compound (**5a**) but not with the cobalt and nickel compounds (**3a** and **4a**). The manganese structure (**1a**) is neither similar to **2a** and **5a** nor to **3a** and **4a**.

In all of the structures $[M^{II}Cl_2(3\text{-CNpy})_2]_n$ (**1a–5a**) the metal ions are octahedrally coordinated by four chlorine atoms and two 3-CNpy ligands, coordinating with their N_{py} atom each. The metal atoms are connected through μ_2-bridging chlorine atoms, resulting in a linear $[M^{II}Cl_2]_n$ chain (Fig. 2). All chains are parallel to the [100] direction. The metal–metal distances within these chains range from 3.5837(3) Å (for **4a**) to 3.7560(1) Å (for **5a**) and correspond to the lattice parameter *a* in each structure (Table 3). The pyridine rings occupy the *trans*-positions of the connected $[M^{II}Cl_2]_n$ blocks and stick nearly perpendicular to the chain (Fig. 2 and Table 4). Neighbouring 3-CNpy ligands are parallel to each other and connected through π–π-interactions. The centre-to-centre distance between two 3-CNpy rings is equivalent to the metal–metal distance and to the lattice parameter *a*. This allows a good π–π-stacking within the chain.

In all structures the chains are arranged in a herringbone packing motif (Fig. 3). The cyano groups of neighbouring chains are orientated antiparallel to optimize the electrostatic interactions of the dipoles.

In compounds **3a** and **4a** two of four neighbouring chains are shifted by $x = 0.5$ in the chain direction (Fig. 4b), resulting in an AABBAA… stacking along [010]. In contrast, in **1a**, **2a** and **5a** the chains are not shifted, leading to an AAAA… stacking (Fig. 4a and c).

The herringbone packing motif is typical for coordination polymers of the composition $[M^{II}X_2(CNpy)_2]_n$ (X = Cl, Br; M =

Table 4 Selected bond lengths and angles in compounds $[M^{II}Cl_2(3\text{-CNpy})_2]_n$ (**1a–5a**). The given standard deviations are those resulting from the Rietveld refinement. The actual accuracy is much lower

	1a	2a	3a	4a	5a
M^{II}	Mn	Fe	Co	Ni	Cu
M–N_{py}(1)/Å	2.302(3)	2.279(5)	2.094(11)	2.060(7)	2.057(2)
M–N_{py}(2)/Å	2.302(3)	2.279(5)	2.226(11)	2.153(7)	2.057(2)
M–Cl(1)/Å	2.503(2)	2.482(4)	2.273(13)	2.430(10)	2.338(2)
M–Cl(2)/Å	2.503(2)	2.482(4)	2.441(15)	2.439(12)	2.338(2)
M–Cl(3)/Å	2.544(2)	2.535(4)	2.482(15)	2.455(12)	2.926(2)
M–Cl(4)/Å	2.544(2)	2.535(4)	2.750(18)	2.493(10)	2.926(2)
Pyridine stacking angle δ/°[a]	88.3	87.0	84.8/88.2[b]	84.3/85.4[b]	85.9

[a] Angle between the pyridine ring mean plane and the chain direction; see Fig. 5b. [b] Structures **3a** and **4a** contain two symmetrically independent 3-CNpy rings each.

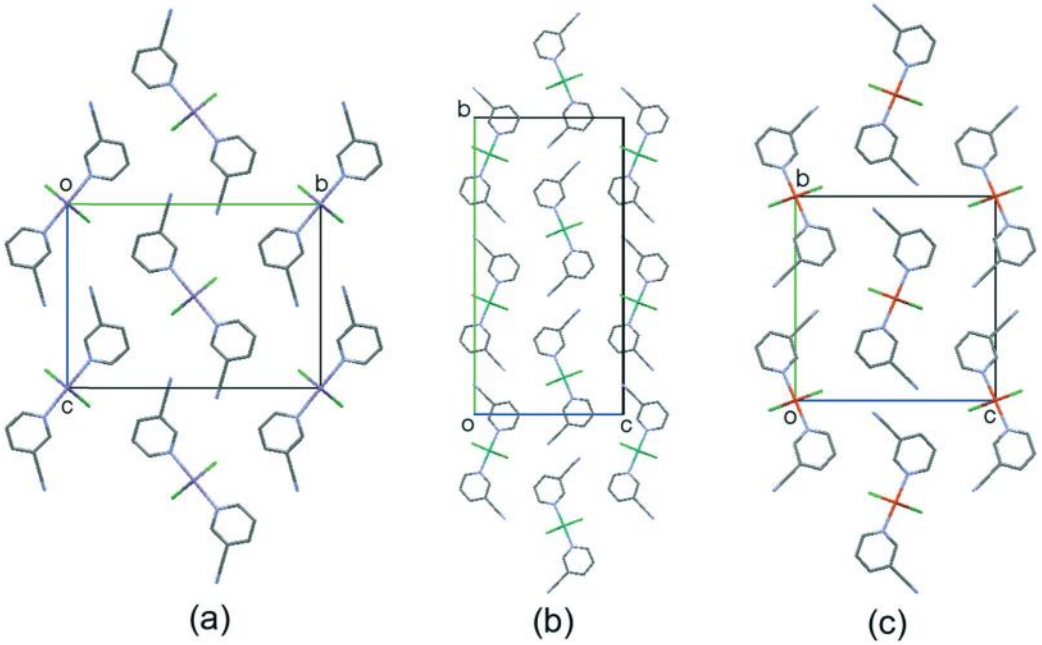

Fig. 3 Herringbone packing motifs of (a) $[MnCl_2(3\text{-}CNpy)_2]_n$ (**1a**), (b) $[NiCl_2(3\text{-}CNpy)_2]_n$ (**4a**) and (c) $[CuCl_2(3\text{-}CNpy)_2]_n$ (**5a**). View direction [$\bar{1}$00]. Color code: Mn rose, Ni dark green, Cu red, Cl light green, N blue, C grey. H atoms are omitted for clarity.

Mn, Fe, Co, Ni, Cu) with CNpy = 3-CNpy or 4-CNpy.[3–6] However, there are small differences between the structures because of the nature of the halogen atom. In the bromine compounds, there is more space for the organic ligand available, resulting in large π–π distances between the cyanopyridine fragments along the chain. Consequently, in the Br series, the 3-CNpy or 4-CNpy ligands can easily be orientated exactly perpendicular to the chain direction.

In the bromo structures, neighbouring cyanopyridine groups along the chain are exactly on top of each other. This allows a crystallographic mirror plane *m* through the cyanopyridine molecules, as shown in Fig. 5a. Together with the

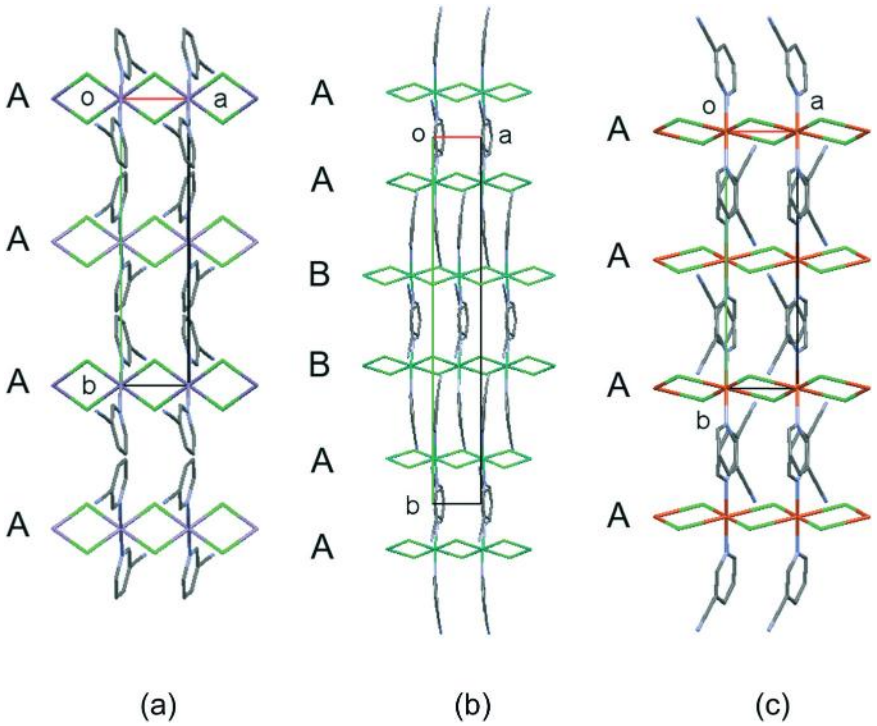

Fig. 4 Crystal structures of (a) $[MnCl_2(3\text{-}CNpy)_2]_n$ (**1a**), (b) $[NiCl_2(3\text{-}CNpy)_2]_n$ (**4a**) and (c) $[CuCl_2(3\text{-}CNpy)_2]_n$ (**5a**). View direction [00$\bar{1}$]. The stacking sequences are highlighted with capital letters. Color code: Mn rose, Ni dark green, Cu red, Cl light green, N blue, C grey. H atoms are omitted for clarity.

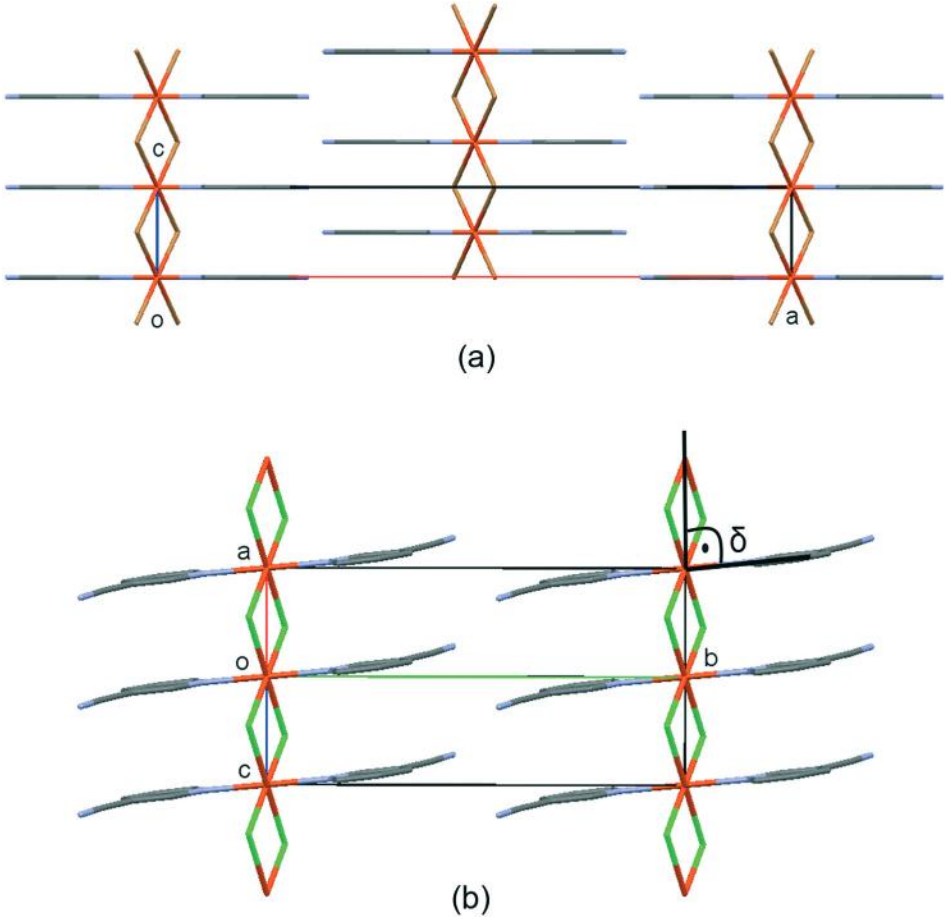

Fig. 5 Effect of the halogen size on the geometry of the chains in $[FeX_2(3\text{-CNpy})_2]_n$, (a) X = Br,[3] view direction [010]; (b) X = Cl, view direction [101], only two chains are shown. The pyridine stacking angle (Table 4) is indicated as δ. Color code: Fe orange, Cl green, Br brown, N blue, C grey. H atoms are omitted for clarity.

inversion symmetry of the chains, the chains gain $\not{p}112/m$ symmetry (rod group No. 11[26]) and indeed $[M^{II}Br_2(3\text{-CNpy})_2]_n$ (with M = Mn, Fe, Co)[3] and $[M^{II}Br_2(4\text{-CNpy})_2]_n$ (with M = Co, Ni)[6] crystallise in the space group $P2_1/n2_1/n2/m$, $Z = 2$ with the metal atom on a $2/m$ site.

In the corresponding chlorine compounds the shorter M···M distances do not allow this arrangement of the cyanopyridine groups. Consequently, the cyanopyridine moieties bend and tilt away from this plane in order to allow a more dense π–π-stacking along the chains (Fig. 5b). Thus, the angle δ between

Table 5 Crystallographic data of $[ZnCl_2(3\text{-CNpy})_2]$ (α-6a, β-6a)

Compound	α-6a $[ZnCl_2(3\text{-CNpy})_2]$	β-6a $[ZnCl_2(3\text{-CNpy})_2]$	$[ZnBr_2(3\text{-CNpy})_2]$[28]	$[ZnCl_2(py)_2]$[29]
CCDC number/CSD code	1904111	1904112	QAHZAC	ZNPYRC01
Structure determined from	Powder	Powder	Single crystal	Single crystal
Formula	$C_{12}H_8Cl_2ZnN_4$	$C_{12}H_8Cl_2ZnN_4$	$C_{12}H_8Br_2ZnN_4$	$C_{10}H_{10}Cl_2ZnN_2$
Crystal system	Orthorhombic	Monoclinic	Orthorhombic	Monoclinic
Space group (no.)	*Pnma* (62)	$P2_1/c$ (14)	*Pbca* (61)	$P2_1/c$ (14)
a/Å	10.6653(3)	11.6619(15)	8.5600(4)	8.580(3)
b/Å	20.3998(5)	15.0731(18)	14.5379(5)	17.677(1)
c/Å	6.6114(17)	8.0572(10)	23.3751(9)	8.397(5)
α/°	90	90	90	90
β/°	90	91.0112(9)	90	101.42(4)
γ/°	90	90	90	90
V/Å^3	1438.4(6)	1416.0(7)	2908.9(2)	1248.3(5)
Z, Z'	4, 1/2	4, 1	8, 1	4, 1
Site symmetry of M^{II}	*.m.*	1	1	1
T/K	298	298	120	295
Radiation type	Cu Kα_1	Cu Kα_1	Mo Kα	Mo Kα

Table 6 Selected bond lengths and bond angles in $[ZnX_2(py)_2]$ compounds. The given standard deviations of α-**6a** and β-**6a** are those resulting from the Rietveld refinement. The actual accuracy is much lower

Compound	α-$[ZnCl_2(3\text{-}CNpy)_2]$ α-**6a**	β-$[ZnCl_2(3\text{-}CNpy)_2]$ β-**6a**	$[ZnBr_2(3\text{-}CNpy)_2]$[28]	$[ZnCl_2(py)_2]$[29]	$[ZnCl_2(4\text{-}CNpy)_2]$[30]
Structure determined from	Powder	Powder	Single crystal	Single crystal	Single crystal
Zn^{II}–N_{py}/Å	2.099(3)	2.038(3)	2.061(3)	2.046(5)	2.059(5)
Zn^{II}–N_{py}/Å	2.099(3)	2.051(3)	2.072(3)	2.052(6)	2.069(6)
Zn^{II}–X/Å	2.148(4)	2.177(3)	2.3369(5)	2.215(2)	2.207(2)
Zn^{II}–X/Å	2.175(4)	2.187(3)	2.3471(5)	2.228(2)	2.218(2)
N_{py}–Zn^{II}–N_{py}/°	97.3(2)	108.51(11)	100.85(11)	106.3(2)	105.0(2)
X–Zn^{II}–X/°	119.5(2)	124.87(11)	121.841(19)	120.9(1)	125.7(1)

the pyridine ring mean plane and the stacking direction deviates from 90° (Table 4). This deviation breaks the mirror symmetry; the symmetry is reduced and the lattice becomes monoclinic. In the case of $[FeCl_2(3\text{-}CNpy)_2]_n$, this results in the space group $P12_1/c1$, with the iron atom on an inversion center. Note that $P12_1/c1$ is a *translationengleiche* subgroup of $P2_1/n2_1/n2/m$.[27]

In all structures of the type $[M^{II}Cl_2(3\text{-}CNpy)_2]_n$ the bond lengths between the M^{II} atoms and the coordinating atoms vary largely (Table 4). For **1a**, **2a**, **3a** and **5a** two M^{II}–Cl bond distances are significantly longer than the other two M^{II}–Cl bond distances, and specifically for **5a**, a Jahn–Teller distortion of the Cu^{2+} octahedron is present.

2.4 Crystal structures and polymorphism of $[ZnCl_2(3\text{-}CNpy)_2]$ (6a)

$[ZnCl_2(3\text{-}CNpy)_2]$ (**6a**) was crystallised at ~8 °C. In the course of a long-time XRPD measurement at room temperature of one of the first samples of **6a**, small foreign reflections appeared with increasing intensity during the measurement. The diffraction pattern of the subsequent measurement of the same sample contained only reflections of the foreign phase. DTA–TG analysis of the measured sample proved that the stoichiometry of this phase was identical to that of the starting material. Apparently, α-**6a** forms at around 8 °C and transforms within several hours at room temperature into β-**6a**. Both crystal structures were determined from XRPD data. Details on the measurements are given in Table S2-2 (ESI†), Rietveld plots of α-**6a** and β-**6a** are shown in Fig. S21 and S22 (ESI†). Relevant crystallographic data are given in Table 5.

Both polymorphs of **6a** form discrete complexes, in which the Zn atom is coordinated by two Cl and two N_{py} atoms in an approximately tetrahedral fashion (Table 6). As expected, the Zn^{2+} atom shows a typical tetrahedral coordination due to its closed shell with a d^{10} configuration. This coordination arrangement has already been reported for similar Zn^{II} compounds, *e.g.* $[ZnBr_2(3\text{-}CNpy)_2]$, $[ZnCl_2(py)_2]$ and $[ZnCl_2(4\text{-}CNpy)_2]$.[28–30]

The structure of β-**6a** is similar to that of $[ZnBr_2(3\text{-}CNpy)_2]$ and $[ZnCl_2(py)_2]$, but the packing of α-**6a** is quite unusual. In α-**6a**, the molecules are stacked like chips in a cylindrical tin following the 2_1 screw axis in the [100] direction, but a straight π–π-stacking is missing (Fig. 6a–c) because the cyanopyridine molecules are not located directly above each other (Fig. 6b). These chip-wise stacks are somehow gridlocked along the [001] direction: the pyridine rings of a neighbouring

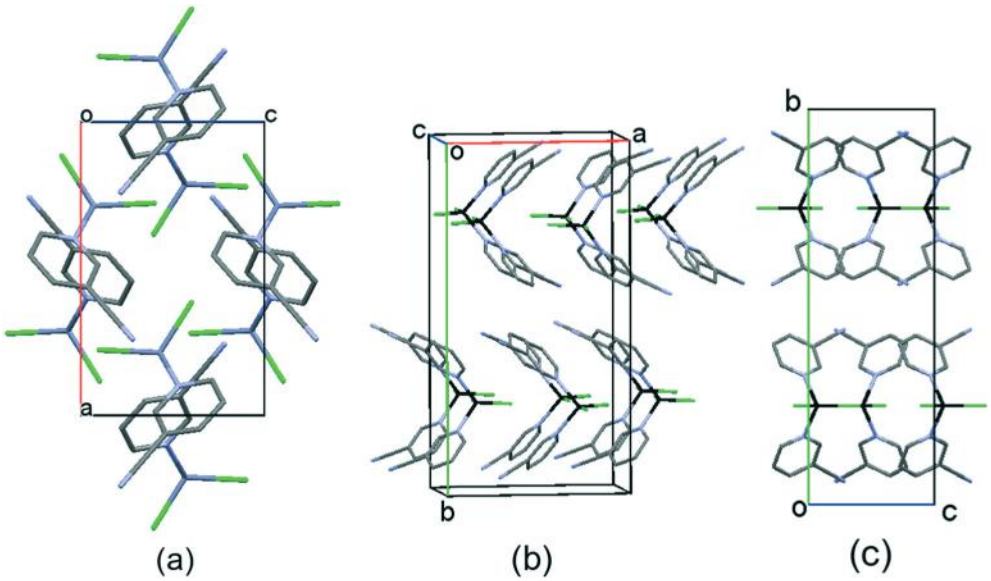

Fig. 6 Crystal structure of α-$[ZnCl_2(3\text{-}CNpy)_2]$: (a) view direction [010], (b) approximately [001], and (c) [100]. Color code: Zn black, Cl green, N blue, C grey. H atoms are omitted for clarity.

molecule point *via* their cyano groups in between two chips; this arrangement is supported by py-C≡N···H contacts. The packing motif of **α-6a** is quite unusual which might explain that this polymorph is metastable at room temperature. Apparently the formation of this polymorph is kinetically favoured by our synthesis, but it transforms rapidly into **β-6a**.

The phase **β-6a** as well as $[ZnBr_2(3\text{-}CNpy)_2]$ and $[ZnCl_2(py)_2]$ shows an exceptional molecular arrangement with two different π–π-stacking motifs, generated by the two different symmetry elements of $P2_1/c$ (Fig. 7a–c). In Fig. 7, the two symmetrically independent pyridine rings are shown in yellow and in violet, respectively. One pyridine ring (marked in yellow) packs *via* the *c* glide plane in an infinite chain along the *c*-axis. The π–π distance is approximately 4.00 Å. The second pyridine ring (marked in violet) forms a pair with the pyridine ring of a neighbouring molecule *via* a centre of symmetry. Here, the π–π-distance is 3.53 Å. These interactions stabilise the packing of **β-6a**, which is denser than the packing of **α-6a**. The easy transformation from **α-6a** to **β-6a** indicates that the molecular packing of **β-6a** is the energetically more favoured one.

2.5 Crystal structures of $[M^{II}Cl_2(3\text{-}CNpy)_1]_n$ (1b, 3b–5b)

The crystal structures of **1b**, **3b**, **4b** and **5b** were determined from XRPD data. The structure of **2b** could not be determined hitherto, because the quality of the powder was always insufficient. Relevant crystallographic data are given in Table 7. Details on the measurements and refinements are given in Table S3 (ESI†). Rietveld plots of structures **1b** and **3b–5b** are shown in Fig. S23–S26 (ESI†).

All compounds (**1b** and **3b–5b**) contain double chains with μ_3-bridging Cl atoms (Fig. 8). These double chains are arranged in a herringbone packing motif (Fig. 9). To date, a polymeric structure of the type $[M^{II}Cl_2(CNpy)_1]_n$ containing double chains was found only once, for M = Cu and CNpy =

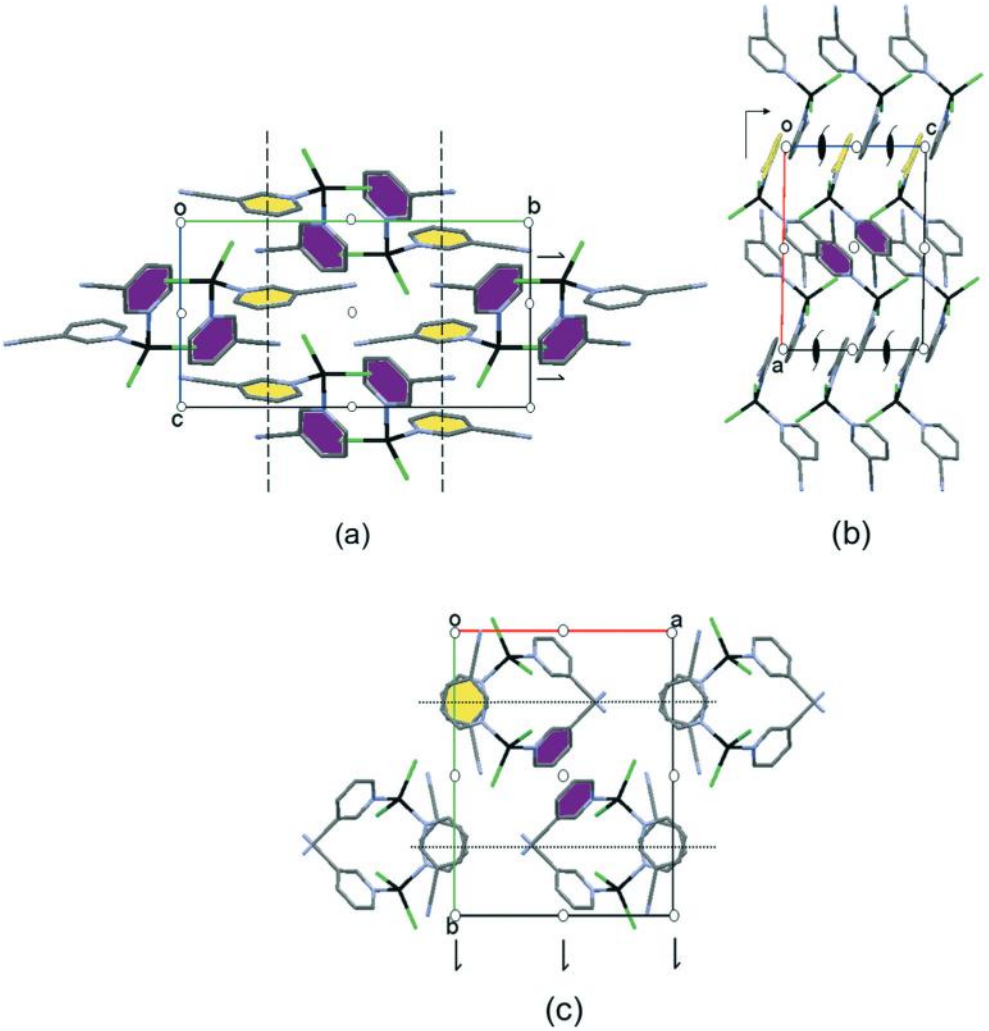

Fig. 7 Crystal structure of β-$[ZnCl_2(3\text{-}CNpy)_2]$ (**β-6a**): view directions (a) [100], (b) [010] and (c) [001]. The symmetry elements of space group $P2_1/c$ are shown as well. The structure contains two symmetrically independent cyanopyridine moieties, shown in yellow and black. Color code: Zn black, Cl green, N blue, C grey. H atoms are omitted for clarity.

Table 7 Crystallographic data of $[M^{II}Cl_2(3\text{-CNpy})_1]_n$ (**1b**, **3b**–**5b**)

	1b	**3b**	**4b**	**5b**
Compound	$[MnCl_2(3\text{-CNpy})_1]_n$	$[CoCl_2(3\text{-CNpy})_1]_n$	$[NiCl_2(3\text{-CNpy})_1]_n$	$[CuCl_2(3\text{-CNpy})_1]_n$
CCDC number	1904108	1904114	1904109	1904115
Structure determined from	Powder	Powder	Powder	Powder
Formula	$C_6H_4Cl_2MnN_2$	$C_6H_4Cl_2CoN_2$	$C_6H_4Cl_2NiN_2$	$C_6H_4Cl_2CuN_2$
Crystal system	Monoclinic	Orthorhombic	Orthorhombic	Monoclinic
Space group (no.)	*Pnma* (62)	*Pnma* (62)	*Pnma* (62)	$P2_1/c$ (14)
a/Å	16.5338(9)	16.0863(5)	15.9027(4)	3.77530(8)
b/Å	3.6933(12)	3.5874(10)	3.5328(6)	13.9311(4)
c/Å	14.4596(9)	14.1910(5)	14.0807(4)	15.6849(3)
α/°	90	90	90	90
β/°	90	90	90	96.114(3)
γ/°	90	90	90	90
V/Å^3	882.96(3)	818.9(1)	791.0(5)	820.2(4)
Z, Z'	4, 1/2	4, 1/2	4, 1/2	4, 1
Site symmetry of M	*.m.*	*.m.*	*.m.*	1
T/K	298	298	298	298
Radiation type	Mo Kα_1	Mo Kα_1	Cu Kα_1	Cu Kα_1

4-cyanopyridine.[6] Structures **1b**, **3b**, **4b** and **5b** are now the first 3-cyanopyridine compounds containing double chains.

Each metal atom is coordinated to five chlorine atoms and – *via* the N_{py} atom – to one 3-cyanoypridine molecule. The double chains are formed by the fusion of two $[M^{II}Cl_2(3\text{-CNpy})_2]_n$ single chains. In fact, the removal of one 3-CNpy from $[M^{II}Cl_2(3\text{-CNpy})_2]_n$ creates a vacancy at the metal atom, which is filled by a Cl atom from the neighboring chain. As a result, the metal atom is coordinated by two μ_2-bridging Cl atoms and three μ_3-bridging Cl atoms (Table 8). The sixth position is occupied by the remaining 3-CNpy ligand, coordinated by N_{py}. The M^{II}–N_{py} distances decrease from 2.243(8) Å (**1b**) to 2.020(6) Å (**4b**) according to the shrinking volume of the metal atom (Table 8).

1b, **3b** and **4b** are isotypic and crystallise in the orthorhombic space group *Pnma* with $Z = 4$. Structure **5b** crystallises in the monoclinic subgroup $P2_1/c$ with $Z = 4$ and is similar to structures **1b**, **3b** and **4b**. In the orthorhombic structures (**1b**, **3b** and **4b**) all atoms are located on mirror planes perpendicular to the chain direction (*.m.* sites) (Fig. 9a). The chain itself has $\nmid 12_1/m1$ symmetry which is a non-standard setting of the rod group $\nmid 112_1/m$ (rod group No. 12[26]). Together with n and a glide planes perpendicular to m, this results in space group $P2_1/n2_1/m2_1/a$. In structures **1b**, **3b** and **4b** the M^{II}–μ_2-Cl bonds are shorter than the M^{II}–μ_3-Cl bonds. In the nickel compound **4b** one M^{II}–μ_3-Cl bond is significantly longer than the other two M^{II}–μ_3-Cl bonds, resulting in a slight axial elongation of the coordination octahedron (Table 8).

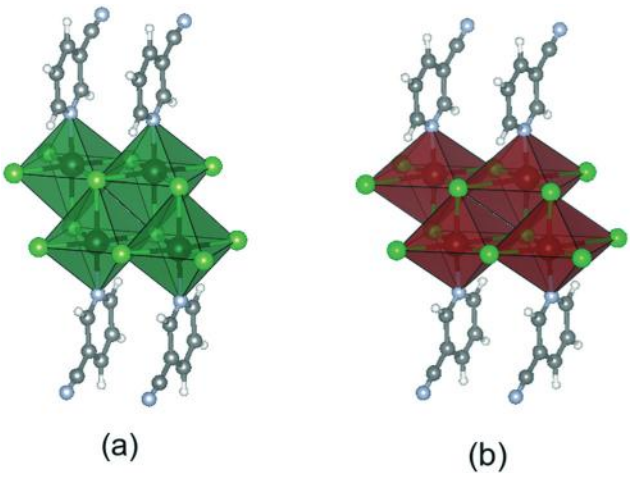

Fig. 8 Part of a double chain in (a) $[NiCl_2(3\text{-CNpy})_1]_n$ (**4b**) and (b) $[CuCl_2(3\text{-CNpy})_1]_n$ (**5b**); the copper coordination octahedron is elongated in the chain direction. Color code: Ni dark green, Cu orange, Cl light green, N blue, C grey, H white.[40]

The copper compound (**5b**) shows a similar topology, but its structure is monoclinic. In fact, in **5b** a Jahn–Teller distortion of the Cu^{2+} coordination octahedron is present (Fig. 8b and Table 8): one Cu–μ_3-Cl and one Cu–μ_2-Cl bond are noticeably longer than the other Cu–Cl bonds, resulting in a stretching of the copper coordination octahedron along the a-axis. A Jahn–Teller distortion is typical for d^9-ions, *e.g.* the Cu^{2+} ion, and was already observed in the crystal structures of the corresponding 4-CNpy phases of $[CuCl_2(4\text{-CNpy})_1]_n$.[6] The distortion of the octahedron results in a reduced symmetry. The 3-CNpy ligands are no longer placed on mirror planes (Fig. 9b) and the Cu atom is located in a general position. This results in a pyridine stacking angle deviating from 90° (Table 8). The symmetry is reduced by an order of 2 from $P2_1/n2_1/m2_1/a$ to its maximal subgroup $P112_1/a$, which is a non-standard setting of $P12_1/c1$ (Fig. 9b).

In contrast to the $[M^{II}Cl_2(3\text{-CNpy})_1]_n$ compounds, all corresponding Br compounds $[M^{II}Br_2(3\text{-CNpy})_1]_n$ consist of a network in which the metal atoms are coordinated by four μ_2-Br atoms.[3] In case of the double chain topology, the metal atoms would be surrounded by five bromine atoms, and due to the size of a bromine atom this arrangement is never observed in $[M^{II}Br_2(3\text{-CNpy})_1]_n$ (nor $[M^{II}Br_2(4\text{-CNpy})_1]_n$)

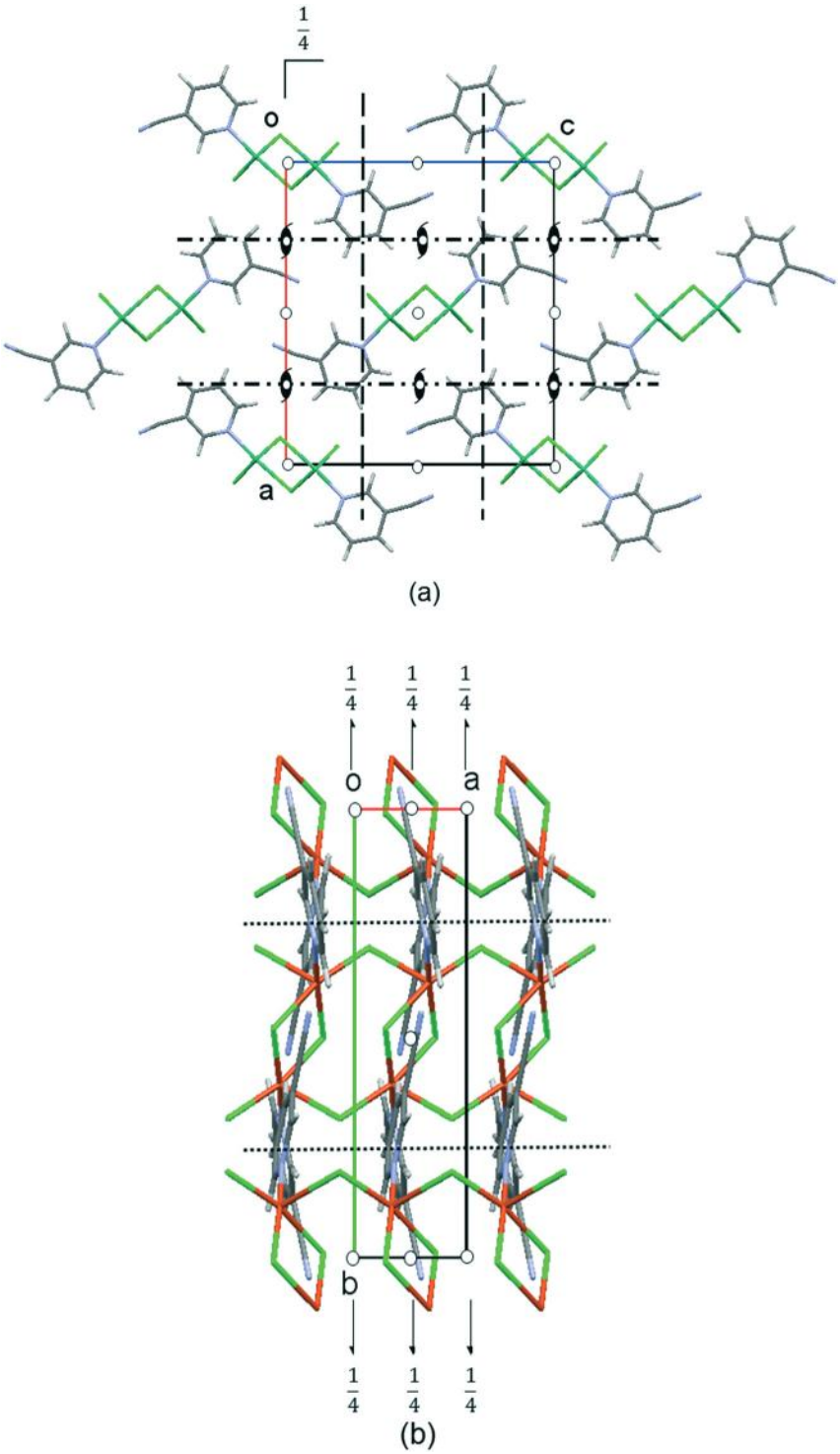

Fig. 9 Crystal structure of (a) $[NiCl_2(3\text{-}CNpy)_1]_n$ (**4b**), view direction [010]; and (b) $[CuCl_2(3\text{-}CNpy)_1]_n$ (**5b**), view direction [001]. Selected symmetry elements are shown. Color code: Ni dark green, Cl light green, N blue, C grey, H white.

compounds. But why do $[M^{II}Cl_2(4\text{-}CNpy)_1]_n$ (with M^{II} = Mn, Fe and Ni) show a two-dimensional network topology, whereas the corresponding 3-CNpy compounds do not? The M^{II}-py-C-N-M^{II} system is stabilized by resonance, as shown in Fig. 10 for the nickel compound. The aromatic stabilization is established by back-bonding from the metal to the coordinated N_{py} atom and, furthermore, by a π-donating bond from the –C≡N– fragment to the next metal atom.

This stabilization is less pronounced for 3-cyanopyridine. Therefore all chlorine compounds $[M^{II}Cl_2(3\text{-}CNpy)_1]_n$ (M = Mn, Co, Ni, Cu) do not contain bridging cyano groups, but double chains.

Table 8 Selected bond lengths in compounds $[M^{II}Cl_2(3\text{-}CNpy)_1]_n$ (**1b**, **3b**, **4b** and **5b**). The given standard deviations are those resulting from the Rietveld refinement. The actual accuracy is much lower

	1b	3b	4b	5b
M^{II}	Mn	Co	Ni	Cu
M^{II}–N_{py}/Å	2.243(8)	2.153(6)	2.106(4)	2.020(6)
M^{II}-μ_2-Cl(1)/Å	2.504(5)	2.443(4)	2.426(2)	2.630(11)[b]
M^{II}-μ_2-Cl(2)/Å	2.504(5)	2.443(4)	2.426(2)	2.239(10)
M^{II}-μ_3-Cl(3)/Å	2.613(5)	2.506(4)	2.459(2)	3.146(10)[b]
M^{II}-μ_3-Cl(4)/Å	2.613(5)	2.506(4)	2.459(2)	2.373(10)
M^{II}-μ_3-Cl(5)/Å	2.616(7)	2.514(5)	2.497(3)	2.278(11)
N_{py}–M^{II}-μ_3-Cl(5)/°	168.1(3)	172.6(2)	175.6(1)	170.6(4)
Pyridine stacking angle δ/°[a]	90	90	90	88.3

[a] Angle between the pyridine ring mean plane and the stacking direction (for **1b**, **3b** and **4b** [100] and for **5b** [001]). [b] Jahn–Teller elongation.

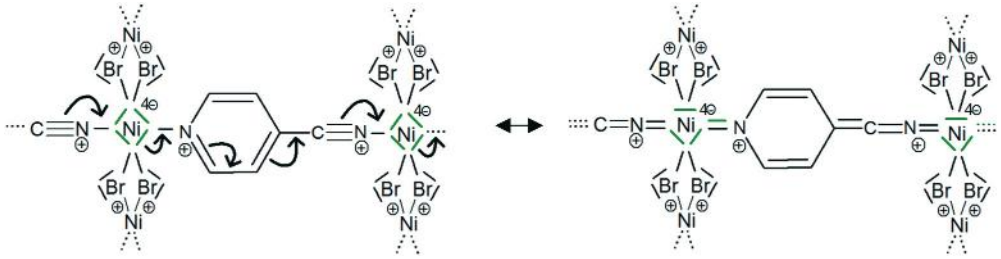

Fig. 10 Resonance stabilization in the Ni^{II}-py-C-N-Ni^{II} system.

3. Experimental section

3.1 Materials

$MnCl_2{\cdot}4H_2O$, $CoCl_2{\cdot}6H_2O$, $NiCl_2{\cdot}6H_2O$, $CuCl_2{\cdot}2H_2O$, $ZnCl_2{\cdot}2H_2O$, methanol and 3-cyanopyridine were purchased from Alfa Aesar. $FeCl_2{\cdot}2H_2O$ and ethanol were purchased from Sigma Aldrich. All chemicals were used without further purification.

3.2 Syntheses

Synthesis of $[M^{II}Cl_2(3\text{-}CNpy)_2]_{(n)}$. Compounds $[M^{II}Cl_2(3\text{-}CNpy)_2]$ (**1a–5a**) were prepared by stirring the reactants in methanol (for **4a** and **5a**) or ethanol (for **1a**, **2a**, **3a** and **6a**) at room temperature. The obtained powders were isolated by filtration, washed with ethanol and dried in air. In the case of $[ZnCl_2(3\text{-}CNpy)_2]$ (**6a**), no powder was obtained after having mixed the dissolved reactants. The solution was placed in a fridge for two days, where a colorless powder slowly formed. XRPD measurements revealed polymorphism of $[ZnCl_2(3\text{-}CNpy)_2]$: **α-6a** forms at ~8 °C and transforms at room temperature within 12 h into **β-6a**. Further details on the syntheses of $[M^{II}Cl_2(3\text{-}CNpy)_2]_n$ can be found in the ESI.†

Preparation of $[M^{II}Cl_2(3\text{-}CNpy)_1]_n$. Compounds $[M^{II}Cl_2(3\text{-}CNpy)_1]_n$ (**1b**, **3b**, **4b** and **5b**) were prepared by thermal decomposition of **1a**, **3a**, **4a** and **5a** at the corresponding temperatures in a thermogravimetric device (DTA); details are given in Table 9. Around 30 mg of the starting material was filled in an Al_2O_3 crucible and heated (heating rate: 5 °C min^{-1}) to the target temperatures under argon atmosphere. The temperatures were kept for several minutes. After cooling under an Ar gas flow, the powders were immediately transferred into a glass capillary; the capillary was sealed afterwards. All powders were characterized by XRPD and IR. Further details on the preparations of $[M^{II}Cl_2(3\text{-}CNpy)_1]_n$ can be found in the ESI.†

3.3 IR-spectroscopy

FT-IR spectra were recorded with a SHIMADZUIRaffinity 1S Fourier transform infrared reflection-absorption spectrometer.

3.4 Differential thermal analysis and thermogravimetry (DTA/TG)

Differential thermal and thermogravimetric analyses (DTA/TG) were performed on a SETARAM (TGA 92) device. The samples were placed into Al_2O_3 crucibles and measured in a dynamic argon atmosphere with a heating rate of 5 °C min^{-1} and a constant flow rate of about 75 mL min^{-1}. The heating

Table 9 Heating temperatures and heating times for the preparation of $[M^{II}Cl_2(3\text{-}CNpy)_1]_n$ (**1b**, **3b**, **4b** and **5b**) by DTA

Compound	1b	3b	4b	5b
Target temperature	240 °C	240 °C	290 °C	230 °C
Heating time at the target temperature	10 min	10 min	10 min	25 min

temperatures range from 293 K to 713 K for the compounds **1a–6a** (for details see Fig. S1–S5 in the ESI†).

3.5 X-ray powder diffraction (XRPD)

XRPD measurements were performed on Stoe STADI-P diffractometers equipped with Ge (111) monochromators. For **1b**, **2a**, **3a** and **3b**, the diffraction data were collected using Mo-Kα_1 radiation (λ = 0.70903 Å) and a Mythen 1K detector (Dectris). Samples **1a**, **4a**, **4b**, **5a**, **5b**, α-**6a** and β-**6a** were measured using Cu-Kα_1 radiation (λ = 1.54056 Å) and a linear position sensitive detector (PSD, Kr/CH_4). The data were collected with the software WinXPOW 3.4.[31] The samples were measured in borosilicate glass capillaries from Hilgenberg (diameter 0.7 mm or 0.5 mm), except **1a** and α-**6a**: the powders were too fluffy to be placed in capillaries and had to be measured between polymer foils. A slight preferred orientation was observed in **1a** and α-**6a** as well as in **4a** which was taken into account in the Rietveld refinement.

3.6 Structure determinations from XRPD data

All powder patterns were indexed with DICVOL91[32] (within the DASH package[33]) and CONOGRAPH,[34,35] using the first 20–25 reasonable reflections. Indexing results from both methods were compared and selected with regard to expected cell volumes using Hofmann's volume increments.[36] The space groups were determined by checking carefully the extinction conditions and considering molecular symmetry as well. All structures were solved by applying the global optimization method of simulated annealing (SA) as implemented in DASH, using a starting structural model in direct space. The starting models were built up from known fragments in AVOGADRO.[37] Structure solution was then performed with respect to the space group and site symmetry. All structures could be solved without problems. Subsequently a Pawley refinement was carried out with TOPAS[38,39] to refine background, zero point error, lattice parameters and peak shape parameters, including peak asymmetry. During the Rietveld refinements the pyridine ring was restrained to be flat; bond lengths for all bonds were restrained to statistical mean values from the CSD; all C–C–C and C–C–H angles of the pyridine ring were restrained to 120°. One overall thermal displacement parameter for the non-hydrogen atoms was used. The displacement parameter of the H atoms was constrained to be 1.2 times that of the non-hydrogen atoms. At the end of the refinement, the restraints for the M–Br and M–N_{py} distances and all restraints on angles involving M atoms (Br–M–N, M–N–C *etc.*) were omitted in order to search for possible Jahn–Teller-distortions of the octahedra.

As mentioned above, no pure-phase samples of **1b** and **5b** could be obtained. In both cases, foreign reflections could be assigned to further decomposition products, probably $[MnCl_2(3\text{-}CNpy)_{1/3}]_n$ (**1c**) and $[CuCl_2(3\text{-}CNpy)_{1/2}]_n$ (**5c**), respectively (Fig. S27 and S28 in the ESI†). Attempts to solve the structures of **1c** and **5c** failed to date despite a reliable and reproducible indexing. Therefore, reflections of $[MnCl_2(3\text{-}CNpy)_{1/3}]_n$ and $[CuCl_2(3\text{-}CNpy)_{1/2}]_n$ were modelled with an additional peak phase.

As already mentioned, α-**6a** transforms into β-**6a** within several hours. Hence, in the powder pattern of α-**6a** reflections of β-**6a** appear during the measurement with growing intensity and were excluded during the refinement.

Further details on structure determination from XRPD data and Rietveld refinement are given in Text S3 in the ESI.† Cif-files can also be found in the ESI.†

4. Conclusion

Ten new coordination compounds built up from $M^{II}Cl_2$ (M = Mn, Fe, Co, Ni, Cu, Zn) and 3-cyanopyridine were synthesised and structurally characterised. All compounds of the composition $[M^{II}Cl_2(3\text{-}CNpy)_2]_{(n)}$ were obtained from solution. For M = Mn, Fe, Co, Ni or Cu the structure consists of single chains in which the metal atoms are linked *via* four μ_2-bridging Cl atoms (**1a–5a**). Two additional 3-cyanoypridine molecules coordinate terminally with their N_{py} atom to each metal atom, resulting in an octahedral coordination of the metal atom. The chains are arranged in different "herringbone" packing ways. For M = Zn two polymorphs were obtained; their structures contain discrete tetrahedral complexes (α-**6a** and β-**6a**) instead of polymeric chains. The Zn atoms are coordinated by two Cl atoms and two 3-cyanopyridine ligands (coordinating with their N_{py} atoms). Upon heating the compounds **1a–5a**, half of the organic ligand evaporates and the remaining single chain fragments merge to form double chains of the composition $[M^{II}Cl_2(3\text{-}CNpy)_1]_n$ (**1b**, **3b–5b**). In **1b** and **3b–5b**, the chains are arranged in a "herringbone" packing manner. The metal atoms are coordinated by one terminal 3-cyanopyridine molecule, two μ_2- and three μ_3-bridging Cl atoms. The Cu structure (**5b**) exhibits a Jahn–Teller distortion of the Cu^{2+} coordination octahedron: the two axial Cu–Cl bonds are noticeably longer than the three equatorial Cu–Cl bonds. A similar behaviour has already been observed in both polymorphs of $[CuCl_2(4\text{-}CNpy)_1]_n$, which is, to the best of our knowledge, the only compound of $M^{II}Cl_2$ and 4-cyanopyridine containing double chains. All other compounds $[M^{II}Cl_2(4\text{-}CNpy)_1]_n$ (with M = Mn, Fe and Ni) consist of two-dimensional networks, in which the 4-cyanopyridine ligand acts as a bridge between two $[M^{II}Cl_2]_n$ chains by connecting two metals *via* the N_{py} and the N_{CN} atom. In contrast to 4-cyanopyridine, 3-cyanopyridine "avoids" a coordination with its N_{CN} to a metal atom due to a less favourable resonance stabilisation of the M^{II}-py-C-N-M^{II} system. Therefore, compounds $[M^{II}Cl_2(3\text{-}CNpy)_1]_n$ do exclusively contain double chains (instead of a network). Next, compounds of $M^{II}F_2$ or $M^{II}I_2$ with 3-CNpy and 4-CNpy should be prepared and their structures should be solved in order to investigate the influence of the halogen atom on the topology of the analogues $[M^{II}F_2(CNpy)_1]_n$ and $[M^{II}I_2(CNpy)_1]_n$ compounds.

Conflicts of interest

There are no conflicts of interest to declare.

Acknowledgements

The authors thank Edith Alig for the TG/DTA and DSC measurements. We thank Maurice Beske and Björn Hohmeier for their support in synthetic investigations.

References

1 C. Janiak, *Dalton Trans.*, 2003, 2781–2804.
2 C. Slabbert and M. Rademeyer, *Coord. Chem. Rev.*, 2015, **288**, 18–49.
3 M. Heine, L. Fink and M. U. Schmidt, *CrystEngComm*, 2018, **20**, 7556–7566.
4 E. Alig, T. Bernert, L. Fink, N. Külcü and T. Yesilkaynak, *Acta Crystallogr., Sect. E: Struct. Rep. Online*, 2010, **66**, m239.
5 Y. Krysiak, L. Fink, T. Bernert, J. Glinnemann, M. Kapuscinski, H. Zhao, E. Alig and M. U. Schmidt, *Z. Anorg. Allg. Chem.*, 2014, **640**, 3190–3196.
6 H. Zhao, A. Bodach, M. Heine, Y. Krysiak, J. Glinnemann, E. Alig, L. Fink and M. U. Schmidt, *CrystEngComm*, 2017, **19**, 2216–2228.
7 X. L. Zhao and T. C. W. Mak, *Dalton Trans.*, 2004, 3212–3217.
8 W. Clegg and R. W. Harrington, 2017, CCDC: JAMQUM; private communication to the CSD.
9 M. K. Broderick, C. Yang, R. D. Pike, A. Nicholas, D. May and H. H. Patterson, *Polyhedron*, 2016, **114**, 333–343.
10 A. Bacchi, G. Cantoni, P. Pelagatti and S. Rizzato, *J. Organomet. Chem.*, 2012, **714**, 81–87.
11 W. H. Leung, W. Lai and I. D. Williams, *J. Organomet. Chem.*, 2000, **604**, 197–201.
12 T. Hu, L. Zhao and T. C. W. Mak, *Organometallics*, 2012, **31**, 7539.
13 A. J. Blake, N. R. Champness, J. E. B. Nicolson and C. Wilson, *Acta Crystallogr., Sect. C: Cryst. Struct. Commun.*, 2011, **57**, 1290.
14 F. H. Allen, *Acta Crystallogr., Sect. B: Struct. Sci.*, 2002, **58**, 380–388.
15 I. J. Bruno, J. C. Cole, P. R. Edgington, M. Kessler, C. F. Macrae, P. McCabe, J. Pearson and R. Taylor, *Acta Crystallogr., Sect. B: Struct. Sci.*, 2002, **58**, 389–397.
16 D. T. Cromer and A. C. Larson, *Acta Crystallogr., Sect. B: Struct. Crystallogr. Cryst. Chem.*, 1972, **28**, 1052–1058.
17 A. J. Graham, P. C. Healy, J. D. Kildea and A. H. White, *Aust. J. Chem.*, 1989, **42**, 177–184.
18 H. Hanika-Heidl, S. E. H. Etaiw, M. S. Ibrahim, A. S. B. Eldin and R. D. Fischer, *J. Organomet. Chem.*, 2003, **684**(1), 329–337.
19 L. Carlucci, G. Ciani, D. M. Proserpio and A. Sironi, *J. Chem. Soc., Chem. Commun.*, 1994, 2755–2756.
20 W. Chen, F. Liu and X. You, *Bull. Chem. Soc. Jpn.*, 2002, **75**, 1559–1560.
21 R. D. Bailey, L. L. Hook and W. T. Pennington, *Chem. Commun.*, 1998, 1181–1182.
22 R. J. H. Clark and C. S. Williams, *Spectrochim. Acta*, 1966, **22**, 1081–1090.
23 R. A. Bailey, S. L. Kozak, T. W. Michelsen and W. N. Mills, *Coord. Chem. Rev.*, 1971, **6**, 407–445.
24 C. Näther, S. Wöhlert, J. Boeckmann, M. Wriedt and I. Jeß, *Z. Anorg. Allg. Chem.*, 2013, **639**, 2696–2714.
25 W.-T. Chen, Z.-G. Luo, Y.-P. Xu and Q.-Y. Luo, *J. Chem. Res.*, 2011, **35**, 253–256.
26 V. Kopský and D. B. Litvin, *Int. Tables for Cryst.*, vol. E, 2010.
27 T. Hahn, *Int. Tables for Cryst.*, vol. A, 2002.
28 R. Ghiasi, *Acta Crystallogr., Sect. E: Struct. Rep. Online*, 2011, **67**, m101.
29 W. L. Steffen and G. J. Palenik, *Acta Crystallogr., Sect. B: Struct. Crystallogr. Cryst. Chem.*, 1976, **32**, 298–300.
30 W. L. Steffen and G. J. Palenik, *Inorg. Chem.*, 1977, **16**(5), 119–1127.
31 STOE & Cie GmbH, STOE WinXPOW 310, 2016, Darmstadt, Germany.
32 A. Boultif and D. Louër, *J. Appl. Crystallogr.*, 2004, **37**, 724–731.
33 W. I. F. David, K. Shankland, J. van de Streek, E. Pidcock, W. D. S. Motherwell and J. C. Cole, *J. Appl. Crystallogr.*, 2006, **39**, 910–915.
34 R. Oishi-Tomiyasu, *J. Appl. Crystallogr.*, 2014, **47**, 593–598.
35 R. Oishi-Tomiyasu, *J. Appl. Crystallogr.*, 2014, **47**, 2055–2059.
36 D. W. M. Hofmann, *Acta Crystallogr., Sect. B: Struct. Sci.*, 2002, **58**, 489–493.
37 *Avogadro Chemistry*, 2018.
38 A. Coelho, TOPAS Acad. User Man. & Tech. Ref, 2009, Brisbane, Australia.
39 A. Coelho, *J. Appl. Crystallogr.*, 2018, **51**, 210–218.
40 K. Momma and F. Izumi, *J. Appl. Crystallogr.*, 2011, **44**, 1272–1276.

Coordination compounds built up from $M^{II}Cl_2$ and 3-cyanopyridine: double chains, single chains and isolated complexes.

Miriam Heine, Lothar Fink, Martin U. Schmidt*

Institute of Inorganic and Analytical Chemistry, Goethe University, Max-von-Laue-Str. 7, 60438 Frankfurt am Main, Germany. E-Mail: m.schmidt@chemie.uni-frankfurt.de; Fax: +49 69798 29235; Tel: +49 69798 29123

Figures

Tables

Experimental details

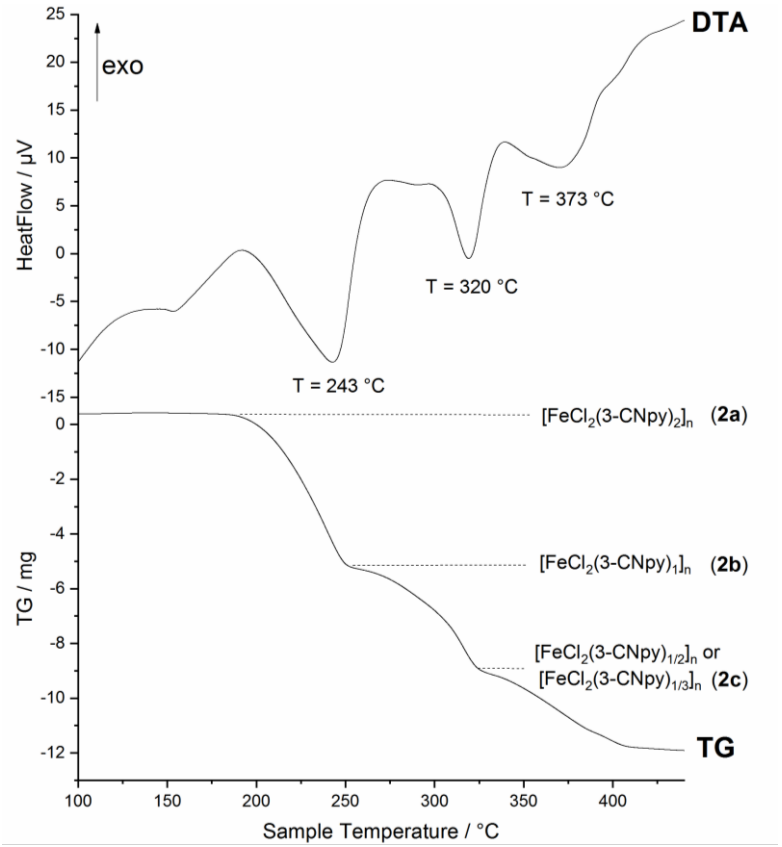

Figure S1. DTA/TG curves of $[FeCl_2(3\text{-}CNpy)_2]_n$ (**2a**). Heating rate: 5 K/min, Ar atmosphere, Al_2O_3 crucible. * DTA-TG results point to the formation of $[FeCl_2(3\text{-}CNpy)_{1/2}]_n$ or $[FeCl_2(3\text{-}CNpy)_{1/3}]_n$, see Tab. S1 in this document.

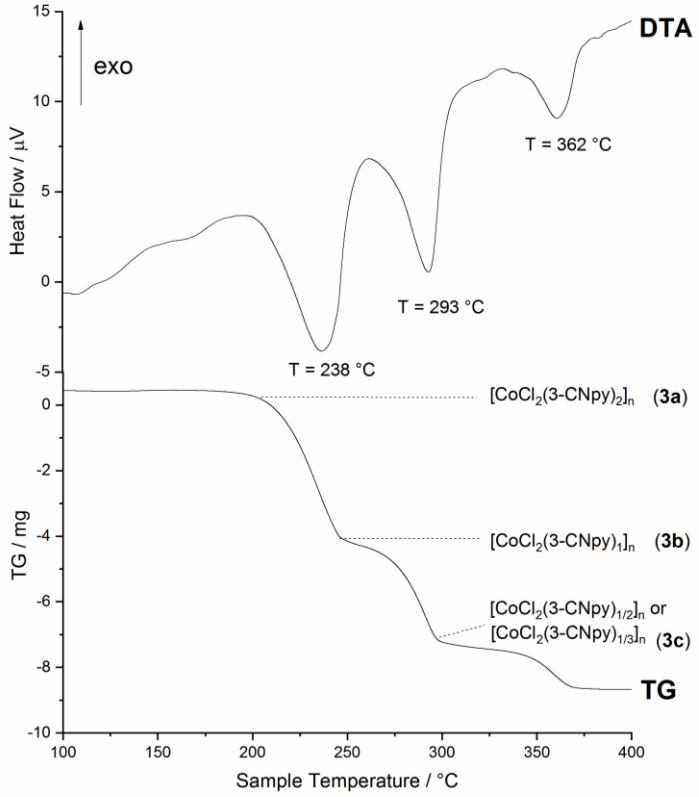

Figure S2. DTA/TG curves of $[CoCl_2(3\text{-}CNpy)_2]_n$ (**3a**). Heating rate: 5 K/min, Ar atmosphere, Al_2O_3 crucible. * DTA-TG results point to the formation of $[CoCl_2(3\text{-}CNpy)_{1/2}]_n$ or $[CoCl_2(3\text{-}CNpy)_{1/3}]_n$, see Tab. S1 in this document.

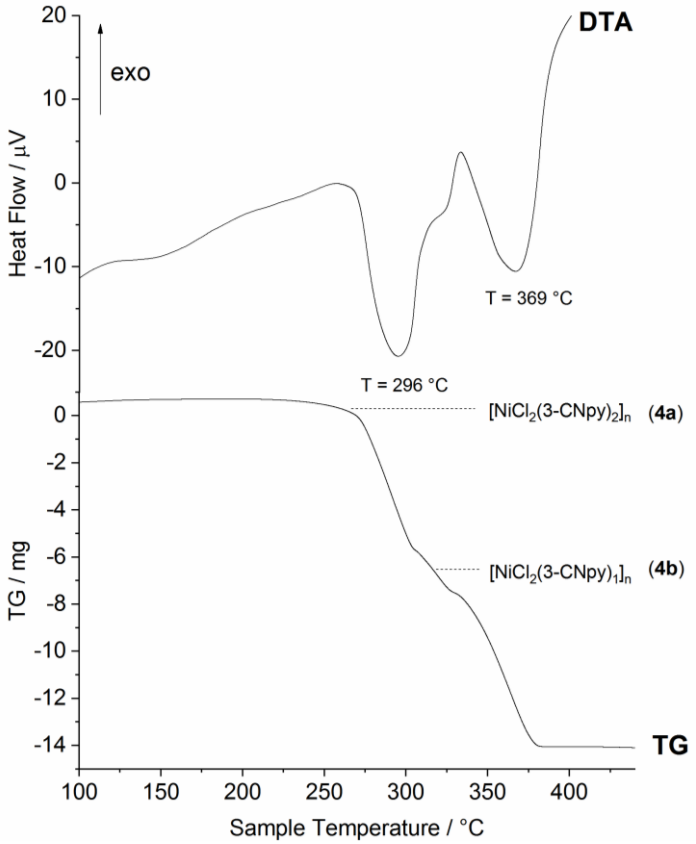

Figure S3. DTA/TG curves of $[NiCl_2(3\text{-}CNpy)_2]_n$ (**4a**). Heating rate: 5 K/min, Ar atmosphere, Al_2O_3 crucible.

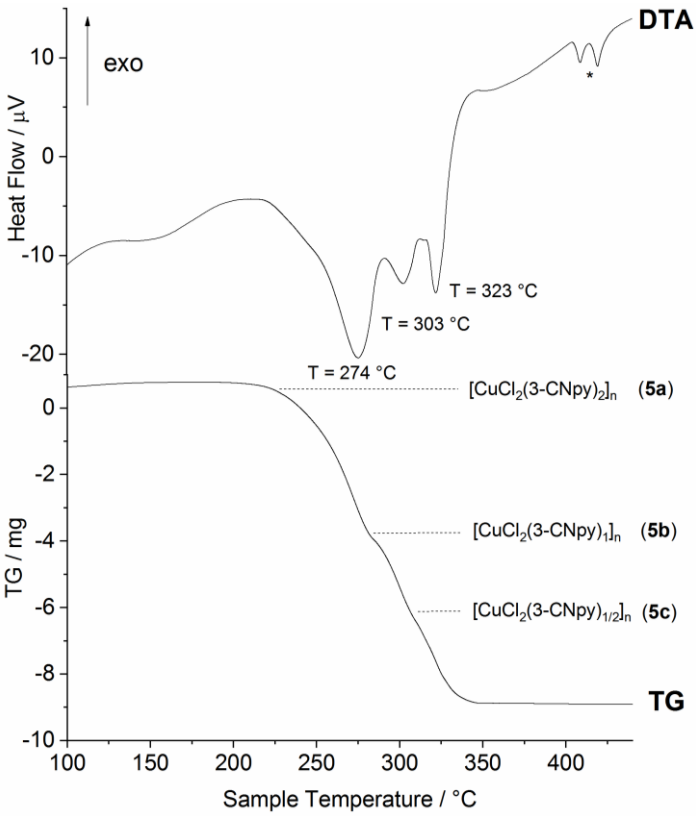

Figure S4. DTA/TG curves of $[CuCl_2(3\text{-}CNpy)_2]_n$ (**5a**). Heating rate: 5 K/min, Ar atmosphere, Al_2O_3 crucible. The endothermic signals marked by the may be attributed to the partial formation of anhydrous CuCl, see Fig. S28 in this document.

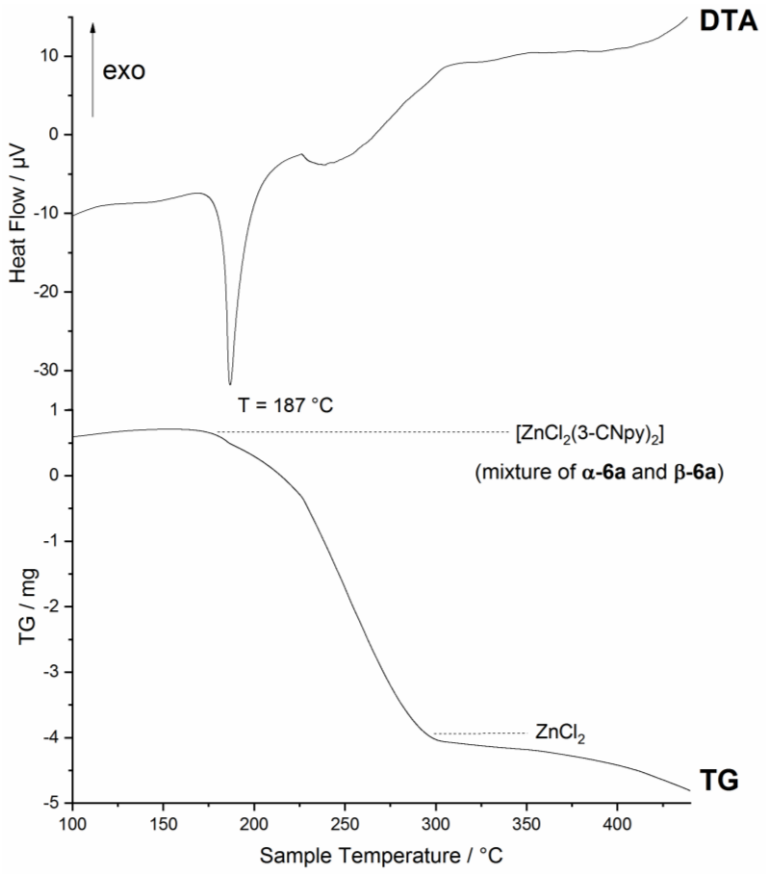

Figure S5. DTA/TG curves of $[ZnCl_2(3\text{-}CNpy)_2]$ (mixture of **α-6a** and **β-6a**). Heating rate: 5 K/min, Ar atmosphere, Al_2O_3 crucible.

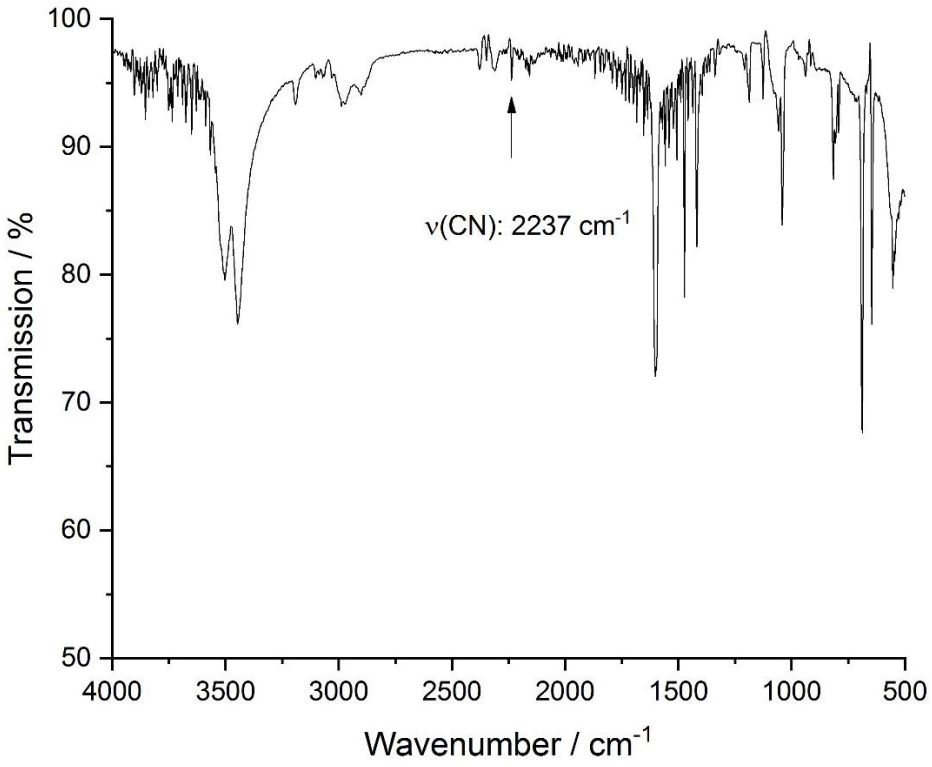

Figure S6. IR spectrum of $[MnCl_2(3\text{-}CNpy)_2]_n$ (**1a**).

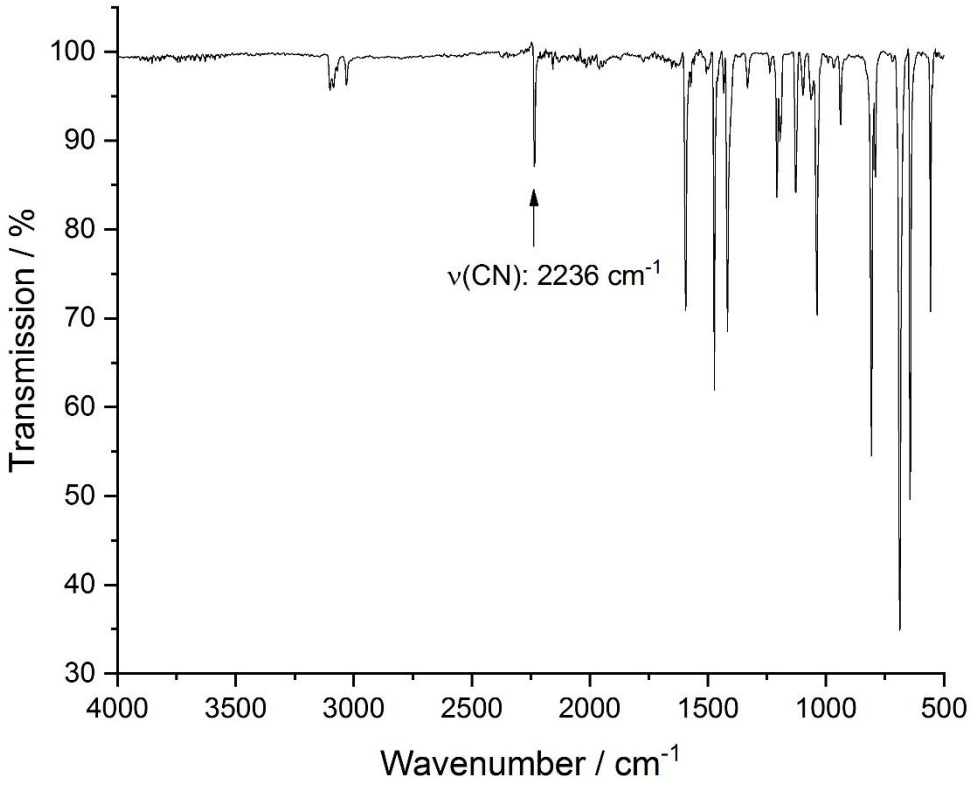

Figure S7. IR spectrum of $[MnCl_2(3\text{-}CNpy)_1]_n$ (**1b**).

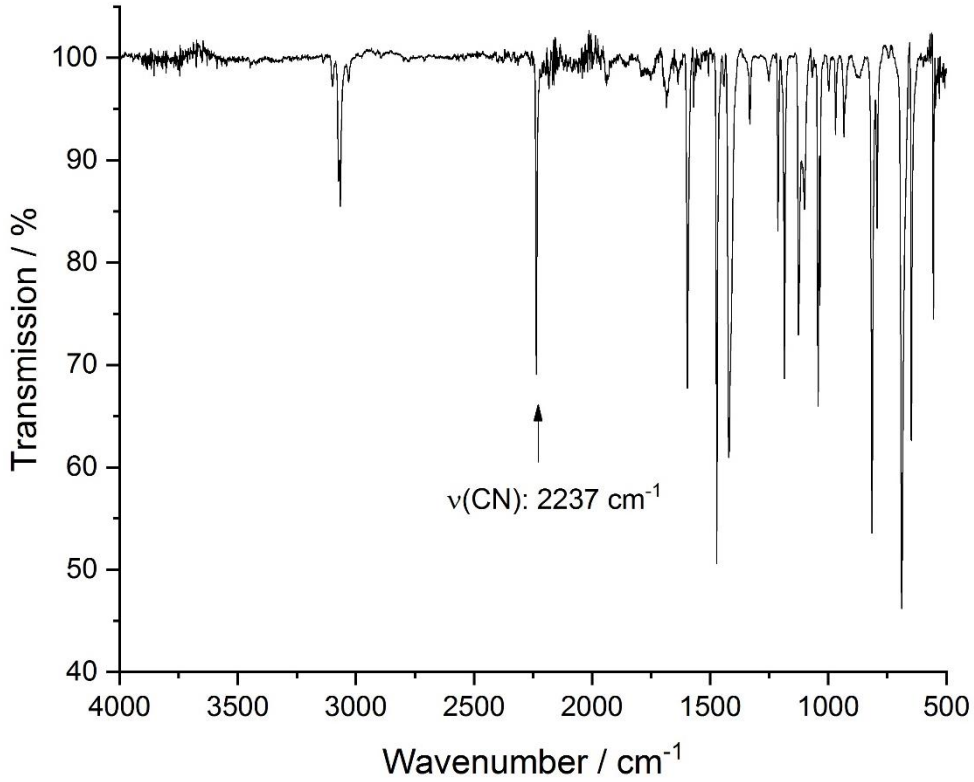

Figure S8. IR spectrum of $[FeCl_2(3\text{-}CNpy)_2]_n$ (**2a**).

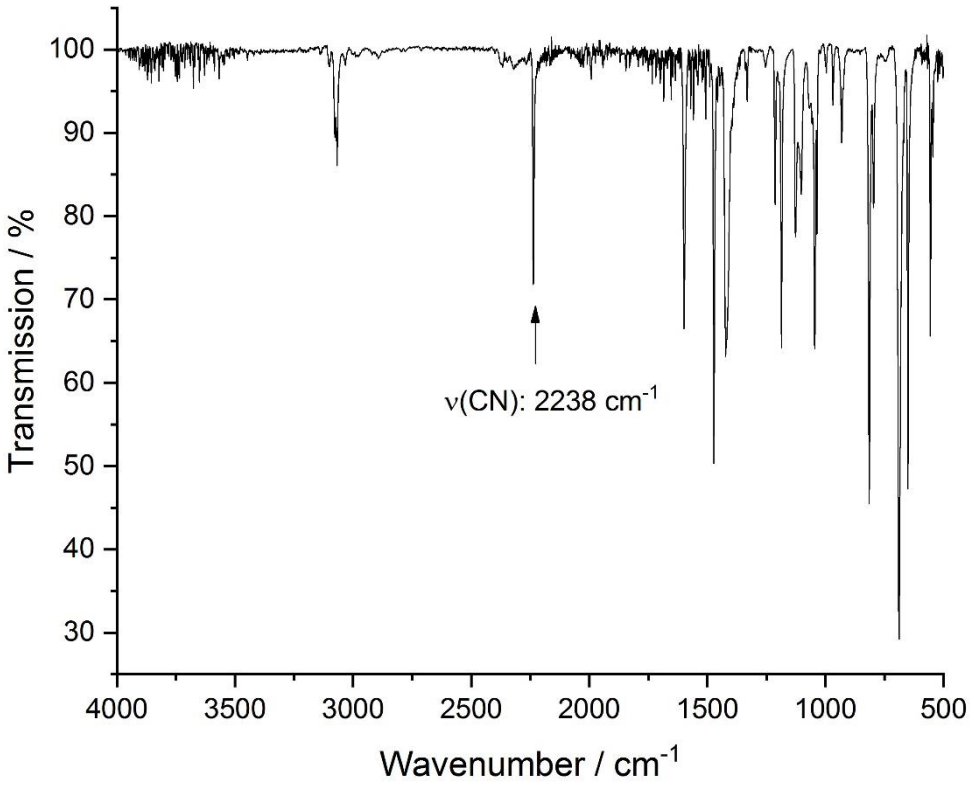

Figure S9. IR spectrum of $[CoCl_2(3\text{-}CNpy)_2]_n$ (**3a**).

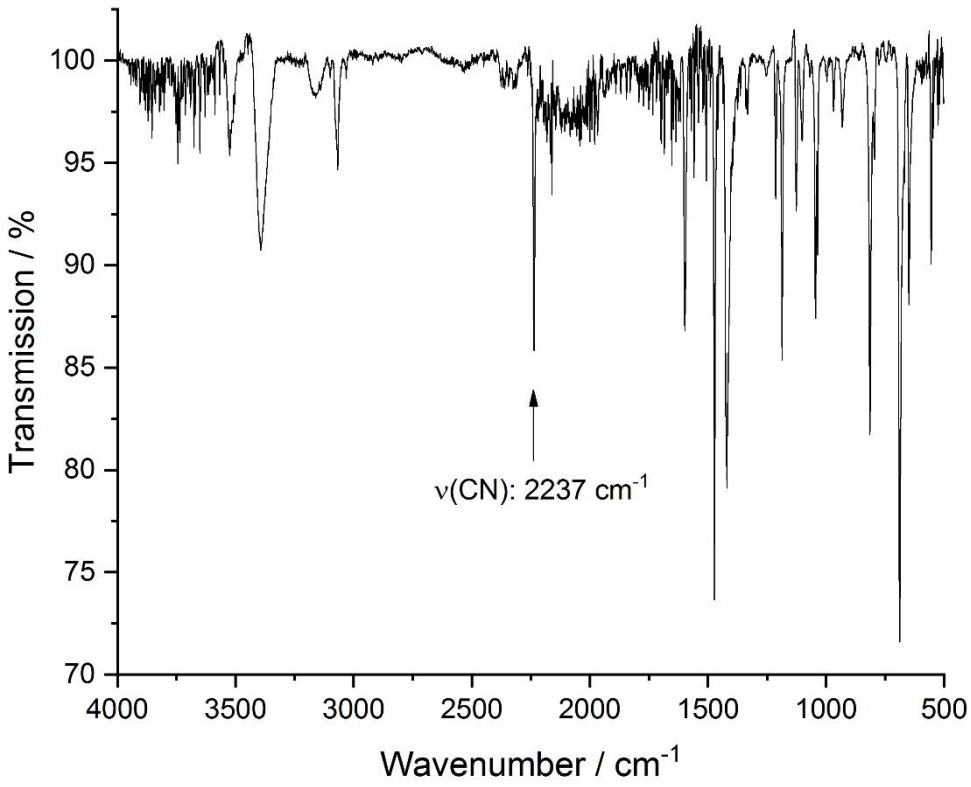

Figure S10. IR spectrum of $[CoCl_2(3\text{-}CNpy)_1]_n$ (**3b**).

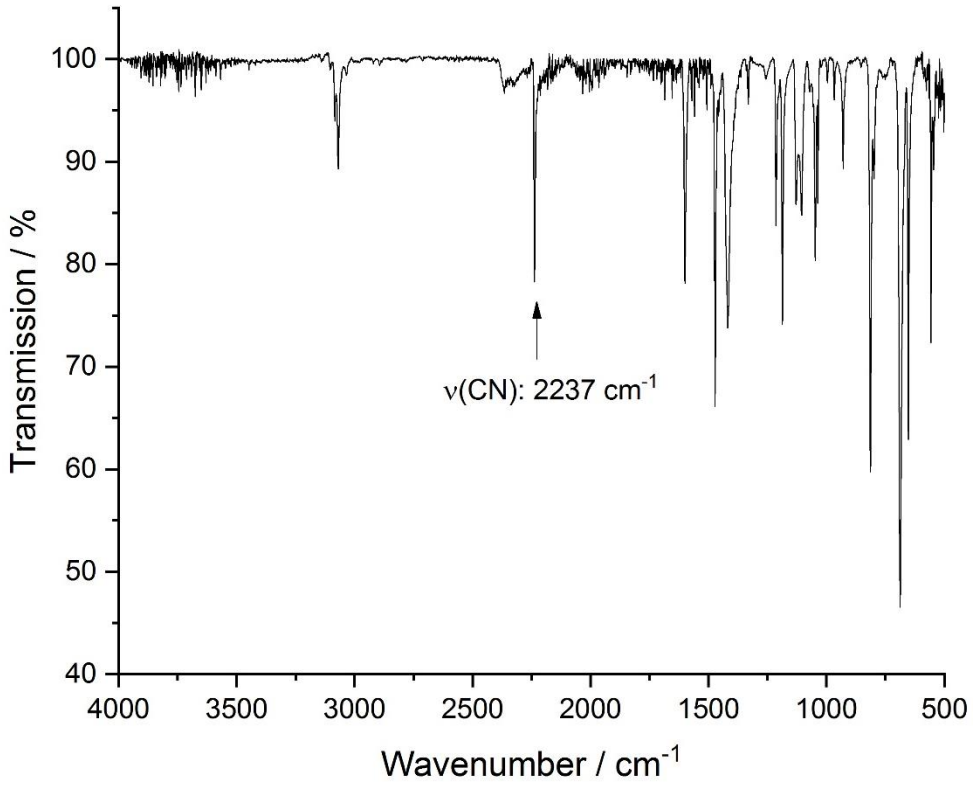

Figure S11. IR spectrum of $[NiCl_2(3\text{-}CNpy)_2]_n$ (**4a**).

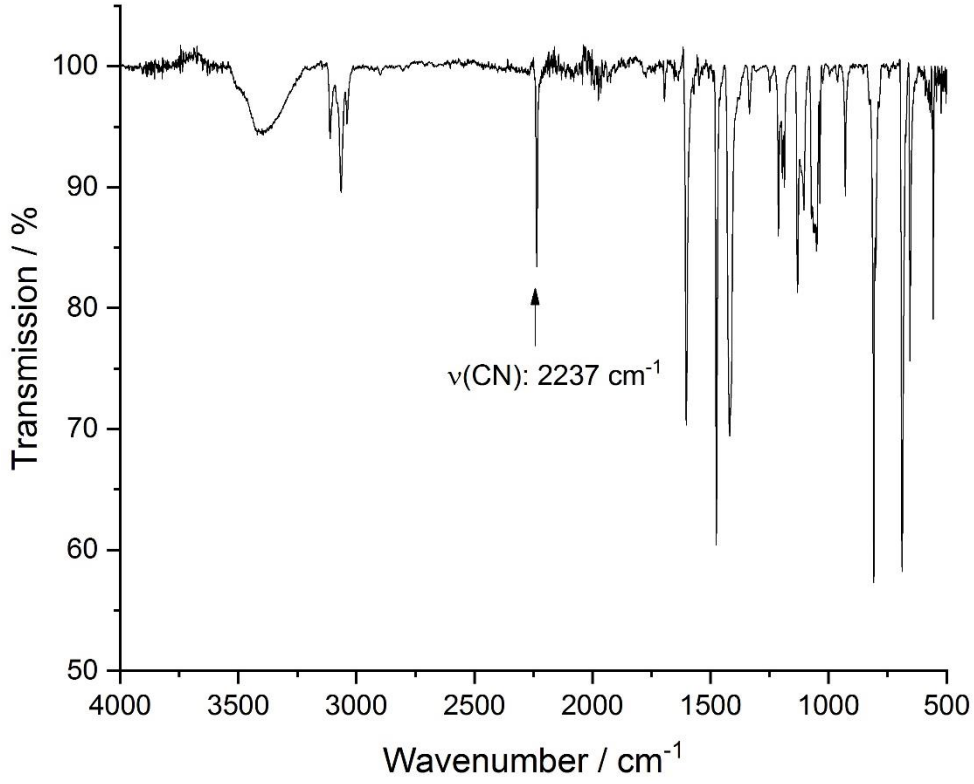

Figure S12. IR spectrum of $[NiCl_2(3\text{-}CNpy)_1]_n$ (**4b**).

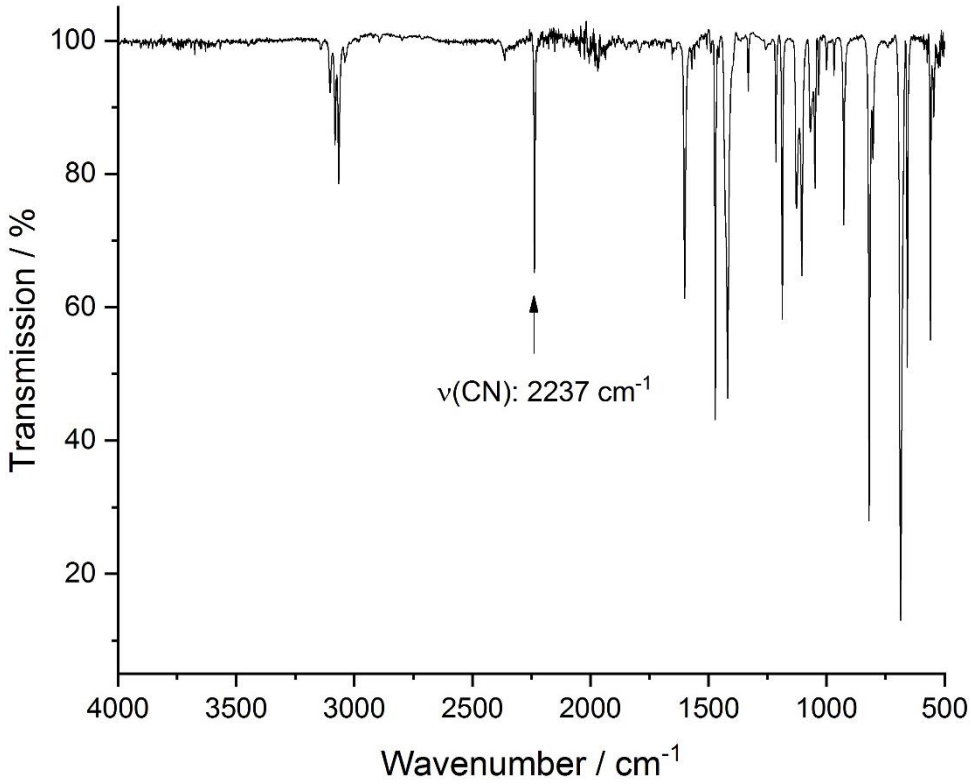

Figure S13. IR spectrum of $[CuCl_2(3\text{-}CNpy)_2]_n$ (**5a**).

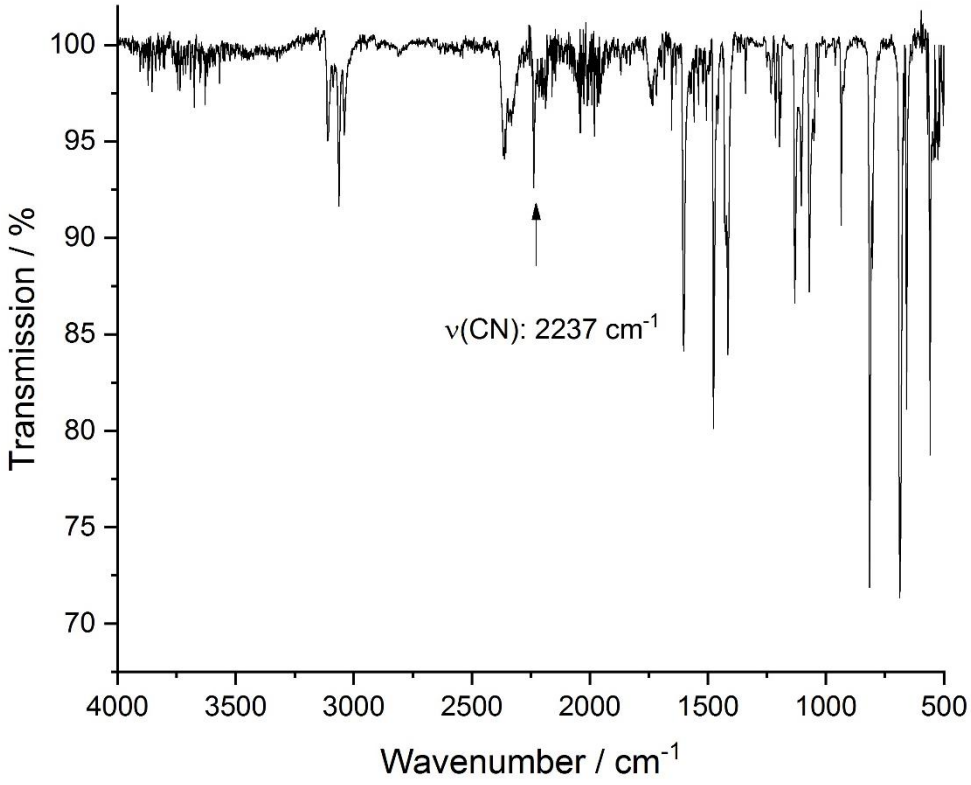

Figure S14. IR spectrum of $[CuCl_2(3\text{-}CNpy)_1]_n$ (**5b**).

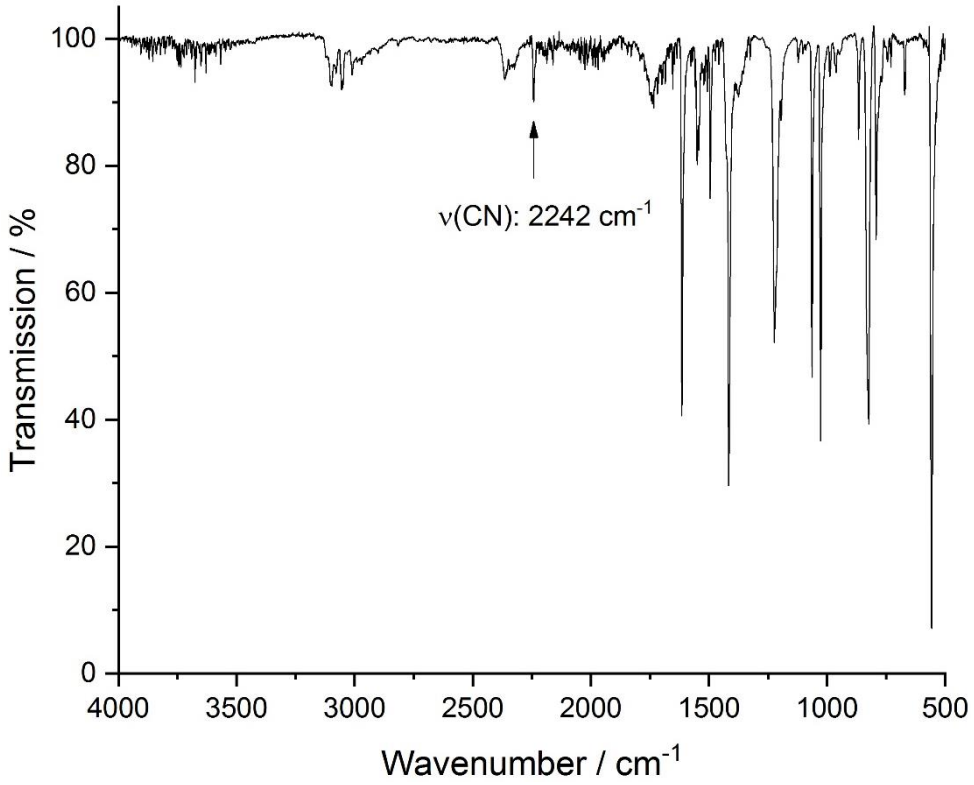

Figure S15. IR spectrum of $[ZnCl_2(3\text{-}CNpy)_2]$: mixture of **α-6** and **β-6**.

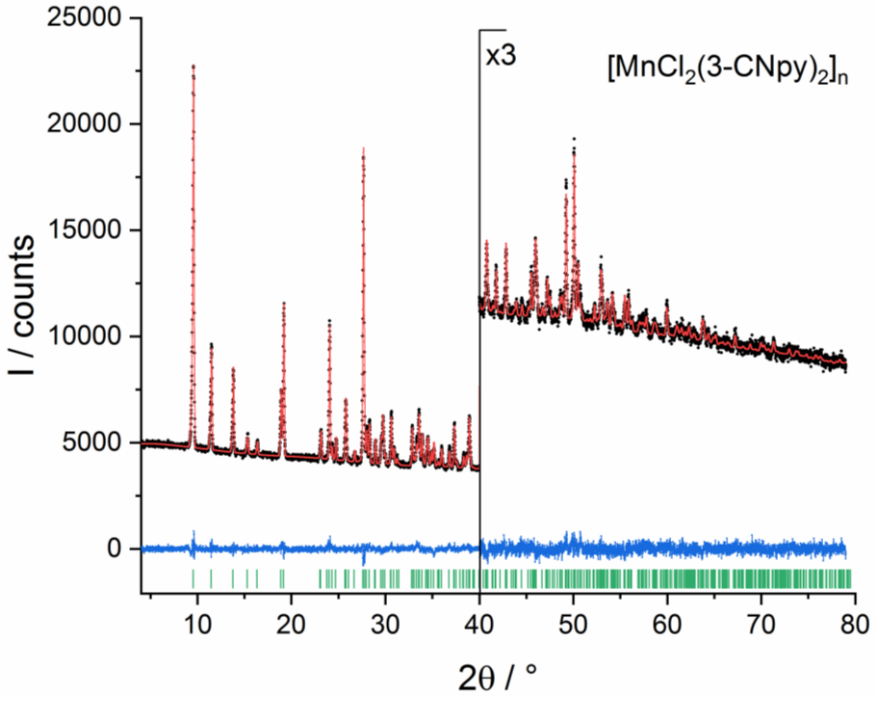

Figure S16. Rietveld plot of $[MnCl_2(3\text{-}CNpy)_2]_n$ (**1a**). Observed powder diagram (black points), simulated powder diagram (red solid line), difference profile (blue solid line) and reflection positions (green tick marks). Change of the scales with corresponding factors is indicated in the diagrams.

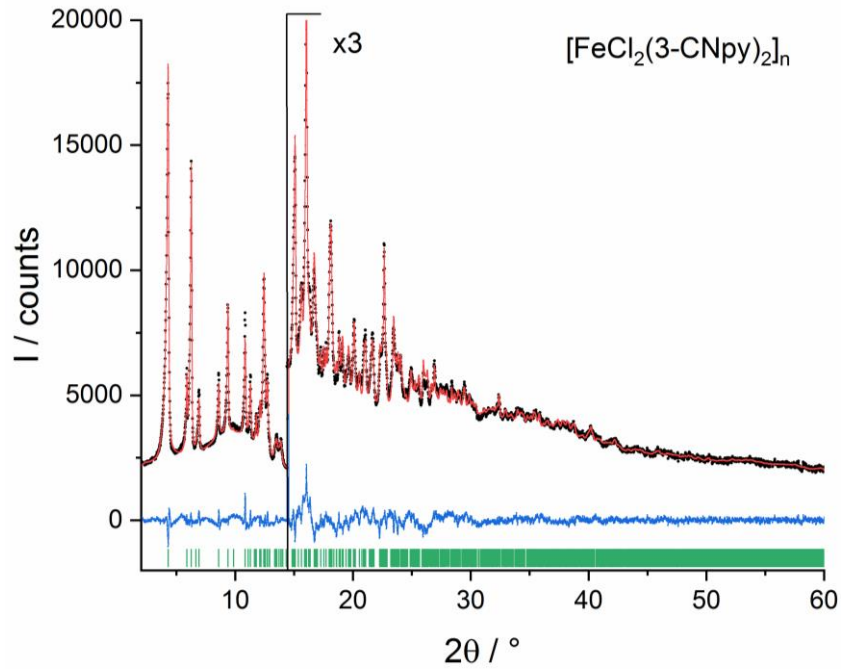

Figure S17. Rietveld plot of $[FeCl_2(3\text{-}CNpy)_2]_n$ (**2a**). Observed powder diagram (black points), simulated powder diagram (red solid line), difference profile (blue solid line) and reflection positions (green tick marks). Change of the scales with corresponding factors is indicated in the diagrams. XRPD data were collected with Mo $K\alpha_1$ radiation.

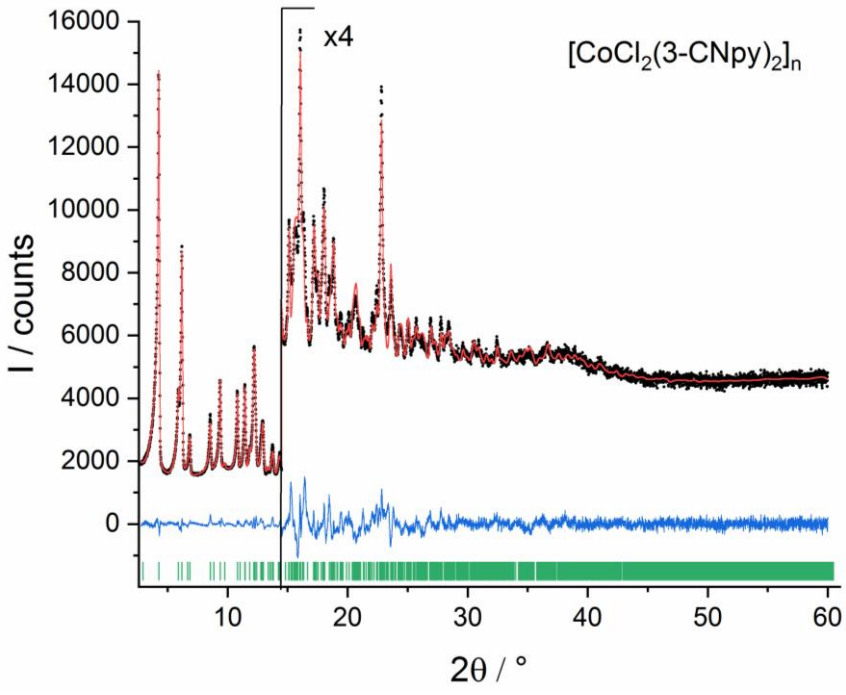

Figure S18. Rietveld plot of $[CoCl_2(3\text{-}CNpy)_2]_n$ (**3a**). Observed powder diagram (black points), simulated powder diagram (red solid line), difference profile (blue solid line) and reflection positions (green tick marks). Change of the scales with corresponding factors is indicated in the diagrams. XRPD data were collected with Mo $K\alpha_1$ radiation.

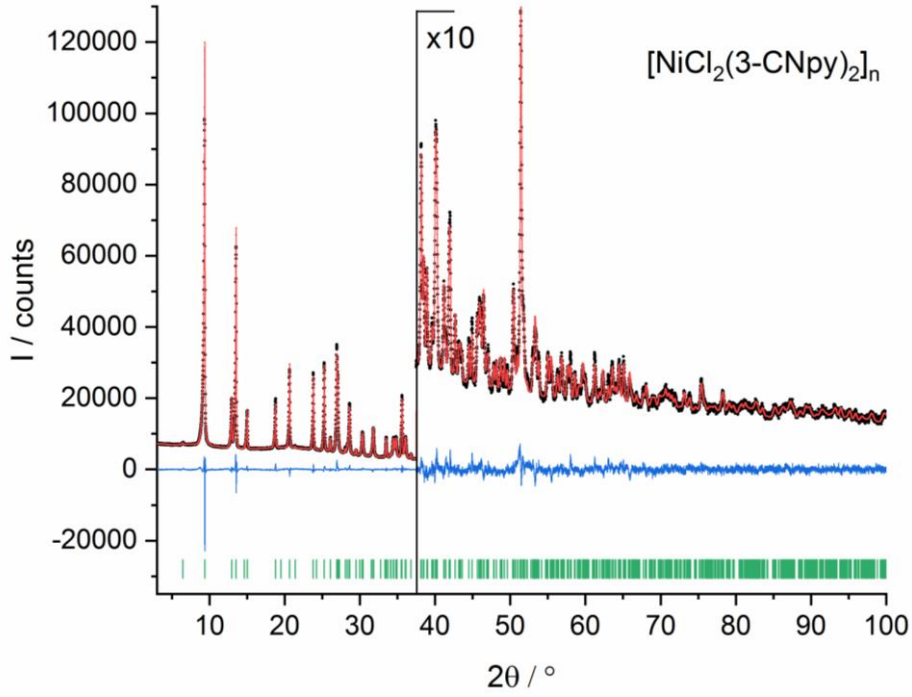

Figure S19. Rietveld plot of $[NiCl_2(3\text{-}CNpy)_2]_n$ (**4a**). Observed powder diagram (black points), simulated powder diagram (red solid line), difference profile (blue solid line) and reflection positions (green tick marks). Change of the scales with corresponding factors is indicated in the diagrams.

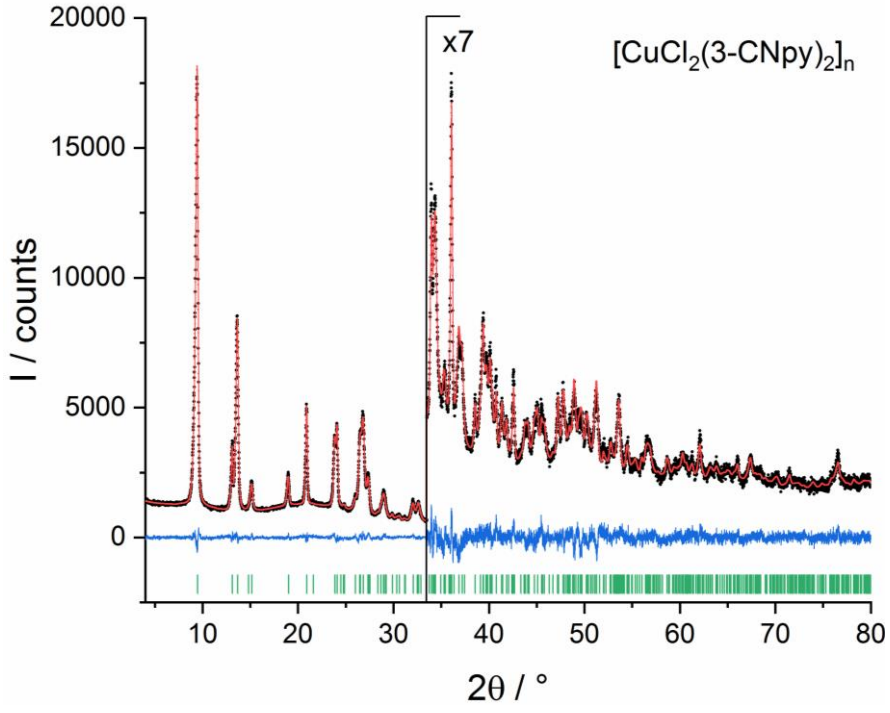

Figure S20. Rietveld plot of $[CuCl_2(3\text{-}CNpy)_2]_n$ (**5a**). Observed powder diagram (black points), simulated powder diagram (red solid line), difference profile (blue solid line) and reflection positions (green tick marks). Change of the scales with corresponding factors is indicated in the diagrams.

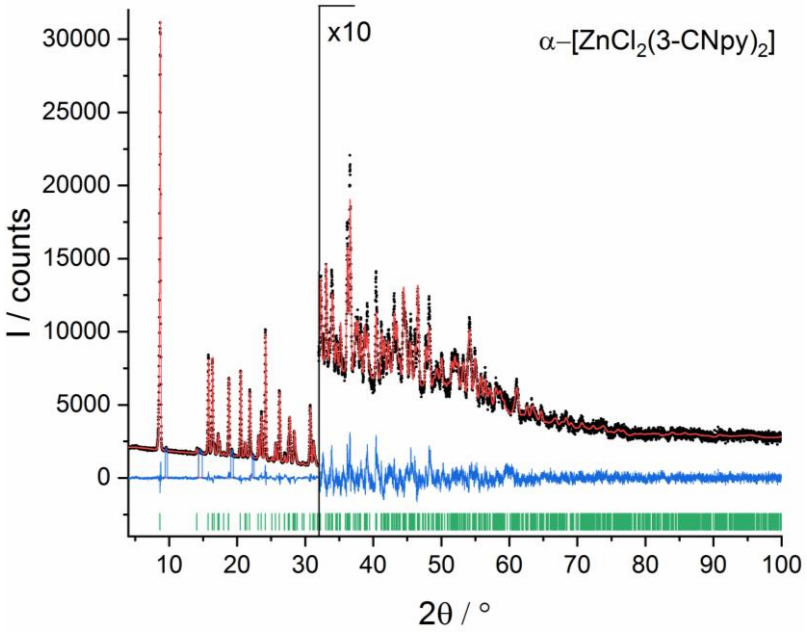

Figure S21. Rietveld plot of α-[$ZnCl_2$(3-CNpy)$_2$] (**α-6a**). Observed powder diagram (black points), simulated powder diagram (red solid line), difference profile (blue solid line) and reflection positions (green tick marks). Reflections of **β-6a** are excluded. Change of the scales with corresponding factors is indicated in the diagrams.

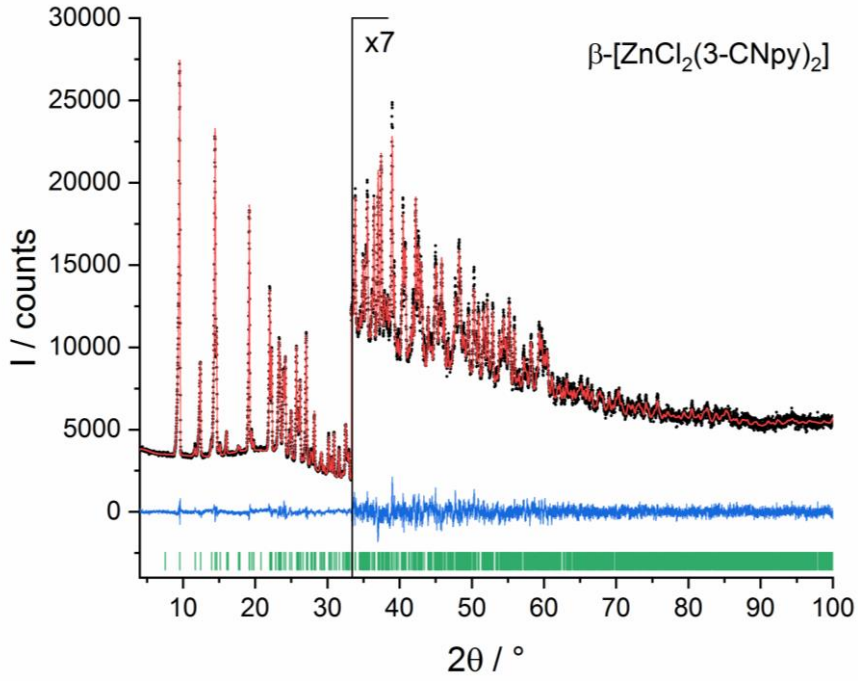

Figure S22. Rietveld plot of β-[$ZnCl_2$(3-CNpy)$_2$] (**β-6a**). Observed powder diagram (black points), simulated powder diagram (red solid line), difference profile (blue solid line) and reflection positions (green tick marks). Change of the scales with corresponding factors is indicated in the diagrams.

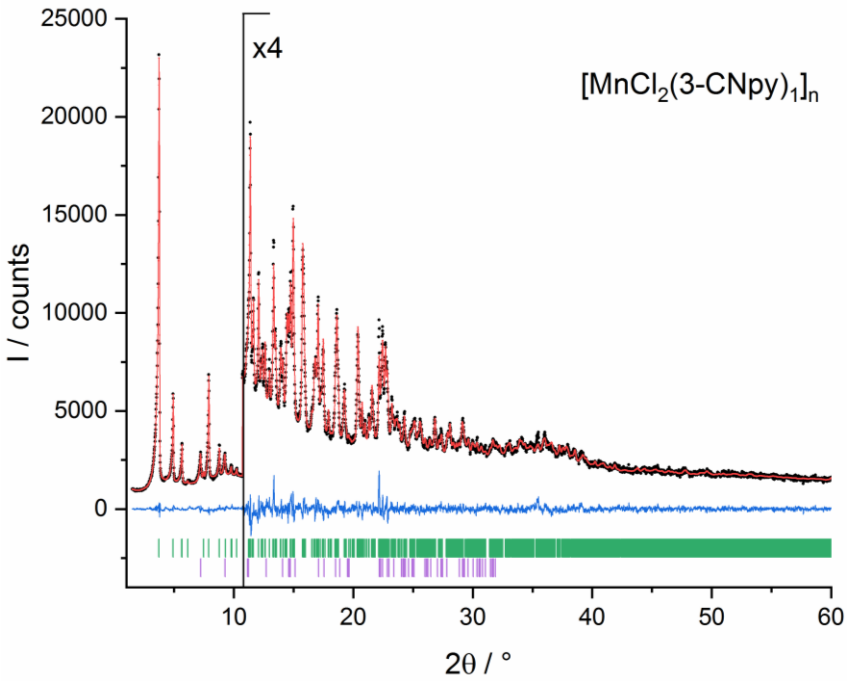

Figure S23. Rietveld plot of $[MnCl_2(3\text{-}CNpy)_1]_n$ (**1b**). Observed powder diagram (black points), simulated powder diagram (red solid line), difference profile (blue solid line) and reflection positions (green tick marks). Change of the scales with corresponding factors is indicated in the diagrams. Reflection positions of $[MnCl_2(3\text{-}CNpy)_{1/3}]_n$ (**1c**) are shown in violet.

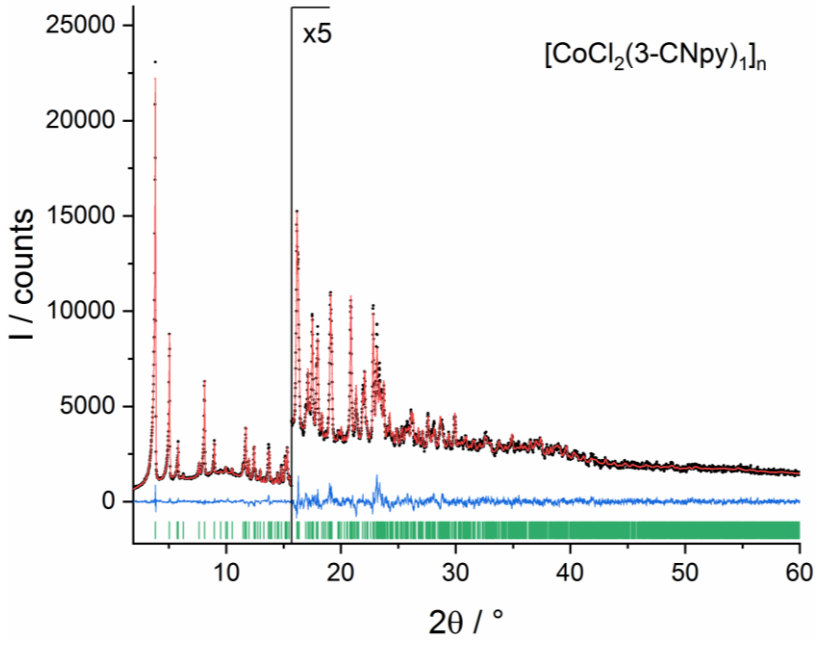

Figure S24. Rietveld plot of $[CoCl_2(3\text{-}CNpy)_1]_n$ (**3b**). Observed powder diagram (black points), simulated powder diagram (red solid line), difference profile (blue solid line) and reflection positions (green tick marks). Change of the scales with corresponding factors is indicated in the diagrams. XRPD data were collected with Mo $K\alpha_1$ radiation.

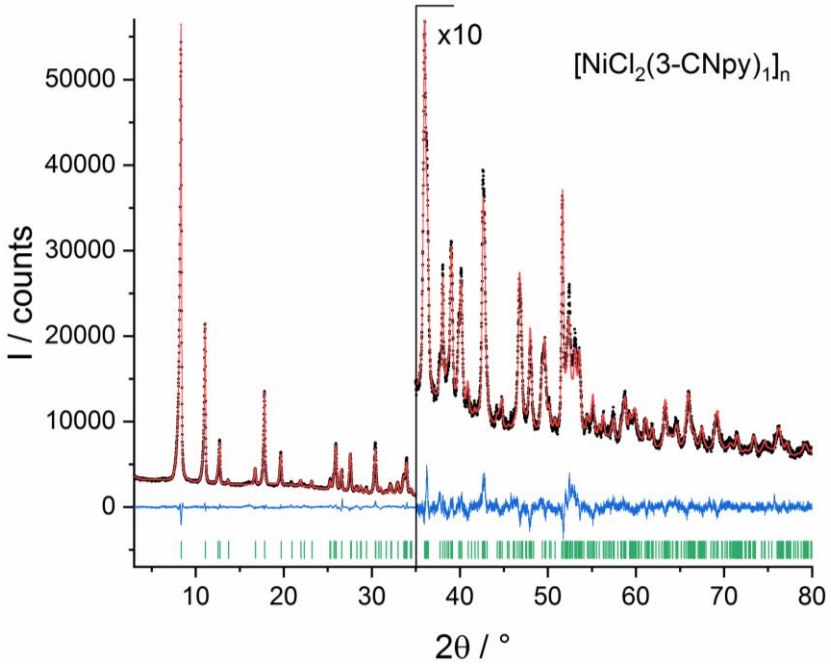

Figure S25. Rietveld plot of $[NiCl_2(3\text{-}CNpy)_1]_n$ (**4b**). Observed powder diagram (black points), simulated powder diagram (red solid line), difference profile (blue solid line) and reflection positions (green tick marks). Change of the scales with corresponding factors is indicated in the diagrams.

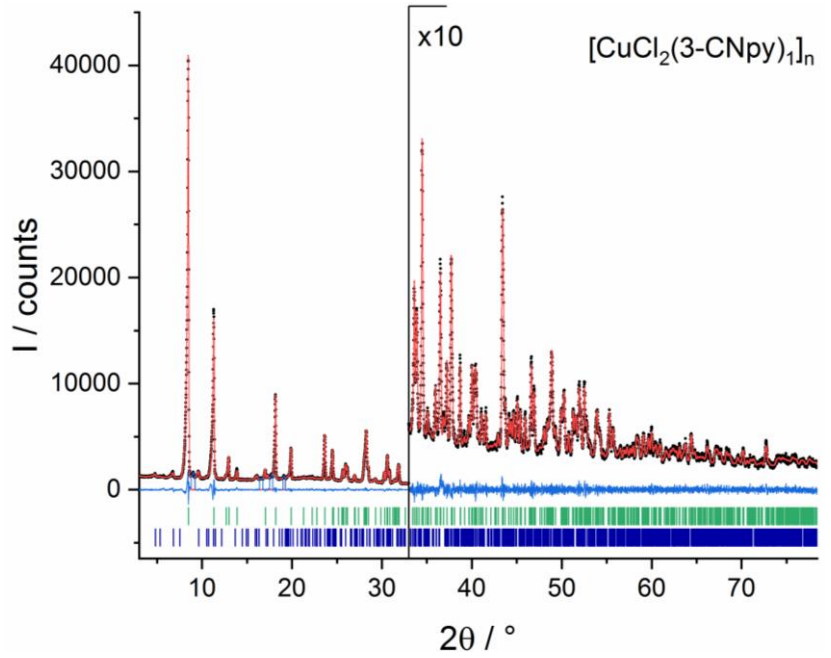

Figure S26. Rietveld plot of $[CuCl_2(3\text{-}CNpy)_1]_n$ (**5b**). Observed powder diagram (black points), simulated powder diagram (red solid line), difference profile (blue solid line) and reflection positions (green tick marks). Reflection positions of $[CuCl_2(3\text{-}CNpy)_{1/2}]_n$ (**5c**) are shown in dark blue. Reflections of a further foreign phase are excluded. Change of the scales with corresponding factors is indicated in the diagram.

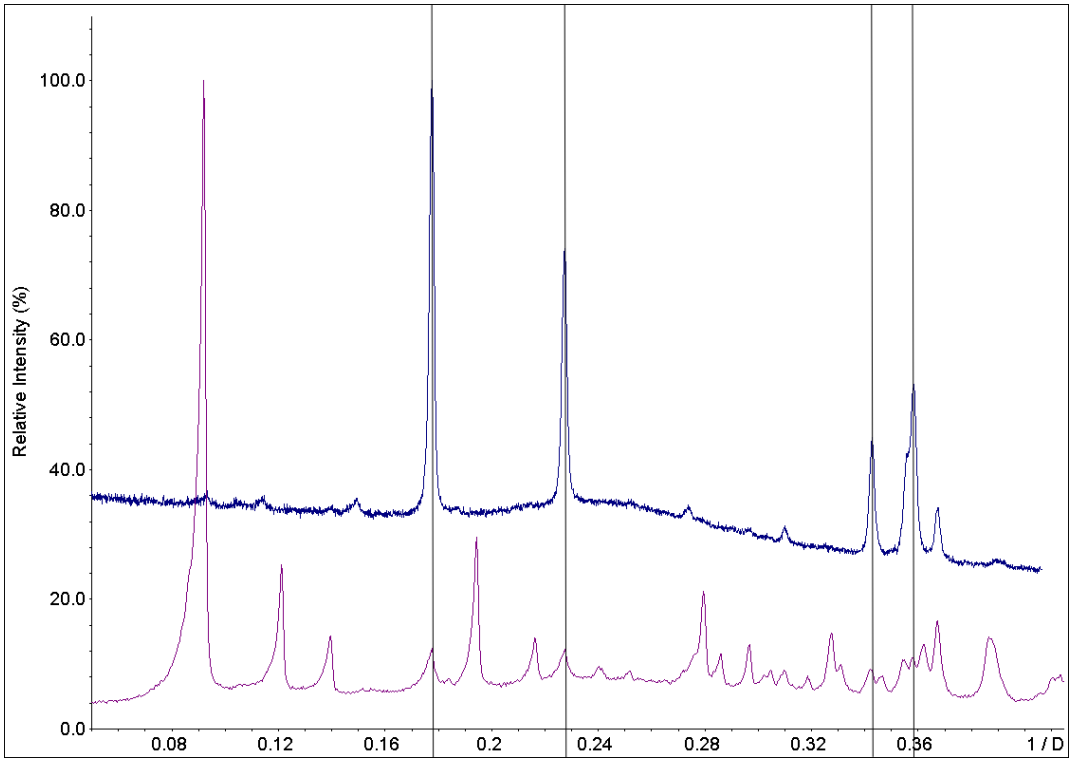

Figure S27. XRPD of $[MnCl_2(3\text{-}CNpy)_1]_n$ (**1b**) (violet pattern) containing foreign reflections (grey lines) of $[MnCl_2(3\text{-}CNpy)_{1/3}]_n$ (**1c**) (blue pattern); reflections XRPD data of **1b** were collected with Mo $K\alpha_1$ radiation. XRPD data of **1c** were collected with Cu $K\alpha_1$ radiation.

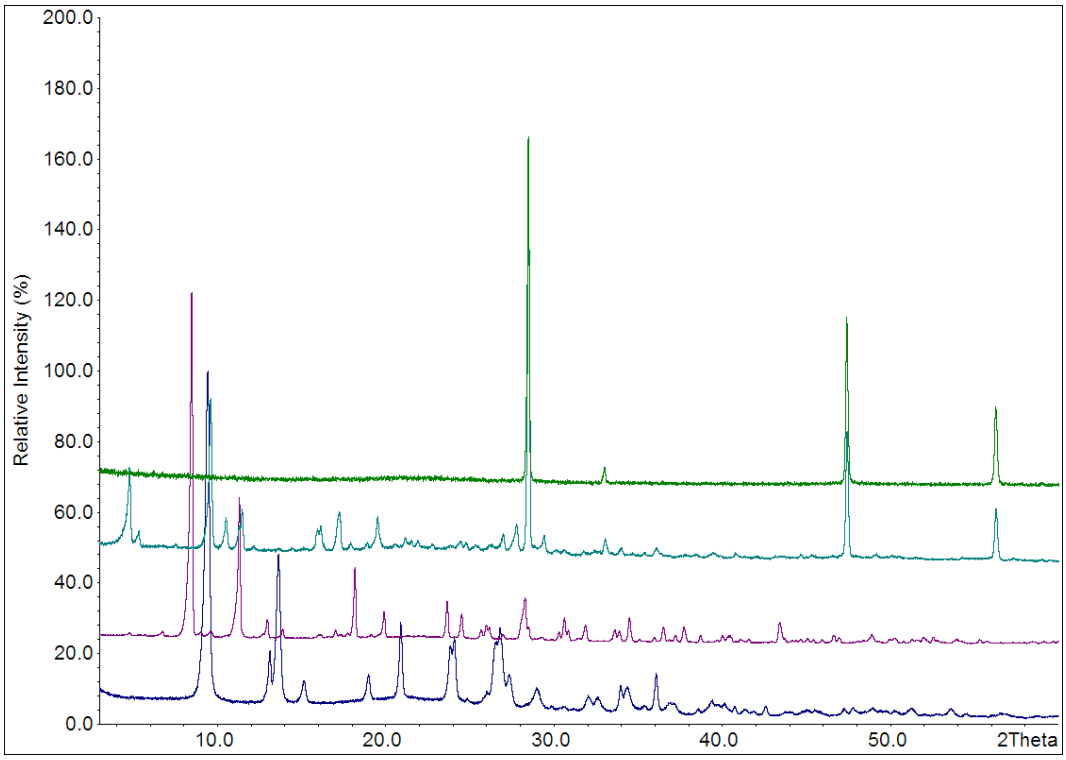

Figure S28. XRPD of the Cu series, showing $[CuCl_2(3\text{-}CNpy)_2]_n$ (**5a**), blue pattern; $[CuCl_2(3\text{-}CNpy)_1]_n$ (**5b**) violet, $[CuCl_2(3\text{-}CNpy)_{1/2}]_n$ (**5c**), light green; and CuCl, dark green (top). XRPD of **5b** contains foreign reflections of **5c**. Further thermal decomposition is accompanied by the formation of CuCl.

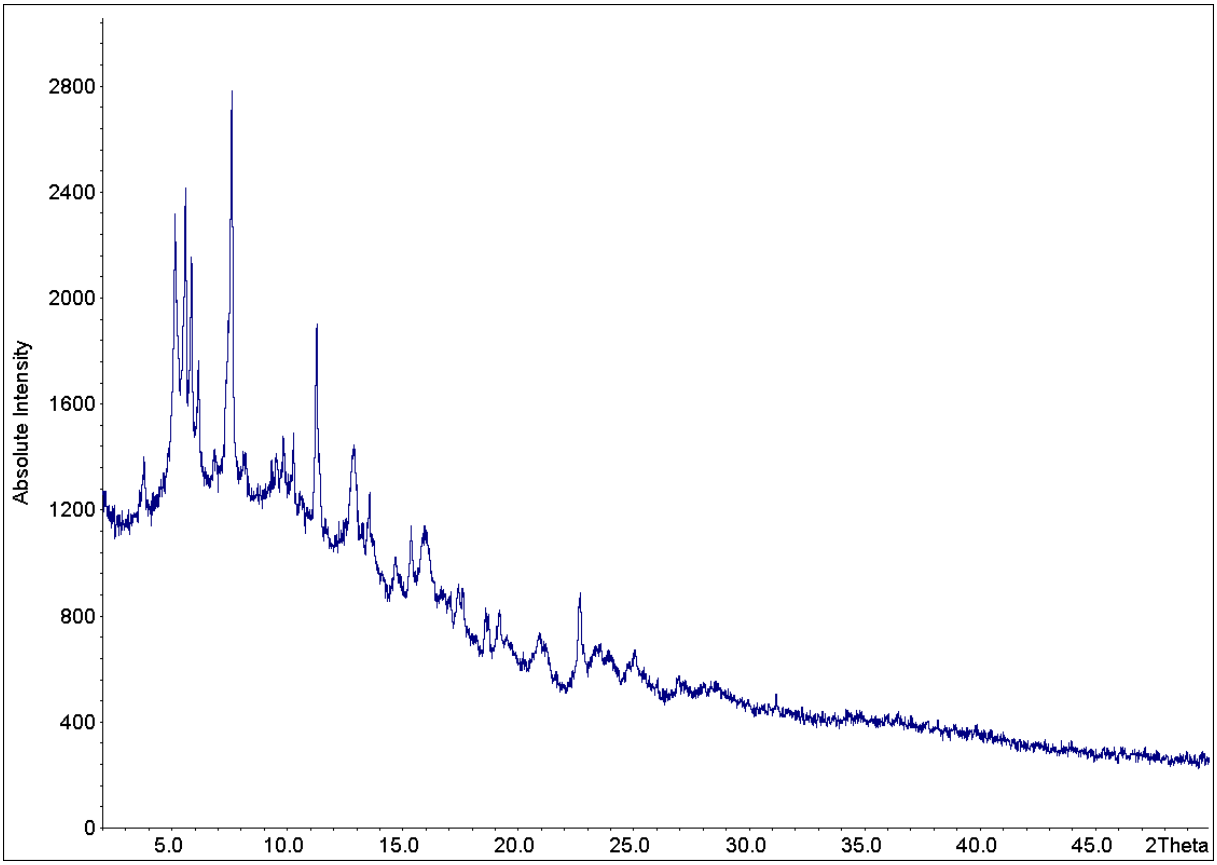

Figure S29. XRPD of $[FeCl_2(3\text{-}CNpy)_1]_n$ (**2b**). The data were collected with Mo $K\alpha_1$ radiation. The structure solution has not been successful.

Table S1. Results of DTA/TG measurements of $[M^{II}Cl_2(3\text{-}CNpy)_2]$ (M^{II} = Mn, Fe, Co, Ni, Cu, Zn). T: DTA peak temperatures, m_0: weight of starting compound, Δm_{exp}: relative experimental weight loss, experimental $\Delta m_{exp}/m_0$, calculated $\Delta m_{cal}/m_0$.

Compound	T / °C	m_0 / mg	Δm_{exp} / mg	$\Delta m_{exp}/m_0$ / %	$\Delta m_{cal}/m_0$ / %
(**1**)					
$[MnCl_2(3\text{-}CNpy)_2]_n$		34.44	0	0	0
$[MnCl_2(3\text{-}CNpy)_1]_n$	246.9*		10.49	30.47	31.16
$[MnCl_2(3\text{-}CNpy)_{1/3}]_n$	275.1		7.27	30.34	30.18
$MnCl_2$	370.9		2.94	17.59	21.61
(**2**)					
$[FeCl_2(3\text{-}CNpy)_2]_n$		23.06	0	0	0
$[FeCl_2(3\text{-}CNpy)_1]_n$	243.4		5.62	24.49	31.08
$[FeCl_2(3\text{-}CNpy)_{1/2}]_n$	319.6		3.78	21.66	22.52
$FeCl_2$	373.4		2.76	19.72	29.11
$[FeCl_2(3\text{-}CNpy)_1]_n$	243.4		5.62	24.49	31.08
$[FeCl_2(3\text{-}CNpy)_{1/3}]_n$	319.6		3.78	21.66	30.07
$FeCl_2$	373.4		2.76	19.72	21.49
(**3**)					
$[CoCl_2(3\text{-}CNpy)_2]_n$		16.03	0	0	0
$[CoCl_2(3\text{-}CNpy)_1]_n$	237.6		4.51	28.13	30.79
$[CoCl_2(3\text{-}CNpy)_{1/3}]_n$	293.4		2.99	25.92	29.67
$CoCl_2$	361.8		1.11	12.98	21.09
$[CoCl_2(3\text{-}CNpy)_1]_n$	237.6		4.51	28.13	30.79
$[CoCl_2(3\text{-}CNpy)_{1/2}]_n$	293.4		2.99	25.92	22.25
$CoCl_2$	361.8		1.11	12.98	28.62
(**4**)					
$[NiCl_2(3\text{-}CNpy)_2]_n$		24.64	0	0	0
$[NiCl_2(3\text{-}CNpy)_1]_n$	295.7		6.054	24.57	30.82
$NiCl_2$	368.9		6.429	34.58	44.55
(**5**)					
$[CuCl_2(3\text{-}CNpy)_2]_n$		14.616			
$[CuCl_2(3\text{-}CNpy)_1]_n$	274.7		4.62	31.61	30.38
$[CuCl_2(3\text{-}CNpy)_{1/2}]_n$	302.9		2.57	25.71	21.81
$CuCl_2$	323.0		2.39	32.18	27.91
(**6**)					
$[ZnCl_2(3\text{-}CNpy)_2]$		13.56	0	0	0
$ZnCl_2$	187.0		4.80	35.44	60.43

Table S2 - Part 1. Crystallographic data of $[M^{II}Cl_2(3\text{-}CNpy)_2]_n$ (**1a**-**4a**).

	1a	**2a**	**3a**	**4a**
Compound	$[MnCl_2(3\text{-}CNpy)_2]_n$	$[FeCl_2(3\text{-}CNpy)_2]_n$	$[CoCl_2(3\text{-}CNpy)_2]_n$	$[NiCl_2(3\text{-}CNpy)_2]_n$
CCDC number/ CSD code	1904113	1904107	1904105	1904110
Structure determined from	Powder	Powder	Powder	Powder
Formula	$C_{12}H_8Cl_2MnN_4$	$C_{12}H_8Cl_2FeN_4$	$C_{12}H_8Cl_2CoN_4$	$C_{12}H_8Cl_2NiN_4$
MW /g·mol^{-1}	334.06	334.96	338.05	337.81
Crystal system	Monoclinic	Monoclinic	Monoclinic	Monoclinic
Space group (No.)	*P* 2$_1$/*c* (14)	*P* 2$_1$/*c* (14)	*C c* (9)	*C c* (9)
***a* /Å**	3.7030(4)	3.6440(2)	3.6186(2)	3.5837(3)
***b* /Å**	15.4310(4)	13.8135(8)	27.504(2)	27.2889(3)
***c* /Å**	11.5780(3)	13.1192(11)	13.2081(12)	13.1815(3)
***α* /°**	90	90	90	90
***ß* /°**	91.438(2)	98.532(7)	97.49(2)	97.715(4)
***γ* /°**	90	90	90	90
***V* /Å^3**	661.3(6)	653.0(8)	1302.6(9)	1277.4(2)
Z, Z'	2, ½	2, ½	4, 1	4, 1
Site symmetry of M^{II}	$\bar{1}$	$\bar{1}$	1	1
***D*$_{calc}$ /Mg·m^{-3}**				
T /K	298	298	298	298
Radiation type	Cu *Kα*$_1$	Mo *Kα*$_1$	Mo *Kα*$_1$	Cu *Kα*$_1$
Wavelength /Å	1.54056	0.70930	0.70930	1.54056
2Θ$_{max}$ /°	80	60	60	100
***R*$_p$ /%**	1.411	2.771	2.348	2.665
***R*$_{wp}$ /%**	1.805	3.448	3.179	3.140
***R*$_{exp}$ /%**	1.562	2.260	2.468	1.617
GOF	1.156	1.525	1.288	1.942
***R*$_p$' /%** [a]	18.327	11.862	11.525	9.804
***R*$_{wp}$' /%** [a]	12.477	11.391	10.777	10.094
***R*$_{exp}$' /%** [a]	10.796	7.467	8.365	5.197
a) *R$_p$'*, *R$_{wp}$'* and *R$_{exp}$'* values are background corrected according to the reference [38].				

Table S2 - Part 2. Crystallographic data of $[M^{II}Cl_2(3\text{-}CNpy)_2]_{(n)}$ (**5a, α-6a, β-6a**).

	5a	**5a [20]**	**α-6a**	**β-6a**
Compound	$[CuCl_2(3\text{-}CNpy)_2]_n$	$[CuCl_2(3\text{-}CNpy)_2]_n$	$[ZnCl_2(3\text{-}CNpy)_2]$	$[ZnCl_2(3\text{-}CNpy)_2]$
CCDC number/ CSD code	1904106	UTIHAH	1904111	1904112
Structure determined from	Powder	Single crystal	Powder	Powder
Formula	$C_{12}H_8Cl_2CuN_4$	$C_{12}H_8Cl_2CuN_4$	$C_{12}H_8Cl_2ZnN_4$	$C_{12}H_8Cl_2ZnN_4$
MW /g·mol^{-1}	342.67	342.67	334.53	334.53
Crystal system	Monoclinic	Monoclinic	Orthorhombic	Monoclinic
Space group (No.)	*P* 2$_1$/*c* (14)	*P* 2$_1$/*c* (14)	*P nma* (62)	*P* 2$_1$/*c* (14)
***a* /Å**	3.7560(1)	3.710(2)	10.6653(3)	11.6619(15)
***b* /Å**	13.4653(3)	13.420(4)	20.3998(5)	15.0731(18)
***c* /Å**	13.0443(5)	12.987(2)	6.6114(17)	8.0572(10)
***α* /°**	90	90	90	90
***ß* /°**	97.347(3)	97.48(?)	90.0	91.0112(9)
***γ* /°**	90	90	90	90
***V* /Å^3**	654.3(4)	641.0(9)	1438.4(6)	1416.0(7)
Z, Z'	2, ½	2, ½	4, ½	4, 1
Site symmetry of M^{II}	$\bar{1}$	$\bar{1}$	*.m.*	1
***D*$_{calc}$ /Mg·m^{-3}**		1.775		
T /K	298	123	298	298
Radiation type	Cu *Kα*$_1$	Mo *Kα*	Cu *Kα*$_1$	Cu *Kα*$_1$
Wavelength /Å	1.54056	0.71073	1.54056	1.54056
2Θ$_{max}$ /°	80		100	100
***R$_p$* /%**	2.996	R_1 = 4.32	3.768	2.172
***R$_{wp}$* /%**	3.925		5.104	2.792
***R$_{exp}$* /%**	3.248		3.188	2.109
GOF	1.208		1.601	1.324
***R$_p$'* /%** [a]	8.133		13.723	9.449
***R$_{wp}$'* /%** [a]	8.579		13.588	9.075
***R$_{exp}$'* /%** [a]	7.099		8.487	6.855
a) *R$_p$'*, *R$_{wp}$'* and *R$_{exp}$'* values are background corrected according to the reference [38].				

Table S3. Crystallographic data of $[M^{II}Cl_2(3\text{-}CNpy)_1]_n$ (**1b, 3b**-**5b**).

	1b	**3b**	**4b**	**5b**
Compound	$[MnCl_2(3\text{-}CNpy)_1]_n$	$[CoCl_2(3\text{-}CNpy)_1]_n$	$[NiCl_2(3\text{-}CNpy)_1]_n$	$[CuCl_2(3\text{-}CNpy)_1]_n$
CCDC number/ CSD code	1904108	1904114	1904109	1904115
Structure determined from	Powder	Powder	Powder	Powder
Formula	$C_6H_4Cl_2MnN_2$	$C_6H_4Cl_2CoN_2$	$C_6H_4Cl_2NiN_2$	$C_6H_4Cl_2CuN_2$
MW /g·mol^{-1}	229.95	233.95	233.71	238.56
Crystal system	Monoclinic	Orthorhombic	Orthorhombic	Monoclinic
Space group (No.)	*Pnma* (62)	*Pnma* (62)	*Pnma* (62)	$P2_1/c$ (14)
***a* /Å**	16.5338(9)	16.0863(5)	15.9026(4)	3.7753(8)
***b* /Å**	3.693(12)	3.5874(10)	3.5328(6)	13.9311(4)
***c* /Å**	14.4596(9)	14.1910(5)	14.0807(4)	15.6849(3)
***α* /°**	90	90	90	90
***ß* /°**	90.0	90	90	96.114(3)
***γ* /°**	90	90	90	90
***V* /Å^3**	882.96(3)	818.9(1)	791.0(5)	820.2(4)
Z, Z'	4, ½	4, ½	4, ½	4, 1
Site symmetry of M^{II}	*.m.*	*.m.*	*.m.*	1
***D*$_{calc}$ /Mg·m^{-3}**				
T /K	298	298	298	298
Radiation type	Mo $K\alpha_1$	Mo $K\alpha_1$	Cu $K\alpha_1$	Cu $K\alpha_1$
Wavelength /Å	0.70930	0.70930	1.54056	1.54056
2Θ$_{max}$ /°	60	60	100	80
***R*$_p$ /%**	2.919	3.106	2.855	3.327
***R*$_{wp}$ /%**	3.846	4.135	3.949	4.454
***R*$_{exp}$ /%**	3.038	3.416	2.235	3.037
GOF	1.266	1.211	1.767	1.467
***R*$_p$' /%** [a]	10.620	11.498	8.994	6.172
***R*$_{wp}$' /%** [a]	11.042	11.403	10.396	7.176
***R*$_{exp}$' /%** [a]	8.722	9.419	5.883	4.893
a) R_p', R_{wp}' and R_{exp}' values are background corrected according to the reference [38].				

Text S1

Details on syntheses of $[M^{II}Cl_2(3\text{-CNpy})_2]_{(n)}$

Synthesis of $[MnCl_2(3\text{-CNpy})_2]_n$ (1a). $MnCl_2 \cdot 4\ H_2O$ (0.5 g, 2.53 mmol) was dissolved in 10mL ethanol, 3-CNpy (1.06 g, 10.18 mmol) was dissolved in 20 mL ethanol. By mixing both solutions, a colorless powder was obtained. IR (cm^{-1}): 3101(w), 2236(m), 1595(m), 1473(s), 1417(s), 1043(m), 1037(m), 806(s), 689(s), 644(s).

Synthesis of $[FeCl_2(3\text{-CNpy})_2]_n$ (2a). $FeCl_2 \cdot 4\ H_2O$ (2.5 g, 12.57 mmol) was dissolved in 20mL ethanol, 3-CNpy (2.5 g, 24.01 mmol) was dissolved in 20 mL ethanol. By mixing both solutions, a yellow powder was obtained. IR (cm^{-1}): 3073(m), 2237(s), 1596(s), 1473(s), 1421(s), 1044(m), 1036(m), 815 (s), 690(s), 648(s).

Synthesis of $[CoCl_2(3\text{-CNpy})_2]_n$ (3a). $CoCl_2 \cdot 6\ H_2O$ (1.0 g, 4.2 mmol) was dissolved in 10 mL methanol, 3-CNpy (0.44 g, 4.4 mmol) was dissolved in 20 mL methanol. By mixing both solutions, a light violet powder was obtained. IR (cm^{-1}): 3068(m), 2238(m), 1599(m), 1473(s), 1045(m), 1036(m), 815(s), 689(s), 651(s).

Synthesis of $[NiCl_2(3\text{-CNpy})_2]_n$ (4a). $NiCl_2 \cdot 6\ H_2O$ (1.0 g, 4.21 mmol) was dissolved in 15 mL methanol, 3-CNpy (0.44 g, 4.4 mmol) was dissolved in 10 mL methanol. By mixing both solutions, a light green powder was obtained. IR (cm^{-1}): 3070(w), 2237(m), 1600(m), 1473(s), 1419(s), 1047(m), 1038(m), 814(s), 688(s), 653(s).

Synthesis of $[CuCl_2(3\text{-CNpy})_2]_n$ (5a). $CuCl_2 \cdot 2\ H_2O$ (0,5 g, 2,93 mmol) was dissolved in 25 mL ethanol, 3-CNpy (1.30 g, 15.8 mmol) was dissolved in 15 mL ethanol. By mixing both solutions, an azure blue powder was obtained. IR (cm^{-1}): 3066(w), 2237(m), 1601(m), 1472(s), 1419(s), 1049(m), 1034(m), 820(s), 687(s), 659(m).

Synthesis of $[ZnCl_2(3\text{-CNpy})_2]$ (α-6a/ β-6a). $ZnCl_2 \cdot 4\ H_2O$ (0.46 g, 2.22 mmol) was dissolved in 3 mL ethanol, 3-CNpy (1.56 g, 15.04 mmol) was dissolved in 6 mL ethanol. The mixture was put in a fridge (~8 °C), and a colorless needle shaped powder (**α-6**) was obtained after slow evaporation of ethanol during two days. **α-6a** transforms within several hours at room temperature into **β-6a.** IR of the mixture (cm^{-1}): 3112(w), 3055(w), 2242(w), 1614(s), 1495(m), 1417(s), 1064(s), 1027(s), 824(s), 672(m).

Text S2

Details on preparation of $[M^{II}Cl_2(3\text{-}CNpy)_1]_n$

Preparation of $[MnCl_2(3\text{-}CNpy)_1]_n$ (1b). 1b was prepared by thermal decomposition of $[MnCl_2(3\text{-}CNpy)_2]_n$ (**1a**). A light brown powder was obtained. Unfortunately, **1b** could not be prepared as pure phase and the measured sample contains a small quantity of $[MnCl_2(3\text{-}CNpy)_{1/3}]_n$. IR of the mixture ($cm^{-1}$): 2237(m), 1603(s), 1473(s), 1420(s), 1045(m), 1042(s), 816 (m), 690(s), 646(s).

Preparation of $[CoCl_2(3\text{-}CNpy)_1]_n$ (3b). 3b was prepared by thermal decomposition of $[CoCl_2(3\text{-}CNpy)_2]_n$ (**3a**)**.** A light violet powder was obtained. IR (cm^{-1}): 3067(w), 2237(m), 1598(s), 1473(s), 1420(s), 1045(m), 1036(m), 815 (m), 687(s), 650(s).

Preparation of $[NiCl_2(3\text{-}CNpy)_1]_n$ (4b). 4b was prepared by thermal decomposition of $[NiCl_2(3\text{-}CNpy)_2]_n$ (**4a**). An ochre powder was obtained. IR (cm^{-1}): 3065(w), 2237(m), 1603(s), 1468(s), 1420(s), 1037(m), 809(s), 689(s), 656(m).

Preparation of $[CuCl_2(3\text{-}CNpy)_1]_n$ (5b). 5b was prepared by thermal decomposition of $[CuCl_2(3\text{-}CNpy)_2]_n$ (**5a**)**.** A light blue powder was obtained. Several heating procedures with different temperatures and rates were performed in order to prepare $[CuCl_2(3\text{-}CNpy)_1]_n$ as pure phase, but remained unsuccessful. Temperature dependent XRPD experiments revealed, that $[CuCl_2(3\text{-}CNpy)_1]_n$ decomposes likely into $[CuCl_2(3\text{-}CNpy)_{1/3}]_n$ or CuCl and could not be prepared on the diffractometer instead (see Fig. S15). IR of the mixture (cm^{-1}): 3063(w), 2237(w), 1603(m), 1477(s), 1416(m), 1071(m), 1034(m), 815(s), 688(s), 659(s).

Text S3

Further details on structure solution and Rietveld refinements.

$[MnCl_2(3\text{-}CNpy)_2]_n$ (1a). The first 20 peaks were selected for indexing in DASH which resulted in an orthorhombic unit cell with $Z = 2$. Structure solution was carried out using simulated annealing with DASH. The molecular fragment ($MnCl_2(3\text{-}CNpy)_1$) was restricted to rotate around the Mn atom on special position (0,0,0). The Cl atom was fixed on $x = {}^1/_2$ during the refinement.

[$MnCl_2(3\text{-}CNpy)_1]_n$ (1b). At first, a Pawley fit was performed in TOPAS refining background and instrumental parameters (zero point, axial divergence). Next, size and strain parameters were refined. The crystal structure crystal structure of $[NiCl_2(3\text{-}CNpy)_1]_n$ was used as starting point for the subsequent structure refinement.

[$FeCl_2(3\text{-}CNpy)_2]_n$ (2a). The first 20 peaks were selected for indexing in CONOGRAPH which resulted in a monoclinic unit cell with $Z = 4$. Structure solution was carried out using simulated annealing with DASH. The molecular fragment ($FeCl_2(3\text{-}CNpy)_1$) was restricted to rotate around the Fe atom on special position (0,0,0).

[$CoCl_2(3\text{-}CNpy)_2]_n$ (3a). At first, a Pawley fit was performed in TOPAS (Coelho, 2018), refining background and instrumental parameters (zero point, axial divergence). Next, size and strain parameters were refined. The crystal structure of $[NiCl_2(3\text{-}CNpy)_2]_n$ (**4a**) was used as starting point for the subsequent structure refinement.

[$CoCl_2(3\text{-}CNpy)_1]_n$ (3b). At first, a Pawley fit was performed in TOPAS, refining background and instrumental parameters (zero point, axial divergence). Next, size and strain parameters were refined. The crystal structure of $[NiCl_2(3\text{-}CNpy)_1]_n$ was used as starting point for the subsequent structure refinement.

[$NiCl_2(3\text{-}CNpy)_2]_n$ (4a). At first, a Pawley fit was performed in TOPAS, background and instrumental parameters (zero point, axial divergence). Next, size and strain parameters were refined. The crystal structure of $[NiBr_2(3\text{-}CNpy)_2]_n$ [1] was used as starting point for the subsequent structure refinement.

[$NiCl_2(3\text{-}CNpy)_1]_n$ (4b). The first 20 peaks were selected for indexing in CONOGRAPH which resulted in an orthorhombic unit cell with $Z = 4$. Structure solution was carried out using simulated annealing in DASH. A molecular starting model was derived from the crystal structure of $[NiCl_2(3\text{-}CNpy)_2]_n$. The Ni atom and the pyridine ring were placed on special position (x, $^1/_4$,z) and the molecular fragment ($NiCl_2(3\text{-}CNpy)_1$) was restricted to rotate around the Ni atom during the simulated annealing. The Ni atom and the pyridine ring were fixed on y = $^1/_4$ and the Cl atoms were fixed on y = $^3/_4$ during the refinement.

$[CuCl_2(3\text{-}CNpy)_2]_n$ (5a). At first, a Pawley fit was performed in TOPAS, refining background and instrumental parameters (zero point, axial divergence). Next, size and strain parameters were refined. The single crystal structure [20] was used as starting point for the subsequent structure refinement.

$[CuCl_2(3\text{-}CNpy)_1]_n$ (5b). The first reliable 20 peaks were selected for indexing in DASH which resulted in a monoclinic unit cell with $Z = 2$. Structure solution was carried out using simulated annealing with DASH. The molecular fragment ($CuCl_2(3\text{-}CNpy)_1$) was restricted to rotate around the Cu atom.

α-$[ZnCl_2(3\text{-}CNpy)_2]$ (α-6a). The first 20 peaks were selected for indexing in CONOGRAPH which resulted in an orthorhombic unit cell with $Z = 4$. Structure solution was carried out using simulated annealing with DASH. A starting molecular model was derived from the crystal structure of $[ZnBr_2(3\text{-}CNpy)_2]$ [28]. The Zn and Cl atoms were placed on special position (x,$^1/_4$,z); the molecular fragment was restricted to rotate around the Zn atom during simulated annealing. Rietveld refinement was carried out with TOPAS. The Zn and Cl atoms were fixed on y = $^1/_4$. Preferred orientation (in [010]-direction) was observed and thus refined.

β-$[ZnCl_2(3\text{-}CNpy)_2]$ (β-6a). The first 20 peaks were selected for indexing in CONOGRAPH, which resulted in a monoclinic unit cell with $Z = 4$. Structure solution was carried out using simulated annealing in DASH using a starting molecular model derived from the crystal structure of α-$[ZnCl_2(3\text{-}CNpy)_2]$ (**α-6a**). The molecular fragment was restricted to rotate around the Zn atom. Rietveld refinement was carried out with TOPAS. The Zn and Cl atoms were fixed on y = $^1/_4$.

[MH4]

4-Cyanopyridine complexes $[MX_2(4\text{-CNpy})_x]_n$ (with X = Cl, Br and x = 1, 2): crystal structures, thermal properties and a comparison with $[MX_2(3\text{-CNpy})_x]_n$ complexes.
Miriam Heine, Lothar Fink and Martin U. Schmidt, In: CrystEngComm, 2020, 22, 2067-2082.

CrystEngComm

ROYAL SOCIETY OF CHEMISTRY

PAPER

View Article Online
View Journal | View Issue

Cite this: *CrystEngComm*, 2020, **22**, 2067

4-Cyanopyridine complexes $[MX_2(4\text{-CNpy})_x]_n$ (with X = Cl, Br and x = 1, 2): crystal structures, thermal properties and a comparison with $[MX_2(3\text{-CNpy})_x]_n$ complexes†

Miriam Heine, Lothar Fink and Martin U. Schmidt *

Received 22nd December 2019,
Accepted 10th February 2020

DOI: 10.1039/c9ce02012h

rsc.li/crystengcomm

Eleven new complexes $[MX_2(4\text{-CNpy})_x]_{(n)}$ with M = Mn, Fe, Co, Ni, Cu, and Zn, X = Cl and Br, 4-CNpy = 4-cyanopyridine, and x = 1 and 2 have been prepared and their structures were characterized by X-ray powder diffraction (XRPD). The reaction of the transition metal halides MX_2 (M = Mn, Fe, Co, Ni, Cu and X = Cl, Br) with 4-CNpy leads to the formation of coordination compounds with the composition $[MX_2(4\text{-CNpy})_2]_n$ first. In all these compounds, the metal atoms are octahedrally coordinated by four halogen atoms and two 4-CNpy ligands. The halogen atoms bridge the metal atoms, leading to infinite $[MX_2]_n$ chains. The 4-CNpy molecules coordinate through their pyridine N atoms (N_{py}) and form lateral "wings" on the $[MX_2]_n$ chains. The manganese compound $[MnBr_2(4\text{-CNpy})_2]_n$ shows polymorphism with a fully reversible phase transition. The thermal behaviour of compounds $[MX_2(4\text{-CNpy})_2]_{(n)}$ was investigated by a combined differential thermal and thermogravimetric analysis (DTA–TG). DTA results show that thermal annealing of $[MX_2(4\text{-CNpy})_2]_n$ at around 240–260 °C leads to compounds of composition $[MX_2(4\text{-CNpy})_1]_n$ (M = Mn, Fe, Co and X = Cl, Br). In these compounds, 4-CNpy acts as a bidentate ligand: the N_{py} and N_{CN} atoms both coordinate to the metal atoms, building (nearly) linear M-py-C≡N–M bridges between the $[MX_2]_n$ chains. This results in two-dimensional (2D) networks, which form the layer structures of the $[MX_2(4\text{-CNpy})_1]_n$ compounds. In all bromo compounds $[MBr_2(4\text{-CNpy})_1]_n$, the 4-CNpy bridges exhibit a head-to-tail-disorder with an inverted orientation of the 4-CNpy molecules between the metal atoms. Further heating of $[MX_2(4\text{-CNpy})_1]_n$ leads to $[MnBr_2(4\text{-CNpy})_{1/2}]_n$, $[FeCl_2(4\text{-CNpy})_{1/3}]_n$, $[CoCl_2(4\text{-CNpy})_{1/3}]_n$ and $[CoBr_2(4\text{-CNpy})_{1/3}]_n$ but their structures could not be determined yet. Additionally, the zinc compound $[ZnBr_2(4\text{-CNpy})_2]$ was prepared. In its both polymorphs, the Zn atoms are tetrahedrally coordinated by two bromine atoms and two 4-CNpy ligands (*via* the N_{py} atoms) to form discrete complexes. Upon heating to 240 °C, the Zn compound decomposes to $ZnBr_2$ without forming intermediate phases. In all compounds $[MX_2(4\text{-CNpy})_x]_{(n)}$, the coordination behavior of the 4-CNpy ligand was investigated by infrared (IR) spectroscopy. A comparison with the structures of the corresponding 3-CNpy compounds is given. This article aims at emphasizing the versatile ability of cyanopyridine to act as a mono- or bidentate ligand to build structures with isolated complexes, chains, double chains and planar or wavy 2D networks.

1. Introduction

In the last decade, investigations on coordination polymers and especially on syntheses of inorganic–organic hybrid materials have become one of the most relevant research fields in inorganic chemistry. In fact, inorganic–organic hybrid compounds offer various useful properties suitable for catalysis, molecular recognition, and gas adsorption and separation.[1] In order to prepare new coordination compounds with the desired properties, structure–property relationships have to be examined first. Coordination polymers built from transition metal (pseudo-)halides and heteroaromatic ligands have attracted much attention throughout the last few years.[2] In this context, we have reported on compounds built from 3d transition metal chlorides or bromides (MX_2) and N-donor ligands pyridine (py), 4-cyanopyridine (4-CNpy) or 3-cyanopyridine (3-CNpy).[3–7] Cyanopyridines are interesting organic ligands because of their two Lewis-donating nitrogen atoms, the N_{py} and N_{CN} atoms, which may connect two metal atoms. However, the Lewis-base character of the N_{py} atom is

Institute of Inorganic and Analytical Chemistry, Goethe University, Max-von-Laue-Str. 7, 60438 Frankfurt am Main, Germany.
E-mail: heine@chemie.uni-frankfurt.de, fink@chemie.uni-frankfurt.de, m.schmidt@chemie.uni-frankfurt.de; Fax: +49 69798 29235; Tel: +49 69798 29171

† Electronic supplementary information (ESI) available. See DOI: 10.1039/c9ce02012h

considerably higher than that of the N_{CN} atom and cyanopyridines mostly act as monodentate ligands through their N_{py} atom only. The Cambridge Structural Database (CSD)[8,9] contains about 250 structures with terminal cyanopyridine molecules (in which the N_{py} atom coordinates to a transition metal atom) and only about 20 structures with cyanopyridine as a bidentate ligand, connecting two metal atoms *via* both N atoms.[10–22] Therefore, we focused on the systematic preparation and structural characterization of new $[MX_2(CNpy)_x]_n$ compounds with bridging cyanopyridine molecules. In previous work, we reported on the syntheses and crystal structures of $[MBr_2(3\text{-CNpy})_1]_n$ (M = Mn, Fe, Co, Ni),[3] $[MCl_2(4\text{-CNpy})_1]_n$ (M = Mn, Ni) and $[NiBr_2(4\text{-CNpy})_1]_n$.[3,4,7] The compounds $[MBr_2(3\text{-CNpy})_1]_n$ are even considered to be the first ones with bidentate 3-CNpy ligands connecting two 3d M^{2+} ions. In the following a brief overview of their structural variety is given. Three main structural motifs can be found in the solid state:

(1) In all compounds $[MX_2(CNpy)_x]_n$ (M = Mn, Fe, Co or Ni, and X = Cl or Br) with $x = 2$ or $x = 1$, the metal atoms are connected to the neighboring metal atoms by four μ-bridging halide atoms, leading to $[MX_2]_n$ single chains in the first instance (Scheme 1a). In the case of $x = 2$ with X = Cl or Br, 3-CNpy and 4-CNpy always behave monodentately.

(2) In all cases of $x = 1$ with X = Br, 3-CNpy and 4-CNpy are both bidentate ligands, connecting the $[MX_2]_n$ chains *via* their two nitrogen atoms into networks (Scheme 1b, Table 1).

(3) Interestingly, in most hitherto known compounds with $x = 1$ and X = Cl, 4-CNpy generally acts as a bidentate ligand (forming network structures), whereas 3-CNpy always behaves monodentately. This results in the formation of polymeric double chains with $[M_2Cl_4]_n$ units (Scheme 1c). To date, $[CuCl_2(4\text{-CNpy})_1]_n$ is the only 1 : 1 compound with 4-CNpy as a monodentate ligand.

Table 1 Overview: space groups and topology of hitherto known compounds $[MX_2(CNpy)_x]_n$ (with M = Mn, Fe, Co, Ni, Cu, Zn; CNpy = 3-CNpy, 4-CNpy, and X = Br, Cl). Structures determined from single crystal data are marked by a star. All other crystal structures were determined from powder data. Structures investigated in this work are denoted as **1a**–**5a**, **1b**–**5b**, **6** and **7**. C = single chains, D = double chains, N = network and I = isolated complexes

	$[MX_2(3\text{-CNpy})_2]_n$				$[MX_2(4\text{-CNpy})_2]_n$			
M^{II}	X = Cl		X = Br		X = Cl		X = Br	
Mn	$P2_1/n$	C	$Pnnm$	C	$*P2_1/n$	C	**1a**	
Fe	$P2_1/n$	C	$Pnnm$	C	**2a**		**3a**	
Co	Cc	C	$Pnnm$	C	$*P2_1/c$	C	**5a**	
			$P\bar{1}$	C	**4a**			
Ni	Cc	C	Cc	C	$P2_1/n$	C	$Pnnm$	C
			$P\bar{1}$	C				
Cu	$*P2_1/c$	C	$P2_1/c$	C	$P2_1/n$	C	**6**	
			$P\bar{1}$	I				
Zn	$Pnma$	I	$*Pbca$	I	$*I2/a$	I	7	
	$P2_1/c$	I						

	$[MX_2(3\text{-CNpy})_1]_n$				$[MX_2(4\text{-CNpy})_1]_n$			
M^{II}	X = Cl		X = Br		X = Cl		X = Br	
Mn	$P2_1/n$	D	$P2_1$	N	$P2/m$	N	**1b**	
Fe	—[a]		$Pmc2_1$	N	**2b**		**3b**	
Co	$Pnma$	D	$Pmc2_1$	N	Pm	N	**5b**	
Ni	$Pnma$	D	$Pmc2_1$	N	Pm	N	$P2/m$	N
Cu	$P2_1/c$	D	—[a]		$P2_1/n$	D	—[b]	
					$P\bar{1}$	D		
Zn	—[b]		—[b]		—[b]		—[b]	

[a] Compound detected by DTA–TG, but the structure is not solved. [b] Compound does not exist according to DTA–TG.

Motivated by these findings, we aimed at investigating further compounds with the composition $[MCl_2(4\text{-CNpy})_1]_n$ and $[MBr_2(4\text{-CNpy})_1]_n$. Will they exhibit network structures, too? And is $[CuCl_2(4\text{-CNpy})_1]_n$ the only structure of the

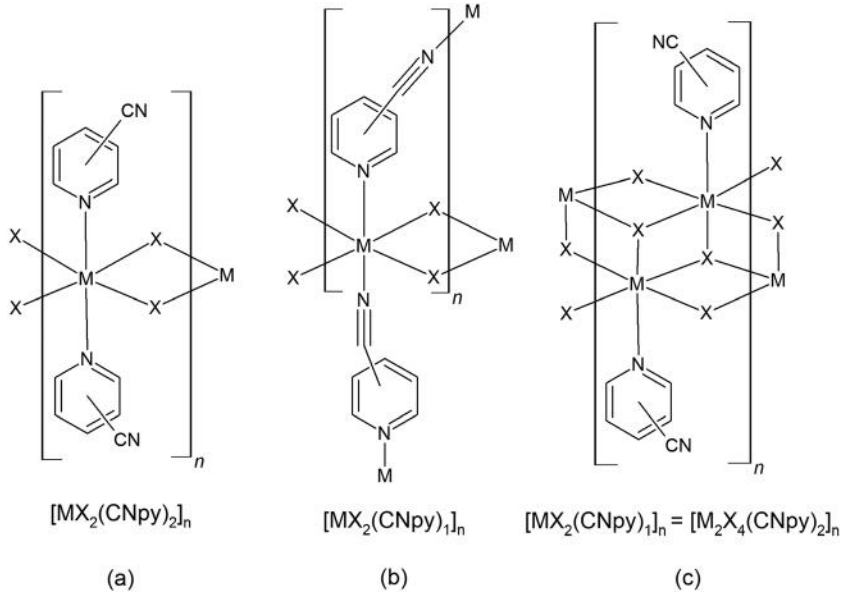

Scheme 1 Connectivity patterns of cyanopyridine compounds $[MX_2(CNpy)_2]_n$ and $[MX_2(CNpy)_1]_n$ with M = Mn, Fe, Co, Ni, and Cu, and X = Cl and Br. (a) Single chains, (b) 2D network with bridging organic ligands, and (c) double chains.

$[MCl_2(4\text{-CNpy})_1]_n$ series that forms double chains instead of networks?

To answer these questions, compounds $[MCl_2(4\text{-CNpy})_1]_n$ (M = Fe, Co) (**2b**, **4b**) and $[MBr_2(4\text{-CNpy})_1]_n$ (M = Mn, Fe, Co) (**1b**, **3b**, **5b**) were prepared by thermal decomposition of $[MX_2(4\text{-CNpy})_2]_n$ (**1a–5a**) under controlled conditions. The precursor compounds **1a–5a**, as well as $[CuBr_2(4\text{-CNpy})_2]_n$ (**6**) and $[ZnBr_2(4\text{-CNpy})_2]$ (**7**), were obtained from solution-based syntheses. Upon heating, **6** and **7** decompose directly into $CuBr_2$ and $ZnBr_2$, and the corresponding 1 : 1 compounds could not be obtained. Compounds **1a** and **7** show polymorphism. The crystal structures of **4a** and **5a** were determined[7,23] previously. All new phases were obtained only as micro- or nanocrystalline powders. Recrystallization was not possible because all compounds, especially **1b–5b**, are insoluble in water and sensitive to moisture and air. Hence, all crystal structures were determined by XRPD. IR spectroscopy was used to determine whether the N_{CN} atom of 4-CNpy coordinates to a metal atom.[24,25] Finally, we give an overview on all transition metal complexes built from MX_2 salts and 3- or 4-CNpy, to which we will refer in the following discussion part (Table 1).

2. Results and discussion

2.1 Syntheses of $[MX_2(4\text{-CNpy})_2]_n$ (1a–7)

Compounds of the composition $[MX_2(4\text{-CNpy})_2]_{(n)}$ were obtained by mixing an alcoholic solution of 4-CNpy and the corresponding MX_2 salt (hydrate). Different molar ratios of MX_2 were reacted with 4-CNpy, which always resulted in the formation of compounds with a metal-to-ligand ratio of 1 : 2. In the 3-CNpy series with MBr_2, this synthetic route even leads to the formation of compounds with a metal-to-ligand ratio of 1 : 4, *i.e.* $[MBr_2(3\text{-CNpy})_4]$. However, with 4-CNpy as a ligand, the analogous ligand-rich phases $[MCl_2(4\text{-CNpy})_4]$ and $[MBr_2(4\text{-CNpy})_4]$ are inaccessible from a solution based synthesis.

2.2 Syntheses of $[MX_2(4\text{-CNpy})_1]_n$ (1b–5b)

Samples of $[MX_2(4\text{-CNpy})_1]_n$ (**1b–5b**) were prepared by thermal decomposition of the corresponding precursors $[MX_2(4\text{-CNpy})_2]_n$ (**1a–5a**) at appropriate temperatures.[26] For details on DTA peak temperatures see Table S1 in the ESI.† In general, the thermal decomposition reaction carried out using a thermogravimetric device leads to samples with a higher crystallinity compared to samples prepared for diffraction measurements. Compounds **1b–3b** were prepared using the thermogravimetric device, subsequently cooled to room temperature and placed in glass capillaries (details are given in the Experimental section). Because of their particular sensitivity to moisture and air, the cobalt compounds **4b** and **5b** had to be prepared *in situ* using a customized heating device coupled to a powder diffractometer.

2.3 Thermoanalytical investigations

The thermal properties of $[MX_2(4\text{-CNpy})_2]_{(n)}$ were investigated by a combined DTA–TG analysis.[26] For example, upon heating $[CoCl_2(4\text{-CNpy})_2]_n$ (**4a**) using a thermobalance to 400 °C, the TG curve exhibits well-separated mass loss steps accompanied by distinct endothermic signals in the DTA curves (Fig. 1, Table S1†). This stepwise process reveals the existence of compounds with a lower metal-to-ligand ratio: the first endothermic signal at 252 °C is assigned to the release of half of the 4-CNpy ligands to form $[CoCl_2(4\text{-CNpy})_1]_n$ (**4b**), see eqn (1). The second endothermic signal at 338 °C is attributed to the decomposition of this intermediate compound to form $[CoCl_2(4\text{-CNpy})_{1/3}]_n$ (**4c**), see eqn (2). The remaining 4-CNpy is released in the third decomposition step at 410 °C, leaving $CoCl_2$, see eqn (3).

$$[CoCl_2(4\text{-CNpy})_2]_n \rightarrow [CoCl_2(4\text{-CNpy})_1]_n + n\ 4\text{-CNpy} \quad (1)$$

$$[CoCl_2(4\text{-CNpy})_1]_n \rightarrow [CoCl_2(4\text{-CNpy})_{1/3}]_n + 2/3n\ 4\text{-CNpy} \quad (2)$$

$$[CoCl_2(4\text{-CNpy})_{1/3}]_n \rightarrow CoCl_2 + 1/3n\ 4\text{-CNpy} \quad (3)$$

From the 1 : 2 compounds **1a–5a**, the corresponding 1 : 1 compounds are available (**1b–5b**). As in the series of **4a** (Fig. 1), the DTA–TG results of $[FeCl_2(4\text{-CNpy})_2]_n$ (**2a**), $[FeBr_2(4\text{-CNpy})_2]_n$ (**3a**) and $[CoBr_2(4\text{-CNpy})_2]_n$ (**5a**) point to the formation of intermediates with a metal-to-ligand ratio of 1 : 1/3, $[FeCl_2(4\text{-CNpy})_{1/3}]_n$ (**2c**), $[FeBr_2(4\text{-CNpy})_{1/3}]_n$ (**3c**) and $[CoBr_2(4\text{-CNpy})_{1/3}]_n$ (**5c**), respectively. In contrast, the thermoanalytical measurements of the manganese series (**1a**) point to the formation of $[MnBr_2(4\text{-CNpy})_{1/2}]_n$ (**1c**). However, the determination of the chemical composition from the TG data at 300–400 °C bears some uncertainties and the given stoichiometry of **1c–5c** should be regarded with caution. The copper compound $[CuBr_2(4\text{-CNpy})_2]_n$ (**6**), as well as the two polymorphs of $[ZnBr_2(4\text{-CNpy})_2]$ (**α-7** and **β-7**), decomposes at around 235–255 °C directly into $CuBr_2$ and $ZnBr_2$, respectively, without any hint of intermediate compounds with $x < 2$. For details on decomposition temperatures and weight loss calculations see Table S1 in the ESI.†

2.4 Spectroscopic investigations

In order to investigate the coordination behaviour of 4-CNpy, IR spectroscopy was used. If the 4-CNpy ligand does not coordinate through its N_{CN} atom but through its N_{py} atom only, then the asymmetric stretching vibration ν_{as}(C≡N) is expected to have a value similar to that of the free 4-CNpy molecule (2238–2240 cm^{-1}).[24,25] For a bidentate 4-CNpy ligand coordinating through its N_{py} and N_{CN} atoms, the asymmetric stretching vibration ν_{as}(C≡N) should be shifted to higher values of about 2275–2298 cm^{-1}, as it is observed in $[MBr_2(3\text{-CNpy})_1]_n$ compounds.[4] In all compounds of the type $[MX_2(4\text{-CNpy})_2]_n$ (**1a–5a**, **6**, **7**), the values of the asymmetric C≡N stretching vibration indicate that the 4-CNpy ligands

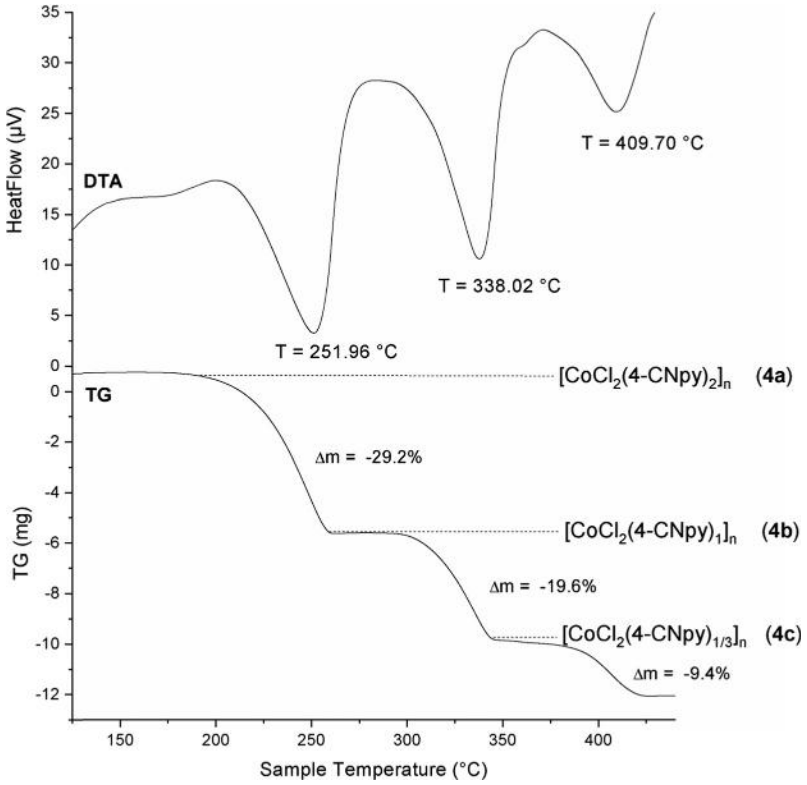

Fig. 1 DTA/TG curves of $[CoCl_2(4\text{-}CNpy)_2]_n$ (**4a**), showing the decomposition of **4a** *via* **4b** and *via* **4c** to $CoCl_2$.

behave monodentately, coordinating through the N_{py} atoms to the metal atoms (Table 2). No measurement of **γ-1a** was run, because this phase is unstable at room temperature.

In contrast, for compounds of the type $[MX_2(4\text{-}CNpy)_1]_n$ (**1b–5b**) the asymmetric stretching vibration $\nu_{as}(C{\equiv}N)$ is clearly shifted, indicating that 4-CNpy coordinates through the N_{py} and N_{CN} atoms. Hence, in **1b–5b** 4-CNpy forms a bridge between two metal atoms, as it is observed for the related $[MBr_2(3\text{-}CNpy)_1]_n$ compounds. Note that the samples of **1b–5b** are particularly sensitive to moisture and air and their IR data should be interpreted with caution. All IR spectra are compiled in the ESI,† Fig. S8 and S19.

2.5 Crystal structures and polymorphism of $[MX_2(4\text{-}CNpy)_2]_n$ (1a–5a, 6, 7). The crystal structures of $[MX_2(4\text{-}CNpy)_2]_n$ (**1a–5a, 6**) were determined from XRPD data. Selected crystallographic data are given in Table 3. Further details on the measurements and refinements are compiled in Table S2 (ESI†), and the Rietveld plots of structures **1a–6** are shown in Fig. S20–S30 (ESI†). In 2011, the crystal structure of **4a** was determined by Chen *et al.* from single

Table 2 Characteristic asymmetric stretching vibrations $\nu_{as}(C{\equiv}N)$ for 4-cyanopyridine, 3-cyanopyridine and their coordination polymers $[MX_2(CNpy)_2]_n$ and $[MX_2(CNpy)_1]_n$

Compound	$\nu_{as}(C{\equiv}N)$ [cm^{-1}]	Interaction
4-Cyanopyridine and its compounds		
4-Cyanopyridine	2238–2240	"Free ligand"
Compounds with a metal–ligand ratio of 1 : 2		
$[MCl_2(4\text{-}CNpy)_2]_n$ (**2a, 4a**)	2241–2242	Terminal ligand
$[MBr_2(4\text{-}CNpy)_2]_n$ (**α-1a, β-1a, 3a, 5a, 6,** α-7, β-7)	2234–2235	Terminal ligand
Compounds with a metal–ligand ratio of 1 : 1		
$[MCl_2(4\text{-}CNpy)_1]_n$ (**2b, 4b**)	2275–2288	Bridging ligand
$[CuCl_2(4\text{-}CNpy)_1]_n$	2243	Terminal ligand
$[MBr_2(4\text{-}CNpy)_1]_n$ (**1b, 3b, 5b**)	2281–2298	Bridging ligand
3-Cyanopyridine and its compounds		
3-Cyanopyridine	2230–2232	"Free ligand"
Compounds with a metal–ligand ratio of 1 : 2		
$[MCl_2(3\text{-}CNpy)_2]_n$	2236–2243	Terminal ligand
$[MBr_2(3\text{-}CNpy)_2]_n$	2236–2239	Terminal ligand
Compounds with a metal–ligand ratio of 1 : 1		
$[MCl_2(3\text{-}CNpy)_1]_n$	2236–2239	Terminal ligand
$[MBr_2(3\text{-}CNpy)_1]_n$	2275–2288	Bridging ligand

Table 3 Selected crystallographic data of $[MX_2(4\text{-CNpy})_2]_n$ (**1a–3a**)

	β-1a	**γ-1a**	**2a**	**3a**
Compound	β-$[MnBr_2(4\text{-CNpy})_2]_n$	γ-$[MnBr_2(4\text{-CNpy})_2]_n$	$[FeCl_2(4\text{-CNpy})_2]_n$	$[FeBr_2(4\text{-CNpy})_2]_n$
CCDC number/CSD code	1956119	1956120	1956117	1956115
Structure determined from	Powder data	Powder data	Powder data	Powder data
Formula	$C_{12}H_8Br_2MnN_4$	$C_{12}H_8Br_2MnN_4$	$C_{12}H_8Cl_2FeN_4$	$C_{12}H_8Br_2FeN_4$
MW/g mol^{-1}	422.96	422.96	334.97	423.87
Crystal system	Monoclinic	Orthorhombic	Monoclinic	Orthorhombic
Space group (No.)	$P2_1/n$ (14)	*Pnnm* (58)	$P2_1/n$ (14)	*Pnnm* (58)
a/Å	27.0744(7)	27.1046(6)	26.5605(10)	26.9168(11)
b/Å	7.38192(18)	7.4288(3)	7.1868(2)	7.3429(2)
c/Å	3.83783(11)	3.86070(12)	3.66280(7)	3.79547(10)
α/°	90	90	90	90
β/°	91.182(3)	90	95.365(3)	90
γ/°	90	90	90	90
V/Å^3	766.87(4)	777.37(4)	696.11(4)	750.17(4)
Z, Z'	2, 1/2	2, 1/4	2, 1/2	2, 1/4
Site symmetry of M	$\bar{1}$	2/*m*	$\bar{1}$	2/*m*
T/K	298	478	298	298
Radiation type	Cu Kα_1	Cu Kα_1	Cu Kα_1	Cu Kα_1
Wavelength/Å	1.54056	1.54056	1.54056	1.54056
$2\theta_{min}$/°	3	3	3	3
$2\theta_{max}$/°	100	100	90	80

crystal X-ray diffraction (SCXRD) data at 298 K.[2,3] Powder data have not been published yet. We redetermined the structure of **4a** at room temperature from powder data, too. The single crystal data of **4a** are included in Table 4.

All samples were investigated for phase purity and polymorphism using XRPD. For **2a–5a** and **6**, no polymorphs were observed.

In contrast, for $[MnBr_2(4\text{-CNpy})_1]_n$ (**1a**), three polymorphic forms were observed (**α-1a**, **β-1a** and **γ-1a**). **β-1a** transforms at room temperature into **α-1a** within several weeks or upon cooling to −100 °C (Fig. S33†). In differential scanning calorimetry (DSC) cycles between room temperature and −120 °C, no signals for a phase transition from **β-1a** to **α-1a** were detectable (Fig. S41 in the ESI†). **α-1a** retransforms into **β-1a** and further on into **γ-1a** upon heating to 120 °C. The phase transition between **β-1a** and **γ-1a** is remarkable and will be discussed later. The crystal structures of the β- and γ-phases could be determined by XRPD. Unfortunately, the structure determination of **α-1a** failed despite reliable and reproducible indexing. Maybe the sample is not phase-pure.

In all crystal structures of $[MX_2(4\text{-CNpy})_2]_n$ (**1a–5a**, **6**) the metal atoms are octahedrally coordinated by four halogen

Table 4 Selected crystallographic data of $[MX_2(4\text{-CNpy})_2]_n$ (**4a**, **5a**, **6**)

	4a-XRPD	**4a**-SCXRD	**5a**	**6**
Compound	$[CoCl_2(4\text{-CNpy})_2]_n$	$[CoCl_2(4\text{-CNpy})_2]_n$	$[CoBr_2(4\text{-CNpy})_2]_n$	$[CuBr_2(4\text{-CNpy})_2]_n$
CCDC number/CSD code	1956112	UTIHIP	LATJOI	1956113
Structure determined from	Powder data	Single crystal data	Powder data	Powder data
Formula	$C_{12}H_8Cl_2CoN_4$	$C_{12}H_8Cl_2CoN_4$	$C_{12}H_8Br_2CoN_4$	$C_{12}H_8Br_2CuN_4$
MW/g mol^{-1}	338.06	338.06	426.96	431.57
Crystal system	Monoclinic	Monoclinic	Orthorhombic	Monoclinic
Space group (no.)	$P2_1/n$ (14)[a]	$P2_1/n$ (14)[a]	*Pnnm* (58)	$P2_1/n$ (14)
a/Å	26.4959(3)[a]	26.4571(2)[a]	26.8461(15)	7.30106(14)
b/Å	7.15642(12)[a]	7.065(5)[a]	7.31908(32)	25.8712(6)
c/Å	3.6288(4)[a]	3.608(3)[a]	3.77080(11)	3.98420(7)
α/°	90	90	90	90
β/°	94.465(5)[a]	95.739(7)[a]	90	97.3176(13)
γ/°	90	90	90	90
V/Å^3	686.02(18)	671.0(6)	740.92(6)	746.44(3)
Z, Z'	2, 1/2	2, 1/2	2, 1/4	2, 1/2
Site symmetry of M	$\bar{1}$	$\bar{1}$	2/*m*	$\bar{1}$
T/K	298	293	298	298
Radiation type	Mo Kα_1	Mo Kα	Mo Kα_1	Cu Kα_1
Wavelength/Å	0.70930	0.71073	0.70930	1.54056
$2\theta_{min}$/°	1.6150	?	1	3
$2\theta_{max}$/°	89.9046	?	60	80

[a] After transformation from $P2_1/c$ to $P2_1/n$ ($a' = -a - c$, $b' = b$, $c' = a$).

atoms and two 4-CNpy molecules coordinating with their N_{py} atoms. The neighbouring coordination octahedra are connected *via* two μ_2-bridging halogen atoms, resulting in a linear chain of edge-sharing octahedra (Fig. 2a). The 4-CNpy ligands occupy the axial positions of the octahedra. Within these chains, the metal–metal distances range from 3.61 Å (for **4b**) to 3.98 Å (for **6**), see Table 5. All chains are orientated parallel to each other and the metal-to-metal distance corresponds to the short lattice parameter *c* in structures $[MX_2(4\text{-CNpy})_2]_n$ (Table 4). The neighbouring pyridine rings of one chain stack always parallel to each other, which allows a good π–π-interaction. Their centroid-to-centroid distance is equivalent to the metal-to-metal distance (and to the short lattice parameter). The chains are arranged in a herringbone packing motif and linked by weak intermolecular C–H···N contacts into a three-dimensional network (Fig. 2b).

Compounds **γ-1a**, **3a** and **5a** are isotypic and crystallize in the space group *Pnnm* (No. 58). The structures of **β-1a**, **2a**, **4a** and **6** are isotypic, too. They crystallize in the space group $P2_1/n$. The alternative space group setting $P2_1/n$ was chosen in order to compare the orthorhombic structures of **γ-1a**, **3a** and **5a** with the monoclinic ones of **β-1a**, **2a** and **6**. The single crystal structure of $[CoCl_2(4\text{-CNpy})_2]_n$ (**4a**) was determined in $P2_1/c$ by Chen *et al.* Here, we use the $P2_1/n$ setting for **4a**. The packings of the $[MX_2(4\text{-CNpy})_2]_n$ compounds (except for **α-1a**) are similar and exhibit only small differences. The structure of **α-1a** could not be solved yet, but the XRD pattern clearly reveals that the structure is not similar to those of **β-1a** and **γ-1a** (see Fig. S33†).

The differences between the monoclinic and orthorhombic structures are visible from a view perpendicular to the chain direction. In the bromo compounds $[MBr_2(4\text{-CNpy})_2]_n$ (**γ-1a**, **3a** and **5a**) the pyridine rings stack exactly perpendicular to the chain direction (and the angle β is 90°). This leads to mirror planes *m* parallel to (001) (Fig. 3). Together with the *n* glide planes perpendicular to *m* this results in the space group $P2_1/n2_1/n2/m$. The asymmetric unit consists of one metal atom (on a 2/*m* site), one 4-CNpy ligand (on a site with *m* symmetry and on the same mirror plane as the metal atom) and a bromine atom (on an *m* site too, but on the neighbouring mirror plane).

In structures **β-1a**, **2a**, **4a** and **6** the 4-CNpy ligands are still co-planar, but no longer perpendicular to the chain (Fig. 4). β inclines from 90° to 91.18° for **β-1a** and 97.32° for **6**. The lattices become monoclinic and the space group is reduced to $P12_1/n1$, which is a maximal "*translationengleiche*" subgroup of $P2_1/n2_1/n2/m$. The metal atoms have a site symmetry of $\bar{1}$ only.

Among the structures with cyanopyridine ligands, $[MX_2(CNpy)_2]_n$ (with M = Mn, Fe, Co, Ni), the chlorine compounds generally crystallize in space groups of lower symmetry compared to the bromo analogues.

We discussed this trend in the case of the $[MX_2(3\text{-CNpy})_2]_n$ series recently.[3,4] In structures with bromine atoms more space is available for the pyridine fragments, which forces the pyridine ligands to pile up exactly above each other. Thus, the ligands are orientated exactly perpendicular to the chain, which generates crystallographic mirror planes perpendicular to the chain direction.

However, this trend is not valid for the copper compounds, which typically exhibit a pronounced Jahn–Teller distortion of the coordination octahedra (Fig. 5a). In $[CuBr_2(4\text{-CNpy})_2]_n$ (**6**), the two Cu–N_{py} and two Cu–Br bonds are quite short with bond lengths about 2.006 Å and 2.418 Å, respectively. (Table 5). The two other Cu–Br bonds are significantly longer with a bond length of 3.154 Å each, which is much longer than in **1a–5a**.

2.5.1. Monitoring the phase transition between β-1a and γ-1a by temperature-dependent X-ray diffraction. The phase transition from **β-1a** to **γ-1a** (and reverse from **γ-1a** to **β-1a**) was investigated in detail, recording powder patterns in the 2θ range from 22° to 37°. A sample of **β-1a** was heated from 20 °C to 32 °C and subsequently cooled back to 20 °C. All powder patterns are plotted in Fig. 6 (further details on the measurement series can be found in Table S8, ESI†). Exemplarily, five pairs of corresponding reflections are highlighted in yellow: the reflection pairs are split in the

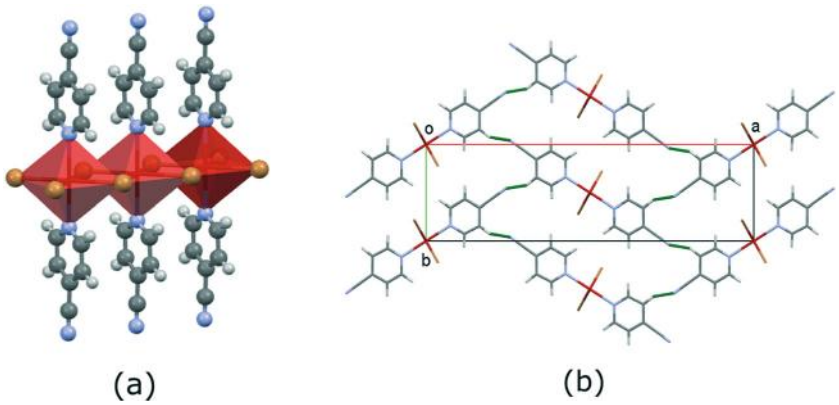

Fig. 2 Crystal structure of $[FeBr_2(4\text{-CNpy})_2]_n$ (**3a**). (a) One chain of $[FeBr_2(4\text{-CNpy})_2]_n$: neighbouring octahedra are connected *via* two Br atoms. (b) View direction [001]: the chains are arranged in a herringbone packing motif. The intermolecular C–H···N contacts are shown as green lines. Color code: Fe, red; Br, orange; N, blue; C, grey; H, white.

Table 5 Selected bond lengths and angles in compounds $[MX_2(4\text{-CNpy})_1]_n$ (**1a–5a** and **6**). The given standard deviations are those resulting from the Rietveld refinement. The actual accuracy is much lower

	β-1a	**γ-1a**	**2a**	**3a**	**4a**	**5a**	**6**
M···M/Å	3.83783(11)	3.86070(12)	3.66280(7)	3.79547(10)	3.628(9)	3.77080(11)	3.98420(7)
M–N_{py}/Å	2 × 2.345(6)	2 × 2.307(6)	2 × 2.333(3)	2 × 2.252(5)	2 × 2.179(3)	2 × 2.202(9)	2 × 2.007(3)
M–X(1)/Å	2 × 2.691(2)	4 × 2.699(2)	4 × 2.654(2)	2 × 2.491(2)	2 × 2.453(2)	4 × 2.617(2)	2 × 2.418(2)
M–X(2)/Å	2 × 2.720(2)			2 × 2.621(2)	2 × 2.516(2)		2 × 3.154(2)
Pyridine stacking angle δ/°[a]	88.98	90	87.33	90	87.83	90	89.94

[a] Angle between the pyridine ring mean plane and the chain direction [001] for **β-1a**, **2a**, **4a** and **6**. For **γ-1a**, **3a** and **5a**, δ corresponds to the angle β.

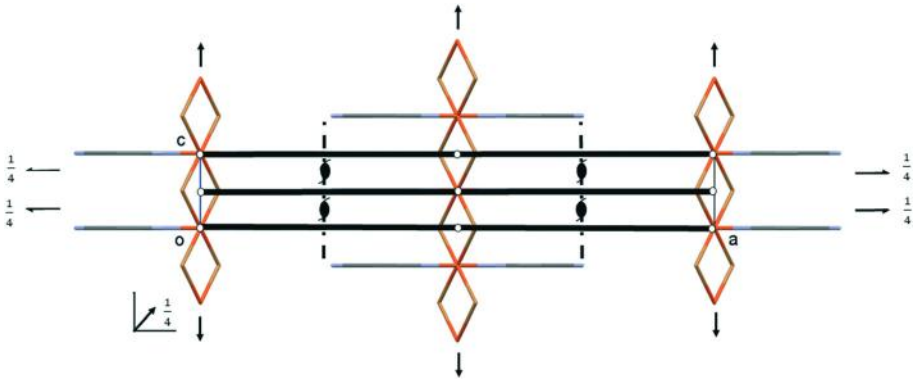

Fig. 3 Crystal structure of $[FeBr_2(4\text{-CNpy})_2]_n$ (**3a**). View direction [010]: the symmetry elements of the space group *Pnnm* (No. 58) are shown. The thick black lines denote the mirror planes. Color code: Fe, red; Br, orange; N, blue; C, grey; H atoms are omitted.

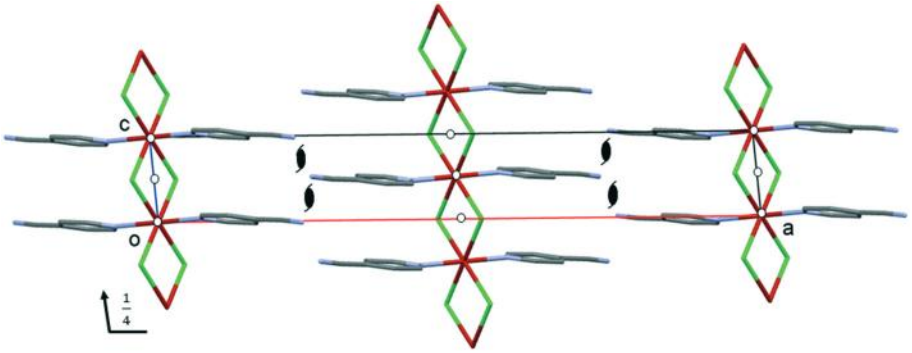

Fig. 4 Crystal structure of $[FeCl_2(4\text{-CNpy})_2]_n$ (**2a**). View direction [010]: the symmetry elements of the space group $P12_1/n1$ (No. 14) are shown. Color code: Fe, red; Cl, light green; N, blue; C, grey; H atoms are omitted.

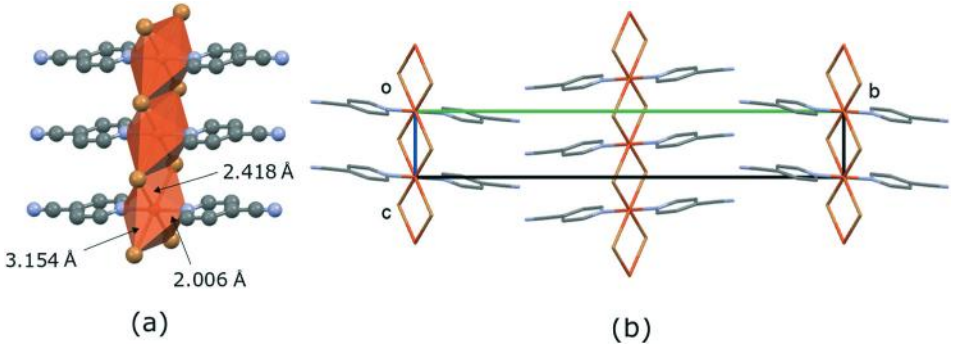

Fig. 5 Crystal structure of $[CuBr_2(4\text{-CNpy})_2]_n$ (**6**). (a) One chain of $[CuBr_2(4\text{-CNpy})_2]_n$: the coordination octahedra are stretched in the chain direction. (b) View direction [100]. Color code: Cu, brown; Br, orange; N, blue; C, grey; H atoms are omitted.

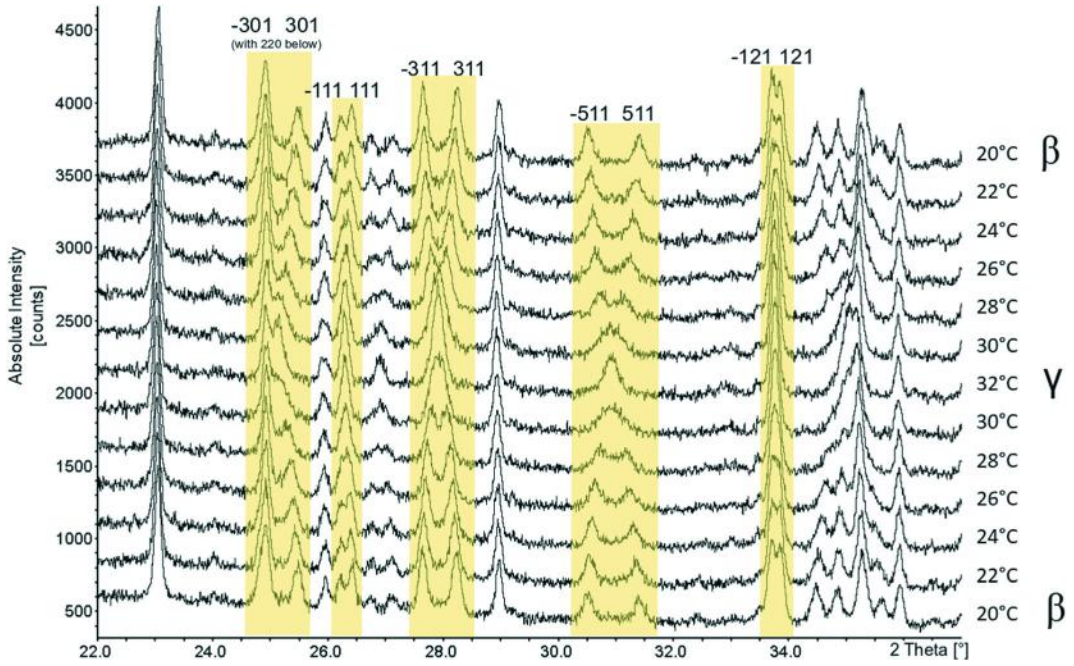

Fig. 6 Temperature-dependent X-ray powder series of $[MnBr_2(4\text{-}CNpy)_2]_n$ (**1a**): powder patterns were recorded in steps of 2 °C. The Miller indices are given for five examples of reflection pairs.

monoclinic system (**β-1a**), but unified in the orthorhombic structure (**γ-1a**). The phase transition is almost completed at 32 °C. No further major changes occurred up to 120 °C (Fig. S34, ESI†). Upon cooling back to 20 °C, the reflection intensities change without hysteresis in the same manner as observed for the heating cycle. Obviously, both polymorphs have similar lattice energies and the energy barrier is small (if any).

We performed a long-term measurement at 120 °C in order to determine the structure of **γ-1a**, in which we denominated the "high-temperature" phase of $[MnBr_2(4\text{-}CNpy)_2]_n$ (**1a**). The temperature-dependent behaviour of $[MnBr_2(4\text{-}CNpy)_2]_n$ is somehow remarkable and an excellent example to study some basic supergroup–subgroup relationships. As discussed above, in the orthorhombic structure of **γ-1a**, all atoms are located on crystallographic mirror planes, whereas in the monoclinic structure of **β-1a**, no mirror planes are present (because the cyanopyridine ligands do not stack exactly perpendicular to the $[MnBr_2]_n$

Table 6 Selected crystallographic data of $[ZnBr_2(4\text{-}CNpy)_2]$ (**α-7**, **β-7**) and related compounds

	α-7		**β-7**	
Compound	α-$[ZnBr_2(4\text{-}CNpy)_2]$	$[ZnCl_2(4\text{-}CNpy)_2]$	β-$[ZnBr_2(4\text{-}CNpy)_2]$	$[ZnCl_2(py)_2]$
CCDC number/CSD code	1956121	CYPYZN[a]	1956122	ZNPYRC01
Structure determined from	Powder data	Single crystal data	Powder data	Single crystal data
Formula	$C_{12}H_8Br_2ZnN_4$	$C_{12}H_8Cl_2ZnN_4$	$C_{12}H_8Cl_2ZnN_4$	$C_{10}H_{10}Cl_2ZnN_2$
Crystal system	Monoclinic	Monoclinic	Monoclinic	Monoclinic
Space group (No.)	*C*2/*c* (15)	*C*2/*c* (15)	$P2_1/c$ (14)	$P2_1/c$ (14)
a/Å	28.4031(3)	28.21(2)	16.0185(4)	8.580(3)
b/Å	7.73326(8)	7.44(3)	12.09069(19)	17.677(1)
c/Å	17.2427(2)	17.22(9)	7.89902(13)	8.397(5)
α/°	90	90	90	90
β/°	126.9230(6)	127.1(08)	94.8775(12)	101.42(4)
γ/°	90	90	90	90
V/Å^3	3027.76(6)	2885.1(7)	1524.30(5)	1248.3(5)
Z, *Z*′	8, 1	8, 1	4, 1	4, 1
Site symmetry of M	1	1	1	1
T/K	298	295	298	295
Radiation type	Cu Kα_1	Mo Kα	Cu Kα_1	Mo Kα
Wavelength/Å	1.54056	0.71069	1.54056	0.71069
$2\theta_{min}$/°	3	0	3	0
$2\theta_{max}$/°	80	45	80	45

[a] Unit cell transformed from the literature data to correspond to **α-7**. Transformation matrix (*P*, *p*): $-a - c$, *b*, *a*; 0, 0, 0.

Table 7 Selected bond lengths and bond angles in $[ZnX_2(py)_2]$ compounds. The given standard deviations of α-7 and β-7 are those resulting from the Rietveld refinement. The actual accuracy is much lower

	α-$[ZnBr_2(4\text{-CNpy})_2]$ α-7	β-$[ZnBr_2(4\text{-CNpy})_2]$ β-7	$[ZnCl_2(4\text{-CNpy})_2]$ CYPYZN	$[ZnCl_2(py)_2]$ ZNPYRC01
Structure determined from	Powder data	Powder data	Single crystal data	Single crystal data
Zn–N_{py}/Å	2.037(3)	2.057(4)	2.059(5)	2.046(5)
Zn–N_{py}/Å	2.063(4)	2.127(3)	2.069(6)	2.052(6)
Zn–X/Å	2.335(2)	2.370(2)	2.207(2)	2.215(2)
Zn–X/Å	2.332(2)	2.327(3)	2.218(2)	2.228(2)
N_{py}–Zn–N_{py}/°	103.42(15)	99.84(11)	105.0(2)	106.3(2)
X–Zn–X/°	124.47(10)	124.95(8)	125.7(1)	120.9(1)

chain). Therefore, reflections that are systematically unified in the orthorhombic structure of γ-1a split in the powder pattern of the low temperature phase. The Miller indices are given exemplarily for five reflection pairs in Fig. 6. Unfortunately, the additional reflections of $0kl$ ($k + l \neq 2n$), for example 021 or 041, are masked by other reflections of the monoclinic system.

2.6 Crystal structures and polymorphism of $[ZnBr_2(4\text{-CNpy})_2]$ (7)

α-$[ZnBr_2(4\text{-CNpy})_2]$ (α-7) was crystallized first while a second synthesis of $[ZnBr_2(4\text{-CNpy})_2]$, using an identical experimental protocol, resulted in the formation of β-$[ZnBr_2(4\text{-CNpy})_2]$ (β-7). The reason for this observation is unclear and should be investigated on a later occasion. Details on the synthesis are given in the Experimental section.

The crystal structures of both $[ZnBr_2(4\text{-CNpy})_2]$ polymorphs were determined from the XRPD data. Selected crystallographic data are given in Table 6. Further details on the measurements and refinements are compiled in Table S2 (ESI†), and the Rietveld plots of structures α-7 and β-7 are shown in Fig. S31 and S32 (ESI†).

α-7 and β-7 both form discrete complexes, in which the Zn atom is coordinated by two Br and two N_{py} atoms in a slightly distorted tetrahedral configuration (Table 7), which is typical for a large number of $[ZnX_2(py)_2]$ compounds with pyridine derivatives.[27–29]

The structure of α-7 is similar to that of $[ZnCl_2(4\text{-CNpy})_2]$. The molecules are connected through two different types of

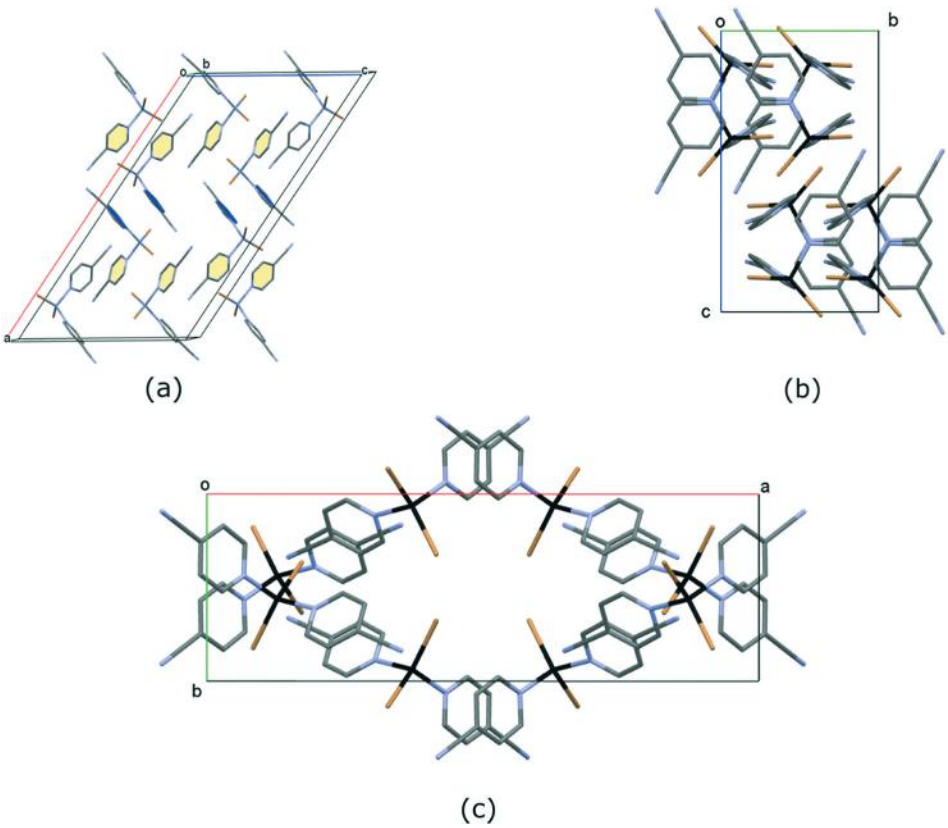

Fig. 7 Crystal structure of α-$[ZnBr_2(4\text{-CNpy})_2]$ (α-7): view directions (a) approx. [010], (b) [100] and (c) [001]. The structure contains two symmetrically independent 4-CNpy moieties, shown in blue and yellow. Color code: Zn, black; Br, orange; N, blue; C, grey. H atoms and delocalized bonds are omitted for clarity.

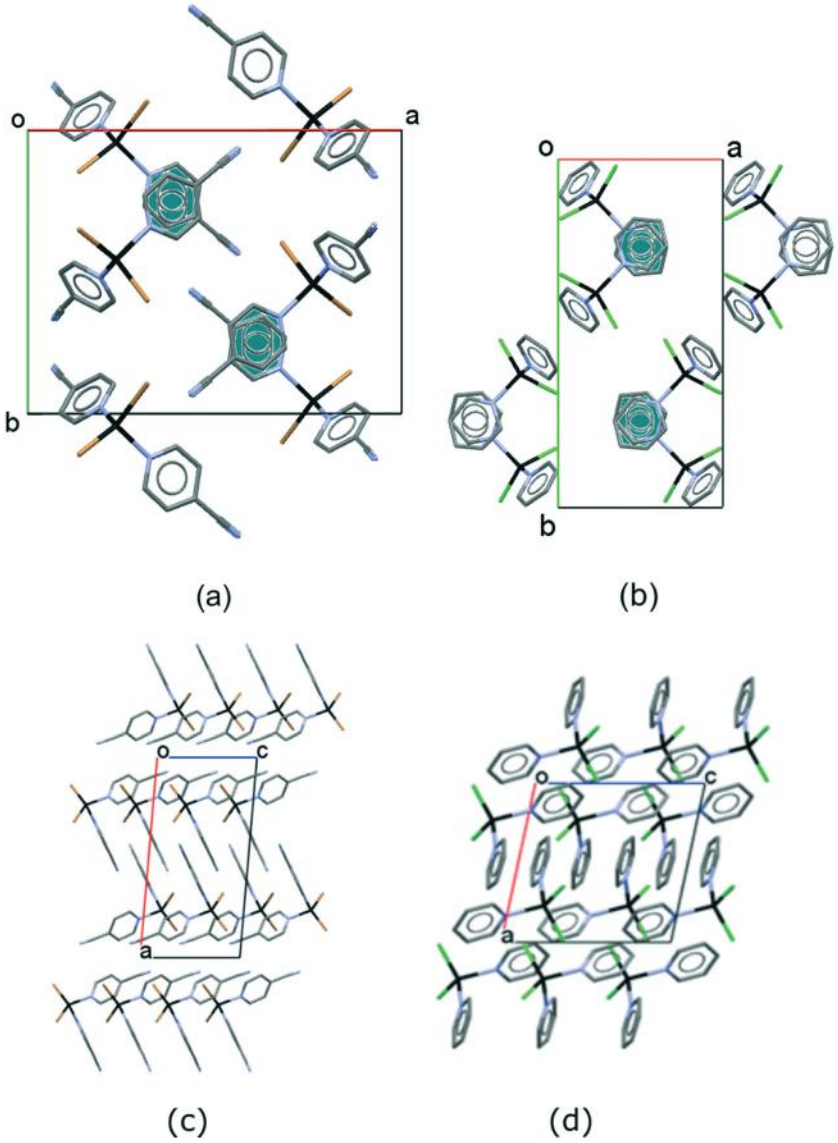

Fig. 8 Crystal structure of β-[$ZnBr_2$(4-CNpy)$_2$] (**β-7**) (a and c) and [$ZnCl_2(py)_2$] (b and d). View direction: [001] (a and b) and [010] (c and d). Color code: Zn, black; Br, orange; Cl, green; N, blue; C, grey; H atoms are omitted.

weak π–π-interactions. One pyridine ring forms a kind of "pair" (marked in yellow in Fig. 7a) with the pyridine ring of a neighbouring molecule, *via* the centre of symmetry. The centroid-to-centroid distance between these rings is approximately 4.6 Å and the rings are quite far apart. The second pyridine ring forms a kind of "pair" too (marked in blue in Fig. 7a), and the centroid-to-centroid distance is shorter of about 3.9 Å. But a straight π–π-stacking is missing in both interaction types and the cyanopyridine molecules stack slightly shifted because of two steric factors, the cyano substituent and the relatively bulky bromine atoms.

The packing of **β-7** (Fig. 8a and c) is similar to that of [$ZnCl_2(py)_2$] (Fig. 8b and d), but in contrast to [$ZnCl_2(py)_2$] and **α-7**, a single π–π-interaction motif is present: one pyridine ring (marked in green in both structures) packs *via* the *c* glide plane in a chain like way along the *c*-axis (Fig. 8a and b). The centroid-to-centroid distance of neighbouring rings is about 4.0 Å. The second pyridine ring points away from this chain and forms a kind of paddle following the *c*-axis (Fig. 8c and d). The π–π-interaction motif is the main factor controlling the packing and is effective in the stabilization of the crystal structure. In both polymorphs, weak intermolecular H···Br contacts of about 2.9 Å are present. In **β-7**, additional N···H contacts of about 2.5 Å are effective.

2.7 Crystal structures of $[MX_2(4\text{-CNpy})_1]_n$ (1b–5b)

The crystal structures of $[MX_2(4\text{-CNpy})_1]_n$ (**1b–5b**) were determined from the XRPD data. The structures of the cobalt compounds (**4b** and **5b**) were determined from the powder data collected at 250 °C within a high-temperature series (Fig. S37–S40†), and the other data were measured at room

Table 8 Selected crystallographic data of $[MX_2(4\text{-CNpy})_1]_n$ (**1b–5b**)

	1b	**2b**	**3b**	**4b**	**5b**
Compound	$[MnBr_2(4\text{-CNpy})_1]_n$	$[FeCl_2(4\text{-CNpy})_1]_n$	$[FeBr_2(4\text{-CNpy})_1]_n$	$[CoCl_2(4\text{-CNpy})_1]_n$	$[CoBr_2(4\text{-CNpy})_1]_n$
CCDC number/CSD code	1956118	1956116	1956114	1956126	1956111
Structure determined from	Powder data	Powder data	Powder data	Powder data	Powder data
Formula	$C_6H_4Br_2MnN_2$	$C_6H_4Cl_2FeN_2$	$C_6H_4Br_2FeN_2$	$C_6H_4Cl_2CoN_2$	$C_6H_4Br_2CoN_2$
MW/g mol^{-1}	318.85	230.86	319.76	233.95	322.85
Crystal system	Monoclinic	Monoclinic	Monoclinic	Monoclinic	Monoclinic
Space group (No.)	*P*2/*m* (10)	*Pm* (6)	*P*2/*m* (10)	*Pm* (6)	*P*2/*m* (10)
a/Å	12.4448(6)	7.6656(8)	12.4397(9)	7.7426(4)	12.4692(10)
b/Å	3.82332(12)	3.57945(15)	3.75800(17)	3.57685(7)	3.76053(17)
c/Å	9.8744(5)	7.7986(10)	9.6919(7)	7.6901(4)	9.6232(7)
α/°	90	90	90	90	90
β/°	90.569(8)	102.157(3)	90.459(8)	102.664(2)	89.870(15)
γ/°	90	90	90	90	90
V/Å^3	469.81(4)	209.18(4)	453.07(5)	207.790(16)	451.24(5)
Z, *Z*′	2, 1/2	1, 1/2	2, 1/2	1, 1/2	2, 1/2
Site symmetry of M	*m*	*m*	*m*	*m*	*m*
T/K	298	298	298	523	523
Radiation type	Cu Kα_1	Cu Kα_1	Cu Kα_1	Mo Kα_1	Mo Kα_1
Wavelength/Å	1.54056	1.54056	1.54056	0.70930	0.70930
$2\theta_{min}$/°	3	3	3	1	1
$2\theta_{max}$/°	90	90	80	50.26	50.26

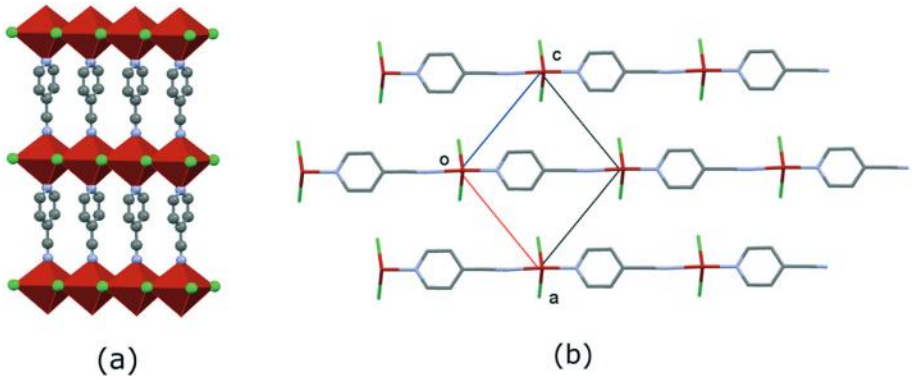

Fig. 9 Crystal structure of $[FeCl_2(4\text{-CNpy})_1]_n$ (**2b**). (a) One single layer. (b) Arrangement of the layers, view direction [010]. All 4-CNpy fragments have the same orientation. Color code: Fe, red; Cl, green; N, blue; C, grey; H atoms are omitted.

Table 9 Selected bond lengths and angles in compounds $[MX_2(4\text{-CNpy})_1]_n$ (**1b–5b**). The given standard deviations are those resulting from the Rietveld refinement. The actual accuracy is much lower

	$[MnBr_2(4\text{-CNpy})_1]_n$ **1b**	$[FeCl_2(4\text{-CNpy})_1]_n$ **2b**	$[FeBr_2(4\text{-CNpy})_1]_n$ **3b**	$[CoCl_2(4\text{-CNpy})_1]_n$ **4b**	$[CoBr_2(4\text{-CNpy})_1]_n$ **5b**
M–N_{py}/Å	2.2134(41)	2.072(16)	2.305(10)	2.1953(68)	2.398(21)
M–X(**1**)/Å	2.6932(33)	2.516(19)	2.600(11)	2.4576(95)	2.559(12)
M–X(2)/Å	2.6932(33)	2.516(19)	2.600(11)	2.4576(95)	2.559(12)
M–X(3)/Å	2.6944(34)	2.575(19)	2.687(12)	2.4675(92)	2.752(14)
M–X(4)/Å	2.6944(34)	2.575(19)	2.687(12)	2.4675(92)	2.752(14)
M–N_{CN}/Å	2.3235(44)	2.244(17)	2.0573(98)	1.9920(87)	1.754(22)
C≡N–M/°	174.86(19)	176.09(87)	179.5(19)	177.51(71)	167.0(48)
δ/°[a]	2.50		1.31	—	6.54

[a] Angle between the $[M_2Br_4]_n$ chain and the (001) plane (for **1b**, **3b** and **5b**).

temperature. Relevant crystallographic data are given in Table 8. Details on the measurements and refinements are given in Table S3 (ESI†), and the Rietveld plots of structures **1b–5b** are shown in Fig. S22–S29 (ESI†).

The structures of the chlorine compounds $[MCl_2(4\text{-CNpy})_1]_n$ (**2b**, **4b**) are isotypic, and they are isotypic to $[NiCl_2(4\text{-CNpy})_1]_n$. The chlorine compounds crystallize in the space group *Pm* (No. 6). Similarly, all bromine compounds

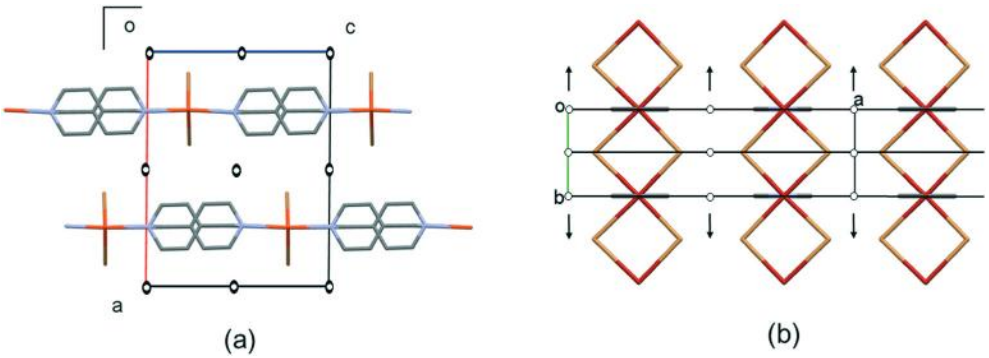

Fig. 10 Crystal structure of $[FeBr_2(4\text{-CNpy})_1]_n$ (**3b**), showing a head-to-tail disorder of the 4-CNpy groups. Symmetry elements of the space group $P12/m1$ are shown as well. (a) View direction [010], (b) view direction [001]. Color code: Fe, red; Br, orange; N, blue; C, grey; H atoms are omitted.

Table 10 *R*-Values of the Rietveld refinements of $[MBr_2(4\text{-CNpy})_1]_n$ (**1b**, **3b**, **5b**) using models with and without disorder. The occupancies for both 4-CNpy orientations are given, too

	$[MnBr_2(4\text{-CNpy})_1]_n$ **1b**		$[FeBr_2(4\text{-CNpy})_1]_n$ **3b**		$[CoBr_2(4\text{-CNpy})_1]_n$ **5b**	
	With disorder	Without disorder	With disorder	Without disorder	With disorder	Without disorder
Occupancy ordered/disordered	0.518(1)/0.482(1)	1 : 0	0.50(2)/0.50(2)	1 : 0	0.51(2)/0.49(2)	1 : 0
R_{Bragg}	1.3150	1.7894	0.7015	1.1749	1.2488	1.6017
R_p/%	1.757	1.934	1.524	1.645	1.480	1.679
R_{wp}/%	2.331	2.605	1.974	2.191	1.984	2.334
R_{exp}/%	1.442	1.443	1.664	1.665	1.404	1.402
GOF	1.616	1.806	1.186	1.316	1.413	1.666
R'_p/%[a]	18.116	20.129	27.077	30.406	19.766	23.433
R'_{wp}/%[a]	14.684	16.472	18.263	20.451	14.496	17.247
R'_{exp}/%[a]	9.087	9.122	15.403	15.535	10.260	10.355

[a] R'_p, R'_{wp} and R'_{exp} values are background corrected according to ref. 38.

$[MBr_2(4\text{-CNpy})_1]_n$ (**1b**, **3b**, **5b**) are isotypic to $[NiBr_2(4\text{-CNpy})_1]_n$. The bromine compounds crystallize in the space group $P2/m$ (No. 10).

In all compounds, 4-cyanopyridine acts as a bidentate ligand, coordinating with its N_{py} and N_{CN} atoms to form a bridge between the metal atoms (Fig. 9a), as indicated by IR spectroscopy. Each metal atom is coordinated by one 4-cyanopyridine ligand with its N_{py} atom, and a second one with its N_{CN} atom. The 4-CNpy bridges connect the $[MX_2]_n$ chains to build layers parallel to $(10\bar{1})$ (Fig. 9b). In the chlorine structures $[MCl_2(4\text{-CNpy})_1]_n$ (**2b**, **4b**) the orientation of the 4-CNpy molecules in all layers is uniform. The 4-CNpy rings stack exactly parallel to each other and all layers are located on crystallographic mirror planes parallel to (010). This results in space group $P1m1$ for the chlorine compounds. The bromine structures $[MBr_2(4\text{-CNpy})_1]_n$ (**1b**, **3b**, **5b**) crystallize in $P12/m1$ (No. 10). They are pseudo-orthorhombic and the monoclinic angle β deviates slightly from 90°. In fact, the MBr_4 planes are not exactly parallel to the (001) plane. In $[CoBr_2(4\text{-CNpy})_1]_n$ (**5b**) the $CoBr_4$ planes form an angle of about 6.5° with it (Table 9). For $[MnBr_2(4\text{-CNpy})_1]_n$ (**1b**) and $[FeBr_2(4\text{-CNpy})_1]_n$ (**3b**) the deviation is 2.5° and 1.3°, respectively. The orthorhombic supergroup would be $P2_1/m2/m2/a$ (*Pmma*, No. 51) with $Z = 2$, and the metal atoms would be situated on sites with *mm*2 symmetry (instead of sites with 1*m*1 symmetry). Recently, we reported the crystal structures of the analogous 3-CNpy compounds $[MBr_2(3\text{-CNpy})_1]_n$ (M = Fe, Co, Ni).[3] They crystallize in the space group $Pmc2_1$ with $Z = 1/2$, which is a minimal *translationengleiche* supergroup of $P2_1$. Regarding this, one would try to refine the structures of **1b**, **3b** and **5b** in a space group of higher symmetry, too. Thus, we performed Rietveld refinements in the space group *Pmma* (see Table S5, ESI†). For **1b** and **3b** the refinements clearly revealed that $P2/m$ is the correct space group. For **5b** the results are less clear: the *R* values are slightly higher in *Pmma*, but the number of parameters is reduced. Together with the monoclinic angle of 89.870(15)° and the limited data quality at higher diffraction angles, it remains ambiguous if the structure should better be described in $P2/m$ or *Pmma*. We chose the $P2/m$ description due to the slightly better *R* values. Fig. 10 shows that due to the disorder the structures of **1b**, **3b** and **5b** are close to having even higher symmetry: $B2/m2/m2/m$, $Z = 2$ (which is a non-standard setting of *Cmmm* (No. 65)). In this space group, the metal ions have site symmetry *mmm* and the bromine atoms 2*mm*. However, even for **5b** the metal atom

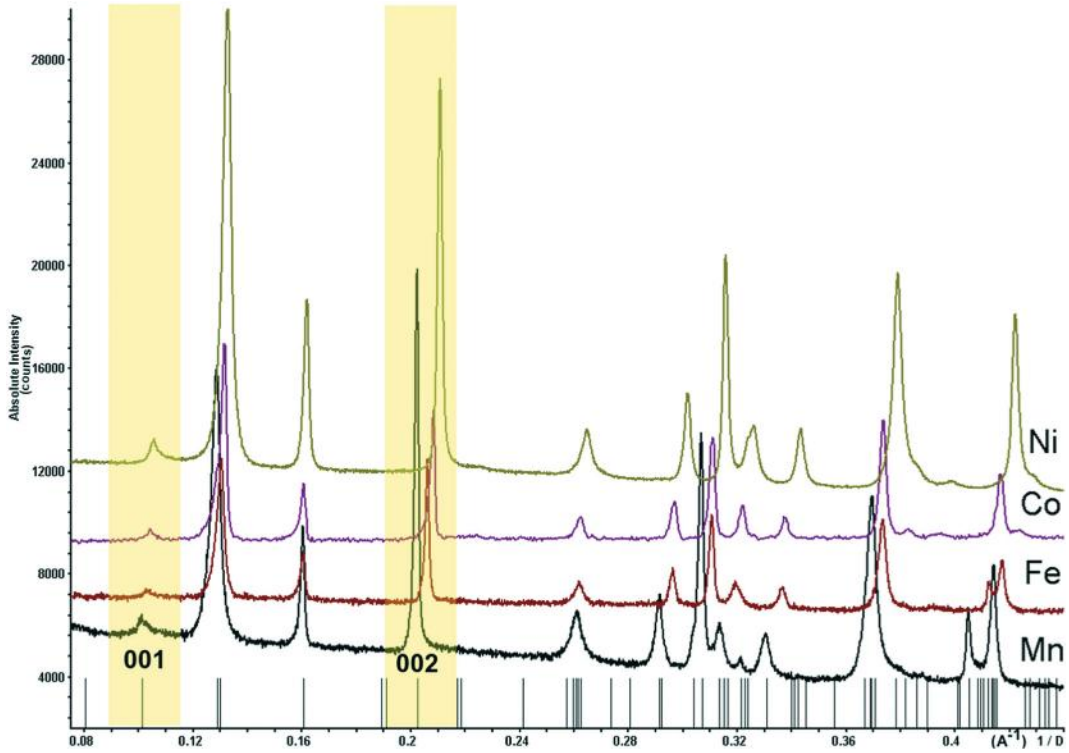

Fig. 11 Low-range part of the powder patterns of $[MBr_2(4\text{-CNpy})_1]_n$: the first two Warren type peaks are indicated. They are particularly visible in the patterns of the Ni, Mn and Fe compounds. Original raw data of the Ni compound were added.[6] λ = 1.54056 Å (Cu Kα_1) for Ni, Mn, and Fe and λ = 0.70930 Å (Mo Kα_1) for Co.

deviates by 0.3 Å and the Br atoms by 0.2 to 0.6 Å from these sites, which proves that the *Bmmm* symmetry is only an approximate one.

2.7.1. Disorder in $[MBr_2(4\text{-CNpy})_1]_n$ compounds (1b, 3b and 5b)

All bromine structures $[MBr_2(4\text{-CNpy})_1]_n$ (**1b**, **3b** and **5b**) are affected by a "head-to-tail" disorder concerning the cyanopyridine bridges (Fig. 10a). In both orientations, both N atoms of the 4-CNpy molecule bind to metal atoms. The refinement of the occupancy parameter ends up in a distribution of about 0.5 to 0.5 in all $[MBr_2(4\text{-CNpy})_1]_n$ compounds (Table 10). This disorder is common to all $[MBr_2(4\text{-CNpy})_1]_n$ structures. Also $[NiBr_2(4\text{-CNpy})_1]_n$ shows this type of disorder.

This disorder causes diffuse scattering perpendicular to c^*, which is particularly visible as Warren type peaks (*i.e.* peaks with a tail to higher diffraction angles) of the 00l reflections in the powder diagrams collected with Cu Kα_1-radiation: $[MnBr_2(4\text{-CNpy})_1]_n$ (**1b**), $[FeBr_2(4\text{-CNpy})_1]_n$ (**3b**) and $[NiBr_2(4\text{-CNpy})_1]_n$ (Fig. 11). In the case of the chlorine compounds **2b** and **4b**, a disorder of the 4-CNpy molecules cannot be completely excluded, but the results of Rietveld refinements (using the disorder model) point against a disorder (see Table S4, ESI†). In $[FeCl_2(4\text{-CNpy})_1]_n$ (**2b**) and $[CoCl_2(4\text{-CNpy})_1]_n$ (**4b**), the layer-to-layer distance is shortened due to the smaller chlorine atoms. Therefore, the 4-CNpy ligands are somehow forced to be accurately orientated and a head-to-tail disorder is sterically hindered.

3. Experimental section

3.1 Materials

$MnBr_2$, $FeBr_2$, $CoCl_2{\cdot}6H_2O$, $CoBr_2$, $ZnBr_2$, methanol and 4-cyanopyridine were purchased from Alfa Aesar. $FeCl_2{\cdot}2H_2O$ and ethanol were obtained from Sigma Aldrich, and $CuBr_2$ was purchased from Riedel-de-Haën. All chemicals were used without further treatment.

3.2 Synthesis of $[MX_2(4\text{-CNpy})_2]_{(n)}$

Compounds $[MX_2(4\text{-CNpy})_2]_{(n)}$ (**1a–5a**, **6**, **α-7**, **β-7**) were prepared by stirring the reactants and dissolved in ethanol (for **1a**, **2a**, **3a**, **5a**, **α-7** and **β-7**) or methanol (for **4a** and **6**) at room temperature. Powders of **2a**, **4a**, **5a**, **6**, **α-7** and **β-7** were obtained within several minutes. In the case of $[MnBr_2(4\text{-CNpy})_2]_n$ (**1a**) and $[FeBr_2(4\text{-CNpy})_2]_n$ (**3a**) no powder was obtained after mixing the solutions. They were placed in a fridge (8 °C) for three days, where precipitates slowly formed. All residues were isolated by filtration, washed with ethanol and dried in air at room temperature. Further details on the syntheses of compounds $[MX_2(4\text{-CNpy})_2]_n$ can be found in the ESI.†

3.3 Preparation of $[MX_2(4\text{-CNpy})_1]_n$

Compounds $[MX_2(4\text{-CNpy})_1]_n$ (**1b–5b**) were prepared by thermal annealing of $[MX_2(4\text{-CNpy})_2]_n$ (**1a–5a**) at the corresponding decomposition temperatures. Two different

Table 11 Preparation types (diffractometer or DTA-device) and target temperatures for the decomposition of **1a–5a** to **1b–5b**, respectively

Compound	**1b**	**2b**	**3b**	**4b**	**5b**
Procedure	DTA	DTA	DTA	Diff.	Diff.
Target temperature/°C	230	220	260	250	250

preparation procedures were applied: (A) compounds **1b–3b** were prepared by thermal decomposition of **1a–3a** using the thermogravimetric device (DTA). Around 20–30 mg of the starting material (**1a–3a**, respectively) was placed in an Al_2O_3 crucible and heated (heating rate: 5 °C min^{-1}) to the target temperature under an argon gas flow (see Table 11). The temperature was kept for ten minutes. After cooling under an Ar flow, the powder was immediately transferred into a glass capillary that was sealed afterwards. (B) $[CoCl_2(4\text{-CNpy})_1]_n$ (**4b**) and $[CoBr_2(4\text{-CNpy})_1]_n$ (**5b**) were obtained during a high-temperature measurement series of $[CoCl_2(4\text{-CNpy})_2]_n$ (**4a**) and $[CoBr_2(4\text{-CNpy})_2]_n$ (**5a**), respectively, on the XRPD diffractometer. The starting material (**4a** or **5a**) was placed in a glass capillary and mounted on a STOE Stadi-P diffractometer, equipped with a customized heating system. The open capillary was heated under a constant nitrogen gas flow to 250 °C. The measurement at 250 °C was run twice. All powders were characterized by XRPD and, wherever possible, by IR. Further details on the preparations of compounds $[MX_2(4\text{-CNpy})_1]_n$ (*e.g.* temperature program for the heating series of **4a** and **5a**) can be found in the ESI.†

3.4 Spectroscopy

FT-IR spectroscopy was performed with a SHIMADZU IRaffinity 1S Fourier transform infrared reflection–absorption spectrometer.

3.5 Differential thermal analysis and thermogravimetry (DTA/TG)

Differential thermal and thermogravimetric analyses (DTA/TG) were performed on a SETARAM (TGA 92) device. Samples of **1a–7** were placed in Al_2O_3 crucibles and heated under an argon atmosphere with a heating rate of 5 K min^{-1} and a constant Ar flow rate of about 75 mL min^{-1}. The DTA–TG curves of **1a–3a** and **5a–7** are shown in the ESI.†

3.6 X-ray powder diffraction (XRPD)

XRPD data were collected on Stoe STADI-P transmission diffractometers, equipped with Ge (111) monochromators.[30] Samples of Mn, Fe, Cu and Zn were measured using Cu-Kα_1 radiation (λ = 1.54056 Å) and a linear position-sensitive detector (PSD, Kr/CH_4). The cobalt compounds were measured using Mo-Kα_1 radiation (λ = 0.70903 Å) and a Mythen 1K detector from Dectris. The powders were placed in Hilgenberg capillaries, and samples of **2a** and **β-7** were placed between thin polymer foil sheets purchased from Stoe.

3.7 Structure determination from XRPD data

The powder patterns of **β-1a**, **γ-1a**, **3a**, **6**, **α-7** and **β-7** were indexed with DICVOL91 (ref. 31) (implemented in the DASH package[32]) and CONOGRAPH[33,34] using the first 20–25 peaks. Indexing results were checked with regard to calculated cell volumes applying Hofmann's volume increment method.[35] Space groups were determined in consideration of known related $[MX_2(4\text{-CNpy})_2]_n$ compounds.[6,36] The structures were solved with the simulated annealing algorithm in DASH, using a starting structure fragment in direct space. Structure solution was carried out with respect to the space group and site symmetry. Next, a Pawley refinement was performed with TOPAS,[37,38] with refining background coefficients, zero point error, lattice parameters, scale factors and peak shape parameters, including peak asymmetry. In the subsequent Rietveld refinement, the pyridine ring was restrained to be flat (for details on bond length and bond angle restraints see Table S6 in the ESI†). The displacement factors were refined isotropically and the displacement parameter of the H atoms was constrained to be 1.2 times that of the non-hydrogen atoms. In the final refinement cycles, all restraints on bond distances and bond angles involving M atoms (X–M–N, M–N–C, *etc.*) were omitted, in order to search for possible Jahn–Teller distortions of the octahedra.

Compounds **2b** and **4b** are isotypic to $[NiCl_2(4\text{-CNpy})_1]_n$, and compounds **1b**, **3b** and **5b** are isotypic to $[NiBr_2(4\text{-CNpy})_1]_n$. Hence, the lattice parameters of $[NiCl_2(4\text{-CNpy})_1]_n$ or $[NiBr_2(4\text{-CNpy})_1]_n$, respectively, were used as starting values for the Pawley fit, and their atomic positions were used for the subsequent Rietveld refinement. Structures of **1b**, **3b** and **5b** exhibit a disordered orientation of the 4-CNpy fragments as already observed in $[NiBr_2(4\text{-CNpy})_1]_n$. A disorder model with variable occupancy for the 4-CNpy orientation (head-to-tail-disorder) was implemented by applying a mirror plane, parallel to (001) between two metal positions. The preferred orientation was observed in some samples and refined using the predefined macro in TOPAS. Further details on structure determination from the XRPD data and Rietveld refinement are given in Text S3 in the ESI.† Cif-files can be found in the ESI,† too.

Table 12 Overview: topologies in crystal structures of the type $[MX_2(CNpy)_1]_n$

$[MX_2(CNpy)_1]_n$	4-CNpy	3-CNpy
X = Cl	2D network (layer) for M = Mn, Fe, Co, Ni Double chains for M = Cu	Double chains (M = Mn, Co, Ni, Cu)
X = Br	2D network (layer) (M = Mn, Fe, Co, Ni)	2D network (wavy layer) (M = Mn, Fe, Co, Ni)

4. Conclusion

Eleven new coordination compounds built from MX_2 (M = Mn, Fe, Co, Ni, Cu, Zn) and 4-cyanopyridine were synthesized and structurally characterized. All compounds of composition $[MnBr_2(4\text{-}CNpy)_2]_n$ were obtained from solution. For M = Mn, Fe, Co, Ni or Cu the structure consists of single chains in which the metal atoms are linked *via* four μ_2-bridging halogen atoms (**1a–5a**, **6**). Two additional 4-cyanoypridine molecules coordinate terminally with their N_{py} atom to each metal atom, resulting in an octahedral coordination of the metal atom. The chains are arranged in different "herringbone" packing ways. The copper compound **6** exhibits the typical Jahn–Teller distortion of the coordination octahedra. $[MnBr_2(4\text{-}CNpy)_2]_n$ (**1a**) shows polymorphism with a reversible phase transition from $P2_1/c$ (**β-1a**) to the supergroup *Pnnm* (**γ-1a**) upon heating. For M = Zn two polymorphs were obtained, too. Their structures contain discrete tetrahedral complexes (**α-7** and **β-7**) instead of polymeric chains. The Zn atoms are coordinated by two Br atoms and two 4-cyanopyridine ligands (coordinating with their N_{py} atoms). Upon heating the compounds **1a–5a**, half of the organic ligand evaporates and the remaining single chain fragments are merged to form two-dimensional networks of the composition $[MX_2(4\text{-}CNpy)_1]_n$ (M = Mn, Fe, Co; **1b–5b**). Here, the 4-cyanopyridine ligand acts as a bridge between two $[MX_2]_n$ chains. It connects two metal atoms *via* the N_{py} and N_{CN} atoms to build layered structures. In the chlorine compounds (**2b**, **4b**), all 4-CNpy moieties are parallel, whereas in the bromine compounds (**1b**, **3b**, **5b**) the 4-CNpy bridges exhibit a "head-to-tail" disorder with occupancies of about 0.5 : 0.5.

In contrast to the $[MCl_2(4\text{-}CNpy)_1]_n$ compounds, the analogous 3-cyanopyridine compounds $[MCl_2(3\text{-}CNpy)_1]_n$ contain double chains (instead of networks). Here, 3-cyanopyridine always acts as a monodentate ligand, coordinating with its N_{py} atom only. To date, $[CuCl_2(4\text{-}CNpy)_1]_n$ is still the only 1 : 1 compound of the 4-CNpy series with 4-CNpy as a monodentate ligand, leading to the double chain topology.

To summarize the results of our investigations on $[MX_2(CNpy)_x]_n$ compounds, three main structural topologies are available: single chains, double chains and two-dimensional networks (Table 12). The degree of polymerization is systematically tuneable by thermal decomposition from chains to double chains or networks.

Conflicts of interest

There are no conflicts of interest to declare.

Acknowledgements

The authors thank Edith Alig for the TG/DTA measurements. We thank Justine Ruhl and Tobias Schelhas for their support in synthetic investigations.

References

1 C. Janiak, *Dalton Trans.*, 2003, 2781–2804.
2 C. Slabbert and M. Rademeyer, *Coord. Chem. Rev.*, 2015, **288**, 18–49.
3 M. Heine, L. Fink and M. U. Schmidt, *CrystEngComm*, 2019, **21**, 4305–4318.
4 M. Heine, L. Fink and M. U. Schmidt, *CrystEngComm*, 2018, **20**, 7556–7566.
5 E. Alig, T. Bernert, L. Fink, N. Külcü and T. Yesilkaynak, *Acta Crystallogr., Sect. E: Struct. Rep. Online*, 2010, **66**, m239.
6 Y. Krysiak, L. Fink, T. Bernert, J. Glinnemann, M. Kapuscinski, H. Zhao, E. Alig and M. U. Schmidt, *Z. Anorg. Allg. Chem.*, 2014, **640**, 3190–3196.
7 H. Zhao, A. Bodach, M. Heine, Y. Krysiak, J. Glinnemann, E. Alig, L. Fink and M. U. Schmidt, *CrystEngComm*, 2017, **19**, 2216–2228.
8 F. H. Allen, *Acta Crystallogr., Sect. B: Struct. Sci.*, 2002, **58**, 380–388.
9 I. J. Bruno, J. C. Cole, P. R. Edgington, M. Kessler, C. F. Macrae, P. McCabe, J. Pearson and R. Taylor, *Acta Crystallogr., Sect. B: Struct. Sci.*, 2002, **58**, 389–397.
10 X. L. Zhao and T. C. W. Mak, *Dalton Trans.*, 2004, 3212–3217.
11 W. Clegg and R. W. Harrington, 2017, CCDC: JAMQUM.
12 M. K. Broderick, C. Yang, R. D. Pike, A. Nicholas, D. May and H. H. Patterson, *Polyhedron*, 2016, **114**, 333–343.
13 A. Bacchi, G. Cantoni, P. Pelagatti and S. Rizzato, *J. Organomet. Chem.*, 2012, **714**, 81–87.
14 W. H. Leung, W. Lai and I. D. Williams, *J. Organomet. Chem.*, 2000, **604**, 197–201.
15 T. Hu, L. Zhao and T. C. W. Mak, *Organometallics*, 2012, **31**, 7539.
16 A. J. Blake, N. R. Champness, J. E. B. Nicolson and C. Wilson, *Acta Crystallogr., Sect. C: Cryst. Struct. Commun.*, 2011, **57**, 1290.
17 D. T. Cromer and A. C. Larson, *Acta Crystallogr., Sect. B: Struct. Crystallogr. Cryst. Chem.*, 1972, **28**, 1052–1058.
18 A. J. Graham, P. C. Healy, J. D. Kildea and A. H. White, *Aust. J. Chem.*, 1989, **42**, 177–184.
19 H. Hanika-Heidl, S. E. H. Etaiw, M. S. Ibrahim, A. S. B. Eldin and R. D. Fischer, *J. Organomet. Chem.*, 2003, **684**, 329–337.
20 L. Carlucci, G. Ciani, D. M. Proserpio and A. Sironi, *J. Chem. Soc., Chem. Commun.*, 1994, 2755–2756.
21 W. Chen, F. Liu and X. You, *Bull. Chem. Soc. Jpn.*, 2002, **75**, 1559–1560.
22 R. D. Bailey, L. L. Hook and W. T. Pennington, *Chem. Commun.*, 1998, 1181–1182.
23 W.-T. Chen, Z.-G. Luo, Y.-P. Xu and Q.-Y. Luo, *J. Chem. Res.*, 2011, **35**, 253–256.
24 R. J. H. Clark and C. S. Williams, *Spectrochim. Acta*, 1966, **22**, 1081–1090.
25 R. A. Bailey, S. L. Kozak, T. W. Michelsen and W. N. Mills, *Coord. Chem. Rev.*, 1971, **6**, 407–445.

26 C. Näther, S. Wöhlert, J. Boeckmann, M. Wriedt and I. Jeß, *Z. Anorg. Allg. Chem.*, 2013, **639**, 2696–2714.
27 R. Ghiasi, *Acta Crystallogr., Sect. E: Struct. Rep. Online*, 2011, **67**, m101.
28 W. L. Steffen and G. J. Palenik, *Acta Crystallogr., Sect. B: Struct. Crystallogr. Cryst. Chem.*, 1976, **32**, 298–300.
29 W. L. Steffen and G. J. Palenik, *Inorg. Chem.*, 1977, **16**(5), 119–1127.
30 STOE & Cie GmbH, STOE WinXPOW 310, Darmstadt, Germany, 2016.
31 A. Boultif and D. Louër, *J. Appl. Crystallogr.*, 2004, **37**, 724–731.
32 W. I. F. David, K. Shankland, J. van de Streek, E. Pidcock, W. D. S. Motherwell and J. C. Cole, *J. Appl. Crystallogr.*, 2006, **39**, 910–915.
33 R. Oishi-Tomiyasu, *J. Appl. Crystallogr.*, 2014, **47**, 593–598.
34 R. Oishi-Tomiyasu, *J. Appl. Crystallogr.*, 2014, **47**, 2055–2059.
35 D. W. M. Hofmann, *Acta Crystallogr., Sect. B: Struct. Sci.*, 2002, **58**, 489–493.
36 T. Hahn, Int. Tables for Cryst. Vol. A, 2002.
37 A. Coelho, TOPAS Acad. User Man. & Tech. Ref, 2009, Brisbane, Australia.
38 A. Coelho, *J. Appl. Crystallogr.*, 2018, **51**, 210–218.

4-Cyanopyridine complexes $[MX_2(4\text{-CNpy})_x]_n$ (with X = Cl, Br and x = 1, 2): Crystal structures, thermal properties and a comparison with $[MX_2(3\text{-CNpy})_x]_n$ complexes

Miriam Heine, Lothar Fink, Martin U. Schmidt*

Institute of Inorganic and Analytical Chemistry, Goethe University, Max-von-Laue-Str. 7, 60438 Frankfurt am Main, Germany. E-Mail: heine@chemie.uni-frankfurt.de, fink@chemie.uni-frankfurt.de, m.schmidt@chemie.uni-frankfurt.de; Fax: +49 69798 29235; Tel: +49 69798 29171

Figures

Tables

Experimental details

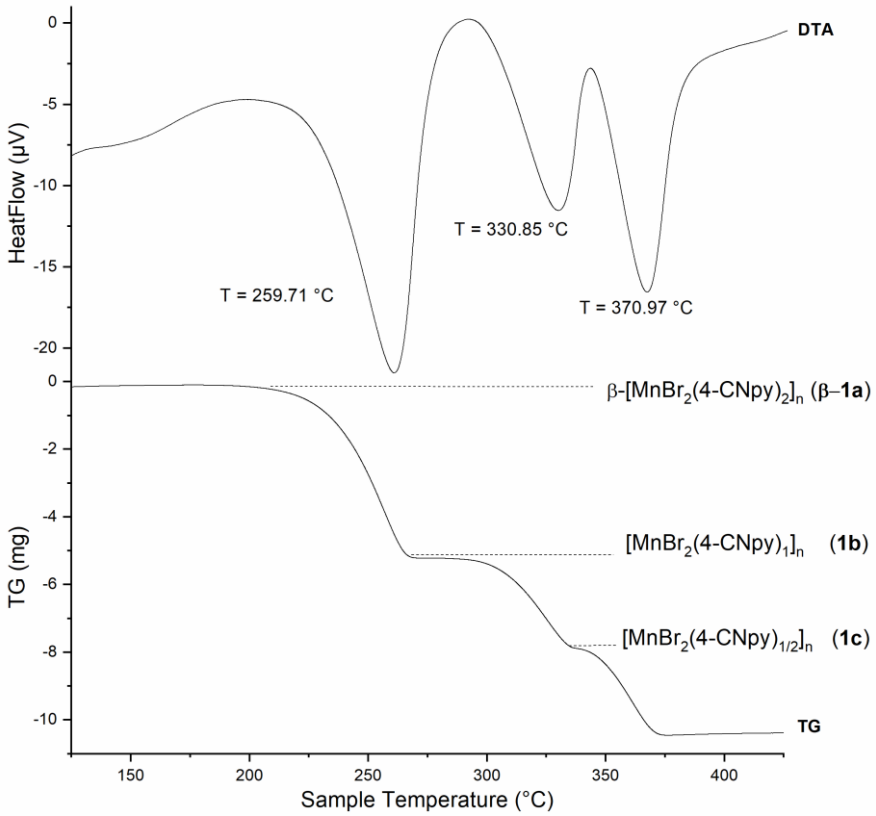

Figure S1. DTA/TG curves of β-$[MnBr_2(4\text{-}CNpy)_2]_n$ (**β-1a**). Heating rate: 5 K/min, Ar atmosphere, Al_2O_3 crucible.

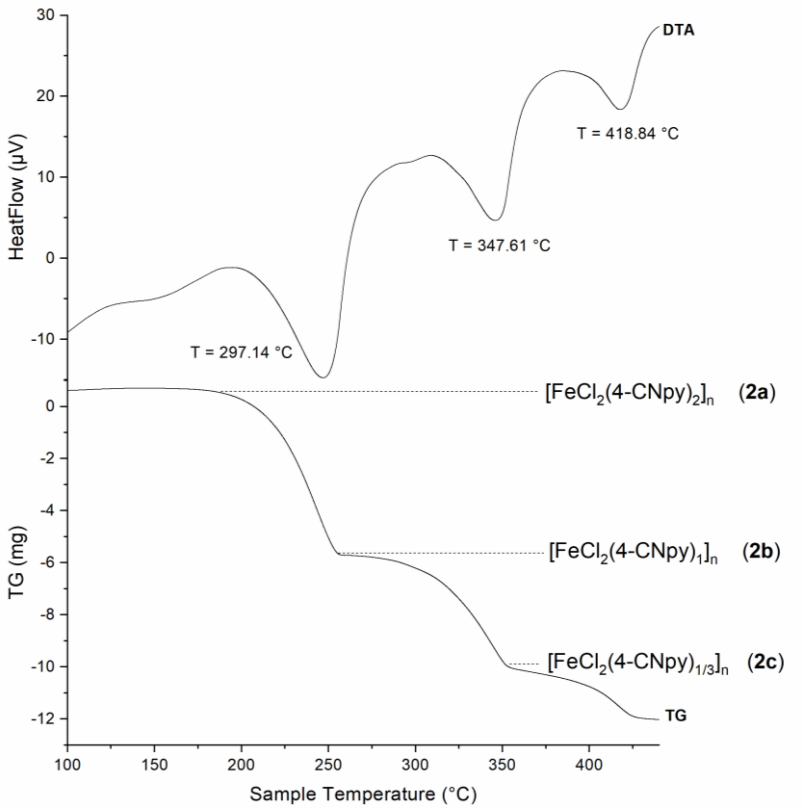

Figure S2. DTA/TG curves of $[FeCl_2(4\text{-}CNpy)_2]_n$ (**2a**). Heating rate: 5 K/min, Ar atmosphere, Al_2O_3 crucible.

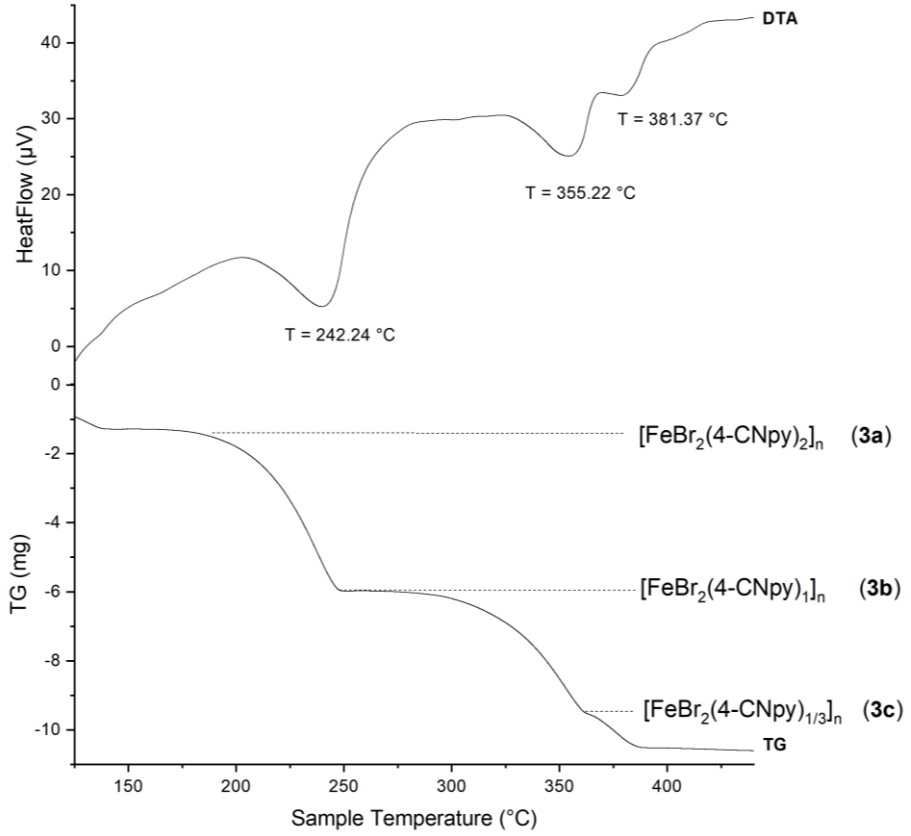

Figure S3. DTA/TG curves of $[FeBr_2(4\text{-}CNpy)_2]_n$ (**3a**). Heating rate: 5 K/min, Ar atmosphere, Al_2O_3 crucible.

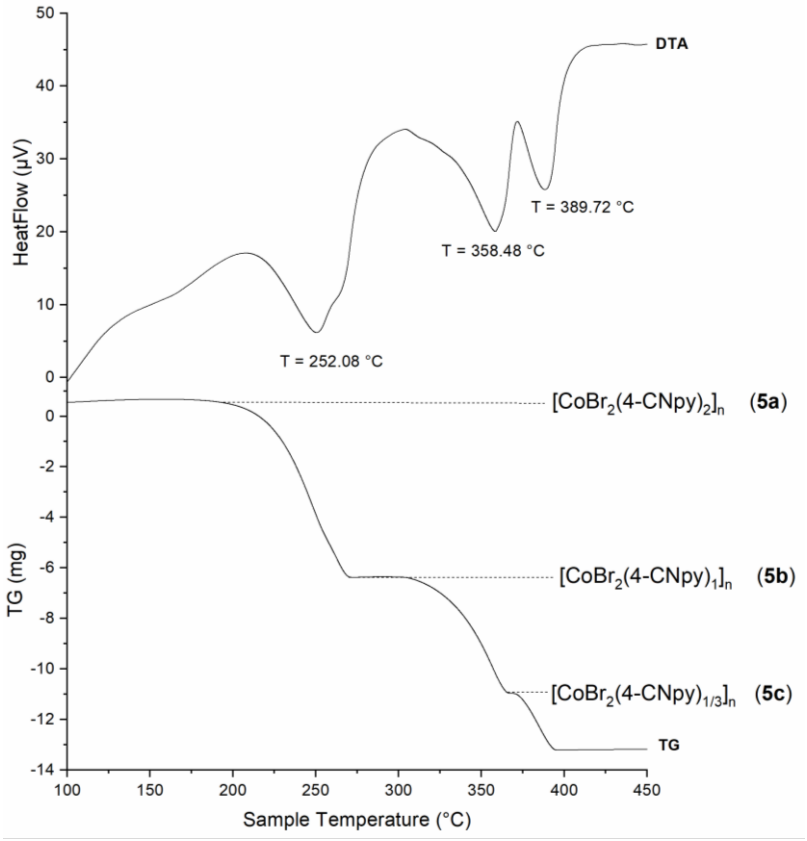

Figure S4. DTA/TG curves of $[CoBr_2(4\text{-}CNpy)_2]_n$ (**5a**). Heating rate: 5 K/min, Ar atmosphere, Al_2O_3 crucible.

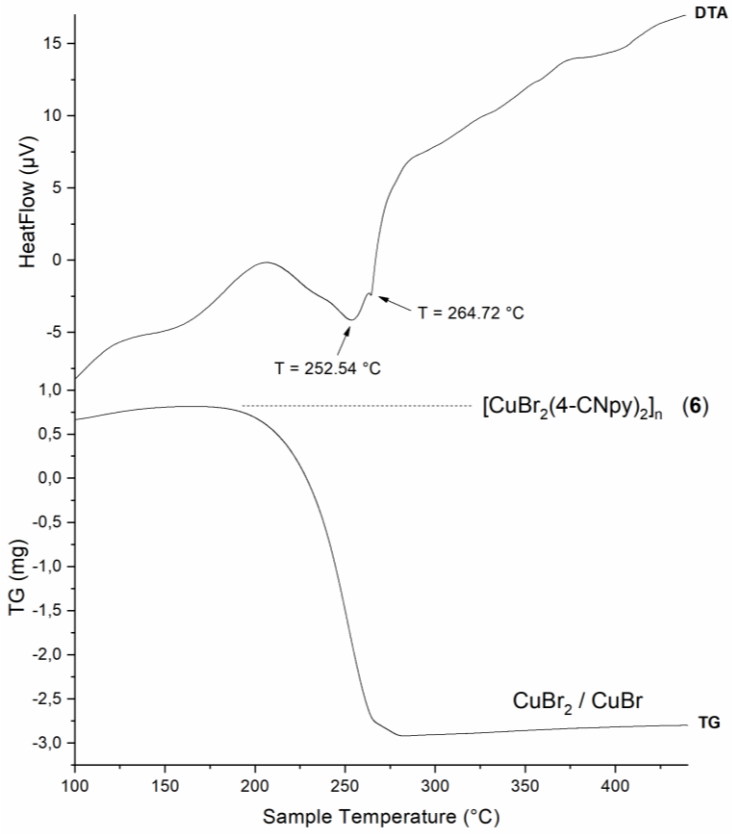

Figure S5. DTA/TG curves of $[CuBr_2(4\text{-}CNpy)_2]_n$ (**6**). Heating rate: 5 K/min, Ar atmosphere, Al_2O_3 crucible.

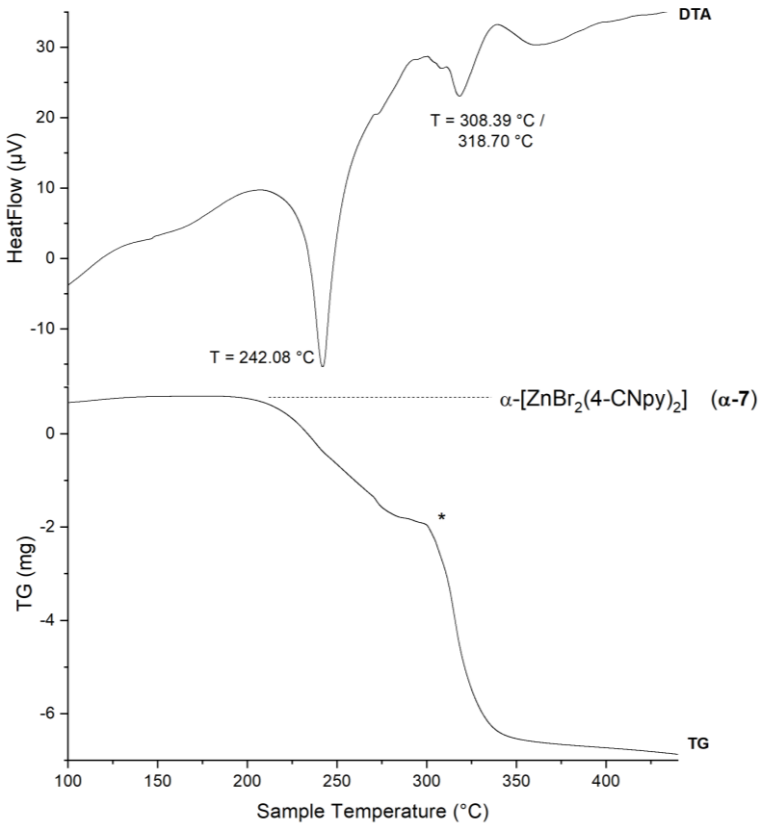

Figure S6. DTA/TG curves of α-[$ZnBr_2$(4-CNpy)$_2$] (**α-7**). The star * marks a phase of unknown composition. Heating rate: 5 K/min, Ar atmosphere, Al_2O_3 crucible.

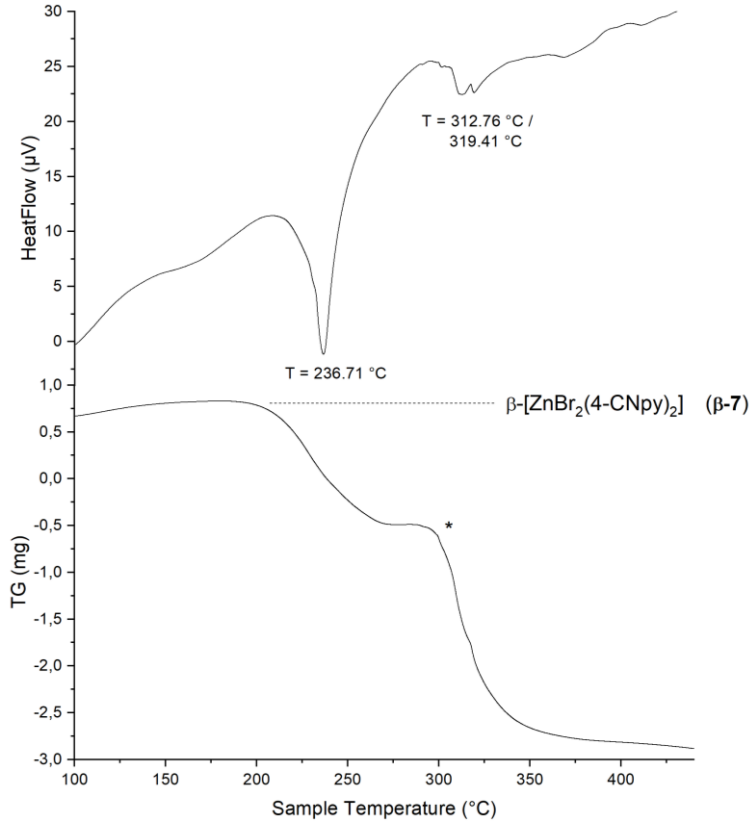

Figure S7. DTA/TG curves of β-[$ZnBr_2$(4-CNpy)$_2$] (**β-7**). The star * marks a phase of unknown composition. Heating rate: 5 K/min, Ar atmosphere, Al_2O_3 crucible.

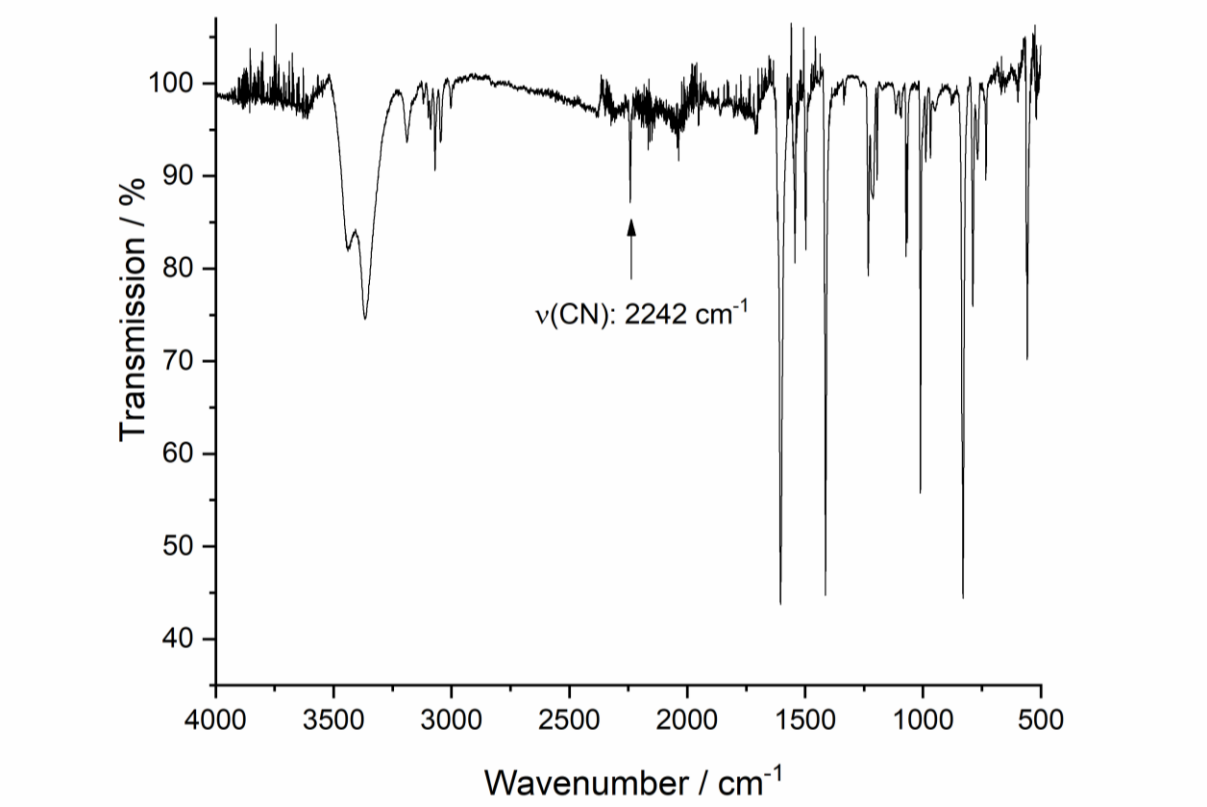

Figure S8. IR spectrum of α-$[MnBr_2(4\text{-}CNpy)_2]_n$ (**α-1a**).

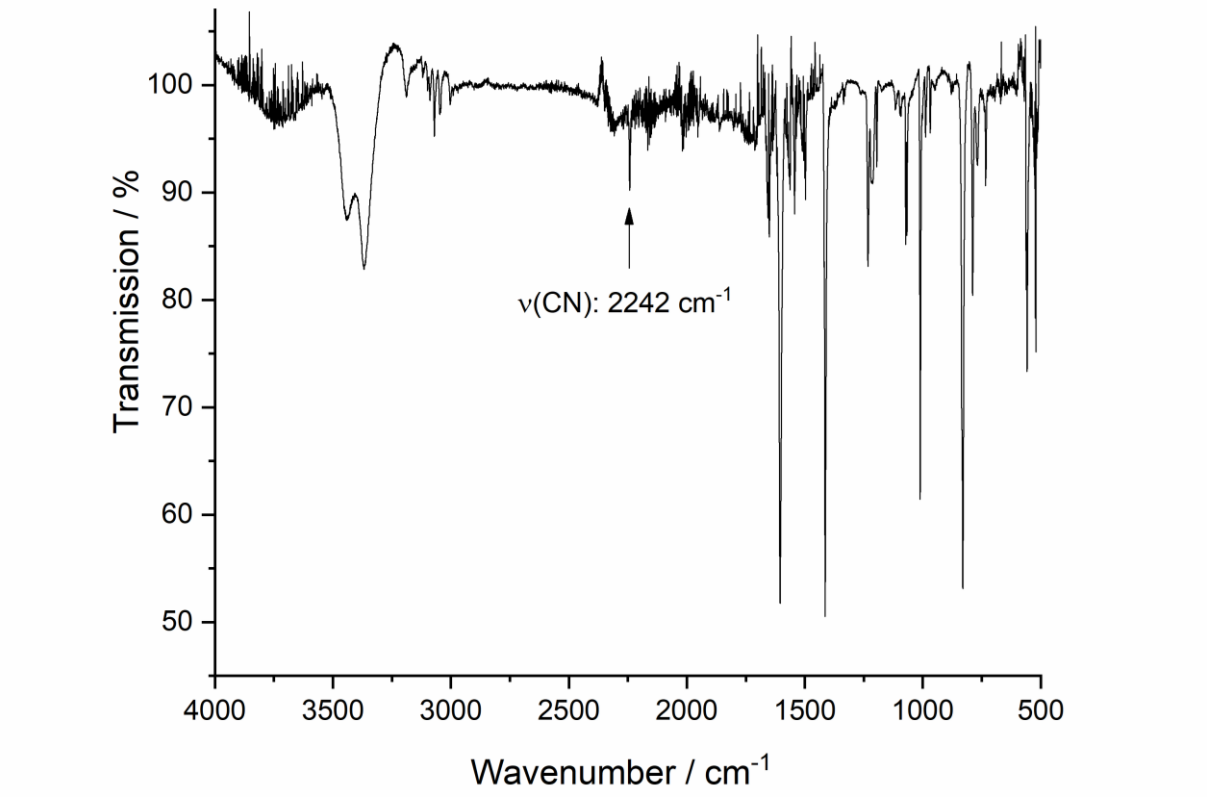

Figure S9. IR spectrum of β-$[MnBr_2(4\text{-}CNpy)_2]_n$ (**β-1a**).

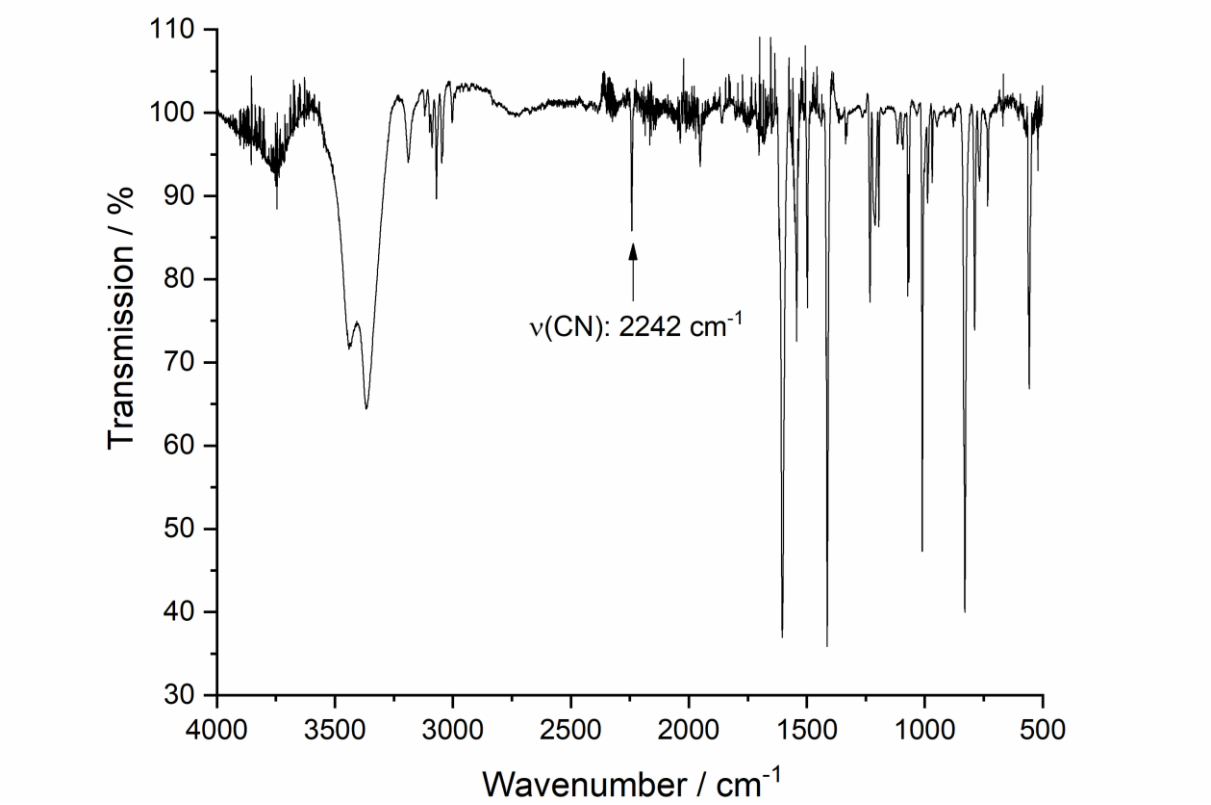

Figure S10. IR spectrum of $[MnBr_2(4\text{-}CNpy)_1]_n$ (**1b**).

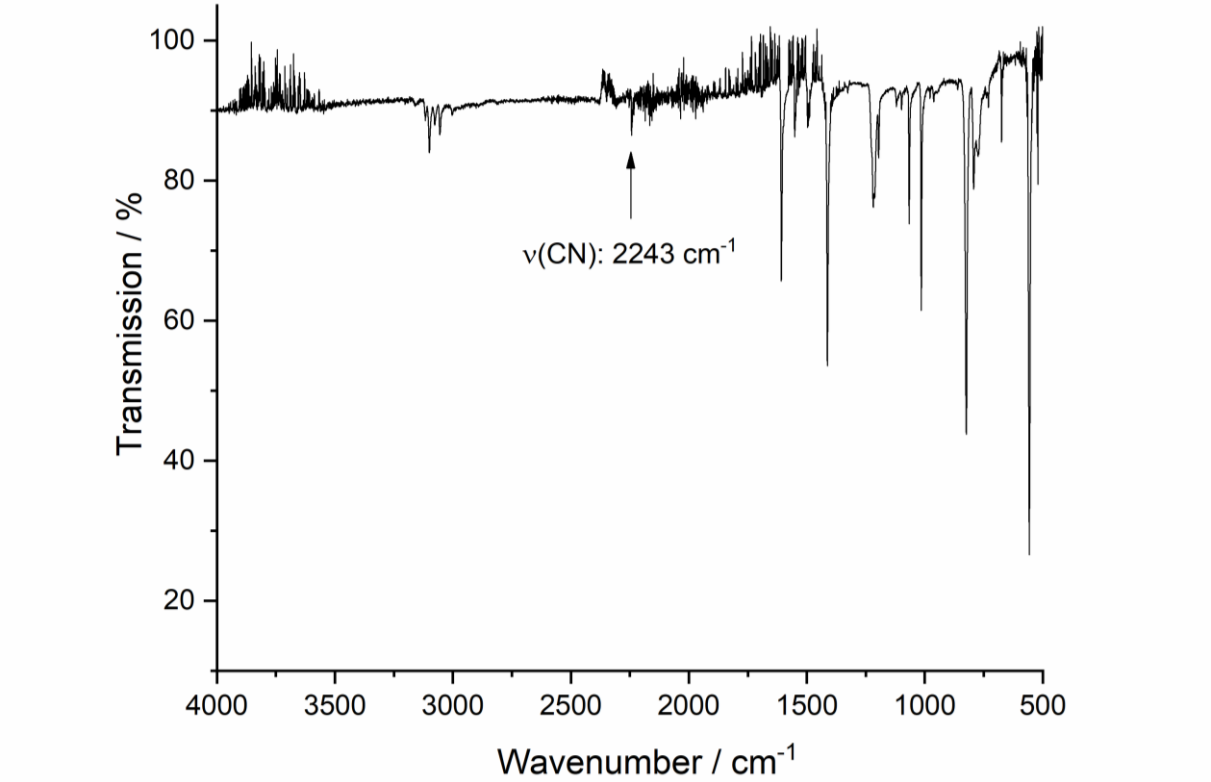

Figure S11. IR spectrum of $[FeCl_2(4\text{-}CNpy)_2]_n$ (**2a**).

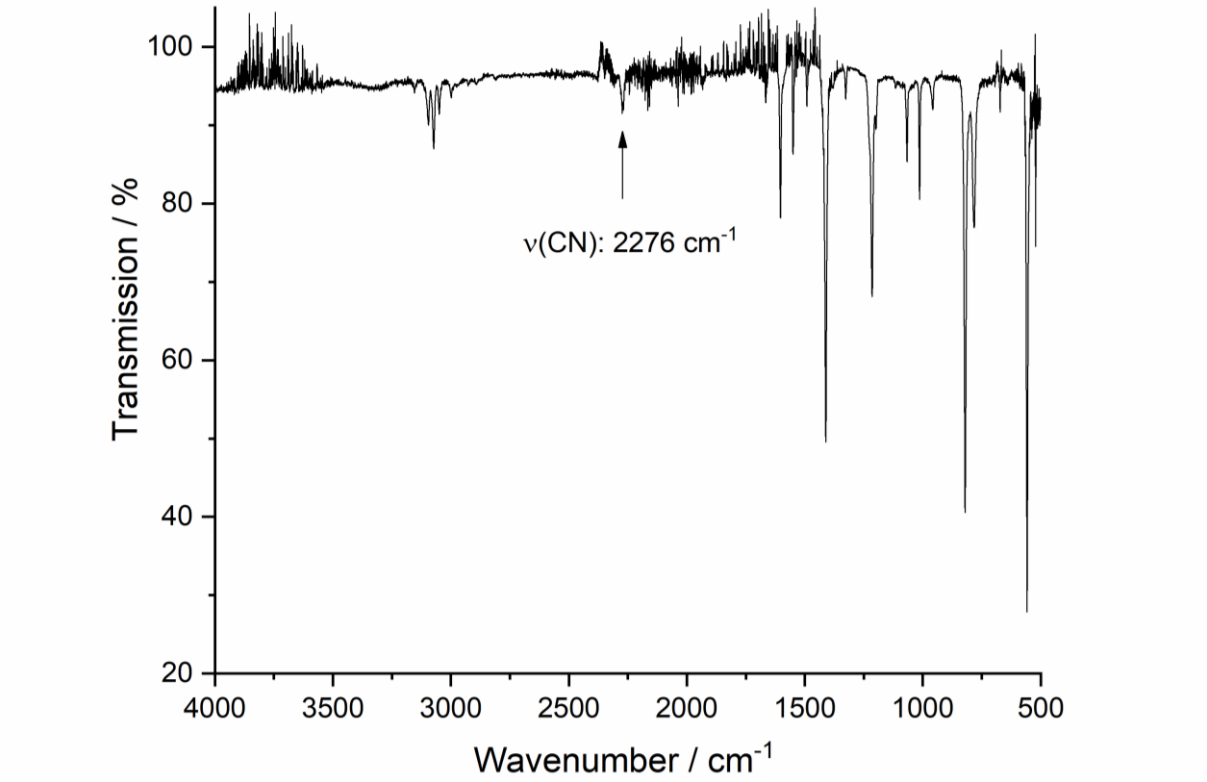

Figure S12. IR spectrum of $[FeCl_2(4\text{-}CNpy)_1]_n$ (**2b**).

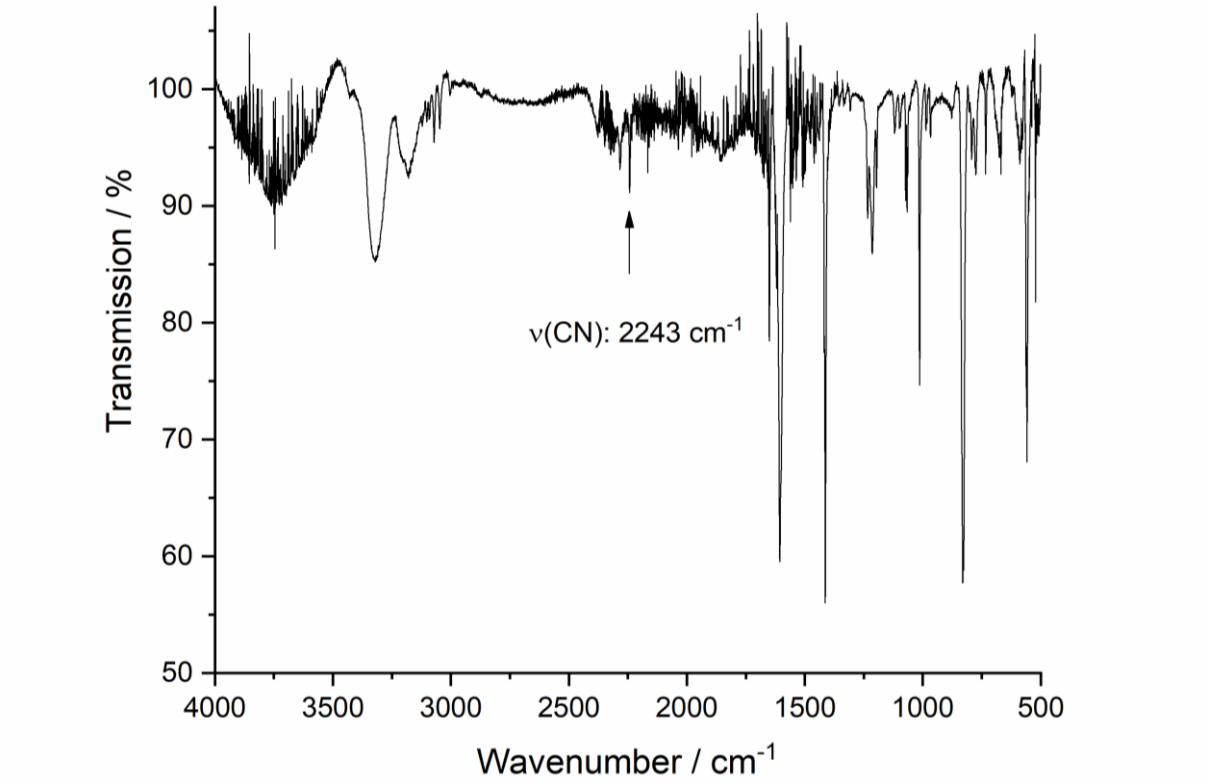

Figure S13. IR spectrum of $[FeBr_2(4\text{-}CNpy)_2]_n$ (**3a**).

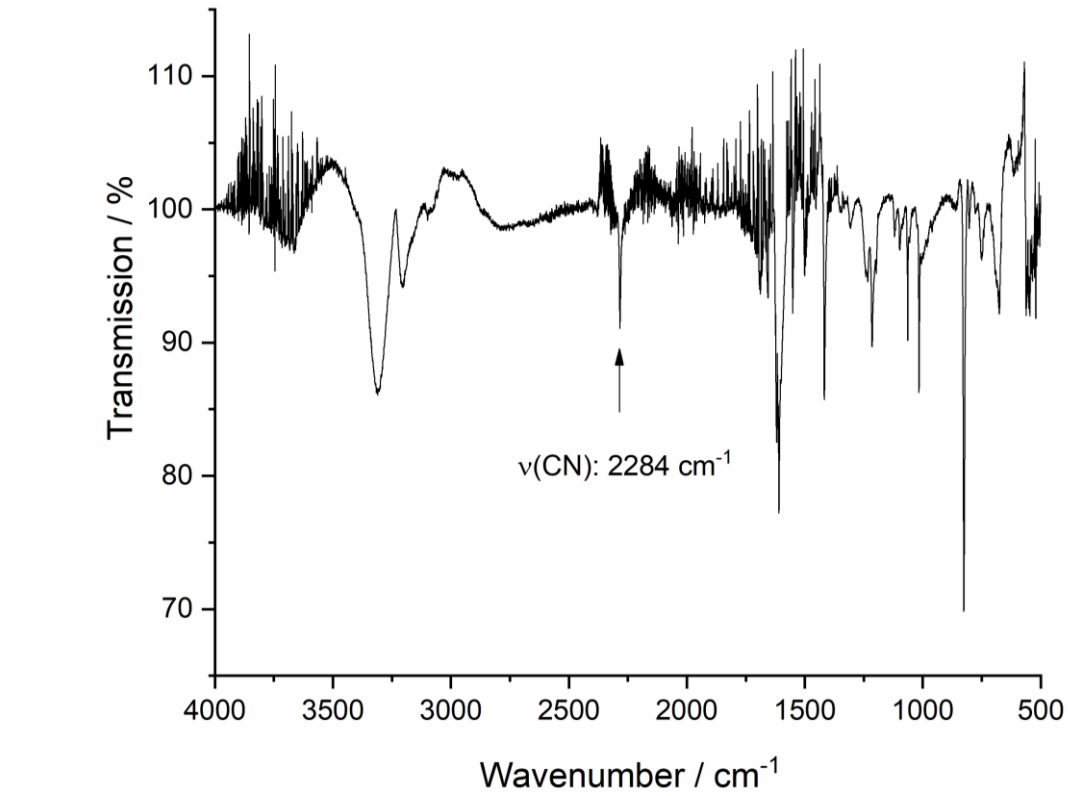

Figure S14. IR spectrum of $[FeBr_2(4\text{-}CNpy)_1]_n$ (**3b**).

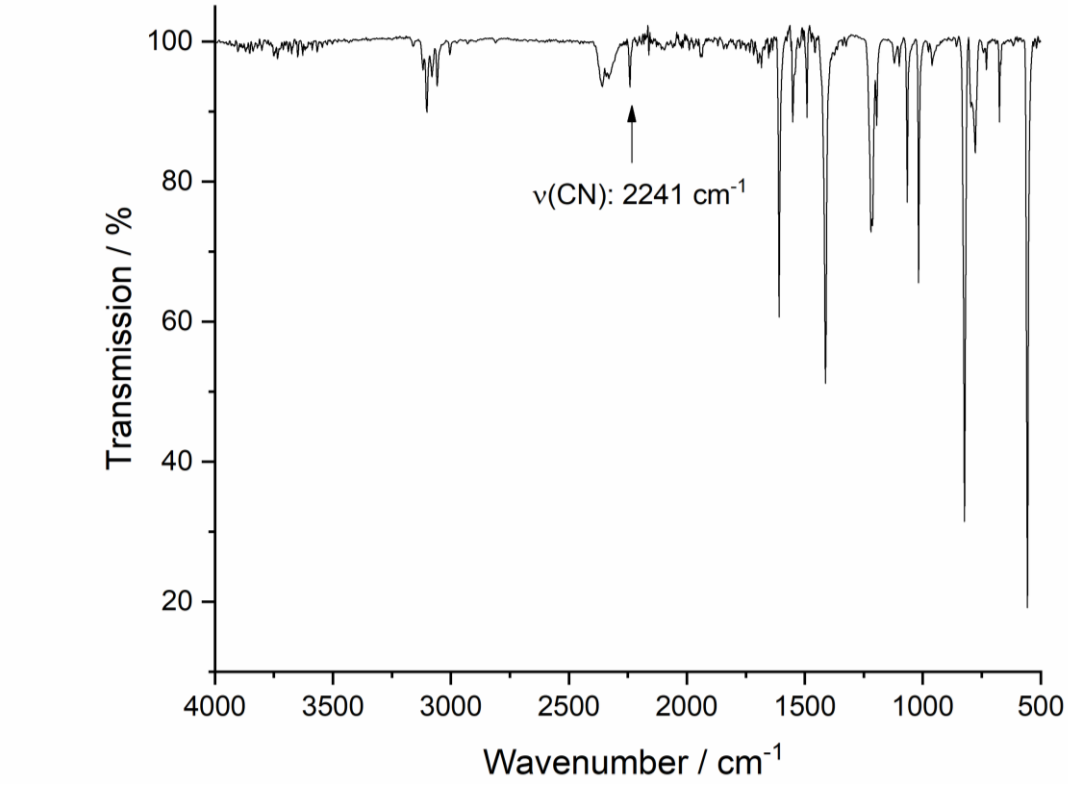

Figure S15. IR spectrum of $[CoCl_2(4\text{-}CNpy)_2]_n$ (**4a**).

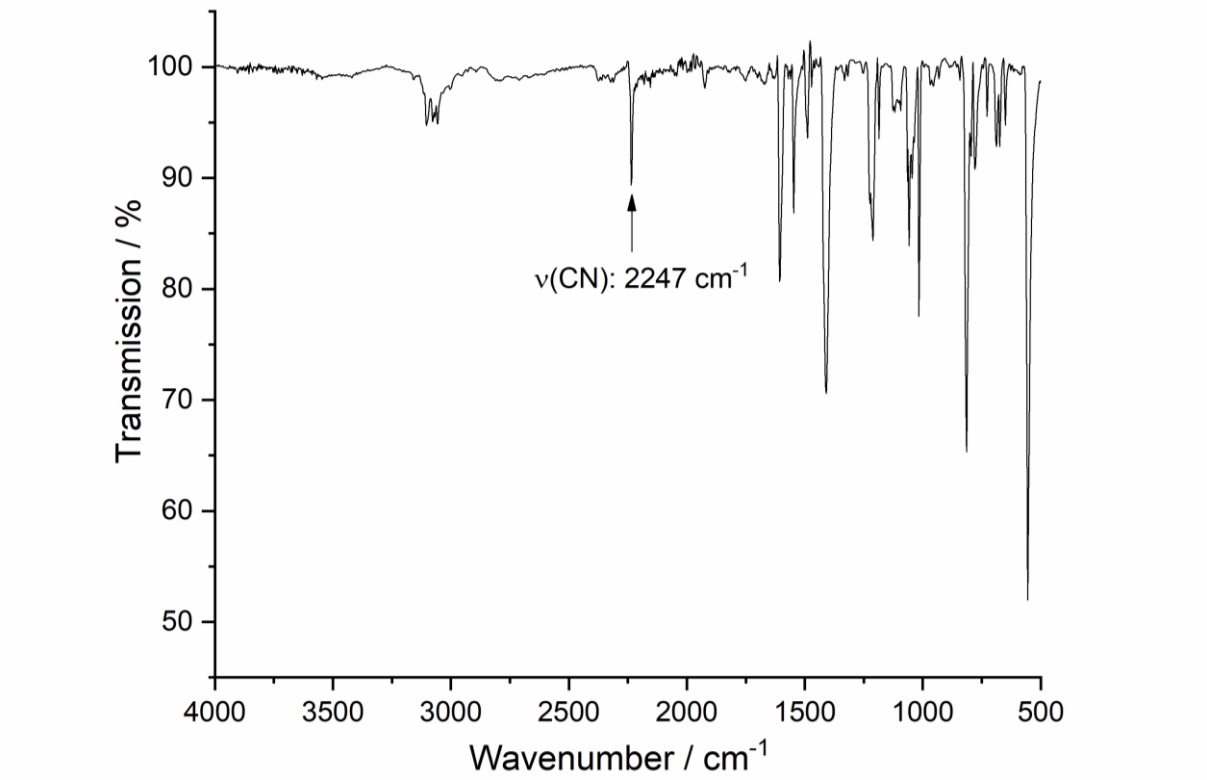

Figure S16. IR spectrum of $[CoBr_2(4\text{-}CNpy)_2]_n$ (**5a**).

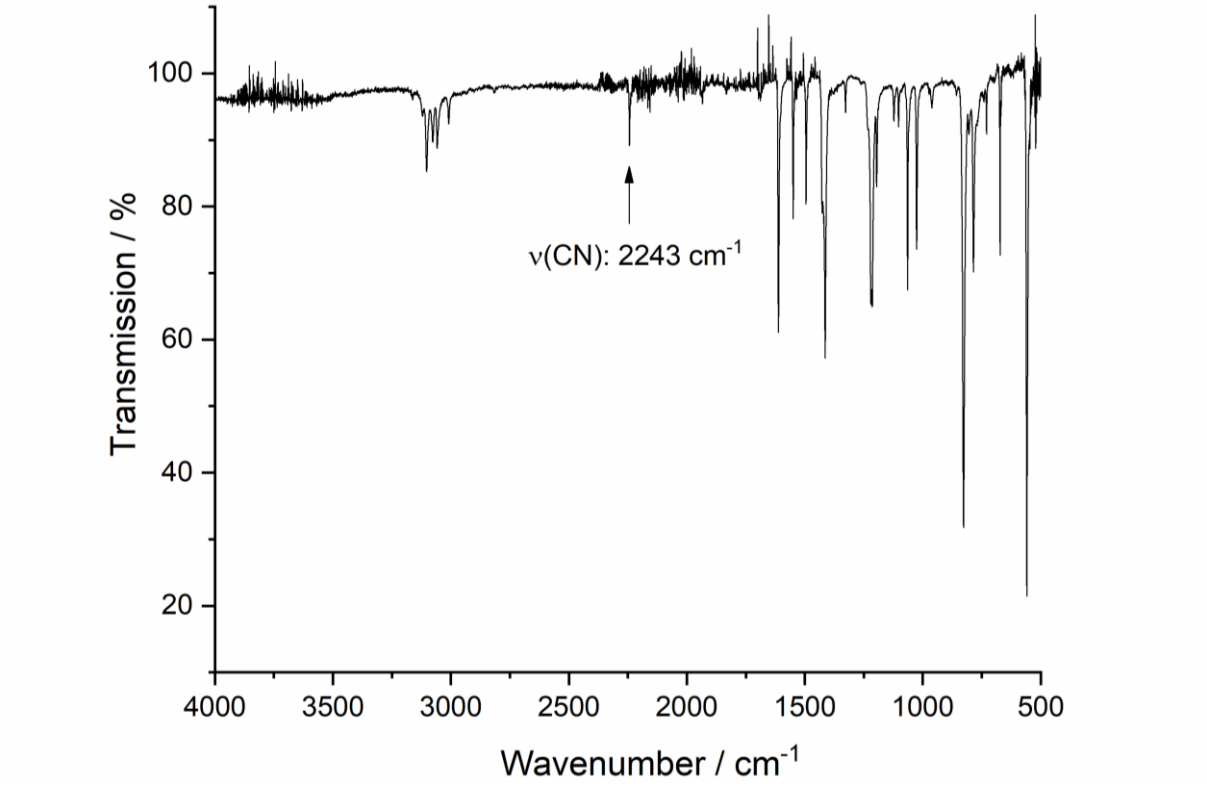

Figure S17. IR spectrum of $[CuBr_2(4\text{-}CNpy)_2]_n$ (**6**).

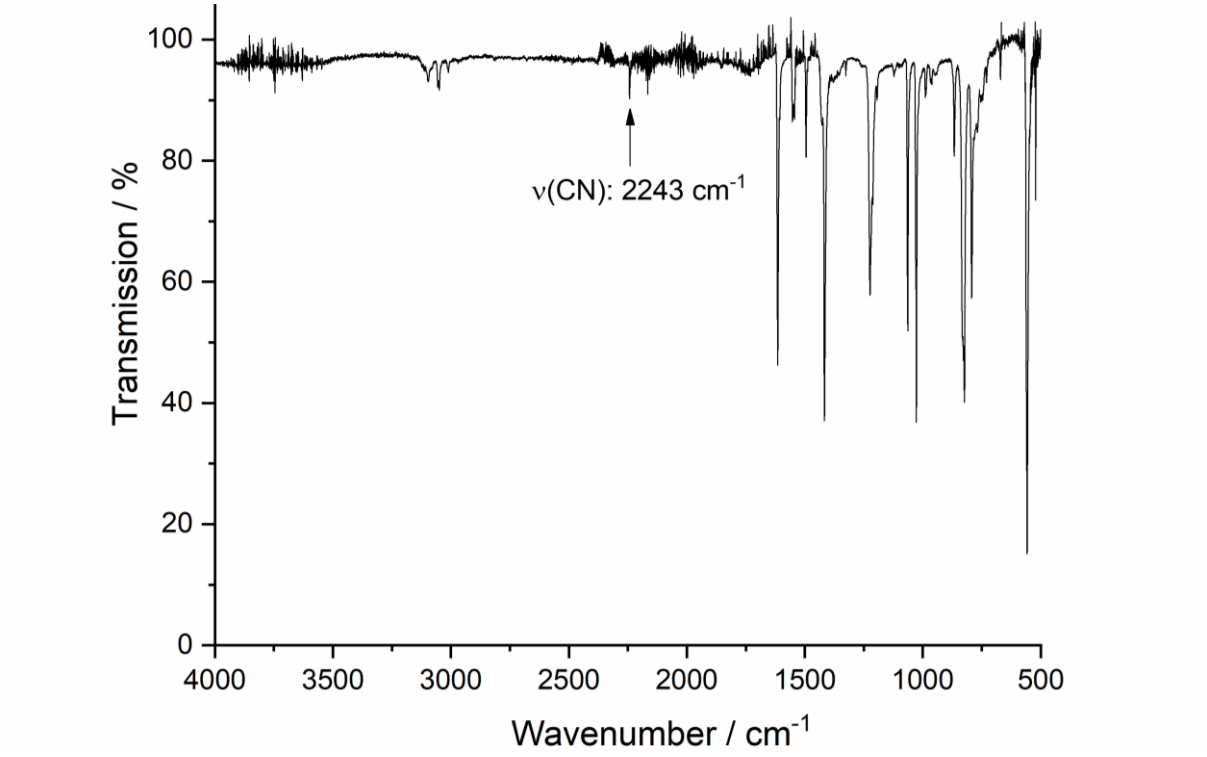

Figure S18. IR spectrum of α-[$ZnBr_2$(4-CNpy)$_2$] (**α-7**).

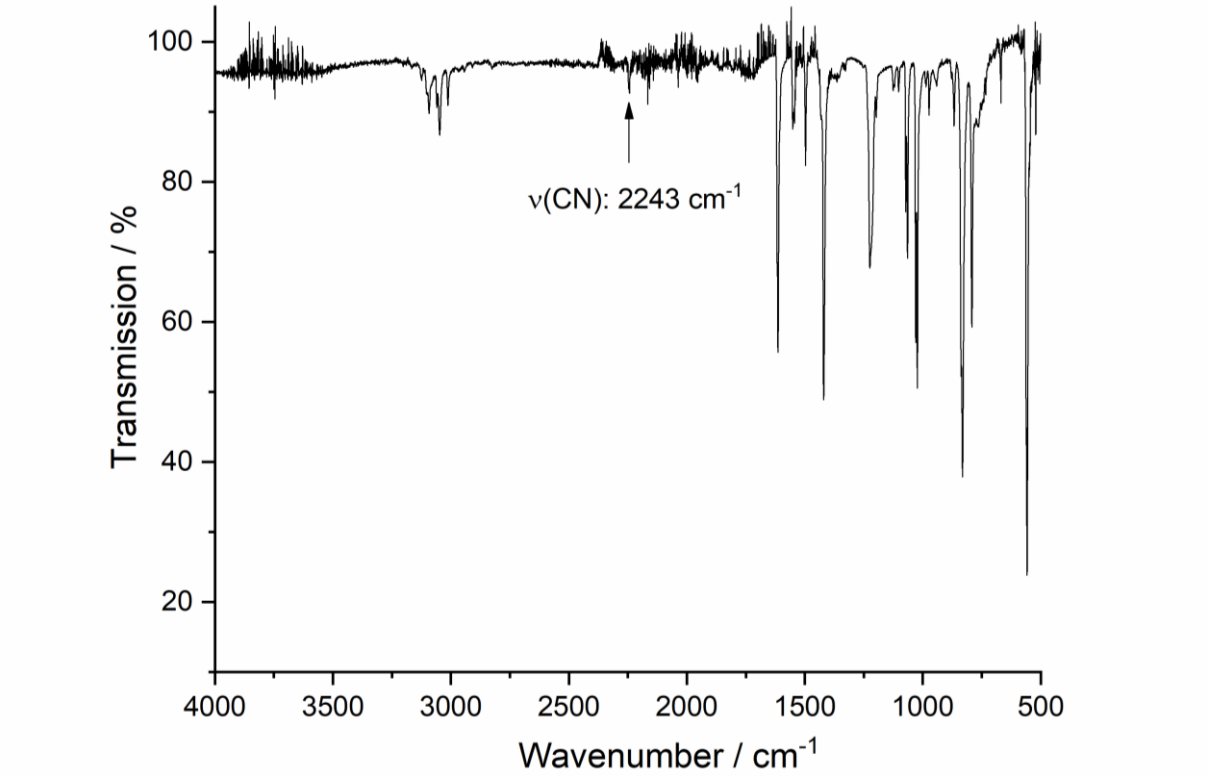

Figure S19. IR spectrum of β-[$ZnBr_2$(4-CNpy)$_2$] (**β-7**).

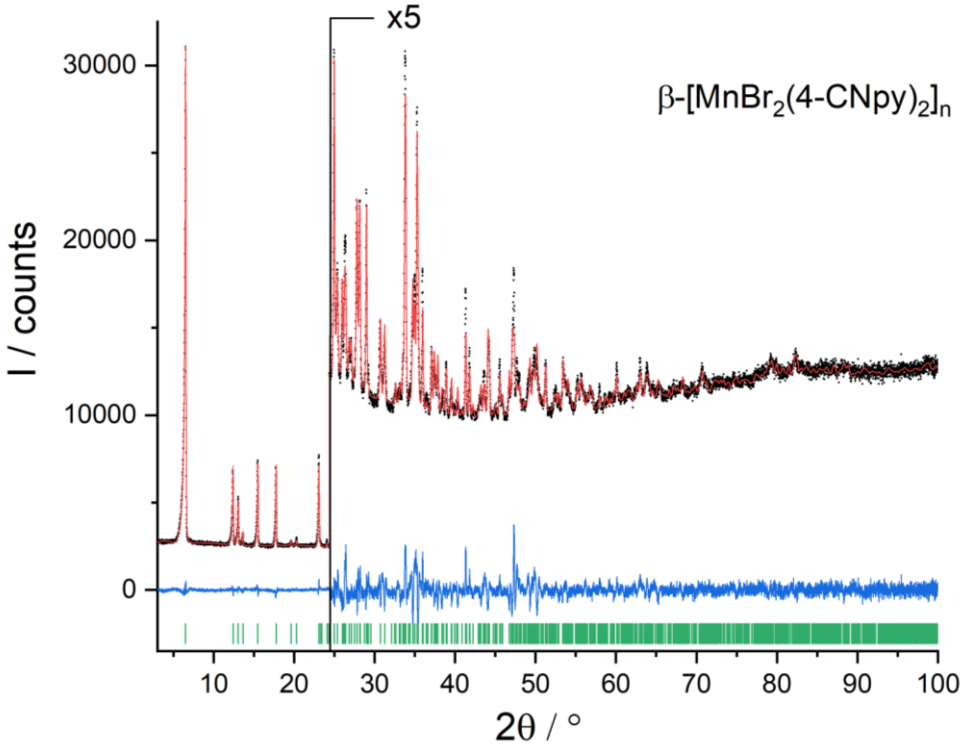

Figure S20. Rietveld plot of (**β-1a**). Observed powder diagram (black points), calculated powder diagram (red solid line), difference curve (blue solid line) and calculated reflection positions (green bars). Change of the scales with corresponding factor is indicated.

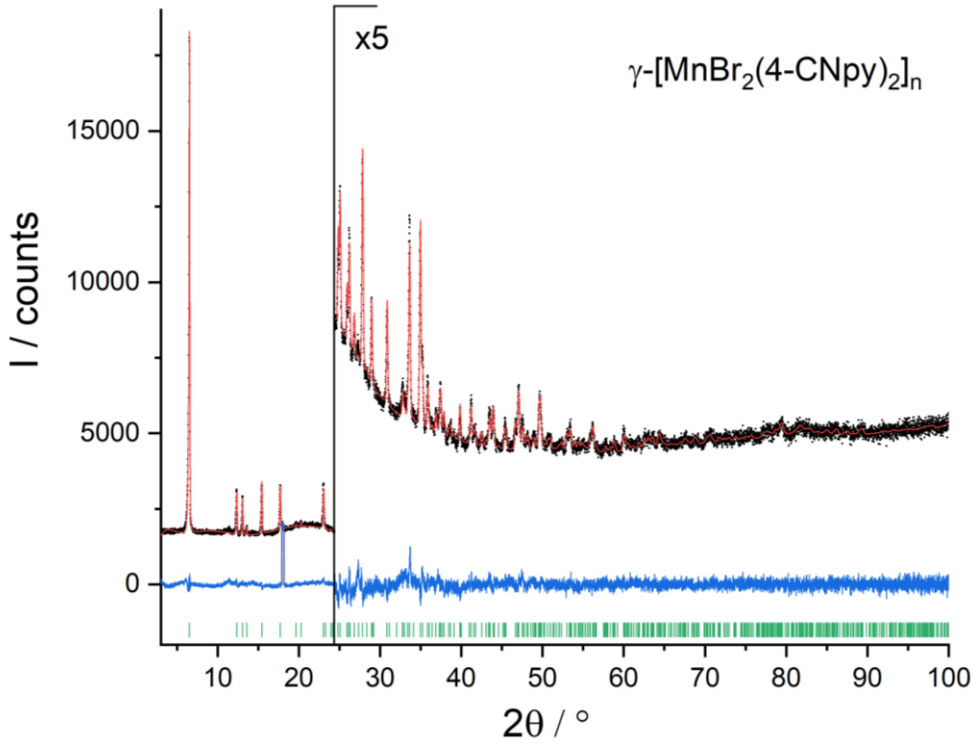

Figure S21. Rietveld plot of (**γ-1a**). Observed powder diagram (black points), calculated powder diagram (red solid line), difference curve (blue solid line) and calculated reflection positions (green bars). One appearing reflection of **1b** was excluded during the refinement. Change of the scales with corresponding factor is indicated.

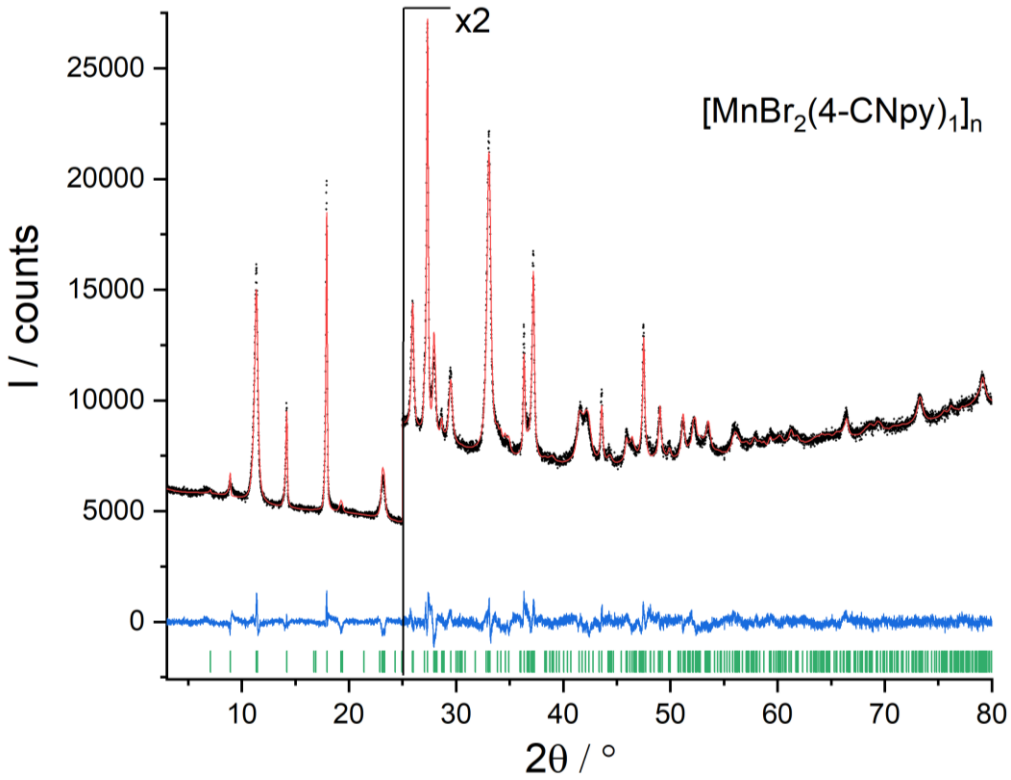

Figure S22. Rietveld plot of (**1b**). Observed powder diagram (black points), calculated powder diagram (red solid line), difference curve (blue solid line) and calculated reflection positions (green bars). Change of the scales with corresponding factor is indicated.

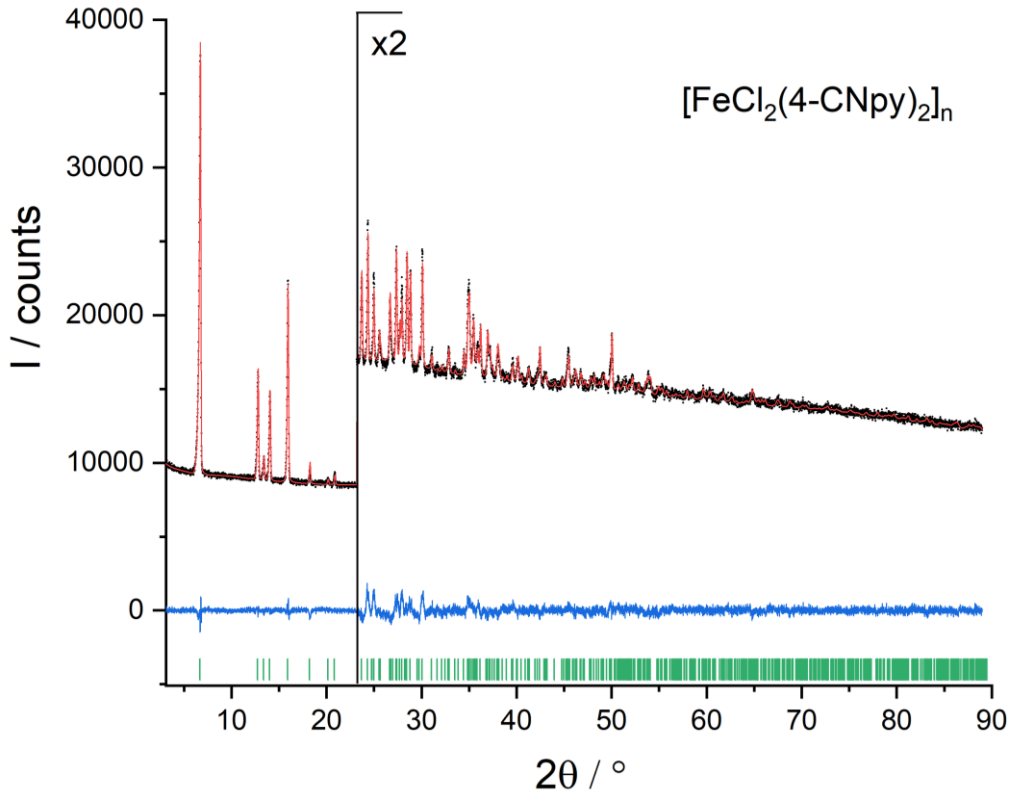

Figure S23. Rietveld plot of (**2a**). Observed powder diagram (black points), calculated powder diagram (red solid line), difference curve (blue solid line) and calculated reflection positions (green bars). Change of the scales with corresponding factor is indicated.

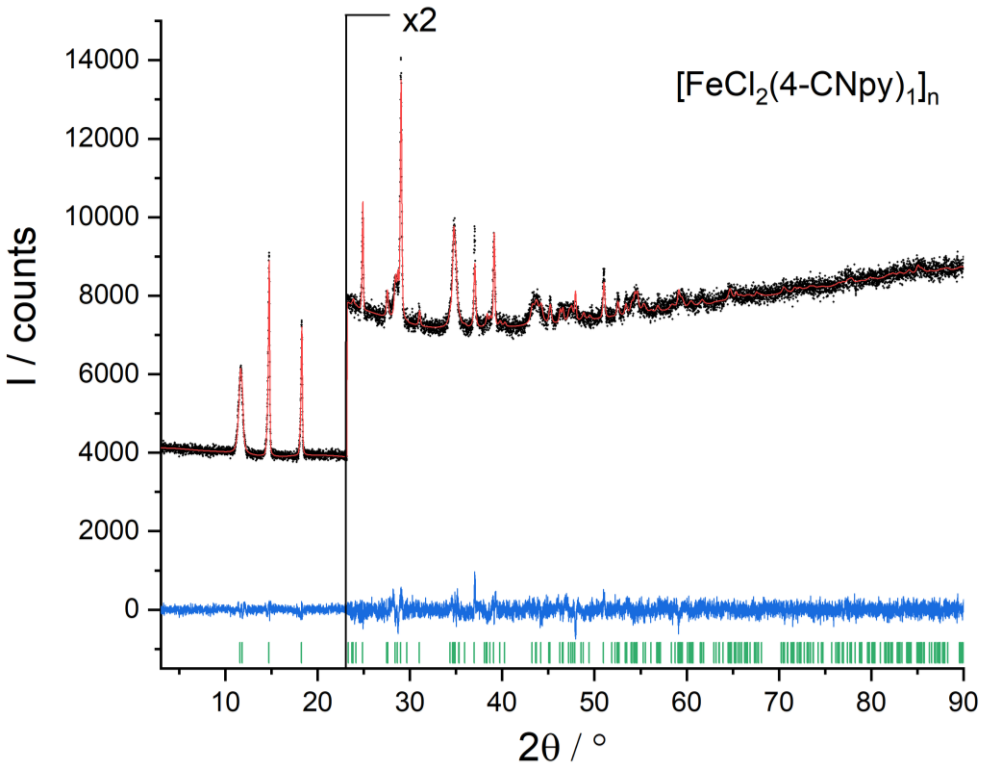

Figure S24. Rietveld plot of (**2b**). Observed powder diagram (black points), calculated powder diagram (red solid line), difference curve (blue solid line) and calculated reflection positions (green bars). Change of the scales with corresponding factor is indicated.

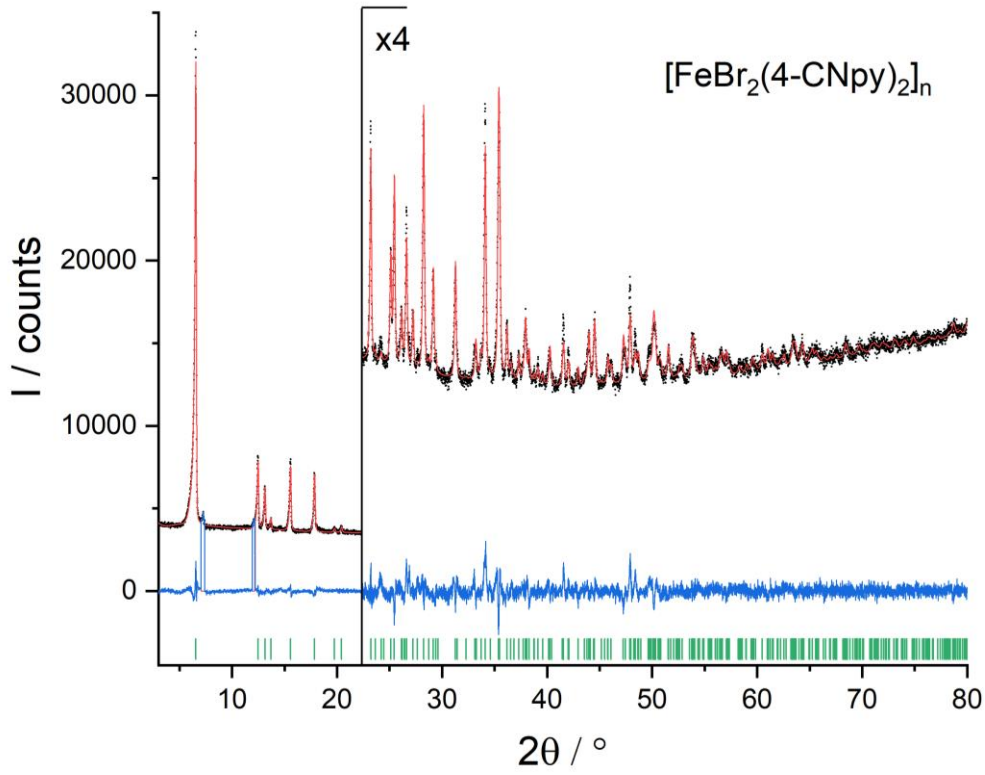

Figure S25. Rietveld plot of (**3a**). Observed powder diagram (black points), calculated powder diagram (red solid line), difference curve (blue solid line) and calculated reflection positions (green bars). Reflections of a foreign phase are excluded. Change of the scales with corresponding factor is indicated

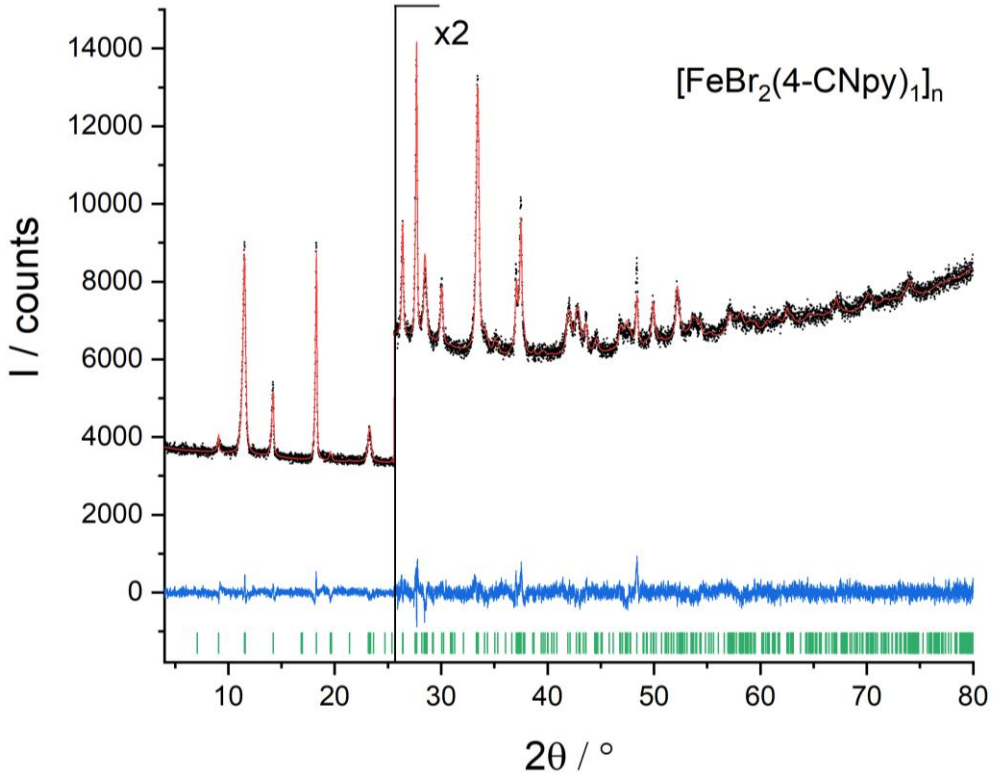

Figure S26. Rietveld plot of (**3b**). Observed powder diagram (black points), calculated powder diagram (red solid line), difference curve (blue solid line) and calculated reflection positions (green bars). Change of the scales with corresponding factor is indicated.

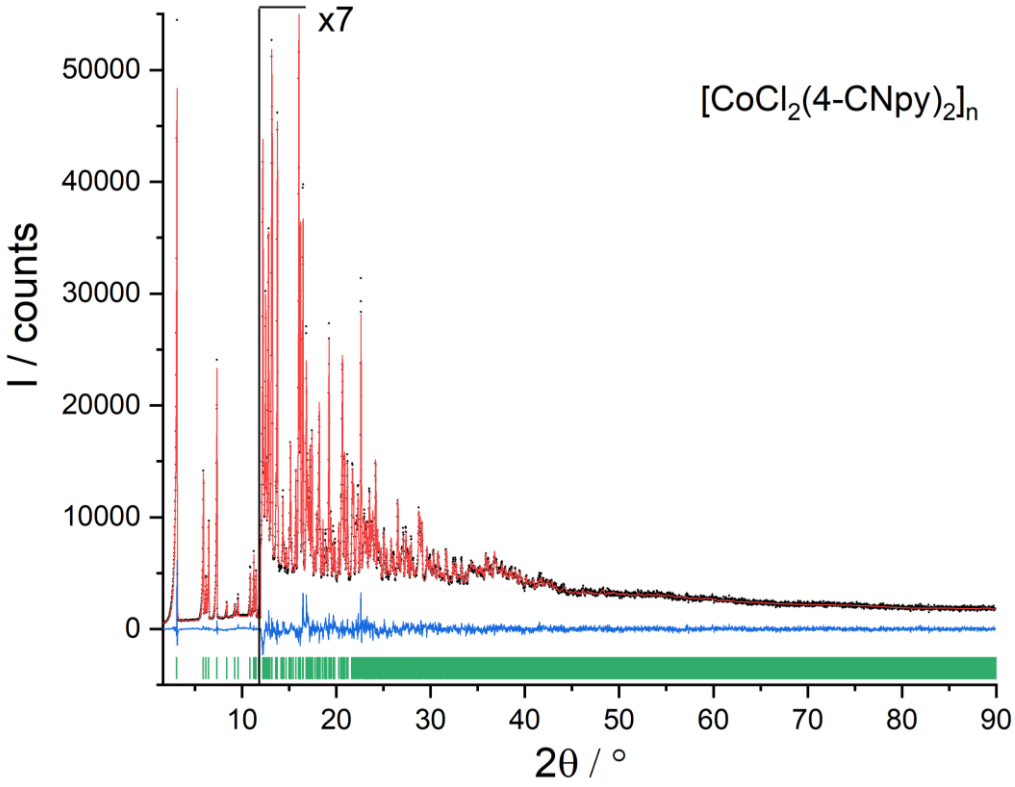

Figure S27a. Full Rietveld plot of (**4a**). Observed powder diagram (black points), calculated powder diagram (red solid line), difference curve (blue solid line) and calculated reflection positions (green bars). Change of the scales with corresponding factor is indicated.

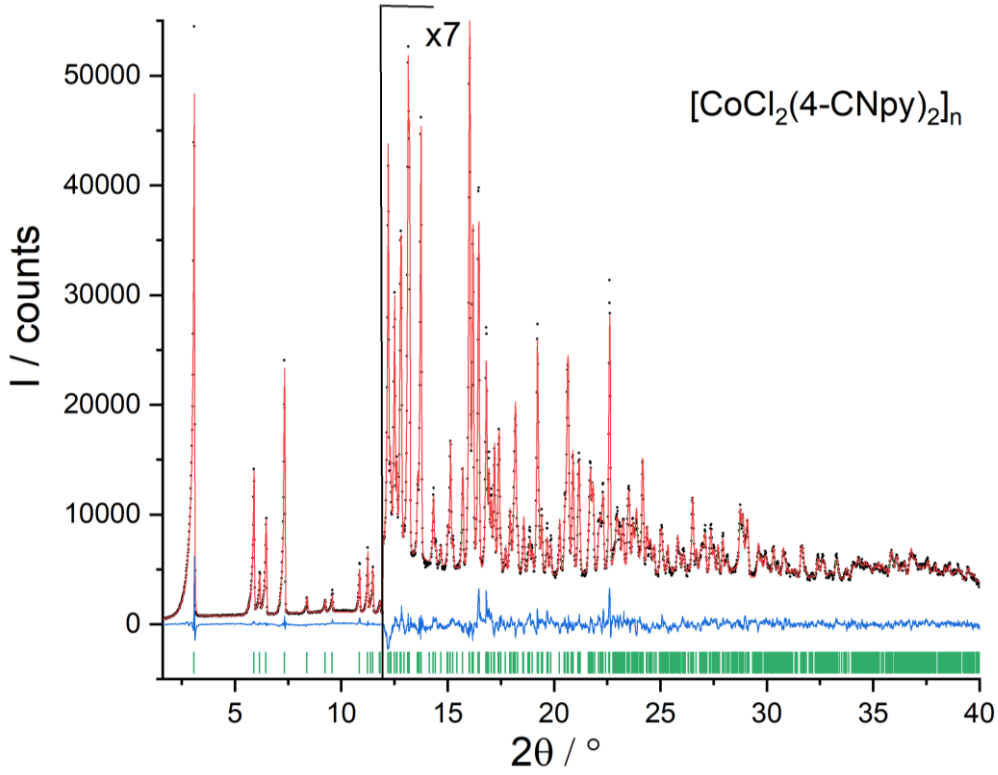

Figure S27b. Rietveld plot of (**4a**) shown until 40° in 2θ. Observed powder diagram (black points), calculated powder diagram (red solid line), difference curve (blue solid line) and calculated reflection positions (green bars). Change of the scales with corresponding factor is indicated.

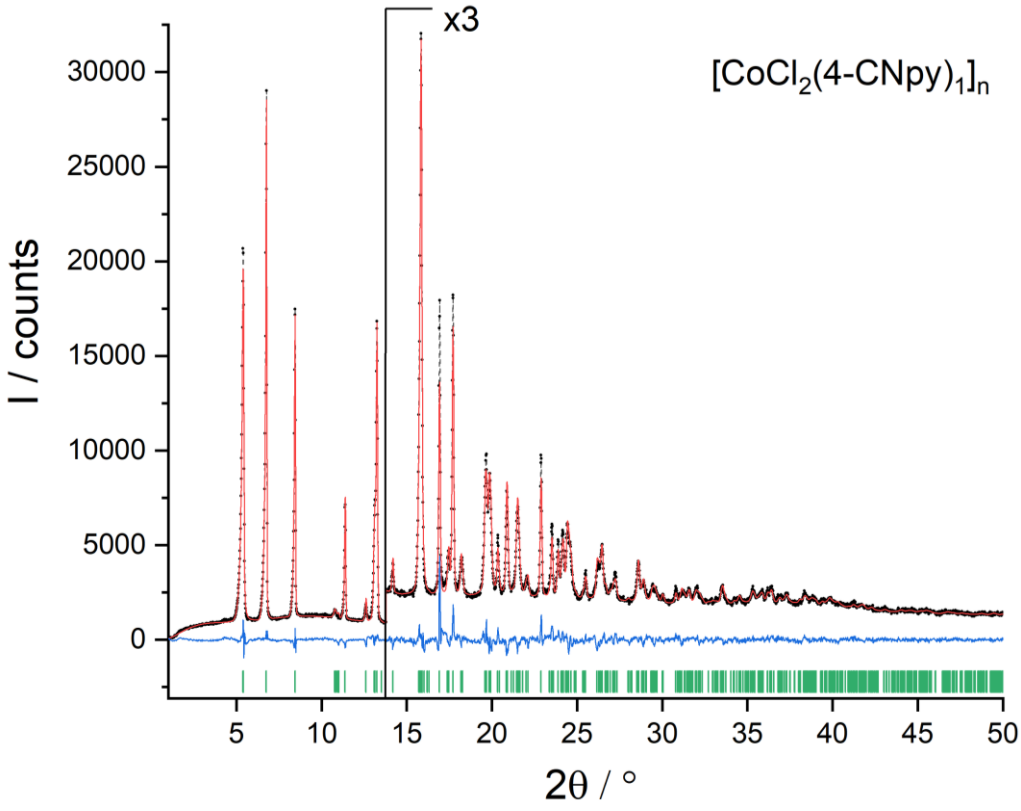

Figure S28. Rietveld plot of (**4b**). Observed powder diagram (black points), calculated powder diagram (red solid line), difference curve (blue solid line) and calculated reflection positions (green bars). Change of the scales with corresponding factor is indicated.

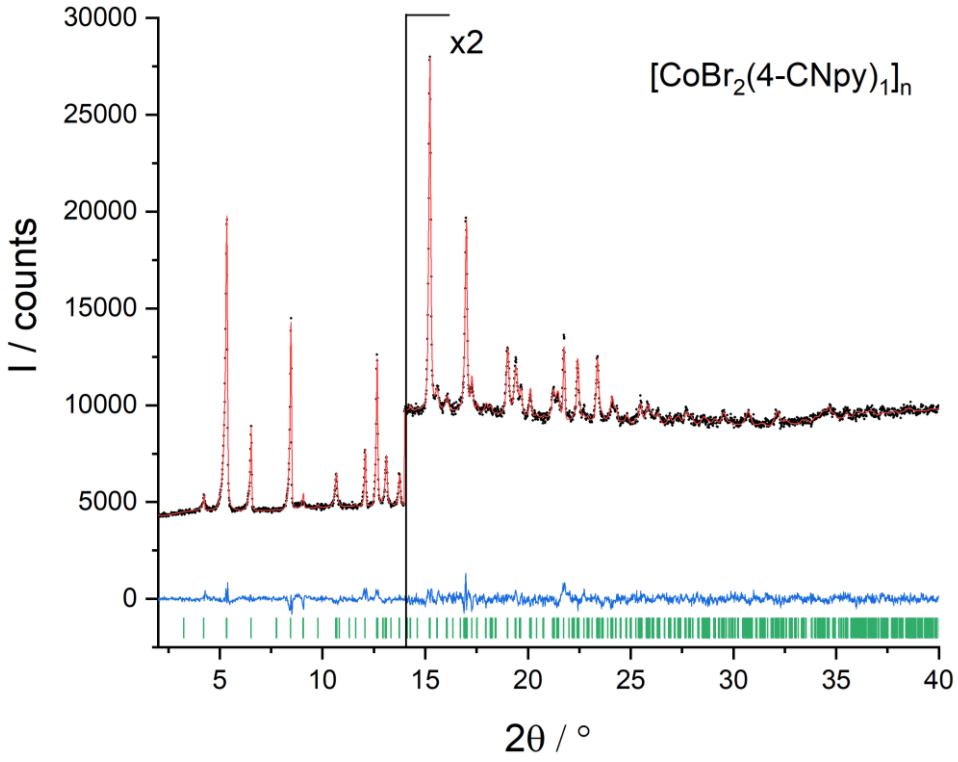

Figure S29. Rietveld plot of (**5b**). Observed powder diagram (black points), calculated powder diagram (red solid line), difference curve (blue solid line) and calculated reflection positions (green bars). Change of the scales with corresponding factor is indicated.

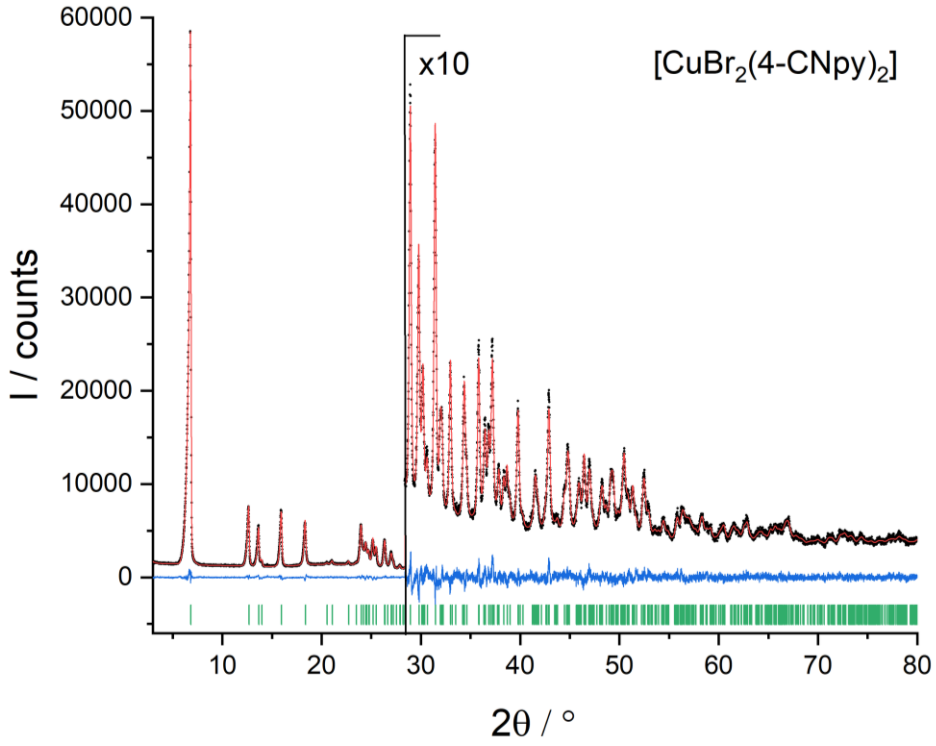

Figure S30. Rietveld plot of (**6**). Observed powder diagram (black points), calculated powder diagram (red solid line), difference curve (blue solid line) and calculated reflection positions (green bars). Change of the scales with corresponding factor is indicated.

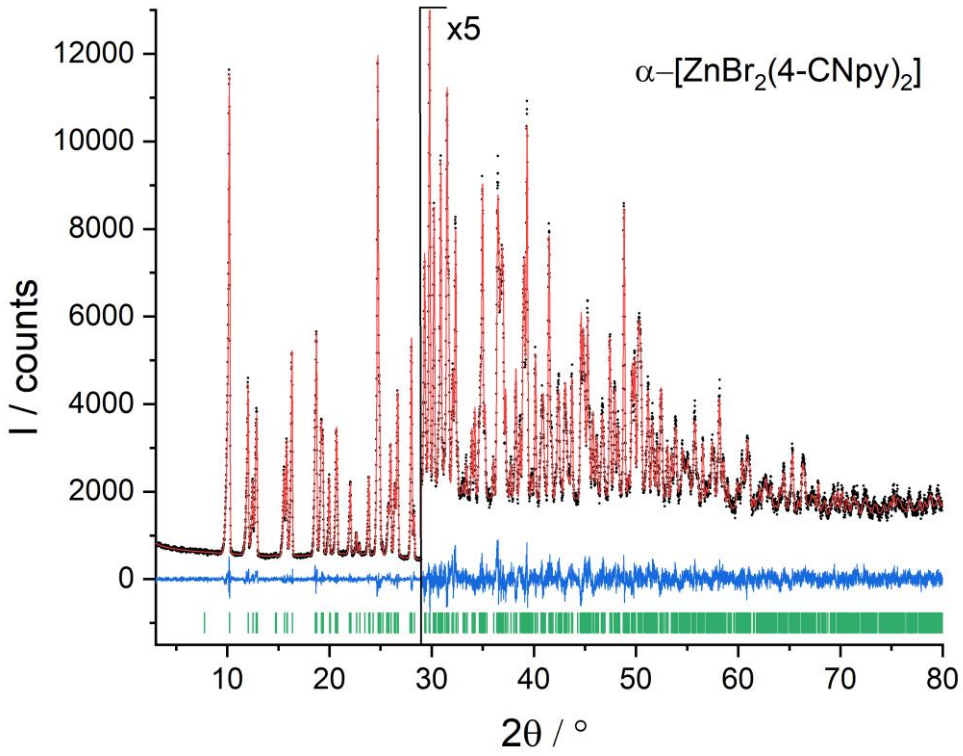

Figure S31. Rietveld plot of (**α-7**). Observed powder diagram (black points), calculated powder diagram (red solid line), difference curve (blue solid line) and calculated reflection positions (green bars). Change of the scales with corresponding factor is indicated.

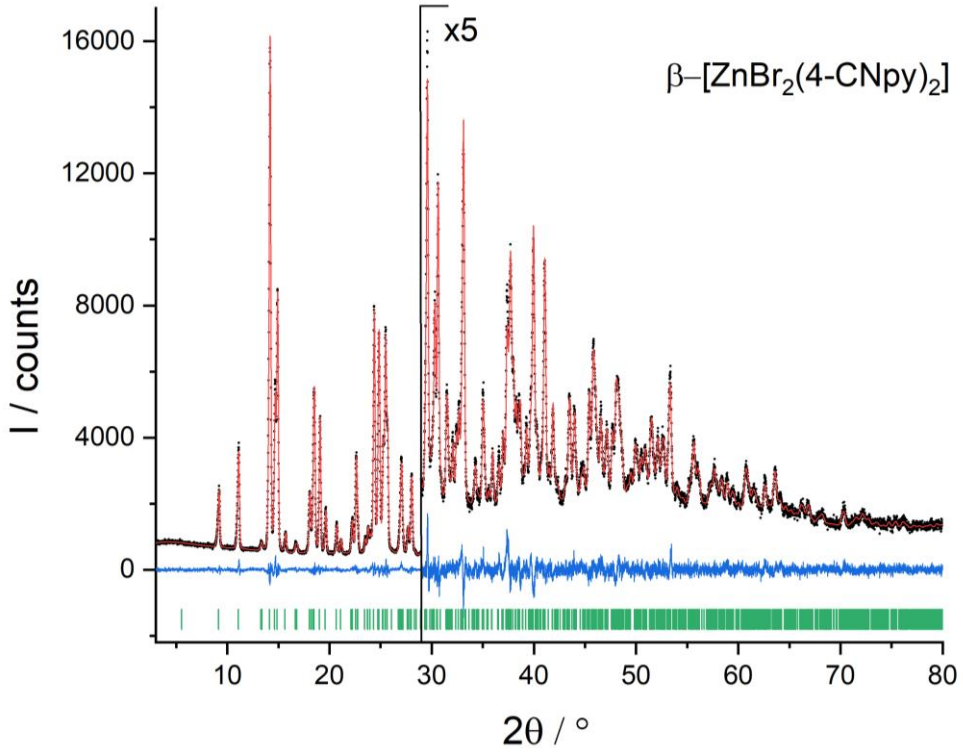

Figure S32. Rietveld plot of (**β-7**). Observed powder diagram (black points), calculated powder diagram (red solid line), difference curve (blue solid line) and calculated reflection positions (green bars). Change of the scales with corresponding factor is indicated.

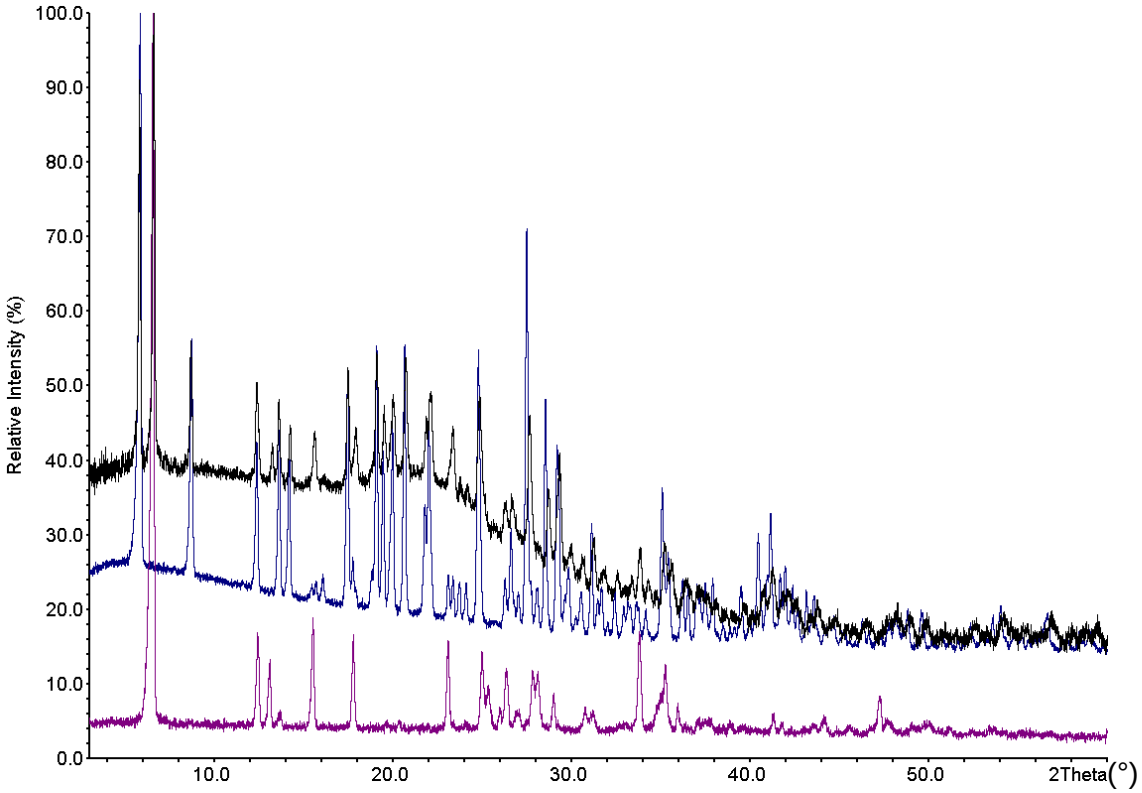

Figure S33. Experimental X-ray powder patterns of $[MnBr_2(4\text{-}CNpy)_2]_n$ (**1a**), collected with Cu-$K_{\alpha1}$ radiation. Violet: initial room temperature measurement of **1a**: pure **β-1a**. Black: measurement of **1a** at -100°C: mixture of **α-1a** + **β-1a**. Blue: new room temperature measurement after several weeks of **1a:** pure **α-1a**.

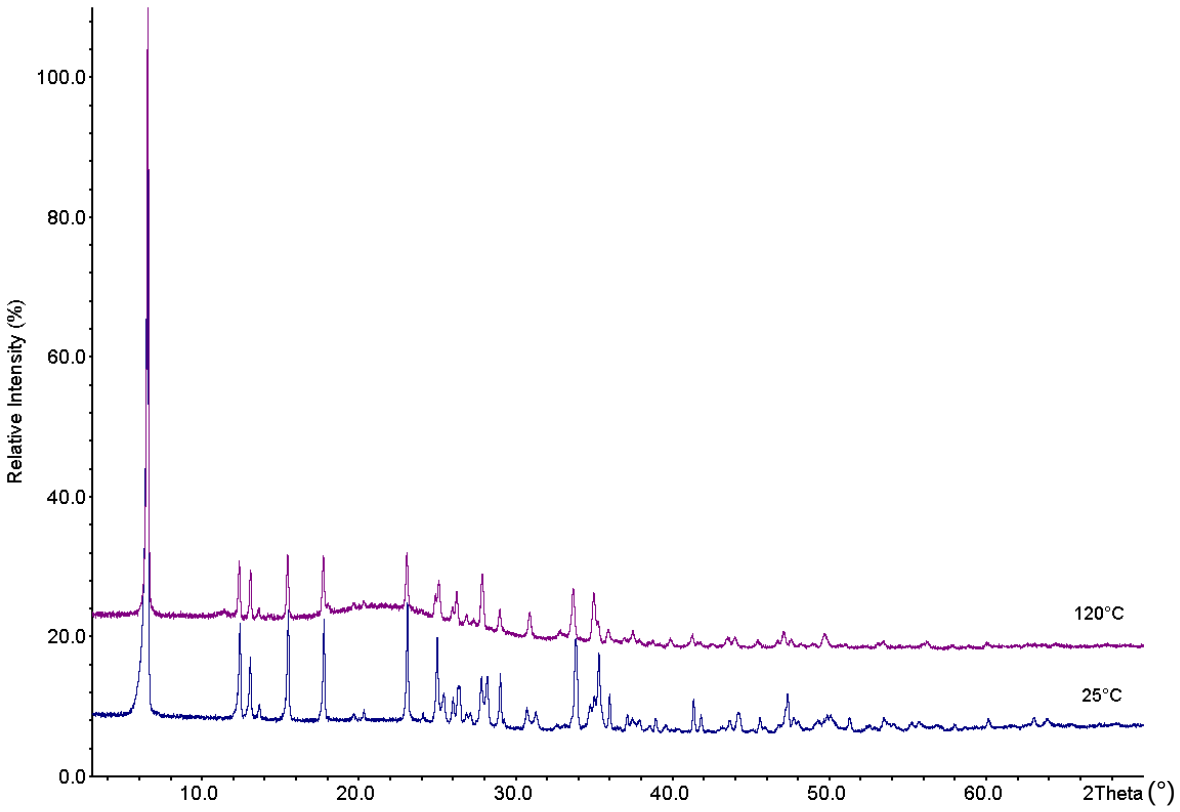

Figure S34. Experimental X-ray powder pattern of **β-1a** (blue) and **γ-1a** (violet), collected with Cu-$K_{\alpha1}$ radiation.

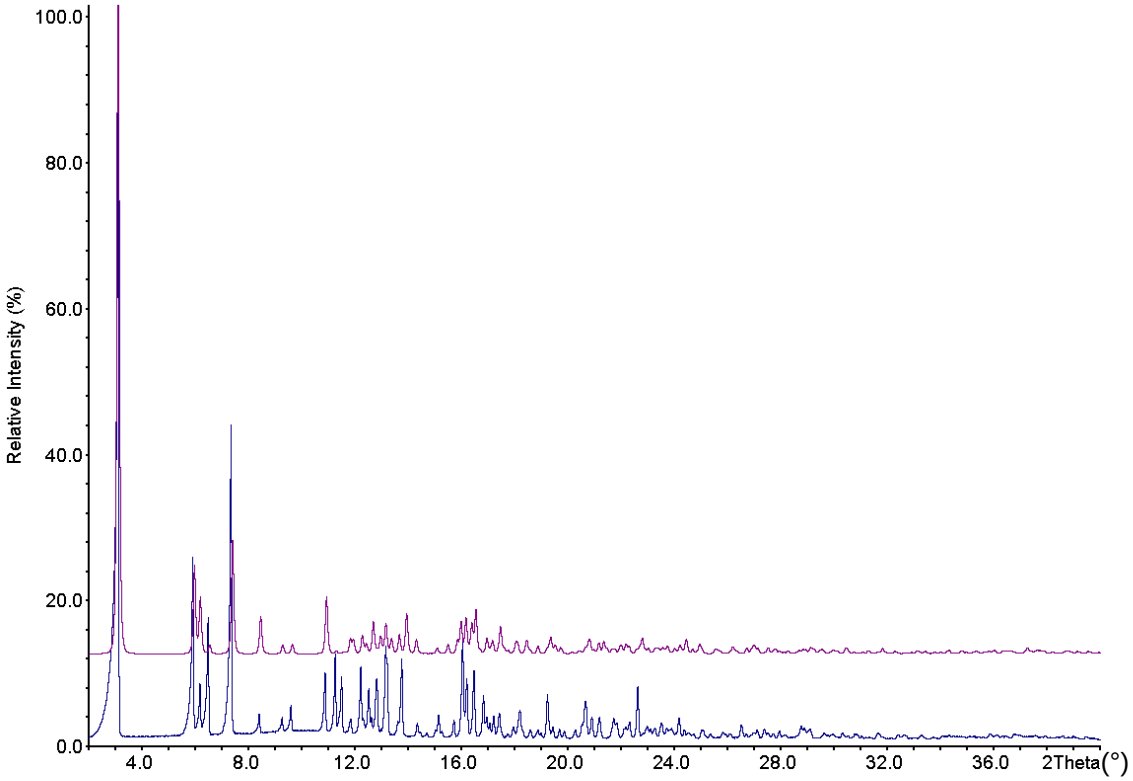

Figure S35. Experimental (blue) and calculated (UTIHIP, violet) X-ray powder pattern of $[CoCl_2(4\text{-}CNpy)_2]_n$ (**4a**) with Mo-$K_{\alpha 1}$ radiation.

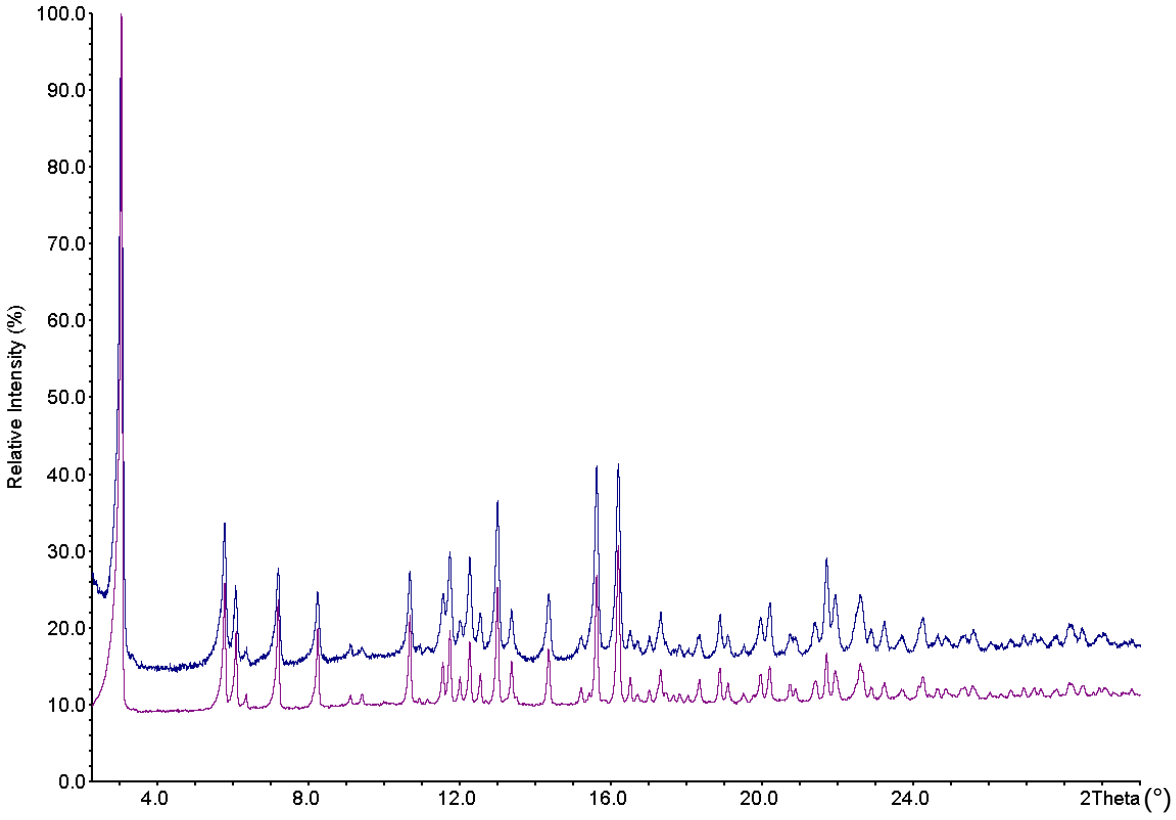

Figure S36. Experimental X-ray powder patterns of $[CoBr_2(4\text{-}CNpy)_2]_n$ (**5a**), collected with Mo-$K_{\alpha 1}$ radiation. Blue: original data for structure determination of **5a** (LATJOI). Violet: data of a new sample of **5a**, obtained in 2019.

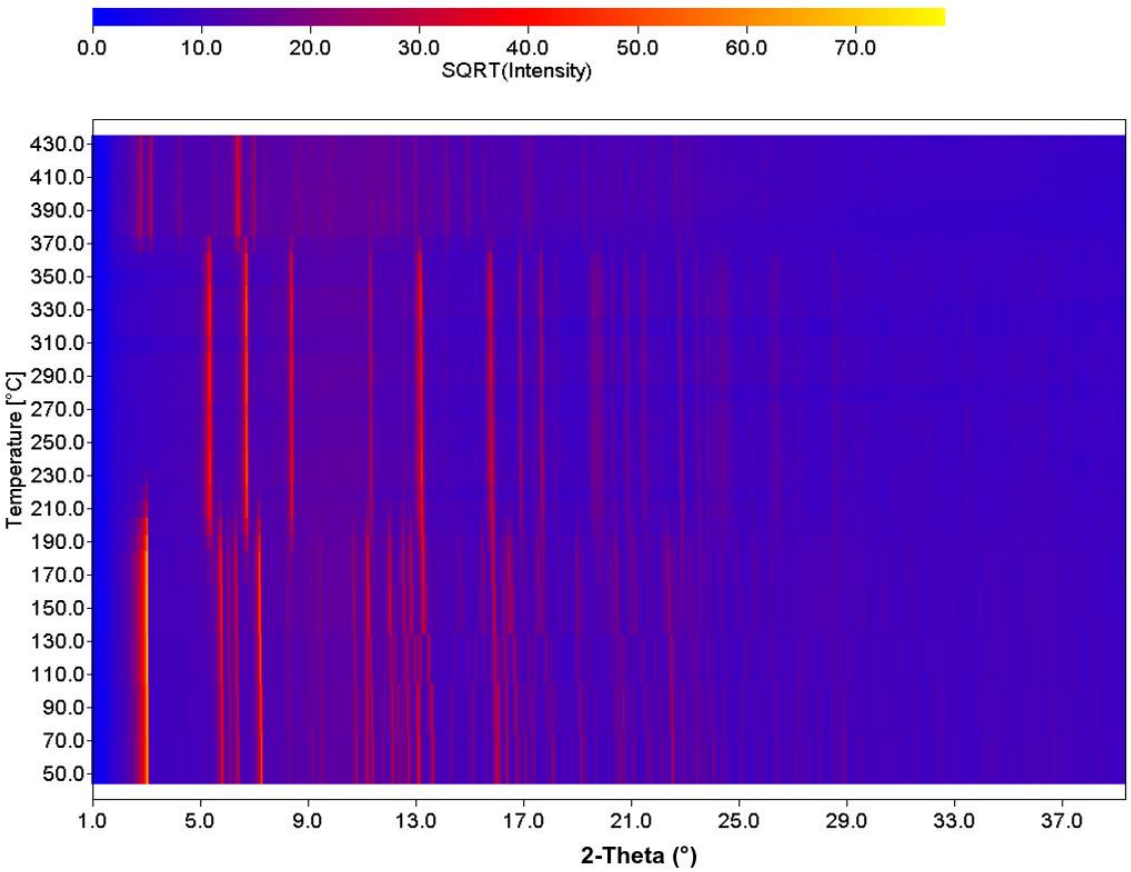

Figure S37. 3D-plot of the high-temperature X-ray measurement of $[CoCl_2(4\text{-}CNpy)_2]_n$ (**4a**), collected with Mo-$K_{\alpha1}$ radiation. Square root of the intensity chosen for better visibility.

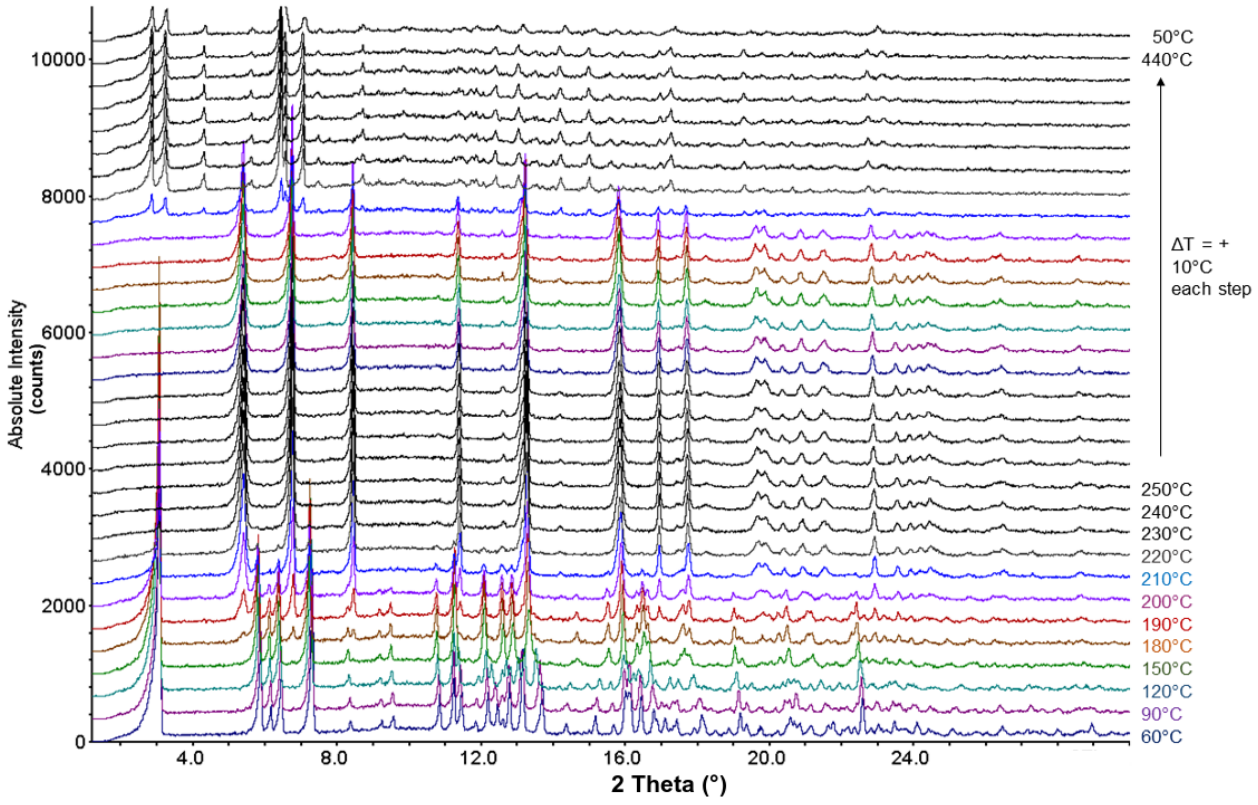

Figure S38. Temperature dependent X-ray powder pattern of **4a** transforming to **4b** and **4c,** collected with Mo-$K_{\alpha1}$ radiation.

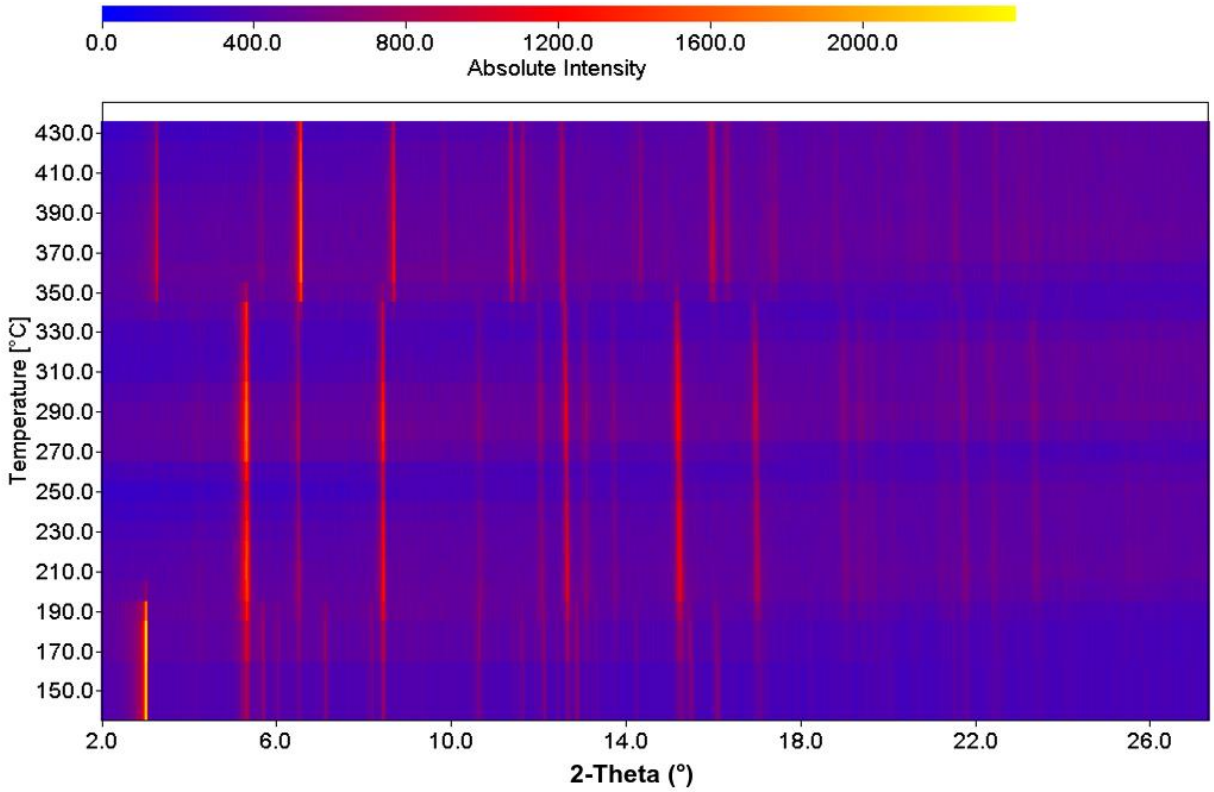

Figure S39. 3D-plot of the high-temperature X-ray measurement of $[CoBr_2(4\text{-}CNpy)_2]_n$ (**5a**), collected with Mo-$K_{\alpha1}$ radiation.

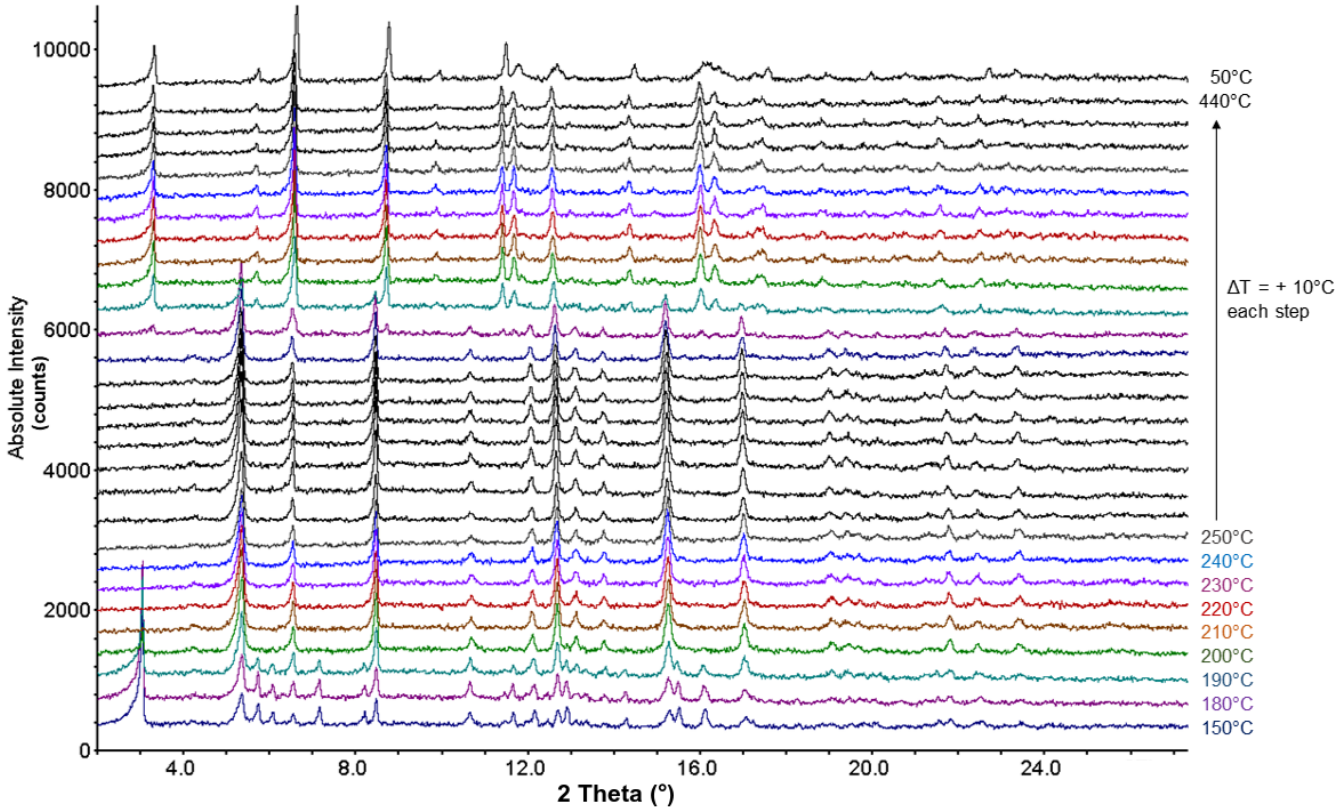

Figure S40. Temperature dependent X-ray powder pattern of **5a,** transforming to **5b** and **5c,** collected with Mo-$K_{\alpha1}$ radiation.

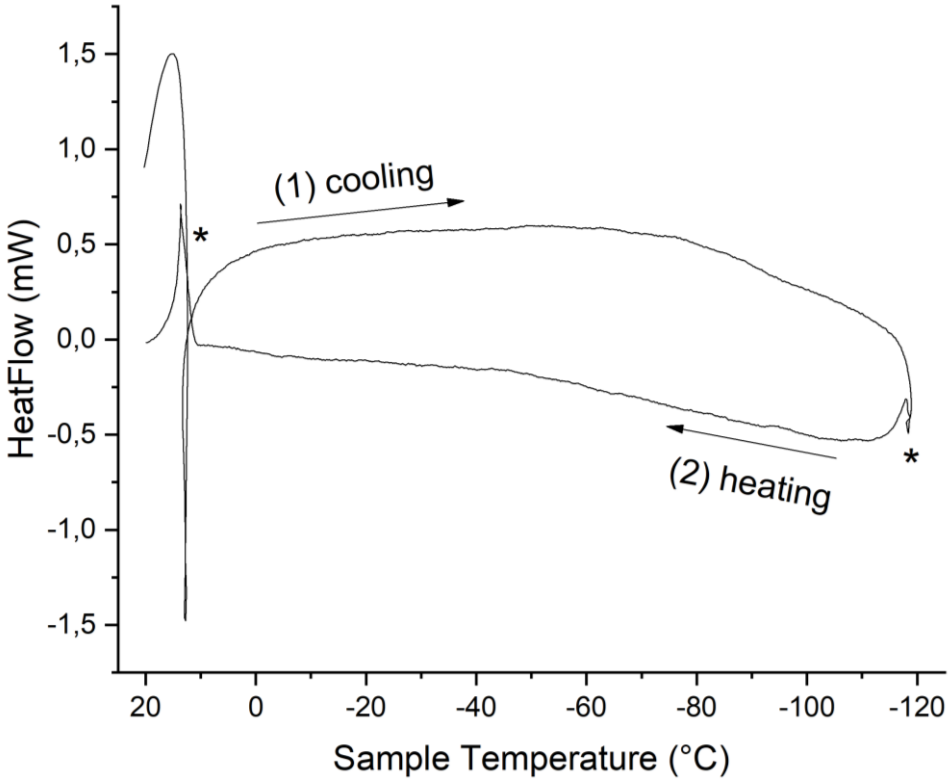

Figure S41. DSC-curve of $[MnBr_2(4\text{-}CNpy)_2]_n$ (**β-1a**): (1) Cooling from room temperature to -120 °C, then (2) heating back to room temperature. Instrumental artefacts are marked by stars.

Table S1 Results of DTA/TG measurements of $[MX_2(4\text{-CNpy})_2]_n$. DTA peak temperatures, m_0: weight of starting compound, Δm_{exp}: relative experimental weight loss, experimental $\Delta m_{exp}/m_0$, calculated $\Delta m_{cal}/m_0$.

Compound	**T [°C]**	**m_0 [mg]**	**Δm_{exp} [mg]**	**$\Delta m_{exp}/m_0$ [%]**	**$\Delta m_{cal}/m_0$ [%]**
β-$[MnBr_2(4\text{-CNpy})_2]_n$ (**β-1a**)		22.328	0	0	0
$[MnBr_2(4\text{-CNpy})_1]_n$ (**1b**)	260.68		5.074	23.51	24.61
$[MnBr_2(4\text{-CNpy})_{1/2}]_n$ (**1c**)	328.38		2.624	15.89	16.32
$MnBr_2$	366.47		2.499	18.00	19.51
$[FeCl_2(4\text{-CNpy})_2]_n$ (**2a**)		21.506	0	0	0
$[FeCl_2(4\text{-CNpy})_1]_n$ (**2b**)	248.51		6.382	29.68	31.07
$[FeCl_2(4\text{-CNpy})_{1/3}]_n$ (**2c**)	347.61		4.294	28.39	30.06
$FeCl_2$	418.84		1.519	14.02	21.49
$[FeBr_2(4\text{-CNpy})_2]_n$ (**3a**)		22.000	0	0	0
$[FeBr_2(4\text{-CNpy})_1]_n$ (**3b**)	242.24		4.652	23.14	24.56
$[FeBr_2(4\text{-CNpy})_{1/3}]_n$ (**3c**)			3.422	19.73	21.70
$FeBr_2$ (→ $FeBr_3$)	355.22		1.003	7,20	13.86
$[CoCl_2(4\text{-CNpy})_2]_n$ (**4a**)		21.713	0	0	0
$[CoCl_2(4\text{-CNpy})_1]_n$ (**4b**)	251.96		6.342	29.21	30.80
$[CoCl_2(4\text{-CNpy})_{1/3}]_n$ (**4c**)	338.02		4.263	27.73	29.66
$CoCl_2$	409.70		2.050	18.45	21.08
$[CoBr_2(4\text{-CNpy})_2]_n$ (**5a**)		29.84	0	0	0
$[CoBr_2(4\text{-CNpy})_1]_n$ (**5b**)	252.08		7.023	23.54	30.80
$[CoBr_2(4\text{-CNpy})_{1/3}]_n$ (**5c**)	358.48		4.614	20.22	21.49
$CoBr_2$	389.72		2.231	12.25	13.69
$[CuBr_2(4\text{-CNpy})_2]$ (**6**)		6.119	0	0	0
$CuBr_2$ (→ CuBr)	252.54		2.405	60.69	48.24
α-$[ZnBr_2(4\text{-CNpy})_2]$ (**α-7**)		31.043	0	0	0
$ZnBr_2$	242.08		7.123	48.03	22.94
β-$[ZnBr_2(4\text{-CNpy})_2]$ (**β-7**)		13.56	0	0	0
$ZnBr_2$	236.71		3.039	48.03	25.89

Table S2-Part 1. Crystallographic data of $[MX_2(4\text{-CNpy})_2]_n$ (**1a**-**5a**).

	β -1a	**γ-1a**	**2a**	**3a**	**4a-PD**	**4a-SC**	**5a**
Compound	β-$[MnBr_2(4\text{-CNpy})_2]_n$	γ-$[MnBr_2(4\text{-CNpy})_2]_n$	$[FeCl_2(4\text{-CNpy})_2]_n$	$[FeBr_2(4\text{-CNpy})_2]_n$	$[CoCl_2(4\text{-CNpy})_2]_n$	$[CoCl_2(4\text{-CNpy})_2]_n$	$[CoBr_2(4\text{-CNpy})_2]_n$
CCDC number/ CSD code	1956119	1956120	1956117	1956115	1956112	UTIHIP	LATJOI
Structure determined from	Powder data	Powder data	Powder data	Powder data	Powder data	Single crystal data	Powder data
Formula	$C_{12}H_8Br_2MnN_4$	$C_{12}H_8Br_2MnN_4$	$C_{12}H_8Cl_2FeN_4$	$C_{12}H_8Br_2FeN_4$	$C_{12}H_8Cl_2CoN_4$	$C_{12}H_8Cl_2CoN_4$	$C_{12}H_8Br_2CoN_4$
MW /g·mol^{-1}	422.96	422.96	334.97	423.87	338.06	338.06	426.96
Crystal system	Monoclinic	Orthorhombic	Monoclinic	Orthorhombic	Monoclinic	Monoclinic	Orthorhombic
Space group (No.)	*P* 2$_1$/*n* (14)	*P nnm* (58)	*P* 2$_1$/*n* (14)	*P nnm* (58)	*P* 2$_1$/*c* (14)	*P* 2$_1$/*c* (14)	*P nnm* (58)
***a* /Å**	27.0744(7)	27.1046(6)	26.5605(10)	26.9168(11)	3.628870(42)	3.608(2)	26.8461(15)
***b* /Å**	7.38192(18)	7.4288(3)	7.1868(2)	7.3429(2)	7.15642(12)	7.065(5)	7.31908(32)
***c* /Å**	3.83783(11)	3.86070(12)	3.66280(7)	3.79547(10)	26.46185(42)	26.342(4)	3.77080(11)
***α* /°**	90	90	90	90	90	90	90
***ß* /°**	91.182(3)	90	95.365(3)	90	93.3930(16)	92.093(6)	90
***γ* /°**	90	90	90	90	90	90	90
***V* /Å^3**	766.87(4)	777.37(4)	696.11(4)	750.17(4)	686.002(18)	671.0(6)	740.920
Z, Z'	2, ½	2, ¼	2, ½	2, ¼	2, ½	2, ½	2, ¼
Site symmetry of M	$\bar{1}$	$\bar{1}$	$\bar{1}$	$\bar{1}$	$\bar{1}$	$\bar{1}$	$\bar{1}$
T /K	298	478	298	298	298	293	298
Radiation type	Cu *Kα*$_1$	Cu *Kα*$_1$	Cu *Kα*$_1$	Cu *Kα*$_1$	Mo *Kα*$_1$	Mo *Kα*	Mo *Kα*$_1$
Wavelength /Å	1.54056	1.54056	1.54056	1.54056	0.70930	0.71073	0.70930
2Θ$_{min}$ /°	3	3	3	3	1.6150	-	1
2Θ$_{max}$ /°	100	100	90	80	89.9046	-	60
psd step in 2Θ /°	0.09	0.09	0.09	0.09	0.125	-	0.09
time/step /sec	120	80	160	130	30	-	180
number of scans	2	2	1	1	2	-	3
***R$_p$* /%**	2.044	2.304	1.118	1.801	3.634	-	1.389
***R$_{wp}$* /%**	2.915	2.914	1.465	2.374	4.834	-	1.891
***R$_{exp}$* /%**	1.976	2.820	1.123	1.632	3.562	-	1.783
GOF	1.476	1.033	1.305	1.455	1.357	1.172	1.060
***R$_p$'* /%** [a]	18.774	11.862	24.007	20.053	9.249	-	17.81
***R$_{wp}$'* /%** [a]	15.827	28.219	17.657	15.685	10.106	-	13.06
***R$_{exp}$'* /%** [a]	10.726	18.035	13.535	10.782	7.446	-	12.32

a) R_p', R_{wp}' and R_{exp}' values are background corrected according to the reference [38].

Table S2-Part 2. Crystallographic data of $[MBr_2(4\text{-}CNpy)_2]_{(n)}$ (**6, α-7, β-7**).

	6	**α-7**	**β-7**
Compound	$[CuBr_2(4\text{-}CNpy)_2]_n$	α-$[ZnBr_2(4\text{-}CNpy)_2]$	β-$[ZnBr_2(4\text{-}CNpy)_2]$
CCDC number/ CSD code	1956113	1956121	1956122
Structure determined from	Powder data	Powder data	Powder data
Formula	$C_{12}H_8Br_2CuN_4$	$C_{12}H_8Br_2ZnN_4$	$C_{12}H_8Cl_2ZnN_4$
MW /g·mol^{-1}	431.57	433.41	433.41
Crystal system	Monoclinic	Monoclinic	Monoclinic
Space group (No.)	*P* $2_1/n$ (14)	*C* 2/*c* (15)	*P* $2_1/c$ (14)
***a* /Å**	7.30106(14)	28.4031(3)	16.0185(4)
***b* /Å**	25.8712(6)	7.73326(8)	12.09069(19)
***c* /Å**	3.98420(7)	17.2427(2)	7.89902(13)
***α* /°**	90	90	90
***ß* /°**	97.3176(13)	126.9230(6)	94.8775(12)
***γ* /°**	90	90	90
***V* /Å^3**	746.44(3)	3027.76(6)	1524.30(5)
Z, Z'	2, ½	8, 1	4, 1
Site symmetry of M	$\bar{1}$	1	1
T /K	298	298	298
Radiation type	Cu $K\alpha_1$	Cu $K\alpha_1$	Cu $K\alpha_1$
Wavelength /Å	1.54056	1.54056	1.54056
2Θ$_{min}$ /°	3	3	3
2Θ$_{max}$ /°	80	80	80
psd step in 2Θ /°	0.09	0.09	0.09
time/step / sec	150	150	120
number of scans	1	1	1
***R$_p$* /%**	2.681	3.380	3.239
***R$_{wp}$* /%**	3.699	4.356	4.213
***R$_{exp}$* /%**	2.904	3.642	3.452
GOF	1.274	1.196	1.220
***R$_p$'* /%** [a]	5.762	7.676	6.397
***R$_{wp}$'* /%** [a]	7.355	8.016	7.149
***R$_{exp}$'* /%** [a]	5.775	6.703	5.858

Table S3. Crystallographic data of $[MX_2(4\text{-}CNpy)_1]_n$ (**1b-5b**).

	1b	**2b**	**3b**	**4b**	**5b**
Compound	$[MnBr_2(4\text{-}CNpy)_1]_n$	$[FeCl_2(4\text{-}CNpy)_1]_n$	$[FeBr_2(4\text{-}CNpy)_1]_n$	$[CoCl_2(4\text{-}CNpy)_1]_n$	$[CoBr_2(4\text{-}CNpy)_1]_n$
CCDC number/ CSD code	1956118	1956116	1956114	1956126	1956111
Structure determined from	Powder data	Powder data	Powder data	Powder data	Powder data
Formula	$C_6H_4Br_2MnN_2$	$C_6H_4Cl_2FeN_2$	$C_6H_4Br_2FeN_2$	$C_6H_4Cl_2CoN_2$	$C_6H_4Br_2CoN_2$
MW /g·mol^{-1}	318.85	230.86	319.76	233.95	322.85
Crystal system	Monoclinic	Monoclinic	Monoclinic	Monoclinic	Monoclinic
Space group (No.)	*P* 2/*m* (10)	*P m* (6)	*P* 2/*m* (10)	*P m* (6)	*P* 2/*m* (10)
***a* /Å**	12.4448(6)	7.6656(8)	12.4397(9)	7.7426(4)	12.4692(10)
***b* /Å**	3.82332(12)	3.57945(15)	3.75800(17)	3.57685(7)	3.76053(17)
***c* /Å**	9.8744(5)	7.7986(10)	9.6919(7)	7.6901(4)	9.6232(7)
***α* /°**	90	90	90	90	90
***ß* /°**	90.569(8)	102.157	90.459(8)	102.664(2)	89.870(15)
***γ* /°**	90	90	90	90	90
***V* /Å^3**	469.81(4)	209.18(4)	453.07(5)	207.790(16)	451.24(5)
Z, Z'	2, ½	1, ½	2, ½	1, ½	2, ½
Site symmetry of M	*m*	*m*	*m*	*m*	*m*
T /K	298	298	298	523	523
Radiation type	Cu $K\alpha_1$	Cu $K\alpha_1$	Cu $K\alpha_1$	Mo $K\alpha_1$	Mo $K\alpha_1$
Wavelength /Å	1.54056	1.54056	1.54056	0.70930	0.70930
$2\Theta_{min}$ /°	3	3	3	1	1
$2\Theta_{max}$ /°	90	90	80	50.26	50.26
psd step in 2Θ /°	0.09	0.09	0.09	0.125	0.125
time/step /sec	160	60	130	120	120
number of scans	1	1	1	2	2
***R_p* /%**	1.757	1.304	1.524	3.882	1.480
***R_{wp}* /%**	2.331	1.681	1.974	5.477	1.984
***R_{exp}* /%**	1.442	1.575	1.664	2.995	1.404
GOF	1.616	1.067	1.186	1.829	1.413
***R_p'* /%** [a]	18.116	40.719	27.077	10.365	19.766
***R_{wp}'* /%** [a]	14.684	23.746	18.263	11.476	14.496
***R_{exp}'* /%** [a]	9.087	22.252	15.403	6.274	10.260

Table S4. R-Values of the Rietveld refinements of $[MCl_2(4\text{-}CNpy)_1]_n$ (**2b, 4b**) in *P* 2/*m* using models with and without disorder.

	$[FeCl_2(4\text{-}CNpy)_1]_n$ (2b)		**$[CoCl_2(4\text{-}CNpy)_1]_n$ (4b)**	
	without disorder model	with disorder model	without disorder model	with disorder model
R_{bragg}	0.7160	0.5962	2.2730	3.2948
R_p /%	1.304	1.298	3.882	4.323
R_{wp} /%	1.681	1.673	5.477	5.749
R_{exp} /%	1.575	1.575	2.995	2.995
GOF	1.067	1.062	1.829	1.920
R_p' /% [a]	40.719	40.641	10.365	11.591
R_{wp}' /% [a]	23.746	23.665	5.477	12.063
R_{exp}' /% [a]	22.252	22.278	6.274	6.283

Table S5. Results of the Rietveld refinements of $[MBr_2(4\text{-}CNpy)_1]_n$ (**1b, 3b, 5b**) in space group *Pmma* without using the disorder-model.

	$[MnBr_2(4\text{-}CNpy)_1]_n$ (1b)	**$[FeBr_2(4\text{-}CNpy)_1]_n$ (3b)**	**$[CoBr_2(4\text{-}CNpy)_1]_n$ (5b)**
R_{bragg}	1.649	1.853	2.473
R_p /%	2.108	3.882	1.727
R_{wp} /%	2.951	3.023	2.484
R_{exp} /%	1.443	1.665	1.407
GOF	2.044	1.815	1.765
R_p' /% [a]	22.087	39.659	24.165
R_{wp}' /% [a]	18.629	28.939	18.214
R_{exp}' /% [a]	9.112	15.943	10.318

Table S6. Restraints applied for the 4-CNpy fragment in the Rietveld refinements.

Type of bond angle	**Angle [°]**	**Type of bond length**	**Length [Å]**
C=C-H	120	N=C	1.34
C=C=C	120	C=C	1.38
C-C≡N	180	C≡N	1.14
N=C=C	120	C-H	0.99
N=C-H	120	C-C	1.44

Table S7. Measurement protocol of the high temperature series to prepare $[CoCl_2(4\text{-}CNpy)_1]_n$ (**4b**) and $[CoBr_2(4\text{-}CNpy)_1]_n$ (**5b**) on the X-ray powder diffractometer.

Elapsed time [min]	Step No.	Mode	Target temperature [°C]	Holding time before next step or measurement [min]	Measurement No.
00:00	1	Ramp	40.0	0	
00:01	2	Ramp	90.0	0	
00:12	3	Hold	90.0	10	
00:13	4	Ramp	140.0	0	
00:23	5	Hold	140.0	10	
00:24	6	Ramp	190.0	0	
00:35	7	Hold	190.0	10	
00:36	8	Ramp	240.0	0	
00:47	9	Hold	240.0	10	
00:47	10	Ramp	250.0	0	
02:58	11	Hold	250.0	10	1
05:09	12	Hold	250.0	10	2

Table S8. Measurement protocol of the temperature series to monitor the phase transition of **β-1a** to **γ-1a** on the powder diffractometer.

Elapsed time [min]	Step No.	Mode	Target temperature [°C]	Holding time before next step or measurement [min]	Measurement No.
00:00	1	Ramp	20.0	0	
01:38	2	Hold	20.0	0	1
01:36	3	Ramp	22.0	0	
03:12	4	Hold	22.0	0	2
03:09	5	Ramp	24.0	0	
04:45	6	Hold	24.0	0	3
04:43	7	Ramp	26.0	0	
06:19	8	Hold	26.0	0	4
06:16	9	Ramp	28.0	0	
07:53	10	Hold	28.0	0	5
07:50	11	Ramp	30.0	0	
09:26	12	Hold	30.0	0	6
09:24	13	Ramp	32.0	0	
11:00	14	Hold	32.0	0	7
10:57	15	Ramp	30.0	0	
12:34	16	Hold	30.0	0	8
12:31	17	Ramp	28.0	0	
14:08	18	Hold	28.0	0	9
14:05	19	Ramp	26.0	0	
15:42	20	Hold	26.0	0	10
15:39	21	Ramp	24.0	0	
17:16	22	Hold	24.0	0	11
17:13	23	Ramp	22.0	0	
18:50	24	Hold	22.0	0	12
18:47	25	Ramp	20.0	0	
20:23	26	Hold	20.0	0	13

Text S1

Details on syntheses of $[MX_2(4\text{-CNpy})_2]_{(n)}$ (1a-5a, 6, 7)

Synthesis of $[MnBr_2(4\text{-CNpy})_2]_n$ (1a). $MnBr_2$ (1.0 g, 4.66 mmol) was dissolved in 15 mL ethanol, 4-CNpy (0.97 g, 9.32 mmol) was dissolved in 35 mL ethanol. No precipitate formed after having mixed the solutions. The mixture was place in a fridge (8 °C), where a light pink powder formed within three days. IR -C≡N: 2242 cm^{-1}.

Synthesis of $[FeCl_2(4\text{-CNpy})_2]_n$ (2a). $FeCl_2 \cdot 6\ H_2O$ (0.5 g, 3.944 mmol) was dissolved in 70 mL ethanol, 4-CNpy (1.64 g, 15.77 mmol) was dissolved in 80 mL ethanol. By mixing both solutions, an orange precipitate formed. IR -C≡N: 2243 cm^{-1}.

Synthesis of $[FeBr_2(4\text{-CNpy})_2]_n$ (3a). $FeBr_2 \cdot x\ H_2O$ (0.45 g, 4.2 mmol) was dissolved in 70 mL ethanol, 4-CNpy (0.91 g, 8.72 mmol) was dissolved in 80 mL methanol. No precipitate formed after having mixed the solutions. The mixture was place in a fridge (8 °C), where a dark orange powder formed within two days. IR -C≡N: 2243 cm^{-1}.

Synthesis of $[CoCl_2(4\text{-CNpy})_2]_n$ (4a). $CoCl_2 \cdot 6\ H_2O$ (1.0 g, 4.21 mmol) was dissolved in 10 mL methanol, 4-CNpy (0.44 g, 4.4 mmol) was dissolved in 10 mL methanol. By mixing both solutions, a lilac precipitate formed. IR -C≡N: 2241 cm^{-1}.

Synthesis of $[CoBr_2(4\text{-CNpy})_2]_n$ (5a). $CoBr_2$ (0,53 g, 2,4 mmol) was dissolved in 8 mL ethanol, 4-CNpy (0.55 g, 5.3 mmol) was dissolved in 5 mL ethanol. No precipitate formed after having mixed the solutions. The mixture was heated to 70°C and a violet powder was obtained within one minute. IR -C≡N: 2247 cm^{-1}.

Synthesis of $[CuBr_2(4\text{-CNpy})_2]_n$ (6). $CuBr_2$ (0.5 g, 2.23 mmol) was dissolved in 40 mL methanol, 4-CNpy (0.93 g, 8.92 mmol) was dissolved in 20 mL methanol. By mixing both solutions, an neon green precipitate formed. IR -C≡N: 2243 cm^{-1}.

Synthesis of $[ZnBr_2(4\text{-CNpy})_2]$ (α-7/ β-7). $ZnBr_2$ (0.46 g, 2.22 mmol) was dissolved in 40 mL ethanol, 4-CNpy (0.49 g, 4.66 mmol) was dissolved in 20 mL ethanol. The solutions were mixed and colorless precipitate formed with two minutes. IR -C≡N: 2243 cm^{-1}.

Text S2

Details on preparation of $[MX_2(4\text{-CNpy})_1]_n$

Preparation of $[MnBr_2(4\text{-CNpy})_1]_n$ (1b). 1b was prepared by thermal decomposition of $[MnBr_2(4\text{-CNpy})_2]_n$ (**1a**) at 230 °C in the DTA-TG device. A greyish powder was obtained. IR -C≡N: 2242 cm^{-1} but should be around 2280 cm^{-1}. $[MnBr_2(4\text{-CNpy})_1]_n$ easily reacts with water and oxygen and, unfortunately, IR data may be incorrect.

Preparation of $[FeCl_2(4\text{-CNpy})_1]_n$ (2b). 2b was prepared by thermal decomposition of $[FeCl_2(4\text{-CNpy})_2]_n$ (**2a**) at 220 °C in the DTA-TG device. A yellow powder was obtained. IR -C≡N: 2276 cm^{-1}.

Preparation of $[FeBr_2(4\text{-CNpy})_1]_n$ (3b). 3b was prepared by thermal decomposition of $[FeBr_2(4\text{-CNpy})_2]_n$ (**3a**) at 260 °C in the DTA-TG device. A dark red powder was obtained. IR -C≡N: 2284 cm^{-1}.

Preparation of $[CoCl_2(4\text{-CNpy})_1]_n$ (4b). 4b was prepared by thermal decomposition of $[CoCl_2(4\text{-CNpy})_2]_n$ (**4a**) at 250 °C on the x-ray powder diffractometer. No IR spectrum was measured, because the sample always was obtained *in-situ*.

Preparation of $[CoBr_2(4\text{-CNpy})_1]_n$ (5b). 5b was prepared by thermal decomposition of $[CoCl_2(4\text{-CNpy})_1]_n$ (**5a**) at 250 °C on the x-ray powder diffractometer. No IR spectrum was measured, because the sample was obtained *in-situ*.

Text S3

Further details on structure solution and Rietveld refinements.

$[MnBr_2(4\text{-CNpy})_2]_n$ (β-1a). The first 20 peaks were selected for indexing in DASH which resulted in a monoclinic unit cell with $Z = 2$. Structure solution was then carried out using simulated annealing with DASH. A starting molecular model was derived from the known crystal structure of $[MnBr_2(4\text{-CNpy})_2]_n$. The molecular fragment was restricted to rotate around the Mn atom. The Mn atom was placed on the origin, the bromine atom was fixed on $(x,z,{}^1/_2)$, 4-CNpy was fixed on (x,y,0).

$[MnBr_2(4\text{-CNpy})_2]_n$ (γ-1a). The first 20 peaks were selected for indexing in DASH which resulted in an orthorhombic unit cell with $Z = 2$. Structure solution was then carried out using simulated annealing with DASH. A starting molecular model was

derived from the known crystal structure of β-$[MnBr_2(4\text{-}CNpy)_2]_n$. The molecular fragment was restricted to rotate around the Mn atom, Mn atom and 4-cyanopyridine were fixed on a special position (0,0,0) during the simulated annealing.

$[MnBr_2(4\text{-}CNpy)_1]_n$ (1b). The structure is isotypic to $[NiBr_2(4\text{-}CNpy)_1]_n$. A Pawley fit was performed in TOPAS using the lattice parameters of $[NiBr_2(4\text{-}CNpy)_1]_n$ as starting values. First, background and instrumental parameters (zero point, axial divergence) were refined. Next, size and strain parameters were refined. Structure solution was then carried out with the simulated annealing algorithm of DASH using a starting molecular model derived from $[NiBr_2(4\text{-}CNpy)_1]_n$. The molecular fragment was restricted to rotate around the Mn atom, Mn atom and 4-cyanopyridine were fixed on a special position (0,0,0) during the simulated annealing. The Rietveld refinement was carried out with TOPAS. The Mn atom was placed on the origin, the bromine atom was fixed on $(x,-^1/_2,z)$, the 4-cyanopyridine was fixed on (x,0,z).

$[FeCl_2(4\text{-}CNpy)_2]_n$ (2a). The first 20 peaks were selected for indexing in CONOGRAPH which resulted in a monoclinic unit cell with $Z = 2$. First, background and instrumental parameters (zero point, axial divergence) were refined. Next, size and strain parameters were refined. Structure solution was then carried out using simulated annealing in DASH. The molecular fragment ($FeCl_2(4cypy)_1$) was restricted to rotate around the Fe atom on special position (0,0,0). Rietveld refinement was carried out with TOPAS.

$[FeCl_2(4\text{-}CNpy)_1]_n$ (2b). $[FeCl_2(4\text{-}CNpy)_1]_n$ is isotypic to $[NiCl_2(4\text{-}CNpy)_1]_n$. At first, a Pawley fit was performed in TOPAS refining background and instrumental parameters (zero point, axial divergence). Next, size and strain parameters were refined. The crystal structure of $[NiCl_2(4\text{-}CNpy)_1]_n$ was used as starting point for the subsequent structure refinement. The Rietveld refinement was carried out with TOPAS.

$[FeBr_2(4\text{-}CNpy)_2]_n$ (3a). The first 20 peaks were selected for indexing in CONOGRAPH and DASH, which both resulted in a orthorhombic unit cell with $Z = 2$. Structure solution was then carried out using simulated annealing with DASH. A starting molecular model was derived from the known crystal structure of $[NiBr_2(4\text{-}CNpy)_2]_n$. The Fe atom was placed on the origin, the bromine atom was fixed on $(x,z,^1/_2)$, the 4-cyanopyridine was restrained flat in the mirror plane. The Rietveld refinement was carried out with TOPAS.

[$FeBr_2(4\text{-}CNpy)_1]_n$ (3b). The structure is isotypic to [$NiBr_2(4\text{-}CNpy)_1]_n$ and [$MnBr_2(4\text{-}CNpy)_1]_n$. A Pawley fit was performed in TOPAS (Coelho, 2018) using the lattice paramters of [$MnBr_2(4\text{-}CNpy)_1]_n$ as starting values. First, background and instrumental parameters (zero point, axial divergence) were refined. Next, size and strain parameters were refined. Structure solution was then carried out with the simulated annealing algorithm of DASH using a starting molecular model derived from [$NiBr_2(4\text{-}CNpy)_1]_n$. The molecular fragment was restricted to rotate around the Fe-atom. The Fe atom was placed on the origin, the bromine atom was fixed on (x,-1/2,z), the 4-cyanopyridine was fixed on (x,0,z). The Rietveld refinement was carried out with TOPAS.

[$CoCl_2(4\text{-}CNpy)_2]_n$ (4a). The structure of [$CoCl_2(4\text{-}CNpy)_2]_n$ was determined from single crystal data (UTIHIP) by Chen et. al in 2011. A Pawley fit was performed in TOPAS using these lattice parameters as starting values. First, background and instrumental parameters (zero point, axial divergence) were refined. Next, size and strain parameters were refined. Structure solution was then carried out with the simulated annealing algorithm of DASH using one Co and one Cl atom, and one 4-CNpy ring as fragments. The Co atom was placed on special position (0,0,0). Rietveld refinement was carried out with TOPAS (Coelho, 2018).

[$CoCl_2(4\text{-}CNpy)_1]_n$ (4b). The compound is isotypic to [$NiCl_2(4\text{-}CNpy)_1]_n$ and [$FeCl_2(4\text{-}CNpy)_1]_n$. A Pawley fit was performed in TOPAS (Coelho, 2018) using the lattice parameters of the isotypic Ni-compound. First background and instrumental parameters (zero point, axial divergence) were refined. Next, size and strain parameters were refined. Structure solution was then carried out with the simulated annealing algorithm of DASH using one Co atom, two Cl atoms and one 4-CNpy ring as fragments. The Co atom was placed on special position (0,0,0), the pyridine ring was placed on (x,0,z) and the Cl atoms were placed on (x,1/2,z). Rietveld refinement was carried out with TOPAS.

[$CoBr_2(4\text{-}CNpy)_1]_n$ (5b). The structure is isotypic to [$MnBr_2(4\text{-}CNpy)_1]_n$, [$FeBr_2(4\text{-}CNpy)_1]_n$ and [$NiBr_2(4\text{-}CNpy)_1]_n$. A Pawley fit was performed in TOPAS (Coelho, 2018) using the lattice parameters of [$NiBr_2(4\text{-}CNpy)_1]_n$ as starting values. First, background and instrumental parameters (zero point, axial divergence) were refined. Next, size and strain parameters were refined. Structure solution was then carried out with the simulated annealing algorithm of DASH using one Co atom, two

Br atoms and one 4-CNpy as fragments. The Co atom was placed on the origin, the bromine atom was fixed on (x,-1/2,z), the 4-cyanopyridine was fixed on (x,0,z).

$[CuBr_2(4\text{-}CNpy)_2]_n$ (6). At first, a Pawley fit was performed in TOPAS to refine background and instrumental parameters (zero point, axial divergence). Next, size and strain parameters were refined. The crystal structure of $[CuCl_2(4\text{-}CNpy)_2]_n$ was used as starting point for the subsequent structure refinement. Rietveld refinement was carried out with TOPAS.

$[ZnBr_2(4\text{-}CNpy)_2]_n$ (α-7). The first 20 peaks were selected for indexing in CONOGRAPH and DASH which resulted unanimously in a monoclinic unit cell with Z = 8. First, background and instrumental parameters (zero point, axial divergence) were refined. Next, size and strain parameters were refined. Structure solution was then carried out using simulated annealing with DASH. A starting molecular model was derived from the crystal structure of $[ZnBr_2(4\text{-}CNpy)_2]$. The molecular fragment was restricted to rotate around the Zn atom during the simulated annealing procedure. Rietveld refinement was carried out with TOPAS.

$[ZnBr_2(4\text{-}CNpy)_2]_n$ (β-7). The first 20 peaks were selected for indexing in CONOGRAPH which resulted in a monoclinic unit cell with Z = 4. First, background and instrumental parameters (zero point, axial divergence) were refined. Next, size and strain parameters were refined. Structure solution was then carried out using simulated annealing with DASH. The starting molecular model for the β-phase was derived from the crystal structure of α-$[ZnBr_2(4\text{-}CNpy)_2]$. The molecular fragment was restricted to rotate around the Zn atom during simulated annealing. Rietveld refinement was carried out with TOPAS.

B Ergänzende Informationen

B1 [$ZnBr_2(3\text{-}CNpy)_2$]

Synthese

Zu einer ethanolischen Lösung von $ZnBr_2$ (0,5 g bzw. 2,22 mmol in 40 mL) wurde eine ethanolische Lösung von 3-Cyanopyridin (0,947 g bzw. 9,10 mmol, in 30 mL) gegeben. Das Reaktionsgemisch wurde kräftig gerührt und abgedeckt bei RT stehen gelassen. Nach ca. 10 min bildeten sich erste Kristalle in der Lösung. Der Niederschlag wurde abfiltriert und mit 10 mL Ethanol gewaschen.

Datensammlung

Die Röntgenpulverdaten wurden auf einem Stoe Stadi-P Diffraktometer mit monochromatischer Kupfer $K\alpha_1$-Strahlung und einem linearen ortsempfindlichen Detektor (linearer PSD) aufgenommen. Dazu wurde die Probe in eine Glaskapillare (d = 0,7 mm, Hilgenberg) gefüllt und in Transmissionsgeometrie vermessen. Die Daten wurden im Bereich von 4 bis 90° in 2θ und in Schritten von 0,2° gesammelt, wobei jeder Messpunkt 120 s lang bestrahlt wurde.

Rietveld-Verfeinerung

Die Rietveld-Verfeinerung wurde dem Programm TOPAS [9] durchgeführt. Die Startstruktur für Pawley- bzw. Rietveld-Fit wurde aus den Einkristalldaten von [$ZnBr_2(3\text{-}CNpy)_2$] abgeleitet (QAHZAC). In einem Pawley-Fit wurden zunächst nacheinander Untergrund, Nullpunkt, Instrumentalfunktion, Skalierungsfaktor, Gitterparameter, Peakform und Peakbreite angepasst. In der anschließenden Rietveld-Verfeinerung wurde die Planarität der beiden Pyridin-Fragmente über zwei unabhängige flatten-Befehle kontrolliert. Die Auslenkungsparameter B_{iso} wurden isotrop verfeinert, wobei alle Nicht-H-Atome über einen Parameter (bnonh) und alle H-Atome über einen zweiten Parameter (bh mit bh = bnonh · 1,2) verfeinert wurden. Im letzten Verfeinerungsschritt wurden alle Bindungslängen und Bindungswinkel des

Zn-Atoms (Zn1-N2, Br5-Ni2-N1, …) freigegeben. Die Ergebnisse der Rietveld-Verfeinerung sind in Tab. B1.3 aufgeführt, der Rietveld-Plot ist in Abb. B1.2 dargestellt.

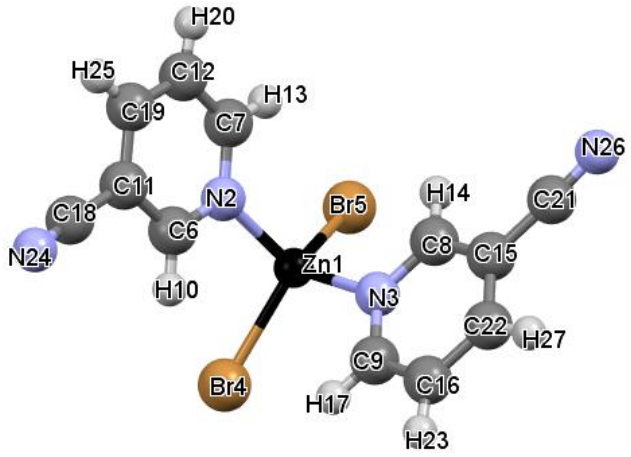

Abbildung B1.1: Startfragment $ZnBr_2(3\text{-}CNpy)_2$ für die Rietveld-Verfeinerung von $[ZnBr_2(3\text{-}CNpy)_2]$.

Tabelle B1.1: Elementarzelle von $[ZnBr_2(3\text{-}CNpy)_2]$: Startwerte des Pawley-Fits.

Verbindung	**$[ZnBr_2(3\text{-}CNpy)_2]$**
CSD Refcode	QAHZAC
Kristallsystem	orthorhombisch
Raumgruppe (Nr.)	*P bca* (61)
***a* /Å**	8,6148(8)
***b* /Å**	14,68087(16)
***c* /Å**	23,6121(2)
***α* /°**	90
***ß* /°**	90
***γ* /°**	90
***V* /Å³**	2986,30(5)
Z, Z'	8, 1
Lagesymmetrie von Zn	1

Tabelle B1.2: Übersicht der gesetzten Restraints auf Bindungslängen (links) und -winkel (rechts) mit Startwerten im Startfragment $ZnBr_2(3\text{-}CNpy)_2$.

Bindung zwischen …	Bindungslänge [Å]
Zn1-N2	2,06121
Zn1-N3	2,07204
Zn1-Br4	2,34712
Zn1-Br5	2,33698
N2-C6	1,33499
N2-C7	1,34712
N3-C8	1,33536
N3-C9	1,34631
C6-H10	0,99
C6-C11	1,39434
C7-C12	1,39203
C7-H13	0,99
C8-H14	0,99
C8-H15	1,39193
C9-C16	1,38578
C9-H17	0,99
C11-C18	1,44374
C11-C19	1,39427
C12-C19	1,37553
C12-H20	0,99
C15-C21	1,43515
C15-C22	1,38688
C16-C22	1,36767
C16-H23	0,99
C18-N24	1,14547
C19-H25	0,99
C21-N26	1,14859
C22-H27	0,99

Winkel zwischen …	Bindungswinkel [°]
C-C-C	120
C-C-H	120
$C\text{-}N_{py}\text{-}C$	120
$N_{Py}\text{-}C\text{-}H$	120
$C\text{-}C\text{-}N_{CN}$	180
$Zn\text{-}N_{py}\text{-}C$	120
N2-Zn1-N3	100,85526
N2-Zn1-Br4	105,62365
N2-Zn1-Br5	111,60011
N3-Zn1-Br4	105,81979
N3-Zn1-Br5	108,97234
Br4-Zn1-Br5	121,84016

Tabelle B1.3: Ergebnisse der Rietveld-Verfeinerung von $[ZnBr_2(3\text{-}CNpy)_2]$.

Verbindung	**$[ZnBr_2(3\text{-}CNpy)_2]$**
CSD Refcode	QAHZAC01
Summenformel	$C_{12}H_8Br_2N_4Zn$
Kristallsystem	orthorhombisch
Raumgruppe (Nr.)	*P bca* (61)
***a* /Å**	8,6148(8)
***b* /Å**	14,68087(16)
***c* /Å**	23,6121(2)
***α* /°**	90
***ß* /°**	90
***γ* /°**	90
***V* /Å³**	2986,30(5)
Z, Z'	8, 1
Lagesymmetrie von Zn	1
T /K	298
Strahlungsart	Cu $K\alpha_1$
Wellenlänge /Å	1,5406
$2\Theta_{min}$ /°	4
$2\Theta_{max}$ /°	90
***R_p* /%**	3,044
***R_{wp}* /%**	3,947
***R_{exp}* /%**	3,001
R_{Bragg}	1,809
GOF	1,315
***R_p'* /%** [a]	10,742
***R_{wp}'* /%** [a]	10,553
***R_{exp}'* /%** [a]	8,025

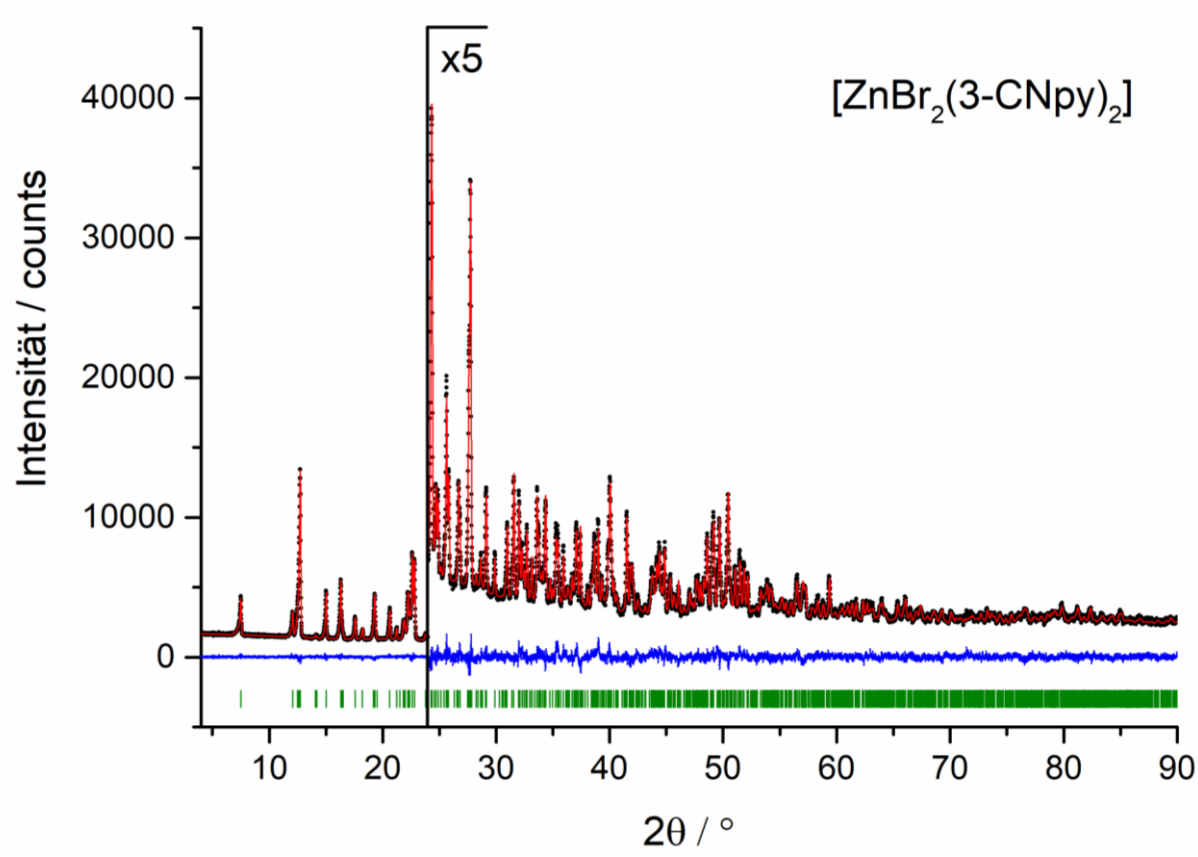

Abbildung B1.2: Rietveld-Plot zu $[ZnBr_2(3\text{-}CNpy)_2]$. Schwarze Punkte: gemessenes Pulverdiffraktogramm; rote Linie: simuliertes Pulverdiffraktogramm; blaue Linie: Differenzkurve; grüne Striche: erlaubte Reflexpositionen.

DTA-TG-Analyse

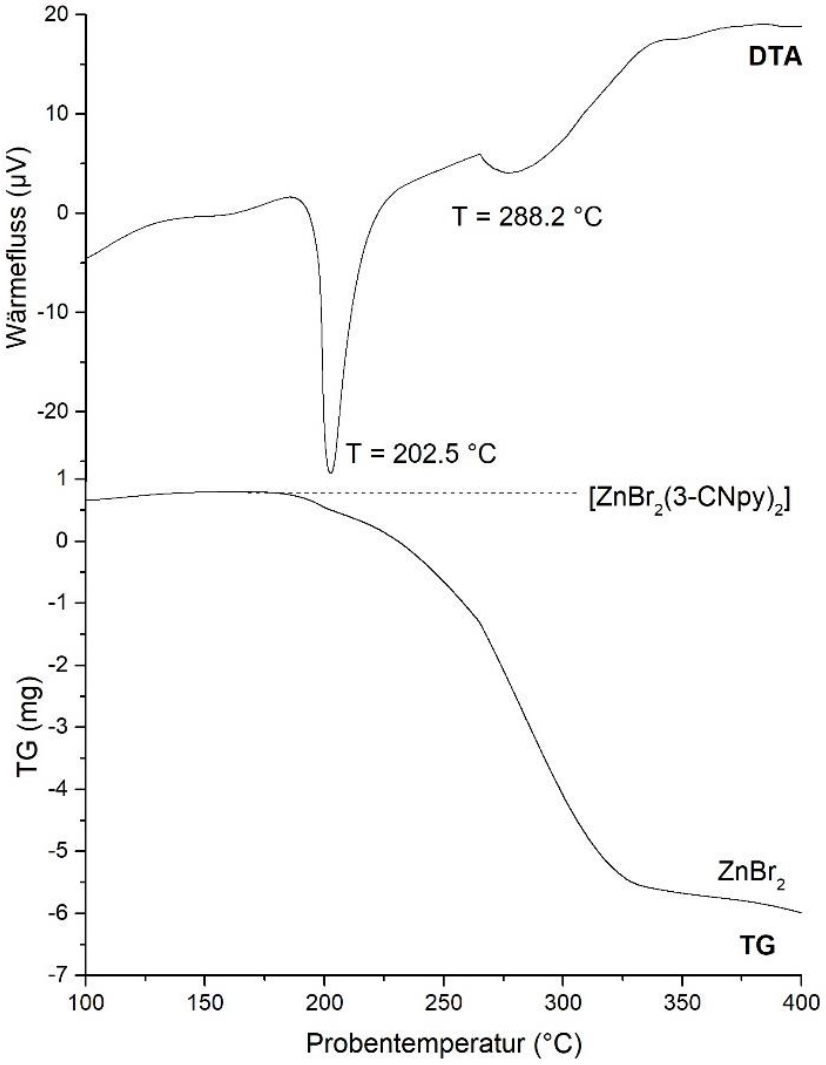

Abbildung B1.3: DTA-TG-Aufnahme von $[ZnBr_2(3\text{-}CNpy)_2]$. Heizrate: 5 K/min, Inertgas: Ar, Probenteller: Al_2O_3.

Tabelle B1.4: Ergebnisse der DTA-TG-Messung von $[ZnBr_2(3\text{-}CNpy)_2]$. T: DTA-Peaktemperatur, m_0: Einwaage der Startverbindung, Δm_{exp}: Masseverlust (absolut), $\Delta m_{exp}/m_0$: experimenteller Masseverlust (relativ), $\Delta m_{cal}/m_0$: theoretischer Masseverlust (relativ). * Leider blieb nach sämtlichen DTA-TG-Aufnahmen stets eine amorphe Substanz zurück, sodass nicht nachvollziehbar war, welche Stoffumwandlung zu diesem unerwartet geringen Masseverlust führte.

Verbindung	T [°C]	m_0 [mg]	Δm_{exp} [mg]	$\Delta m_{exp}/m_0$ [%]	$\Delta m_{cal}/m_0$ [%]
$[ZnBr_2(3\text{-}CNpy)_2]$		23,753	0	0	0
* $ZnBr_2$	202,5		6,62	* 28,00	* 51,96

B2 $[NiCl_2(3,5\text{-}CNpy)_2]_n$

Synthese

Zu einer methanolischen Lösung von $NiCl_2 \times 6\ H_2O$ (368 mg bzw. 1,55 mmol in 10 mL) wurde eine methanolische Lösung von 3,5-Dicyanopyridin (400 mg bzw. 3,10 mmol, in 40 mL) gegeben. Die Darstellung von 3,5-CNpy erfolgte nach [40]. Das Reaktionsgemisch wurde auf 100 °C erwärmt, bis das gesamte Lösemittel entfernt war. Es fiel sofort ein blass grüner, fein kristalliner Niederschlag an (Ausbeute: 581 mg bzw. 1,50 mmol). Dieser wurde solange mit Methanol gewaschen, bis die Waschflüssigkeit farblos blieb.

Datensammlung

Die Röntgenpulverdaten wurden auf einem Stoe Stadi-P Diffraktometer mit monochromatischer Kupfer $K\alpha_1$-Strahlung und einem linearen ortsempfindlichen Detektor (linearer PSD) aufgenommen. Dazu wurde die Probe zwischen zwei Polyacetat-Folien eingespannt und in Transmissionsgeometrie vermessen. Die Daten wurden im Bereich von 3 bis 82° in 2θ und in Schritten von 0,2° gesammelt, wobei jeder Messpunkt 150 s lang bestrahlt wurde.

Indizierung und Strukturlösung

Die Indizierung des Pulverdiffraktogramms erfolgte mit dem Programm DASH [10, 11, 12] bzw. dem darin implementierten Programm DICVOL91 [6]. Alle Indizierversuche führten zu einer reproduzierbaren monoklinen Elementarzelle, die gemäß den Hofmann' schen Volumeninkrementen [24] zwei Formeleinheiten (Z = 2) enthält.

Tabelle B2.1: Gewählte Elementarzelle für die Strukturlösung von $[NiCl_2(3,5\text{-}CNpy)_2]_n$ (inklusive Gütewerte dieses Indiziervorschlags aus DASH (M nach [16] und F nach [43]).

Verbindung	**$[NiCl_2(3,5\text{-}CNpy)_2]_n$**
Kristallsystem	monoklin
***a* /Å**	27,132(7)
***b* /Å**	7,631(3)
***c* /Å**	3,6311(11)
***α* /°**	90
***ß* /°**	91,81(7)
***γ* /°**	90
***V* /Å³**	751,46(3)
Z	2
M_{15}	24,5
F_{15}	23,3

Die Strukturlösung wurde ebenfalls mit DASH durchgeführt, das die *Simulated-Annealing*-Methode enthält. Nach Prüfung auf systematische Auslöschungen wurde eine Strukturlösung in der Raumgruppe $P\,2_1/n$ vorgenommen. Das Startfragment wurde aus der bereits bekannten Kristallstruktur von $[NiCl_2(4\text{-}CNpy)_2]_n$ (LATKOJ) abgeleitet. Da in $P\,2_1/n$ bei $Z = 2$ spezielle Lagen zu besetzen sind, wurde das Ni-Atom bei der Strukturlösung auf (0, 0, 0) fixiert und als Rotationsdrehpunkt festgelegt.

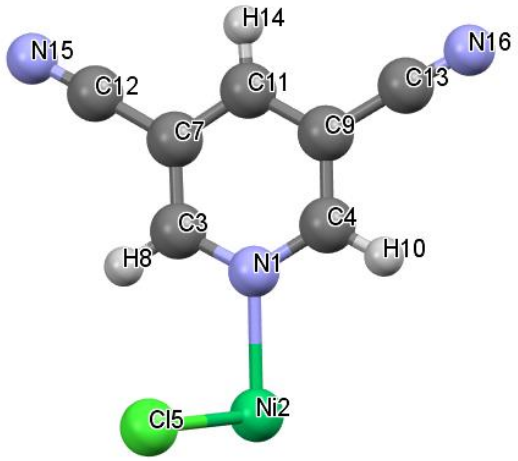

Abbildung B2.1: Startfragment $NiCl_1(3,5\text{-}CNpy)_1$ zur Strukturlösung von $[NiCl_2(3,5\text{-}CNpy)_2]_n$.

Tabelle B2.2: Übersicht der gesetzten Restraints auf Bindungslängen (links) und -winkel (rechts) mit Startwerten im Startfragment $NiCl_1(3,5\text{-}CNpy)_1$.

Bindung zwischen …	Bindungslänge [Å]
Ni2-Cl5	2,12
Ni2-N1	2,43
N1-C3	1,34
N1-C4	1,34
C3-C7	1,38
C3-H8	0,99
C4-C9	1,38
C4-H10	0,99
C7-C11	1,38
C7-C12	1,44
C9-C11	1,38
C9-C13	1,44
C12-N15	1,14
C13-N16	1,14

Winkel zwischen …	Bindungswinkel [°]
C-C-C	120
C-C-H	120
$C\text{-}N_{py}\text{-}C$	120
$N_{Py}\text{-}C\text{-}H$	120
$Cl\text{-}Ni\text{-}N_{py}$	90
$C\text{-}C\text{-}N_{CN}$	180

Rietveld-Verfeinerung

Die Rietveld-Verfeinerung wurde dem Programm TOPAS [9] durchgeführt. Zunächst wurde ein Pawley-Fit zur Anpassung von Untergrund, Nullpunkt, Instrumentalfunktion, Skalierungsfaktor, Gitterparameter, Peakform und Peakbreite durchgeführt. In der anschließenden Rietveld-Verfeinerung wurde die Planarität des Pyridin-Fragments über den flatten-Befehl kontrolliert. Die Auslenkungsparameter B_{iso} wurden isotrop verfeinert, wobei alle Nicht-H-Atome über einen Parameter (bnonh) und alle H-Atome über einen zweiten Parameter (bh mit bh = bnonh · 1,2) verfeinert wurden. Im letzten Verfeinerungsschritt wurden alle Bindungslängen und Bindungswinkel des Ni-Atoms (Ni2-N1, Cl5-Ni2-N1, …) freigegeben. Die Ergebnisse der Rietveld-Verfeinerung sind in Tab. B2.3 aufgeführt, der Rietveld-Plot ist in Abb. B2.2 dargestellt.

Tabelle B2.3: Ergebnisse der Rietveld-Verfeinerung von $[NiCl_2(3,5\text{-}CNpy)_2]_n$.

Verbindung	**$[NiCl_2(3,5\text{-}CNpy)_2]_n$**
CSD Refcode	DUQTIV
Summenformel	$C_{14}H_6Cl_2N_6Ni$
Kristallsystem	monoklin
Raumgruppe (Nr.)	*P* $2_1/n$ (14)
***a* /Å**	27,1288(4)
***b* /Å**	7,62666(15)
***c* /Å**	3,6101(2)
***α* /°**	90
***ß* /°**	91,389(7)
***γ* /°**	90
***V* /Å³**	746,72(5)
Z, Z'	2, ½
Lagesymmetrie von Ni	$\bar{1}$
T /K	298
Strahlungsart	Cu $K\alpha_1$
Wellenlänge /Å	1,5406
$2\Theta_{min}$ /°	3
$2\Theta_{max}$ /°	82
***R_p* /%**	2,205
***R_{wp}* /%**	3,153
***R_{exp}* /%**	2,657
R_{Bragg}	1,227
GOF	1,187
***R_p'* /%**	19,301
***R_{wp}'* /%**	16,438
***R_{exp}'* /%**	13,854

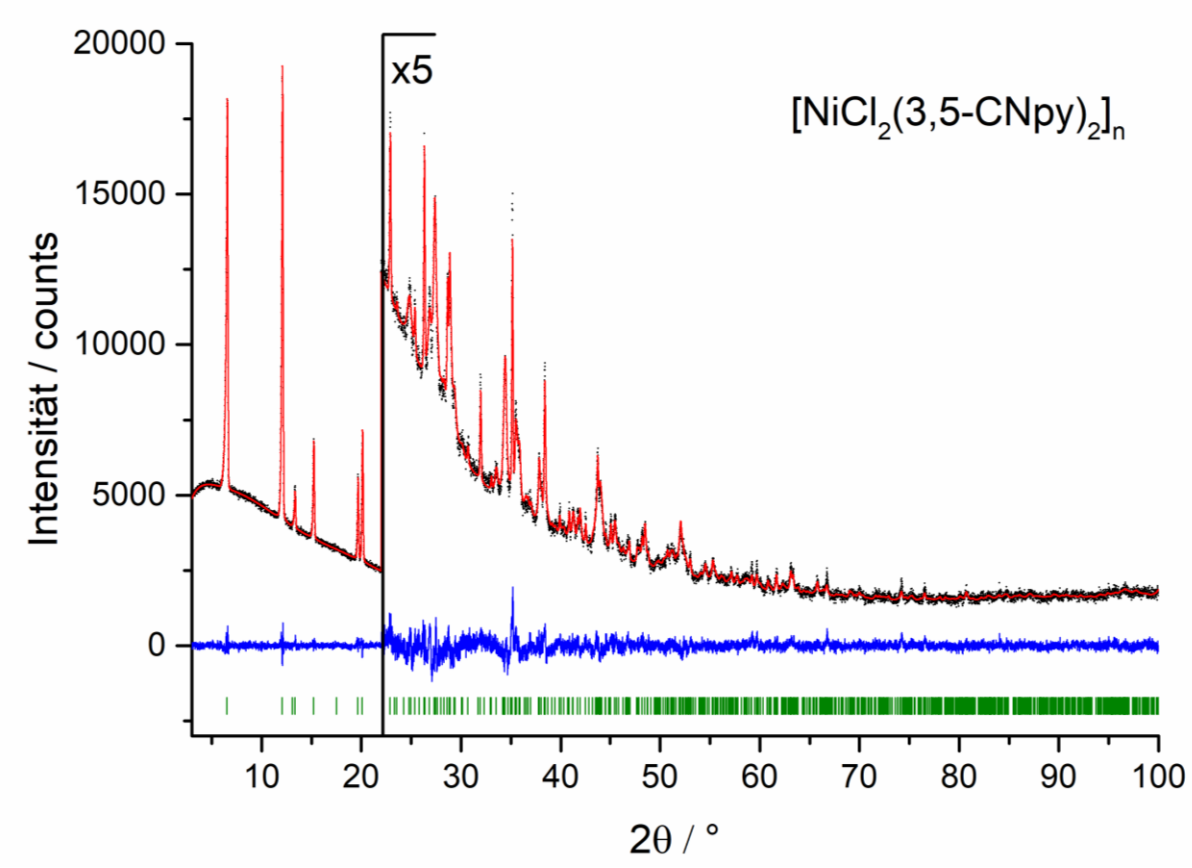

Abbildung B2.2: Rietveld-Plot zu $[NiCl_2(3,5\text{-}CNpy)_2]_n$. Schwarze Punkte: gemessenes Pulverdiffraktogramm; rote Linie: simuliertes Pulverdiffraktogramm; blaue Linie: Differenzkurve; grüne Striche: erlaubte Reflexpositionen.

IR-Aufnahmen

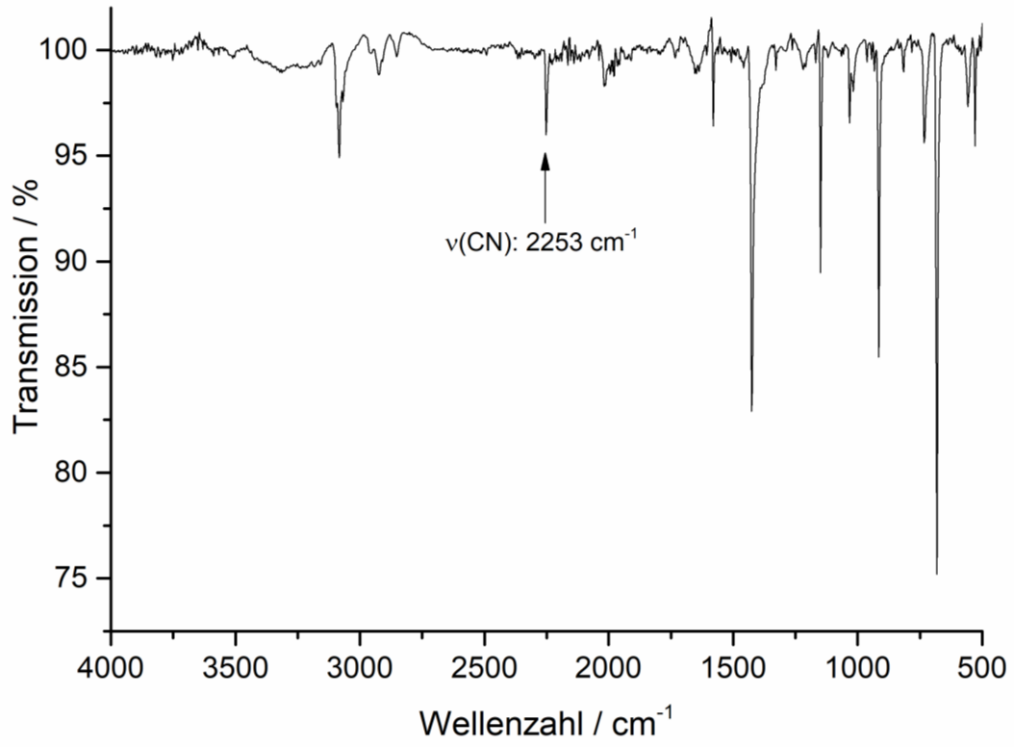

Abbildung B2.3: IR-Spektrum von $[NiCl_2(3,5\text{-}CNpy)_2]_n$.

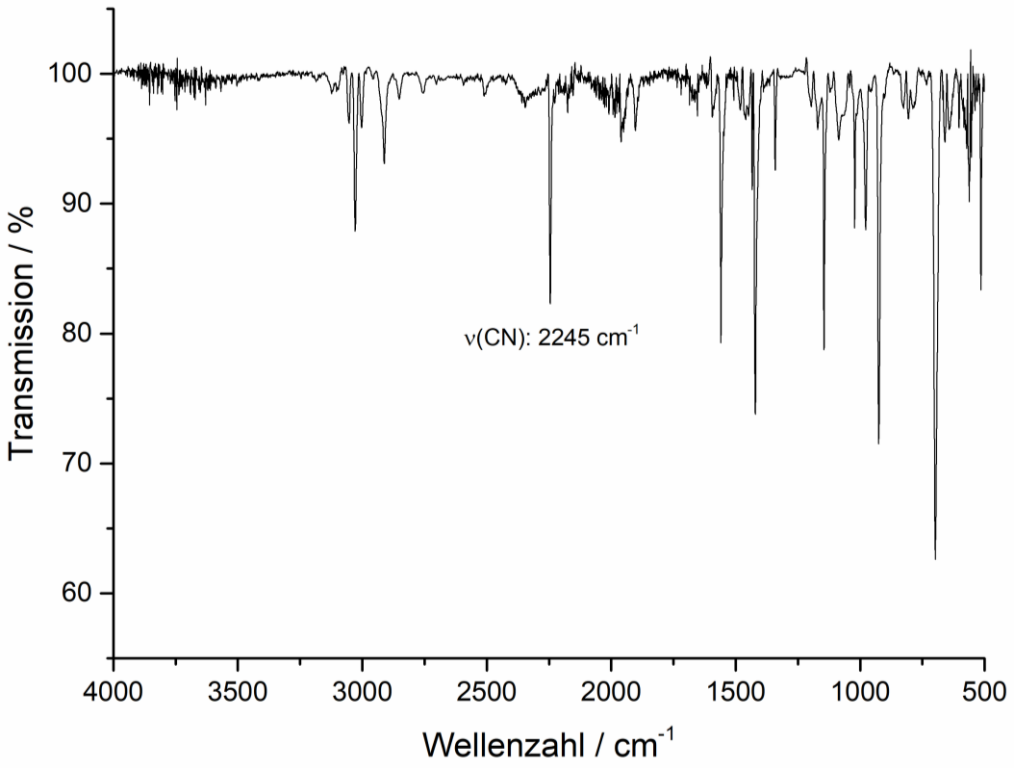

Abbildung B2.4: IR-Spektrum von 3,5-CNpy.

DTA-TG-Messung

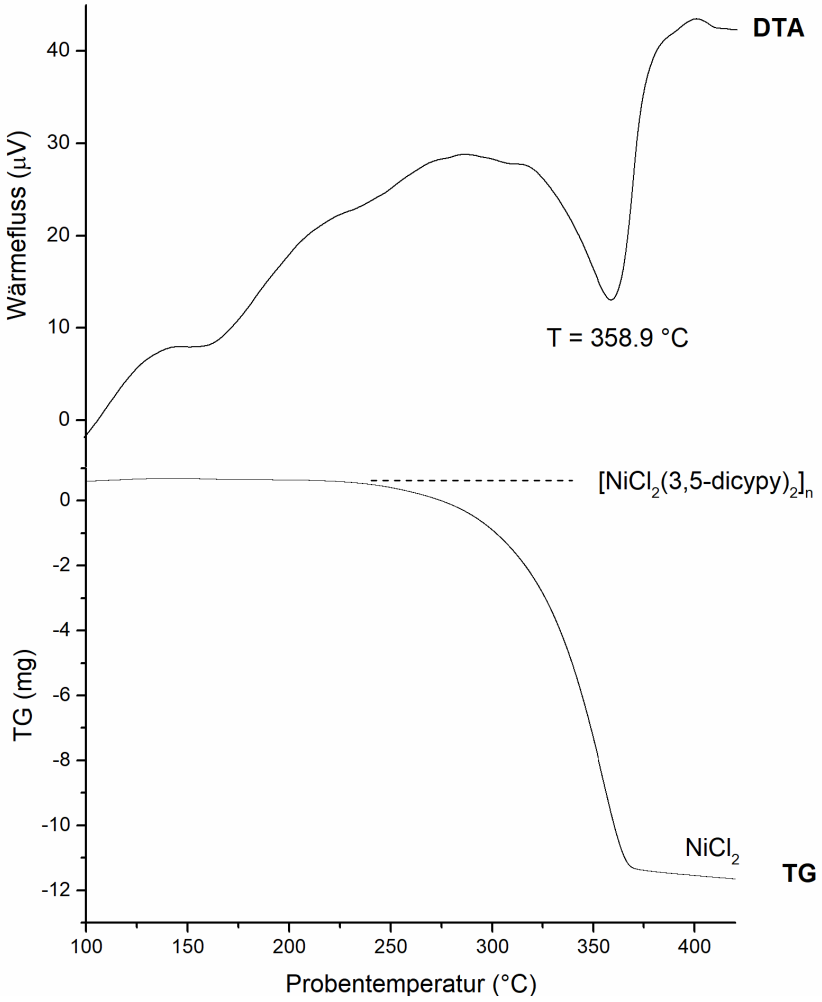

Abbildung B2.5: DTA-TG-Aufnahme von $[NiCl_2(3,5\text{-}CNpy)_2]_n$. Heizrate: 5 K/min, Inertgas: Ar, Probenteller: Al_2O_3.

Tabelle B2.4: Ergebnisse der DTA-TG-Messung von $[NiCl_2(3,5\text{-}CNpy)_2]_n$. T: DTA-Peaktemperatur, m_0: Einwaage der Startverbindung, Δm_{exp}: Masseverlust (absolut), $\Delta m_{exp}/m_0$: experimenteller Masseverlust (relativ), $\Delta m_{cal}/m_0$: theoretischer Masseverlust (relativ).

Verbindung	T [°C]	m_0 [mg]	Δm_{exp} [mg]	$\Delta m_{exp}/m_0$ [%]	$\Delta m_{cal}/m_0$ [%]
$[NiCl_2(3,5\text{-}CNpy)_2]_n$		21,31	0	0	0
$NiCl_2$	358,9		11,567	58,16	66,58

B3 β-$[CuBr_2(3\text{-}CNpy)_2]_n$

Synthese

Zu einer methanolischen Lösung von $CuBr_2$ (0,5 g bzw. 2,23 mmol in 40 mL) wurde eine methanolische Lösung von 3-Cyanopyridin (0,93 g bzw. 8,92 mmol, in 20 mL) gegeben. Es bildete sich sofort ein giftgrüner Niederschlag. Dieser wurde abfiltriert und solange mit Methanol gewaschen, bis die Waschflüssigkeit farblos blieb.

Datensammlung

Die Röntgenpulverdaten wurden auf einem Stoe Stadi-P Diffraktometer mit monochromatischer Kupfer $K\alpha_1$-Strahlung und einem linearen ortsempfindlichen Detektor (linearer PSD) aufgenommen. Dazu wurde die Probe zwischen zwei Polyacetat-Folien eingespannt und in Transmissionsgeometrie vermessen. Die Daten wurden im Bereich von 3 bis 80° in 2θ und in Schritten von 0,2° gesammelt, wobei jeder Messpunkt 120 s lang bestrahlt wurde.

Indizierung und Strukturlösung

Die Indizierung des Pulverdiffraktogramms erfolgte mit dem Programm DASH [10, 11, 12] bzw. dem darin implementierten Programm DICVOL91 [6]. Reflexe einer weiteren Phase (möglicherweise einer dritten Phase von $[CuBr_2(3\text{-}CNpy)_2]_n$) wurden dabei ignoriert. Alle Indizierversuche führten zu einer reproduzierbaren monoklinen Elementarzelle, die gemäß den Hofmann' schen Volumeninkrementen [24] zwei Formeleinheiten (Z = 2) enthält.

Die Strukturlösung wurde ebenfalls mit der *Simulated-Annealing*-Methode in DASH durchgeführt. Nach Prüfung auf systematische Auslöschungen wurde eine Strukturlösung in der Raumgruppe $P\,2_1/c$ vorgenommen. Das Startfragment wurde aus der bereits bekannten Kristallstruktur α-$[CuBr_2(3\text{-}CNpy)_2]_n$ abgeleitet (MAHVOH [30]). Mit Z = 2 sind in $P\,2_1/c$ spezielle Lagen zu besetzen. Daher wurde das Cu-Atom bei der Strukturlösung auf (0, 0, 0) fixiert und als Rotationsdrehpunkt festgelegt.

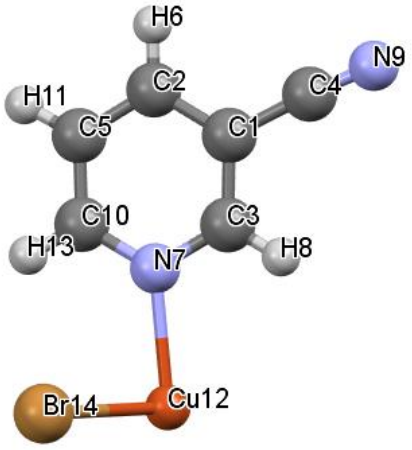

Abbildung B3.1: Startfragment $CuBr_1(3\text{-}CNpy)_1$ zur Strukturlösung von β-$[CuBr_2(3\text{-}CNpy)_2]_n$.

Tabelle B3.1: Gewählte Elementarzelle für die Strukturlösung von β-$[CuBr_2(3\text{-}CNpy)_2]_n$ (inklusive Gütewerte dieses Indiziervorschlags aus DASH (M nach [16] und F nach [43]).

Verbindung	**β-$[CuBr_2(3\text{-}CNpy)_2]_n$**
Kristallsystem	monoklin
***a* /Å**	3,932(2)
***b* /Å**	7,188(4)
***c* /Å**	26,141(18)
***α* /°**	90
***ß* /°**	92,54(11)
***γ* /°**	90
***V* /Å³**	737,12(3)
Z	2
M_{16}	21,2
F_{16}	31,3

Rietveld-Verfeinerung

Die Rietveld-Verfeinerung wurde dem Programm TOPAS [9] durchgeführt. Bereiche mit Reflexen einer Fremdphase mussten über den exclude-Befehl von der Verfeinerung (9-9,6°, 13-13,3°, 18,8-19,1° und 23,0-23,5° in 2θ) ausgenommen werden, da es nicht gelang eine reproduzierbare Indizierung zu finden, auf deren Grundlage eine PONKCS-Phase hätte beschrieben werden können. Zunächst wurde ein Pawley-Fit zur Anpassung von Untergrund, Nullpunkt, Instrumentalfunktion,

Skalierungsfaktor, Gitterparameter, Peakform und Peakbreite durchgeführt. In der anschließenden Rietveld-Verfeinerung wurde die Planarität des Pyridin-Fragments über den flatten-Befehl kontrolliert. Die Auslenkungsparameter B_{iso} wurden isotrop verfeinert, wobei alle Nicht-H-Atome über einen Parameter (bnonh) und alle H-Atome über einen zweiten Parameter (bh mit: bh = bnonh · 1,2) verfeinert wurden. Im letzten Verfeinerungsschritt wurden alle Restraints auf Bindungslängen und -winkel des Cu-Atoms (Cu12-N7, Br14-Cu12-N7, …) entfernt, um eine unverfälschte Verzerrung des Koordinationsoktaeders zu erhalten. Die Ergebnisse der Rietveld-Verfeinerung sind in Tab. B3.3 aufgeführt, der Rietveld-Plot ist in Abb. B3.2 dargestellt.

Tabelle B3.2: Übersicht der gesetzten Restraints auf Bindungslängen (links) und -winkel (rechts) mit Startwerten im Startfragment $CuBr_2(3\text{-}CNpy)_1$.

Bindung zwischen …	**Bindungslänge [Å]**
Cu12-Br14	2,42
Cu12-N7	2,01
C1-C2	1,38
C1-C3	1,38
C1-C4	1,44
C2-C5	1,38
C2-H8	0,99
C3-N7	1,34
C3-H8	0,99
C4-N9	1,14
C5-C2	1,38
C5-H11	0,99
N7-C10	1,34
C10-H13	0,99

Winkel zwischen …	**Bindungswinkel [°]**
C-C-C	120
C-C-H	120
$C\text{-}N_{py}\text{-}C$	120
$N_{Py}\text{-}C\text{-}H$	120
$Br\text{-}Cu\text{-}N_{py}$	90
$C\text{-}C\text{-}N_{CN}$	180

Tabelle B3.3: Ergebnisse der Rietveld-Verfeinerung von β-$[CuBr_2(3\text{-}CNpy)_2]_n$. Hinweis: Diese Kristallstruktur wurde in der Standardaufstellung $P2_1/c$ in die CSD eingepflegt und in Kap. 4.7 zwecks besserer Vergleichbarkeit mit den anderen Strukturen in $P2_1/n$ diskutiert.

	β-$[CuBr_2(3\text{-}CNpy)_2]_n$
Refcode	DUNVIU
Summenformel	$C_{12}H_8Br_2CuN_4$
Kristallsystem	monoklin
Raumgruppe (Nr.)	$P2_1/c$ (14)
***a* /Å**	3,93786(8)
***b* /Å**	7,21068(16)
***c* /Å**	26,2265(7)
***α* /°**	90
***ß* /°**	92,249(2)
***γ* /°**	90
***V* /Å^3**	744,12(3)
Z, Z'	2, ½
Lagesymmetrie von Cu	$\bar{1}$
T /K	298
Strahlungsart	Cu $K\alpha_1$
Wellenlänge /Å	1,5406
$2\Theta_{min}$ /°	3
$2\Theta_{max}$ /°	82
***R_p* /%**	3,111
***R_{wp}* /%**	4,231
***R_{exp}* /%**	2,656
R_{Bragg}	1,718
GOF	1,593
***R_p'* /%**	8,328
***R_{wp}'* /%**	9,502
***R_{exp}'* /%**	5,965

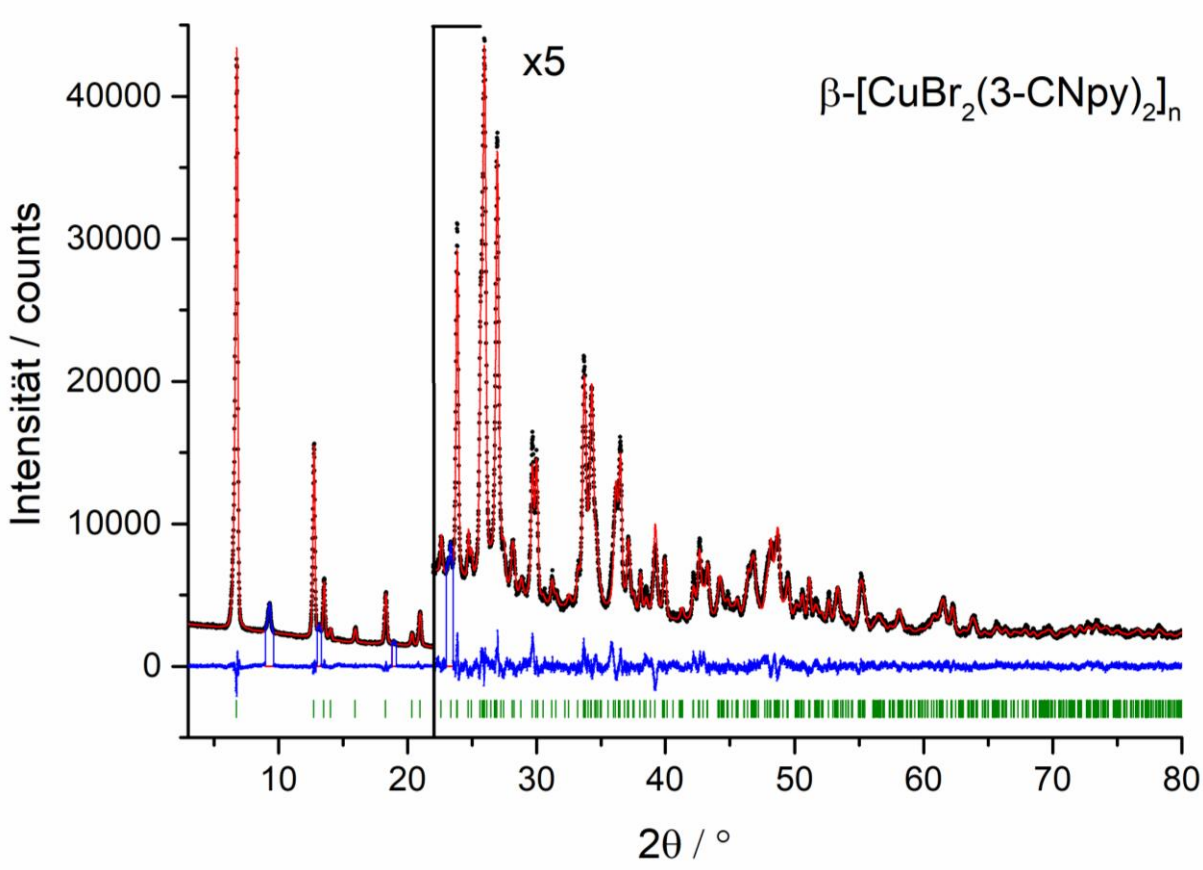

Abbildung B3.2: Rietveld-Plot zu β-$[CuBr_2(3\text{-}CNpy)_2]_n$. Schwarze Punkte: gemessenes Pulverdiffraktogramm; rote Linie: simuliertes Pulverdiffraktogramm; blaue Linie: Differenzkurve; grüne Striche: erlaubte Reflexpositionen.

IR-Aufnahme

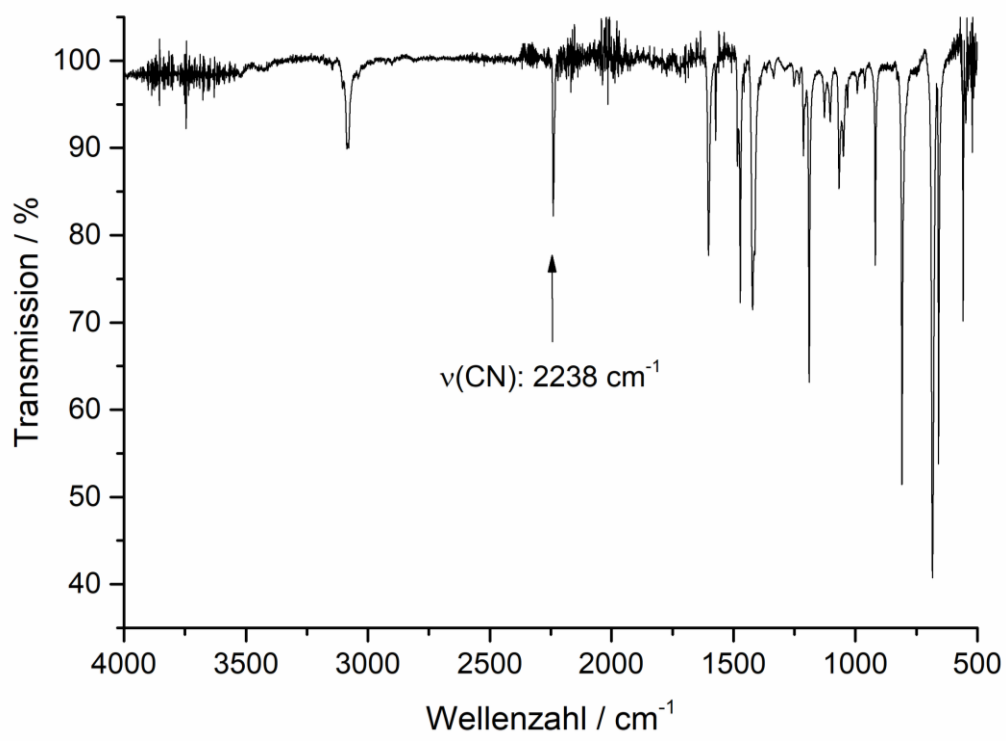

Abbildung B3.3: IR-Spektrum von β-$[CuBr_2(3\text{-}CNpy)_2]_n$.

DTA-TG-Analyse

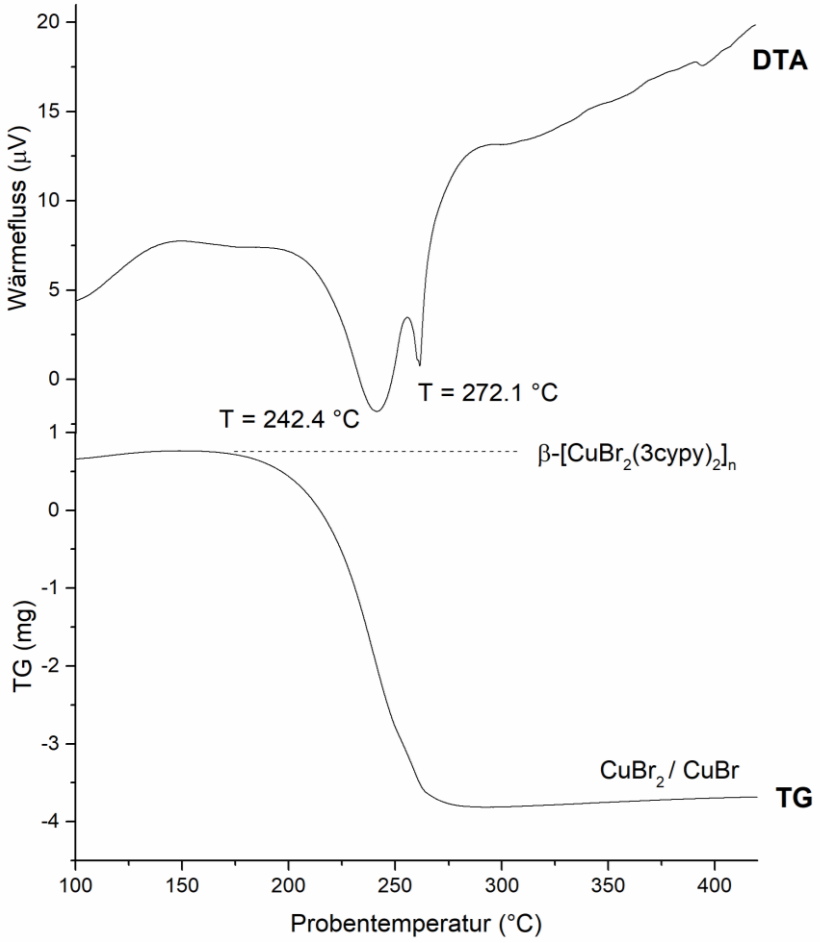

Abbildung B3.4: DTA-TG-Aufnahme von β-$[CuBr_2(3\text{-}CNpy)_2]_n$. $CuBr_2$ wird bei der Messung ab ca. 270 °C teilweise zu CuBr reduziert. Heizrate: 5K/min, Inertgas: Ar, Probenteller: Al_2O_3.

Tabelle B3.4: Ergebnisse der DTA-TG-Messung von β-$[CuBr_2(3\text{-}CNpy)_2]_n$. T: DTA-Peaktemperatur, m_0: Einwaage der Startverbindung, Δm_{exp}: Masseverlust (absolut), $\Delta m_{exp}/m_0$: experimenteller Masseverlust (relativ), $\Delta m_{cal}/m_0$: theoretischer Masseverlust (relativ). * $CuBr_2$ wird bei der Messung teilweise zu CuBr reduziert.

Verbindung	**T [°C]**	**m_0 [mg]**	**Δm_{exp} [mg]**	**$\Delta m_{exp}/m_0$ [%]**	**$\Delta m_{cal}/m_0$ [%]**
β-$[CuBr_2(3\text{-}CNpy)_2]_n$		7,521	0	0	0
$CuBr_2$ (* CuBr)	242,4 272,1		4,566	60,07	51,75

C Lebenslauf

D Darstellung des Eigenanteils an MH1-4

Experimente und Ergebnisse

Zur Charakterisierung meiner Proben dienten im Wesentlichen IR-Spektroskopie, DTA-TG, DSC und (temperaturabhängige) XRPD bzw. im weiteren Verlauf die Röntgenstrukturanalyse. Mit Ausnahme der DTA-TG- und DSC-Aufnahmen habe ich die übrigen Messungen eigenständig durchgeführt und ausgewertet. Über die finalen Ergebnisse der Kristallstrukturbestimmungen habe ich mich mit Prof. Schmidt und Dr. Fink ausgetauscht.

Anfertigung der Publikationen

Die Manuskripte der Publikationen MH2, MH3 und MH4 habe ich selbst aufgesetzt. Für Publikation MH1 habe ich sämtliche Textpassagen, Tabellen und Abbildungen zu meinen dort diskutierten Kristallstrukturen (d.h. $[NiBr_2(4cypy)_2]_n$ und $[NiBr_2(4cypy)_1]_n$) erstellt. Anschließend wurden die Manuskripte Prof. Schmidt bzw. Dr. Fink vorgelegt und überarbeitet. Der Eigenanteil verteilt sich etwa wie folgt:

Publikation	Titel und Autoren	Anzahl neu bestimmter Kristallstrukturen	geschätzter Eigenanteil
MH1	*4-Cyanopyridine, a versatile mono- and bidentate ligand. Crystal structures of related coordination polymers determined by X-ray powder diffraction.* H. Zhao, A. Bodach, M. Heine, Y. Krysiak, J. Glinnemann, E. Alig, L. Fink, M. U. Schmidt	8 (2 von mir)	10%
MH2	*3-Cyanopyridine as a bridging and terminal ligand in coordination polymers.* M. Heine, L. Fink, M. U. Schmidt	14 (alle von mir)	80-90%
MH3	*Coordination compounds built up from $M^{II}Cl_2$ and 3-cyanopyridine: double chains, single chains and isolated complexes.* M. Heine, L. Fink, M. U. Schmidt	11 (alle von mir)	80-90%
MH4	*4-Cyanopyridine complexes $[MX_2(4\text{-}CNpy)_x]_n$ (with X = Cl, Br and x = 1, 2): crystal structures, thermal properties and a comparison with $[MX_2(3\text{-}CNpy)_x]_n$ complexes.* M. Heine, L. Fink, M. U. Schmidt	13 (alle von mir)	80-90%

E Posterbeiträge

1 *Syntheses and crystal structures of transition-metal bromide complexes with pyridine-type ligands: $[MBr_2(3\text{-cypy})_4]$ and $[MBr_2(3\text{-cypy})_2]_n$.*

Miriam Heine, Lothar Fink, Martin U. Schmidt (2016)
European Crystallographic Meeting (ECM-30), Basel, Schweiz

2 *Crystal structure determination of $[NiBr_2(4\text{-cypy})_2]_n$ and $[NiBr_2(4\text{-cypy})_1]_n$ by X-ray powder diffraction.*

Miriam Heine, Lothar Fink, Martin U. Schmidt (2017)
Jahrestagung der Deutschen Gesellschaft für Kristallographie (DGK-25), Karlsruhe, Deutschland

3 *Crystal structures of transition-metal halide complexes with cyanopyridine ligands: single chains, double chains, and networks.*

Miriam Heine, Lothar Fink, Martin U. Schmidt (2019)
European Crystallographic Meeting (ECM-31), Wien, Österreich

F Akademische Lehrer

Chemie

Anorganische Chemie:

Dr. L. Fink, Dr. J. Glinnemann, Prof. Dr. M. Wagner

Organische Chemie:

Prof. Dr. E. Egert, Prof. Dr. J. Engels, Prof. Dr. M. Göbel, Prof. Dr. H. Schwalbe

Physikalische Chemie:

Dr. M. Braun, Prof. Dr. B. Brutschy, Prof. Dr. T. Prisner, Prof. Dr. J. Wachtveitl

Didaktik der Chemie:

Prof. Dr. H. J. Bader, Dr. B. Drechsler-Köhler, Prof. Dr. A. Lühken

Französisch

Sprachwissenschaften:

Prof. Dr. J. Erfurt

Literaturwissenschaften:

Dr. F. Estelmann, Prof. Dr. R. Spiller

Fremdsprachenausbildung:

S. Niepceron

Fachdidaktik:

Dr. G. Birken-Silverman